frontiers | Research Topics

Nanodomain regulation of muscle physiology and alterations in disease

Edited by
Niall Macquaide, Nina D. Ullrich, William E. Louch
and Manuel F. Navedo

Published in
Frontiers in Physiology

ISSN 1664-8714
ISBN 978-2-83251-026-1
DOI 10.3389/978-2-83251-026-1

About Frontiers

Frontiers is more than just an open access publisher of scholarly articles: it is a pioneering approach to the world of academia, radically improving the way scholarly research is managed. The grand vision of Frontiers is a world where all people have an equal opportunity to seek, share and generate knowledge. Frontiers provides immediate and permanent online open access to all its publications, but this alone is not enough to realize our grand goals.

Frontiers journal series

The Frontiers journal series is a multi-tier and interdisciplinary set of open-access, online journals, promising a paradigm shift from the current review, selection and dissemination processes in academic publishing. All Frontiers journals are driven by researchers for researchers; therefore, they constitute a service to the scholarly community. At the same time, the *Frontiers journal series* operates on a revolutionary invention, the tiered publishing system, initially addressing specific communities of scholars, and gradually climbing up to broader public understanding, thus serving the interests of the lay society, too.

Dedication to quality

Each Frontiers article is a landmark of the highest quality, thanks to genuinely collaborative interactions between authors and review editors, who include some of the world's best academicians. Research must be certified by peers before entering a stream of knowledge that may eventually reach the public - and shape society; therefore, Frontiers only applies the most rigorous and unbiased reviews. Frontiers revolutionizes research publishing by freely delivering the most outstanding research, evaluated with no bias from both the academic and social point of view. By applying the most advanced information technologies, Frontiers is catapulting scholarly publishing into a new generation.

What are Frontiers Research Topics?

Frontiers Research Topics are very popular trademarks of the *Frontiers journals series*: they are collections of at least ten articles, all centered on a particular subject. With their unique mix of varied contributions from Original Research to Review Articles, Frontiers Research Topics unify the most influential researchers, the latest key findings and historical advances in a hot research area.

Find out more on how to host your own Frontiers Research Topic or contribute to one as an author by contacting the Frontiers editorial office: frontiersin.org/about/contact

Nanodomain regulation of muscle physiology and alterations in disease

Topic editors

Niall Macquaide — Glasgow Caledonian University, United Kingdom
Nina D. Ullrich — Heidelberg University, Germany
William E. Louch — University of Oslo, Norway
Manuel F. Navedo — University of California, Davis, United States

Citation

Macquaide, N., Ullrich, N. D., Louch, W. E., Navedo, M. F., eds. (2022). *Nanodomain regulation of muscle physiology and alterations in disease*.
Lausanne: Frontiers Media SA. doi: 10.3389/978-2-83251-026-1

Table of contents

frontiers | Frontiers in Physiology

TYPE Editorial
PUBLISHED 29 November 2022
DOI 10.3389/fphys.2022.1092304

OPEN ACCESS

EDITED AND REVIEWED BY
Ruben Coronel,
University of Amsterdam, Netherlands

*CORRESPONDENCE
Niall Macquaide,
Niall.Macquaide@gcu.ac.uk

SPECIALTY SECTION
This article was submitted to Cardiac Electrophysiology,
a section of the journal
Frontiers in Physiology

RECEIVED 07 November 2022
ACCEPTED 10 November 2022
PUBLISHED 29 November 2022

CITATION
Louch WE, Ullrich ND, Navedo MF and Macquaide N (2022), Editorial: Nanodomain regulation of muscle physiology and alterations in disease.
Front. Physiol. 13:1092304.
doi: 10.3389/fphys.2022.1092304

Editorial: Nanodomain regulation of muscle physiology and alterations in disease

William E Louch[1,2], Nina D Ullrich[3,4], Manuel F Navedo[5] and Niall Macquaide[6]*

[1]Institute for Experimental Medical Research, Oslo University Hospital, University of Oslo, Oslo, Norway, [2]K. G. Jebsen Center for Cardiac Research, University of Oslo, Oslo, Norway, [3]Institute of Physiology and Pathophysiology, Division of Cardiovascular Physiology, Heidelberg University, Heidelberg, Germany, [4]DZHK (German Center for Cardiovascular Research), Partner Site Heidelberg/Mannheim, Heidelberg University, Heidelberg, Germany, [5]Department of Pharmacology, School of Medicine, University of California, Davis, CA, United States, [6]School of Health and Life Sciences, Glasgow Caledonian University, Glasgow, United Kingdom

KEYWORDS

cardiac, smooth muscle (physiology), excitation-contraction (E-C) coupling, electrophyiology, calcium, phosphorylation, ryanodine receptor (RyR), CaV1.2 Ca channels 2+

Editorial on the Research Topic
Nanodomain Regulation of Muscle Physiology and Alterations in Disease

Introduction

Cardiac, skeletal and smooth muscle are vastly different in their function and structure. However, in all three types of muscle, calcium ions (Ca^{2+}) serve as the primary second messenger controlling contraction, and this function is modulated by the autonomic nervous system. Disruption of Ca^{2+} signalling and muscle function are evident in pathologies linked to both inherited and acquired conditions, including hypertension, diabetes, muscular dystrophy, and heart disease. Evidence has shown that remodelling of Ca^{2+} signalling nanodomains, as well as other signalling cascades, contribute to these pathological changes. However, our understanding of these mechanisms remains in its infancy. More information is needed to further our comprehension of nanoscale cellular physiology and develop treatments to counteract the changes that occur in disease. This Research Topic has collected 11 high-quality papers from authors focusing on nanodomains and alterations in disease.

The dyadic space

Early electron microscopy (EM) measurements described the existence of a ~12–15 nm gap between the sarcolemmal (SL) and sarcoplasmic reticulum (SR) membrane in cardiac and skeletal myocytes called the dyad or triad, respectively (Page and Niedergerke, 1972; Franzini-Armstrong et al., 1999). In healthy ventricular myocytes, most of the estimated ~20,000 clusters of Ca^{2+} release channels (Ryanodine Receptors, RyRs) are coupled to invaginations of the membrane called transverse(t)-tubules. A sparser network of t-tubules has been observed in atrial myocytes.

Dyadic remodelling in heart failure

The dyadic space is maintained by junctophilin-2 (JPH2), which spans both SR and SL membranes, and maintains the two membranes in functional dyads. Remodelling of the cardiac dyad has been observed in a host of animal models of heart disease (Heinzel et al., 2002; Quinn et al., 2003; Louch et al., 2004; Song et al., 2006; du Sert et al., 2020) with a loss or remodelling, resulting in an increase in non-coupled (Dries et al., 2013) or orphaned (Song et al., 2006) RyR clusters. Non-coupled RyRs rely on diffusion to trigger Ca^{2+} release resulting in reduced efficiency of Ca^{2+} release. New evidence on nanoscale organisation on JPH2 by Hou et al. shows remodelling of the t-tubule with an increased thickening into branched t-tubule structures called T-sheets, similar to those seen in patient samples observed in block section EM (Pinali et al., 2013), but with no evidence of reduced JPH2 expression. Smaller RyR clusters and reduced RyR expression were also observed, which may contribute to reduced E-C coupling efficiency in heart failure (Beuckelmann et al., 1992; Gómez et al., 2001).

A lack of consensus on correlations of JPH2 expression with t-tubule morphology shows that more work is needed to fully understand the role of this protein in t-tubule sustainment. Indeed, amphiphysin-II (Bin1) is recognised as being an important structural modulator of t-tubule formation and maintenance. Zhou et al. showed the importance of phosphatidylinositol-4,5-bisphosphate (PIP_2) in this process. Depletion of PIP_2 caused a loss of t-tubules and a reduction of E-C coupling. New therapies targeting these processes could reverse changes in heart disease.

One observation that does show consistency is the loss of t-tubules in heart failure with reduced ejection fraction. Increasing evidence demonstrates that this subcellular remodelling results in a larger percentage of uncoupled RyRs, with subsequent loss of Ca^{2+} synchrony (Louch et al., 2006). Further ramifications of this form of remodelling are observed through altered regulation of orphaned RyR clusters by kinases and reactive oxygen species (ROS) (Dries et al., 2013; Dries et al., 2018). Indeed, in this issue, Belevych et al. show that detubulated myocytes have a reduced response to sympathetic stimulation upon cholinergic activity. This is the first report of this type of regulation; further work could shed light on a new cholinergic-sympathetic signalling nexus in the ventricular myocyte.

The remodelling of RyR clusters themselves has been reported in cardiac pathologies including heart failure (Kolstad et al., 2018) and atrial fibrillation (Macquaide et al., 2015). Indeed, new imaging information shows altered nanoscale orientation of neighbouring RyRs during acute phosphorylation (Asghari et al., 2020), while chronic phosphorylation during chronic β-adrenergic stimulation leads to RyR dispersion (Shen et al., 2022). These observations have ramifications for heart failure, where chronic β-adrenergic stimulation and CaMKII activation are well described (Swaminathan et al., 2012). Interestingly, similar remodelling of RyRs was observed in the cerebral microvasculature in Duchenne muscular dystrophy (Pritchard et al., 2018). While Bin1 has been implicated in the recruitment of phosphorylated RyRs to the t-tubules during acute β-adrenergic stimulation (Fu et al., 2016), it is unclear whether this protein plays a role in the dispersion of RyRs during longer-term stimulation.

Similar detail is beginning to emerge regarding the plasticity of modular arrangement on the other side of the dyad; i.e., the positioning of L-type Ca^{2+} channels. Clusters of these channels have been reported to increase by 20% in size upon β-adrenergic stimulation (del Villar et al., 2021), resulting in increased inter-channel cooperativity in these "superclusters." These exciting data appear to recapitulate findings from human disease, where increased channel activity and density are observed in human dilated cardiomyopathy patients. This remodelling may be linked to increased CaMKII expression and activity during heart failure (Anderson et al., 2011). Interestingly, Bin1 has also been implicated in the organisation of the L-type Ca^{2+} channel in t-tubules (Hong et al., 2012), although the role of phosphorylation in this process has not been investigated.

Na^+ gradients in the dyad

The importance of dyadic Na^+ ion concentration is highlighted in the review by Skogestad and Aronsen who explore the subcellular localisation and function of the sodium-potassium-ATPase (NKA) in cardiomyocytes. Specifically, they review data indicating that the presence of the alpha-2 isoform (NKAα2) in the dyad vs. NKAα1 outside the dyad may set up subcellular Na^+ and Ca^{2+} gradients within the myocyte; findings which have implications for the role of NKAα2 in triggering cardiac hypertrophy and arrhythmia. These processes may be important to set the scene for further dyadic remodelling that occurs in disease and may augment the increased NCX activity that is often observed.

Ageing effects on cAMP microdomains

In the sinoatrial node, pacemaker cells utilise L-type Ca^{2+} signalling as part of the Ca^{2+} clock mechanism, which regulates heart rate. Choi et al. have presented elegant work to correlate nanostructural alterations in aged mice, which leads to declining β-adrenergic responsiveness. It appears that fewer β-adrenenergic receptors colocalise with L-type Ca^{2+} channels in ageing myocytes, with possible roles for caveolin-3 and AKAP150. This observation highlights that the location of both inside caveolae nanosignalling domains is of utmost importance for their effective interaction.

New insights from computational modelling and superresolution imaging

In the current Research Topic, the nanoscale structures of ion channel clusters, including RyR and L-type Ca^{2+} channel clusters, are elegantly reviewed by Dixon, with a presented relevance to disease and physiological β-adrenergic agonism. Interesting future directions are highlighted, leveraging new super-resolution imaging methods. Indeed, these new imaging technologies have yielded unprecedented levels of structural detail informing present and future modelling endeavours, as reviewed by Louch et al.

Here, new paradigms with high spatial detail are explored with ramifications in disease. The scale of modelling from sub-sarcomere to whole organ is explored in the review by Colman et al. This article highlights the utility and perils of spatial computational modelling in interpreting and scaling up this cellular information to a full organ model with realistic anatomy. The paper by Iaparov et al. is an original model incorporating coupled gating of realistic-sized RyR clusters to explore how Mg^{2+} affects the sensitivity of RyR and how this affects Ca^{2+} release events. This work may provide new information on how drugs requiring Mg^{2+} for their action can be better understood and to produce more realistic models of RyR cluster behaviour.

Neurohormonal inputs influence muscle nanodomains

A number of our submissions discuss the consequences of sympathetic activity of RyR and L-type Ca^{2+} channel clusters and activity. In Franzoso et al., the role of localised neurotransmitter release from sympathetic nerves is explored in the context of a neuro-cardiac junction akin to the neuro-muscular junction in skeletal muscle. These nerves appear to be very densely distributed, effectively innervating single myocytes, with some myocytes receiving multiple inputs. Ramifications for disease are discussed, introducing interesting new paradigms of localised hyper-adrenergic activation increasing cellular cAMP acting as a trigger for arrhythmic Ca^{2+} release.

Another form of cardiovascular neurohormonal activation is discussed in Salazar-Enciso et al. , where new research shows that upregulation of Ca^{2+} signalling channels and pumps ($Ca_v1.2$ and SERCA2) occurs in the plasmalemmal-SR nanodomain in the vascular smooth muscle of mesenteric arteries in response to aldosterone signalling. This increase in SERCA expression importantly occurs in concert with an increased $Ca_v1.2$ expression, to modulate Ca^{2+} cycling and prevent vasoconstriction and enhance vasorelaxation.

Summary

In conclusion, the scientific work presented in this Research Topic has provided intriguing new insight into structure-function relationships within nanosignalling domains. This understanding is expected to provide new avenues for research in cardiovascular disease to facilitate novel, targeted approaches. Indeed, the increasing array of druggable targets offers new hope for tackling complex cardiovascular disease phenotypes. Nevertheless, given the analogies described here, caution must be taken, and an integrative approach should be considered when coordinating the effects of these drugs across multiple organ systems.

Author contributions

NM wrote the first draft of the manuscript. NM, WL, MN, and NU wrote sections of the manuscript. All authors contributed to the manuscript revision, read, and approved the submitted version.

Conflict of interest

The authors declare that the research was conducted in the absence of any commercial or financial relationships that could be construed as a potential conflict of interest.

Publisher's note

References

Anderson, M. E., Brown, J. H., and Bers, D. M. (2011). CaMKII in myocardial hypertrophy and heart failure. *J. Mol. Cell. Cardiol.* 51, 468–473. doi:10.1016/j.yjmcc.2011.01.012

Asghari, P., Scriven, D. R. L., Ng, M., Panwar, P., Chou, K. C., van Petegem, F., et al. (2020). Cardiac ryanodine receptor distribution is dynamic and changed by auxiliary proteins and post-translational modification. *Elife* 9, 51602. doi:10.7554/eLife.51602

Beuckelmann, D. J., Näbauer, M., and Erdmann, E. (1992). Intracellular calcium handling in isolated ventricular myocytes from patients with terminal heart failure. *Circulation* 85, 1046–1055. doi:10.1161/01.CIR.85.3.1046

del Villar, S. G., Voelker, T. L., Westhoff, M., Reddy, G. R., Spooner, H. C., Navedo, M. F., et al. (2021). β-Adrenergic control of sarcolemmal CaV1.2 abundance by small GTPase Rab proteins. *Proc. Natl. Acad. Sci. U. S. A.* 118, e2017937118. doi:10.1073/pnas.2017937118

Dries, E., Bito, V., Lenaerts, I., Antoons, G., Sipido, K. R., and Macquaide, N. (2013). Selective modulation of coupled ryanodine receptors during microdomain activation of calcium/calmodulin-dependent kinase II in the dyadic cleft. *Circ. Res.* 113, 1242–1252. doi:10.1161/CIRCRESAHA.113.301896

Dries, E., Santiago, D. J., Gilbert, G., Lenaerts, I., Vandenberk, B., Nagaraju, C. K., et al. (2018). Hyperactive ryanodine receptors in human heart failure and ischaemic cardiomyopathy reside outside of couplons. *Cardiovasc. Res.* 114, 1512–1524. doi:10.1093/cvr/cvy088

du Sert, N. P., Ahluwalia, A., Alam, S., Avey, M. T., Baker, M., Browne, W. J., et al. (2020). Reporting animal research: Explanation and elaboration for the arrive guidelines 2.0. *PLoS Biol.* 18, e3000411. doi:10.1371/journal.pbio.3000411

Franzini-Armstrong, C., Protasi, F., and Ramesh, V. (1999). Shape, size, and distribution of Ca2+ release units and couplons in skeletal and cardiac muscles. *Biophys. J.* 77, 1528–1539. doi:10.1016/S0006-3495(99)77000-1

Fu, Y., Shaw, S., Naami, R., Vuong, C., Basheer, W. A., Guo, X., et al. (2016). Isoproterenol promotes rapid ryanodine receptor movement to bridging integrator 1 (BIN1)-organized dyads. *Circulation* 115, 388–397. doi:10.1161/CIRCULATIONAHA.115.018535

Gómez, A. M., Guatimosim, S., Dilly, K. W., Vassort, G., and Lederer, W. j. (2001). Heart failure after myocardial infarction: Altered excitation-contraction coupling. *Circulation* 104, 688–693. doi:10.1161/HC3201.092285

Heinzel, F. R., Bito, V., Volders, P. G. A., Antoons, G., Mubagwa, K., and Sipido, K. R. (2002). Spatial and temporal inhomogeneities during Ca2+ release from the sarcoplasmic reticulum in pig ventricular myocytes. *Circ. Res.* 91, 1023–1030. doi:10.1161/01.RES.0000045940.67060.dd

Hong, T. T., Smyth, J. W., Chu, K. Y., Vogan, J. M., Fong, T. S., Jensen, B. C., et al. (2012). BIN1 is reduced and Cav1.2 trafficking is impaired in human failing cardiomyocytes. *Heart rhythm.* 9, 812–820. doi:10.1016/j.hrthm.2011.11.055

Kolstad, T. R., van den Brink, J., MacQuaide, N., Lunde, P. K., Frisk, M., Aronsen, J. M., et al. (2018). Ryanodine receptor dispersion disrupts Ca 2+ release in failing cardiac myocytes. *Elife* 7, e39427. doi:10.7554/eLife.39427

Louch, W. E., Bito, V., Heinzel, F. R., Macianskiene, R., Vanhaecke, J., Flameng, W., et al. (2004). Reduced synchrony of Ca2+ release with loss of T-tubules - a comparison to Ca2+ release in human failing cardiomyocytes. *Cardiovasc. Res.* 62, 63–73. doi:10.1016/j.cardiores.2003.12.031

Louch, W. E., Mørk, H. K., Sexton, J., Strømme, T. A., Laake, P., Sjaastad, I., et al. (2006). T-tubule disorganization and reduced synchrony of Ca2+ release in murine cardiomyocytes following myocardial infarction. *J. Physiol.* 574, 519–533. doi:10.1113/JPHYSIOL.2006.107227

Macquaide, N., Tuan, H. T. M., Hotta, J.-I., Sempels, W., Lenaerts, I., Holemans, P., et al. (2015). Ryanodine receptor cluster fragmentation and redistribution in persistent atrial fibrillation enhance calcium release. *Cardiovasc. Res.* 108, 387–398. doi:10.1093/cvr/cvv231

Page, S. G., and Niedergerke, R. (1972). Structures of physiological interest in the frog heart ventricle. *J. Cell Sci.* 11, 179–203. doi:10.1242/JCS.11.1.179

Pinali, C., Bennett, H., Davenport, J. B., Trafford, A. W., and Kitmitto, A. (2013). Three-dimensional reconstruction of cardiac sarcoplasmic reticulum reveals a continuous network linking transverse-tubules: This organization is perturbed in heart failure. *Circ. Res.* 113, 1219–1230. doi:10.1161/CIRCRESAHA.113.301348

Pritchard, H. A. T., Pires, P. W., Yamasaki, E., Thakore, P., and Earley, S. (2018). Nanoscale remodeling of ryanodine receptor cluster size underlies cerebral microvascular dysfunction in Duchenne muscular dystrophy. *Proc. Natl. Acad. Sci. U. S. A.* 115, E9745–E9752. doi:10.1073/pnas.1804593115

Quinn, F. R., Currie, S., Duncan, A. M., Miller, S., Sayeed, R., Cobbe, S. M., et al. (2003). Myocardial infarction causes increased expression but decreased activity of the myocardial Na+-Ca2+ exchanger in the rabbit. *J. Physiol.* 553, 229–242. doi:10.1113/jphysiol.2003.050716

Shen, X., van den Brink, J., Bergan-Dahl, A., Kolstad, T. R., Norden, E. S., Hou, Y., et al. (2022). Prolonged β-adrenergic stimulation disperses ryanodine receptor clusters in cardiomyocytes and has implications for heart failure. *Elife* 11, e77725. doi:10.7554/eLife.77725

Song, L. S., Sobie, E. A., McCulle, S., Lederer, W. J., Balke, C. W., and Cheng, H. (2006). Orphaned ryanodine receptors in the failing heart. *Proc. Natl. Acad. Sci. U. S. A.* 103, 4305–4310. doi:10.1073/pnas.0509324103

Swaminathan, P. D., Purohit, A., Hund, T. J., and Anderson, M. E. (2012). Calmodulin-dependent protein kinase II: Linking heart failure and arrhythmias. *Circ. Res.* 110, 1661–1677. doi:10.1161/CIRCRESAHA.111.243956

Zhou, J., Singh, N., Monnier, C., Marszalec, W., Gao, L., Jin, J., et al. (2012). Phosphatidylinositol-4,5-Bisphosphate Binding to Amphiphysin-II Modulates T-Tubule Remodeling: Implications for Heart Failure. *Front. Physiol.* 12, 2271. doi:10.3389/FPHYS.2021.782767

frontiers in Physiology

ORIGINAL RESEARCH
published: 26 August 2021
doi: 10.3389/fphys.2021.725798

Acute Detubulation of Ventricular Myocytes Amplifies the Inhibitory Effect of Cholinergic Agonist on Intracellular Ca^{2+} Transients

***Andriy E. Belevych*[1,2]*, *Vladimir Bogdanov*[1,2], *Dmitry A. Terentyev*[1,2] and *Sandor Gyorke*[1,2]**

[1] Department of Physiology and Cell Biology, The Ohio State University, Columbus, OH, United States, [2] Davis Heart and Lung Research Institute, The Ohio State University Wexner Medical Center, Columbus, OH, United States

OPEN ACCESS

Edited by:
Manuel F. Navedo,
University of California, Davis,
United States

Reviewed by:
Caoimhin Griffin,
University of Nevada, Reno,
United States
Leighton Izu,
University of California, Davis,
United States
Timothy Domeier,
University of Missouri, United States
Elena N. Dedkova,
University of California, Davis,
United States

****Correspondence:***
Andriy E. Belevych
Andriy.Belevych@osumc.edu

Specialty section:
This article was submitted to
Cardiac Electrophysiology,
a section of the journal
Frontiers in Physiology

Received: *15 June 2021*
Accepted: *02 August 2021*
Published: *26 August 2021*

Citation:
Belevych AE, Bogdanov V,
Terentyev DA and Gyorke S (2021)
Acute Detubulation of Ventricular
Myocytes Amplifies the Inhibitory
Effect of Cholinergic Agonist on
Intracellular Ca^{2+} Transients.
Front. Physiol. 12:725798.
doi: 10.3389/fphys.2021.725798

Muscarinic receptors expressed in cardiac myocytes play a critical role in the regulation of heart function by the parasympathetic nervous system. How the structural organization of cardiac myocytes affects the regulation of Ca^{2+} handling by muscarinic receptors is not well-defined. Using confocal Ca^{2+} imaging, patch-clamp techniques, and immunocytochemistry, the relationship between t-tubule density and cholinergic regulation of intracellular Ca^{2+} in normal murine ventricular myocytes and myocytes with acute disruption of the t-tubule system caused by formamide treatment was studied. The inhibitory effect of muscarinic receptor agonist carbachol (CCh, 10 μM) on the amplitude of Ca^{2+} transients, evoked by field-stimulation in the presence of 100 nM isoproterenol (Iso), a β-adrenergic agonist, was directly proportional to the level of myocyte detubulation. The timing of the maximal rate of fluorescence increase of fluo-4, a Ca^{2+}-sensitive dye, was used to classify image pixels into the regions functionally coupled or uncoupled to the sarcolemmal Ca^{2+} influx (I_{Ca}). CCh decreased the fraction of coupled regions and suppressed Ca^{2+} propagation from sarcolemma inside the cell. Formamide treatment reduced I_{Ca} density and decreased sarcoplasmic reticulum (SR) Ca^{2+} content. CCh did not change SR Ca^{2+} content in Iso-stimulated control and formamide-treated myocytes. CCh inhibited peak I_{Ca} recorded in the presence of Iso by ~20% in both the control and detubulated myocytes. Reducing I_{Ca} amplitude up to 40% by changing the voltage step levels from 0 to –25 mV decreased Ca^{2+} transients in formamide-treated but not in control myocytes in the presence of Iso. CCh inhibited CaMKII activity, whereas CaMKII inhibition with KN93 mimicked the effect of CCh on Ca^{2+} transients in formamide-treated myocytes. It was concluded that the downregulation of t-tubules coupled with the diminished efficiency of excitation–contraction coupling, increases the sensitivity of Ca^{2+} release and propagation to muscarinic receptor-mediated inhibition of both I_{Ca} and CaMKII activity.

Keywords: excitation-contraction coupling, t-tubule, muscarinic receptor agonist, calcium microdomains, ventricular myocyte

INTRODUCTION

The autonomic nervous system exerts its effects on the mechanical and electrical activity of the heart in part *via* β-adrenergic and muscarinic receptors expressed in ventricular myocytes. β-Adrenergic receptors mediate stimulatory effects of the sympathetic nervous system *via* cAMP-dependent activation of Ca^{2+} handling proteins, such as the L-type Ca^{2+} channels, sarcoplasmic reticulum (SR) Ca^{2+} ATPase, and RyR2, SR Ca^{2+} release channels (Bers, 2001). Muscarinic receptors contribute to the inhibitory effects of the parasympathetic system mostly by antagonizing β-adrenergic responses (Löffelholz and Pappano, 1985; Harvey and Belevych, 2003). In cardiac diseases, such as heart failure, the abnormal autonomic regulation of cardiac function is usually accompanied by the structural remodeling of the heart that at the cellular level is often associated with downregulation of the t-tubule system (Guo et al., 2013; Poláková and Sobie, 2013). T-tubules, branched invaginations of sarcolemma occurring at the Z-lines in ventricular myocytes, provide critical support for excitation–contraction coupling (ECC) by aligning the sarcolemmal Ca^{2+} influx channels (L-type) with the SR Ca^{2+} release channels (RyR2s) (Brette and Orchard, 2003). The juxtaposition of t-tubule and SR membranes creates a unique dyadic microdomain, characterized by high Ca^{2+} fluxes and distinct patterns of Ca^{2+}-dependent signaling (Bers, 2001; Brette and Orchard, 2003; Jones et al., 2018). Accordingly, RyR2 coupled to t-tubules and those that are not associated with the dyadic domain (uncoupled) display different functional properties (Biesmans et al., 2011; Dries et al., 2013; Belevych et al., 2017). Growing evidence suggests that β-adrenergic receptors differentially regulate the L-type and RyR2 Ca^{2+} channels in dyadic vs. extra-dyadic compartments (Nikolaev et al., 2010; Dries et al., 2016; Belevych et al., 2017). However, little is known about the role of t-tubules in muscarinic receptor–mediated regulation of intracellular Ca^{2+} handling in ventricular myocytes.

In the present study, the mechanisms underlying the regulation of ECC by muscarinic receptor stimulation in the setting of acute t-tubule disruption were addressed. Using formamide treatment, a well-characterized approach to detubulate ventricular myocytes, it was found that the downregulation of t-tubules amplifies the inhibitory effects of muscarinic receptor stimulation on ECC. Mechanistically, this effect was attributed to the increased sensitivity of ECC to muscarinic receptor-mediated effects, inhibition of the L-type Ca^{2+} channels, and decrease in CaMKII-dependent activity of RyR2.

MATERIALS AND METHODS

Ventricular Myocyte Isolation

All animal procedures were approved by the Ohio State University Institutional Animal Care and Use Committee and conformed to the Guide for the Care and Use of Laboratory Animals published by the US National Institute of Health (NIH Publication No. 85-23, revised 2011). Ventricular myocytes were isolated from 2 to 6-month-old C57BL/6J mice (Jackson Laboratory Stock No: 000664) of either sex. Mice were anesthetized with 5% isoflurane in 95% oxygen, hearts were rapidly excised and cannulated through the aorta for perfusion with an ice-cold calcium-free solution containing (in mM): 140 NaCl, 5.4 KCl, 0.5 $MgCl_2$, 10 HEPES, and 5.5 glucose with pH 7.4. Using the Langendorff apparatus, hearts were perfused with the a Ca^{2+}-free solution at 37°C for 5 min that was followed by perfusion with a Ca^{2+}-free solution containing Liberase TH (0.24U; Roche). Following enzymatic digestion (10–20 min), hearts were minced and triturated in the perfusion solution containing 2% BSA. Following two rounds of gravity sedimentation, ventricular myocytes were plated on the laminin (40 μg/ml) and stored at room temperature (RT). Isolated cells were used for experiments within 6 h after isolation.

Ca^{2+} Imaging and Patch-Clamp Techniques

The cellular experiments were performed using an open bath imaging chamber (Warner Instruments, CT, United States) that was continuously perfused with an external solution containing the following (in mM): 140 NaCl, 5.4 KCl, 2.0 $CaCl_2$, 0.5 $MgCl_2$, 5.6 glucose, and 10 HEPES (pH 7.4). Myocytes were incubated in a low Ca^{2+} external solution (0.5 mM $CaCl_2$) containing 9 μM Fluo-4 AM (Thermo Fisher Scientific, MA, United States) for 20 min at RT. Following 15–20 min of de-esterification in the dye-free external solution, intracellular Ca^{2+} transients were induced by electrical field stimulation (SD9 stimulator, Grass Technologies/Astro-Med Inc., RI, United States) using a pair of platinum electrodes. The following extracellular solution was used for the field-stimulation experiments (mM): 140 NaCl, 5.4 KCl, 2.0 $CaCl_2$, 0.5 $MgCl_2$, 10 HEPES, and 5.6 glucose (pH 7.4).

In experiments directed to study the regulation of the L-type Ca^{2+} channels by muscarinic receptor agonist, Ca^{2+} currents were recorded in the extracellular solution containing 1 mM $CaCl_2$ and 5.4 mM CsCl replacing KCl. Patch pipettes were filled with a solution that contained in mM: 123 CsCl, 20 TEACl, 5 MgATP, 10 NaCl, 1 $MgCl_2$, 0.1 Tris GTP, 5 EGTA, and 10 HEPES (pH 7.2). Whole-cell patch-clamp configuration was established using an Axopatch 200B amplifier coupled to Digidata1440 data acquisition system (Axon Instruments Inc./Molecular Devices, CA, United States). In these experiments, the Ca^{2+} currents were evoked by 100 ms depolarization steps to 0 mV every 10 s. The depolarization steps were preceded by a 100 ms step from −80 to −50 mV to inactivate Na^+ currents.

Imaging of the intracellular Ca^{2+} transients was performed using Olympus FluoView FV 1000 (Olympus America Inc., PA, United States) confocal microscope system equipped with x60 oil-immersion objective lens (NA 1.4). Fluo-4 was excited with a 488 nm line of argon laser, and the signal was collected at 500–600 nm wavelengths. Linescan images were acquired along the central axis of the myocytes at a speed of 2.1 ms per line. Fluorescence signals were normalized to the baseline cellular fluorescence (F_0).

To record Ca^{2+} currents simultaneously with the intracellular Ca^{2+} transients, the extracellular solution containing 1 mM

$CaCl_2$ was used and in the patch pipette solution, 5 mM EGTA was replaced with 0.1 mM fluo-3 K_5 (ThermoFisher Scientific, MA, United States). In these experiments, the following voltage protocol was used: 100 ms voltage ramp was applied from the holding potential of −80 to −45 mV, at which level the voltage was kept for 500 ms followed by a 50 ms depolarization step to either −25, or −20, or 0 mV to induce the Ca^{2+} currents of different amplitude. The Ca^{2+} currents were evoked every 8 s. A train of 10 pulses from −80 to −10 mV was applied at 2 Hz to maintain steady SR Ca^{2+} loading before each Ca^{2+} current-inducing voltage protocol.

The SR Ca^{2+} content was assessed by the rapid application of an extracellular solution containing 5 mM caffeine and 20 mM 2,3-butanedione monoxime, as previously described (Kashimura et al., 2010). All recordings were made at RT.

Detubulation of the myocytes was induced following 15 min incubation in the low-Ca^{2+} external solution containing 1.5 M formamide (Brette et al., 2002). T-tubules were labeled with 3.3 μg/ml of di4-AN(F)EPPTEA at RT for 5–10 min.

Immunocytochemistry

Plated on laminin cardiomyocytes were incubated for 10 min in the external solution containing either isoproterenol (Iso, 100 nM), or Iso (100 nM) plus carbachol (CCh) (10 μM), or Iso (100 nM) plus KN93 (2 μM). Myocytes were electrically stimulated for 1 min at 2 Hz and 1 min at 1 Hz. Following stimulation protocol, cells were immediately fixed with 4% paraformaldehyde (10 min at RT) and washed with phosphate-buffered saline (PBS, 3 × 10 min at RT). Fixed myocytes were permeabilized with 0.25% Triton X-100 in PBS (15 min, RT) and incubated in blocking solution (BlockAid^{TM} Blocking Solution, Thermo Fisher Scientific, MA, United States) for 60 min at RT. Following overnight incubation at 4°C in the blocking solution containing primary antibody (1:150 dilution, anti-CaMKII (phospho T286) antibody, ab32678, Abcam, Cambridge, United Kingdom) and several rounds of PBS washes, myocytes were incubated in the blocking solution containing secondary antibody (1:500 dilution, goat anti-rabbit IgG [H + L], Invitrogen) for 90 min at RT. After 3 × 5 min of PBS washes, the samples were mounted using ProLong^{TM} Gold Antifade Mountant (Thermo Fisher Scientific, MA, United States). Images were acquired using an Olympus FluoView FV 1000 (Olympus America Inc., PA, United States) confocal microscope system equipped with a ×60 oil-immersion objective lens (NA 1.4). Following subtraction of the non-cellular background signal, average fluorescence, excluding nuclear area, was calculated for each myocyte and normalized to the value of mean fluorescence value obtained from a group of myocytes incubated in 100 nM Iso.

Image Analysis

The activation time of Ca^{2+} release during the electrical stimulation was used to assess the proximity to the sarcolemma (Dries et al., 2013, 2016; Belevych et al., 2017). Time to the peak of fluorescence derivative (dF/dt) during the rising phase of Ca^{2+} transients was calculated for each pixel. The obtained distribution of time to $(dF/dt)_{max}$ was used to classify pixels into "early" and "delayed," as described in the "Results" section. T-tubule density was analyzed according to Wagner et al. (2014).

Statistical Analysis

Images were analyzed using MATLAB (2017b, The MathWorks, Inc., MA, United States) and ImageJ (Rasband, W.S., ImageJ, US National Institutes of Health, Bethesda, Maryland, United States[1], 1997–2018) software. Aggregate data were analyzed using the R software environment (The R Project for Statistical Computing[2]) and OriginPro 2020b (OriginLab Corp, MA, United States). Results are expressed as the mean ± SEM. Statistical significance was determined using either ANOVA with Tukey's *post hoc* test or Student's *t*-test with *p*-values of 0.05. Linear fits to the data were compared using the *F* test.

Reagents

All materials were obtained from Sigma-Aldrich (St. Louis, MI, United States) unless specified otherwise.

RESULTS

Effect of Muscarinic Receptor Stimulation on Intracellular Ca^{2+} Transients in Control and Detubulated Ventricular Myocytes

We studied the effects of the muscarinic receptor agonist, CCh, on Ca^{2+} transients evoked by 1 Hz electrical field stimulation in ventricular myocytes isolated from WT mouse heart. In ventricular myocytes, the effect of muscarinic receptor stimulation is generally attributed to the modulation of cAMP-dependent responses coupled to β-adrenergic receptor stimulation (Löffelholz and Pappano, 1985; Endoh, 1999; Harvey and Belevych, 2003). Indeed, in the absence of β-adrenergic receptor stimulation, CCh (10 μM) did not affect the properties of Ca^{2+} transients (**Figure 1**). However, in the presence of 3–10 nM isoproterenol (Iso), a β-adrenergic receptor agonist, CCh inhibited the amplitude and decay rate of Ca^{2+} transients by 25–30% (**Figure 1**). The inhibitory effects of CCh on Ca^{2+} transients were not observed in the presence of 30–100 nM Iso in control ventricular myocytes (**Figure 1** and **Supplementary Table 1**).

In cardiac myocytes, deep invaginations of the sarcolemma, known as t-tubules, have a significant impact on the regulation of intracellular Ca^{2+} handling (Brette and Orchard, 2003). To test whether the regulation of Ca^{2+} handling by muscarinic receptors in ventricular myocytes depends on the spatial organization of t-tubules, the effects of CCh in myocytes with reduced t-tubule density resulting from formamide treatment were studied (Brette et al., 2002). As shown in **Figures 2A–C**, formamide treatment reduced t-tubules density in the ventricular myocytes by ∼70%. The formamide-treated myocytes, CCh (10 μM) inhibited the amplitude of Ca^{2+} transients in the presence of 3, 10, and 30 nM Iso, and slowed Ca^{2+} transient decay in the

---

[1] https://imagej.nih.gov/ij/

[2] https://www.r-project.org

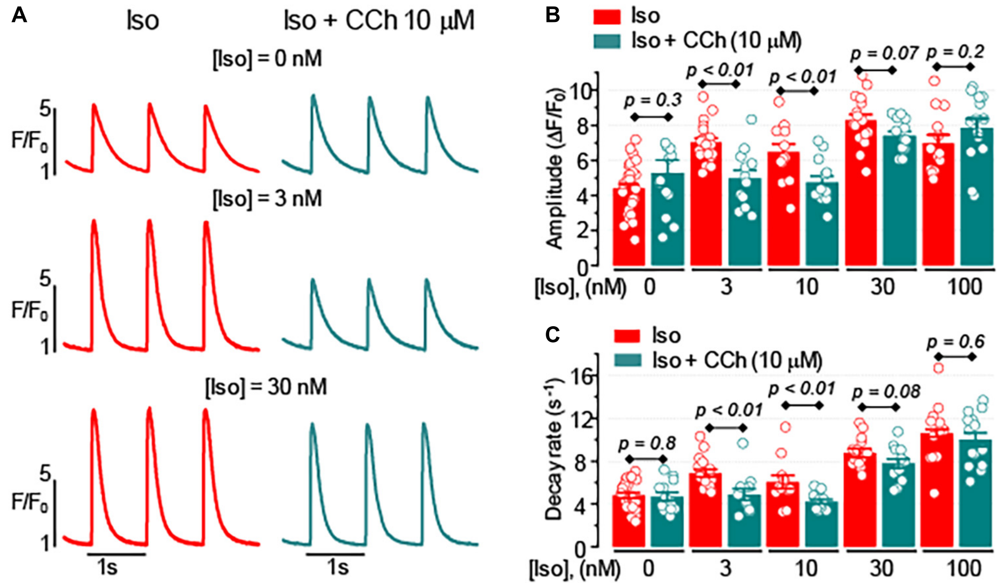

FIGURE 1 | The effect of muscarinic receptor stimulation on cytoplasmic Ca^{2+} transients depends on the level of β-adrenergic receptor stimulation. **(A)** Representative fluorescence profiles obtained from the line-scan images recorded in mouse ventricular myocytes electrically stimulated at 1 Hz in the presence of isoproterenol (Iso) alone or the presence of Iso plus 10 μM carbachol (CCh). Bar graphs with individual data points illustrate the effect of 10 μM CCh on the amplitude **(B)** and the decay rate **(C)** of Ca^{2+} transients recorded in the presence of various concentrations of Iso.

presence of Iso at all concentrations studied (**Figures 2E,F** and **Supplementary Table 2**). Comparison of CCh-induced changes in Ca^{2+} transients in control vs. formamide-treated myocytes (**Figures 2G,H**) revealed that t-tubule downregulation was associated with the more pronounced inhibitory effect on CCh on the amplitude of Ca^{2+} transients recorded in the presence of 30 and 100 nM Iso.

The Relationship Between T-Tubule Density and CCh Effect on Ca^{2+} Transients in Ventricular Myocytes

The time delay between the electrical stimulus and activation of Ca^{2+} release has been previously used to characterize the proximity of Ca^{2+} release units to the sarcolemma (Dries et al., 2013, 2016; Belevych et al., 2017). We recorded Ca^{2+} transients induced by 1 Hz stimulation in the presence of Iso (100 nM) in control and formamide-treated myocytes and obtained time distribution of maximal rate of fluorescence increase $(dF/dt)_{max}$ for each line-scan pixel in each myocyte (**Figure 3**). As demonstrated in **Figures 3A,C**, in control myocytes, Ca^{2+} release was highly synchronous [$(dF/dt)_{max}$ for 98% of line-scan pixels occurred within 6.3 ms]. Formamide-treatment decreased the fraction of fast response regions (first 4.2 ms) by about 50% and significantly increased the fraction of regions displaying $(dF/dt)_{max}$ after 6.3 ms (**Figures 3B,C**). Assuming that the effects of formamide treatment on Ca^{2+} transients stem mostly from decreased t-tubule density (Brette et al., 2002), we classified regions displaying $(dF/dt)_{max}$ after 8.5 ms as "delayed," or uncoupled from the t-tubules, whereas line-scan pixels with $(dF/dt)_{max}$ occurring within first 4.2 ms were classified as "early," or coupled to t-tubule regions.

Following formamide treatment, the proportion of the delayed regions was on average 44% in myocytes treated with Iso alone and 42% in cells challenged with Iso plus CCh ($p = 0.8$). **Figures 4A,B** shows line-scan images of myocytes displaying a low and a high proportion of delayed Ca^{2+} release regions. As illustrated in **Figures 4A,C**, the proportion of the delayed regions did not significantly affect the amplitude of Ca^{2+} transients observed in the presence of 100 nM Iso. In contrast, peak Ca^{2+} transient recorded in the presence of Iso plus CCh inversely correlated with the proportion of the delayed regions (**Figures 4B,D**). Thus, the anti-adrenergic effect of muscarinic receptor stimulation on the amplitude of Ca^{2+} transients appears to be more pronounced with the increased level of detubulation of ventricular myocytes. Of note, the rate of Ca^{2+} transients decay did not correlate with the level of detubulation: in the presence of 100 nM Iso alone, the Pearson's correlation coefficient was −0.27 and the slope of the regression curve was not different from 0 ($p = 0.14$). In the presence of 100 nM Iso plus 10 μM CCh, the relationship between the rate of Ca^{2+} transients decay and detubulation levels was fitted to the linear curve with the correlation coefficient −0.05 and the slope that was not different from 0 ($p = 0.78$).

The analysis of site-specific regulation of Ca^{2+} signaling revealed that CCh did not significantly affect the relationship between Ca^{2+} release from the coupled regions and the level of myocyte detubulation (**Figure 4E**). In contrast, the propagation of Ca^{2+} signal from sarcolemma, measured as the ratio of $(dF/dt)_{max}$ recorded at the delayed regions to that recorded at the early regions, was significantly inhibited by the CCh

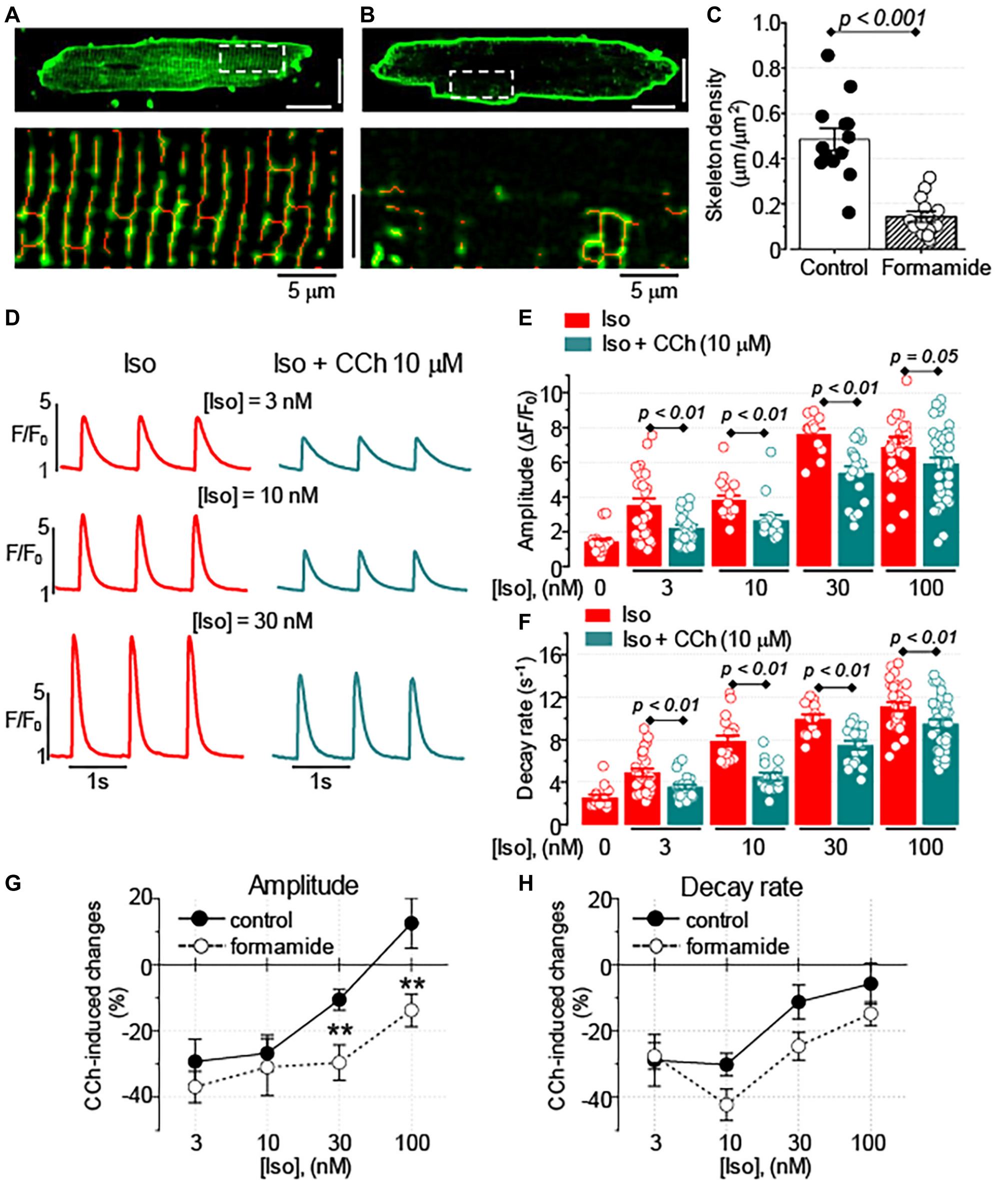

FIGURE 2 | Formamide treatment disrupts t-tubule organization and amplifies the inhibitory effect of CCh. Representative images of control **(A)** and formamide-treated **(B)** ventricular myocytes stained with membrane dye Di-4-AN(F)EPPTEA. Lower panels represent scaled-up regions indicated by white line rectangles and illustrate morphological skeletons of t-tubules (red lines). White scale bars are 20 μm. **(C)** Summary data along with the individual data points are shown for the density of t-tubules in control (n = 13) and formamide-treated (n = 13) ventricular myocytes, respectively. **(D)** Representative fluorescence profiles were obtained from the line-scan images recorded in formamide-treated ventricular myocytes electrically stimulated at 1 Hz in the presence of Iso alone or the presence of Iso plus 10 μM CCh. Bar graphs with individual data points illustrate the effect of 10 μM CCh on the amplitude **(E)** and the decay rate **(F)** of Ca^{2+} transients recorded in the presence of various concentrations of Iso in formamide-treated myocytes. CCh–induced changes in the amplitude **(G)** and the decay rate **(H)** of Ca^{2+} transients recorded in control and formamide-treated myocytes are plotted against the concentration of Iso. $^{**}p < 0.01$ (control *vs.* formamide).

(**Figure 4F**). It should be noted that the timing of Ca^{2+} release is affected not only by proximity to the sarcolemma but also by the functional properties of the sarcolemmal and SR Ca^{2+} channels (Zhou et al., 2009; Bryant et al., 2015). Therefore, we studied the effect of CCh on the timing of Ca^{2+} release by comparing the properties of Ca^{2+} transients recorded in the presence of Iso and Iso plus CCh in the same myocytes. First, we plotted the CCh-induced changes in the amplitude of Ca^{2+} transient vs. the fraction of delayed regions measured in the presence of Iso alone and confirmed that the inhibitory effect of CCh correlates with the level of myocyte detubulation (**Figure 4G**). Second, we found that CCh indeed produced a small (6%) but significant reduction of early regions and increased fraction of delayed regions by 8% (**Figure 4H**).

Taken together, these data suggest that downregulation of t-tubules in ventricular myocytes enhances the impact of

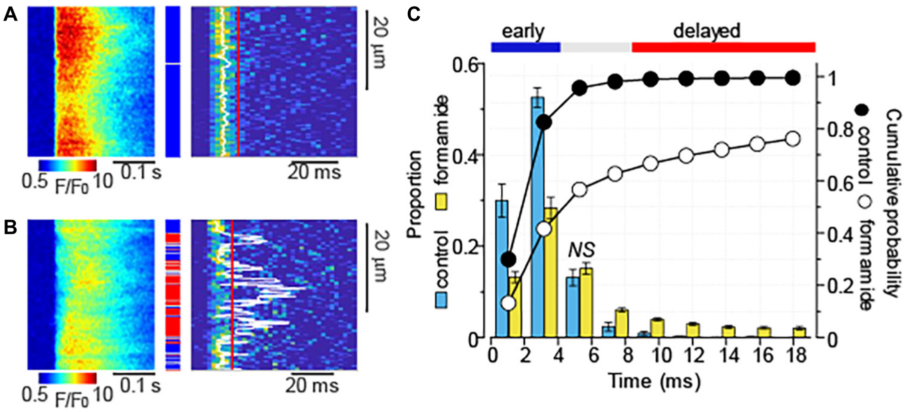

FIGURE 3 | Formamide treatment delays Ca^{2+} release activation. **(A,B)** Linescan images of fluo-4 fluorescence (left panels) and corresponding images illustrating the rate of fluorescence change (right panels) recorded in control **(A)** and formamide-treated **(B)** ventricular myocytes in the presence of Iso (100 nM). Ca^{2+} transients were induced by electrical field stimulation at 1 Hz. White lines indicate the maximal rate of fluorescence increase [$(dF/dt)_{max}$] that was calculated by averaging data from at least five consecutive Ca^{2+} transients. **(C)** Average time distribution of $(dF/dt)_{max}$ obtained from the line-scan images of control (n = 12) and formamide-treated (n = 33) myocytes. Time distribution in each myocyte was adjusted to the timing of fastest $(dF/dt)_{max}$. The time distribution bin is 2.1 ms. Formamide treatment significantly changed the relative frequency of occurrence of $(dF/dt)_{max}$ at each time interval except where indicated by NS (not significant). Blue and red lines indicate the time intervals used for the classification of image pixels into the "early" [blue rectangles in panel **(A,B)**] and "delayed" [red rectangles in panel **(A,B)**] regions, respectively.

muscarinic receptor stimulation on intracellular Ca^{2+} transient. This effect of CCh was associated with the inhibition of a small fraction of coupled SR Ca^{2+} release sites and weakened Ca^{2+} signal propagation from junctional release sites to uncoupled regions.

CCh Does Not Affect the SR Ca^{2+} Content in Control and Formamide-Treated Ventricular Myocytes

The SR Ca^{2+} release is known to be tightly regulated by the intra-SR Ca^{2+} levels (Györke et al., 2017). The effect of CCh on the SR Ca^{2+} content was assessed by studying caffeine-induced Ca^{2+} transients in myocytes loaded with fluo-4 FF Ca^{2+} sensitive dye. As illustrated in **Figure 5**, 10 µM CCh did not affect the SR Ca^{2+} content recorded in the presence of 100 nM Iso in control and in formamide-treated ventricular myocytes. Noticeably, the formamide treatment significantly reduced the SR Ca^{2+} load in myocytes challenged with either Iso alone or Iso plus CCh. Similar to the results obtained with fluo-4 dye, in experiments using fluo-4FF, CCh did not change the amplitude of field-stimulated at 1 Hz Ca^{2+} transients in control myocytes (1.77 ± 0.11 $\Delta F/F_0$, $n = 14$ in the presence of 100 nM Iso and 1.70 ± 0.12 $\Delta F/F_0$, $n = 14$ in the presence of 100 nM Iso plus 10 µM CCh, $p = 0.66$), but significantly inhibited it in formamide-treated myocytes (1.35 ± 0.12 $\Delta F/F_0$, $n = 10$ in the presence of 100 nM Iso and 0.92 ± 0.14 $\Delta F/F_0$, $n = 6$ in the presence of 100 nM Iso plus 10 µM CCh, $p = 0.04$). Furthermore, CCh significantly reduced fractional release in myocytes with reduced t-tubules density (**Figure 5D**). Analysis of time to peak of field stimulated Ca^{2+} transients revealed that the formamide treatment significantly increased this parameter for both Iso and Iso plus CCh groups indicating dyssynchrony of Ca^{2+} release activation consistent with the downregulation of t-tubules (Iso group: 33.75 ± 1.21 ms in control *vs.* 39.09 ± 1.72 ms in formamide-treated myocytes ($p = 0.02$); Iso plus CCh group: 33.43 ± 0.79 ms in control vs. 53.84 ± 4.52 ms in formamide-treated myocytes ($p < 0.001$) (Louch et al., 2010).

These results indicate that the inhibitory effect of CCh on the amplitude of Ca^{2+} transients cannot be explained by changes in the SR Ca^{2+} load. Rather, these point to the potential role of decreased Ca^{2+} influx and/or reduced Ca^{2+} sensitivity of the SR Ca^{2+} release channels as potential mechanisms mediating the effect of a muscarinic receptor agonist.

Regulation of Sarcolemmal Ca^{2+} Channels by CCh

To test whether the signaling cross-talk between muscarinic and β-adrenergic receptor systems is different between t-tubular and peripheral sarcolemma, we compared the regulation of the L-type Ca^{2+} channel current (I_{Ca}) was compared with Iso and CCh in control and formamide-treated ventricular myocytes. Formamide treatment reduced the cell capacitance by 33% and decreased the density of baseline Ca^{2+} current by 58% (**Figures 6C,D**). The application of 100 nM Iso to control and formamide-treated myocytes produced a similar 50–70% increase in the amplitude of peak Ca^{2+} current (**Figures 6A–C,E**). CCh (10 µM) inhibited this Iso-mediated increase in I_{Ca}, on average, by 50% in both control and formamide-treated myocytes. However, when the effect of CCh was normalized to the amplitude of I_{Ca} recorded in the presence of Iso, it resulted in ~20% inhibition of I_{Ca} in both groups (**Figures 6A–C,F**). These data indicate that signaling mediated by β-adrenergic and muscarinic receptors is similar for peripheral and t-tubular membranes, respectively.

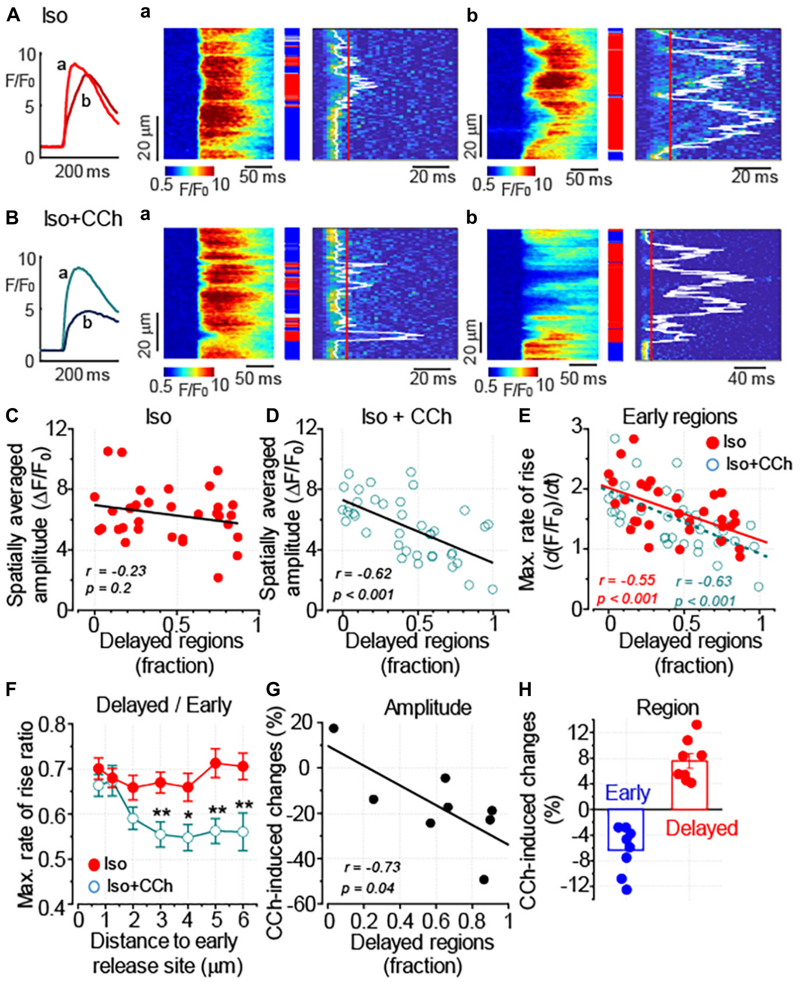

FIGURE 4 | Downregulation of t-tubules augments the anti-adrenergic effect of CCh on the amplitude of Ca^{2+} transients. **(A,B)** Ca^{2+} transients were recorded in formamide-treated ventricular myocyte in the presence of 100 nM Iso alone (**A**, *n* = 32) and the presence of 100 nM Iso plus 10 µM CCh (**B**, *n* = 39). The inset on the left illustrates spatially averaged fluorescence profiles recorded from the cells displaying moderate (a, corresponding to the line-scan image in panel a) and pronounced (b, corresponding to the line-scan image in panel b) levels of detubulation, respectively. **(A**,a,b,**B**,a,b**)** Linescan images of fluo-4 fluorescence (left) and corresponding images illustrating the rate of fluorescence change (right). White lines indicate the timing of $(dF/dt)_{max}$, and red lines indicate the time point used to differentiate delayed regions (red rectangles). Early and intermediate regions are indicated by blue and gray rectangles, respectively. **(C,D)** Regression analysis of the relationship between the detubulation level and the amplitude of Ca^{2+} transients showed the lack of correlation for the transients recorded in a presence of Iso alone **(C)** and the inverse correlation for the transients recorded in a presence of Iso plus CCh **(D)**. **(E)** The relationships between the detubulation level and $(dF/dt)_{max}$ at the early Ca^{2+} release regions recorded in the presence of Iso alone and in the presence of Iso plus CCh are shown along with the linear fits to the data. The two datasets were not significantly different (*F* test, $p = 0.3$). **(F)** CCh suppressed propagation of Ca^{2+} signal from the sarcolemma inside the cell. The propagation of Ca^{2+} was characterized by plotting the ratio of $(dF/dt)_{max}$ recorded at the delayed regions to that measured at the early regions vs. the distance to the nearest early Ca^{2+} release site ($^*p < 0.05$; $^{**}p < 0.01$). **(G)** CCh-induced changes in the Ca^{2+} transient amplitude plotted against the level of myocyte detubulation. Ca^{2+} transients were recorded in the presence of Iso (100 nM) alone and the presence of Iso (100 nM) plus CCh (10 µM) in the same myocytes. The delayed region fraction used in this graph was calculated from the line-scan images obtained before the application of CCh (in the presence of Iso alone). **(H)** CCh reduces the fraction of early and increases the fraction of delayed regions, respectively. **(C–E,G)** *r*, Pearson's correlation coefficient; *p*, the probability that the slope of the regression curve is different from 0.

Formamide-Treatment Reduces Functional Reserve of Excitation–Contraction (EC) Coupling in Ventricular Myocytes

The results demonstrate that in both control and formamide-treated ventricular myocytes, CCh similarly reduced I_{Ca} and did not affect the SR Ca^{2+} content. However, the inhibitory effect of CCh on Ca^{2+} transients in formamide-treated myocytes was observed in the context of significant reduction of both peak I_{Ca} density and the SR Ca^{2+} content. We hypothesize that the effect of CCh in formamide-treated myocytes is associated with the increased sensitivity of the SR Ca^{2+} release to changes in depolarization-induced Ca^{2+} influx. To test this hypothesis we studied how Ca^{2+} transients respond to changes in ICa amplitude in control and formamide-treated voltage-clamped

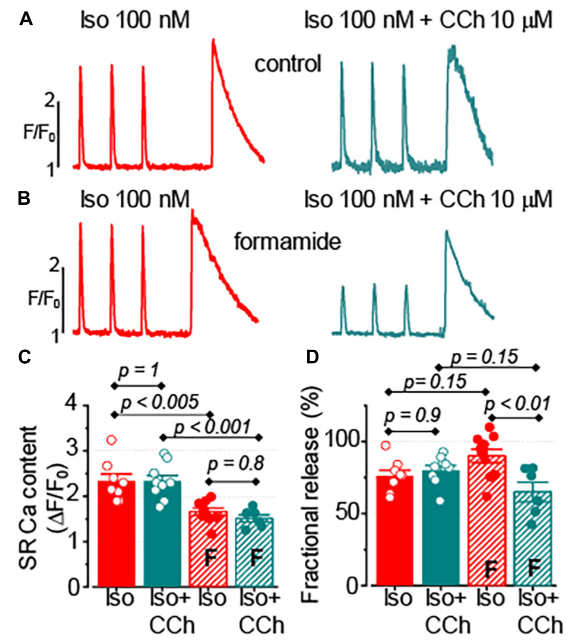

FIGURE 5 | Muscarinic receptor stimulation does not affect the sarcoplasmic reticulum (SR) Ca^{2+} content in control and formamide-treated ventricular myocytes. **(A,B)** spatially averaged fluo-4FF fluorescence profiles illustrating field-stimulated (1 Hz) and caffeine-induced Ca^{2+} transients recorded in control **(A)** and formamide-treated **(B)** ventricular myocytes in the presence of 100 nM Iso alone, and in the presence of 100 nM Iso plus 10 μM CCh. Bar graphs with data points demonstrate the effect of CCh on the amplitude caffeine-induced Ca^{2+} transients **(C)** and fractional release **(D)** in control and formamide-treated (F) myocytes. The fractional release was calculated as the ratio of amplitudes of electrically-stimulated to caffeine-induced Ca^{2+} transients, respectively. Multiple pairwise comparisons were performed with Tukey's test. The number of control myocytes studied was 14 for both Iso and Iso plus CCh groups. Number of formamide-treated myocytes studied was 10 for the Iso group and 6 for the Iso plus CCh group.

myocytes. In these experiments, performed in the presence of 100 nM Iso, we sought to mimic the CCh-mediated inhibition of I_{Ca} by using different voltage protocols. As illustrated in **Figure 7**, in control ventricular myocytes changing the depolarization level from 0 to –25 mV resulted in 38 ± 6.5% ($n = 5$) reduction in the peak I_{Ca}. This experimental protocol produced similar decrease in I_{Ca} amplitude (43 ± 3.0%, $n = 6$) in formamide-treated myocytes. However, in control ventricular myocytes, this decrease in I_{Ca} was not associated with the changes in Ca^{2+} transient (peak Ca^{2+} transients observed at –25 mV was 95 ± 5.2% of that recorded at 0 mV, $n = 5$, $p = 0.4$, paired t-test). In contrast, in formamide-treated myocytes, Ca^{2+} transients were significantly reduced by such a decrease in I_{Ca} (amplitude of Ca^{2+} transients observed at –25 mV was 66 ± 11% of that recorded at 0 mV, $n = 6$, $p = 0.03$, paired t-test) (**Figure 7D**). Accordingly, EC coupling gain measured at 0 mV in formamide-treated myocytes was 67 ± 4% of that measured in control myocytes ($p = 0.05$), whereas the gain recorded at –25 mV in formamide-treated myocytes was only 46 ± 6% of that measured in control myocytes ($p = 0.02$; **Figure 6C**). In aggregate, these data indicate the presence of a significant functional reserve (redundancy) of EC coupling in control myocytes during β-adrenergic receptor stimulation. Furthermore, the results show that the downregulation of t-tubules reduces EC coupling functional reserve thereby increasing the sensitivity of SR Ca^{2+} release to changes in the depolarization-induced Ca^{2+} influx.

Inhibition of CaMKII With KN93 Mimics the Effect of CCh in Formamide-Treated Myocytes

The results that Ca^{2+} signal propagation is inhibited by CCh (**Figure 4F**) suggest that muscarinic receptor activation may affect the Ca^{2+} sensitivity of RyR2. Since no effect of CCh was found on the SR Ca^{2+} content, Ca^{2+} spark activity can serve as an indicator of Ca^{2+} sensitivity of RyR2s. Therefore, the frequency of Ca^{2+} sparks was examined following 1 Hz field-stimulation in formamide-treated myocytes that were challenged sequentially by Iso 100 nM alone and by Iso100 nM plus CCh 10 μM. Indeed, CCh significantly reduced Ca^{2+} spark frequency (**Supplementary Figure 1**) thereby supporting our hypothesis on the inhibition of RyR2 Ca^{2+} sensitivity by muscarinic receptor agonist in formamide-treated myocytes.

It has been previously reported that in control and failing ventricular myocytes CCh reduced CaMKII-dependent phosphorylation of RyR2, a post-translational modification that is strongly associated with the increased sensitivity of RyR2 to Ca^{2+} (Ho et al., 2016). In this study, the effect of CCh on CaMKII activity was examined in Iso-stimulated control and formamide-treated ventricular myocytes. In agreement with the results from field-stimulation experiments in control myocytes, in the presence of 100 nM Iso, CCh did not affect activation of CaMKII (**Supplementary Figure 2**). In contrast, in formamide-treated myocytes, in the presence of 100 nM Iso, CCh reduced CaMKII activation by 20% (**Figure 8**). For comparison, KN93 (2 μM), a well-characterized CaMKII inhibitor (Anderson et al., 1998), reduced CaMKII activity by 58% (**Figure 8**). Next, the effect of KN-93 was studied on the properties of Ca^{2+} release in formamide-treated myocytes in the presence of 100 nM Iso. As demonstrated in **Figure 9**, KN93 mimicked the effect of CCh on Ca^{2+} transients in formamide-treated myocytes. First, following KN93 treatment Ca^{2+} transient amplitude showed inverse correlation with the levels of detubulation, as in the case of CCh (**Figures 9A,B**). Second, in the presence of KN93 propagation of Ca^{2+} from coupled to delayed regions, as evidenced by normalized $(dF/dt)_{max}$, was indistinguishable from that recorded in the presence of CCh (**Figure 9D**). In addition, the slope of the regression curve between $(dF/dt)_{max}$ at early regions and delayed regions fraction was similar in myocytes treated with Iso plus KN93 and Iso plus CCh (**Figures 4E**, **9B**). To test whether CCh produces any effects on Ca^{2+} propagation inside the cell in the presence of KN93, the $(dF/dt)_{max}$ ratio was examined in myocytes treated with Iso plus CCh plus KN93. As shown in **Figure 9D**, the $(dF/dt)_{max}$ ratio was not significantly affected by CCh, suggesting that CCh had no effects on Ca^{2+} propagation under these conditions.

Overall, these results suggest that the inhibitory effect of muscarinic receptor stimulation on Ca^{2+} transients observed

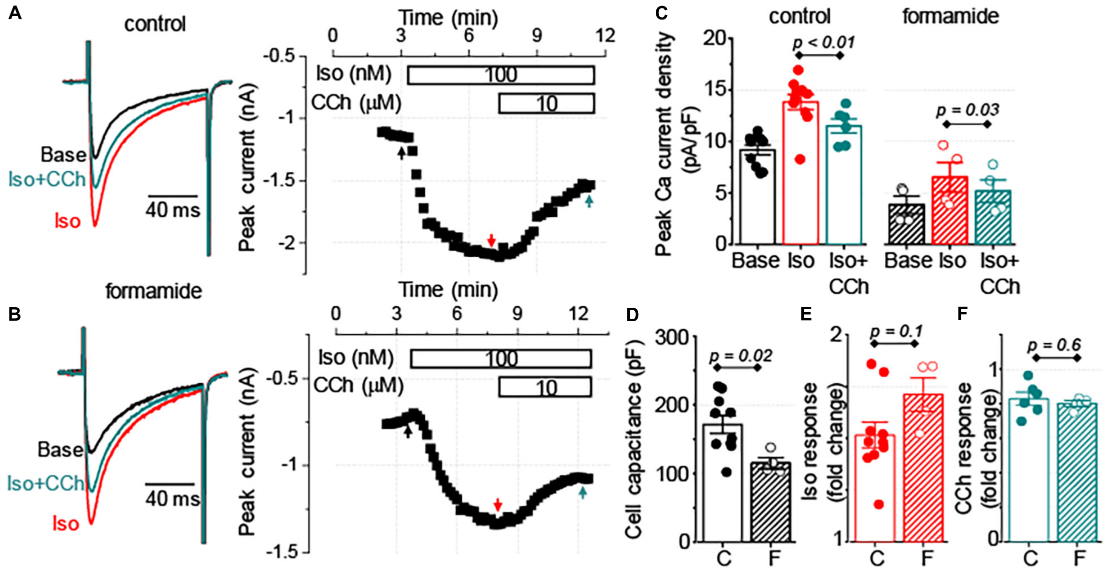

FIGURE 6 | Similar regulation of sarcolemmal Ca^{2+} influx by muscarinic receptor stimulation in control and detubulated myocytes. **(A,B)** Representative traces of Ca^{2+} currents and corresponding time-courses of changes in the amplitude of Ca^{2+} currents observed at the baseline (Base), in response to application of 100 nM Iso alone followed by application of 100 nM Iso plus 10 μM CCh. Currents were recorded in control (**A**, *n* = 6–10) and formamide-treated (**B**, *n* = 4) ventricular myocytes. **(C)** Bar graphs with data points show the peak Ca^{2+} current density recorded at the baseline (Base), in the presence of Iso alone, and in the presence of Iso plus CCh in control **(C)** and formamide-treated **(F)** ventricular myocytes, respectively. Summary data along with individual data points are shown for myocyte capacitance **(D)**, peak Ca^{2+} current response to Iso, normalized to the baseline **(E)**, and peak Ca^{2+} current response to CCh, normalized to the peak Ca^{2+} current recorded in the presence of Iso **(F)**.

in myocytes with downregulated t-tubules can be attributed, at least partially, to the reduced levels of CaMKII-dependent phosphorylation of RyR2.

DISCUSSION

A well-organized t-tubule system is critical for maintaining the robust excitation–contraction (EC) coupling in ventricular myocytes, whereas disorganization and downregulation of t-tubules have been consistently associated with the defective SR Ca^{2+} release in cardiac disease (Brette and Orchard, 2003; Louch et al., 2010; Guo et al., 2013; Poláková and Sobie, 2013). In this study, the mechanisms underlying the regulation of intracellular Ca^{2+} handling by muscarinic receptors in ventricular myocytes were addressed in the context of acutely disrupted t-tubules. Our main finding is that the downregulation of t-tubules amplified the inhibitory effect of muscarinic receptor agonist CCh on cytosolic Ca^{2+} transients. This effect is attributed to the increased dependency of SR Ca^{2+} release on CCh-mediated inhibition of both the L-type Ca^{2+} channel and RyR2.

Muscarinic Receptor Signaling at the Surface Sarcolemma vs. T-Tubular Domain

In ventricular myocytes, the negative ionotropic effect associated with the stimulation of muscarinic receptors is predominantly attributed to the inhibition of β-adrenergic receptor–mediated stimulatory effects on Ca^{2+} transients and myocyte shortening (Hartzell, 1988; Endoh, 1999; Harvey and Belevych, 2003). Accordingly, we found that inhibitory effects of CCh on Ca^{2+} transients occurred only during β-adrenergic receptor stimulation with Iso (**Figure 1**). In this study, CCh at 10 μM was used to ensure maximal activation of muscarinic receptor–mediated functional responses (Vandecasteele et al., 1999). Growing evidence suggests that t-tubules have an important role not only in establishing and regulating compartmentalized Ca^{2+} and Na^{+} signaling (Bers, 2001; Brette and Orchard, 2003; Jones et al., 2018), but also for the local regulation of G-protein coupled receptor-mediated signaling, including signaling mediated by β-adrenergic receptors (Gorelik et al., 2013). To test the functional significance of muscarinic receptor signaling localized to t-tubular microdomains, we used a well characterized approach to acutely disrupt t-tubules with formamide treatment (Brette et al., 2002). In our experiments, the formamide treatment significantly reduced t-tubule density (**Figures 2A–C**) and enhanced the CCh-mediated inhibitory effect on the amplitude of Ca^{2+} transients (**Figure 2G**). We used the timing of maximal rate of increase of fluo-4 fluorescence as an index of proximity between the SR Ca^{2+} release sites and t-tubule sarcolemma (Dries et al., 2013, 2016; Belevych et al., 2017) to study the relationship between Ca^{2+} transient and detubulation level for each myocyte. This analysis showed that the amplitude of Ca^{2+} transients recorded in the presence of 100 nM Iso alone was not significantly affected by the extent of detubulation (**Figure 4C**). In contrast, the inhibitory effect of CCh was directly proportional to the degree of t-tubule downregulation (**Figures 4D,G**).

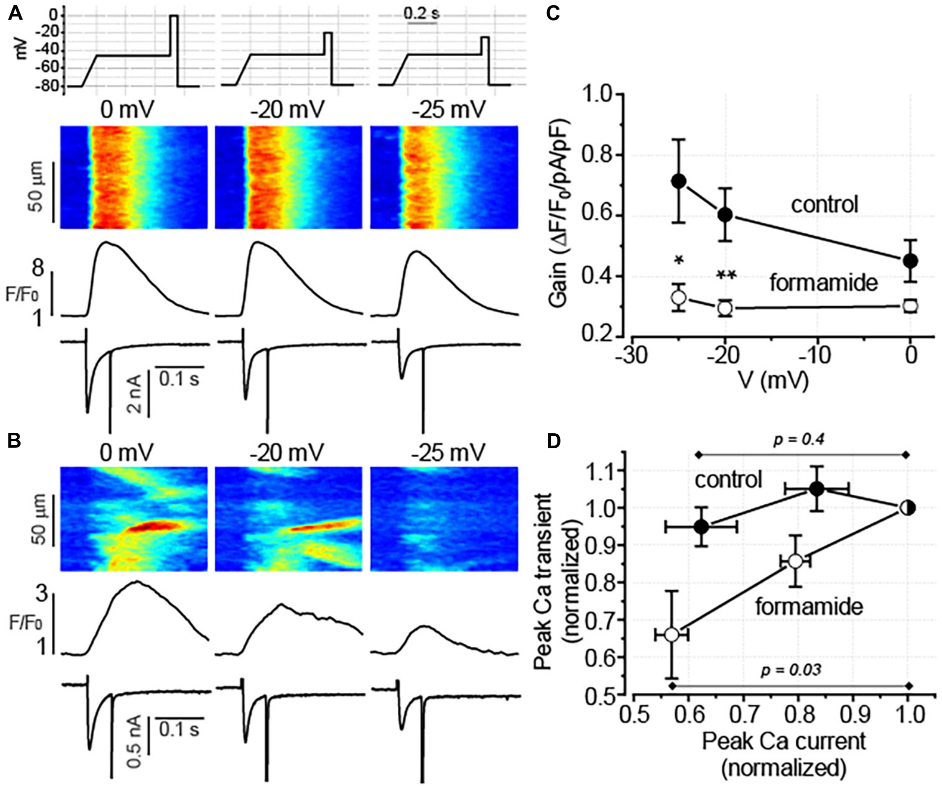

FIGURE 7 | Detubulation reduces the fidelity of excitation-contraction (EC) coupling. **(A,B)** Representative line-scan images of fluo-4 fluorescence with the corresponding spatially averaged fluorescence profiles and I_{Ca} traces recorded in control **(A)** and formamide-treated **(B)** ventricular myocytes in a presence of 100 nM Iso. Depolarization levels used to evoke I_{Ca} are indicated above each line scan image. The upper panel in **A** illustrates the voltage protocol used to evoke Ca^{2+} currents. **(C)** The relationship between EC coupling gain and membrane voltage is shown for control (n = 5) and formamide-treated (n = 6) myocytes, respectively $^*p < 0.05$; $^{**}p < 0.01$ (control vs. formamide). **(D)** Voltage-dependent reduction in I_{Ca} decreased the amplitude of Ca^{2+} transients in formamide-treated but not in control myocytes, respectively. Data shown in panel C were transformed so that for each myocyte both peak Ca^{2+} transients and peak I_{Ca} were normalized to the corresponding values recorded at 0 mV.

To explain this effect, we considered the possibility that β-adrenergic receptor and/or muscarinic receptor-mediated signaling is different at the surface sarcolemma vs. t-tubular domain. Indeed, Brette et al. (2004) showed different sensitivity of I_{Ca} to Iso in control and detubulated rat ventricular myocytes. Nikolaev et al. (2010) attributed the difference in β-adrenergic receptor-mediating signaling in surface vs. t-tubular membrane domain to the preferential localization of β2-adrenergic receptor to the t-tubular membrane of rat and mouse ventricular myocytes. Kashihara et al. (2014) reported preferential inhibition of t-tubular vs. surface sarcolemma Ca^{2+} channels by signaling mediated *via* β2-adrenergic and muscarinic receptors in mouse model of heart failure. However, in our experiment we did not find a significant difference in the sensitivity of I_{Ca} to Iso between the control and detubulated myocytes (**Figure 6E**), suggesting that in mouse ventricular myocytes β2-adrenergic receptor do not significantly contribute to the stimulatory effect of Iso. Importantly, no difference was observed in the response of I_{Ca} to CCh in control and detubulated ventricular myocytes (**Figure 6F**). Therefore, our data indicate that the molecular crosstalk between β-adrenergic and muscarinic receptor signaling is similar in t-tubular and surface membrane domains, at least at the level of L-type Ca^{2+} channel regulation.

The Role of Excitation–Contraction-Coupling Reserve in Muscarinic Receptor Regulation of Ca^{2+} Transients

In ventricular myocytes, t-tubules support the spatial alignment of the L-type Ca^{2+} channels and RyR2, thus permitting the high fidelity coupling between the membrane depolarization and SR Ca^{2+} release (Franzini-Armstrong et al., 1999; Bers, 2001; Brette and Orchard, 2003). Downregulation of t-tubules drastically reduces depolarization-induced Ca^{2+} influx, significantly increases the fraction of RyR2s uncoupled from the L-type Ca^{2+} channels, and thereby, increases the contribution of regenerative Ca^{2+} release to the global Ca^{2+} transient (Brette et al., 2004). In the current experiments, formamide treatment was associated with a 50% decrease in I_{Ca} density in the presence of 100 nM Iso (**Figure 6**). Remarkably, despite these changes, the amplitude of Ca^{2+} transients was not affected by detubulation (**Figure 4C**). These results demonstrate the

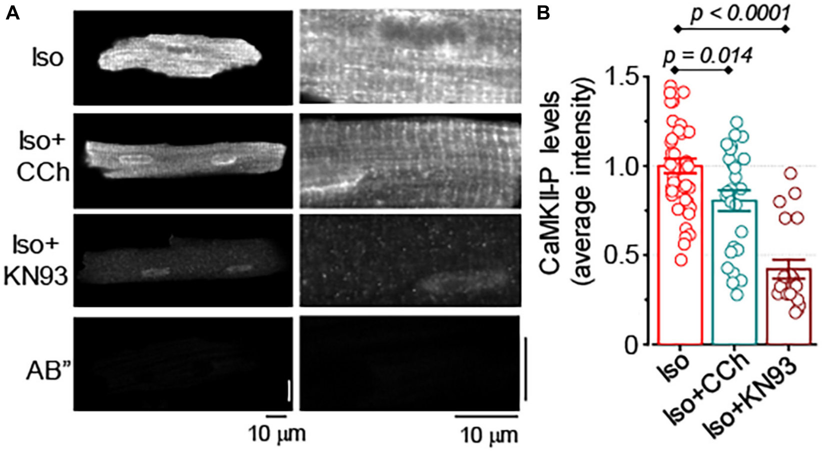

FIGURE 8 | Muscarinic receptor stimulation reduces CaMKII activation in formamide-treated myocytes. **(A)** Representative images of formamide-treated myocytes immunostained for activated CaMKII (phospho T286). Right panels are the scaled-up parts of the corresponding left panel images. AB” images illustrate myocyte labeling with secondary antibody only. **(B)** Summary data along with individual data points illustrate average myocyte fluorescence observed in formamide-treated ventricular myocytes incubated with 100 nM Iso alone ($n = 41$), 100 nM Iso plus 10 μM CCh ($n = 26$), and 100 nM Iso and 2 μM KN93, a CaMKII inhibitor ($n = 20$). In all groups, myocytes were field-stimulated for 1 min at 2 Hz followed by 1 min at 1 Hz. Multiple pairwise comparisons were performed with Tukey’s test.

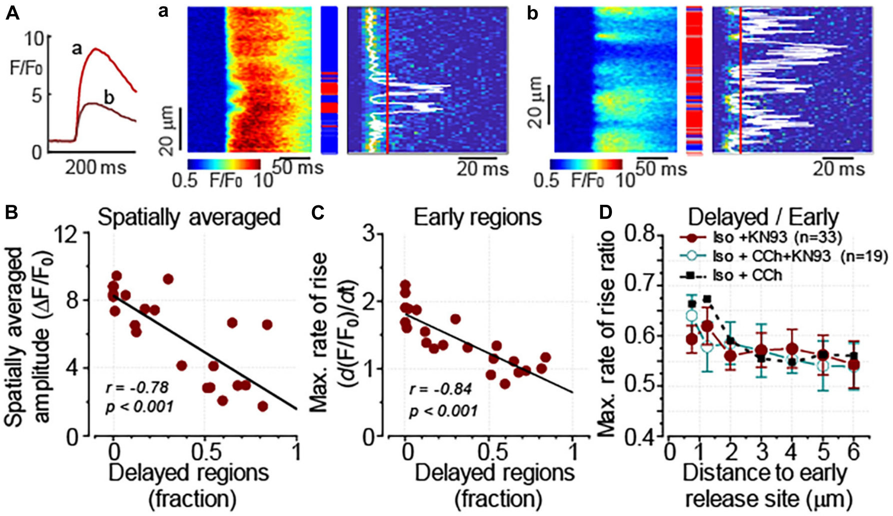

FIGURE 9 | CaMKII inhibitor KN93 mimics the effect of CCh on Ca^{2+} transients in formamide-treated myocytes. Ca^{2+} transients were recorded in formamide-treated ventricular myocytes in the presence of 100 nM Iso and KN93 (2 μM). **(A)** Inset on the left shows spatially averaged fluorescence profiles recorded from the cell displaying moderate (a, corresponding to the line-scan image in panel a) and pronounced (b, corresponding to the line-scan image in panel b) levels of detubulation, respectively. **(A**,a,b**)** Linescan images of fluo-4 fluorescence (left) and corresponding images illustrating the rate of fluorescence change (right). The white line indicates the timing of $(dF/dt)_{max}$, and the red line indicates the time point used to differentiate delayed regions (red rectangles). Early and intermediate regions are indicated by blue and gray rectangles, respectively. **(B)** The amplitude of Ca^{2+} transients is inversely correlated with the fraction of the delayed regions. **(C)** The relationship between $(dF/dt)_{max}$ at the early Ca^{2+} release regions and the delayed region fraction recorded in the presence of Iso plus KN93 is shown along with a linear fit to the data. The slope of the regression line (–1.2 ± 0.2) was not significantly different (F test, $p = 0.09$) from that recorded in the presence of Iso plus CCh (shown in **Figure 3E**, –1.0 ± 0.2). **(D)** The propagation of Ca^{2+} from the sarcolemma was similarly affected by KN93 and CCh. The propagation was characterized by plotting the ratio of $(dF/dt)_{max}$ recorded at the delayed regions to that measured at the early regions *vs.* the distance to the nearest early Ca^{2+} release site. Furthermore, CCh did not produce further changes in the $(dF/dt)_{max}$ max ratio when added to the cells treated with KN93. Data obtained in the presence of Iso plus CCh (as in **Figure 3F**) are shown for comparison. **(B,C)** r, Pearson’s correlation coefficient; p, the probability that the slope of the regression curve is different from 0.

presence of a significant functional reserve of EC coupling in ventricular myocytes during β-adrenergic receptor stimulation. As it has been noticed in earlier studies, the linear relationship between sarcolemmal Ca^{2+} influx and SR Ca^{2+} release observed at baseline becomes flattened during β-adrenergic stimulation (Hussain and Orchard, 1997; Song et al., 2001). In other words, the increase in I_{Ca} amplitude beyond a certain level becomes redundant as it does not produce a further increase in the amplitude of Ca^{2+} transients. Accordingly, our experiments indicate that the presence of 100 nM Iso voltage-dependent reduction of I_{Ca} peak by 40% did not significantly change the amplitude of Ca^{2+} transients in control ventricular myocytes (**Figure 7**). In myocytes with downregulated t-tubules density, EC coupling reserve is significantly diminished and the SR Ca^{2+} release becomes more sensitive to changes in I_{Ca} density as demonstrated in experiments illustrated in **Figure 7**. Therefore, a similar reduction of I_{Ca} in control and detubulated ventricular myocytes induced by CCh (**Figure 6F**) may have a more pronounced effect on the Ca^{2+} transients in formamide-treated than in control myocytes.

Regulation of Coupled and Uncoupled Ca^{2+} Release Sites by Muscarinic Receptor Stimulation

Analysis of time-dependent changes in fluorescence response to field stimulation (**Figures 2D–F**) allowed us to assess the effect of CCh on Ca^{2+} release sites functionally coupled and uncoupled from the t-tubules. The initial experiments in formamide-treated myocytes indicated that muscarinic receptor stimulation did not affect the properties of coupled Ca^{2+} release sites (**Figure 4E**). Further experiments in which we studied Ca^{2+} transients in the presence of Iso and Iso plus CCh in the same myocytes revealed that CCh reduced the fraction of coupled Ca^{2+} release sites by only 6% (**Figure 4H**). These results suggest that in the presence of Iso at 100 nM, a concentration producing a maximal stimulatory effect on Ca^{2+} transients (**Figures 1**, **2**), muscarinic receptor stimulation has rather limited effects on regulation of adjacent to sarcolemma Ca^{2+} release sites. In contrast, the CCh significantly inhibited Ca^{2+} release at the uncoupled Ca^{2+} release sites (**Figure 4F**). This effect became evident with an apparent increase in the distance between coupled and uncoupled Ca^{2+} release sites, thus suggesting that CCh suppressed propagation of the Ca^{2+} signal from sarcolemma inside the cell. Propagation of Ca^{2+} under these conditions strongly relies on regenerative Ca^{2+} release at the uncoupled sites. This process is regulated by Ca^{2+} concentration inside the SR and by the sensitivity of RyR2 to cytosolic Ca^{2+} which is determined by both SR Ca^{2+} content and post-translational modifications of the protein (Brette et al., 2005; Venetucci et al., 2007; Belevych et al., 2013). In our experiments, CCh did not affect the SR Ca^{2+} content recorded in paced control and formamide-treated myocytes (**Figure 5**), suggesting a potential contribution of post-translational modifications of RyR2s in the CCh effect. β-Adrenergic receptor stimulation in ventricular myocytes has been associated with increased phosphorylation of RyR2 at Ser2808 and Ser2814 sites (Wehrens et al., 2005; Belevych et al., 2013) and oxidation-dependent intersubunit cross-linking (Bovo et al., 2012; Nikolaienko et al., 2018). All of these post-translational modifications result in the stimulation of RyR2 activity. We previously showed that CCh reduces phosphorylation at Ser2814, a CaMKII-dependent phosphorylation site (Ho et al., 2016). This effect was attributed to muscarinic receptor-mediated suppression of reactive oxygen species (ROS) generation and inhibition of downstream ROS signaling including activation of CaMKII. In this study, we showed that CCh inhibits activation of CaMKII in formamide-treated myocytes response to field stimulation in the presence of 100 nM Iso (**Figure 8**). Furthermore, myocyte pretreatment with KN93, a well-characterized inhibitor of CaMKII (Anderson et al., 1998), completely recapitulated the effect of CCh on Ca^{2+} transients in formamide-treated ventricular myocytes (**Figure 9**). Taken together, these data suggest that the inhibitory effect of CCh on the amplitude of Ca^{2+} transients in ventricular myocytes with disrupted t-tubules critically depends on inhibition of CaMKII-dependent phosphorylation of uncoupled RyR2 clusters.

CaMKII-dependent phosphorylation of RyR2 has been associated mostly with pathological remodeling and manifested as the increased myocyte propensity to arrhythmogenic Ca^{2+} waves (Anderson et al., 2011; Belevych et al., 2013; Mustroph et al., 2017). The previous studies showed that arrhythmogenesis in heart failure myocytes was attributable to CaMKII-dependent facilitation of coupled Ca^{2+} release site activity (Belevych et al., 2017). CaMKII-dependent activation of non-coupled Ca^{2+} release sites was also found important for Ca-dependent arrhythmogenesis in heart failure (Dries et al., 2018). The results of the present study suggest that CaMKII-dependent phosphorylation of uncoupled RyR2 may have physiological significance as the mechanism underlying EC coupling reserve.

Limitations

Acute disruption of t-tubule organization in ventricular myocytes by formamide has been an invaluable tool for the research of the functional role of t-tubule domain and domain-related proteins (Brette et al., 2002, 2004, 2005; Despa et al., 2003; Chase and Orchard, 2011; Bryant et al., 2018). Furthermore, formamide-induced reduction of t-tubule density may resemble changes in the t-tubule system observed at the advanced stages of heart failure (Guo et al., 2013). However, in chronic cardiac diseases, such as heart failure, remodeling of the t-tubule system has been associated not only with reduced density and organization level but with changes in domain-specific protein expression and activity (Dries et al., 2013, 2016; Belevych et al., 2017; Jones et al., 2018). These changes may not be reproduced by acute detubulation protocol. Therefore, caution should be used when extrapolating these findings to disease settings.

CONCLUSION

Heart failure has been associated with the diminished contribution of the parasympathetic nervous system in the regulation of cardiac function (Gold et al., 2016; van Bilsen et al., 2017). Although muscarinic receptors expressed in ventricular myocytes are known to play a significant role in mediating the effects of the parasympathetic nerve system, how heart failure affects muscarinic receptor-mediated signaling is not well defined (Fernandez and Canty, 2015). In this study, we described a novel t-tubule-dependent mechanism of cholinergic regulation of intracellular Ca^{2+} handling in ventricular myocytes that may be of importance in cardiac diseases, such as heart failure, which is associated with downregulated t-tubules (Brette and Orchard, 2003; Louch et al., 2010; Guo et al., 2013). The present study indicates that therapies involving parasympathetic augmentation

(Hanna et al., 2018) may be associated with an unwanted muscarinic receptor-mediated inhibition of mechanical function in failing hearts.

DATA AVAILABILITY STATEMENT

The original contributions presented in the study are included in the article/**Supplementary Material**, further inquiries can be directed to the corresponding author.

ETHICS STATEMENT

The animal study was reviewed and approved by The Ohio State University Institutional Animal Care and Use Committee.

AUTHOR CONTRIBUTIONS

AB, DT, and SG planned the research and wrote the manuscript. AB and VB designed and performed the experiments and analyzed the experimental data. All authors contributed to the article and approved the submitted version.

FUNDING

This work was supported by NIH NHLBI Grants HL063043 and HL074045 (SG), and HL121796 and HL142588 (DT).

ACKNOWLEDGMENTS

The authors thank Benjamin Hernandez Orengo for excellent technical assistance.

SUPPLEMENTARY MATERIAL

The Supplementary Material for this article can be found online at: https://www.frontiersin.org/articles/10.3389/fphys.2021.725798/full#supplementary-material

REFERENCES

Anderson, M. E., Braun, A. P., Wu, Y., Lu, T., Wu, Y., Schulman, H., et al. (1998). KN-93, an inhibitor of multifunctional Ca++/calmodulin-dependent protein kinase, decreases early afterdepolarizations in rabbit heart. *J. Pharmacol. Exp. Ther.* 287, 996–1006.

Anderson, M. E., Brown, J. H., and Bers, D. M. (2011). CaMKII in myocardial hypertrophy and heart failure. *J. Mol. Cell. Cardiol.* 51, 468–473. doi: 10.1016/j.yjmcc.2011.01.012

Belevych, A. E., Ho, H.-T., Bonilla, I. M., Terentyeva, R., Schober, K. E., Terentyev, D., et al. (2017). The role of spatial organization ofCa^{2+} release sites in the generation of arrhythmogenic diastolic Ca^{2+} release in myocytes from failing hearts. *Basic Res. Cardiol.* 112:44. doi: 10.1007/s00395-017-0633-2

Belevych, A. E., Radwański, P. B., Carnes, C. A., and Györke, S. (2013). "Ryanopathy": causes and manifestations of RyR2 dysfunction in heart failure. *Cardiovasc. Res.* 98, 240–247. doi: 10.1093/cvr/cvt024

Bers, D. M. (2001). *Excitation-Contraction Coupling and Cardiac Contractile Force*, 2nd Edn. Dordrecht: Kluwer Academic Publishers.

Biesmans, L., Macquaide, N., Heinzel, F. R., Bito, V., Smith, G. L., and Sipido, K. R. (2011). Subcellular heterogeneity of ryanodine receptor properties in ventricular myocytes with low T-tubule density. *PLoS One* 6:e25100. doi: 10.1371/journal.pone.0025100

Bovo, E., Lipsius, S. L., and Zima, A. V. (2012). Reactive oxygen species contribute to the development of arrhythmogenic Ca^{2+} waves during β-adrenergic receptor stimulation in rabbit cardiomyocytes. *J. Physiol.* 590, 3291–3304. doi: 10.1113/jphysiol.2012.230748

Brette, F., Despa, S., Bers, D. M., and Orchard, C. H. (2005). Spatiotemporal characteristics of SR Ca^{2+} uptake and release in detubulated rat ventricular myocytes. *J. Mol. Cell. Cardiol.* 39, 804–812. doi: 10.1016/j.yjmcc.2005.08.005

Brette, F., Komukai, K., and Orchard, C. H. (2002). Validation of formamide as a detubulation agent in isolated rat cardiac cells. *Am. J. Physiol. Heart Circ. Physiol.* 283, H1720–H1728. doi: 10.1152/ajpheart.00347.2002

Brette, F., and Orchard, C. (2003). T-tubule function in mammalian cardiac myocytes. *Circ. Res.* 92, 1182–1192. doi: 10.1161/01.RES.0000074908.17214.FD

Brette, F., Rodriguez, P., Komukai, K., Colyer, J., and Orchard, C. H. (2004). β-adrenergic stimulation restores the Ca transient of ventricular myocytes lacking t-tubules. *J. Mol. Cell. Cardiol.* 36, 265–275. doi: 10.1016/j.yjmcc.2003.11.002

Bryant, S. M., Kong, C. H. T., Cannell, M. B., Orchard, C. H., and James, A. F. (2018). Loss of caveolin-3-dependent regulation of ICa in rat ventricular myocytes in heart failure. *Am. J. Physiol. Heart Circ. Physiol.* 314, H521–H529. doi: 10.1152/ajpheart.00458.2017

Bryant, S. M., Kong, C. H. T., Watson, J., Cannell, M. B., James, A. F., and Orchard, C. H. (2015). Altered distribution of I_{Ca} impairs Ca release at the t-tubules of ventricular myocytes from failing hearts. *J. Mol. Cell. Cardiol.* 86, 23–31. doi: 10.1016/j.yjmcc.2015.06.012

Chase, A., and Orchard, C. H. (2011). Ca efflux via the sarcolemmal Ca ATPase occurs only in the t-tubules of rat ventricular myocytes. *J. Mol. Cell. Cardiol.* 50, 187–193. doi: 10.1016/j.yjmcc.2010.10.012

Despa, S., Brette, F., Orchard, C. H., and Bers, D. M. (2003). Na/Ca exchange and Na/K-ATPase function are equally concentrated in transverse tubules of rat ventricular myocytes. *Biophys. J.* 85, 3388–3396. doi: 10.1016/S0006-3495(03)74758-4

Dries, E., Bito, V., Lenaerts, I., Antoons, G., Sipido, K. R., and Macquaide, N. (2013). Selective modulation of coupled ryanodine receptors during microdomain activation of calcium/calmodulin-dependent kinase II in the dyadic cleft. *Circ. Res.* 113, 1242–1252. doi: 10.1161/CIRCRESAHA.113.301896

Dries, E., Santiago, D. J., Gilbert, G., Lenaerts, I., Vandenberk, B., Nagaraju, C. K., et al. (2018). Hyperactive ryanodine receptors in human heart failure and ischaemic cardiomyopathy reside outside of couplons. *Cardiovasc. Res.* 114, 1512–1524. doi: 10.1093/cvr/cvy088

Dries, E., Santiago, D. J., Johnson, D. M., Gilbert, G., Holemans, P., Korte, S. M., et al. (2016). Calcium/calmodulin-dependent kinase II and nitric oxide synthase 1-dependent modulation of ryanodine receptors during β-adrenergic stimulation is restricted to the dyadic cleft. *J. Physiol.* 594, 5923–5939. doi: 10.1113/JP271965

Endoh, M. (1999). Muscarinic regulation of Ca^{2+} signaling in mammalian atrial and ventricular myocardium. *Eur. J. Pharmacol.* 375, 177–196. doi: 10.1016/S0014-2999(99)00231-9

Fernandez, S. F., and Canty, J. M. (2015). Adrenergic and cholinergic plasticity in heart failure. *Circ. Res.* 116, 1639–1642. doi: 10.1161/CIRCRESAHA.115.306439

Franzini-Armstrong, C., Protasi, F., and Ramesh, V. (1999). Shape, size, and distribution of Ca^{2+} release units and couplons in skeletal and cardiac muscles. *Biophys. J.* 77, 1528–1539. doi: 10.1016/S0006-3495(99)77000-1

Gold, M. R., Van Veldhuisen, D. J., Hauptman, P. J., Borggrefe, M., Kubo, S. H., Lieberman, R. A., et al. (2016). Vagus nerve stimulation for the treatment of heart failure: the INOVATE-HF Trial. *J. Am. Coll. Cardiol.* 68, 149–158. doi: 10.1016/j.jacc.2016.03.525

Gorelik, J., Wright, P. T., Lyon, A. R., and Harding, S. E. (2013). Spatial control of the βAR system in heart failure: the transverse tubule and beyond. *Cardiovasc. Res.* 98, 216–224. doi: 10.1093/cvr/cvt005

Guo, A., Zhang, C., Wei, S., Chen, B., and Song, L.-S. (2013). Emerging mechanisms of T-tubule remodelling in heart failure. *Cardiovasc. Res.* 98, 204–215. doi: 10.1093/cvr/cvt020

Györke, S., Belevych, A. E., Liu, B., Kubasov, I. V., Carnes, C. A., and Radwański, P. B. (2017). The role of luminal Ca regulation in Ca signaling refractoriness and cardiac arrhythmogenesis. *J. Gen. Physiol.* 149, 877–888. doi: 10.1085/jgp.201711808

Hanna, P., Shivkumar, K., and Ardell, J. L. (2018). Calming the nervous heart: autonomic therapies in heart failure. *Card. Fail. Rev.* 4, 92–98. doi: 10.15420/cfr.2018.20.2

Hartzell, H. C. (1988). Regulation of cardiac ion channels by catecholamines, acetylcholine and second messenger systems. *Prog. Biophys. Mol. Biol.* 52, 165–247. doi: 10.1016/0079-6107(88)90014-4

Harvey, R. D., and Belevych, A. E. (2003). Muscarinic regulation of cardiac ion channels. *Br. J. Pharmacol.* 139, 1074–1084. doi: 10.1038/sj.bjp.0705338

Ho, H.-T., Belevych, A. E., Liu, B., Bonilla, I. M., Radwański, P. B., Kubasov, I. V., et al. (2016). Muscarinic stimulation facilitates sarcoplasmic reticulum Ca release by modulating ryanodine receptor 2 phosphorylation through protein pinase G and Ca/calmodulin-dependent protein kinase II. *Hypertension* 68, 1171–1178. doi: 10.1161/HYPERTENSIONAHA.116.07666

Hussain, M., and Orchard, C. H. (1997). Sarcoplasmic reticulum Ca^{2+} content, L-type Ca^{2+} current and the Ca^{2+} transient in rat myocytes during b-adrenergic stimulation. *J. Physiol.* 505, 385–402.

Jones, P. P., MacQuaide, N., and Louch, W. E. (2018). Dyadic plasticity in cardiomyocytes. *Front. Physiol.* 9:1773. doi: 10.3389/fphys.2018.01773

Kashihara, T., Hirose, M., Shimojo, H., Nakada, T., Gomi, S., Hongo, M., et al. (2014). β_2-Adrenergic and M_2-muscarinic receptors decrease basal t-tubular L-type $Ca2^{+}$ channel activity and suppress ventricular contractility in heart failure. *Eur. J. Pharmacol.* 724, 122–131. doi: 10.1016/j.ejphar.2013.12.037

Kashimura, T., Briston, S. J., Trafford, A. W., Napolitano, C., Priori, S. G., Eisner, D. A., et al. (2010). In the RyR2(R4496C) mouse model of CPVT, beta-adrenergic stimulation induces Ca waves by increasing SR Ca content and not by decreasing the threshold for Ca waves. *Circ. Res.* 107, 1483–1489.

Löffelholz, K., and Pappano, A. J. (1985). The parasympathetic neuroeffector junction of the heart. *Pharmacol. Rev.* 37, 1–24.

Louch, W. E., Sejersted, O. M., and Swift, F. (2010). There goes the neighborhood: pathological alterations in T-tubule morphology and consequences for cardiomyocyte Ca^{2+} handling. *J. Biomed. Biotechnol.* 2010:e503906. doi: 10.1155/2010/503906

Mustroph, J., Neef, S., and Maier, L. S. (2017). CaMKII as a target for arrhythmia suppression. *Pharmacol. Ther.* 176, 22–31. doi: 10.1016/j.pharmthera.2016.10.006

Nikolaev, V. O., Moshkov, A., Lyon, A. R., Miragoli, M., Novak, P., Paur, H., et al. (2010). β2-Adrenergic receptor redistribution in heart failure changes cAMP compartmentation. *Science* 327, 1653–1657. doi: 10.1126/science.1185988

Nikolaienko, R., Bovo, E., and Zima, A. V. (2018). Redox dependent modifications of ryanodine receptor: basic mechanisms and implications in heart diseases. *Front. Physiol.* 9:1775. doi: 10.3389/fphys.2018.01775

Poláková, E., and Sobie, E. A. (2013). Alterations in T-tubule and dyad structure in heart disease: challenges and opportunities for computational analyses. *Cardiovasc. Res.* 98, 233–239. doi: 10.1093/cvr/cvt026

Song, L. S., Wang, S. Q., Xiao, R. P., Spurgeon, H., Lakatta, E. G., and Cheng, H. (2001). β-Adrenergic stimulation synchronizes intracellular Ca^{2+} release during excitation-contraction coupling in cardiac myocytes. *Circ. Res.* 88, 794–801. doi: 10.1161/hh0801.090461

van Bilsen, M., Patel, H. C., Bauersachs, J., Böhm, M., Borggrefe, M., Brutsaert, D., et al. (2017). The autonomic nervous system as a therapeutic target in heart failure: a scientific position statement from the Translational Research Committee of the Heart Failure Association of the European Society of Cardiology. *Eur. J. Heart Fail.* 19, 1361–1378. doi: 10.1002/ejhf.921

Vandecasteele, G., Eschenhagen, T., Scholz, H., Stein, B., Verde, I., and Fischmeister, R. (1999). Muscarinic and beta-adrenergic regulation of heart rate, force of contraction and calcium current is preserved in mice lacking endothelial nitric oxide synthase. *Nat. Med.* 5, 331–334. doi: 10.1038/6553

Venetucci, L. A., Trafford, A. W., and Eisner, D. A. (2007). Increasing ryanodine receptor open probability alone does not produce arrhythmogenic calcium waves: threshold sarcoplasmic reticulum calcium content is required. *Circ. Res.* 100, 105–111.

Wagner, E., Brandenburg, S., Kohl, T., and Lehnart, S. E. (2014). Analysis of tubular membrane networks in cardiac myocytes from atria and ventricles. *J. Vis. Exp.* 92:e51823. doi: 10.3791/51823

Wehrens, X. H., Lehnart, S. E., and Marks, A. R. (2005). Intracellular calcium release and cardiac disease. *Annu. Rev. Physiol.* 67, 69–98.

Zhou, P., Zhao, Y.-T., Guo, Y.-B., Xu, S.-M., Bai, S.-H., Lakatta, E. G., et al. (2009). β-Adrenergic signaling accelerates and synchronizes cardiac ryanodine receptor response to a single L-type Ca^{2+} channel. *Proc. Natl. Acad. Sci. U.S.A.* 106, 18028–18033. doi: 10.1073/pnas.0906560106

Conflict of Interest: The authors declare that the research was conducted in the absence of any commercial or financial relationships that could be construed as a potential conflict of interest.

frontiers in Physiology

ORIGINAL RESEARCH
published: 08 October 2021
doi: 10.3389/fphys.2021.724372

Nanoscale Organisation of Ryanodine Receptors and Junctophilin-2 in the Failing Human Heart

Yufeng Hou [1,2], ***Jizhong Bai*** [1], ***Xin Shen*** [1,2], ***Oscar de Langen*** [1], ***Amy Li*** [3], ***Sean Lal*** [4], ***Cristobal G. dos Remedios*** [5], ***David Baddeley*** [6], ***Peter N. Ruygrok*** [7], ***Christian Soeller*** [8]* **and** ***David J. Crossman*** [1]*

[1] Department of Physiology, University of Auckland, Auckland, New Zealand, [2] Institute for Experimental Medical Research, Oslo University Hospital, University of Oslo, Oslo, Norway, [3] Department of Pharmacy and Biomedical Science, Health and Engineering, La Trobe University, Bendigo, VIC, Australia, [4] Faculty of Medicine and Science, University of Sydney, Sydney, NSW, Australia, [5] Victor Chang Cardiac Research Institute, Darlinghurst, Sydney, NSW, Australia, [6] Auckland Bioengineering Institute, University of Auckland, Auckland, New Zealand, [7] Department of Cardiology, Auckland City Hospital, Auckland, New Zealand, [8] Biomedical Physics, University of Exeter, Exeter, United Kingdom

OPEN ACCESS

Edited by:
Nina D. Ullrich,
Heidelberg University, Germany

Reviewed by:
Thomas Seidel,
University of Erlangen Nuremberg, Germany
Andrew Trafford,
The University of Manchester, United Kingdom

***Correspondence:**
David J. Crossman
d.crossman@auckland.ac.nz
Christian Soeller
c.soeller@exeter.ac.uk;
christian.soeller@unibe.ch

Specialty section:
This article was submitted to Cardiac Electrophysiology, a section of the journal Frontiers in Physiology

Received: *13 June 2021*
Accepted: *03 September 2021*
Published: *08 October 2021*

Citation:
Hou Y, Bai J, Shen X, de Langen O, Li A, Lal S, dos Remedios CG, Baddeley D, Ruygrok PN, Soeller C and Crossman DJ (2021) Nanoscale Organisation of Ryanodine Receptors and Junctophilin-2 in the Failing Human Heart.
Front. Physiol. 12:724372.
doi: 10.3389/fphys.2021.724372

The disrupted organisation of the ryanodine receptors (RyR) and junctophilin (JPH) is thought to underpin the transverse tubule (t-tubule) remodelling in a failing heart. Here, we assessed the nanoscale organisation of these two key proteins in the failing human heart. Recently, an advanced feature of the t-tubule remodelling identified large flattened t-tubules called t-sheets, that were several microns wide. Previously, we reported that in the failing heart, the dilated t-tubules up to ∼1 μm wide had increased collagen, and we hypothesised that the t-sheets would also be associated with collagen deposits. Direct stochastic optical reconstruction microscopy (dSTORM), confocal microscopy, and western blotting were used to evaluate the cellular distribution of excitation-contraction structures in the cardiac myocytes from patients with idiopathic dilated cardiomyopathy (IDCM) compared to myocytes from the non-failing (NF) human heart. The dSTORM imaging of RyR and JPH found no difference in the colocalisation between IDCM and NF myocytes, but there was a higher colocalisation at the t-tubule and sarcolemma compared to the corbular regions. Western blots revealed no change in the JPH expression but did identify a ∼50% downregulation of RyR ($p = 0.02$). The dSTORM imaging revealed a trend for the smaller t-tubular RyR clusters (∼24%) and reduced the t-tubular RyR cluster density (∼35%) that resulted in a 50% reduction of t-tubular RyR tetramers in the IDCM myocytes ($p < 0.01$). Confocal microscopy identified the t-sheets in all the IDCM hearts examined and found that they are associated with the reticular collagen fibres within the lumen. However, the size and density of the RyR clusters were similar in the myocyte regions associated with t-sheets and t-tubules. T-tubule remodelling is associated with a reduced RyR expression that may contribute to the reduced excitation-contraction coupling in the failing human heart.

Keywords: t-tubules, ryanodine receptor, collagen VI, fibrosis, junctophilin

INTRODUCTION

The highly ordered nature of the excitation-contraction coupling (ECC) machinery of ventricular myocytes is recognised as the key cellular structure enabling a tightly regulated and synchronised contraction (Bers, 2002). This includes the extraordinarily complex invaginations of the ventricular myocyte sarcolemma, namely, the transverse tubules (t-tubules), although this term is not always correct as axial tubules are also present (Soeller and Cannell, 1999). The t-tubules facilitate the rapid conduction of action potential to the cell interior, facilitating a nearly simultaneous calcium ion (Ca^{2+}) release, and hence, contractions across the cell volume (Crocini et al., 2014). The initiation of the cell-wide Ca^{2+} transient occurs at specialised nanostructures called the cardiac junction or dyadic cleft, which lies in close apposition of the sarcolemma with the sarcoplasmic reticulum (Page and Surdyk-Droske, 1979). Upon depolarisation, the L-type Ca^{2+}channels located on the sarcolemma side of the dyad open, triggering the Ca^{2+} to enter the cell. The gap between the sarcolemma and the sarcoplasmic reticulum (SR) at the dyad is ∼10 nm and provides a restricted volume that concentrates the incoming Ca^{2+} to the levels required to trigger the opening of the SR Ca^{2+} released from the ryanodine receptor (RyR)-2, thereby, initiating a cell-wide Ca^{2+}release (Takeshima et al., 2000).

It is now well-recognised that the pathological remodelling of the ECC machinery, particularly the loss of t-tubules, is a major driver of the loss of contractile function in the failing heart. Several studies have demonstrated the loss of the t-tubules in heart failure (HF), including studies on animal models (Louch et al., 2006; Song et al., 2006; Heinzel et al., 2008) and humans (Heling et al., 2000; Crossman et al., 2011; Zhang et al., 2013; Guo et al., 2015; Wang et al., 2018). Furthermore, physiological studies have demonstrated that the loss of t-tubules is linked to the loss of cardiac function. Isolated myocyte studies have confirmed that cells lacking t-tubules, either from failing hearts or through experimental detubulation, have reduced and dyssynchronous Ca^{2+} release (Kawai et al., 1999; Louch et al., 2006; Song et al., 2006). Live-cell imaging of whole rat hearts demonstrated that t-tubule remodelling is correlated with cardiac function and precedes the development of HF, implicating its causative role in HF (Wei et al., 2010). In findings, it is consistent that the t-tubule remodelling in HF is associated with a loss of transverse components and an increase in axial components (Song et al., 2006). For example, we have reported that contractile function within the failing human heart is strongly associated with the number of transverse components (Crossman et al., 2015c). This would result in the loss of dyads or initiations sites required to trigger Ca^{2+} transients, as the transverse components of the t-tubules are aligned with the Z discs where the majority of the sarcoplasmic reticulum Ca^{2+} release channels and the RyR are located. Notably, a quantitative electron microscopy study has demonstrated that the loss of t-tubules is also associated with the loss of dyads in the failing human heart (Zhang et al., 2013).

The protein junctophilin (JPH)-2 is proposed as a key driver in the t-tubule remodelling in HF (Beavers et al., 2014). It forms a physical link between the plasma membrane and the RyR on the SR and is critical for the formation of dyads. The knockout of this protein is embryonically lethal, demonstrating that it is fundamental for life (Takeshima et al., 2000). Furthermore, cardiac-specific knockdown in adult mice results in the loss of t-tubule, impaired calcium handling, and the development of HF (Van-Oort et al., 2011). Super-resolution imaging of these animals revealed a loss of JPH co-localisation with the RyR (Munro et al., 2016). The JPH down-regulation was also found in the hypertrophic and dilated mouse models of HF (Minamisawa et al., 2004). In the rat thoracic aortic banding model of HF, there was a loss of t-tubules which is correlated with the drop in JPH expression (Wei et al., 2010). However, these results may be model dependent as JPH expression is not linked to t-tubule remodelling in the sheep and ferret models of HF (Caldwell et al., 2014). Nevertheless, reduced levels of JPH have been reported in human hypertrophic cardiomyopathy, dilated cardiomyopathy and ischaemic cardiomyopathy suggesting its important role in human HF (Landstrom et al., 2007; Zhang et al., 2013; Guo et al., 2015; Xiao et al., 2018). However, it is not known if the loss of co-localisation between JPH and RyR occurs in the failing human heart. This would be expected if the JPH down-regulation were driving the t-tubule remodelling.

Ryanodine receptors are organised into multiunit clusters within the cardiac myocytes which are responsible for producing Ca^{2+} sparks, which constitute the fundamental unit of Ca^{2+} release from the SR (Cheng et al., 1993). RyR clustering was first observed in electron microscopy studies where the giant tetrameric RyR molecule (∼2 MDa) was attributed to electron-dense particles packing the cardiac junctions with an approximate centre to centre spacing of 29 nm (Franzini-Armstrong et al., 1999). Epifluorescence and confocal microscopy of the immune-labelled cells and tissue have confirmed the organisation of RyR into rows of discrete puncta, aligned with the Z discs (Soeller et al., 2007). The co-labelling of the t-tubules revealed that many of the RyR puncta were not part of the cardiac junction (Jayasinghe et al., 2012b) and Ca^{2+} release from these clusters was thought to be initiated by Ca^{2+} released from neighbouring clusters (Soeller et al., 2007). However, it was not possible to acquire a detailed image of the RyR cluster organisation in diffraction-limited imaging due to the resolution limit of ∼250 nm. New insight was provided by the advent of super-resolution microscopy with a ∼10-fold improvement in the resolution which demonstrated that RyR cluster sizes in rat myocytes followed an exponential distribution dominated by very small clusters, many of which were not detected by the diffraction-limited imaging (Baddeley et al., 2009). Many of these small clusters were within <100 nm of the neighbouring clusters and were proposed to act functionally as a single calcium release unit (CRU) or supercluster (Baddeley et al., 2009).

A super-resolution imaging of atrial myocytes in sheep with persistent atrial fibrillation (AF) demonstrated that the RyR clusters were more densely crowded. The CRUs were larger and contained increased individual clusters, although the average cluster size was similar to control animals. This geometric arrangement was associated with a higher spark frequency, increased numbers of larger sparks, and slowed kinetics that would contribute to increased Ca^{2+} release in AF (Macquaide et al., 2015). Recently, a super-resolution imaging of rat ventricle myocytes with ischaemic HF identified smaller RyR clusters but organised into geometrically larger calcium release units containing more clusters but fewer RyRs (Kolstad et al., 2018). The increased fraction of smaller clusters were linked to a rise in the non-spark "silent" Ca^{2+} leaks. The larger dispersed CRUs were associated with an increased spark mass with slowed kinetics and desynchronised total Ca^{2+} transient (Kolstad et al., 2018). In a third study, expansion microscopy was used to examine the isolated right ventricular myocytes of a rat model with pulmonary hypertension that causes right-sided HF. This study revealed RyR cluster fragmentation as well as a non-uniform hyper-phosphorylation within the cluster centre with a diminished ability to initiate Ca^{2+} release in simulations (Sheard et al., 2019).

These data support the premise that RyR cluster organisation contributes to the kinetics of Ca^{2+} release within the myocyte. In contrast to these detailed animal model-based studies, the nanoscale organisation of RyR in human cardiac myocytes and the impact that disease may have on this organisation are currently unknown.

Recently, a 3D confocal microscopy study of the failing human heart identified a new previously unappreciated feature of t-tubule remodelling, namely, large flattened sheet-like structures called t-sheets. Their presence was associated with larger RyR-to-sarcolemma distances and delayed Ca^{2+} transient (Seidel et al., 2017a) compared with patients with fewer t-sheet structures. The authors suggested 2D imaging, which was used in previous studies and resulted in t-sheets mistakenly identified as axial tubules. In a different study of t-tubule changes in human hearts, we reported that dilated t-tubules in the failing human heart contain increased collagen, suggesting that fibrosis could be a contributing factor driving t-tubule remodelling (Crossman et al., 2017). We suspected that t-sheets, like dilated t-tubules, would also contain collagen. This proposition is supported by a previous study that used wheat germ agglutinin (WGA) labelling to visualise t-sheets (Seidel et al., 2017a). We identified that a major component of WGA labelling in the failing human heart was collagen VI (Crossman et al., 2017), an observation that indicates that t-sheets likely contain collagen.

The work presented here has three objectives: (1) To determine if reduced co-localisation of JPH and RyR is correlated with the loss of t-tubules and cardiac junctions previously documented in the failing human heart; (2) Determine if there are changes in RyR cluster organisation in human HF that could contribute to disrupted Ca^{2+} release in human HF; (3) Determine if t-sheets were associated with luminal collagen deposition and changes in RyR cluster organisation. To achieve these objectives we used a combination of confocal and super-resolution microscopy coupled with western blots to examine non-failing (NF) donor hearts and the hearts of patients with idiopathic dilated cardiomyopathy (IDCM).

METHODS

Human Cardiac Tissue

Idiopathic dilated cardiomyopathy tissue samples were obtained from the Auckland City Hospital, New Zealand. The NF human tissue was supplied by the Organ Donation New Zealand, and from the University of Sydney in collaboration with St Vincent's Hospital, Sydney. The human tissue used in this study was collected with the informed and written consent of transplant patients or from the families of the organ donors of NF hearts following the principles in the Declaration of Helsinki. Ethical approval was provided by the Health and Disability Ethics Committees in New Zealand (NTY/05/08/050/AM05), Human Research Ethics Committees at the University of Sydney (2016/7326), and St Vincent's Hospital (H03/118). The tissue samples were preserved as previously described (Crossman et al., 2017). The patient details are presented in **Table 1**.

Immunohistochemistry

For the direct stochastic optical reconstruction microscopy (dSTORM) imaging, sections with 10 µm thickness were cut from the frozen tissue blocks and mounted on coverslips coated with poly-d-lysine. The sections were then permeabilized with 1% Triton X100 in phosphate buffered saline (PBS) for 15 min, washed in PBS followed by incubation with FX signal enhancer (ThermoFisher) for 1 h. For JPH, RyR, and WGA labelling, the sections were incubated overnight at 4°C with polyclonal rabbit anti-JPH [1:100, custom made (Van-Oort et al., 2011)] and mouse monoclonal anti-RyR (1:100, MA3-916, ThermoFisher). The sections were washed and incubated with goat anti-rabbit Alexa Fluor 680 (1:100, ThermoFisher), rabbit anti-mouse Alexa Fluor 750 (1:100, ThermoFisher) and WGA Alexa Fluor 594 (1:200, ThermoFisher). For the RyR and WGA labelling, the sections were incubated similarly with anti-RyR (1:100, MA3-916, ThermoFisher), followed by goat anti-mouse Alexa Fluor 680 (1:100, ThermoFisher) and WGA Alexa Fluor 488 (1:100, ThermoFisher). For confocal imaging, the same general labelling procedure was followed. For Col-I, WGA, and RyR labelling, the sections were first incubated with rabbit anti-Col I (ab292, Abcam) and anti-RyR (1:100, MA3-916, ThermoFisher) followed by goat anti-rabbit Alexa Fluor 488 (1:100, ThermoFisher), goat anti-mouse Alexa Fluor 647 (1:100, ThermoFisher), and WGA Alexa Fluor 594 (1:200 ThermoFisher). For Col-VI and RyR labelling, the sections were first incubated with rabbit-anti Col-VI (1:100, ab6588, Abcam) and anti-RyR (1:100, MA3-916, ThermoFisher) followed by goat anti-rabbit Alexa Fluor 488 (1:200, ThermoFisher) and goat anti-mouse Alexa Fluor 647 (1:200, ThermoFisher).

Confocal Imaging

The samples prepared for confocal imaging were mounted in 90% glycerol in PBS. The samples previously used for super-resolution imaging were imaged in the switching buffer as described below. Confocal images were obtained on a Zeiss LSM 710 inverted confocal microscope. 3D image stacks were collected with a 63× NA 1.4 oil-immersion objective (94 × 94 pixel spacing, 250 nm Z-slicing). The image stacks were then deconvolved with the Richardson-Lucy algorithm as previously described (Soeller and Cannell, 1999). The volume rendering of t-sheets was performed with the 3D Viewer in the Fiji distribution of ImageJ and Paraview.

TABLE 1 | Donor and patient characteristics.

Donor			**IDCM**					
Age, y	**Sex**	**Code**	**Age, y**	**Sex**	**NYHA**	**LVEF, %**	**LVEDD, mm**	**LVESD, mm**
62	F		57	F	III	15	72	65
57	F		54	M	III–IV	18	80	74
54	F		52	M	III–IV	17	67	61
48	F	5.089	18	M	IV	15	68	65
53	M	4.083	49	F	III	21	74	64
44	F	5.090	48	F	III–IV	18	69	65
19	M	7.012	54	M	IV	∼35%	48	NA
			58	M	II–IV	9	82	NA
			21	M	III–IV	19	76	68
			60	M	I on LVAD	25	76	65
			17	F	III–IV	20	98	82
			21	M	III	14	90	82

NYHA, New York Heart Association classification; LVAD, left ventricle assist device; LVEF, left ventricle ejection fraction; LVEDD, left ventricle end-diastolic diameter; LVESD, left ventricle end-systolic diameter; Code, Sydney Heart Bank de-identified sample code.

Correlative Confocal and dSTORM Super-Resolution Imaging

The correlative confocal and super-resolution imaging was performed as previously described (Soeller et al., 2017). Briefly, the tissue sections were mounted with an imaging buffer containing 90% glycerol and 10 mM cysteamine (MEA) in PBS an hour before imaging. The dSTORM images were collected on a Nikon TE200 inverted total internal reflection microscope modified for dual colour localisation microscopy. This involved focusing a solid-state 671 nm laser through a 60x NA 1.49 oil-immersion TIRF objective (Nikon) as a highly inclined light sheet to achieve a $\sim 10^9$ W/m^2 non-TIRF illumination within a 20 µm-wide area up to several microns deep within the sample. The emitted light was then passed through a dichroic mirror (Q680LP, Chroma Technology) and an emission filter (XF3104-690ALP, Omega optical) before being split into two spectral channels using a custom-built splitter device built as previously described (Baddeley et al., 2011). This provided a 2D axial super-resolution imaging with a localisation precision of ∼15 nm as previously reported (Baddeley et al., 2011). There were numerous single RyR with a ∼30 nm full width half maximum. Fourier ring correlation indicated a resolution of ∼60 nm. The axial resolution of dSTORM was diffraction limited at ∼700 nm. The actively switching transversely orientated myocytes were imaged for 20,000–40,000 frames at a rate of 50 ms per frame. The light emitting from the sample was captured on two halves of the cooled EM-CCD chip of an IXon DV887DCS-BV camera (Andor Technology, Belfast). After a super-resolution imaging, correlative confocal Z-stacks of WGA labelling was captured to provide imaging of the t-tubules and cell border (see confocal imaging section for microscope details).

dSTORM Image Analysis

Custom written algorithms coded in Python were used to identify single-molecule events and determine fluorophore designation by ratio-metric analysis of camera channels (Baddeley et al., 2011). The localisations points were then rendered using jittered triangulation onto 5 nm × 5 nm pixel spacing 2D TIFF image. The colocalisation of RyR and JPH was determined using the method previously described (Jayasinghe et al., 2012a) with the addition of separating the labelling of RyR and JPH into the t-tubular, sarcolemma, and corbular regions based on a binary mask created from the correlative confocal image of WGA (Crossman et al., 2015a). The term "corbular" refers to the regions of the SR without cardiac junctions, alternatively called non-junctional SR. The RyR cluster size was calculated from the rendered images thresholded using the PYME signal fraction method set to 50%. The cluster sizes were then measured *via* a custom python code utilising the scipy ndimages library. A filter was applied to the measured sizes where all clusters areas below 1 RyR were excluded from the analysis. For the cluster edge to edge nearest neighbour distances, each cluster was iterated over with a Euclidean distance transform (EDT). A cluster with the lowest transform range from the selected cluster was determined to be the nearest neighbour. The superclusters were identified through an EDT of the RyR mask inverse and all pixels with the value $<$ 50 nm were selected. The cluster analyses were separated into the t-tubular, sarcolemma and corbular regions. The cluster and tetramer densities were expressed per cell area and rather than in the area of the t-tubular, sarcolemma and corbular masks. These structures were below the resolution limit and could not be accurately estimated for normalisation. The JPH event counts associated with each RyR cluster were measured using the regions of interest obtained from RyR cluster masks to measure events in the corresponding JPH channel. Each JPH image was normalised to the mean event count.

Western Blotting

Tissue samples were homogenised in urea/thiourea extraction buffer (87% glycerol, 7 M Urea, 2 M thiourea, 15 mM PBS at pH 8, 0.8% Triton X-100, 10 mM DTT, 5 mM EDTA, and complete protease inhibitor Roche). The homogenates were centrifuged (13,000 × g, 4°C, 10 min) and the supernatants were removed. The supernatants were assayed using the Bio-Rad protein assay to determine the loading concentration. The supernatants were then mixed with a loading buffer, incubated at 55°C for 15 min, and separated by SDS-PAGE (4–15% Mini-PROTEAN TGX Stain-Free, Bio-Rad,). The Trans-Blot Turbo Transfer System (Bio-Rad) was used to transfer proteins onto Polyvinylidene Fluoride (PVDF) membranes. The total protein concentration for the transfer efficiency and blot normalisation was assessed using the stain-free system. This involved exposing the gels to UV and imaging before and after transfer using the ChemiDoc MP System (Bio-Rad). For JPH, the staining blots were incubated with rabbit anti-JPH antibody [1: 1,000, custom made (Van-Oort et al., 2011)] overnight at 4°C, and then incubated with the goat anti-rabbit Alexa Fluor 647 antibody (1: 20,000, ThermoFisher) for 1 h at room temperature. For RyR, the staining blots were incubated with the mouse anti-RyR antibody (1:500, MA3-916, ThermoFisher) overnight at 4°C, and then incubated with the goat anti-mouse Alexa Fluor 647 antibody (1:20,000, ThermoFisher) for 1 h at room temperature. The blots were imaged at 700 nm with a 1 min integration time using the Odyssey Fc system (LI-COR Biosciences, Nebraska, USA).

Statistics

A Linear Mixed-Effects (LME) model was used to analyse the hierarchical nature of our data for colocalisation and RyR cluster parameters. For comparisons between NF and IDCM patients, the fixed effects were in the disease status (IDCM, NF) and cell region (t-tubules, sarcolemma, corbular) and the random effects were in the heart. For the analysis of the t-sheets, the fixed effects were in the cell region (t-sheets, t-tubules, none) and the random effects were in the heart. *A post-hoc* comparison of the marginal means was performed with a Sidak multiple comparisons test. For the assessment of the RyR cluster size and JPH counts a least-squares linear regression was used. For the comparison of western blot data, a two-tail *t*-test was utilised. Statistical tests were carried out in IBM SPSS Statistics 25.

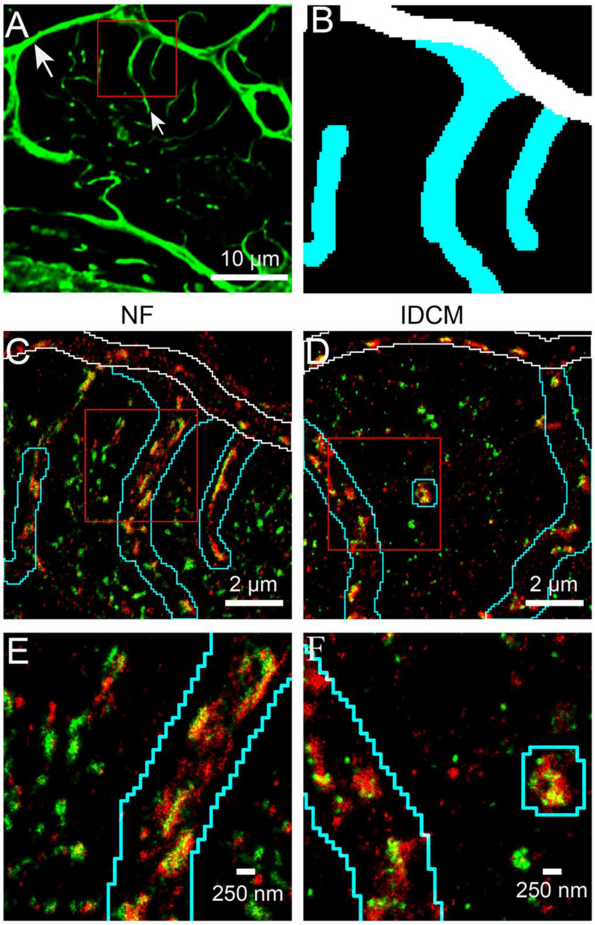

FIGURE 1 | Super-resolution imaging of RyR and JPH in donor and IDCM human cardiomyocytes segmented into t-tubular, sarcolemmal and corbular SR regions. **(A)** Confocal imaging of the WGA labelled donor cardiac myocyte (transversely orientated). The WGA labelling identifies the sarcolemma (large arrow) and t-tubules (small arrow). **(B)** Binary mask of regions near t-tubules (cyan), surface sarcolemma (white) and corbular SR (Black) generated from the WGA labelling of the red box in "**(A)**". **(C)** Super-resolution imaging of RyR (green) and JPH (red) in donor myocyte indicated by the red box in "**(A)**". The outline of the t-tubule mask is shown in cyan and the sarcolemma mask in white. Cellular areas outside these outlines contain the corbular SR. **(D)** Super-resolution image of RyR and JPH in an IDCM myocyte, outlines for t-tubule and sarcolemma masks as in "**(C)**". **(E)** Enlargement of the red box from donor myocyte in "**(C)**". **(F)** Enlargement of the red box from IDCM myocyte in "**(D)**".

RESULTS

Nanoscale Distribution of RyR and JPH

Super-resolution imaging was used to examine the nanoscale distribution of RyR and JPH in cardiac myocytes from NF and IDCM hearts (**Figure 1**). The distribution of these proteins was separated into cellular regions based on correlative confocal imaging as previously described (Soeller et al., 2017). This segmentation was achieved by labelling the sections with WGA that labels the t-tubules, sarcolemma, and extra-cellular matrix (**Figure 1A**). A binary mask was then created from the WGA labelling to separate the cell into the following cellular regions; t-tubule, surface sarcolemma, and corbular (**Figure 1B**). Visual inspection of the RyR and JPH labelling suggests there is a close association between the two proteins at the t-tubules and surface sarcolemma. The paradoxical appearance of RyR and JPH labelling within the t-tubule mask is due to the ∼700 nm Z resolution of 2D dSTORM. Within the corbular regions, there was an evident spatial separation in the RyR and JPH labelling compared with the other regions. Upon the visual inspection of the RyR and JPH distribution, there was no observable difference between the NF and IDCM human hearts.

A distance-based colocalisation analysis was used to quantify the relative nanoscale distribution of RyR and JPH in each of the three cellular compartments (**Figure 2**). This involved calculating the amount of RyR labelling as a function of distance, in 20 nm bins, from the edge of JPH labelling. The reverse, i.e., the amount of JPH labelling as a function of distance from the edge of RyR labelling, was also calculated.

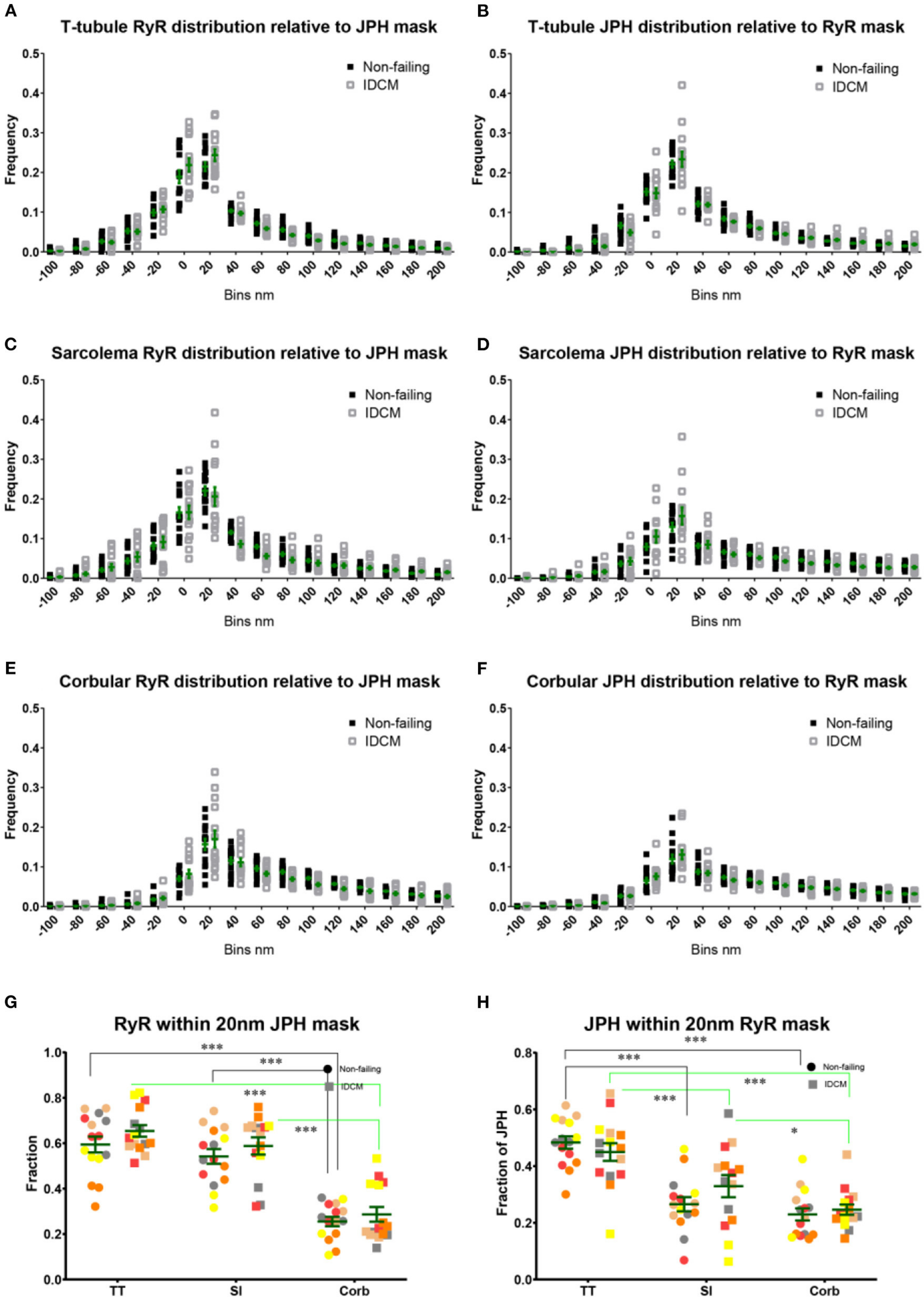

FIGURE 2 | Nanoscale distribution of RyR and JPH labelling in donor and IDCM human cardiac myocytes at t-tubular, sarcolemmal and corbular regions. **(A)** Frequency plot of RyR distribution relative to the mask of JPH labelling at the T-tubule regions. **(B)** Frequency plot of JPH distribution relative to the mask of RyR labelling at the T-tubule regions. **(C)** Frequency plot of RyR distribution relative to the mask of JPH labelling at the sarcolemmal regions. **(D)** Frequency plot of JPH

(Continued)

FIGURE 2 | distribution relative to the mask of RyR labelling at the sarcolemmal regions. **(E)** Frequency plot of RyR distribution relative to the mask of JPH labelling at the corbular SR regions. **(F)** Frequency plot of JPH distribution relative to the mask of RyR labelling at the corbular SR regions. **(G)** Total fraction of RyR with 20 nm of JPH mask for the t-tubular, sarcolemma and corbular SR regions. **(H)** Total fraction of JPH with 20 nm of RyR mask for the t-tubular, sarcolemma and corbular SR regions. Distributions were estimated from $n = 5$ donor hearts, $n = 5$ IDCM hearts, 3 cells were analysed from each heart. For "**(G,H)**" groups linked with a line are significantly different at either $p < 0.05$ and $p < 0.001$ as indicated by * and *** respectively. LME model was used to test for the effects of the disease status (IDCM, NF) and cell region (t-tubules, sarcolemma, corbular) and random effects were in the heart. *P*-values reported are *post-hoc* comparisons of marginal means using a Sidak test for multiple comparisons. Symbols of the same colour in "**(G,H)**" are from the same heart.

For simplicity, these parameters are herein referred to as RyR or JPH colocalisation, respectively. This distance-based analysis demonstrated a greater RyR colocalisation at the t-tubules and sarcolemma compared with the corbular regions (**Figures 2A,C,E**). A similar colocalisation pattern was seen for JPH (**Figures 2B,D,F**) confirming the visual impression of the labelling patterns. The ability to quantify the distribution of each protein in 20 nm bins allowed for selecting a biological relevant distance range to measure the total colocalisation for each protein. For the RyR and JPH, a total fraction of label within 20 nm of the mask of the other channel was chosen, based on the ∼27 nm size of RyRs (Wagenknecht et al., 1989). The total RyR and JPH colocalisation were calculated from the distance-based histogram analysis and are presented in **Figures 2G,H**, respectively. The Linear Mixed-Effects (LME) modelling found no change in the total RyR colocalisation between the NF and IDCM myocytes (0.46 ± 0.036 and 0.51 ± 0.036, respectively) but found a change in the total RyR colocalisation between the t-tubule, sarcolemma, and corbular regions (0.62 ± 0.029, 0.56 ± 0.029, and 0.27 ± 0.029, respectively, $p < 0.001$). A *post-hoc* pairwise comparison of the marginal means, in general, confirmed the findings from the LME model and are presented in **Figure 2G**. The total JPH colocalisation pattern was similar with LME model, finding no difference between the NF and IDCM myocytes (0.33 ± 0.028 and 0.34 ± 0.028, respectively) but a difference between the regions (0.47 ± 0.023, 0.3 ± 0.023, 0.24 ± 0.023, $p < 0.001$). A *post-hoc* pairwise comparison of the marginal means, in general, confirmed the findings from the LME model and are presented in **Figure 2H**. In summary, there was increased total colocalisation of both the RyR and JPH in the t-tubule and sarcolemma regions compared with the corbular regions in both NF and IDCM myocytes.

RyR Cluster Analysis

The RyR cluster size, RyR supercluster size and nearest neighbour distances between RyR clusters were estimated from the super-resolution images (**Figure 3**, **Supplementary Figure 2A**). For this analysis, The RyR images were converted to a binary mask of RyR clusters and were partitioned into the t-tubule, sarcolemma and corbular regions based on the masks generated from the correlative confocal WGA images (**Figures 3D,E**). The analysis of the RyR cluster sizes demonstrated an exponential distribution at the t-tubule, sarcolemma, and corbular regions with ∼60% of clusters containing less than five RyR tetramers with no appreciable difference in the distribution between the NF heart myocytes and IDCM myocytes (**Supplementary Figures 1A,C,E**). The LME model found no significant change in RyR cluster size between the NF and IDCM myocytes (13 ± 1.7 and 11 ± 1.7, respectively) but statistically significant ($p < 0.001$) differences were identified between the t-tubule, sarcolemma, and corbular regions (15 ± 1.4, 12 ± 1.4, and 10 ± 1.4). The *post-hoc* pairwise comparisons of the marginal means for this analysis are presented in **Figure 3E**. The LME model revealed no significant change in the RyR supercluster size between the NF and IDCM myocytes (18 ± 2.4 and 15 ± 2.4, respectively) but statistically significant ($p < 0.001$) differences were identified between the t-tubule, sarcolemma, and corbular regions (22 ± 1.9, 6 ± 1.9, and 13 ± 1.9). The *post-hoc* pairwise comparisons of the marginal means for this analysis are presented in **Supplementary Figure 2A**. The nearest neighbour distances between the RyR clusters also followed an exponential distribution at the t-tubule, sarcolemma, and corbular regions with ∼60% of the inter-cluster distances closer than 140 nm (**Supplementary Figures 1B,D,F**). The LME model analysis of inter RyR cluster distances revealed a significant ($p = 0.02$) difference between the NF and IDCM myocytes (131 ± 12, and 176 ± 12, respectively) and a significant ($p < 0.001$) difference between the t-tubule, sarcolemma, and corbular regions (114 ± 12, 182 ± 12, and 163 ± 12, respectively). The *post-hoc* pairwise comparisons between the groups are presented in **Figure 3F**. A smaller inter RyR cluster distance was identified at the sarcolemma and corbular SR in non-failing myocytes compared with IDCM myocytes ($p < 0.01$ and $p < 0.5$, respectively). The linear regression between the RyR cluster size and the mean JPH events within each cluster showed a poor fit in both the NF and IDCM myocytes (**Figure 3G**). However, a good fit was found between RyR cluster size and total JPH events in each cluster (**Figure 3H**). In summary, the RyR cluster sizes were similar in the NF and IDCM myocytes but reduced intercluster distances were observed in the NF myocytes relative to IDCM myocytes.

Quantification of RyR Expression

The western blot analysis revealed no change in the expression of JPH in the NF and IDCM left ventricle but there was a ∼2-fold decrease in the RyR expression in the IDCM tissue ($p = 0.02$, **Figures 4A,B**). To explore where these differences occurred within the cardiac myocytes, super-resolution images were quantified for the number of RyR clusters per cell area and the number of RyR tetramers per cell area (**Figures 4C,D**). The normalisation per cell area means that the number of clusters (or tetramers) per cell region, e.g., t-tubules, was normalised to total cell area, as an accurate estimation of the t-tubular area for normalisation was not possible from the diffraction-limited confocal imaging. The LME model showed that the mean RyR cluster density between the NF and IDCM myocytes was similar (1.1 ± 0.15 and 0.77 ± 0.15 clusters μm^{-2} respectively)

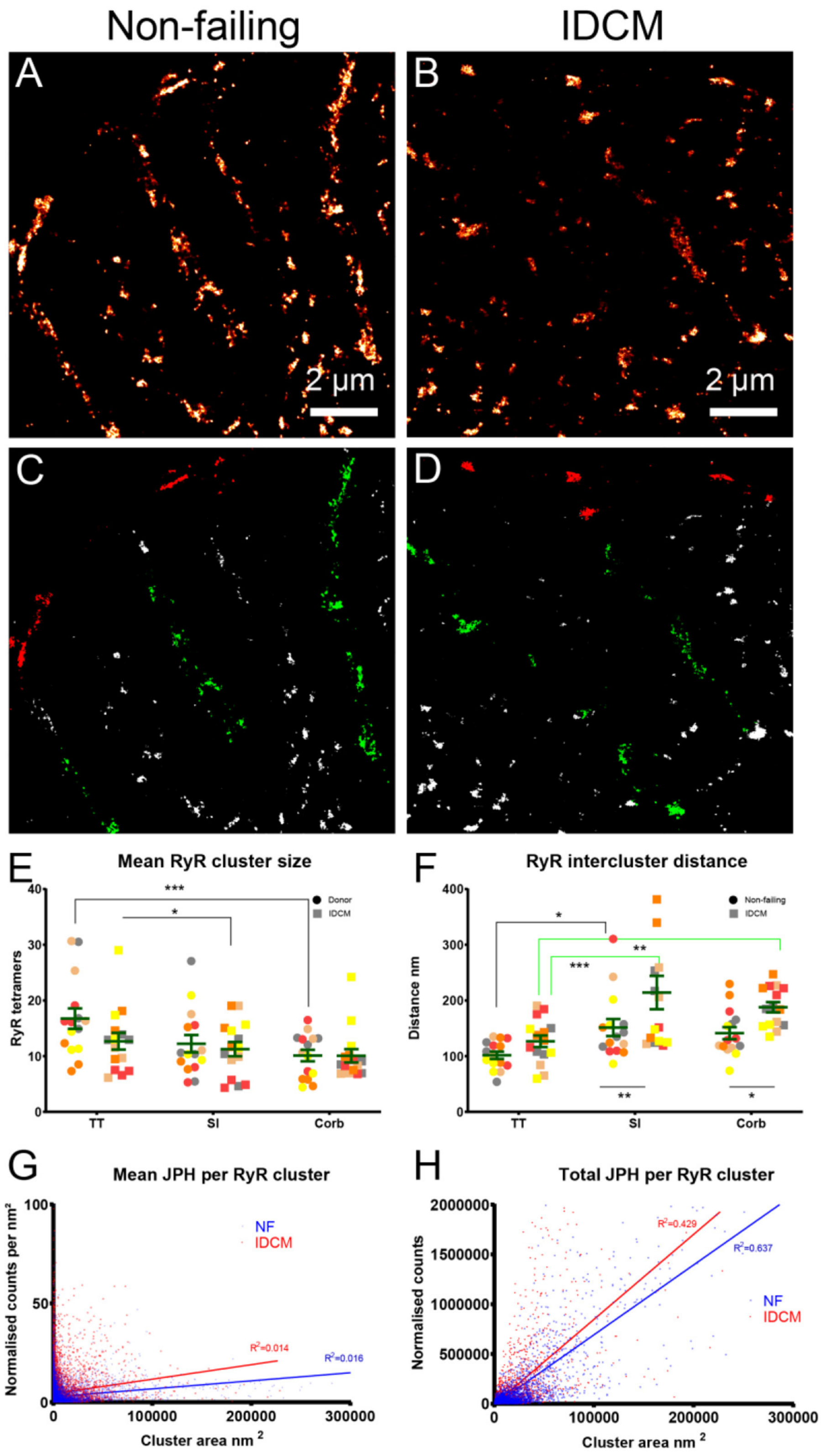

FIGURE 3 | Super-resolution imaging of RyR clusters in donor and IDCM human hearts. **(A)** RyR clusters in Donor myocyte. **(B)** RyR clusters in IDCM myocyte. **(C)** Binary mask of "**(A)**" segmented into TT (green), SI (red), and Corb regions (white). **(B)** RyR clusters in IDCM myocyte. **(D)** Binary mask of "**(B)**" segmented into TT, SI, and Corb regions. **(E)** Mean RyR clusters size in NF and IDCM hearts. **(F)** Mean RyR intercluster distance in NF and IDCM hearts. Symbols of the same colour in

(Continued)

FIGURE 3 | "**(E,F)**" are from the same heart. **(G)** Mean number of JPH counts per RyR cluster. **(H)** Total number of JPH counts per RyR cluster. Groups linked with a line are significantly different in *post-hoc* pairwise comparison at either $p < 0.05$, $p < 0.01$, and $p < 0.001$ as indicated by *, **, and *** respectively. LME model was used to test for the effects of disease status (IDCM, NF) and cell region (t-tubules, sarcolemma, corbular) and random effects were in the heart. *P*-values reported are *post-hoc* comparisons of marginal means using a Sidak test for multiple comparisons.

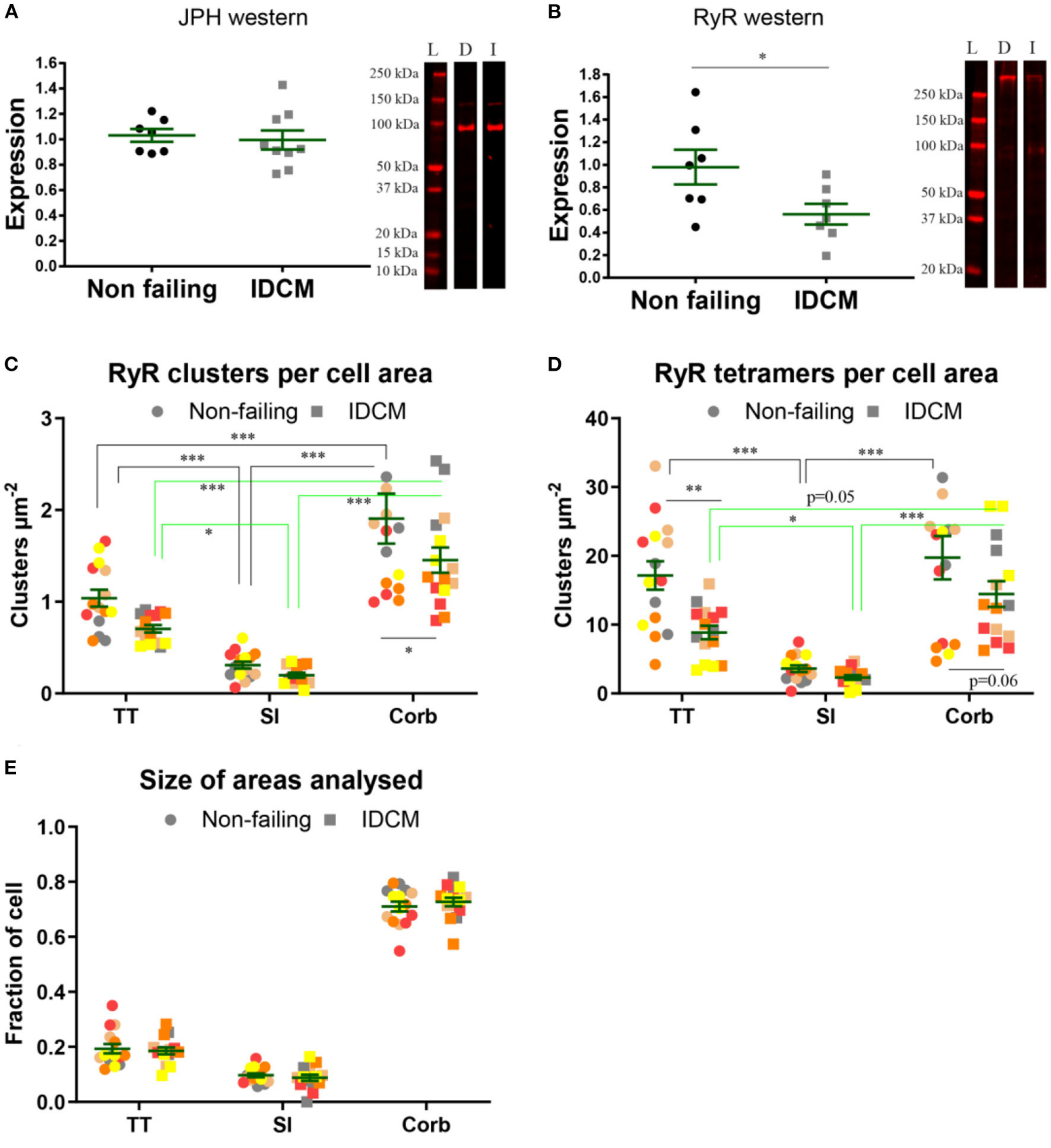

FIGURE 4 | Quantification of expression of JPH and RyR in normal and IDCM hearts. **(A)** JPH western, two-tailed *t*-test $p = 0.79$ $n = 8$ donor, and $n = 9$ IDCM hearts. **(B)** RyR western, two-tailed *t*-test $p = 0.02^*$ $n = 8$ donor, and $n = 7$ IDCM hearts. For each western exemplar, lanes are shown. L, ladder; D, donor; and I, IDCM. **(C)** Mean number of RyR clusters, $n = 5$ donor, $n = 5$ IDCM hearts, 3 cells were analysed from each heart. The number of clusters per cell area was calculated for TT, SI, Corb regions. **(C)** Mean number of RyR clusters per cell area coming from TT, SI, and Corb regions, $n = 5$ non-failing, $n = 5$ IDCM hearts, 3 cells were analysed from each heart. $P < 0.05^*$ for Corb. **(D)** Mean number of RyR tetramers per cell area coming from TT, SI, and Corb regions, from $n = 5$ non-failing, $n = 5$ IDCM hearts, 3 cells were analysed from each heart. $P < 0.05^*$ for TT and $P = 0.7$ for Corb. For "**(C,D)**" Groups linked with a line are significantly different at either $p < 0.05$, $p < 0.01$, and $p < 0.001$ as indicated by *, **, and *** respectively. LME model was used to test for the effects of the disease status (IDCM, non-failing) and cell region (t-tubules, sarcolemma, corbular) and random effects were in the heart. *P*-values reported are *post-hoc* comparisons of marginal means using a Sidak test for multiple comparisons. **(E)** Size of the area fractions TT, SI, and Corb analysed in "**(C,D)**". Note normalisation per cell area in "**(C,D)**" means the number of clusters (or tetramers) per cell region, e.g., t-tubules was normalised to total cell area, as an accurate estimation of t-tubular area for normalisation was not possible from diffraction-limited confocal imaging. Symbols of the same colour in "**(C–E)**" are from the same heart.

whereas, there were differences between the t-tubule, sarcolemma and corbular regions (0.9 ± 0.13, 0.26 ± 0.13, 1.7 ± 0.13, clusters μm^{-2}, respectively, $p < 0.001$). The *post-hoc* pairwise comparisons between the groups are presented in **Figure 4C**. The mean RyR tetramer density, however, was higher in the NF myocytes compared with IDCM myocytes in the LME model (14 ± 1.7 and 8.4 ± 1.7 tetramers μm^{-2}, respectively, $p = 0.03$). Furthermore, there were changes between the t-tubule, sarcolemma and corbular regions (13 ± 1.5, 2.9 ± 0.16, 17 ± 1.5, clusters μm^{-2}, respectively, $p < 0.001$). The *post-hoc* pairwise comparisons between the groups are presented in **Figure 4D**, notably, a decrease in RyR tetramers was found in the IDCM myocytes compared with NF myocytes at the t-tubular regions ($p < 0.01$). From these data, the main effect observed from analysing the super-resolution images was a reduction in the RyR tetramer density at the t-tubules in IDCM cells that correlates with the observed reduction of RyR expression in western blots in **Figure 4**.

3D Confocal Imaging of T-Sheets in IDCM Cardiac Myocytes

To investigate the structure of t-sheets, we used confocal microscopy due to its ability to capture 3D data in an extended volume, whereas, typically 3D dSTORM imaging is limited to a small axial range of ~1 µm deep. This is due to the out of focus bleaching limiting the capture at multiple Z-positions. The confocal Z-stacks, ~10 µm deep, of WGA labelled tissue were analysed to determine if the recently described t-sheets were present in the IDCM human heart samples (**Figure 5**). We did not observe t-sheets within the NF hearts. In all five IDCM hearts examined, the membrane structures exhibiting the characteristics of t-sheets were readily observed, i.e., large flattened membrane invaginations that display strong WGA labelling and have a sheet-like appearance when examined in 3D images. **Figure 5A** is an example of a cell with apparent "axial" t-tubules in a 2D view. However, close inspection of the confocal Z-stack demonstrated that these "axial" tubules persist for several microns within the image volume. A 3D rendering (**Figure 5B**) of the highlighted region reveals that these are sheet-like structures that are comparable to the t-sheets described by Seidel et al. (2017a). Furthermore, the careful examination of WGA-labelled IDCM heart tissue identified examples of t-sheets that extended along the lateral imaging plane of the confocal microscope (white arrows **Figures 5C,D**). At the higher resolution provided by in-plane imaging, it was observed that t-sheets are composed of multiple apparently "fused" t-tubules. Also, there are numerous regions where two or more adjacent t-tubules appeared to intertwine and become fused (white box **Figures 5E,F**).

Previously, we demonstrated that dilated t-tubules in IDCM hearts contain increased amounts of collagen (Crossman et al., 2017). To determine that collagen was a component of t-sheets, tissue sections were labelled for collagen types I and VI. The confocal Z-stacks of these tissue samples demonstrated sheet-like structures made up of multiple fibres of both types I and VI collagen (white arrows **Figures 5G,H**) consistent with the conclusion that the t-sheet luminal spaces also contain collagen.

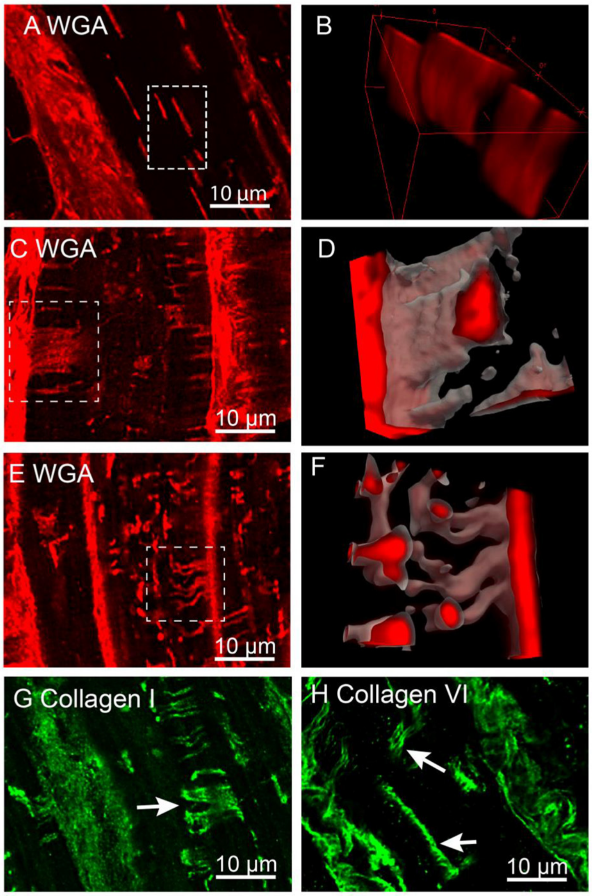

FIGURE 5 | Confocal imaging of t-sheets in the IDCM human heart. **(A)** WGA labelling of t-sheets that superficially appear as axial tubules in the single-plane image. **(B)** 3D projection of the white rectangular region from "**(A)**" confirm the presence of sheet-like structures. **(C)** Confocal stack Z-projection 1.5 µm deep of in-plane WGA labelled t-sheet (white arrow). **(D)** 3D projection of t-sheet from "**(C)**". **(E)** Confocal stack Z-projection 1.5 µm deep of WGA labelling indicating the presence of two t-tubules that have appeared to fuse (white arrow). **(F)** 3D projection of fused t-tubules from "**(E)**". **(G)** Confocal stack Z-projection 1.5 µm deep of collagen I labelling of t-sheets (white arrow). **(H)** Confocal stack Z-projection 1.5 µm deep of collagen VI labelling of t-sheets (white arrows). For each label $n = 5$ IDCM hearts, 3 cells were imaged from each heart.

To assess the organisation of RyR Ca^{2+} release clusters in relation to the t-sheets (**Figure 6**) confocal Z-stacks of WGA and RyR labelled HF tissue were captured. The RyR clusters were apparent and immediately adjacent to the t-sheets and appeared to follow the outline of the WGA labelling that delineates the t-sheets (**Figure 6B**). This was particularly apparent in the large oblique t-tubules where the normal striated appearance of RyR cluster rows was disrupted with the RyR clusters following the diagonal direction of the WGA labelling (**Figures 6C,D**). In the other enlarged but less prominently remodelled t-tubules, a similar association between the RyR clusters and WGA labelling was observed (**Figures 6E,F**). Of particular note, there were

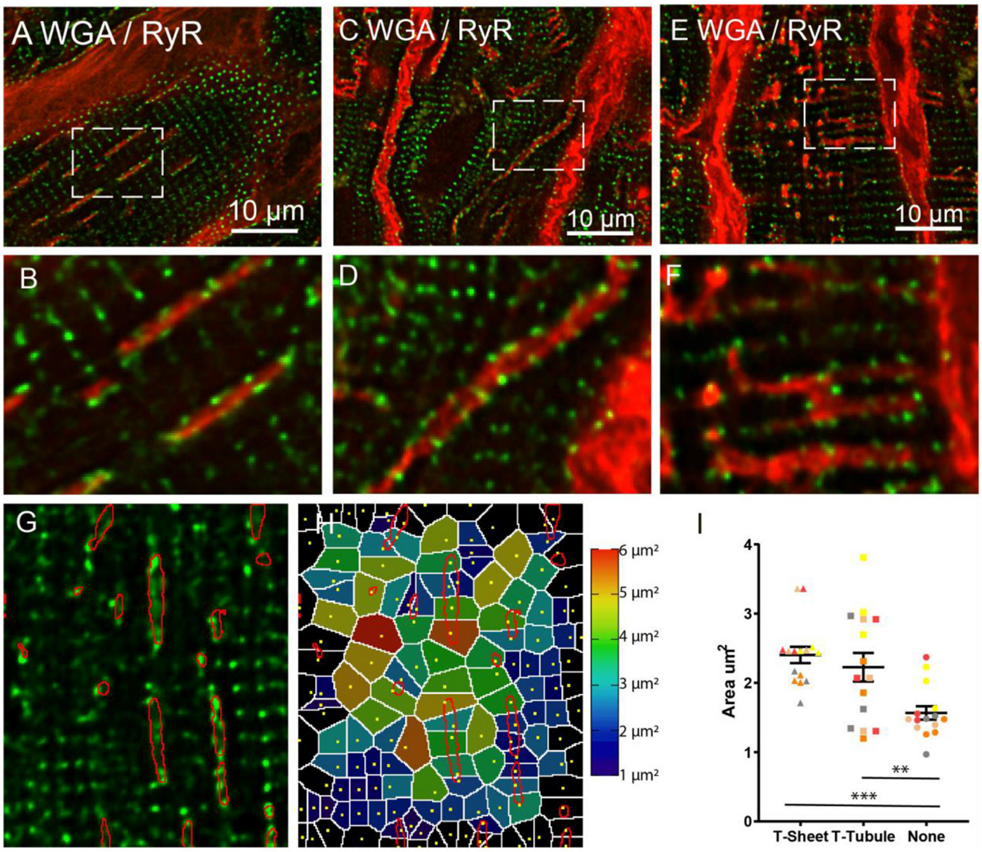

FIGURE 6 | Confocal imaging of WGA labelled t-sheets (red) and ryanodine receptors (green) in the IDCM human heart. **(A)** 1.5 µm Z-projection of t-sheets perpendicularly orientated to the image plane. The white arrow points to the plane image of the sarcolemma showing WGA labelling and RyR clusters. **(B)** Enlargement of the region in "**(A)**", note area between adjacent t-sheets lacking RyR. **(C)** T-sheet/enlarged oblique running t-tubule. **(D)** Enlargement of the region in "**(B)**", note area between adjacent to t-sheet/t-tubule lacking RyR. **(E)** Dilated t-tubules. **(F)** Enlargement of the white box in "**(E)**" showing fused t-tubules. **(G)** Single plane confocal image of region RyR labelling with t-sheet masks highlighted in red. **(H)** Voronoi diagram showing the area covered by each RyR cluster, RyR cluster location indicated by yellow dots. **(I)** The average Voronoi areas from regions with t-sheets, t-tubules, and no WGA labelling (None). For each region $n = 5$ IDCM hearts, 3 cells were imaged from each heart. $^{**}p < 0.01$ and $^{***}p < 0.001$. LME model was used to test for effects of the region (t-sheets, t-tubules, and no WGA labelling) and random effects were in the heart. *P*-values reported are *post-hoc* comparisons of marginal means using a Sidak test for multiple comparisons. Symbols of the same colour in "**(I)**" are from the same heart.

areas devoid of RyR clusters near the t-sheets and t-tubules (**Figure 6G**) that disrupted the usual sarcomeric grid-like pattern. To quantify these visual observations, we analysed the RyR clusters in regions associated with t-sheets, t-tubules and with no WGA. This involved determining RyR cluster centroids; from these centroids, a Voronoi diagram was generated which determined the area of pixels that were closest to the particular centroid relative to other centroids (**Figure 6H**). The associated Voronoi areas provided an index that is inversely proportional to local RyR density. The LME model revealed a difference in the mean Voronoi areas between the t-sheet, t-tubule and regions without WGA staining (2.4 ± 0.1, 2.2 ± 0.1, and 1.6 ± 0.1, respectively, $p < 0.001$). A *post-hoc* comparison of the marginal means demonstrated that the t-sheets and t-tubule regions had greater Voronoi areas (i.e., lower local RyR density) than regions without WGA labelling ($p < 0.001$ and 0.01, respectively, **Figure 6I**).

Super-Resolution Imaging of RyR Clusters at T-Sheets

We used super-resolution microscopy to provide a nanoscale analysis of the RyR clusters at both the t-sheet and t-tubule regions of the IDCM myocytes to determine if t-sheet remodelling drives nanoscale changes in the RyR cluster organisation (**Figure 7**). Epifluorescence microscopy of WGA labelling was first used to identify transversely orientated cell regions containing either t-tubules or t-sheets (**Figures 7A,B**). In the same region, super-resolution microscopy was then used to acquire images of the RyR clusters (**Figures 7C,D**). The analysis of the RyR cluster sizes revealed an exponential distribution with ∼60% of the clusters containing less than five RyR tetramers with no appreciable difference in the distribution between the t-tubule and t-sheet regions (**Supplementary Figure 1G**). The LME model of the mean RyR cluster sizes demonstrated no statistical difference between

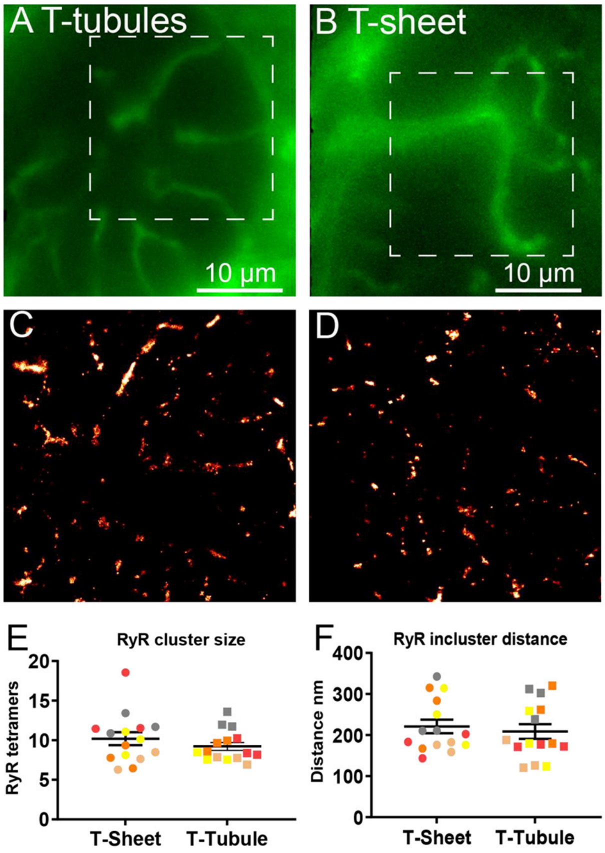

FIGURE 7 | Comparison of RyR clusters between t-tubules and t-sheets regions in IDCM human hearts. **(A)** Epifluorescence image of WGA labelled t-tubules recorded on super-resolution microscope before subsequent nanoscale imaging of RyR clusters. **(B)** Epifluorescence image of WGA labelled t-sheet recorded on super-resolution microscope before subsequent nanoscale imaging of RyR clusters. The t-sheet identification was confirmed by changing the focus by several microns and the structure designated a t-sheet if it was visible throughout the change in focus. **(C)** Super-resolution image of RyR clusters from t-tubular region recorded from the white box in "**(A)**". **(D)** Super-resolution image of RyR clusters from t-sheet region recorded from the white box in "**(B)**". **(E)** Mean RyR cluster size in the t-tubule and t-sheet regions. **(F)** Mean RyR cluster nearest neighbour distance in the t-tubule and t-sheet regions. Five IDCM hearts were analysed with 3 t-tubule and 3 t-sheet regions imaged from each heart. LME model was used to test for effects of the region (t-sheets and t-tubules) and random effects were in the heart. For RyR cluster size $p = 0.53$ and for RyR cluster nearest neighbour $p = 0.19$. Symbols of the same colour in "**(E,F)**" are from the same heart.

t-tubules and t-sheets (**Figure 7E**). Similarly, superclusters were not statistically different between t-tubules and t-sheets (**Supplementary Figure 2B**). The nearest neighbour distances between the RyR clusters also followed an exponential distribution with ∼60% of the inter-cluster distances closer than 140 nm (**Supplementary Figure 1H**). The LME model of the mean RyR nearest neighbour distances demonstrated no statistical difference between t-tubules and t-sheets (**Figure 7F**).

DISCUSSION

RyR and JPH Co-Localisation

We found that there is an increased co-localisation between RyR and JPH at the t-tubules and sarcolemmas compared with corbular regions. This finding is consistent with the role of JPH in forming cardiac junctions by providing a structural link between the SR and sarcolemma (Takeshima et al., 2000). However, contrary to our *a priori* hypothesis, we found no change in the co-localisation of the RyR with the JPH between the donor and end-stage IDCM myocytes. Furthermore, the western blot analysis showed no change in JPH expression. These data suggest that changes in JPH expression are not primarily responsible for t-tubule remodelling in the IDCM hearts we examined. Previously, the knockdown of JPH expression in mice reduced the colocalisation of RyR and JPH (Munro et al., 2016), promoted t-tubule remodelling and resulted in the loss of cardiac junctions, and impaired calcium release that resulted in acute HF (Van-Oort et al., 2011). Furthermore, downregulation of JPH has been observed in several animal models and in human HF including dilated cardiomyopathy (DCM) (Minamisawa et al., 2004; Landstrom et al., 2007; Wei et al., 2010; Zhang et al., 2013; Guo et al., 2015; Wang et al., 2018; Xiao et al., 2018).

These conflicting observations, explained by the downregulation of JPH in experimental HF, is not a consistent finding and may be model specific. For example, tachycardia-induced HF in sheep and thoracic aortic banding in ferrets result in HF with t-tubule loss but no change in JPH expression (Caldwell et al., 2014). With regards to human HF, the samples in our study are clinically described as idiopathic DCM whereas in other publications were described as non-specified DCM (Zhang et al., 2013; Guo et al., 2015; Xiao et al., 2018). It is thus, possible, that the DCM samples between the studies represent different aetiologies. DCM is a multifactorial disease that can result from a diverse range of causes including inherited mutations, infection and inflammation, autoimmunity, metabolic syndrome, and peripartum cardiomyopathy (Schultheiss et al., 2019). Idiopathic and inherited forms are the most commonly recorded cases of DCM. However, to accurately identify a case as idiopathic, it would require the exclusion of all known causes of DCM, which presents a diagnostic challenge, particularly as the availability of the required diagnostic procedures vary widely between hospitals (Schultheiss et al., 2019). The data shown here indicate that in at least some forms of DCM, JPH down-regulation does not appear to be the driving factor in t-tubule remodelling. This conclusion is supported by a recent study that found no change in the mRNA levels of JPH in DCM patients (Frisk et al., 2021). Furthermore, the JPH cluster density did not change between the non-failing and HF hearts, although there was a decrease with age in the non-failing heart (Lyu et al., 2021). JPH has been proposed as a therapeutic target for HF to improve the t-tubule structure and cardiac function (Reynolds et al., 2016). Our data suggest that this may only be effective in certain subpopulations of patients. This highlights the need for personalised medicine where underlying molecular defects can be characterised so that targeted therapies can be utilised effectively. This goal could be achieved by greater utilisation of endomyocardial biopsy and a combination of molecular methods including confocal and super-resolution microscopy to identify the underlying pathology involved (Crossman et al., 2015b).

RyR Expression and Cluster Geometry

The data presented here indicate an overall reduction in the density of RyR within IDCM cardiac myocytes and may contribute to the reduced Ca^{2+} release as previously documented in myocytes from the failing human heart (Beuckelmann et al., 1992) and should be considered alongside the well-documented defects in sarcoplasmic reticulum Ca^{2+} ATPase SERCA expression in HF (Lipskaia et al., 2010). This conclusion is supported by the ∼50% reduction of RyR expression in IDCM hearts as measured by the western blot. Previous analyses have produced conflicting results (Hasenfuss et al., 1997). Our results were confirmed through super-resolution microscopy and the difference between studies may reflect the underlying pathology. Super-resolution imaging indicated that the reduced expression of RyR was predominately due to the decreased RyR cluster density, as previously documented (Crossman et al., 2011) and to a lesser extent, a change in the RyR cluster size. In IDCM, RyR cluster density was lower at the corbular regions as measured by both the increased RyR inter-cluster distance and the decreased number of RyR clusters. An increased distance between non-junction RyR clusters could reduce the ability of the calcium transient to propagate to adjacent non-junctional RyR clusters. This could have a substantial impact as a large portion of RyR clusters are non-junctional in human ventricular myocytes (Crossman et al., 2011; Seidel et al., 2017a) (**Figure 4**). This contrasts with the rat ventricular myocytes where the junctional clusters dominate (Jayasinghe et al., 2009, 2012b; Scriven et al., 2010) but is closer to the rabbit, pig, and dog ventricular myocytes (Sachse et al., 2009, 2012; Biesmans et al., 2011).

In IDCM myocytes there was a trend for smaller t-tubular RyR clusters (∼24%) and reduced t-tubule RyR cluster density (∼35%), although this did not reach statistical significance. However, the total t-tubular RyR tetramers per cell decreased by ∼50% in the IDCM myocytes, a parameter that includes the effects of both RyR cluster size and density. Decreased t-tubular RyR tetramers would likely reduce the release flux of junctional Ca^{2+} release thereby reducing the amplitude of the Ca^{2+} transient. Overall, the RyR cluster and supercluster size did not differ between the donor and IDCM myocytes. However, there were larger RyR clusters and superclusters at the t-tubular and sarcolemmal regions compared with the corbular regions in NF myocytes. This size difference between the junctional and non-junctional RyR clusters was lost in the IDCM myocytes. Larger junctional RyR clusters size may increase their sensitivity to trigger Ca^{2+} because the larger RyR clusters size was found to increase the frequency of spontaneous sparks in the rat ventricular myocytes (Galice et al., 2018). In summary, the loss of RyR tetramers and reduced cluster sizes at the t-tubules in IDCM could reduce the potential of junctional RyRs to activate. This would be further exacerbated by the increased distances between the non-junctional RyR clusters, decreasing the ability of the cell to generate a robust calcium transient.

T-Sheets in Human Heart Failure

In agreement with Seidel et al. (2017a), we identified t-sheets in all of our IDCM human hearts. The 3D confocal imaging of the WGA-labelled sections several microns deep allowed the extent of t-sheet structures to be visualised (**Figure 5**). In general, only parts of the t-sheets could be visualised in single confocal micrographs (**Figure 5A**) notably when viewed in isolation, i.e., 2D optical sections could be mistaken for axial tubules (Seidel et al., 2017a). Careful examination of the tissue sections captured t-sheets orientated parallel to the imaging plane providing the benefit of a ∼3-fold higher lateral resolution (**Figure 5C**). These images indicated that t-sheets had the appearance of several t-tubules that had fused, compatible with the idea that t-sheets may represent an advanced state of the t-tubule remodelling. Furthermore, there were numerous examples of small or perhaps "immature" t-sheets that contained only two t-tubules that were fused over only part of their lengths (**Figure 5D**). Consistent with this proposition, more t-sheets were found in patients with prolonged HF, and in patients that failed to functionally recover while mechanically unloaded with a left ventricle assist device (Seidel et al., 2017a). These data suggest that t-sheets are associated with the pathology of advanced HF.

We have previously proposed that increased fibrosis could directly drive the remodelling of t-tubules based on the finding of increased collagen, particularly type VI, within the lumen of the t-tubules in IDCM patients (Crossman et al., 2017). Here, we report multiple reticular fibres (Ushiki, 2002), of both type I and type VI collagen, within the t-sheets indicating that fibrosis could drive both t-tubule and t-sheet remodelling in HF. This suggests a direct link between load, fibrosis, and t-tubule disarray. Consistent with this hypothesis, t-tubule remodelling, including the formation of t-sheets, was associated with local fibrosis in a rabbit model of myocardial infarction (Seidel et al., 2017b). Notably, in that study, the fibrosis was estimated based on WGA labelling. We have previously demonstrated that collagen VI comprises a large component of the WGA signal (Crossman et al., 2017) indicating that this collagen may also be a feature of t-tubule/t-sheet remodelling in this animal model.

RyR Clusters Organisation at T-Sheets and T-Tubules

The confocal analysis demonstrated that the WGA labelled t-sheets and t-tubules colocalised with numerous RyR clusters. Presumably, these RyR clusters would be directly stimulated by the action potential which travels down the t-tubules. Given the tortuous and highly variable t-sheet and t-tubule architecture in the myocytes of the IDCM myocardium, this would be expected to lead to highly variable and asynchronous Ca^{2+} release and contraction compared to the much more regular organisation of the t-tubules and RyR in the non-failing myocardium (Crossman et al., 2011). Notably, the RyR clusters appeared to follow the morphology of remodelled t-sheets/t-tubules breaking the symmetry of RyR cluster organisation. For example, this was particularly noticeable in regions with oblique running t-tubules (**Figure 6B**) where there was a diagonal arrangement of RyR clusters along with the WGA labelling that disrupted the usual sarcomere grid-like arrangement of the RyR clusters. These observations indicate that the process that drives the t-tubule remodelling also leads to a disruption in the organisation of the sarcoplasmic reticulum and agrees with previous electron tomography that revealed remodelling of both t-tubules and the sarcoplasmic reticulum in the failing sheep heart (Pinali et al., 2013). Moreover, we noticed that many regions adjacent to the t-sheet and t-tubules in the failing heart had an absence of RyR clusters that was quantified by the enlarged Voronoi areas in these regions. A similar finding has been found for dyssynchronous HF in dogs where increased RyR density has been reported in regions of reduced t-tubule density at cell ends (Li et al., 2015). The Voronoi areas give an estimate of the area that would be dominated by Ca^{2+} released from its respective RyR centroid assuming uniform Ca^{2+} release. Larger Voronoi areas indicate a sparser local density of RyR clusters and these would be expected to contribute to the slowed Ca^{2+} release in these regions, consistent with the previously documented delayed Ca^{2+} release documented in the failing human heart (Beuckelmann et al., 1992). Super-resolution imaging of the RyR cluster geometry found no difference in the RyR cluster size and RyR inter-cluster distances between the cell regions with t-tubules and cell regions with t-sheets (**Figure 7**) and agrees with the confocal data on the Voronoi cell size, an independent measure of RyR cluster density. Therefore, our data indicate that t-sheet remodelling has a negligible effect on RyR clusters size.

LIMITATIONS

Cardiac junctions have a reported gap of ∼10 nm (Takeshima et al., 2000) estimated from electron microscopy measurements, which is less than the ∼30 nm resolution we previously reported for our dSTORM microscopy (Baddeley et al., 2011). Therefore, it is not possible to draw a definitive conclusion on the remodelling of cardiac junctions with the methods we employed. Furthermore, our study was based on a 2D analysis that will not resolve the complex 3D geometry previously reported for the RyR imaged in the isolated rat cardiac myocytes (Shen et al., 2019). This is largely a technical issue associated with imaging optically thick tissue sections that will likely be resolved in the future. Moreover, the regions corresponding to the t-tubules, sarcolemma and corbular were estimated from diffraction-limited confocal imaging and therefore reflect a generalised region rather than a precise measurement of these sub-resolution structures.

CONCLUSIONS

Given the previous reports on the expression of JPH in HF, we expected a reduced co-localisation of RyR and JPH in IDCM. However, we found that there was no change in the distribution of RyR and JPH at the nano-scale. In addition, western blot analysis found no change in the JPH protein expression but did report a downregulation of RyR. Analysis of the RyR cluster sizes identified a similar near-exponential size distribution as previously identified in rodents. The average RyR cluster size was not changed in HF but the density of total RyRs was decreased in agreement with western blot data. Confocal microscopy identified that t-sheets were present in all HF examples examined and that these were associated with the presence of reticular collagen fibres within their lumen. Super-resolution imaging demonstrated no difference in RyR clusters in cell regions containing t-sheets compared to cell regions containing t-tubules.

DATA AVAILABILITY STATEMENT

The raw data supporting the conclusions of this article will be made available by the authors, without undue reservation.

ETHICS STATEMENT

The studies involving human participants were reviewed and approved by the human tissue used in this study was collected with the informed and written consent of transplant patients or from the families of organ donors of non-failing hearts in accordance with the principles in the Declaration of Helsinki. Ethical approval was provided by Health and Disability Ethics Committees New Zealand (NTY/05/08/050/AM05), Human Research Ethics Committees at the University of Sydney (2016/7326), and St Vincent's Hospital (H03/118). The patients/participants provided their written informed consent to participate in this study.

AUTHOR CONTRIBUTIONS

DC, CS, and YH contributed to the conception, design, and drafting of the manuscript. YH, DC, JB, XS, OL, AL, SL, CR, and PR contributed to the data acquisition and experiments. DC, YH, CS, and DB contributed to the data analysis. All authors revised and approved the manuscript.

ACKNOWLEDGMENTS

We gratefully acknowledge the assistance of Auckland City Hospital and St Vincent's Hospital staff for their assistance in obtaining tissue, and transplant recipients, and donor families for donating tissue. We are grateful for the financial support provided by the Health Research Council of New Zealand (Project Grants: DJC and SC) and the Auckland Medical Research Foundation (Project Grant: DC).

SUPPLEMENTARY MATERIAL

The Supplementary Material for this article can be found online at: https://www.frontiersin.org/articles/10.3389/fphys.2021.724372/full#supplementary-material

REFERENCES

Baddeley, D., Crossman, D., Rossberger, S., Cheyne, J. E. J. E., Montgomery, J. M. J. M., Jayasinghe, I. D. I. D., et al. (2011). 4D super-resolution microscopy with conventional fluorophores and single wavelength excitation in optically thick cells and tissues. *PLoS ONE* 6:e20645. doi: 10.1371/journal.pone.0020645

Baddeley, D., Jayasinghe, I. D., Lam, L., Rossberger, S., Cannell, M. B., and Soeller, C. (2009). Optical single-channel resolution imaging of the ryanodine receptor distribution in rat cardiac myocytes. *Proc. Natl. Acad. Sci. U.S.A.* 106, 22275–22280. doi: 10.1073/pnas.0908971106

Beavers, D. L., Landstrom, A. P., Chiang, D. Y., and Wehrens, X. H. T. (2014). Emerging roles of junctophilin-2 in the heart and implications for cardiac diseases. *Cardiovasc. Res.* 103, 198–205. doi: 10.1093/cvr/cvu151

Bers, D. (2002). Cardiac excitation–contraction coupling. *Nature* 415, 198–205. doi: 10.1038/415198a

Beuckelmann, D. J., Näbauer, M., and Erdmann, E. (1992). Intracellular calcium handling in isolated ventricular myocytes from patients with terminal heart failure. *Circulation* 85, 1046–55. doi: 10.1161/01.CIR.85.3.1046

Biesmans, L., Macquaide, N., Heinzel, F. R., Bito, V., Smith, G. L., and Sipido, K. R. (2011). Subcellular heterogeneity of ryanodine receptor properties in ventricular myocytes with low T-tubule density. *PLoS ONE* 6:e25100. doi: 10.1371/journal.pone.0025100

Caldwell, J. L., Smith, C. E., Taylor, R. F., Kitmitto, A., Eisner, D., a, Dibb, K. M., et al. (2014). Dependence of cardiac transverse tubules on the BAR domain protein amphiphysin II (BIN-1). *Circ. Res.* 115, 986–996. doi: 10.1161/CIRCRESAHA.116.303448

Cheng, H., Lederer, W. J. J., and Cannell, M. B. B. (1993). Calcium sparks: elementary events underlying excitation-contraction coupling in heart muscle. *Science* 262, 740–744. doi: 10.1126/science.8235594

Crocini, C., Coppini, R., Ferrantini, C., Yan, P., Loew, L. M., Tesi, C., et al. (2014). Defects in T-tubular electrical activity underlie local alterations of calcium release in heart failure. *Proc. Natl. Acad. Sci. U.S.A.* 111, 15196–15201. doi: 10.1073/pnas.1411557111

Crossman, D. J., Hou, Y., Jayasinghe, I., Baddeley, D., and Soeller, C. (2015a). Combining confocal and single molecule localisation microscopy: a correlative approach to multi-scale tissue imaging. *Methods* 88, 45–55. doi: 10.1016/j.ymeth.2015.03.011

Crossman, D. J., Ruygrok, P. N., Hou, Y. F., and Soeller, C. (2015b). Next-generation endomyocardial biopsy: the potential of confocal and super-resolution microscopy. *Heart Fail. Rev.* 20, 203–214. doi: 10.1007/s10741-014-9455-6

Crossman, D. J., Ruygrok, P. R., Soeller, C., and Cannell, M. B. (2011). Changes in the organization of excitation-contraction coupling structures in failing human heart. *PLoS ONE* 6:e17901. doi: 10.1371/annotation/061613ea-0f01-420f-bc3f-af36e5c35790

Crossman, D. J., Shen, X., Jüllig, M., Munro, M., Hou, Y., Middleditch, M., et al. (2017). Increased collagen within the transverse tubules in human heart failure. *Cardiovasc. Res.* 113, 879–891. doi: 10.1093/cvr/cvx055

Crossman, D. J., Young, A. A., Ruygrok, P. N., Nason, G. P., Baddelely, D., Soeller, C., et al. (2015c). t-tubule disease: Relationship between t-tubule organization and regional contractile performance in human dilated cardiomyopathy. *J. Mol. Cell. Cardiol.* 84, 170–178. doi: 10.1016/j.yjmcc.2015.04.022

Franzini-Armstrong, C., Protasi, F., and Ramesh, V. (1999). Shape, size, and distribution of Ca(2+) release units and couplons in skeletal and cardiac muscles. *Biophys. J.* 77, 1528–1539. doi: 10.1016/S0006-3495(99)77000-1

Frisk, M., Le, C., Shen, X., Hou, Y., Manfra, O., Silva, G. J. J., et al. (2021). Etiology-dependent impairment of diastolic cardiomyocyte calcium homeostasis in heart failure with preserved ejection fraction. *J. Am. Coll. Cardiol.* 77, 405–419. doi: 10.1016/j.jacc.2020.11.044

Galice, S., Xie, Y., Yang, Y., Sato, D., and Bers, D. M. (2018). Size matters: Ryanodine receptor cluster size affects arrhythmogenic sarcoplasmic reticulum calcium release. *J. Am. Heart Assoc.* 7, 1–13. doi: 10.1161/JAHA.118.008724

Guo, A., Hall, D., Zhang, C., Peng, T., Miller, J. D., Kutschke, W., et al. (2015). Molecular determinants of calpain-dependent cleavage of junctophilin-2 protein in cardiomyocytes. *J. Biol. Chem.* 290, 17946–17955. doi: 10.1074/jbc.M115.652396

Hasenfuss, G., Meyer, M., Schillinger, W., Preuss, M., Pieske, B., and Just, H. (1997). Calcium handling proteins in the failing human heart. *Basic Res. Cardiol.* 92, 87–93. doi: 10.1007/BF00794072

Heinzel, F. R., Bito, V., Biesmans, L., Wu, M., Detre, E., von Wegner, F., et al. (2008). Remodeling of T-tubules and reduced synchrony of Ca2+ release in myocytes from chronically ischemic myocardium. *Circ. Res.* 102, 338–346. doi: 10.1161/CIRCRESAHA.107.160085

Heling, A., Kostin, S., Maeno, Y., Hein, S., Devaux, B., Bauer, E., et al. (2000). Extracellular proteins in failing human myocardium. *Circ. Res.* 86, 846–853. doi: 10.1161/01.RES.86.8.846

Jayasinghe, I. D., Baddeley, D., Kong, C. H. T., Wehrens, X. H. T., Cannell, M. B., and Soeller, C. (2012a). Nanoscale organization of junctophilin-2 and ryanodine receptors within peripheral couplings of rat ventricular cardiomyocytes. *Biophys. J.* 102, L19–L21. doi: 10.1016/j.bpj.2012.01.034

Jayasinghe, I. D., Cannell, M. B., and Soeller, C. (2009). Organization of ryanodine receptors, transverse tubules, and sodium-calcium exchanger in rat myocytes. *Biophys. J.* 97, 2664–2673. doi: 10.1016/j.bpj.2009.08.036

Jayasinghe, I. I. D., Crossman, D. D. J., Soeller, C., and Cannell, M. B. M. (2012b). Comparison of the organization of T-tubules, sarcoplasmic reticulum and ryanodine receptors in rat and human ventricular myocardium. *Clin. Exp. Pharmacol. Physiol.* 39, 469–476. doi: 10.1111/j.1440-1681.2011.05578.x

Kawai, M., Hussain, M., and Orchard, C. H. (1999). Excitation-contraction coupling in rat ventricular myocytes after formamide-induced detubulation. *Am. J. Physiol.* 277, H603–H609. doi: 10.1152/ajpheart.1999.277.2.H603

Kolstad, T. R., van den Brink, J., Macquaide, N., Lunde, P. K., Frisk, M., Aronsen, J. M., et al. (2018). Ryanodine receptor dispersion disrupts Ca 2+ release in failing cardiac myocytes. *Elife* 7:e39427. doi: 10.7554/eLife.39427.022

Landstrom, A. P., Weisleder, N., Batalden, K. B., Martijn Bos, J., Tester, D. J., Ommen, S. R., et al. (2007). Mutations in JPH2-encoded junctophilin-2 associated with hypertrophic cardiomyopathy in humans. *J. Mol. Cell. Cardiol.* 42, 1026–1035. doi: 10.1016/j.yjmcc.2007.04.006

Li, H., Lichter, J., Seidel, T., Tomaselli, G. F., Bridge, J. H., S. F., et al. (2015). Cardiac resynchronization therapy reduces subcellular heterogeneity of ryanodine receptors, T-tubules, and Ca2+ sparks produced by dyssynchronous heart failure. *Circ Hear. Fail* 8, 1105–1114. doi: 10.1161/CIRCHEARTFAILURE.115.002352

Lipskaia, L., Chemaly, E. R., Hadri, L., Lompre, A. M., and Hajjar, R. J. (2010). Sarcoplasmic reticulum Ca2 ATPase as a therapeutic target for heart failure. *Expert Opin. Biol. Ther.* 10, 29–41. doi: 10.1517/14712590903321462

Louch, W. E., Mørk, H. K., Sexton, J., Strømme, T., a, Laake, P., Sjaastad, I., et al. (2006). T-tubule disorganization and reduced synchrony of Ca2+ release in murine cardiomyocytes following myocardial infarction. *J. Physiol.* 574, 519–533. doi: 10.1113/jphysiol.2006.107227

Lyu, Y., Verma, V. K., Lee, Y., Taleb, I., Badolia, R., Shankar, T. S., et al. (2021). Remodeling of t-system and proteins underlying excitation- contraction coupling in aging versus failing human heart. *NPJ Aging Mech. Dis.* 7, 16. doi: 10.1038/s41514-021-00066-7

Macquaide, N., Tuan, H. T. M., Hotta, J. I., Sempels, W., Lenaerts, I., Holemans, P., et al. (2015). Ryanodine receptor cluster fragmentation and redistribution in persistent atrial fibrillation enhance calcium release. *Cardiovasc. Res.* 108, 387–398. doi: 10.1093/cvr/cvv231

Minamisawa, S., Oshikawa, J., Takeshima, H., Hoshijima, M., Wang, Y., Chien, K. R., et al. (2004). Junctophilin type 2 is associated with caveolin-3 and is down-regulated in the hypertrophic and dilated cardiomyopathies. *Biochem. Biophys. Res. Commun.* 325, 852–856. doi: 10.1016/j.bbrc.2004.10.107

Munro, M. L., Jayasinghe, I. D., Wang, Q., Quick, A., Wang, W., Baddeley, D., et al. (2016). Junctophilin-2 in the nanoscale organisation and functional signalling of ryanodine receptor clusters in cardiomyocytes. *J. Cell Sci.* 129, 4388–4398. doi: 10.1242/jcs.196873

Page, E., and Surdyk-Droske, M. (1979). Distribution, surface density, and membrane area of diadic junctional contacts between plasma membrane and terminal cisterns in mammalian ventricle. *Circ. Res.* 45, 260–267. doi: 10.1161/01.RES.45.2.260

Pinali, C., Bennett, H., Davenport, J. B., Trafford, A. W., and Kitmitto, A. (2013). 3-D reconstruction of the cardiac sarcoplasmic reticulum reveals a continuous network linking T-tubules: this organization is perturbed in heart failure. *Circ. Res.* 113, 1219–1230. doi: 10.1161/CIRCRESAHA.113.301348

Reynolds, J. O., Quick, A. P., Wang, Q., Beavers, D. L., Philippen, L. E., Showell, J., et al. (2016). Junctophilin-2 gene therapy rescues heart failure by normalizing RyR2-mediated Ca2 + release. *Int. J. Cardiol.* 225, 371–380. doi: 10.1016/j.ijcard.2016.10.021

Sachse, F., Torres, N., Savio-Galimberti, E., Aiba, T., Kass, D., Tomaselli, G., et al. (2012). Subcellular structures and function of myocytes impaired during heart failure are restored by cardiac resynchronization therapy. *Circ. Res.* 110, 588–597. doi: 10.1161/CIRCRESAHA.111.257428

Sachse, F. B., Savio-Galimberti, E., Goldhaber, J. I., and Bridge, J. H. B. (2009). Towards computational modeling of excitation-contraction coupling in cardiac myocytes: Reconstruction of structures and proteins from confocal imaging. *Pac. Symp. Biocomput.* 2009, 328–339. doi: 10.1142/9789812836939_0031

Schultheiss, H.-P., Fairweather, D., Caforio, A. L. P., Escher, F., Hershberger, R. E., Lipshultz, S. E., et al. (2019). Dilated cardiomyopathy. *Nat. Rev. Dis. Prim.* 5:32. doi: 10.1038/s41572-019-0084-1

Scriven, D. R. L., Asghari, P., Schulson, M. N., and Moore, E. D. W. (2010). Analysis of Cav1.2 and ryanodine receptor clusters in rat ventricular myocytes. *Biophys. J.* 99, 3923–3929. doi: 10.1016/j.bpj.2010.11.008

Seidel, T., Navankasattusas, S., Ahmad, A. A., Diakos, N. A., Xu, W. D., Tristani-Firouzi, M., et al. (2017a). Sheet-like remodeling of the transverse tubular system in human heart failure impairs excitation-contraction coupling and functional recovery by mechanical unloading. *Circulation* 135, 1632–1645. doi: 10.1161/CIRCULATIONAHA.116.024470

Seidel, T., Sankarankutty, A. C., and Sachse, F. B. (2017b). Remodeling of the transverse tubular system after myocardial infarction in rabbit correlates with local fibrosis: a po1. *Prog. Biophys. Mol. Biol.* 130, 302–314. doi: 10.1016/j.pbiomolbio.2017.07.006

Sheard, T. M. D., Hurley, M. E., Colyer, J., White, E., Norman, R., Pervolaraki, E., et al. (2019). Three-dimensional and chemical mapping of intracellular signaling nanodomains in health and disease with enhanced expansion microscopy. *ACS Nano* 13, 2143–2157. doi: 10.1021/acsnano.8b08742

Shen, X., van den Brink, J., Hou, Y., Colli, D., Le, C., Kolstad, T. R., et al. (2019). 3D dSTORM imaging reveals novel detail of ryanodine receptor localization in rat cardiac myocytes. *J. Physiol.* 597, 399–418. doi: 10.1113/JP277360

Soeller, C., and Cannell, M. B. (1999). Cardiac rat myocytes by 2-photon microscopy and digital image–processing techniques. *Circ. Res.* 84, 266–275. doi: 10.1161/01.RES.84.3.266

Soeller, C., Crossman, D., Gilbert, R., and Cannell, M. B. B. (2007). Analysis of ryanodine receptor clusters in rat and human cardiac myocytes. *Proc. Natl. Acad. Sci. U.S.A.* 104, 14958–14963. doi: 10.1073/pnas.0703016104

Soeller, C., Hou, Y., Jayasinghe, I. D., Baddeley, D., and Crossman, D. (2017). Correlative single-molecule localization microscopy and confocal microscopy. *Methods Mol. Biol.* 1663, 205–217. doi: 10.1007/978-1-4939-7265-4_17

Song, L.-S., Sobie, E., a, McCulle, S., Lederer, W. J., Balke, C. W., and Cheng, H. (2006). Orphaned ryanodine receptors in the failing heart. *Proc. Natl. Acad. Sci. U.S.A.* 103, 4305–4310. doi: 10.1073/pnas.0509324103

Takeshima, H., Komazaki, S., Nishi, M., Iino, M., and Kangawa, K. (2000). Junctophilins: a novel family of junctional membrane complex proteins. *Mol. Cell* 6, 11–22. doi: 10.1016/S1097-2765(05)00005-5

Ushiki, T. (2002). Collagen fibers, reticular fibers and elastic fibers. A comprehensive understanding from a morphological viewpoint. *Arch. Histol. Cytol.* 65, 109–126. doi: 10.1679/aohc.65.109

Van-Oort, R. J., Garbino, A., Wang, W., Dixit, S. S., Landstrom, A. P., Gaur, N., et al. (2011). Disrupted junctional membrane complexes and hyperactive ryanodine receptors after acute junctophilin knockdown in mice. *Circulation* 123, 979–988. doi: 10.1161/CIRCULATIONAHA.110.006437

Wagenknecht, T., Grassucci, R., Frank, J., Saito, A., Inui, M., and Fleischer, S. (1989). Three-dimensional architecture of the calcium channel/foot structure of sarcoplasmic reticulum. *Nature* 338, 167–170. doi: 10.1038/338167a0

Wang, Y., Chen, B., Huang, C. K., Guo, A., Wu, J., Zhang, X., et al. (2018). Targeting calpain for heart failure therapy: implications from multiple murine models. *JACC Basic Transl. Sci.* 3, 503–517. doi: 10.1016/j.jacbts.2018.05.004

Wei, S., Guo, A., Chen, B., Kutschke, W., Xie, Y.-P.-P., Zimmerman, K., et al. (2010). T-tubule remodeling during transition from hypertrophy to heart failure. *Circ. Res.* 107, 520–531. doi: 10.1161/CIRCRESAHA.109.212324

Xiao, H., Li, H., Wang, J. J., Zhang, J. S., Shen, J., An, X. B., et al. (2018). IL-18 cleavage triggers cardiac inflammation and fibrosis upon β-Adrenergic insult. *Eur. Heart J.* 39. doi: 10.1093/eurheartj/ehx261

Zhang, H.-B., Li, R.-C., Xu, M., Xu, S.-M., Lai, Y.-S., Wu, H.-D., et al. (2013). Ultrastructural uncoupling between T-tubules and sarcoplasmic reticulum in human heart failure. *Cardiovasc. Res.* 98, 269–276. doi: 10.1093/cvr/cvt030

Conflict of Interest: The authors declare that the research was conducted in the absence of any commercial or financial relationships that could be construed as a potential conflict of interest.

frontiers in Physiology

ORIGINAL RESEARCH
published: 23 December 2021
doi: 10.3389/fphys.2021.782767

Phosphatidylinositol-4,5-Bisphosphate Binding to Amphiphysin-II Modulates T-Tubule Remodeling: Implications for Heart Failure

Junlan Zhou[1]†, Neha Singh[1]†, Chloe Monnier[1], William Marszalec[1], Li Gao[1], Jing Jin[1], Michael Frisk[2,3], William E. Louch[2,3], Suresh Verma[1], Prasanna Krishnamurthy[1], Elsa Nico[1], Maaz Mulla[1], Gary L. Aistrup[1], Raj Kishore[1] and J. Andrew Wasserstrom[1]*

[1] Department of Medicine (Cardiology), Feinberg Cardiovascular Research Institute, Northwestern University Feinberg School of Medicine, Chicago, IL, United States, [2] Institute for Experimental Medical Research (IEMR), Oslo University Hospital, Oslo, Norway, [3] K. G. Jebsen Cardiac Research Center, University of Oslo, Oslo, Norway

Edited by:
Rosana A. Bassani,
State University of Campinas, Brazil

Reviewed by:
Kenneth Ginsburg,
UC Davis, United States
Alicia Mattiazzi,
Consejo Nacional de Investigaciones Científicas y Técnicas (CONICET), Argentina

***Correspondence:**
J. Andrew Wasserstrom
ja-wasserstrom@northwestern.edu

† These authors have contributed equally to this work and share first authorship

Specialty section:
This article was submitted to Striated Muscle Physiology, a section of the journal Frontiers in Physiology

Received: *24 September 2021*
Accepted: *19 November 2021*
Published: *23 December 2021*

Citation:
Zhou J, Singh N, Monnier C, Marszalec W, Gao L, Jin J, Frisk M, Louch WE, Verma S, Krishnamurthy P, Nico E, Mulla M, Aistrup GL, Kishore R and Wasserstrom JA (2021) Phosphatidylinositol-4,5-Bisphosphate Binding to Amphiphysin-II Modulates T-Tubule Remodeling: Implications for Heart Failure. Front. Physiol. 12:782767. doi: 10.3389/fphys.2021.782767

BIN1 (amphyphysin-II) is a structural protein involved in T-tubule (TT) formation and phosphatidylinositol-4,5-bisphosphate (PIP2) is responsible for localization of BIN1 to sarcolemma. The goal of this study was to determine if PIP2-mediated targeting of BIN1 to sarcolemma is compromised during the development of heart failure (HF) and is responsible for TT remodeling. Immunohistochemistry showed co-localization of BIN1, Cav1.2, PIP2, and phospholipase-Cβ1 (PLCβ1) in TTs in normal rat and human ventricular myocytes. PIP2 levels were reduced in spontaneously hypertensive rats during HF progression compared to age-matched controls. A PIP Strip assay of two native mouse cardiac-specific isoforms of BIN1 including the longest (cardiac BIN1 #4) and shortest (cardiac BIN1 #1) isoforms as well human skeletal BIN1 showed that all bound PIP2. In addition, overexpression of all three BIN1 isoforms caused tubule formation in HL-1 cells. A triple-lysine motif in a short loop segment between two helices was mutated and replaced by negative charges which abolished tubule formation, suggesting a possible location for PIP2 interaction aside from known consensus binding sites. Pharmacological PIP2 depletion in rat ventricular myocytes caused TT loss and was associated with changes in Ca^{2+} release typically found in myocytes during HF, including a higher variability in release along the cell length and a slowing in rise time, time to peak, and decay time in treated myocytes. These results demonstrate that depletion of PIP2 can lead to TT disruption and suggest that PIP2 interaction with cardiac BIN1 is required for TT maintenance and function.

Keywords: BIN-1, heart failure, PIP2—phosphatidylinositol-4,5-bisphosphate, T-tubule disruption, Ca^{2+} transients

INTRODUCTION

Transverse tubules (TTs) are membranous invaginations primarily associated with mammalian ventricular myocytes. These inward projections of the external sarcolemmal membrane bring voltage-gated calcium channels on the surface membrane into proximity with the sarcoplasmic reticulum (SR), the main intracellular Ca^{2+} store within the myocyte. Ca^{2+} influx across the sarcolemma activates Ca^{2+}-sensitive ryanodine receptors in the SR promoting a synchronous cell-wide Ca^{2+} release via the phenomenon of calcium-induced calcium release (CICR), ultimately leading to myocyte contraction. Many studies have demonstrated TT loss in ventricular myocytes during heart failure (HF) in small animal models such as mice (Louch et al., 2006) and rats (Lyon et al., 2009; Wasserstrom et al., 2009) as well as in larger mammals such as dogs (He et al., 2001; Balijepalli et al., 2003), pigs (Louch et al., 2004; Heinzel et al., 2008), and humans (Louch et al., 2004; Lyon et al., 2009; Crossman et al., 2011). Furthermore, work from several investigators has demonstrated that the loss of TTs may be responsible for the development of diastolic and systolic dysfunction (Song et al., 2006; Wei et al., 2010; Shah et al., 2014) making it of far greater importance to understand the mechanisms of normal TT formation as well as of TT remodeling during HF.

The mechanisms underlying normal TT formation and maintenance are poorly understood. A growing body of evidence suggests that the cardiac isoform(s) of amphiphysin-II (BIN1) may play a more central role in TT formation in skeletal and heart muscle. Isoform 8 of BIN1 has the ability to form TTs in skeletal muscle cells (Lee et al., 2002) and mutation of the amphiphysin-II gene was associated with a disrupted TT network (Razzaq et al., 2001). Other studies showed an association of BIN1 with muscular dystrophy as well (Nicot et al., 2007; Fugier et al., 2011). BIN1 knockdown also produces a cardiomyopathy (Muller et al., 2003), making this protein a potential mediator for TT remodeling during the development of HF.

The role of a phosphatidylinositol-4,5-bisphosphate (PIP_2) interaction with Bin1 in TT formation and maintenance is established skeletal muscle but unclear in the heart. Skeletal BIN1 contains a unique sequence domain of 15 amino-acids called Exon10 (Ramjaun and McPherson, 1998). The primary structure of Exon10 is very similar to a binding motif for PIP2 (Martin, 1998) and Lee et al. (2002) showed that Exon10 has a high specificity to associate with PIP_2. In addition, PIP_2 binding to BIN1 opens the SH3 domain to protein-protein interactions, providing a means by which BIN1 could assemble a structural backbone for TT formation, raising the question of whether BIN1 localization and subsequent sarcolemmal TT formation might in fact be PIP_2-dependent. Although little is known about changes in PIP_2 during the early stages of HF, there is a clear reduction of PIP_2 in end-stage HF (Tappia et al., 1999; Ziegelhoffer et al., 2001). This could reduce targeting of BIN1 to the sarcolemmal membrane and thereby disrupt maintenance of the TT structure. However, an important study by Hong et al. (2014) found that none of the four identified cardiac BIN1 (cBIN1) isoforms in mouse heart contained the critical exon 10 (re-named Exon 11 in mouse heart). The implication of these results was that this exon *could* not bind PIP2 and that therefore TT formation was independent of PIP2-BIN1 interactions. To explore the possible interaction between PIP2 and BIN1 and the role of PIP2 in TT formation, through a pivotal role of PIP_2 in BIN1 organization, we investigated the idea that PIP2 is important for cardiac TT formation and maintenance and that the depletion of sarcolemmal PIP_2 results in TT degeneration.

MATERIALS AND METHODS

Animal and Human Tissue Samples

Animal Studies

All experiments using animals were performed according to a protocol approved by Institutional Animal Care and Use Committee of the Northwestern University and according to the NIH guidelines for animal use. Hearts were obtained from Sprague Dawley rats (aged 4–6 months) and age-matched Wistar Kyoto and spontaneously hypertensive rats (SHR) ranging between 2 and 20 months of age. Rats were injected with 750 units of heparin 5 min prior to anesthesia induced by an injection mixture (80 mg/kg:10 mg/kg) of ketamine and xylazine. When the rats were fully anesthetized, the heart was quickly excised and processed for myocyte isolation, protein extraction or tissue fixation.

Human Samples

Normal human tissue samples were obtained from The Gift of Hope of Illinois. All samples were obtained from healthy organ donors whose hearts were considered unsuitable for transplantation. Upon harvest, these hearts were immediately placed in cold cardioplegia solution. Tissue samples were then perfused with 2% paraformaldehyde for subsequent processing. The protocol for tissue use was reviewed by the Institutional Review Board of Northwestern University (exemption 4) and informed consent was obtained from families of organ donors before tissue was collected for research purposes.

All reasonable requests for original data analyses will be fulfilled upon written request to the corresponding author in support of transparency and reproducibility requirements. Full details of all methods are provided in the online **Supplementary Material**.

RESULTS

Molecular Interactions Between Amphiphysin-II Isoforms and Phosphatidylinositol-4,5-Bisphosphate

Amphiphysin-II, Phosphatidylinositol-4,5-Bisphosphate, and Phospholipase-Cβ1 Are Distributed Along Transverse Tubules

Immunohistochemistry co-localization studies of BIN1 with Cav1.2, the L-type Ca^{2+} channel protein present at a high density in TTs, indicated that isoforms of cardiac Bin1 (cBIN1) co-localized with Cav1.2 along the TTs in both normal rat (Wistar Kyoto or WKY rats) and human ventricular tissue (**Figures 1A,B**). The distribution pattern of PIP2 and phospholipase-Cβ1 (PLCβ1) in rat ventricular tissue showed that both co-localized at TTs with cBIN1 (**Figures 1C–E**). These observations demonstrate that all four proteins are present exclusively in the TTs, raising the possibility that an important relationship exists between Ca1.2, cBIN1, PIP2, and PLCβ 1.

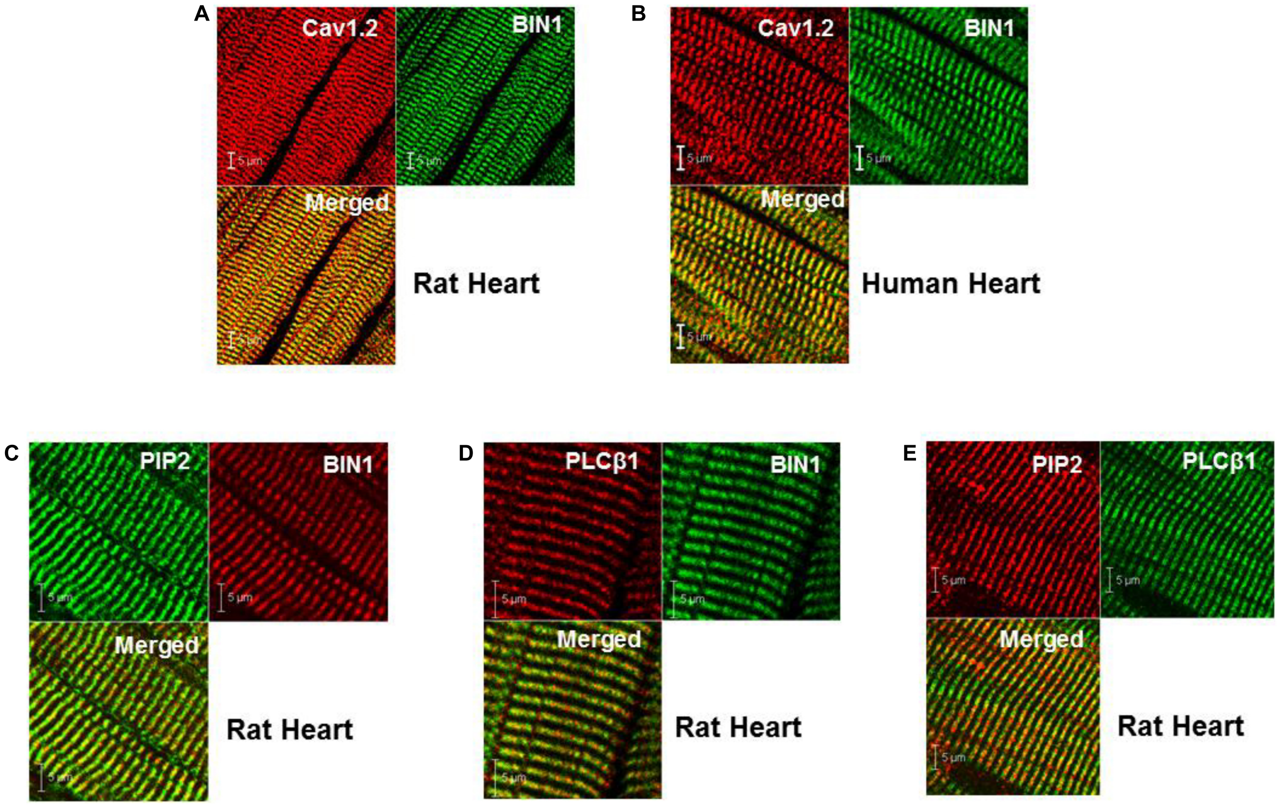

FIGURE 1 | Cellular localization of BIN1, PIP2, and PLCβ1 at TTs in both rat and human heart. **(A,B)** Co-localization of BIN1 with Cav1.2 in rat and human ventricle. **(C–E)** PIP2 and PLCβ1 are also localized at t-tubules in rat heart. Pixel size was 0.02–0.04 µm/pixel and all images were obtained with the pinhole adjusted to Airey units = 1.

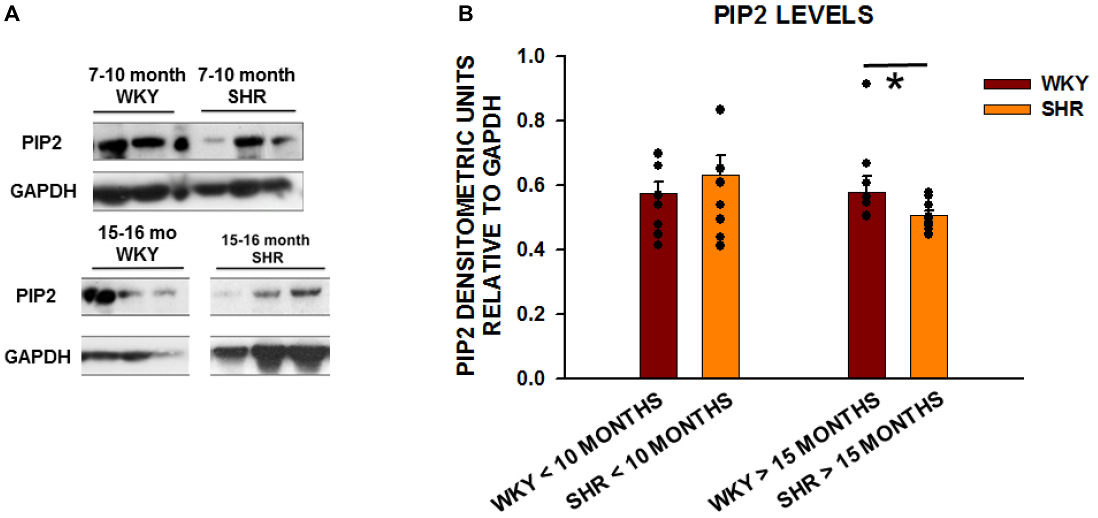

FIGURE 2 | PIP2 levels are reduced with age in SHRs in comparison to control WKY rats. **(A)** Expression of PIP2 from left ventricular tissue in two different age group of animals with young animals < 10 months of age (WKY *n* = 8 rats; SHR *n* = 6 rats) and old animals > 15 months (WKY *n* = 8 rats; SHR *n* = 9 rats). **(B)** Graph of relative protein expression normalized to GAPDH. Values indicated mean ± SEM here and in all subsequent experiments. Comparisons were made using an unpaired *t*-test. $^*p < 0.05$.

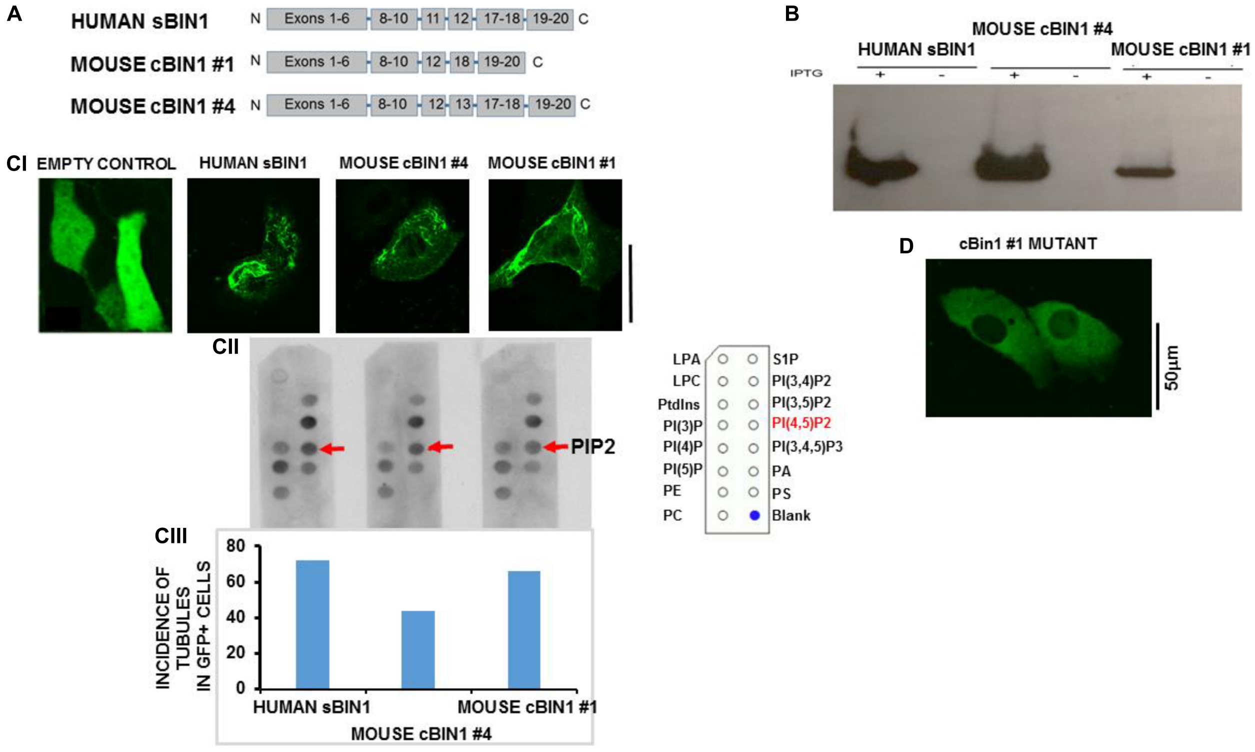

FIGURE 3 | *In vitro* model of HL1 cells shows tubules after BIN1 overexpression. **(A)** Gene organization for two splice variants of mouse cardiac muscle BIN1 as well as human skeletal muscle BIN1. **(B)** The expression of BIN1 proteins induced by isopropyl-b-D-thiogalactoside (IPTG) in bacteria. **(C)** The interaction between purified Bin1 and PIP2. **(CI)** Tubule formation in Hl-1 cells 48 h after overexpression with each of the Bin1 constructs. The inset shows that no tubules formed in the overexpression of empty vector. **(CII)** PIP Strip assays were performed using BIN1 antibody. Representative results from 3 separate experiment are shown and all PIP strip results were confirmed in 1–2 additional strips for each protein. The template describing location of dots for all phospholipids is shown in **Supplementary Figure 3**. **(CIII)** Incidence of tubule formation induced by over expressed BIN1 in HL1 cells for each construct. No tubules were formed in cells with empty vector. (*N* = 48 cells/3 cultures for each including empty vector). **(D)** Example of an HL-1 cell over-expressing a construct with triple mutations of Lys164Glu/Lys165Glu/Lys166Glu in a loop segment of the N-BAR coiled-coil domain completely abolished tubule formation. No tubulation was found in any GFP-positive cells (*N* = 36 cells/3 cultures). Note that the vector contains a GFP tag so Bin1 can be easily visualized. Pixel size was 0.11 μm/pixel and all images were obtained with the pinhole adjusted to Airey units = 1.

Reduction in Phosphatidylinositol-4,5-Bisphosphate Levels During the Progressive Development of Heart Failure in Spontaneously Hypertensive Rats

SHRs develop severe cardiac structural and functional changes as they age (Shah et al., 2014). We next investigated whether the levels of BIN1 and PIP2 change in left ventricular tissue from SHRs from young (<10 month) and old (>15 month) rats with WKY rats as the normal controls. We found no change in BIN1 protein expression in SHRs as a function of age (**Supplementary Figure 1**). However, when we also measured PIP2 levels in these same cardiac samples in young (2–10 months old) and aged (15–20 months old) (**Figure 2A**), we found that PIP2 levels were unchanged in the younger animals but decreased significantly in old SHRs in comparison to WKYs (**Figure 2B**).

Amphiphysin-II Overexpression Induces Sarcolemmal Tubular Extensions in HL1 Cells

To investigate the interaction between cBIN1 and PIP2, we cloned two splice variants of mouse cBIN1 (#1 and #4) as well as human skeletal muscle BIN1 (isoform 8) in pET6xHN. These cBIN1 splice variants exclude mouse exon11 (previously exon10) and either include 13 and 17 (full-length variant #4) or exclude these two exons (variant #1, as shown in **Figure 3A**). cBIN1 expression was confirmed in bacteria by western blotting (**Figure 3B**). PIP Strip assays further confirmed an interaction between purified cBIN1 and PIP2 (**Figure 3CII**). Interestingly, both cBIN1 and human skeletal muscle BIN1 interacted with other phosphoinositides, including phosphatidylinositol-4,(or 3, or 5)-phosphate and PIP2, [PI(3,5)P_2] [PI(3,4)P_2] [PI(3,4,5)P_3], but not with phosphatidylinositol (PI), phosphatidylserine (PS), phosphatidylcholine (PC), and phosphatidic acid (PA).

Next, the ability of each isoform to induce tubule formation was examined. We developed an *in vitro* model that permitted the study of tubule formation and biochemical signaling pathways that are responsible for both TT loss and maintenance. For purposes of comparison, we performed di-4-ANEPPs staining in intact normal rat ventricle which showed a well-organized and dense TT network (**Supplementary Figure 2A**). In contrast, staining of HL-1 cells showed a lack of tubulation. We then assayed for BIN1 expression using Western blot analysis and found no protein expression for BIN1 in HL-1 cells (**Supplementary Figure 2B**), confirming that HL-1 cells had no tubules and lacked BIN1. Overexpression of both isoforms of cBIN1 in HL1 cells induced tubule formation as did human sBIN1 (**Figure 3CI**). Moreover, all isoforms induced tubule formation in a very large percentage of GFP+ cells, ranging from 72 to 44% (**Figure 3CIII**). These results indicate that both the shortest and longest splice variants of cBIN1 are capable of inducing tubule formation and that all are capable of binding PIP2 similar to their skeletal counterpart despite the absence of exon 11. Furthermore, binding of PIP2 to cBIN1 does not require the presence of exons 11, 13, or 17 and must reside at another site or sites on the cardiac isoforms. Note that HL-1 cells transfected with empty vector failed to produce any tubules (**Figure 3CI**).

In order to explore the role of PIP2 binding and tubule formation, we then created a mutant variant of cBIN1 #4 by substituting three lysine residues with negatively charged aspartic acid residues in a loop segment of the N-BAR coiled-coil domain. When this Lys164Glu/Lys165Glu/Lys166Glu mutant was transfected to HL-1 cells, there was no observable tubule formation (**Figure 3D**), suggesting the structural importance of positive charges in the loop segment in anchoring cBIN1 lattice to phospholipids in promoting tubule formation.

Depletion of Phosphatidylinositol-4,5-Bisphosphate Levels by Pharmacologic Intervention

To determine if depletion of PIP_2 underlies TT remodeling, we performed a series of experiments with pharmacological agents known to decrease cellular PIP_2 levels by either interfering with PIP2 production or increasing its catalysis. Wortmannin inhibits phosphoinositol-4 kinase (PI4K), an enzyme required for PIP_2 synthesis (Brown et al., 2007; Albert et al., 2008). Inhibition of PI4K interferes with PIP_2 regeneration and thus reduces its membrane levels. Endothelin-1 (Et-1) is the endogenous activator of a receptor-mediated signaling cascade involving a Gαq activation of several isoforms of phospholipase C (including sarcolemmal PLCβ1) by which PIP_2 is hydrolyzed to diacylglycerol and inositol-3-phosphate (DAG and IP_3). Finally, m-3M3FBS is a direct activator of PLCβ (and subsequent PIP2 hydrolysis).

To demonstrate that TT loss mediated by these pharmacological interventions was indeed a result of PIP2 depletion/reduction, PIP2 levels were measured following each of these treatments. First HL1 cells were transfected with a PLCδ1-PH-GFP construct that acts indirectly as a PIP2 reporter. PLCδ1-PH-GFP binds with sarcolemmal PIP2 but is released in the cytosol when PIP2 levels decline. We monitored PH-GFP translocation after treating Bin1- cells with either 15 μM wortmannin (2 h), 200 nmol/L Et-1 (for 48 h), 30 μm m-3M3FBS (30 μmol/L; for 3 h) or the combination of Et-1 and m-3M3FBS (for 45 min) (**Figure 4**). In the absence of any pharmacological treatments, PIP2 was localized in the sarcolemma (**Figure 4A**). In contrast, the construct was translocated to the cytoplasm after treatment with wortmannin, Et-1, m-3M3FBS and the combination of Et-1 and m-3M3FBS (**Figures 4B–F**). Note also that PIP2 depletion was more effective via direct activation of PLCβ1 with m-3M3FBS than with wortmannin. These results support the notion that each of these agents causes PIP2 depletion from the sarcolemma.

To confirm that the treatments indeed cause PIP2 depletion of PIP2 through activation of PLCβ1, the enzyme activity was measured directly using an ELISA assay kit for IP1 which is an easily measured downstream metabolite of PIP2 and IP3 since the latter is extremely difficult to measure directly. We found that IP1 was significantly increased in response to wortmannin ($p < 0.05$), Et-1 ($p < 0.05$), m-3M3FBS ($p < 0.05$), and the combination of Et-1 and m-3M3FBS ($p < 0.05$) (**Figure 4G**). Our results thus suggest that increased PIP2 metabolism and subsequent PIP2 depletion can be responsible for tubule disruption and strongly indicate that PIP2 is required for TT maintenance.

Effects of Phosphatidylinositol-4,5-Bisphosphate Depletion on Transverse Tubule Density and Excitation-Contraction Coupling in Adult Rat Ventricular Myocytes

Phosphatidylinositol-4,5-Bisphosphate Depletion Causes Transverse Tubule Disruption in Isolated Adult Rat Ventricular Myocytes

In order to extend our observation that PIP2 plays a key role in tubule disruption in a cell culture system to adult ventricular myocytes, we investigated the effects of pharmacological depletion of PIP2 on TTs in isolated adult rat ventricular myocytes (ARVMs). We have previously described our measurements of TT organization, measured as organization index (OI), in adult myocytes using di-4-ANNEPS staining (Aistrup et al., 2013).

Figure 5A (left panel) shows a typical ventricular myocyte with TTs that traverse the entire cell width at even spacing of about 2 μm. Severe TT remodeling was observed in cardiomyocytes exposed to wortmannin treatment (**Figure 5A**, right panel). Similar results were obtained in myocytes treated with Et-1 (**Figure 5B**), m-3M3FBS (**Figure 5C**), and in combination (**Figure 5D**). **Figure 5E** summarizes these results and demonstrates that all four treatments that deplete PIP2 also significantly reduced OI in rat ventricular myocytes.

Finally, we wanted to demonstrate that TT disruption was directly responsible for altered Ca^{2+} release properties in adult myocytes following pharmacologically-induced PIP2 depletion. We and others have demonstrated that progressive heart failure is characterized by TT loss and profound disruption of sarcoplasmic reticulum Ca^{2+} release and reuptake (Louch et al., 2006, 2012; Frisk et al., 2016). Therefore, we measured Ca^{2+} rise times, times-to-peak and decay times in order to determine if they were affected by pharmacological disruption of TTs in a manner similar to that reported to occur following TT disruption in heart failure. **Figures 6A–D** show longitudinal confocal line scan recordings of Ca^{2+} transients in isolated ARVMs both under control conditions and following treatment with each of the agents inducing PIP2 depletion and TT loss. The 2-D images show representative myocytes in control (**Figure 6A**) and following treatment with wortmannin (**Figure 6B**), m-3M3FBS (**Figure 6C**), and combination of the Et-1 and m-3M3FBS (**Figure 6D**). Note the high OI in the untreated control and corresponding low values of OI in the treated cells.

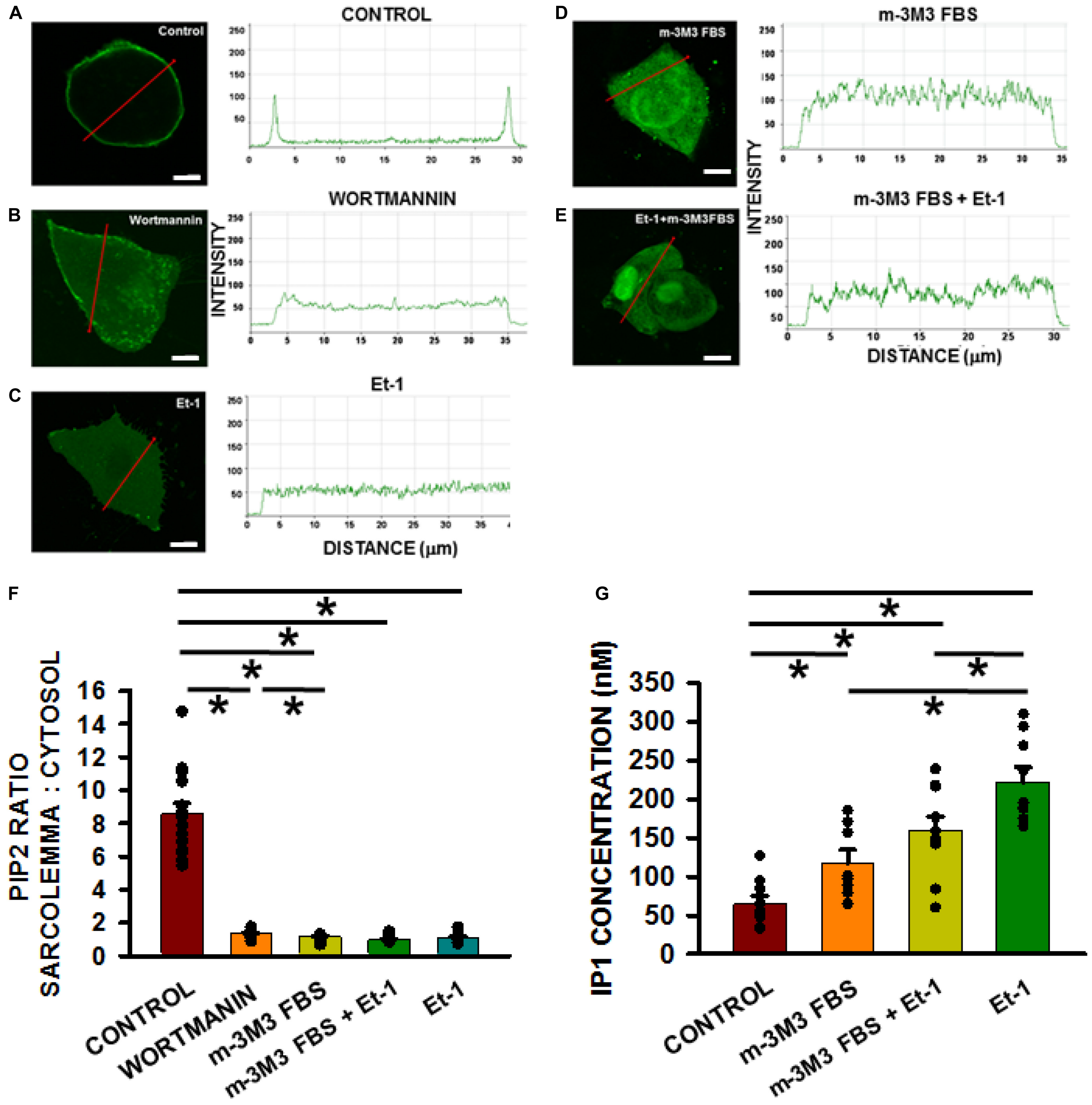

FIGURE 4 | Membrane PIP2 levels decrease significantly in HL-1 cells with active treatments compared to non-treated controls. PIP2 depletion measurements in HL1 cells transfected with the PLCδ1-PH-GFP construct. Quantification measured as the fluorescence intensity change along the red line from membrane to cytosol (**A–E**, scale bar = 5 μm). Pixel size was 0.11 μm/pixel and all images were obtained with the pinhole adjusted to Airey units = 1. Bar graph **(F)** shows results of controls (*n* = 15 wells) compared to cells pre-incubated with wortmannin (*n* = 13), m-3M3FBS (*n* = 12 wells), Et-1 (*n* = 12), and combination of Et-1 and m-3M3FBS (*n* = 15 wells) from 3 separate cultures each. **(G)** Measurements of IP1 in different treatment groups. Control *n* = 9 wells; Et-1 *n* = 8; m-3M3FBS *n* = 9; m-3M3FBS+Et-1 *n* = 10 obtained from 3 cultures each. Statistical comparisons were made using a one-way ANOVA in **(F,G)**. *$p < 0.05$.

When we measured Ca^{2+} transients at slow (BCL = 2,000 ms) and rapid (BCL = 1,000 ms) pacing rates in the control myocyte, Ca^{2+} release was rapid and uniform along the entire cell length and the decay of the transient was also rapid at both rates (linescan images in **Figure 6A**), In contrast, each linescan image from the drug-treated cells showed regions of late release (arrow heads) at the slow rate that were exaggerated during rapid pacing (linescan images in **Figures 6B–D**). The result is a slowing in overall rise time and decay time of the transients that was exaggerated at the faster rates in each of the cells with poor TT organization, as indicated by the average fluorescence intensity profiles at the right of each image. The summary graphs for the Ca^{2+} transients during rapid pacing (**Figures 6E–G**) show that the overall rates of Ca^{2+} release and sequestration were delayed in all the drug-treated myocytes compared to untreated cells as indicated by the significant

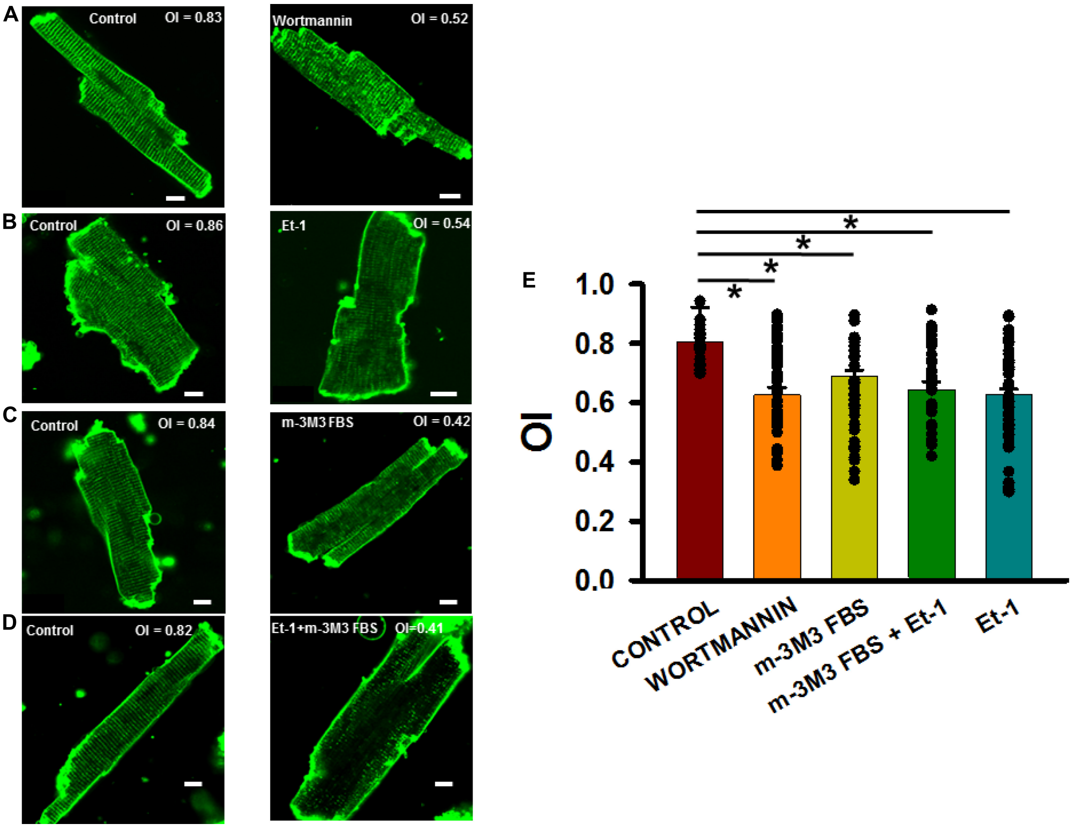

FIGURE 5 | PIP2 depleting agents adversely affected organizational index (OI) of TTs in isolated adult rat ventricular myocytes. **(A–D)** 2-D images of control (left panels) and treated (right panels) myocytes. **(E)** Summary of OI changes untreated cells (35 myocytes in 3 rats) and after treatment with wortmannin (15 μmol/L, 2 h, $n = 35/3$), m-3M3FBS (30μmol/L, 3 h, $n = 37/5$), and Et-1(400 nmol/L) + m-3M3FBS (30 μmol/L, 45 min, $n = 35/4$) and Et-1 (400 nmol/L, 6 h, $n = 54/4$). $^{*}p < 0.05$ using Dunn's test following a one-way ANOVA performed on all cells. Pixel size was 0.45 μm with the pinhole adjusted to Airey units = 1.

increases in rise times, times-to-peak and decay times of the Ca^{2+} transients.

When rise time, time to peak and decay time were plotted for all cells treated with PIP2-depleting agents as a function of mean OI (**Figure 7**), close inverse relationships were observed, indicative of slowed Ca^{2+} release and removal with decreased OI (**Figures 7A–C**). The left panels show myocytes that were treated with wortmannin, m-3M3FBS, or the combination of m-3M3FBS + Et-1 and each treatment is individually color-coded. Control cells (open circles) have high OI and are characterized by rapid Ca^{2+} release and recovery. In contrast, treated cells (filled circles) show dramatic slowing in release and recovery properties as OI decreases. There is no obvious departure of any cell group from the overall relationship, suggesting a commonality in mechanism, in this case the decrease in OI. These data suggest that the relationship between OI and each characteristic of Ca^{2+} release or removal occurs along a continuum that is largely independent from the specific treatment involved so that the slowing of release and of removal is reliant on the reduction in OI and not on how it was achieved. This is best demonstrated in the graphs in the right panels in which the linear fit for each overall relationship is shown. Each graph shows a significant reliance of Ca^{2+} release and reuptake on OI that is not related to the specific treatment by which reduced OI was induced. We have previously shown nearly identical results in individual myocytes from aged SHRs (Singh et al., 2017) which strongly suggests the critical role of TT remodeling on Ca^{2+} cycling even in myocytes where TT loss was acutely and artificially induced through pharmacological means but which yields results that are nearly identical to those found in HF. We have previously shown nearly identical results in individual myocytes from aged SHRs (Singh et al., 2017). Taken together, these results demonstrate that TT disruption induced by PIP2 depletion causes morphological and physiological alterations that share a very close resemblance with those found in HF.

DISCUSSION

Cardiac Amphiphysin-II Isoforms and Transverse Tubule Formation

Although cardiac TT remodeling and associated dysfunction of Ca^{2+} release have been extensively reported in HF (Balijepalli et al., 2003; Louch et al., 2004, 2012; Song et al., 2006), the processes underlying the formation and maintenance of TTs in general are not known, although we do know that BIN1 seems

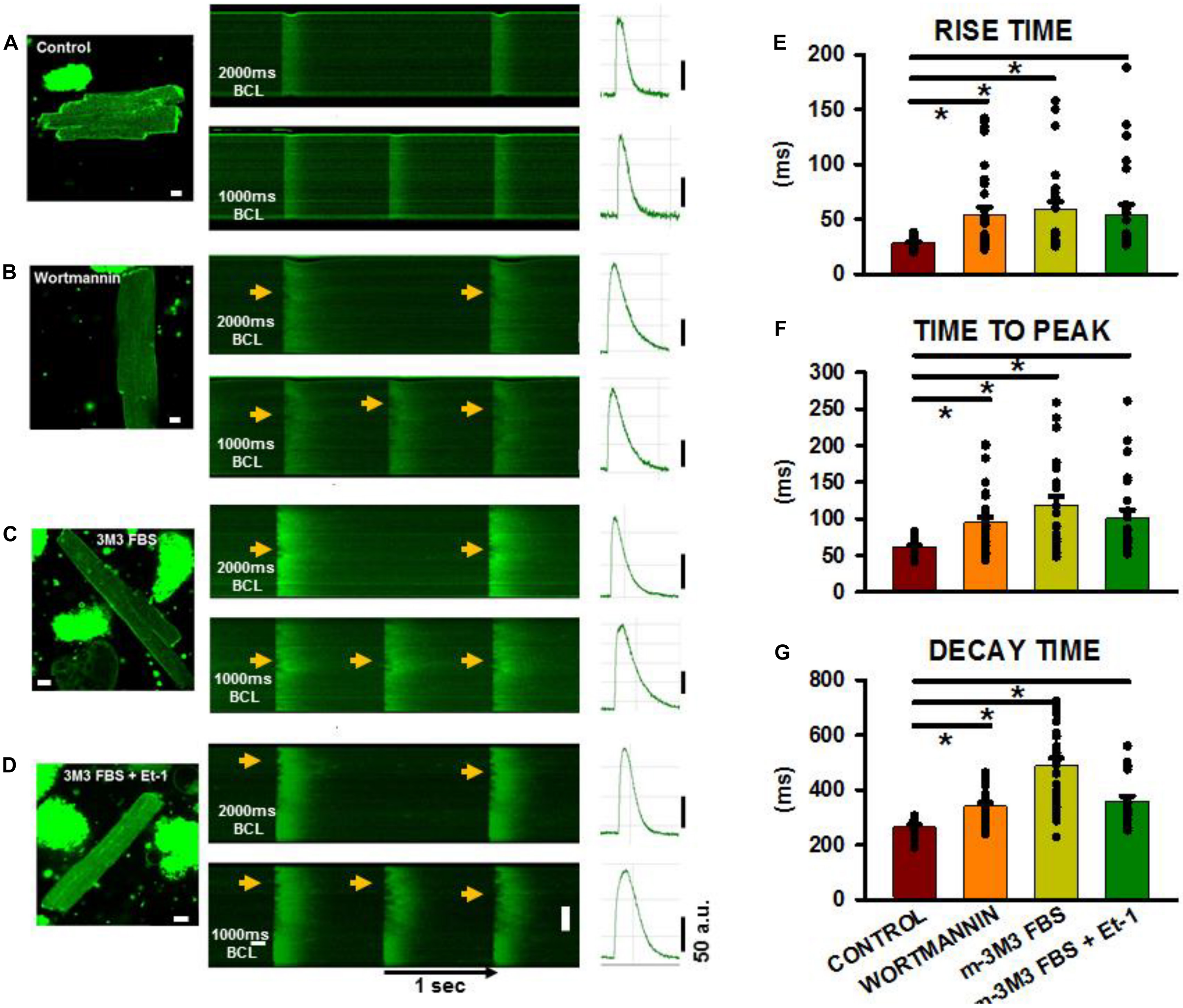

FIGURE 6 | Calcium transients in isolated adult ventricular myocytes after PIP2 depletion. **(A–D)** 2-D images with associated linescan images from treated and non-treated myocytes. Pacing was performed at basic cycle lengths of 2,000 and 1,000 ms. Arrows shows areas of delayed Ca^{2+} release along the cell length in the myocytes. **(E–G)** Shows summaries of rise time, time to peak and decay time from control and treated cells at a pacing cycle length of 1,000 ms. Control (*n* = 18–28 myocytes from 6 rats), wortmannin (27–36/5), m-3M3FBS (27/3), Et-1+m-3M3FBS (*n* = 22–24/3). $^*p < 0.05$ using a Dunn's test following a one-way ANOVA performed on cells. Pixel size was 0.2 μm with the pinhole adjusted to Airey units = 1.

to be a critical component of TT assembly. In skeletal muscle, this protein has several unique features that make it well-suited for this role, including a natural curvature, a charge profile that allows anchoring in the negatively charged phospholipids in the membrane bilayer, and a PIP2 binding site in Exon 10 that is unique to the muscle (and TT bearing) isoform of the amphiphysin-II protein family. With the exception of Exon 10, nearly all of these properties appear to be shared by the cardiac isoforms of this protein leaving us with an incomplete understanding of these processes in heart.

In cardiomyocytes, Hong et al., 2014 have shown that one of four cBIN1 isoforms in mouse adult cardiomyocyte (BIN1+13+17) was involved in cardiomyopathy and arrhythmia by regulating ion flux and TT morphology (Hong et al., 2014). It has been shown that exon 10 of BIN1 contains a basic amino-acid sequence (RKKSKLFSRLRRKKN) that is important to TT biogenesis in skeletal muscle and the interaction of Exon10 with PIP2 appears to be crucial for localization of BIN1 to TTs in skeletal muscle (Lee et al., 2002). However, our data show that mouse cBIN1 without Exon10/11 still binds a number of phosphoinositides including PIP2. Moreover, overexpressed cBIN1 was capable of tubule formation. These data indicate that Exon 10/11 is not essential for the interaction between cBIN1 and PIP2 for cardiac TT formation. Furthermore, we found that at least one critical PIP2 binding site on cBIN1 is not located at either exon13 or exon17 but does appear to adjoin the BAR domain where its mutation prevented tubule formation. Thus, the current study suggests a novel mechanism that allows cBIN1 and PIP2 to play a crucial role in TT biogenesis. It is also important to note that recent work has also identified the presence of exon 11-containing isoform 8 in rat (Li et al., 2020) but not apparently in mouse (Hong et al., 2014)

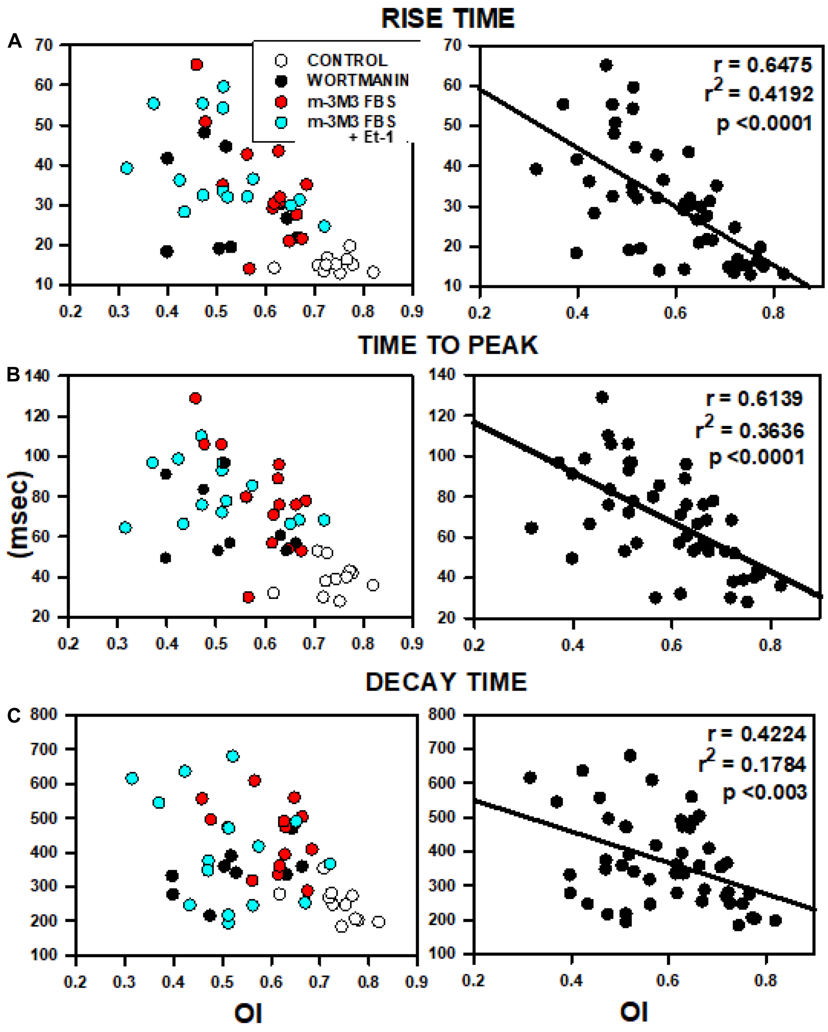

FIGURE 7 | Relationships between OI and rise time **(A)**, time to peak **(B)** and decay time **(C)**. Data were obtained from 5 rats from the analyses presented in **Figure 6** including data from control myocytes (open circles), myocytes treated with wortmannin (filled circles), 3M3FBS (red circles) and combination Et-1 + 3M3FBS (cyan circles).

myocardium. Furthermore, Guo et al. (2021) have shown that at least two different exon 11-containing isoforms 8 and 13 (i.e., Bin1+11 and Bin1+11+17, respectively) are also present in human heart. These results indicate that there are indeed exon 11-containing isoforms in hearts other than mouse that are likely to interact with PIP2 through this motif as well as possible additional binding sites described here that do not rely on the presence of exon 11.

Phosphatidylinositol-4,5-Bisphosphate, Phospholipase-Cβ1, Amphiphysin-II, and Transverse Tubules

One important finding is the co-localization of PLCβ1, BIN1, and PIP2, at TTs in adult ventricular myocytes. This is likely to be the PLCβ1b isoform since the other minor cardiac isoform (PLCβ1a) is located in the cytoplasm unlike membrane-bound PLCβ1b (Grubb et al., 2008, 2011). TT disruption in HF abolished both the normal striated patterns of Cav1.2 and of BIN1 organization without an overall loss of BIN1 (**Supplementary Figure 4**). Thus, BIN1 organization is lost in HF without reduced protein levels when PIP2 is no longer available to insure BIN1 membrane insertion and its absence also reduces BIN1 interactions with neighboring proteins. Finally, this co-localization of PLCβ1, BIN1, and PIP2 at TTs also suggests the existence of a signalasome responsible for TT formation and maintenance, supporting the idea that TT remodeling may result from a loss of one or more members of a putative signaling complex.

Phospholipase-Cβ1 Activity, Phosphatidylinositol-4,5-Bisphosphate Depletion and Transverse Tubules

Hypertension and other cardiovascular diseases that often develop into HF are known to increase levels of endothelin-1 (Miyauchi et al., 1989; Yasuda et al., 1990; Tsuji et al., 1991;

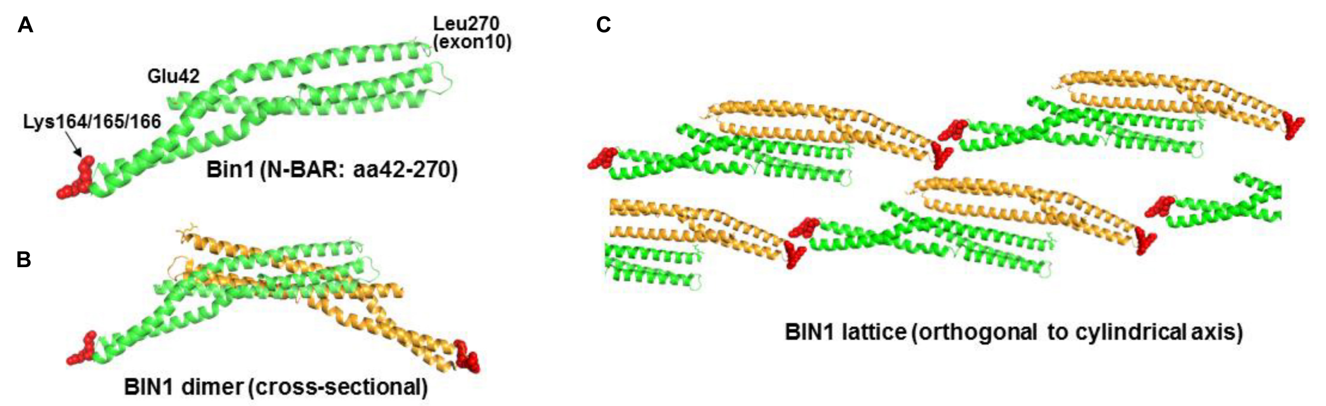

FIGURE 8 | Proposed model of BIN1 in T-tubule formation. **(A)** Crystal structure of N-BAR of BIN1 (PDB ID: 2FIC) consists of a coiled-coil domain. The short loop segment between helix 2 and 3 has three lysine residues from amino acid 164 to 166 (red). **(B)** Two BIN1 N-BARs (one in green color and the other in orange color) form a "banana"-shaped curve through their lateral interactions. **(C)** In T-tubule formation, BIN1 N-BAR domain oligomerizes to form a patterned lattice (modeled based on F-BAR domain) around the lipid bilayer.

Bohm and Pernow, 2007) and angiotensin-II (Gray et al., 1998; Strawn et al., 2000; Molkentin and DornII, 2001; Ayabe et al., 2006; Palaniyandi et al., 2009). These factors serve as agonists for a G protein-coupled signaling cascade through Gαq activation which in turn activates several isoforms of phospholipase C, including PLCβ1, found in the sarcolemma. In addition, mRNA and protein levels of PLCβ1 are increased in ischemia (Asemu et al., 2003) and in stroke-prone SHRs as young as 8–10 months there is increased sarcolemmal protein kinase C (PKC) activity (Kawaguchi et al., 1993), suggesting increased PLCβ1 activity. Here, we propose that it is the resulting decrease in membrane PIP2 content itself that has important consequences for TT maintenance and efficient excitation-contraction (EC) coupling.

In order to investigate the role of PIP2, we first focused on the properties of BIN1. Recently, it has been reported that BIN1 serves as an anchor for $Ca_v1.2$ localization to cardiac TTs, thus promoting specific microtubule-induced trafficking of new $Ca_v1.2$ molecules to the T-tubular membranes (Hong et al., 2010). This is an important observation because it demonstrates that BIN1 may insure the localization of proteins crucial for EC coupling to the TT and thus serve as an important candidate around which to build the structural and functional TT unit. With this in mind, we measured BIN1 protein expression in SHRs in comparison to normal WKY rats from ages 2–20 months and found no change in BIN1 levels with HF progression but rather extensive disorganization of this protein. We have previously reported that SHRs show significant abnormalities in systolic and diastolic function by 12–17 months as a sign of advancing HF (Shah et al., 2014). In the same study we showed that SHRs show TT disorganization in some myocytes as early as 9-months and that by the age of 17-months a significant reduction in TT organization is apparent in nearly all myocytes. Our current results show that PIP2 levels were significantly decreased during HF development in SHRs especially after the age of 12 months which is consistent with the onset of TT loss during HF development.

Amphiphysin-II Overexpression and Tubulation in HL-1 Cells

In this study, we wanted to explore the properties of BIN1 in a cell system that did not have inherent expression of this protein or TTs. This approach allowed us to examine the properties of BIN1 in tubule formation and how it would respond to PIP2 depletion. We used mouse HL1 cells which do not express BIN1 and found that the exogenous overexpression of all isoforms of BIN1 induced tubulation. We then used this model system to demonstrate that PIP2 depletion could be accomplished in any number of ways including activation of PLCβ or by inhibition of PIP2 synthesis via PI4-kinase (PI4K), both of which subsequently were found to abolish TTs in adult ventricular myocytes. The translocation of the membrane PIP2-binding reporter PLCδ1-PH-GFP from sarcolemma to cytosol following these pharmacological treatments suggested that tubule loss was a result of sarcolemma PIP2 depletion. These results suggest that not only does BIN1 have the potential to promote tubulation but it also requires the presence of membrane PIP2 to do so.

A Molecular Model for the Role of Cardiac BIN1 in Transverse Tubule Formation

We postulated that the N-BAR domain alone, without the Exon 10/11 sequence such as in cBIN1 isoforms, can still bind PIP2. In fact, the concept of structurally related F-BAR domains capable of binding phosphoinositol was studied previously by Frost et al. (2008) Mutagenesis analysis of the F-BAR domain of FBP17 protein showed that combined Lys56Glu and Arg104Asp substitutions resulted in an absence of tubulation. Considering that Lys56 and Arg104 are residuals of the α-helices that may be directly involved in the integrity of the helical structures or in maintaining coil-to-coil interactions, the argument of these cationic residues being the anchoring sites for phospholipid interactions remains inconclusive. The

N-BAR domain of BIN1 also forms oligomeric lattices with narrower tubules than those induced by F-BAR proteins (Frost et al., 2009). We noticed a triple-lysine motif (Lys164-Lys165-Lys166) in a short loop segment between two helices and subsequently demonstrated that mutations of these cationic residues abolished tubule formation. This cationic motif is located at the distal tips of an N-BAR dimer and the mutant is not expected to affect the integrity of the BAR domain structure (**Figures 8A,B**). When we modeled the BIN1 lattice in self-assembly during tubule induction and highlighted the pattern of tip-to-tip locations in **Figure 8C**, we found an alternative scenario of unified T-tubule formation through a charge-based BIN1-to-phosphoinositol interaction. These theoretical results support the idea of a novel mechanism by which PIP2 may induce BIN1 oligomerization with resulting TT formation and maintenance.

A Role for Cardiac BIN1 and Phosphatidylinositol-4,5-Bisphosphate Interaction in Cardiac Transverse Tubule Formation

In order to extend our observations in the HL-1 cell culture system to native cardiac myocyte structure and function, we repeated the PIP2 depletion experiments in native ventricular myocytes and found a similar dramatic reduction of TT organization following pharmacological PIP2 depletion. PIP2 depletion induced by either PI4K inhibition or PLCβ1 activation had virtually identical effects to disrupt TT organization to that reported for HF myocytes. As postulated earlier, PLCβ1 activation, as a member of putative BIN1, PIP2, and PLCβ1 complex located in the TTs, may lower endogenous PIP2 membrane levels in a manner similar to what we observed in culture. Thus, PIP2 depletion via PLCβ1 hydrolysis may eventually disrupt BIN1 targeting to plasma membranes where PIP2 ordinarily helps to localize this protein causing the cBIN1/PIP2 complex to lose its ability to maintain TTs and inducing TT remodeling in HF.

Effect of Transverse Tubule Loss in Failing Heart

HF myocytes show a reduction of both the rate and magnitude of SR Ca^{2+} release that contribute to poor contractile performance at the subcellular and cellular levels and ultimately to systolic dysfunction in the heart. Slow rise times and times to peak in myocytes after PIP2 depletion is consistent with the finding that PIP2 loss disrupts TTs thereby reducing Ca^{2+} influx through L-type Ca^{2+} channels and impairing CICR from SR. This point is important since cellular regions lacking TTs then have large distances across which remote TT Ca^{2+} influx must diffuse to reach the SR membrane (and so-called orphaned RyRs) in order to induce CICR compared to areas with normal TTs. Thus, instead of a simultaneous activation of contraction throughout the cell, individual cell regions without local TTs will do so with a delay resulting in a dyssynchronous contraction, reducing contractile efficiency. Another feature of altered Ca^{2+} cycling is slow reuptake (Beuckelmann et al., 1992; Balke and Shorofsky, 1998; O'Rourke et al., 1999; Gomez et al., 2001; Wasserstrom et al., 2009) and we observed a slower decay time of Ca^{2+} transients in these cells, affecting the synchrony of relaxation. The primary reason for this slowing is that the time to peak release is slowed and, furthermore, there is increased heterogeneity of release along the cell length. This variability in release presumably occurs where orphaned RyRs must wait for CICR from nearby release units to increase local Ca^{2+} concentration and activate release at those sites which no longer have nearby L-type Ca^{2+} current to trigger release. Because of the delay in release, there is a slowing in rise time and time-to-peak as seen both in our experiments with pharmacologically-induced PIP2 depletion and TT loss (**Figure 6**) as well as in HF (Louch et al., 2006, 2012; Song et al., 2006; Shah et al., 2014; Singh et al., 2017). The result is also a slowing in recovery of the Ca^{2+} transient as different regions of the cell go through delayed release and resulting removal of cytoplasmic Ca^{2+}.

Sarcolemmal PIP2 may also help localize other sarcolemmal proteins including K^+ channels and the Na-Ca exchanger, thereby affecting cytosolic Ca^{2+} homeostasis through other mechanisms (Hilgemann and Ball, 1996; Huang et al., 1998). The progressive amplification at the multicellular level of this intracellular phenomenon probably contributes to the impairment of overall myocardial function observed in HF.

Limitations

It is possible that the immunohistochemistry results may be affected by some experimental artifact that could bias our interpretation of apparent co-localization between these proteins. However, we took great care to insure that Cav1.2 was used as an indicator of the location of TTs and that any subsequent localization of the other proteins was aligned with this accepted standard for the localization of TTs. The close alignment between Cav1.2 and Bin1 (**Figures 1A,B**) as indicated in the merged overlap image cannot be explained as resulting due to chance without invoking explanations that are clearly unrealistic. Thus, although there may be some minor experimental artifacts that might reduce the accuracy of co-localization, such as poor alignment in the z-plane due to the point spread function inherent in confocal microscopy, it is highly unlikely that our results and interpretation are inaccurate overall.

Overall, our work provides extensive evidence that (1) PIP2 binds to Bin1, which has been a highly controversial issue in the heart, (2) Bin1 isoforms are capable of inducing tubule formation, and (3) PIP2 depletion causes loss of TTs in the heart in a manner that mimics the TT remodeling that occurs in HF. On the other hand, we have not provided definitive proof that the PIP2 depletion is directly responsible for TT loss. Our current methodologies do not permit us to measure this interaction directly but our results provide critical new evidence that PIP2 depletion occurs in HF and that pharmacological PIP2 depletion is associated with the loss of TTs in cardiac myocytes. The hope is that, in the future, we will be able to observe this relationship with higher precision in order to provide definitive proof of this reliance of TT remodeling on PIP2 regulation during the development of cardiac disease.

Clinical Implications

Our data suggest that BIN1 localization at the sarcolemma is required for TT formation and that PIP2 functions as a membrane-targeting and stabilization element for the formation of TTs. These observations are crucial to our understanding of TT remodeling in HF since reduced sarcolemmal PIP2 levels would then be expected to reduce BIN1 targeting to the sarcolemma and hence tubulation. This finding suggests a novel mechanism for TT formation and maintenance, both normal and abnormal. Approximately 80% or more of all L-type Ca^{2+} channels are present on TTs, which in turn are critical for the synchronous release of Ca^{2+} in myocytes and normal EC coupling in heart. Our observation that both delayed Ca^{2+} release and reuptake are closely related to TT organization due to PIP2 depletion strongly suggests that the loss of PIP2 may be the mechanism for TT disruption during disease development and the resulting defects in Ca^{2+} cycling and progressive decline in myocardial mechanics. Our study provides important new insights into the mechanistic understanding of TT organization and its implications in Ca^{2+} dynamics in normal and diseased states.

Based on our results, it might be possible to interfere with degenerative TT remodeling by targeting pathways leading to PIP2 loss. A better mechanistic understanding of the roles of BIN1 and PIP2 in TT remodeling may be important to the development of novel therapeutic interventions aimed at the restoration of this putative phospholipid-protein interactive complex both for the prevention of and the reversal of HF once it has developed.

DATA AVAILABILITY STATEMENT

The original contributions presented in the study are included in the article/**Supplementary Material**, further inquiries can be directed to the corresponding author/s.

ETHICS STATEMENT

The studies involving human participants were reviewed and approved by the Northwestern University Institutional Review Board, Northwestern University, Evanston, IL. Written informed consent for participation was not required for this study in accordance with the national legislation and the institutional requirements. The animal study was reviewed and approved by the Institutional Animal Care and Use Committee, Northwestern University, Evanston, IL.

AUTHOR CONTRIBUTIONS

JZ, NS, JW, and JJ designed and performed experiments, analyzed the data, wrote parts of the manuscript, and approved the final version. CM, WM, and LG designed and performed the experiments, analyzed the data, and approved the final version. MF, WL, PK, SV, RK, and GA designed the experiments and approved the final version. EN and MM analyzed the data and approved the final version. All authors contributed to the article and approved the submitted version.

FUNDING

Funding was provided in part by the HL119095 (to JW) and HL09193 (to RK).

SUPPLEMENTARY MATERIAL

The Supplementary Material for this article can be found online at: https://www.frontiersin.org/articles/10.3389/fphys.2021.782767/full#supplementary-material

REFERENCES

Aistrup, G. L., Gupta, D. K., Kelly, J. E., O'toole, M. J., Nahhas, A., Chirayil, N., et al. (2013). Inhibition of the late sodium current slows t-tubule disruption during the progression of hypertensive heart disease in the rat. *Am. J. Physiol. Heart Circ. Physiol.* 305, H1068–H1079. doi: 10.1152/ajpheart.00401.2013

Albert, A. P., Saleh, S. N., and Large, W. A. (2008). Inhibition of native TRPC6 channel activity by phosphatidylinositol 4,5-bisphosphate in mesenteric artery myocytes. *J. Physiol.* 586, 3087–3095. doi: 10.1113/jphysiol.2008.153676

Asemu, G., Tappia, P. S., and Dhalla, N. S. (2003). Identification of the changes in phospholipase C isozymes in ischemic-reperfused rat heart. *Arch. Biochem. Biophys.* 411, 174–182. doi: 10.1016/s0003-9861(02)00733-6

Ayabe, N., Babaev, V. R., Tang, Y., Tanizawa, T., Fogo, A. B., Linton, M. F., et al. (2006). Transiently heightened angiotensin II has distinct effects on atherosclerosis and aneurysm formation in hyperlipidemic mice. *Atherosclerosis* 184, 312–321. doi: 10.1016/j.atherosclerosis.2005.05.016

Balijepalli, R. C., Lokuta, A. J., Maertz, N. A., Buck, J. M., Haworth, R. A., Valdivia, H. H., et al. (2003). Depletion of T-tubules and specific subcellular changes in sarcolemmal proteins in tachycardia-induced heart failure. *Cardiovasc. Res.* 59, 67–77. doi: 10.1016/s0008-6363(03)00325-0

Balke, C. W., and Shorofsky, S. R. (1998). Alterations in calcium handling in cardiac hypertrophy and heart failure. *Cardiovasc. Res.* 37, 290–299. doi: 10.1016/s0008-6363(97)00272-1

Beuckelmann, D. J., Nabauer, M., and Erdmann, E. (1992). Intracellular calcium handling in isolated ventricular myocytes from patients with terminal heart failure. *Circulation* 85, 1046–1055.

Bohm, F., and Pernow, J. (2007). The importance of endothelin-1 for vascular dysfunction in cardiovascular disease. *Cardiovasc. Res.* 76, 8–18. doi: 10.1016/j.cardiores.2007.06.004

Brown, D. A., Hughes, S. A., Marsh, S. J., and Tinker, A. (2007). Regulation of M(Kv7.2/7.3) channels in neurons by PIP(2) and products of PIP(2) hydrolysis: significance for receptor-mediated inhibition. *J. Physiol.* 582, 917–925. doi: 10.1113/jphysiol.2007.132498

Crossman, D. J., Ruygrok, P. N., Soeller, C., and Cannell, M. B. (2011). Changes in the organization of excitation-contraction coupling structures in failing human heart. *PLoS One* 6:e17901. doi: 10.1371/journal.pone.0017901

Frisk, M., Ruud, M., Espe, E. K., Aronsen, J. M., Roe, A. T., Zhang, L., et al. (2016). Elevated ventricular wall stress disrupts cardiomyocyte t-tubule structure and calcium homeostasis. *Cardiovasc. Res.* 112, 443–451. doi: 10.1093/cvr/cvw111

Frost, A., Perera, R., Roux, A., Spasov, K., Destaing, O., Egelman, E. H., et al. (2008). Structural basis of membrane invagination by F-BAR domains. *Cell* 132, 807–817. doi: 10.1016/j.cell.2007.12.041

Frost, A., Unger, V. M., and De Camilli, P. (2009). The BAR domain superfamily: membrane-molding macromolecules. *Cell* 137, 191–196. doi: 10.1016/j.cell.2009.04.010

Fugier, C., Klein, A. F., Hammer, C., Vassilopoulos, S., Ivarsson, Y., Toussaint, A., et al. (2011). Misregulated alternative splicing of BIN1 is associated with T tubule alterations and muscle weakness in myotonic dystrophy. *Nat. Med.* 17, 720–725. doi: 10.1038/nm.2374

Gomez, A. M., Guatimosim, S., Dilly, K. W., Vassort, G., and Lederer, W. J. (2001). Heart failure after myocardial infarction: altered excitation-contraction coupling. *Circulation* 104, 688–693. doi: 10.1161/hc3201.092285

Gray, M. O., Long, C. S., Kalinyak, J. E., Li, H. T., and Karliner, J. S. (1998). Angiotensin II stimulates cardiac myocyte hypertrophy via paracrine release of TGF-beta 1 and endothelin-1 from fibroblasts. *Cardiovasc. Res.* 40, 352–363. doi: 10.1016/s0008-6363(98)00121-7

Grubb, D. R., Iliades, P., Cooley, N., Yu, Y. L., Luo, J., Filtz, T. M., et al. (2011). Phospholipase Cbeta1b associates with a Shank3 complex at the cardiac sarcolemma. *FASEB J.* 25, 1040–1047. doi: 10.1096/fj.10-171470

Grubb, D. R., Vasilevski, O., Huynh, H., and Woodcock, E. A. (2008). The extreme C-terminal region of phospholipase Cbeta1 determines subcellular localization and function; the "B" splice variant mediates alpha1-adrenergic receptor responses in cardiomyocytes. *FASEB J.* 22, 2768–2774. doi: 10.1096/fj.07-102558

Guo, J., Tian, Q., Barth, M., Xian, W., Ruppenthal, S., Schaefers, H. J., et al. (2021). Human BIN1 isoforms grow, maintain and regenerate excitation-contraction couplons in adult rat and human stem cell-derived cardiomyocytes. *Cardiovasc. Res.* 2021:cvab195. doi: 10.1093/cvr/cvab195

He, J., Conklin, M. W., Foell, J. D., Wolff, M. R., Haworth, R. A., Coronado, R., et al. (2001). Reduction in density of transverse tubules and L-type Ca(2+) channels in canine tachycardia-induced heart failure. *Cardiovasc. Res.* 49, 298–307. doi: 10.1016/s0008-6363(00)00256-x

Heinzel, F. R., Bito, V., Biesmans, L., Wu, M., Detre, E., Von Wegner, F., et al. (2008). Remodeling of T-tubules and reduced synchrony of Ca2+ release in myocytes from chronically ischemic myocardium. *Circ. Res.* 102, 338–346. doi: 10.1161/CIRCRESAHA.107.160085

Hilgemann, D. W., and Ball, R. (1996). Regulation of cardiac Na+,Ca2+ exchange and KATP potassium channels by PIP2. *Science* 273, 956–959. doi: 10.1126/science.273.5277.956

Hong, T., Yang, H., Zhang, S. S., Cho, H. C., Kalashnikova, M., Sun, B., et al. (2014). Cardiac BIN1 folds T-tubule membrane, controlling ion flux and limiting arrhythmia. *Nat. Med.* 20, 624–632. doi: 10.1038/nm.3543

Hong, T. T., Smyth, J. W., Gao, D., Chu, K. Y., Vogan, J. M., Fong, T. S., et al. (2010). BIN1 localizes the L-type calcium channel to cardiac T-tubules. *PLoS Biol.* 8:e1000312. doi: 10.1371/journal.pbio.1000312

Huang, C. L., Feng, S., and Hilgemann, D. W. (1998). Direct activation of inward rectifier potassium channels by PIP2 and its stabilization by Gbetagamma. *Nature* 391, 803–806. doi: 10.1038/35882

Kawaguchi, H., Sano, H., Iizuka, K., Okada, H., Kudo, T., Kageyama, K., et al. (1993). Phosphatidylinositol metabolism in hypertrophic rat heart. *Circ. Res.* 72, 966–972. doi: 10.1161/01.res.72.5.966

Lee, E., Marcucci, M., Daniell, L., Pypaert, M., Weisz, O. A., Ochoa, G. C., et al. (2002). Amphiphysin 2 (Bin1) and T-tubule biogenesis in muscle. *Science* 297, 1193–1196. doi: 10.1126/science.1071362

Li, L. L., Guo, Q. J., Lou, H. Y., Liang, J. H., Yang, Y., Xing, X., et al. (2020). Nanobar array assay revealed complementary roles of BIN1 splice isoforms in cardiac T-tubule morphogenesis. *Nano Lett.* 20, 6387–6395. doi: 10.1021/acs.nanolett.0c01957

Louch, W. E., Bito, V., Heinzel, F. R., Macianskiene, R., Vanhaecke, J., Flameng, W., et al. (2004). Reduced synchrony of Ca2+ release with loss of T-tubules-a comparison to Ca2+ release in human failing cardiomyocytes. *Cardiovasc. Res.* 62, 63–73. doi: 10.1016/j.cardiores.2003.12.031

Louch, W. E., Mork, H. K., Sexton, J., Stromme, T. A., Laake, P., Sjaastad, I., et al. (2006). T-tubule disorganization and reduced synchrony of Ca2+ release in murine cardiomyocytes following myocardial infarction. *J. Physiol.* 574, 519–533. doi: 10.1113/jphysiol.2006.107227

Louch, W. E., Stokke, M. K., Sjaastad, I., Christensen, G., and Sejersted, O. M. (2012). No rest for the weary: diastolic calcium homeostasis in the normal and failing myocardium. *Physiology (Bethesda)* 27, 308–323. doi: 10.1152/physiol.00021.2012

Lyon, A. R., Macleod, K. T., Zhang, Y., Garcia, E., Kanda, G. K., Lab, M. J., et al. (2009). Loss of T-tubules and other changes to surface topography in ventricular myocytes from failing human and rat heart. *Proc. Natl. Acad. Sci. U.S.A.* 106, 6854–6859. doi: 10.1073/pnas.0809777106

Martin, T. F. (1998). Phosphoinositide lipids as signaling molecules: common themes for signal transduction, cytoskeletal regulation, and membrane trafficking. *Annu. Rev. Cell Dev. Biol.* 14, 231–264. doi: 10.1146/annurev.cellbio.14.1.231

Miyauchi, T., Yanagisawa, M., Tomizawa, T., Sugishita, Y., Suzuki, N., Fujino, M., et al. (1989). Increased plasma concentrations of endothelin-1 and big endothelin-1 in acute myocardial infarction. *Lancet* 2, 53–54. doi: 10.1016/s0140-6736(89)90303-6

Molkentin, J. D., and Dorn, G. W. II (2001). Cytoplasmic signaling pathways that regulate cardiac hypertrophy. *Annu. Rev. Physiol.* 63, 391–426. doi: 10.1146/annurev.physiol.63.1.391

Muller, A. J., Baker, J. F., Duhadaway, J. B., Ge, K., Farmer, G., Donover, P. S., et al. (2003). Targeted disruption of the murine Bin1/Amphiphysin II gene does not disable endocytosis but results in embryonic cardiomyopathy with aberrant myofibril formation. *Mol. Cell Biol.* 23, 4295–4306. doi: 10.1128/MCB.23.12.4295-4306.2003

Nicot, A. S., Toussaint, A., Tosch, V., Kretz, C., Wallgren-Pettersson, C., Iwarsson, E., et al. (2007). Mutations in amphiphysin 2 (BIN1) disrupt interaction with dynamin 2 and cause autosomal recessive centronuclear myopathy. *Nat. Genet.* 39, 1134–1139. doi: 10.1038/ng2086

O'Rourke, B., Kass, D. A., Tomaselli, G. F., Kaab, S., Tunin, R., and Marban, E. (1999). Mechanisms of altered excitation-contraction coupling in canine tachycardia-induced heart failure, I: experimental studies. *Circ. Res.* 84, 562–570. doi: 10.1161/01.res.84.5.562

Palaniyandi, S. S., Sun, L., Ferreira, J. C., and Mochly-Rosen, D. (2009). Protein kinase C in heart failure: a therapeutic target? *Cardiovasc. Res.* 82, 229–239. doi: 10.1093/cvr/cvp001

Ramjaun, A. R., and McPherson, P. S. (1998). Multiple amphiphysin II splice variants display differential clathrin binding: identification of two distinct clathrin-binding sites. *J. Neurochem.* 70, 2369–2376. doi: 10.1046/j.1471-4159.1998.70062369.x

Razzaq, A., Robinson, I. M., Mcmahon, H. T., Skepper, J. N., Su, Y., Zelhof, A. C., et al. (2001). Amphiphysin is necessary for organization of the excitation-contraction coupling machinery of muscles, but not for synaptic vesicle endocytosis in Drosophila. *Genes Dev.* 15, 2967–2979. doi: 10.1101/gad.207801

Shah, S. J., Aistrup, G. L., Gupta, D. K., O'toole, M. J., Nahhas, A. F., Schuster, D., et al. (2014). Ultrastructural and cellular basis for the development of abnormal myocardial mechanics during the transition from hypertension to heart failure. *Am. J. Physiol. Heart Circ. Physiol.* 306, H88–H100. doi: 10.1152/ajpheart.00642.2013

Singh, J. K., Barsegyan, V., Bassi, N., Marszalec, W., Tai, S., Mothkur, S., et al. (2017). T-tubule remodeling and increased heterogeneity of calcium release during the progression to heart failure in intact rat ventricle. *Physiol. Rep.* 5, e13540. doi: 10.14814/phy2.13540

Song, L. S., Sobie, E. A., Mcculle, S., Lederer, W. J., Balke, C. W., and Cheng, H. (2006). Orphaned ryanodine receptors in the failing heart. *Proc. Natl. Acad. Sci. U.S.A.* 103, 4305–4310. doi: 10.1073/pnas.0509324103

Strawn, W. B., Dean, R. H., and Ferrario, C. M. (2000). Novel mechanisms linking angiotensin II and early atherogenesis. *J. Renin Angiotensin Aldosterone Syst.* 1, 11–17. doi: 10.3317/jraas.2000.001

Tappia, P. S., Liu, S. Y., Shatadal, S., Takeda, N., Dhalla, N. S., and Panagia, V. (1999). Changes in sarcolemmal PLC isoenzymes in postinfarct congestive heart failure: partial correction by imidapril. *Am. J. Physiol.* 277, H40–H49. doi: 10.1152/ajpheart.1999.277.1.H40

Tsuji, S., Sawamura, A., Watanabe, H., Takihara, K., Park, S. E., and Azuma, J. (1991). Plasma endothelin levels during myocardial ischemia and reperfusion. *Life Sci.* 48, 1745–1749. doi: 10.1016/0024-3205(91)90211-s

Wasserstrom, J. A., Sharma, R., Kapur, S., Kelly, J. E., Kadish, A. H., Balke, C. W., et al. (2009). Multiple defects in intracellular calcium cycling in whole failing rat heart. *Circ. Heart Fail* 2, 223–232. doi: 10.1161/CIRCHEARTFAILURE.108.811539

Wei, S., Guo, A., Chen, B., Kutschke, W., Xie, Y. P., Zimmerman, K., et al. (2010). T-tubule remodeling during transition from hypertrophy to heart failure. *Circ. Res.* 107, 520–531. doi: 10.1161/circresaha.109.212324

Yasuda, M., Kohno, M., Tahara, A., Itagane, H., Toda, I., Akioka, K., et al. (1990). Circulating immunoreactive endothelin in ischemic heart disease. *Am. Heart J.* 119, 801–806. doi: 10.1016/s0002-8703(05)80315-1

Ziegelhoffer, A., Tappia, P. S., Mesaeli, N., Sahi, N., Dhalla, N. S., and Panagia, V. (2001). Low level of sarcolemmal phosphatidylinositol 4,5-bisphosphate in cardiomyopathic hamster (UM-X7.1) heart. *Cardiovasc. Res.* 49, 118–126. doi: 10.1016/s0008-6363(00)00209-1

Conflict of Interest: The authors declare that the research was conducted in the absence of any commercial or financial relationships that could be construed as a potential conflict of interest.

REVIEW
published: 05 January 2022
doi: 10.3389/fphys.2021.810408

Nanoscale Organization, Regulation, and Dynamic Reorganization of Cardiac Calcium Channels

*Rose E. Dixon**

Department of Physiology and Membrane Biology, School of Medicine, University of California, Davis, Davis, CA, United States

The architectural specializations and targeted delivery pathways of cardiomyocytes ensure that L-type Ca^{2+} channels (CaV1.2) are concentrated on the t-tubule sarcolemma within nanometers of their intracellular partners the type 2 ryanodine receptors (RyR2) which cluster on the junctional sarcoplasmic reticulum (jSR). The organization and distribution of these two groups of cardiac calcium channel clusters critically underlies the uniform contraction of the myocardium. Ca^{2+} signaling between these two sets of adjacent clusters produces Ca^{2+} sparks that in health, cannot escalate into Ca^{2+} waves because there is sufficient separation of adjacent clusters so that the release of Ca^{2+} from one RyR2 cluster or supercluster, cannot activate and sustain the release of Ca^{2+} from neighboring clusters. Instead, thousands of these Ca^{2+} release units (CRUs) generate near simultaneous Ca^{2+} sparks across every cardiomyocyte during the action potential when calcium induced calcium release from RyR2 is stimulated by depolarization induced Ca^{2+} influx through voltage dependent CaV1.2 channel clusters. These sparks summate to generate a global Ca^{2+} transient that activates the myofilaments and thus the electrical signal of the action potential is transduced into a functional output, myocardial contraction. To generate more, or less contractile force to match the hemodynamic and metabolic demands of the body, the heart responds to β-adrenergic signaling by altering activity of calcium channels to tune excitation-contraction coupling accordingly. Recent accumulating evidence suggests that this tuning process also involves altered expression, and dynamic reorganization of CaV1.2 and RyR2 channels on their respective membranes to control the amplitude of Ca^{2+} entry, SR Ca^{2+} release and myocardial function. In heart failure and aging, altered distribution and reorganization of these key Ca^{2+} signaling proteins occurs alongside architectural remodeling and is thought to contribute to impaired contractile function. In the present review we discuss these latest developments, their implications, and future questions to be addressed.

Keywords: CaV1.2 Ca^{2+} channel, RyR2, EC-coupling, heart failure, β-adrenergic regulation, L-type calcium channels, ion channel clustering

Edited by:
William E. Louch,
University of Oslo, Norway

Reviewed by:
Xin Shen,
University of Oslo, Norway
Michelle Munro,
University of Otago, New Zealand

***Correspondence:**
Rose E. Dixon
redickson@ucdavis.edu
orcid.org/0000-0003-0655-690X

Specialty section:
This article was submitted to Membrane Physiology and Membrane Biophysics, a section of the journal Frontiers in Physiology

Received: 06 November 2021
Accepted: 30 November 2021
Published: 05 January 2022

Citation:
Dixon RE (2022) Nanoscale Organization, Regulation, and Dynamic Reorganization of Cardiac Calcium Channels.
Front. Physiol. 12:810408.
doi: 10.3389/fphys.2021.810408

INTRODUCTION

During action potential (AP)-driven membrane depolarization in ventricular myocytes, Ca^{2+} influx across the plasma membrane occurs through voltage-gated L-type CaV1.2 channels. The level of calcium influx through CaV1.2 channels triggers a graded amount of calcium induced calcium release (CICR) from the type 2 ryanodine receptors (RyR2) on the juxtaposed junctional sarcoplasmic reticulum (jSR) at specialized nanodomains between the sarcoplasmic reticulum (SR) and the t-tubule or surface plasma membrane (PM). These SR-PM junctions termed dyads or calcium release units (CRUs), house the fundamental ion channel machinery for EC-coupling, bringing clusters of CaV1.2 channels into nanometer proximity of their intracellular Ca^{2+} channel partners RyR2 (**Figure 1**). These two cardiac calcium channel partners participate in feedforward and feedback signaling to permit the faithful beat-to-beat coupling of electrical excitation to Ca^{2+}-driven mechanical contraction. Here we review the nanoscale organization of CaV1.2 and RyR2 channels, and how it can be regulated by a key stress signaling pathway (β-adrenergic receptor (β-AR) signaling). We also highlight nanoscale reorganization of these two calcium channels that occurs during heart failure (HF) and aging and discuss the implications for contractile function.

CaV1.2 CHANNEL LOCALIZATION IN VENTRICULAR MYOCYTES

CaV1.2 are heteromeric channel complexes consisting of a pore-forming and voltage-sensing α_{1C} subunit (~250 kDa), associated with CaVβ (~52–72 kDa depending on the isoform), CaV$\alpha_2\delta$ (~175 kDa), and sometimes CaVγ (~32 kDa) auxiliary subunits in a 1:1:1:1 stoichiometry (Catterall, 2011; Zamponi et al., 2015; Dolphin, 2016; Westhoff and Dixon, 2021). To directly influence EC-coupling, CaV1.2 channels must be located at dyadic junctions in the vicinity of the sarcomeres where the influx of Ca^{2+} can be coupled to CICR from RyR2 on the jSR. Dyads are predominantly found at interfaces between the jSR and the t-tubule membrane, but there are a significant number of functional dyads on the axial/longitudinal tubule interfaces and at the sarcolemmal crest interface (Asghari et al., 2009). It should be noted that despite the continued use of t-tubules as the standard nomenclature for the non-surface, tubular network of sarcolemma, a convention we maintain herein, around 40% of the network is not transverse at all but rather lies longitudinally or axially along the length of the cell between the z-lines in rat ventricular myocytes (Soeller and Cannell, 1999), although the proportion of longitudinally-orientated tubules varies between species (Setterberg et al., 2021).

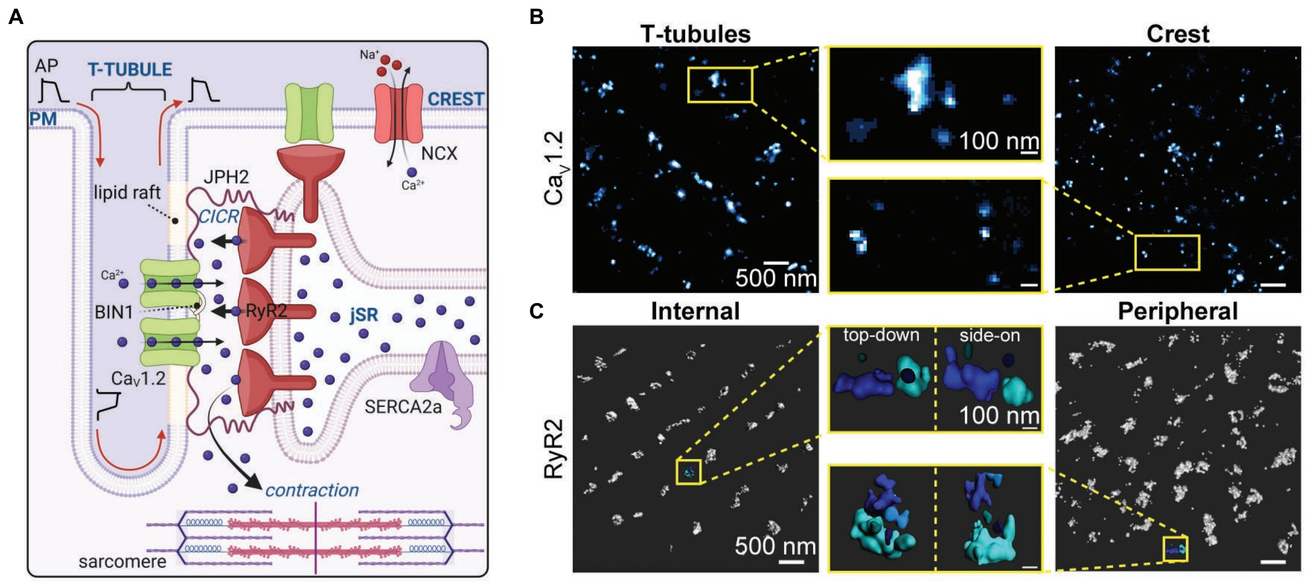

FIGURE 1 | Calcium channel organization/clustering in the Dyad. **(A)** Illustration depicting the cardiac dyad where CaV1.2 channels are delivered along microtubules to BIN1-hubs on the t-tubule membrane. There they concentrate and form clusters of variable sizes, opposite clusters of RyR2 on the junctional sarcoplasmic reticulum. The dyad is held together by JPH2 which anchors the jSR within 12–15 nm of the t-tubule sarcolemma. JPH2 interacts with both CaV1.2 and RyR2, affecting RyR2 gating, and potentially playing a role in CaV1.2 retention in the dyad. Not all CaV1.2 channels and RyR2 are found in these t-tubule:jSR junctional complexes, some are found in junctions at the sarcolemmal crest and others (not illustrated) are found at junctions along longitudinally oriented axial-tubules. **(B)** CaV1.2 channel clusters at the t-tubule (*left*) and crest (*right*) sarcolemma are seen in super-resolution Ground State Depletion (GSD) localization maps from fixed, immunostained mouse ventricular myocytes. Yellow boxes indicate zoomed-in regions (*middle*). Reproduced and modified with permission from (Del Villar et al., 2021). **(C)** RyR2 clusters are observed in 3D-renderings of 3D-STORM images of internal and peripherally located RyR2s in fixed, immunostained rat cardiomyocytes. Yellow boxes indicate zoomed-in regions of each image from top-down, and side-on perspectives. Panel C was reproduced and modified with permission from (Shen et al., 2019). Illustrations were created in *Biorender*.

In health, the vast majority of CaV1.2 channels are located on the t-tubule membranes (Scriven et al., 2000) where the channel density is around 9 times that of the surface sarcolemma (Bers, 2001). This preferential t-tubular distribution of CaV1.2 channels is apparent in immuno-stained myocytes using conventional fluorescence (Carl et al., 1995) and super-resolution imaging approaches (Dixon et al., 2015; Ito et al., 2019; Del Villar et al., 2021). Detubulation of rat ventricular myocytes with formamide, an approach that severs the transverse and axial tubules but allows their openings at the surface sarcolemma to reseal, leads to loss of ~25% of the cell capacitance but an ~75% reduction in I_{Ca}, indicating that the t-tubular membrane constitutes around a quarter of the total sarcolemmal area but houses almost three quarters of the functional CaV1.2 channels (Kawai et al., 1999). The remaining 25% of CaV1.2 represent the surface membrane subpopulation of channels which are thought to play a critical role in SR Ca^{2+} loading since detubulination does not significantly affect SR Ca^{2+} load.

Super-resolution single molecule localization microscopy (SMLM) has revealed that CaV1.2 channels are not just homogenously distributed along the sarcolemma but rather, preferentially form clusters in both the t-tubules (Dixon et al., 2015, 2017; Ito et al., 2019; Del Villar et al., 2021) and sarcolemmal crest of ventricular myocytes (Del Villar et al., 2021; see **Figure 1B**), as well as human embryonic stem cell derived cardiomyocytes (hESC-CMs; De La Mata et al., 2019). Stepwise photobleaching experiments have been used to quantify the number of channels per cluster, likely limited to the surface sarcolemma since these experiments were performed in TIRF (Dixon et al., 2015; Ito et al., 2019). In those studies, myocytes were transduced with photoactivatable GFP-tagged CaVβ subunits which bind to CaVα_{1C} with a 1:1 stoichiometry allowing them to function as fluorescent biosensors of channel location when they are photoactivated. Using this approach, the mean number of channels per surface cluster is 6–8 although this is likely a gross underestimate given that most channels are likely bound to endogenous, non-fluorescent CaVβ and remain uncounted. Cryo-EM structures of the related skeletal muscle L-type Ca^{2+} channel, CaV1.1 have revealed the widest aspect of the channel as 100 Å (10 nm; Wu et al., 2015, 2016). Assuming a single CaV1.2 channel occupies a similar maximum area of 100 nm^2, then t-tubule clusters may contain on the order of ~20–37 channels based on published cluster areas. Crest cluster areas have only been measured in one study thus far but were not significantly different from t-tubule cluster areas (Del Villar et al., 2021) so a similar channel content may be inferred there. In both instances, these estimates assume tight packing of channels with no space between them and are thus likely overestimates. Future studies are needed to accurately quantify the number of channels per cluster. As discussed in Section “RyR2 Localization in Ventricular Myocytes”, cluster size can be regulated by signal transduction pathways including β-adrenergic signaling, with repercussions for channel function, Ca^{2+} influx, and inotropy (Ito et al., 2019; Del Villar et al., 2021).

Targeted delivery of CaV1.2 to the t-tubule membrane is thought to occur *via* microtubules anchored by a protein called bridging integrator 1 (BIN1; Hong et al., 2010, 2012). BIN1 also plays a role in the formation of t-tubules which relies on its ability to curve membranes upon dimerization of its N-terminal BAR domain (Lee et al., 2002; Frost et al., 2009; Hong et al., 2010). Channel conveyance to BIN1 delivery hubs on the membrane is, however not dependent on membrane tubulation as demonstrated by the abrogation of CaV1.2 delivery in cells expressing a truncated BIN1(1–282) which retains the BAR domain and tubulation ability but lacks the coiled-coil and SH3 domains that form the remainder of the full-length BIN1 structure (Hong et al., 2010). This implies that targeted delivery of CaV1.2 is reliant on the coiled-coil and/or SH3 domains of BIN1. In addition, a cardiac specific isoform of BIN1 (BIN1 + 13 + 17) is thought to generate microfolds on the t-tubule membrane which support the formation of diffusion-restricted microdomains and facilitate clustering of CaV1.2 channels already at the t-tubules (Hong et al., 2014). The role of BIN1 in CaV1.2 and RyR2 displacement and mis-regulation during cardiac pathology is discussed in detail in section “Role of Bridging Integrator 1” below.

Non-dyadic CaV1.2 channel subpopulations are present in caveolae, and non-caveolar lipid rafts as reviewed elsewhere (Maguy et al., 2006; Best and Kamp, 2012). These extra-dyadic populations (Levin and Page, 1980) have been reported to contribute to EC-coupling by affecting the efficiency of Ca^{2+} release from the SR (Calaghan and White, 2006), while other reports suggest they do not contribute directly to EC-coupling (Balijepalli et al., 2006; Correll et al., 2017). Lipid rafts have been proposed to form platforms for dyads in cultured rat ventricular myocytes with the dyadic spacer and SR/PM tethering protein junctophilin-2 (JPH2) associating with cholesterol and the muscle isoform of caveolin (Cav3) to form junctional membrane complexes to which CaV1.2 channels are recruited (Poulet et al., 2021). JPH2 is discussed in greater detail in Section “Role of Junctophilin 2”.

RYR2 LOCALIZATION IN VENTRICULAR MYOCYTES

RyR2 are very large (~2.2 MDa) intracellular, Ca^{2+} activated calcium channels found on the ER/SR membrane of most cells (Lanner et al., 2010). These largest known ion channels are homotetrameric assemblies with individual subunits of ~565 kDa (Van Petegem, 2015). Electron microscopy studies have revealed that RyR2 are predominantly, but not exclusively localized to the jSR at t-tubule adjacent locations in junctional complexes/dyads (Franzini-Armstrong et al., 1999). The 3D geometry of RyR2 clusters is variable, complex, and dynamic with them often observed wrapping around t-tubules (Soeller et al., 2007; Hou et al., 2015) and forming larger or smaller clusters depending on their phosphorylation state and/or association with immunophilins FKBP12 or FKBP12.6 (Asghari et al., 2020).

In recent years, super-resolution microscopy techniques have been employed to image RyR2 with 20–30 nm lateral resolution, revealing that the large RyR2 clusters visualized in diffraction-limited confocal microscopy (Chen-Izu et al., 2006) are often ‘superclusters’ composed of several smaller clusters which are proposed to work together as a single CRU (Baddeley et al., 2009; Hou et al., 2015). Delineation of CRU boundaries has varied between publications and investigators with a 3D-STORM study dilating clusters by 50 nm in x, y, and z and then fusing the overlapping clusters to decide on the CRU boundary (Shen et al., 2019) while other 2D studies have assigned clusters to the same CRU if they lie within an edge-to-edge distance of 100 nm (Baddeley et al., 2009; Hou et al., 2015) or 150 nm of each other (MacQuaide et al., 2015). These numbers have stemmed from the *in silico* finding that RyRs located within <100 nm of an activated cluster are exposed to sufficiently high levels of Ca^{2+} (>10 μM) to permit their activation (Sobie et al., 2006). Variation in the reported number of RyRs per CRU from study to study may be partially explained by this inconsistency in CRU boundary delineation (Kolstad et al., 2018).

Clusters present on the coverslip adherent surface of myocytes form peripheral couplons and appear in a double-row pattern visible either side of the z-disk (Chen-Izu et al., 2006), with dSTORM imaging revealing a mean of ~14 RyR2 per cluster (Baddeley et al., 2009), and DNA-PAINT approaches reporting 7–9 RyR2 per peripheral cluster (Jayasinghe et al., 2018; Sheard et al., 2019). Deeper inside the cell, internal clusters are larger and contain ~63 RyR2 on average with >80% of clusters containing ≥100 channels (Hou et al., 2015). More recent 3D super-resolution imaging has suggested that peripheral CRUs contain an average of ~18 and internal CRUs ~23 RyR2 (Shen et al., 2019), with the average cluster containing ~10 channels in the periphery and ~13 channel in the internal fraction (see **Figure 1C**). While an expansion microscopy study in which expanded samples were imaged on an Airyscan confocal microscope reported peripheral clusters contained ~9 RyR2 on average while internal clusters contained ~8 (Sheard et al., 2019). At both locations, there is a high degree of colocalization between RyR2 and JPH2 confirming their dyadic locale (Baddeley et al., 2009; Jayasinghe et al., 2012; Hou et al., 2015). Size of RyR2 clusters has recently been reported to directly influence Ca^{2+} spark frequency (Galice et al., 2018) and amplitude (Xie et al., 2019). This idea will be revisited later in Section "Nanoscale Re-Organization of RyR2".

β-ADRENERGIC RECEPTOR SIGNALING STIMULATES ALTERATIONS IN THE FUNCTION AND NANOSCALE DISTRIBUTION OF CaV1.2

During episodes of acute stress and exercise, catecholamine binding to β-ARs on cardiomyocyte sarcolemmas initiates a cellular signaling cascade resulting in activation of adenylyl cyclase, enhanced cAMP production and a subsequent boost in protein kinase A (PKA) activity and downstream phosphorylation of multiple molecular targets and effectors as recently reviewed (Man et al., 2020). One of those effectors is the cardiac CaV1.2 channel complex. When phosphorylated, CaV1.2 channel open probability (P_o) and gating properties are altered in favor of increased activity and longer mode 2 openings (Tsien et al., 1972; Yue et al., 1990), that has recently been proposed to be due to removal of the inhibitory effects of Rad on CaV1.2 (Liu et al., 2020; Papa et al., 2021).

Along with the increased channel activity, another aspect of β-adrenergic regulation of CaV1.2 is the apparent increase in the number of functional channels in the membrane. This was first observed in some of the earliest reports of adrenergic regulation of these channels (Sperelakis and Schneider, 1976; Reuter and Scholz, 1977; Bean et al., 1984) but remained unexplained until our recent studies examining CaV1.2 channel dynamics and clustering (Ito et al., 2019; Del Villar et al., 2021). We reported PKA-dependent (H-89 and PKI inhibited), enhanced clustering and expression of CaV1.2 channels on the t-tubule membrane of adult mouse cardiomyocytes after stimulation with ISO (**Figures 2A,B**). Within these enlarged clusters, channels are packed tightly together, facilitating physical communication between adjacent CaV1.2 such that the opening of one channel in the cluster can drive the opening of other physically interacting channels *via* an allosteric mechanism. This cooperative gating behavior manifests as the simultaneous opening and/or closing of multiple channels. The exact details of the allosteric mechanism are still incompletely understood but is thought to involve Ca^{2+}/calmodulin (Ca^{2+}•CaM) bridging of neighboring channels *via* their C-terminal tails (Dixon et al., 2015). The overall impact of these interactions between groups of channels in a cluster is an amplification of Ca^{2+} influx into the cell as the highest P_o channel in the cluster, drives the opening of the others. Since PKA-mediated phosphorylation of CaV1.2 increases channel P_o an implication of these findings is that a small number of phospho-channels could have a disproportionately large effect as they can drive activity of attached non-phosphorylated channels in their cluster. This effectively increases the number of functional channels, allowing enhanced Ca^{2+} influx during the action potential plateau thus facilitating an inotropic response. Indeed EC-coupling studies of rat ventricular myocytes biolistically transfected with CaV1.2 channels tagged with a light activated dimerization system confirmed that CaV1.2-CaV1.2 interactions and the ensuing amplification of Ca^{2+} influx leads to larger amplitude Ca^{2+} transients indicating enhanced CICR and favoring inotropy (Dixon et al., 2012).

Along with this ISO-stimulated cooperative gating effect on the functional availability of channels, β-AR activation also incites an ~20% increase in the total number of channels in the t-tubule membrane as indicated by super-resolution SMLM studies of CaV1.2, gating current measurements, and biochemical studies of CaV1.2 protein expression (Ito et al., 2019; Del Villar et al., 2021). This ISO-stimulated dynamic augmentation of channel expression was demonstrated in live-cell TIRF experiments on adult mouse cardiomyocytes using a 'biosensor' approach whereby a photoactivatable FP-fused CaVβ subunit isoform was packaged into an adeno-associated virus serotype 9 (AAV9) and transduced *in vivo* upon retro-orbital injection of AAV9-CaVβ_{2a}-paGFP into anesthetized adult mice (see **Figures 2C,D**). This smaller (1.8 kb) auxiliary subunit of the channel binds to α_{1C} with a 1:1 stoichiometry; thus, when fused to an FP it can be used as a fluorescent reporter of

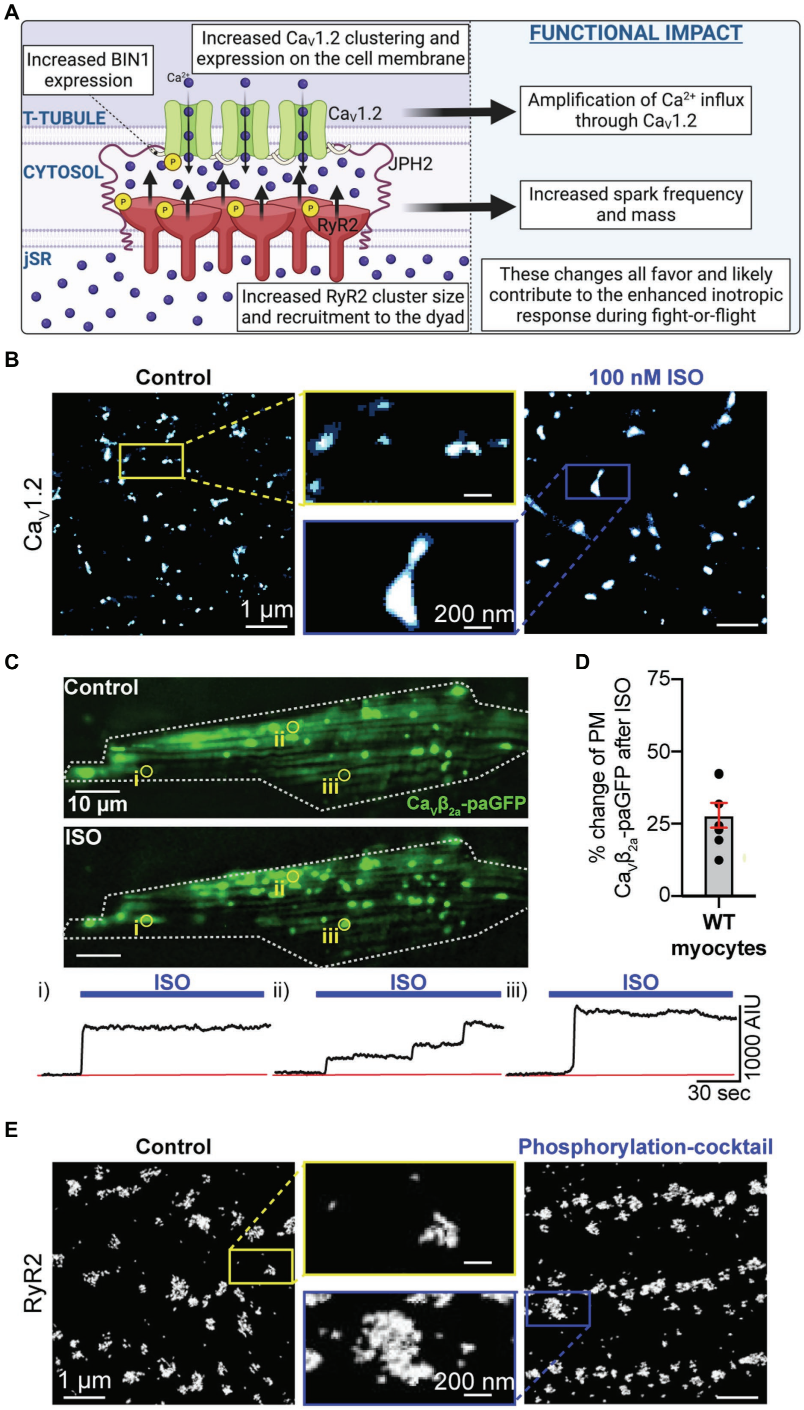

FIGURE 2 | Phosphorylation-mediated expansion of CaV1.2 and RyR2. **(A)** Illustration of phosphorylation-dependent expansion of CaV1.2 and RyR2 in the dyad and its physiological consequences. **(B)** Super-resolution Ground State Depletion (GSD) localization maps from isolated cardiomyocytes immunostained to visualize CaV1.2 channel clusters at the t-tubules in untreated control cells (left) and cells treated with 100 nM ISO for 8 min at room temperature prior to fixation (right). CaV1.2 cluster expansion is evident. (**C**) Show the results of dynamic TIRF imaging performed on mouse ventricular myocytes transduced with AAV9-CaVβ_2-paGFP which acts as a fluorescent CaV1.2 channel biosensor. The images show the GFP-fluorescence emission from channel located on the surface of a myocyte before and after addition of 100 nM ISO. Individual ROIs are indicated (i, ii, and iii) and show time courses of the changes in GFP-emission at each site where channel clusters are seen to undergo stimulated insertion in response to ISO. (**D**) Histogram summarizing the percentage increase in PM CaVβ_2-paGFP stimulated by ISO treatment. Panels **B**, **C**, and **D** are reproduced, with permission from (Del Villar et al., 2021). **(E)** Surface RyR2 cluster expansion in response to a phosphorylation cocktail is observed in panel **E** which was reproduced and modified with permission from (Asghari et al., 2020) under the terms of the Creative Commons Attribution 4.0 International Public License (CC-BY 4.0; https://creativecommons.org/licenses/by/4.0/) associated with that article. Illustrations were created in *Biorender*.

channel location, albeit a subset of channels since most channels are expected to associate with endogenously expressed CaVβ subunit. Stepwise-photobleaching experiments performed on these transduced myocytes also revealed the presence of larger channel clusters after ISO (Ito et al., 2019). The striking visual of stimulated insertion of CaV1.2 channels into the TIRF footprint of cardiomyocytes invited the question, where are these additional channels coming from?

A subsequent study revealed the presence of a sub-sarcolemmal reservoir of preformed, endosome-localized channels that can be mobilized to the membrane by β-AR stimulation (Del Villar et al., 2021). Mobile vesicular/endosomal CaV1.2 channels had been previously observed in tsA cells (Ghosh et al., 2018), and HL-1 cells (Conrad et al., 2018) but this was the first report of an endosomal reservoir of CaV1.2 channels in primary cardiomyocytes. This internal reserve of channels was posited to contribute to the "functional reserve" of the myocardium that can be accessed during sympathetic activation. Subpopulations of Rab4a-positive early endosomes and Rab11a-positive recycling endosomes were seen to co-localize with CaV1.2 channels, and upon ISO-stimulation the co-localization was reduced coincident with enhanced t-tubule expression of the channels suggesting that the endosomal channels were mobilized to the membrane. SMLM studies revealed the t-tubule membrane as the primary insertion location perhaps related to tighter coupling of the channels with juxta-positioned β-AR*s* there (Balijepalli et al., 2006; Chase et al., 2010). Mobilization of these endosomal channels to the membrane was shown to occur along fast Rab4a-dependent and slower Rab11a-dependent recycling pathways which require microtubule polymerization to move the endosomes and their cargo. Given that BIN1, AKA amphiphysin II, anchors microtubules at the t-tubule membrane and is important for t-tubule targeting of CaV1.2, BIN1 expression levels and/or localization may be critical for this stimulated insertion response (Hong et al., 2010). This important hypothesis is currently an open question that should be tested in the future.

β-ADRENERGIC RECEPTOR SIGNALING STIMULATES ALTERATIONS IN THE NANOSCALE DISTRIBUTION OF RYR2

β-AR stimulation is also associated with reorganization of RyR2 in a manner that appears to involve BIN1-mediated recruitment of phosphorylated-RyR2 (**Figure 2A**). As discussed above, BIN1 is best known for its role in t-tubule formation and targeted delivery of CaV1.2 channels but there is accumulating evidence that suggests interactions also occur between BIN1 and RyR2. In three-color super-resolution STORM imaging experiments, CaV1.2 and RyR2 clusters were observed with BIN1 'sandwiched' between them (Fu et al., 2016). Along with these immunostaining-observed interactions, CaV1.2 and BIN1 co-immunoprecipitate in HeLa cells (Hong et al., 2010), as do BIN1 and RyR2 in human heart lysates (Fu et al., 2016). β-AR stimulation with ISO has been found to produce a rapid augmentation of BIN1 expression in the t-tubules and this is accompanied by an increase in recruitment of phosphorylated RyR2 (p2808-RyR2) to the dyad, shown with diffraction-limited confocal microscopy (Fu et al., 2016). In cardiac specific BIN1 heterozygous (HT) knockout mice, there is of course less BIN1 and so β-AR stimulation with ISO increases BIN1 in the t-tubules to a lesser extent than in WT mice, accompanied by a reduced ability to recruit p2808-RyR2 to the dyads. In parallel, ISO-stimulated BIN1$^{+/-}$ HT myocytes were more predisposed to spontaneous Ca^{2+} release events supporting the postulate that the unrecruited pool of p2808-RyR2 may have been left stranded, or 'orphaned' in non-dyadic locations, promoting arrhythmogenesis.

In HF, BIN1 expression is reduced, and in the Hong et al. study this was seen to be accompanied by a reduced co-immunoprecipitation of BIN1 with pS2808-RyR2. It is noteworthy however that there is ongoing controversy (addressed in editorial commentaries (Bers, 2012; Valdivia, 2012)) around the original idea from Andy Mark's lab that pS2808-RyR2 are hyperactive/leaky and enhanced in HF (Marx et al., 2000). Regardless, Hong's finding of a BIN1-choreographed reorganization of RyR2 upon β-AR stimulation remains an interesting and novel finding and others have since reported phosphorylation dependent increases in RyR2 cluster size in the surface membrane (Asghari et al., 2020; **Figure 2E**). Future studies should examine whether similar aggregation of RyR2 occurs after phosphorylation in internally localized clusters. In addition, further investigations are required to determine whether BIN1 organizes a similar β-AR stimulated recruitment of CaMKII-phosphorylated pS2814-RyR2 to the dyads in healthy and HF models.

DYADIC CALCIUM CHANNEL DISPLACEMENT AND MIS-REGULATION DURING CARDIAC PATHOLOGY

HF can be defined as the progressive inability of the heart to adequately pump blood to meet the demands of the body. We focus here on changes observed in CaV1.2 and RyR2 calcium channels during HF with reduced ejection fraction (HFrEF) which commonly occurs after cardiac injury eg. ischemia, or with sustained stress eg. hypertension. There remains a limited understanding of the effects of HF with preserved ejection fraction (HFpEF) on CaV1.2 and RyR2 channel function and regulation, hampered by difficulties in generating an accurate animal model (Eisner et al., 2020; Benitah et al., 2021). The current state of our knowledge of Cav1.2 and RyR2 channel reorganization in HF is summarized in **Figure 3A** and is discussed in detail in this section. Several investigators have demonstrated reduced efficiency of signal transduction between CaV1.2 channels and RyR2 during HF (Gomez et al., 1997; Louch et al., 2004). Reduced functional coupling between these two calcium channels has deleterious implications for cardiac EC-coupling. There are several possibilities to explain reduced functional coupling between these two channels for example:

(1) remodeling of the t-tubule network and reduced number/length of dyadic junctions; (2) remodeling of the SR – with consequences for dyad integrity; (3) decreased expression and/or function of CaV1.2 and/or RyR2; (4) mis-localization or nanoscale reorganization of CaV1.2 and/or RyR2. We discuss each of these possibilities in more detail below.

Remodeling of the T-Tubule Network

The effects of HF and myocardial infarction (MI) on the t-tubule network, dyad integrity, and SR positioning has been previously (Guo et al., 2013) and very recently reviewed (Setterberg et al., 2021). We refer the reader there for a detailed discussion of the architectural changes in myocytes during cardiac pathologies. However, since the t-tubules are critical ultrastructural components that constitute the setting for efficient CaV1.2 participation in EC-coupling, we briefly discuss these changes. Remodeling of the t-tubule network is observed as compensated cardiac hypertrophy transitions into HF, representing somewhat of a watershed event that tips the balance toward failure (Wei et al., 2010). The network undergoes extensive architectural remodeling during HF involving t-tubule loss (He et al., 2001; Balijepalli et al., 2003; Wei et al., 2010; Wu et al., 2012), disorganization (Louch et al., 2006; Song et al., 2006), dilation (Maron et al., 1975; Schaper et al., 1991; Kostin et al., 1998) and appearance of a larger number of longitudinally orientated tubules (Kaprielian et al., 2000; Song et al., 2006) reminiscent of architecture of immature myocytes (Lipsett et al., 2019). While we continue to focus on HFrEF here, it bears mentioning that myocytes from HFpEF patients and rats apparently do not display the typical HFrEF associated reduced t-tubule density, rather t-tubule density in HFpEF is either maintained or even increased relative to healthy myocytes (Frisk et al., 2021). Returning to the 'immature' phenotype idea, this refers to the fact that t-tubules are not present at birth in many species and only begin to develop around 10 days afterwards, initially in a disorganized fashion, only forming a mature network by around 3 weeks post-birth in mice (Hamaguchi et al., 2013), rats (Ziman et al., 2010), and rabbits (Haddock et al., 1999). In addition, the immature phenotype has been linked to the re-emergence of fetal gene expression profiles (Rajabi et al., 2007). For example, the formation of t-tubules and dyads coincides with the expression of JPH2 during development (Ziman et al., 2010), and knockdown of JPH2 during development inhibits t-tubule maturation (Reynolds et al., 2013), but in HF some groups have reported JPH2 expression is downregulated in a regression towards an immature phenotype (Minamisawa et al., 2004; Landstrom et al., 2007; Wei et al., 2010; Zhang et al., 2013; Guo et al., 2015). Similarly, the membrane curvature-mediating, and CaV1.2-targeting protein BIN1 has been demonstrated to play an early role in t-tubule biogenesis in muscle (Lee et al., 2002), but is downregulated in HF (Hong et al., 2012; Caldwell et al., 2014). We consider these two proteins and their role in t-tubule formation and stability, and dyad integrity in more detail below.

Role of Junctophilin 2

Junctophilin 2 is a junctional complex-forming protein that spans the width of the dyadic cleft with its hydrophobic C-terminal transmembrane domain anchored in the SR-membrane while its eight N-terminal Membrane Occupation Recognition Nexus (MORN) motifs bind phospholipids to form the sarcolemmal anchor (Takeshima et al., 2000). Acute

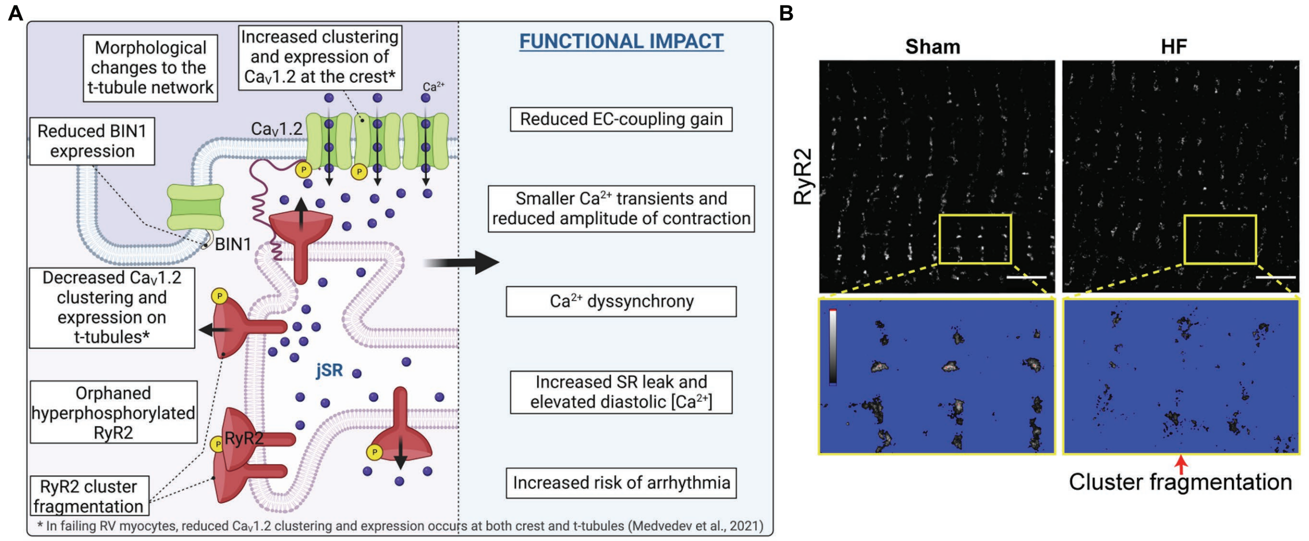

FIGURE 3 | CaV1.2 and RyR2 reorganization and cluster fragmentation in Heart Failure. **(A)** Illustration of the current state of knowledge on CaV1.2 and RyR2 channel reorganization in heart failure. **(B)** dSTORM images of sham-operated control and post-infarction HF rat cardiomyocytes show RyR2 channel cluster fragmentation/dispersal. Yellow boxes indicate zoomed-in regions which are thresholded below to identify channel clusters. Panel B is reproduced and modified with permission from (Kolstad et al., 2018) under the terms of the Creative Commons Attribution 4.0 International Public License (CC-BY 4.0; https://creativecommons.org/licenses/by/4.0/) associated with that article. Illustrations were created in *Biorender*.

knockdown of JPH2 in adult mice precipitates HF (Wei et al., 2010; van Oort et al., 2011), while AAV9-mediated restoration of JPH2 in TAC mice has been demonstrated to improve cardiac function, prevent t-tubule loss, and reduce aberrant Ca^{2+} leak (Reynolds et al., 2016). Loss of JPH2 effectively removes the tether that holds the SR and PM together and precipitates t-tubule drift away from the jSR leading to increased dyadic cleft width, and/or orphaning of RyR2. As a result of this aberrant physical distancing of RyR2 from CaV1.2 and the Ca^{2+} signal for CICR, dyssynchronous SR Ca^{2+} release occurs as RyR2 no longer open in unison during the AP but must wait a little longer for the Ca^{2+} trigger to reach them (Litwin et al., 2000; Louch et al., 2006; Song et al., 2006; Louch et al., 2013; Shiferaw et al., 2020). This dyssynchronous Ca^{2+} release does not favor efficient and uniform contraction and contributes to the contractile dysfunction of HF. Also contributing to the Ca^{2+} signaling irregularities, physical association of JPH2 with RyR2 stabilizes the closed state of the channel (van Oort et al., 2011). Loss of JPH2 thus eliminates this allosteric regulation, resulting in enhanced RyR2 activity and diastolic Ca^{2+} leak that impairs contractility and can trigger arrhythmias (Wang et al., 2014). Transgenic overexpression of JPH2 has been linked with enhanced RyR2 cluster size but reduced spark frequency, again attributed to the inhibitory influence of JPH2 on RyR2 opening (Munro et al., 2016).

Proteomic analyses have further revealed the serine/threonine protein kinase SPEG (striated muscle preferentially expressed protein kinase) as a binding partner of both JPH2 and RyR2, and thus another component of this dyadic protein complex (Quick et al., 2017). In that study, tamoxifen-inducible cardiac specific SPEG knockout in adult mice resulted in t-tubule and dyad loss that preceded HF and correlated with reduced SPEG-mediated phosphorylation of JPH2. This link between JPH2 phosphorylation and architectural remodeling remains correlative and the exact residue on JPH2 that is phosphorylated by SPEG remains to be determined. Another post-translational modification, namely S-palmitoylation has recently been revealed as a critical determinant of the tethering function of JPH2 to both the PM and SR/ER membranes (Jiang et al., 2019). A previous study reported that the palmitoylation status of BK potassium channels determines the ability of PKA to phosphorylate them, suggesting cross-talk between these two post-translational modifications confers conditional regulation of the channel (Tian et al., 2008). Future studies should examine the pathogenicity of JPH2 hypo-phosphorylation, and whether there is any cross-talk between JPH2 phosphorylation and the S-palmitoylation conferred stability of JPH2 tethers.

On the other hand, SPEG-mediated phosphorylation of RyR2 has been pin-pointed to residue S2367 and this post-translation modification inhibits diastolic Ca^{2+} leak, exerting a cardioprotective effect (Campbell et al., 2020). This effect was illustrated in a series of experiments from Xander Wehrens' lab in which knock-in mice with constitutively activated RyR2-S2367D were more resistant to pacing-induced atrial fibrillation (AFib), while knock-in mice with a non-phosphorylatable alanine substitution at that same site (RyR2-S2367A) were more susceptible to AFib (Campbell et al., 2020). SPEG is also known to phosphorylate another critical regulator of cardiomyocyte Ca^{2+} homeostasis, SERCA2a at residue T484 to enhance SR Ca^{2+} reuptake (Quan et al., 2019). Furthermore, human loss-of-function mutations in SPEG are associated with dilated cardiomyopathy [as reviewed in (Campbell et al., 2021)] suggesting reduced SPEG activity is a risk factor for cardiac pathology.

Recent reports have suggested a role for JPH2-dependent recruitment of CaV1.2 channels to the dyads on the t-tubule plasma membrane *via* a physical interaction between the 'joining region' of JPH2 and an unknown portion of the CaV1.2 α_{1C} subunit (Gross et al., 2021; Poulet et al., 2021). In skeletal muscle, an association between CaV1.1 and the junctophilin isoforms JPH1 and JPH2 reportedly occurs through an interaction between the proximal C-terminal tail of the channel at amino acids 1,595–1,606 (Nakada et al., 2018), and amino acids 230–369 on JPH1 or 216–399 on JPH2 (Golini et al., 2011). In a chicken or the egg type of scenario it is difficult to determine whether mutant JPH2 fails to recruit CaV1.2 to the dyad because JPH2-CaV1.2 interactions are critical for dyad assembly or because the dyads are not there in the first place because the mutant JPH2 does not support them. Overexpression of JPH2 has been found to preserve t-tubule structure, an effect that was said to depend on the presence of cholesterol since membrane cholesterol depletion with methyl β-cyclodextrin (MβCD) counteracted the positive effects of JPH2 (Poulet et al., 2021). This idea remains to be tested in freshly isolated cells and is somewhat complicated by the fact that acute (Zhu et al., 2016) or chronic (Bryant et al., 2018b) disruption of lipid rafts and caveolae, and the mere act of myocyte culturing itself (Lipp et al., 1996; Louch et al., 2004; Pavlovic et al., 2010), each lead to t-tubule and dyad disruption. Furthermore, MβCD will deplete cholesterol from all cellular membranes (Zidovetzki and Levitan, 2007), not just the plasma membrane and will thus change patterns of gene transcription [e.g., *via* sterol response element binding protein, SREBP (Eid et al., 2017)] and mTOR activation (Castellano et al., 2017) with implications for metabolism, cellular growth, and contractility (Xu and Brink, 2016). Furthermore, previous studies have shown that alterations in cholesterol homeostasis lead to profound changes in the phospholipid landscape (Vivas et al., 2019; Kutchukian et al., 2021), and as mentioned above, JPH2 is known to associate with the plasma membrane *via* interactions between MORN motifs in its N-terminal with phosphatidylserine and phosphoinositol lipids PIP, $PI(3,4,5)P_3$, and to a lesser extent $PI(4,5)P_2$ (Takeshima et al., 2000; Bennett et al., 2013). Further investigations are needed to disentangle the fundamental role of JPH2 in dyad formation and integrity from a potential role in recruiting or retaining CaV1.2 at those sites.

As noted above, there have been some reports of JPH2 downregulation in failing myocytes from a thoracic-aortic banding induced pressure-overload rat model (Wei et al., 2010), transgenic mouse models of hypertrophic or dilated cardiomyopathies (Minamisawa et al., 2004), and human hypertrophic cardiomyopathy (Landstrom et al., 2007), dilated cardiomyopathy and ischemic cardiomyopathy (Zhang et al., 2013; Guo et al., 2015). However, sheep and ferret HF models display t-tubule loss with no change in JPH2 (Caldwell et al., 2014) and more recent investigations have reported no change in JPH2 expression in myocytes from human patients with idiopathic dilated cardiomyopathy (Hou et al., 2021) or in *jph2* transcript expression in left ventricular tissue samples from patients with dilated cardiomyopathy (Frisk et al., 2021). These conflicting results suggest that reduced JPH2 expression is not a universal feature of HF and may point to species and model-dependent differences, extending even to the different etiologies of human HF. These discrepancies in JPH2 expression also raise some questions about the proposed role of JPH2 as a key driver of t-tubule loss in HF.

Role of Bridging Integrator 1

We have already discussed the role of BIN1 in t-tubule formation (Lee et al., 2002; Frost et al., 2009; Hong et al., 2010), and the finding that BIN1 is downregulated in HF (Hong et al., 2012; Caldwell et al., 2014; see **Figure 3A**). Here we focus on evidence supporting a role of reduced BIN1 in the pathogenesis of HF. The link between reduced BIN1 expression and HF was first appreciated when *Bin1* gene deletion was found to cause perinatal lethality in newborn mice who succumbed to severe ventricular cardiomyopathy within the first 24–48 h of birth (Muller et al., 2003) while cardiac specific cre-recombinase driven *Bin1* knockouts were found to develop age-associated dilated cardiomyopathy (Laury-Kleintop et al., 2015).

Efficient EC-coupling in adult ventricular myocytes requires concentration of CaV1.2 channels at the t-tubules and this is achieved through channel delivery along BIN1-anchored microtubules (Hong et al., 2010, 2012). In HF, CaV1.2 expression at the t-tubules decreases as discussed in Section "Nanoscale Reorganization of CaV1.2" below, could this be linked to reduced transcriptional expression of BIN1? Super-resolution STORM imaging of CaV1.2 in ventricular myocytes revealed smaller clusters in *Bin1*$^{+/-}$ HET knockout myocytes compared to controls (Hong et al., 2014), while surface biotinylation biochemistry revealed reduced membrane expression of CaV1.2 in mouse cardiomyocytes after shRNA-mediated BIN1 knockdown (Hong et al., 2012). Furthermore, lentiviral-mediated BIN1 overexpression in hESC-CMs has been demonstrated to favor tubular membrane formation, and CaV1.2 clustering and recruitment to those BIN1 positive tubules to form functional CaV1.2-RyR2 containing CRUs (De La Mata et al., 2019). A separate study revealed AAV9-delivered BIN1 increases survival of mice with pressure-overload induced cardiomyopathy using the transverse aortic constriction (TAC) model, normalizing t-tubule membrane intensity and CaV1.2 and RyR2 distribution (Li et al., 2020). Collectively, these studies suggest BIN1 plays a role in enrichment and clustering of CaV1.2 on t-tubules and may stabilize CRUs with the implication that downregulation of BIN1 in HF is detrimental to t-tubular CaV1.2 recruitment, dyad integrity, and EC-coupling.

Interestingly, AAV9-delivered SERCA2a to failing rat hearts has also been reported to normalize t-tubule density, reduce Ca^{2+} dyssynchrony, and normalize BIN1 but not JPH2 levels suggesting that JPH2 was not required to restore a functional t-tubule network in that post-infarction rat model of left ventricular HF (Lyon et al., 2012) and implying a link between normalization of calcium signaling and reverse remodeling. It is tempting to speculate that elevations in diastolic Ca^{2+} levels during HF may reduce the ability of microtubules to polymerize and thus destabilize the t-tubule network and cause mis-localization of key ion channels and receptors. Indeed, elevated Ca^{2+} levels have long been known to trigger microtubule depolymerization (Weisenberg, 1972; Sandoval and Weber, 1978).

Remodeling of the SR

The jSR structure and dynamics remains less studied than that of the t-tubule network although as the other half of the junctional membrane complex, its positioning is arguably of equal importance when considering the efficiency of cardiac EC-coupling. A recent study developed a new methodology to examine the mobility of the jSR using an AAV9-packaged photoactivatable GFP-tagged triadin (TRD-paGFP) that was transduced into cardiomyocytes *via* retro-orbital injections of live mice (Drum et al., 2020). Triadin localizes to the jSR where it anchors the Ca^{2+}-binding protein calsequestrin (Casq2) to RyR2 (Zhang et al., 1997). Photoactivation of TRD-paGFP in discrete regions of interest permitted tracking of the jSR over time. While a subset of TRD-paGFP containing jSR elements were observed to remain statically secured in the vicinity of the t-tubule membrane, the majority were mobile and were frequently observed emerging toward, or retracting away from nearby t-tubules (Drum et al., 2020). Furthermore, jSR mobility and structural changes were regulated by microtubules and associated motor proteins in neonatal mouse, (Vega et al., 2011), adult mouse (Drum et al., 2020), and adult rat cardiomyocytes (Vega et al., 2011). The mobility was demonstrated to be reduced by co-transduction of a dominant negative motor-less form of kinesin 5b (Kif5b-DN) or by treatment with small hairpin RNA against dynein (Dnchc1-shRNA). Kinesin is a plus-end directed motor protein that carries cargo along microtubules away from the trans-Golgi while dynein is a minus-end directed motor protein that carries cargo in the opposite direction. In other cell types where fluorescent labeling of the ER is more easily achieved and distinguished from non-invaginating PMs, ER mobility has long been appreciated and indeed the ER is thought of as a highly dynamic organelle with ER-tubules tracking along microtubules as they undergo polymerization and growth or catastrophe and shrinkage (Pendin et al., 2011). Envisioning the jSR being propelled to-and-fro along microtubules brings-to-mind the Prosser lab's elegant Airyscan acquired movies of microtubules buckling into spring-like structures as the cell contracts during systole and recoiling into the more familiar linear structures as the cell relaxes during diastole (Robison et al., 2016). If indeed the jSR tubules are anchored onto microtubules, what does this mechanical action do to the dyadic cleft? An elegant study from the Kohl lab recently demonstrated that t-tubule membranes experience the mechanical stresses and strains of systole and diastole with their membranes undergoing deformation on a beat-to-beat basis (Rog-Zielinska et al., 2021). It seems reasonable to assume the jSR suffers similar stresses and strains that could push it toward the t-tubule PM during contraction and pull it away again as the cell relaxes. The spacer function of JPH2 and the size of the cytosolic portion of RyR2 may act to prevent the total collapse of the dyadic cleft but the consequences of these dyadic deformations for EC-coupling remain to be fully explored.

There is little information on alterations in jSR motility during HF although disrupted SR networks have been observed in HF models (Pinali et al., 2013), and altered distributions of SR proteins are observed in hypertrophic myocytes (Hadipour-Lakmehsari et al., 2019). Microtubule growth and stability is decreased by the oxidative stress of MI, resulting in enhanced rates of microtubule catastrophe and impaired delivery of $K_V4.2$ and $K_V4.3$ potassium channels in mouse ventricular myocytes (Drum et al., 2016). Since jSR mobility relies on motor protein mediated transport along the microtubules, the effects of microtubule instability on jSR positioning and dynamics is an interesting prospect for future studies.

Nanoscale Reorganization of CaV1.2

At the other side of the dyad, CaV1.2 channel localization and function is also altered in HF models. In the late 90s, cell-attached patch recordings from failing human left ventricular myocytes revealed enhanced CaV1.2 channel activity in what were likely overwhelmingly crest-located channel clusters but whole cell current density (I_{Ca}) was unchanged compared to healthy control myocytes and it was prophetically posited that the 'increased activity of superficial channels compensates for a reduced channel expression in the t-tubules' (Schroder et al., 1998). A subsequent report from Clive Orchard's lab interrogated the effect of detubulation on I_{Ca} in failing rat ventricular myocytes post coronary artery ligation (Bryant et al., 2015). Despite an overall preservation of I_{Ca} density in intact (tubulated) failing myocytes compared to healthy sham controls, detubulation revealed that the proportion of channels contributing to that current had shifted in their distribution from a predominantly t-tubular locale in health (24:76% crest:t-tubule ratio) to a more even distribution in failure (45.55% crest:t-tubule ratio; Bryant et al., 2015). Failing myocytes from TAC mice show a similar reduction in t-tubular I_{Ca} density but do not show an increase in density at the cell surface resulting in a diminished I_{Ca} compared to controls (Bryant et al., 2018a). This redistribution with fewer channels in the t-tubules, and sometimes more in the crest (depending on the species/HF model), combined with the alterations in t-tubule morphology in HF was linked to reduced expression of caveolin-3 (Bryant et al., 2018a) and has consequences for EC-coupling since the nanodomain Ca^{2+} signaling and functional coupling between t-tubular CaV1.2 and jSR RyR2 is impaired. Illustrating this, Ca^{2+} transients are reduced in amplitude in failing versus healthy sham controls despite similar I_{Ca} density reflecting a reduced ability of CaV1.2-mediated Ca^{2+} influx to trigger SR Ca^{2+} release, i.e., reduced EC-coupling gain (Gomez et al., 1997; Bryant et al., 2015). Early studies on changes in I_{Ca} with HF are reviewed here (Benitah et al., 2002) but we focus our remaining attentions on recent advances.

One relatively recent technical advance that has brought illuminatingly enhanced resolution to this field and enabled mapping and functional comparison of t-tubule versus crest-localized CaV1.2 channels are the super-resolution patch clamp experiments from the Gorelik lab. Using this approach, Bhargava confirmed other findings that CaV1.2 channels are concentrated (Kawai et al., 1999) and clustered on the t-tubules (Scriven et al., 2010; Dixon et al., 2015, 2017; Ito et al., 2019; Sato et al., 2019; Del Villar et al., 2021), finding that they were 4.3-times more likely to observe CaV1.2 activity from cell-attached patches in the t-tubules versus those in the crest (Bhargava et al., 2013). In subsequent studies on failing left ventricular myocytes CaV1.2 channels reportedly relocate from their usual preferred position on the t-tubules, to occupy new positions on the crest (surface sarcolemma; Sanchez-Alonso et al., 2016; see **Figure 3A**). In failing rat and human ventricular myocytes, the probability of landing the pipette on a patch of crest membrane with CaV1.2 channel activity was improved ~4-fold over that seen healthy cell crests (Sanchez-Alonso et al., 2016). Furthermore, the relocated crest-localized channels exhibited a 3 to 4.5-fold enhancement in P_o (Sanchez-Alonso et al., 2016) which was attributed to increased levels of constitutive channel phosphorylation due to elevated expression and activity of CaMKII in HF (Hoch et al., 1999; Kirchhefer et al., 1999; Zhang et al., 2003; Ai et al., 2005). Indeed, inhibition of CaMKII with KN-93 was seen to normalize the crest channel P_o to healthy levels and reduce arrhythmogenic Ca^{2+} oscillations (Sanchez-Alonso et al., 2016).

In failing right ventricular myocytes after left coronary artery ligation (an ischemic cardiomyopathy (ICM) model) the phosphorylating kinase was identified as PKA and the channel population displaying increased activity was on the t-tubules, not the crest (Medvedev et al., 2021). Interestingly, the phosphorylated channels on the t-tubules displayed overtly cooperative behavior that was inhibited by H-89, reminiscent of our previous work where we demonstrated PKA-dependent enhancement in channel cooperativity and stimulated insertion of multi-channel clusters into the t-tubule membrane [see Section (Ito et al., 2019; Del Villar et al., 2021)]. Whether PKA-triggered augmentation of t-tubular CaV1.2 channel expression similarly occurs in failing right ventricular myocytes remains to be tested. Overall, both crest and t-tubular CaV1.2 density was reduced in failing right ventricular myocytes, indicated by a reduced likelihood of recording CaV1.2 channel activity in cell-attached patches positioned in those locations in the failing myocytes compared to controls. Whether the likelihood of recording channel activity in t-tubule localized patches was further reduced by PKA-inhibition was not reported. Channel hyperphosphorylation and redistribution of channels has thus been reported in several cardiomyopathies including dilated cardiomyopathy (DCM), and ICM (Sanchez-Alonso et al., 2020). However, while CaMKII-mediated phosphorylation underlies the enhanced P_o of crest localized channels in DCM, PKA-mediated phosphorylation underlies the elevated P_o of t-tubule localized in ICM (Sanchez-Alonso et al., 2020) suggesting distinct nanodomain signaling pathways are differentially activated in these two pathologies.

Nanoscale Re-Organization of RyR2

Work from Jon Lederer's lab around the turn of the millennium revealed reduced functional coupling between CaV1.2 channels and RyR2 during HF secondary to hypertension (Gomez et al., 1997) or MI (Gomez et al., 2001). I_{Ca} was found to be maintained in HF myocytes but calcium transient amplitude and the ability to trigger Ca^{2+} sparks was reduced. Spatial remodeling was postulated as the cause of this reduced EC-coupling gain with three scenarios proposed, (1) mismatch where the t-tubule network remained unaltered by the CaV1.2 and RyR2 channels were misaligned; (2) increased width of the dyadic cleft; and (3) altered t-tubule networks resulting in 'orphaned' RyR2 whereby spatial reorganization of the t-tubule network would leave stranded jSR elements behind without juxtaposed CaV1.2 cluster partners. Remodeling of the t-tubule network had already been reported by Tim Kamp's group (He et al., 2001) and so the 'orphaned' scenario gained favor and was later confirmed by Lederer's group (Song et al., 2006). RyR2 orphaning was seen to occur in HF myocytes just as predicted, when the t-tubule network reorganized and became somewhat chaotic in appearance compared to the regular grid-like pattern observed in healthy myocytes. This leads to a loss of local control of RyR2 by CaV1.2. Cultured myocytes were seen to exhibit a similar t-tubule network reorganization and descendance into chaos as the culture period extended (Louch et al., 2004) and examination of the Ca^{2+} transient wavefront on line-scans from Ca^{2+} indicator loaded, paced myocytes revealed that cultured and failing myocytes displayed more frequent delays in activation of some RyR2 in agreement with an earlier report of dyssynchronous sparks in failing rabbit hearts post-MI (Litwin et al., 2000).

Orphaned, and/or smaller clusters of RyR are thought to contribute to the enhanced leak, and are posited to operate in an a silent or "invisible" mode where 1–5 RyR2 open in response to a lower intracellular Ca^{2+} trigger and produce no detectable spark (Sobie et al., 2006; Cheng and Lederer, 2008). While some SR Ca^{2+} leak occurs in healthy hearts, enhanced SR Ca^{2+} leak is a feature of many cardiopathies including MI, HF, and AFib (Shannon et al., 2003; Terentyev et al., 2008; Neef et al., 2010; Fauconnier et al., 2011; Fischer et al., 2014; Li et al., 2014). The increased leak reduces SR Ca^{2+} content leading to reduced amplitude transients, weaker contractions, and impaired relaxation due to elevated diastolic Ca^{2+} levels. The latter can lead to enhanced NCX activity precipitating arrhythmia (Molkentin et al., 1998; Chelu et al., 2009). Hyperphosphorylation of RyR2 by CaMKII has been proposed to underlie the enhanced activity at rest that generates the leak but this is not the full story as while CaMKII inhibitors can restore SR Ca^{2+} content, they do not fully normalize the amplitude of the Ca^{2+} transient (Ai et al., 2005) possibly because CaMKII also increases the fractional release of Ca^{2+} from the SR during systole (Li et al., 1997). These hyperactive CaMKII phosphorylated RyR2 are predominantly located in non-dyadic, 'orphaned' locations (Dries et al., 2018).

More recently, alterations in the nanoscale organization of RyR2 has been linked to the deviant Ca^{2+} signaling and reduced contractility in HF and AFib (MacQuaide et al., 2015; Kolstad et al., 2018). In a mathematical modeling study, RyR2 cluster size heterogeneity was linked to arrhythmogenic Ca^{2+} release from the SR (Xie et al., 2019). In their model, large clusters were found to open more easily, requiring a lower threshold Ca^{2+} trigger and generating a larger fractional release from the SR, resulting in locally reduced SR content due to larger, more frequent Ca^{2+} sparks and non-spark leak (Zima et al., 2010). Thus, although large clusters are predicted to increase diastolic Ca^{2+} levels, the likelihood that they will generate propagating arrhythmogenic Ca^{2+} waves is low because the low SR content they leave in their wake limits propagation through the cell. Small-sized clusters on the other hand were found to be less excitable, with a higher threshold for activation and lower leak, generating local regions of high SR Ca^{2+} load but again, a low propensity for Ca^{2+} wave propagation due to their low excitability. However, small clusters interspersed among larger ones, releases the brake on propagation as the small clusters help maintain the average SR Ca^{2+} concentration, allowing waves originating at large cluster hot-spots to propagate through the cell.

In HF and AFib, fragmentation of RyR2 clusters has been reported, which perhaps increases the heterogeneity of cluster sizes (MacQuaide et al., 2015; Kolstad et al., 2018; Sheard et al., 2019; **Figures 3A**,**B**). In the MacQuaide et al. study of a long-term paced sheep model of persistent AFib, although individual cluster size in atrial myocytes was unchanged by AFib, when one considers the CRU, defined as functionally grouped clusters within 150 nm edge-to-edge of one another, heterogeneity was present. AFib CRUs were more fragmented and contained more RyRs, dispersed over a larger area than healthy cell controls (MacQuaide et al., 2015). However, in a recent study of RyR2 clustering in diseased atrial myocytes from human AFib patients, no dispersion or reorganization of RyR2 was observed suggesting that RyR2 reorganization is not a necessary component of the Ca^{2+} leak and arrhythmogenicity associated with human AFib (Munro et al., 2021).

In the Kolstad et al study, myocytes isolated from post-infarction HF rats had a larger number of small RyR2 clusters than cells isolated from control rats. CRUs were also found to be smaller on average and more fragmented (Kolstad et al., 2018; **Figure 3B**). Mathematical modeling suggested that the smaller clusters generated more 'silent' or non-spark leak, and the cluster dispersal led to low fidelity Ca^{2+} sparks, slow spread of Ca^{2+}, and overall dyssynchrony. In this special issue a study by Hou et al. also reported a trend toward smaller, more dispersed t-tubule adjacent RyR2 clusters and ~ 50% reduction in RyR2 expression in human myocytes isolated from heart samples obtained from patients with idiopathic dilated cardiomyopathy, compared to non-failing controls (Hou et al., 2021). These smaller clusters separated by larger distances were postulated to contribute to smaller Ca^{2+} transients and reduced amplitude of contraction. The rat and sheep studies discussed above suggest that altered nanoscale organization of RyR2 in cardiomyopathies can contribute to the altered kinetics of Ca^{2+} release and the disease phenotype in these species. Further investigations are needed to determine whether the same can be said for multi-factorial human cardiomyopathies given that human AFib does not appear to exhibit this phenomenon (Munro et al., 2021).

AGING-RELATED CHANGES IN VENTRICULAR CaV1.2 CHANNEL FUNCTION AND DISTRIBUTION

Cardiac health and function progressively decline with aging and in the ventricles, is associated with altered L-type calcium channel function and Ca^{2+} signaling (Zhou et al., 1998; Lakatta and Sollott, 2002; Fares and Howlett, 2010; Feridooni et al., 2015), and hyperphosphorylation (Kandilci et al., 2011) and hyper-glycation of RyR2 associated with enhanced SR leak (Ruiz-Meana et al., 2019). There is some evidence that, CaV1.2 channels undergo changes in their function and distribution in the aging ventricular myocardium in a manner somewhat reminiscent of the changes seen in HF. In aging (24 month old) rat ventricular myocytes, single channel recordings of CaV1.2 activity and ensemble currents from crest/surface sarcolemma localized cell-attached patches revealed increased channel number, P_o, and functional availability compared to cells isolated from young 3-month old rats (Josephson et al., 2002). However, like the majority of HF studies, despite an increased number and P_o of a subpopulation of channels, whole cell I_{Ca} is generally preserved (Walker et al., 1993; Xiao et al., 1994) or decreased with aging (Feridooni et al., 2017; Kong et al., 2018). These results suggest that in aging ventricles the t-tubule localized channel population may be reduced with a reciprocal expansion of the crest population. Indeed detubulation experiments on ventricular myocytes isolated from aged, 24-month old mice revealed t-tubular I_{Ca} density was ~50% lower compared to 3-month old mice (Kong et al., 2018). However, in that same study surface I_{Ca} density was reportedly unchanged in apparent conflict with the findings of Josephson *et al* (Josephson et al., 2002), albeit with a different animal model (mice versus rats). Di8-ANEPPS visualization of t-tubule density by the same group revealed an ~12% decrease in t-tubule density with aging, with no apparent change in their orientation. A study of human left ventricular myocardium from patients aged between 19 and 75 also reported t-tubule network alterations and reduced JPH2 expression and clustering with aging, raising the question of dyad integrity (Lyu et al., 2021). These remain the only studies on t-tubule network integrity and channel localization in aged models and thus further investigation is required to reconcile the prior report of enhanced surface single channel activity with these findings. It could be that there are species-dependent differences in these parameters between mice and rats or that consideration of the frailty index could begin to tease out differences in the groups. The frailty index takes into account that people and animals age at different rates, in other words people/animals may be chronologically the same age but some will become 'frail' (more predisposed to adverse health outcomes) faster than others (Heinze-Milne et al., 2019).

CONCLUDING REMARKS AND FUTURE DIRECTIONS

It is apparent that nanoscale organization of CaV1.2 and RyR2 channels in clusters on their respective membranes contributes to the efficiency of Ca^{2+} release on the cellular level, and myocardial contractility on the tissue level. These variably-sized clusters are formed by stochastic self-assembly processes (Baddeley et al., 2009; Sato et al., 2019) and are dynamic and constantly maintained by cycles of endocytosis, delivery, and recycling that ensures a stable population of dyadic channels. However, the populations can be expanded when required as illustrated by the enhanced clustering of each channel that occurs during acute stress to augment Ca^{2+} release and contractility, contributing to the inotropic response. While aberrant reorganization, consisting of channel redistribution and cluster fragmentation occurs in heart failure and at least for CaV1.2, reorganization also appears to occur in aging too. However, much remains to be explored in the aging myocardium to fully elucidate any reorganization of CaV1.2 and RyR2 channels, and morphological changes in the t-tubule network that may have implications for EC-coupling gain.

Future studies should examine RyR2 clustering, organization, and SR remodeling in the aging myocardium. The field would benefit from a super-resolution patching study to assay channel activity at the t-tubules versus the crest. In addition, a study of the phosphorylation status of the channel subpopulations may provide insight into the enhanced channel activity observed at the crest (Josephson et al., 2002). Certainly, aging is associated with an enhanced sympathetic drive at rest and impaired reuptake of norepinephrine that would favor enhanced PKA activity (Kaye and Esler, 2005), yet the aging heart exhibits progressive age-associated loss of βAR responsivity (Lakatta et al., 1975; Stratton et al., 1992; Lakatta, 1993; White et al., 1994; Xiao et al., 1994; Cerbai et al., 1995; Xiao et al., 1998) which diminishes cardiac reserve capacity, rendering the heart less able to cope with acute stress and lowering the threshold for the development of HF (Strait and Lakatta, 2012). Deletion of the PKA regulatory subunit RIIβ has been reported to prolong lifespan and be cardioprotective in male but not female mice (Enns et al., 2009) while CaMKII activity/expression has not been well studied in the context of aging.

The full mechanistic picture of how CaV1.2 channels are recruited to the t-tubule membrane and retained there in dyadic nanodomains is still evolving with putative roles for JPH2, BIN1, Cav3, and lipid rafts as discussed herein. One tangible link between each of these proteins and even lipid rafts is the reliance on, or association with membrane lipids. JPH2 MORN motifs bind phospholipids to form the sarcolemmal anchor (Takeshima et al., 2000), BIN1 presence at the PM, and membrane curving-abilities are reliant on electrostatic interactions with phospholipids (Wu and Baumgart, 2014). PI(4,5)P_2 reportedly accumulates in caveolae where the basic residues on caveolins are posited to play a role in sequestering it (Fujita et al., 2009) and lipid rafts have been proposed to serve as scaffolds of G-protein coupled receptors and PIP_2 signaling (Myeong et al., 2021). Thus, alterations in the lipid profile of cardiomyocytes could impact everything from t-tubule formation, to CaV1.2 channel delivery, to dyadic integrity, and compartmentalization of receptor signaling. Future studies should examine the lipid and phospholipid profile of cardiomyocytes in health, disease, and aging.

To conclude, nanoscale organization of CaV1.2 and RyR2 calcium channels in clusters as a means to control the amplitude of Ca^{2+} entry, SR Ca^{2+} release and myocardial function is an emerging concept. This concept is not just applicable to the heart but has been identified as a regulatory mechanism in several other physiological processes including vascular tone (Pritchard et al., 2018), skeletal muscle mitochondrial biogenesis (Place et al., 2015), and neuronal excitability (Moreno et al., 2016). One hopes that the continued development of nanobodies and and affimers (Carrington et al., 2019; Dong et al., 2019), coupled with newer light microscopy approaches like MINFLUX (Balzarotti et al., 2017; Gwosch et al., 2020) and MINSTED (Weber et al., 2021) which each boast molecular scale resolutions on the order of 1–3 nm in x, y, and impressively ~2 nm axially (Gwosch et al., 2020) will aid continued exploration and new discoveries into how ion channel cluster organization and reorganization can influence physiological processes in health and disease.

AUTHOR CONTRIBUTIONS

The author confirms being the sole contributor of this work and has approved it for publication.

FUNDING

This work was supported by an R01 grant from the US National Institutes of Health to RD (R01AG063796).

ACKNOWLEDGMENTS

We thank Taylor Voelker, Heather Spooner, and Drs. Eamonn Dickson, Silvia Garcia del Villar, and Maartje Westhoff for critically reading the manuscript.

REFERENCES

Ai, X., Curran, J. W., Shannon, T. R., Bers, D. M., and Pogwizd, S. M. (2005). Ca^{2+}/calmodulin-dependent protein kinase modulates cardiac ryanodine receptor phosphorylation and sarcoplasmic reticulum Ca^{2+} leak in heart failure. *Circ. Res.* 97, 1314–1322. doi: 10.1161/01.RES.0000194329.41863.89

Asghari, P., Schulson, M., Scriven, D. R., Martens, G., and Moore, E. D. (2009). Axial tubules of rat ventricular myocytes form multiple junctions with the sarcoplasmic reticulum. *Biophys. J.* 96, 4651–4660. doi: 10.1016/j.bpj.2009.02.058

Asghari, P., Scriven, D. R., Ng, M., Panwar, P., Chou, K. C., van Petegem, F., et al. (2020). Cardiac ryanodine receptor distribution is dynamic and changed by auxiliary proteins and post-translational modification. *elife* 9:e51602. doi: 10.7554/eLife.51602

Baddeley, D., Jayasinghe, I. D., Lam, L., Rossberger, S., Cannell, M. B., and Soeller, C. (2009). Optical single-channel resolution imaging of the ryanodine receptor distribution in rat cardiac myocytes. *Proc. Natl. Acad. Sci. U. S. A.* 106, 22275–22280. doi: 10.1073/pnas.0908971106

Balijepalli, R. C., Foell, J. D., Hall, D. D., Hell, J. W., and Kamp, T. J. (2006). Localization of cardiac L-type Ca^{2+} channels to a caveolar macromolecular signaling complex is required for β_2-adrenergic regulation. *Proc. Natl. Acad. Sci. U. S. A.* 103, 7500–7505. doi: 10.1073/pnas.0503465103

Balijepalli, R. C., Lokuta, A. J., Maertz, N. A., Buck, J. M., Haworth, R. A., Valdivia, H. H., et al. (2003). Depletion of T-tubules and specific subcellular changes in sarcolemmal proteins in tachycardia-induced heart failure. *Cardiovasc. Res.* 59, 67–77. doi: 10.1016/S0008-6363(03)00325-0

Balzarotti, F., Eilers, Y., Gwosch, K. C., Gynna, A. H., Westphal, V., Stefani, F. D., et al. (2017). Nanometer resolution imaging and tracking of fluorescent molecules with minimal photon fluxes. *Science* 355, 606–612. doi: 10.1126/science.aak9913

Bean, B. P., Nowycky, M. C., and Tsien, R. W. (1984). Beta-adrenergic modulation of calcium channels in frog ventricular heart cells. *Nature* 307, 371–375. doi: 10.1038/307371a0

Benitah, J. P., Gomez, A. M., Fauconnier, J., Kerfant, B. G., Perrier, E., Vassort, G., et al. (2002). Voltage-gated Ca^{2+} currents in the human pathophysiologic heart: a review. *Basic Res. Cardiol.* 97, I11–I18. doi: 10.1007/s003950200023

Benitah, J. P., Perrier, R., Mercadier, J. J., Pereira, L., and Gomez, A. M. (2021). RyR2 and calcium release in heart failure. *Front. Physiol.* 12:734210. doi: 10.3389/fphys.2021.734210

Bennett, H. J., Davenport, J. B., Collins, R. F., Trafford, A. W., Pinali, C., and Kitmitto, A. (2013). Human junctophilin-2 undergoes a structural rearrangement upon binding PtdIns(3,4,5)P_3 and the S101R mutation identified in hypertrophic cardiomyopathy obviates this response. *Biochem. J.* 456, 205–217. doi: 10.1042/BJ20130591

Bers, D.M. (2001). *Excitation-Contraction Coupling and Cardiac Contractile Force*. Dordrecht, The Netherlands: Springer.

Bers, D. M. (2012). Ryanodine receptor S2808 phosphorylation in heart failure: smoking gun or red herring. *Circ. Res.* 110, 796–799. doi: 10.1161/CIRCRESAHA.112.265579

Best, J. M., and Kamp, T. J. (2012). Different subcellular populations of L-type Ca^{2+} channels exhibit unique regulation and functional roles in cardiomyocytes. *J. Mol. Cell. Cardiol.* 52, 376–387. doi: 10.1016/j.yjmcc.2011.08.014

Bhargava, A., Lin, X., Novak, P., Mehta, K., Korchev, Y., Delmar, M., et al. (2013). Super-resolution scanning patch clamp reveals clustering of functional ion channels in adult ventricular myocyte. *Circ. Res.* 112, 1112–1120. doi: 10.1161/CIRCRESAHA.111.300445

Bryant, S. M., Kong, C. H., Watson, J., Cannell, M. B., James, A. F., and Orchard, C. H. (2015). Altered distribution of I_{Ca} impairs ca release at the t-tubules of ventricular myocytes from failing hearts. *J. Mol. Cell. Cardiol.* 86, 23–31. doi: 10.1016/j.yjmcc.2015.06.012

Bryant, S. M., Kong, C. H. T., Watson, J. J., Gadeberg, H. C., James, A. F., Cannell, M. B., et al. (2018a). Caveolin 3-dependent loss of t-tubular I_{Ca} during hypertrophy and heart failure in mice. *Exp. Physiol.* 103, 652–665. doi: 10.1113/EP086731

Bryant, S. M., Kong, C. H. T., Watson, J. J., Gadeberg, H. C., Roth, D. M., Patel, H. H., et al. (2018b). Caveolin-3 KO disrupts t-tubule structure and decreases t-tubular I_{Ca} density in mouse ventricular myocytes. *Am. J. Physiol. Heart Circ. Physiol.* 315, H1101–H1111. doi: 10.1152/ajpheart.00209.2018

Calaghan, S., and White, E. (2006). Caveolae modulate excitation-contraction coupling and beta2-adrenergic signalling in adult rat ventricular myocytes. *Cardiovasc. Res.* 69, 816–824. doi: 10.1016/j.cardiores.2005.10.006

Caldwell, J. L., Smith, C. E. R., Taylor, R. F., Kitmitto, A., Eisner, D. A., Dibb, K. M., et al. (2014). Dependence of cardiac transverse tubules on the BAR domain protein Amphiphysin II (BIN-1). *Circ. Res.* 115, 986–996. doi: 10.1161/CIRCRESAHA.116.303448

Campbell, H., Aguilar-Sanchez, Y., Quick, A. P., Dobrev, D., and Wehrens, X. H. T. (2021). SPEG: a key regulator of cardiac calcium homeostasis. *Cardiovasc. Res.* 117, 2175–2185. doi: 10.1093/cvr/cvaa290

Campbell, H. M., Quick, A. P., Abu-Taha, I., Chiang, D. Y., Kramm, C. F., Word, T. A., et al. (2020). Loss of SPEG inhibitory phosphorylation of ryanodine receptor Type-2 promotes atrial fibrillation. *Circulation* 142, 1159–1172. doi: 10.1161/CIRCULATIONAHA.120.045791

Carl, S. L., Felix, K., Caswell, A. H., Brandt, N. R., Ball, W. J. Jr., Vaghy, P. L., et al. (1995). Immunolocalization of sarcolemmal dihydropyridine receptor and sarcoplasmic reticular triadin and ryanodine receptor in rabbit ventricle and atrium. *J. Cell Biol.* 129, 673–682. doi: 10.1083/jcb.129.3.673

Carrington, G., Tomlinson, D., and Peckham, M. (2019). Exploiting nanobodies and Affimers for superresolution imaging in light microscopy. *Mol. Biol. Cell* 30, 2737–2740. doi: 10.1091/mbc.E18-11-0694

Castellano, B. M., Thelen, A. M., Moldavski, O., Feltes, M., van der Welle, R. E., Mydock-McGrane, L., et al. (2017). Lysosomal cholesterol activates mTORC1 via an SLC38A9-Niemann-pick C1 signaling complex. *Science* 355, 1306–1311. doi: 10.1126/science.aag1417

Catterall, W. A. (2011). Voltage-gated calcium channels. *Cold Spring Harb. Perspect. Biol.* 3:a003947. doi: 10.1101/cshperspect.a003947

Cerbai, E., Guerra, L., Varani, K., Barbieri, M., Borea, P. A., and Mugelli, A. (1995). Beta-adrenoceptor subtypes in young and old rat ventricular myocytes: a combined patch-clamp and binding study. *Br. J. Pharmacol.* 116, 1835–1842. doi: 10.1111/j.1476-5381.1995.tb16671.x

Chase, A., Colyer, J., and Orchard, C. H. (2010). Localised Ca channel phosphorylation modulates the distribution of L-type Ca current in cardiac myocytes. *J. Mol. Cell. Cardiol.* 49, 121–131. doi: 10.1016/j.yjmcc.2010.02.017

Chelu, M. G., Sarma, S., Sood, S., Wang, S., van Oort, R. J., Skapura, D. G., et al. (2009). Calmodulin kinase II-mediated sarcoplasmic reticulum Ca^{2+} leak promotes atrial fibrillation in mice. *J. Clin. Invest.* 119, 1940–1951. doi: 10.1172/jci37059

Cheng, H., and Lederer, W. J. (2008). Calcium sparks. *Physiol. Rev.* 88, 1491–1545. doi: 10.1152/physrev.00030.2007

Chen-Izu, Y., McCulle, S. L., Ward, C. W., Soeller, C., Allen, B. M., Rabang, C., et al. (2006). Three-dimensional distribution of ryanodine receptor clusters in cardiac myocytes. *Biophys. J.* 91, 1–13. doi: 10.1529/biophysj.105.077180

Conrad, R., Stölting, G., Hendriks, J., Ruello, G., Kortzak, D., Jordan, N., et al. (2018). Rapid turnover of the cardiac L-Type CaV1.2 channel by endocytic recycling regulates its cell surface availability. *iScience* 7, 1–15. doi: 10.1016/j.isci.2018.08.012

Correll, R. N., Makarewich, C. A., Zhang, H. Y., Zhang, C., Sargent, M. A., York, A. J., et al. (2017). Caveolae-localized L-type Ca^{2+} channels do not contribute to function or hypertrophic signalling in themouse heart. *Cardiovasc. Res.* 113, 749–759. doi: 10.1093/cvr/cvx046

De La Mata, A., Tajada, S., O'Dwyer, S., Matsumoto, C., Dixon, R. E., Hariharan, N., et al. (2019). BIN1 induces the formation of T-tubules and adult-Like Ca^{2+} release units in developing cardiomyocytes. *Stem Cells* 37, 54–64. doi: 10.1002/stem.2927

Del Villar, S. G., Voelker, T. L., Westhoff, M., Reddy, G. R., Spooner, H. C., Navedo, M. F., et al. (2021). Beta-adrenergic control of sarcolemmal CaV1.2 abundance by small GTPase Rab proteins. *Proc. Natl. Acad. Sci. U. S. A.* 118:e2017937118. doi: 10.1073/pnas.2017937118

Dixon, R. E., Moreno, C. M., Yuan, C., Opitz-Araya, X., Binder, M. D., Navedo, M. F., et al. (2015). Graded Ca^{2+}/calmodulin-dependent coupling of voltage-gated CaV1.2 channels. *elife* 4:e05608. doi: 10.7554/eLife.05608

Dixon, R. E., Vivas, O., Hannigan, K. I., and Dickson, E. J. (2017). Ground state depletion super-resolution imaging in mammalian cells. *J. Vis. Exp.* 129:56239. doi: 10.3791/56239

Dixon, R. E., Yuan, C., Cheng, E. P., Navedo, M. F., and Santana, L. F. (2012). Ca^{2+} signaling amplification by oligomerization of L-type CaV1.2 channels. *Proc. Natl. Acad. Sci. U. S. A.* 109, 1749–1754. doi: 10.1073/pnas.1116731109

Dolphin, A. C. (2016). Voltage-gated calcium channels and their auxiliary subunits: physiology and pathophysiology and pharmacology. *J. Physiol.* 594, 5369–5390. doi: 10.1113/JP272262

Dong, J. X., Lee, Y., Kirmiz, M., Palacio, S., Dumitras, C., Moreno, C. M., et al. (2019). A toolbox of nanobodies developed and validated for use as intrabodies and nanoscale immunolabels in mammalian brain neurons. *Elife* 8:e48750. doi: 10.7554/eLife.48750

Dries, E., Santiago, D. J., Gilbert, G., Lenaerts, I., Vandenberk, B., Nagaraju, C. K., et al. (2018). Hyperactive ryanodine receptors in human heart failure and ischaemic cardiomyopathy reside outside of couplons. *Cardiovasc. Res.* 114, 1512–1524. doi: 10.1093/cvr/cvy088

Drum, B. M., Yuan, C., de la Mata, A., Grainger, N., and Santana, L. F. (2020). Junctional sarcoplasmic reticulum motility in adult mouse ventricular myocytes. *Am. J. Physiol. Cell Physiol.* 318, C598–C604. doi: 10.1152/ajpcell.00573.2019

Drum, B. M., Yuan, C., Li, L., Liu, Q., Wordeman, L., and Santana, L. F. (2016). Oxidative stress decreases microtubule growth and stability in ventricular myocytes. *J. Mol. Cell. Cardiol.* 93, 32–43. doi: 10.1016/j.yjmcc.2016.02.012

Eid, W., Dauner, K., Courtney, K. C., Gagnon, A., Parks, R. J., Sorisky, A., et al. (2017). mTORC1 activates SREBP-2 by suppressing cholesterol trafficking to lysosomes in mammalian cells. *Proc. Natl. Acad. Sci. U. S. A.* 114, 7999–8004. doi: 10.1073/pnas.1705304114

Eisner, D. A., Caldwell, J. L., Trafford, A. W., and Hutchings, D. C. (2020). The control of diastolic calcium in the heart: basic mechanisms and functional implications. *Circ. Res.* 126, 395–412. doi: 10.1161/CIRCRESAHA.119.315891

Enns, L. C., Morton, J. F., Treuting, P. R., Emond, M. J., Wolf, N. S., Dai, D. F., et al. (2009). Disruption of protein kinase A in mice enhances healthy aging. *PLoS One* 4:e5963. doi: 10.1371/journal.pone.0005963

Fares, E., and Howlett, S. E. (2010). Effect of age on cardiac excitation-contraction coupling. *Clin. Exp. Pharmacol. Physiol.* 37, 1–7. doi: 10.1111/j.1440-1681.2009.05276.x

Fauconnier, J., Meli, A. C., Thireau, J., Roberge, S., Shan, J., Sassi, Y., et al. (2011). Ryanodine receptor leak mediated by caspase-8 activation leads to left ventricular injury after myocardial ischemia-reperfusion. *Proc. Natl. Acad. Sci. U. S. A.* 108, 13258–13263. doi: 10.1073/pnas.1100286108

Feridooni, H. A., Dibb, K. M., and Howlett, S. E. (2015). How cardiomyocyte excitation, calcium release and contraction become altered with age. *J. Mol. Cell. Cardiol.* 83, 62–72. doi: 10.1016/j.yjmcc.2014.12.004

Feridooni, H. A., Kane, A. E., Ayaz, O., Boroumandi, A., Polidovitch, N., Tsushima, R. G., et al. (2017). The impact of age and frailty on ventricular structure and function in C57BL/6J mice. *J. Physiol.* 595, 3721–3742. doi: 10.1113/JP274134

Fischer, T. H., Eiringhaus, J., Dybkova, N., Forster, A., Herting, J., Kleinwachter, A., et al. (2014). Ca^{2+}/calmodulin-dependent protein kinase II equally induces sarcoplasmic reticulum Ca^{2+} leak in human ischaemic and dilated cardiomyopathy. *Eur. J. Heart Fail.* 16, 1292–1300. doi: 10.1002/ejhf.163

Franzini-Armstrong, C., Protasi, F., and Ramesh, V. (1999). Shape, size, and distribution of Ca(2+) release units and couplons in skeletal and cardiac muscles. *Biophys. J.* 77, 1528–1539. doi: 10.1016/S0006-3495(99)77000-1

Frisk, M., Le, C., Shen, X., Roe, A. T., Hou, Y., Manfra, O., et al. (2021). Etiology-dependent impairment of diastolic cardiomyocyte calcium homeostasis in heart failure with preserved ejection fraction. *J. Am. Coll. Cardiol.* 77, 405–419. doi: 10.1016/j.jacc.2020.11.044

Frost, A., Unger, V. M., and De Camilli, P. (2009). The BAR domain superfamily: membrane-molding macromolecules. *Cell* 137, 191–196. doi: 10.1016/j.cell.2009.04.010

Fu, Y., Shaw, S. A., Naami, R., Vuong, C. L., Basheer, W. A., Guo, X., et al. (2016). Isoproterenol promotes rapid ryanodine receptor movement to bridging integrator 1 (BIN1)-organized dyads. *Circulation* 133, 388–397. doi: 10.1161/CIRCULATIONAHA.115.018535

Fujita, A., Cheng, J., Tauchi-Sato, K., Takenawa, T., and Fujimoto, T. (2009). A distinct pool of phosphatidylinositol 4,5-bisphosphate in caveolae revealed by a nanoscale labeling technique. *Proc. Natl. Acad. Sci. U. S. A.* 106, 9256–9261. doi: 10.1073/pnas.0900216106

Galice, S., Xie, Y., Yang, Y., Sato, D., and Bers, D. M. (2018). Size matters: ryanodine receptor cluster size affects arrhythmogenic sarcoplasmic reticulum calcium release. *J. Am. Heart Assoc.* 7:e008724. doi: 10.1161/JAHA.118.008724

Ghosh, D., Nieves-Cintron, M., Tajada, S., Brust-Mascher, I., Horne, M. C., Hell, J. W., et al. (2018). Dynamic L-type CaV1.2 channel trafficking facilitates CaV1.2 clustering and cooperative gating. *Biochim. Biophys. Acta* 1865, 1341–1355. doi: 10.1016/j.bbamcr.2018.06.013

Golini, L., Chouabe, C., Berthier, C., Cusimano, V., Fornaro, M., Bonvallet, R., et al. (2011). Junctophilin 1 and 2 proteins interact with the L-type Ca^{2+} channel dihydropyridine receptors (DHPRs) in skeletal muscle. *J. Biol. Chem.* 286, 43717–43725. doi: 10.1074/jbc.M111.292755

Gomez, A. M., Guatimosim, S., Dilly, K. W., Vassort, G., and Lederer, W. J. (2001). Heart failure after myocardial infarction: altered excitation- contraction coupling. *Circulation* 104, 688–693. doi: 10.1161/hc3201.092285

Gomez, A. M., Valdivia, H. H., Cheng, H., Lederer, M. R., Santana, L. F., Cannell, M. B., et al. (1997). Defective excitation-contraction coupling in experimental cardiac hypertrophy and heart failure. *Science* 276, 800–806. doi: 10.1126/science.276.5313.800

Gross, P., Johnson, J., Romero, C. M., Eaton, D. M., Poulet, C., Sanchez-Alonso, J., et al. (2021). Interaction of the joining region in Junctophilin-2 with the L-type Ca^{2+} channel is pivotal for cardiac dyad assembly and intracellular $Ca^{(2+)}$ dynamics. *Circ. Res.* 128, 92–114. doi: 10.1161/CIRCRESAHA.119.315715

Guo, A., Hall, D., Zhang, C., Peng, T., Miller, J. D., Kutschke, W., et al. (2015). Molecular determinants of calpain-dependent cleavage of junctophilin-2 protein in cardiomyocytes. *J. Biol. Chem.* 290, 17946–17955. doi: 10.1074/jbc.M115.652396

Guo, A., Zhang, C., Wei, S., Chen, B., and Song, L. S. (2013). Emerging mechanisms of T-tubule remodelling in heart failure. *Cardiovasc. Res.* 98, 204–215. doi: 10.1093/cvr/cvt020

Gwosch, K. C., Pape, J. K., Balzarotti, F., Hoess, P., Ellenberg, J., Ries, J., et al. (2020). MINFLUX nanoscopy delivers 3D multicolor nanometer resolution in cells. *Nat. Methods* 17, 217–224. doi: 10.1038/s41592-019-0688-0

Haddock, P. S., Coetzee, W. A., Cho, E., Porter, L., Katoh, H., Bers, D. M., et al. (1999). Subcellular [Ca2+]i gradients during excitation-contraction coupling in newborn rabbit ventricular myocytes. *Circ. Res.* 85, 415–427. doi: 10.1161/01.RES.85.5.415

Hadipour-Lakmehsari, S., Driouchi, A., Lee, S. H., Kuzmanov, U., Callaghan, N. I., Heximer, S. P., et al. (2019). Nanoscale reorganization of sarcoplasmic reticulum in pressure-overload cardiac hypertrophy visualized by dSTORM. *Sci. Rep.* 9:7867. doi: 10.1038/s41598-019-44331-y

Hamaguchi, S., Kawakami, Y., Honda, Y., Nemoto, K., Sano, A., Namekata, I., et al. (2013). Developmental changes in excitation-contraction mechanisms of the mouse ventricular myocardium as revealed by functional and confocal imaging analyses. *J. Pharmacol. Sci.* 123, 167–175. doi: 10.1254/jphs.13099FP

He, J., Conklin, M. W., Foell, J. D., Wolff, M. R., Haworth, R. A., Coronado, R., et al. (2001). Reduction in density of transverse tubules and L-type Ca^{2+} channels in canine tachycardia-induced heart failure. *Cardiovasc. Res.* 49, 298–307. doi: 10.1016/S0008-6363(00)00256-X

Heinze-Milne, S. D., Banga, S., and Howlett, S. E. (2019). Frailty assessment in animal models. *Gerontology* 65, 610–619. doi: 10.1159/000501333

Hoch, B., Meyer, R., Hetzer, R., Krause, E. G., and Karczewski, P. (1999). Identification and expression of delta-isoforms of the multifunctional Ca^{2+}/calmodulin-dependent protein kinase in failing and nonfailing human myocardium. *Circ. Res.* 84, 713–721. doi: 10.1161/01.RES.84.6.713

Hong, T. T., Smyth, J. W., Chu, K. Y., Vogan, J. M., Fong, T. S., Jensen, B. C., et al. (2012). BIN1 is reduced and CaV1.2 trafficking is impaired in human failing cardiomyocytes. *Heart Rhythm.* 9, 812–820. doi: 10.1016/j.hrthm.2011.11.055

Hong, T. T., Smyth, J. W., Gao, D., Chu, K. Y., Vogan, J. M., Fong, T. S., et al. (2010). BIN1 localizes the L-type calcium channel to cardiac T-tubules. *PLoS Biol.* 8:e1000312. doi: 10.1371/journal.pbio.1000312

Hong, T., Yang, H., Zhang, S. S., Cho, H. C., Kalashnikova, M., Sun, B., et al. (2014). Cardiac BIN1 folds T-tubule membrane, controlling ion flux and limiting arrhythmia. *Nat. Med.* 20, 624–632. doi: 10.1038/nm.3543

Hou, Y., Bai, J., Shen, X., de Langen, O., Li, A., Lal, S., et al. (2021). Nanoscale organisation of ryanodine receptors and junctophilin-2 in the failing human heart. *Front. Physiol.* 12:724372. doi: 10.3389/fphys.2021.724372

Hou, Y., Jayasinghe, I., Crossman, D. J., Baddeley, D., and Soeller, C. (2015). Nanoscale analysis of ryanodine receptor clusters in dyadic couplings of rat cardiac myocytes. *J. Mol. Cell. Cardiol.* 80, 45–55. doi: 10.1016/j.yjmcc.2014.12.013

Ito, D. W., Hannigan, K. I., Ghosh, D., Xu, B., Del Villar, S. G., Xiang, Y. K., et al. (2019). Beta-adrenergic-mediated dynamic augmentation of sarcolemmal CaV1.2 clustering and co-operativity in ventricular myocytes. *J. Physiol.* 597, 2139–2162. doi: 10.1113/JP277283

Jayasinghe, I. D., Baddeley, D., Kong, C. H., Wehrens, X. H., Cannell, M. B., and Soeller, C. (2012). Nanoscale organization of junctophilin-2 and ryanodine receptors within peripheral couplings of rat ventricular cardiomyocytes. *Biophys. J.* 102, L19–L21. doi: 10.1016/j.bpj.2012.01.034

Jayasinghe, I., Clowsley, A. H., Lin, R., Lutz, T., Harrison, C., Green, E., et al. (2018). True molecular scale visualization of variable clustering properties of ryanodine receptors. *Cell Rep.* 22, 557–567. doi: 10.1016/j.celrep.2017.12.045

Jiang, M., Hu, J., White, F. K. H., Williamson, J., Klymchenko, A. S., Murthy, A., et al. (2019). S-Palmitoylation of junctophilin-2 is critical for its role in tethering the sarcoplasmic reticulum to the plasma membrane. *J. Biol. Chem.* 294, 13487–13501. doi: 10.1074/jbc.RA118.006772

Josephson, I. R., Guia, A., Stern, M. D., and Lakatta, E. G. (2002). Alterations in properties of L-type Ca channels in aging rat heart. *J. Mol. Cell. Cardiol.* 34, 297–308. doi: 10.1006/jmcc.2001.1512

Kandilci, H. B., Tuncay, E., Zeydanli, E. N., Sozmen, N. N., and Turan, B. (2011). Age-related regulation of excitation-contraction coupling in rat heart. *J. Physiol. Biochem.* 67, 317–330. doi: 10.1007/s13105-011-0077-3

Kaprielian, R. R., Stevenson, S., Rothery, S. M., Cullen, M. J., and Severs, N. J. (2000). Distinct patterns of dystrophin organization in myocyte sarcolemma and transverse tubules of normal and diseased human myocardium. *Circulation* 101, 2586–2594. doi: 10.1161/01.CIR.101.22.2586

Kawai, M., Hussain, M., and Orchard, C. H. (1999). Excitation-contraction coupling in rat ventricular myocytes after formamide-induced detubulation. *Am. J. Phys.* 277, H603–H609. doi: 10.1152/ajpheart.1999.277.2.H603

Kaye, D., and Esler, M. (2005). Sympathetic neuronal regulation of the heart in aging and heart failure. *Cardiovasc. Res.* 66, 256–264. doi: 10.1016/j.cardiores.2005.02.012

Kirchhefer, U., Schmitz, W., Scholz, H., and Neumann, J. (1999). Activity of cAMP-dependent protein kinase and Ca^{2+}/calmodulin-dependent protein kinase in failing and nonfailing human hearts. *Cardiovasc. Res.* 42, 254–261. doi: 10.1016/S0008-6363(98)00296-X

Kolstad, T. R., van den Brink, J., MacQuaide, N., Lunde, P. K., Frisk, M., Aronsen, J. M., et al. (2018). Ryanodine receptor dispersion disrupts Ca^{2+} release in failing cardiac myocytes. *Elife* 7:e39427. doi: 10.7554/eLife.39427

Kong, C. H. T., Bryant, S. M., Watson, J. J., Gadeberg, H. C., Roth, D. M., Patel, H. H., et al. (2018). The effects of aging on the regulation of T-tubular I_{Ca} by caveolin in mouse ventricular myocytes. *J. Gerontol. A Biol. Sci. Med. Sci.* 73, 711–719. doi: 10.1093/gerona/glx242

Kostin, S., Scholz, D., Shimada, T., Maeno, Y., Mollnau, H., Hein, S., et al. (1998). The internal and external protein scaffold of the T-tubular system in cardiomyocytes. *Cell Tissue Res.* 294, 449–460. doi: 10.1007/s004410051196

Kutchukian, C., Vivas, O., Casas, M., Jones, J. G., Tiscione, S. A., Simo, S., et al. (2021). NPC1 regulates the distribution of phosphatidylinositol 4-kinases at Golgi and lysosomal membranes. *EMBO J.* 40:e105990. doi: 10.15252/embj.2020105990

Lakatta, E. G. (1993). Deficient neuroendocrine regulation of the cardiovascular-system with advancing age in healthy humans. *Circulation* 87, 631–636. doi: 10.1161/01.CIR.87.2.631

Lakatta, E. G., Gerstenblith, G., Angell, C. S., Shock, N. W., and Weisfeldt, M. L. (1975). Diminished inotropic response of aged myocardium to catecholamines. *Circ. Res.* 36, 262–269. doi: 10.1161/01.RES.36.2.262

Lakatta, E. G., and Sollott, S. J. (2002). Perspectives on mammalian cardiovascular aging: humans to molecules. *Comp. Biochem. Physiol. A Mol. Integr. Physiol.* 132, 699–721. doi: 10.1016/S1095-6433(02)00124-1

Landstrom, A. P., Weisleder, N., Batalden, K. B., Bos, J. M., Tester, D. J., Ommen, S. R., et al. (2007). Mutations in JPH2-encoded junctophilin-2 associated with hypertrophic cardiomyopathy in humans. *J. Mol. Cell. Cardiol.* 42, 1026–1035. doi: 10.1016/j.yjmcc.2007.04.006

Lanner, J. T., Georgiou, D. K., Joshi, A. D., and Hamilton, S. L. (2010). Ryanodine receptors: structure, expression, molecular details, and function in calcium release. *Cold Spring Harb. Perspect. Biol.* 2:a003996. doi: 10.1101/cshperspect.a003996

Laury-Kleintop, L. D., Mulgrew, J. R., Heletz, I., Nedelcoviciu, R. A., Chang, M. Y., Harris, D. M., et al. (2015). Cardiac-specific disruption of Bin1 in mice enables a model of stress- and age-associated dilated cardiomyopathy. *J. Cell. Biochem.* 116, 2541–2551. doi: 10.1002/jcb.25198

Lee, E., Marcucci, M., Daniell, L., Pypaert, M., Weisz, O. A., Ochoa, G. C., et al. (2002). Amphiphysin 2 (Bin1) and T-tubule biogenesis in muscle. *Science* 297, 1193–1196. doi: 10.1126/science.1071362

Levin, K. R., and Page, E. (1980). Quantitative studies on plasmalemmal folds and caveolae of rabbit ventricular myocardial cells. *Circ. Res.* 46, 244–255. doi: 10.1161/01.RES.46.2.244

Li, J., Agvanian, S., Zhou, K., Shaw, R. M., and Hong, T. (2020). Exogenous cardiac bridging integrator 1 benefits mouse hearts with pre-existing pressure overload-induced heart failure. *Front. Physiol.* 11:708. doi: 10.3389/fphys.2020.00708

Li, N., Chiang, D. Y., Wang, S., Wang, Q., Sun, L., Voigt, N., et al. (2014). Ryanodine receptor-mediated calcium leak drives progressive development of an atrial fibrillation substrate in a transgenic mouse model. *Circulation* 129, 1276–1285. doi: 10.1161/CIRCULATIONAHA.113.006611

Li, L., Satoh, H., Ginsburg, K. S., and Bers, D. M. (1997). The effect of Ca^{2+}-calmodulin-dependent protein kinase II on cardiac excitation-contraction coupling in ferret ventricular myocytes. *J. Physiol.* 501, 17–31. doi: 10.1111/j.1469-7793.1997.017bo.x

Lipp, P., Huser, J., Pott, L., and Niggli, E. (1996). Spatially non-uniform Ca^{2+} signals induced by the reduction of transverse tubules in citrate-loaded Guinea-pig ventricular myocytes in culture. *J. Physiol.* 497, 589–597. doi: 10.1113/jphysiol.1996.sp021792

Lipsett, D. B., Frisk, M., Aronsen, J. M., Norden, E. S., Buonarati, O. R., Cataliotti, A., et al. (2019). Cardiomyocyte substructure reverts to an immature phenotype during heart failure. *J. Physiol.* 597, 1833–1853. doi: 10.1113/JP277273

Litwin, S. E., Zhang, D., and Bridge, J. H. (2000). Dyssynchronous Ca^{2+} sparks in myocytes from infarcted hearts. *Circ. Res.* 87, 1040–1047. doi: 10.1161/01.RES.87.11.1040

Liu, G., Papa, A., Katchman, A. N., Zakharov, S. I., Roybal, D., Hennessey, J. A., et al. (2020). Mechanism of adrenergic CaV1.2 stimulation revealed by proximity proteomics. *Nature* 577, 695–700. doi: 10.1038/s41586-020-1947-z

Louch, W. E., Bito, V., Heinzel, F. R., Macianskiene, R., Vanhaecke, J., Flameng, W., et al. (2004). Reduced synchrony of Ca^{2+} release with loss of T-tubules-a comparison to Ca^{2+} release in human failing cardiomyocytes. *Cardiovasc. Res.* 62, 63–73. doi: 10.1016/j.cardiores.2003.12.031

Louch, W. E., Hake, J., Mork, H. K., Hougen, K., Skrbic, B., Ursu, D., et al. (2013). Slow Ca^{2+} sparks de-synchronize Ca^{2+} release in failing cardiomyocytes: evidence for altered configuration of Ca^{2+} release units? *J. Mol. Cell. Cardiol.* 58, 41–52. doi: 10.1016/j.yjmcc.2013.01.014

Louch, W. E., Mork, H. K., Sexton, J., Stromme, T. A., Laake, P., Sjaastad, I., et al. (2006). T-tubule disorganization and reduced synchrony of Ca^{2+} release in murine cardiomyocytes following myocardial infarction. *J. Physiol.* 574, 519–533. doi: 10.1113/jphysiol.2006.107227

Lyon, A. R., Nikolaev, V. O., Miragoli, M., Sikkel, M. B., Paur, H., Benard, L., et al. (2012). Plasticity of surface structures and beta(2)-adrenergic receptor localization in failing ventricular cardiomyocytes during recovery from heart failure. *Circ. Heart Fail.* 5, 357–365. doi: 10.1161/CIRCHEARTFAILURE.111.964692

Lyu, Y., Verma, V. K., Lee, Y., Taleb, I., Badolia, R., Shankar, T. S., et al. (2021). Remodeling of t-system and proteins underlying excitation-contraction coupling in aging versus failing human heart. *NPJ Aging Mech. Dis.* 7:16. doi: 10.1038/s41514-021-00066-7

MacQuaide, N., Tuan, H. T., Hotta, J., Sempels, W., Lenaerts, I., Holemans, P., et al. (2015). Ryanodine receptor cluster fragmentation and redistribution in persistent atrial fibrillation enhance calcium release. *Cardiovasc. Res.* 108, 387–398. doi: 10.1093/cvr/cvv231

Maguy, A., Hebert, T. E., and Nattel, S. (2006). Involvement of lipid rafts and caveolae in cardiac ion channel function. *Cardiovasc. Res.* 69, 798–807. doi: 10.1016/j.cardiores.2005.11.013

Man, K. N. M., Bartels, P., Horne, M. C., and Hell, J. W. (2020). Tissue-specific adrenergic regulation of the L-type Ca^{2+} channel CaV1.2. *Sci. Signal.* 13:eabc6438. doi: 10.1126/scisignal.abc6438

Maron, B. J., Ferrans, V. J., and Roberts, W. C. (1975). Ultrastructural features of degenerated cardiac muscle cells in patients with cardiac hypertrophy. *Am. J. Pathol.* 79, 387–434.

Marx, S. O., Reiken, S., Hisamatsu, Y., Jayaraman, T., Burkhoff, D., Rosemblit, N., et al. (2000). PKA phosphorylation dissociates FKBP12.6 from the calcium release channel (ryanodine receptor): defective regulation in failing hearts. *Cell* 101, 365–376. doi: 10.1016/S0092-8674(00)80847-8

Medvedev, R. Y., Sanchez-Alonso, J. L., Mansfield, C. A., Judina, A., Francis, A. J., Pagiatakis, C., et al. (2021). Local hyperactivation of L-type Ca^{2+} channels increases spontaneous Ca^{2+} release activity and cellular hypertrophy in right ventricular myocytes from heart failure rats. *Sci. Rep.* 11:4840. doi: 10.1038/s41598-021-84275-w

Minamisawa, S., Oshikawa, J., Takeshima, H., Hoshijima, M., Wang, Y., Chien, K. R., et al. (2004). Junctophilin type 2 is associated with caveolin-3 and is down-regulated in the hypertrophic and dilated cardiomyopathies. *Biochem. Biophys. Res. Commun.* 325, 852–856. doi: 10.1016/j.bbrc.2004.10.107

Molkentin, J. D., Lu, J. R., Antos, C. L., Markham, B., Richardson, J., Robbins, J., et al. (1998). A calcineurin-dependent transcriptional pathway for cardiac hypertrophy. *Cell* 93, 215–228. doi: 10.1016/S0092-8674(00)81573-1

Moreno, C. M., Dixon, R. E., Tajada, S., Yuan, C., Opitz-Araya, X., Binder, M. D., et al. (2016). Ca^{2+} entry into neurons is facilitated by cooperative gating of clustered CaV1.3 channels. *Elife* 5:e15744, 10.7554/eLife.15744

Muller, A. J., Baker, J. F., DuHadaway, J. B., Ge, K., Farmer, G., Donover, P. S., et al. (2003). Targeted disruption of the murine Bin1/Amphiphysin II gene does not disable endocytosis but results in embryonic cardiomyopathy with aberrant myofibril formation. *Mol. Cell. Biol.* 23, 4295–4306. doi: 10.1128/MCB.23.12.4295-4306.2003

Munro, M. L., Jayasinghe, I. D., Wang, Q., Quick, A., Wang, W., Baddeley, D., et al. (2016). Junctophilin-2 in the nanoscale organisation and functional signalling of ryanodine receptor clusters in cardiomyocytes. *J. Cell Sci.* 129, 4388–4398. doi: 10.1242/jcs.196873

Munro, M. L., van Hout, I., Aitken-Buck, H. M., Sugunesegran, R., Bhagwat, K., Davis, P. J., et al. (2021). Human atrial fibrillation is not associated with remodeling of ryanodine receptor clusters. *Front. Cell Dev. Biol.* 9:633704. doi: 10.3389/fcell.2021.633704

Myeong, J., Park, C. G., Suh, B. C., and Hille, B. (2021). Compartmentalization of phosphatidylinositol 4,5-bisphosphate metabolism into plasma membrane liquid-ordered/raft domains. *Proc. Natl. Acad. Sci. U. S. A.* 118:e2025343118. doi: 10.1073/pnas.2025343118

Nakada, T., Kashihara, T., Komatsu, M., Kojima, K., Takeshita, T., and Yamada, M. (2018). Physical interaction of junctophilin and the CaV1.1 C terminus is crucial for skeletal muscle contraction. *Proc. Natl. Acad. Sci. U. S. A.* 115, 4507–4512. doi: 10.1073/pnas.1716649115

Neef, S., Dybkova, N., Sossalla, S., Ort, K. R., Fluschnik, N., Neumann, K., et al. (2010). CaMKII-dependent diastolic SR Ca^{2+} leak and elevated diastolic Ca^{2+} levels in right atrial myocardium of patients with atrial fibrillation. *Circ. Res.* 106, 1134–1144. doi: 10.1161/CIRCRESAHA.109.203836

Papa, A., Kushner, J., Hennessey, J. A., Katchman, A. N., Zakharov, S. I., Chen, B. X., et al. (2021). Adrenergic CaV1.2 activation via rad phosphorylation converges at alpha1C I-II loop. *Circ. Res.* 128, 76–88. doi: 10.1161/CIRCRESAHA.120.317839

Pavlovic, D., McLatchie, L. M., and Shattock, M. J. (2010). The rate of loss of T-tubules in cultured adult ventricular myocytes is species dependent. *Exp. Physiol.* 95, 518–527. doi: 10.1113/expphysiol.2009.052126

Pendin, D., McNew, J. A., and Daga, A. (2011). Balancing ER dynamics: shaping, bending, severing, and mending membranes. *Curr. Opin. Cell Biol.* 23, 435–442. doi: 10.1016/j.ceb.2011.04.007

Pinali, C., Bennett, H., Davenport, J. B., Trafford, A. W., and Kitmitto, A. (2013). Three-dimensional reconstruction of cardiac sarcoplasmic reticulum reveals a continuous network linking transverse-tubules: this organization is perturbed in heart failure. *Circ. Res.* 113, 1219–1230. doi: 10.1161/CIRCRESAHA.113.301348

Place, N., Ivarsson, N., Venckunas, T., Neyroud, D., Brazaitis, M., Cheng, A. J., et al. (2015). Ryanodine receptor fragmentation and sarcoplasmic reticulum Ca^{2+} leak after one session of high-intensity interval exercise. *Proc. Natl. Acad. Sci. U. S. A.* 112, 15492–15497. doi: 10.1073/pnas.1507176112

Poulet, C., Sanchez-Alonso, J., Swiatlowska, P., Mouy, F., Lucarelli, C., Alvarez-Laviada, A., et al. (2021). Junctophilin-2 tethers T-tubules and recruits functional L-type calcium channels to lipid rafts in adult cardiomyocytes. *Cardiovasc. Res.* 117, 149–161. doi: 10.1093/cvr/cvaa033

Pritchard, H. A. T., Pires, P. W., Yamasaki, E., Thakore, P., and Earley, S. (2018). Nanoscale remodeling of ryanodine receptor cluster size underlies cerebral microvascular dysfunction in Duchenne muscular dystrophy. *Proc. Natl. Acad. Sci. U. S. A.* 115, E9745–E9752. doi: 10.1073/pnas.1804593115

Quan, C., Li, M., Du, Q., Chen, Q., Wang, H., Campbell, D., et al. (2019). SPEG controls calcium reuptake into the sarcoplasmic reticulum through regulating SERCA2a by its second kinase-domain. *Circ. Res.* 124, 712–726. doi: 10.1161/CIRCRESAHA.118.313916

Quick, A. P., Wang, Q., Philippen, L. E., Barreto-Torres, G., Chiang, D. Y., Beavers, D., et al. (2017). SPEG (striated muscle preferentially expressed protein kinase) is essential for cardiac function by regulating junctional membrane complex activity. *Circ. Res.* 120, 110–119. doi: 10.1161/CIRCRESAHA.116.309977

Rajabi, M., Kassiotis, C., Razeghi, P., and Taegtmeyer, H. (2007). Return to the fetal gene program protects the stressed heart: a strong hypothesis. *Heart Fail. Rev.* 12, 331–343. doi: 10.1007/s10741-007-9034-1

Reuter, H., and Scholz, H. (1977). The regulation of the calcium conductance of cardiac muscle by adrenaline. *J. Physiol.* 264, 49–62. doi: 10.1113/jphysiol.1977.sp011657

Reynolds, J. O., Chiang, D. Y., Wang, W., Beavers, D. L., Dixit, S. S., Skapura, D. G., et al. (2013). Junctophilin-2 is necessary for T-tubule maturation during mouse heart development. *Cardiovasc. Res.* 100, 44–53. doi: 10.1093/cvr/cvt133

Reynolds, J. O., Quick, A. P., Wang, Q., Beavers, D. L., Philippen, L. E., Showell, J., et al. (2016). Junctophilin-2 gene therapy rescues heart failure by normalizing RyR2-mediated Ca^{2+} release. *Int. J. Cardiol.* 225, 371–380. doi: 10.1016/j.ijcard.2016.10.021

Robison, P., Caporizzo, M. A., Ahmadzadeh, H., Bogush, A. I., Chen, C. Y., Margulies, K. B., et al. (2016). Detyrosinated microtubules buckle and bear load in contracting cardiomyocytes. *Science* 352:aaf0659. doi: 10.1126/science.aaf0659

Rog-Zielinska, E. A., Scardigli, M., Peyronnet, R., Zgierski-Johnston, C. M., Greiner, J., Madl, J., et al. (2021). Beat-by-beat cardiomyocyte T-tubule deformation drives tubular content exchange. *Circ. Res.* 128, 203–215. doi: 10.1161/CIRCRESAHA.120.317266

Ruiz-Meana, M., Minguet, M., Bou-Teen, D., Miro-Casas, E., Castans, C., Castellano, J., et al. (2019). Ryanodine receptor glycation favors mitochondrial damage in the senescent heart. *Circulation* 139, 949–964. doi: 10.1161/CIRCULATIONAHA.118.035869

Sanchez-Alonso, J. L., Bhargava, A., O'Hara, T., Glukhov, A. V., Schobesberger, S., Bhogal, N., et al. (2016). Microdomain-specific modulation of L-type calcium channels leads to triggered ventricular arrhythmia in heart failure. *Circ. Res.* 119, 944–955. doi: 10.1161/CIRCRESAHA.116.308698

Sanchez-Alonso, J. L., Loucks, A., Schobesberger, S., van Cromvoirt, A. M., Poulet, C., Chowdhury, R. A., et al. (2020). Nanoscale regulation of L-type calcium channels differentiates between ischemic and dilated cardiomyopathies. *EBioMedicine* 57:102845. doi: 10.1016/j.ebiom.2020.102845

Sandoval, I. V., and Weber, K. (1978). Calcium-induced inactivation of microtubule formation in brain extracts. Presence of a calcium-dependent protease acting on polymerization-stimulating microtubule-associated proteins. *Eur. J. Biochem.* 92, 463–470. doi: 10.1111/j.1432-1033.1978.tb12768.x

Sato, D., Hernandez-Hernandez, G., Matsumoto, C., Tajada, S., Moreno, C. M., Dixon, R. E., et al. (2019). A stochastic model of ion channel cluster formation in the plasma membrane. *J. Gen. Physiol.* 151, 1116–1134. doi: 10.1085/jgp.201912327

Schaper, J., Froede, R., Hein, S., Buck, A., Hashizume, H., Speiser, B., et al. (1991). Impairment of the myocardial ultrastructure and changes of the cytoskeleton in dilated cardiomyopathy. *Circulation* 83, 504–514. doi: 10.1161/01.CIR.83.2.504

Schroder, F., Handrock, R., Beuckelmann, D. J., Hirt, S., Hullin, R., Priebe, L., et al. (1998). Increased availability and open probability of single L-type calcium channels from failing compared with nonfailing human ventricle. *Circulation* 98, 969–976. doi: 10.1161/01.CIR.98.10.969

Scriven, D. R., Asghari, P., Schulson, M. N., and Moore, E. D. (2010). Analysis of CaV1.2 and ryanodine receptor clusters in rat ventricular myocytes. *Biophys. J.* 99, 3923–3929. doi: 10.1016/j.bpj.2010.11.008

Scriven, D. R., Dan, P., and Moore, E. D. (2000). Distribution of proteins implicated in excitation-contraction coupling in rat ventricular myocytes. *Biophys. J.* 79, 2682–2691. doi: 10.1016/S0006-3495(00)76506-4

Setterberg, I. E., Le, C., Frisk, M., Li, J., and Louch, W. E. (2021). The physiology and pathophysiology of T-tubules in the heart. *Front. Physiol.* 12:718404. doi: 10.3389/fphys.2021.718404

Shannon, T. R., Pogwizd, S. M., and Bers, D. M. (2003). Elevated sarcoplasmic reticulum Ca^{2+} leak in intact ventricular myocytes from rabbits in heart failure. *Circ. Res.* 93, 592–594. doi: 10.1161/01.RES.0000093399.11734.B3

Sheard, T. M. D., Hurley, M. E., Colyer, J., White, E., Norman, R., Pervolaraki, E., et al. (2019). Three-dimensional and chemical mapping of intracellular signaling nanodomains in health and disease with enhanced expansion microscopy. *ACS Nano* 13, 2143–2157. doi: 10.1021/acsnano.8b08742

Shen, X., van den Brink, J., Hou, Y., Colli, D., Le, C., Kolstad, T. R., et al. (2019). 3D dSTORM imaging reveals novel detail of ryanodine receptor localization in rat cardiac myocytes. *J. Physiol.* 597, 399–418. doi: 10.1113/JP277360

Shiferaw, Y., Aistrup, G. L., Louch, W. E., and Wasserstrom, J. A. (2020). Remodeling promotes proarrhythmic disruption of calcium homeostasis in failing atrial myocytes. *Biophys. J.* 118, 476–491. doi: 10.1016/j.bpj.2019.12.012

Sobie, E. A., Guatimosim, S., Gomez-Viquez, L., Song, L. S., Hartmann, H., Saleet Jafri, M., et al. (2006). The Ca^{2+}+ leak paradox and rogue ryanodine receptors: SR Ca^{2+} efflux theory and practice. *Prog. Biophys. Mol. Biol.* 90, 172–185. doi: 10.1016/j.pbiomolbio.2005.06.010

Soeller, C., and Cannell, M. B. (1999). Examination of the transverse tubular system in living cardiac rat myocytes by 2-photon microscopy and digital image-processing techniques. *Circ. Res.* 84, 266–275. doi: 10.1161/01.RES.84.3.266

Soeller, C., Crossman, D., Gilbert, R., and Cannell, M. B. (2007). Analysis of ryanodine receptor clusters in rat and human cardiac myocytes. *Proc. Natl. Acad. Sci. U. S. A.* 104, 14958–14963. doi: 10.1073/pnas.0703016104

Song, L. S., Sobie, E. A., McCulle, S., Lederer, W. J., Balke, C. W., and Cheng, H. (2006). Orphaned ryanodine receptors in the failing heart. *Proc. Natl. Acad. Sci. U. S. A.* 103, 4305–4310. doi: 10.1073/pnas.0509324103

Sperelakis, N., and Schneider, J. A. (1976). A metabolic control mechanism for calcium ion influx that may protect the ventricular myocardial cell. *Am. J. Cardiol.* 37, 1079–1085. doi: 10.1016/0002-9149(76)90428-8

Strait, J. B., and Lakatta, E. G. (2012). Aging-associated cardiovascular changes and their relationship to heart failure. *Heart Fail. Clin.* 8, 143–164. doi: 10.1016/j.hfc.2011.08.011

Stratton, J. R., Cerqueira, M. D., Schwartz, R. S., Levy, W. C., Veith, R. C., Kahn, S. E., et al. (1992). Differences in cardiovascular responses to isoproterenol in relation to age and exercise training in healthy men. *Circulation* 86, 504–512. doi: 10.1161/01.CIR.86.2.504

Takeshima, H., Komazaki, S., Nishi, M., Iino, M., and Kangawa, K. (2000). Junctophilins: a novel family of junctional membrane complex proteins. *Mol. Cell* 6, 11–22. doi: 10.1016/s1097-2765(00)00003-4

Terentyev, D., Gyorke, I., Belevych, A. E., Terentyeva, R., Sridhar, A., Nishijima, Y., et al. (2008). Redox modification of ryanodine receptors contributes to sarcoplasmic reticulum Ca^{2+} leak in chronic heart failure. *Circ. Res.* 103, 1466–1472. doi: 10.1161/CIRCRESAHA.108.184457

Tian, L., Jeffries, O., McClafferty, H., Molyvdas, A., Rowe, I. C., Saleem, F., et al. (2008). Palmitoylation gates phosphorylation-dependent regulation of BK potassium channels. *Proc. Natl. Acad. Sci. U. S. A.* 105, 21006–21011. doi: 10.1073/pnas.0806700106

Tsien, R. W., Giles, W., and Greengard, P. (1972). Cyclic AMP mediates the effects of adrenaline on cardiac purkinje fibres. *Nat. New Biol.* 240, 181–183. doi: 10.1038/newbio240181a0

Valdivia, H. H. (2012). Ryanodine receptor phosphorylation and heart failure: phasing out S2808 and "criminalizing" S2814. *Circ. Res.* 110, 1398–1402. doi: 10.1161/CIRCRESAHA.112.270876

van Oort, R. J., Garbino, A., Wang, W., Dixit, S. S., Landstrom, A. P., Gaur, N., et al. (2011). Disrupted junctional membrane complexes and hyperactive ryanodine receptors after acute junctophilin knockdown in mice. *Circulation* 123, 979–988. doi: 10.1161/CIRCULATIONAHA.110.006437

Van Petegem, F. (2015). Ryanodine receptors: allosteric ion channel giants. *J. Mol. Biol.* 427, 31–53. doi: 10.1016/j.jmb.2014.08.004

Vega, A. L., Yuan, C., Votaw, V. S., and Santana, L. F. (2011). Dynamic changes in sarcoplasmic reticulum structure in ventricular myocytes. *J. Biomed. Biotechnol.* 2011:382586. doi: 10.1155/2011/382586

Vivas, O., Tiscione, S. A., Dixon, R. E., Ory, D. S., and Dickson, E. J. (2019). Niemann-pick type C disease reveals a link between lysosomal cholesterol and PtdIns(4,5)P2 That regulates neuronal excitability. *Cell Rep.* 27, 2636–2648 e2634. doi: 10.1016/j.celrep.2019.04.099

Walker, K. E., Lakatta, E. G., and Houser, S. R. (1993). Age associated changes in membrane currents in rat ventricular myocytes. *Cardiovasc. Res.* 27, 1968–1977. doi: 10.1093/cvr/27.11.1968

Wang, W., Landstrom, A. P., Wang, Q., Munro, M. L., Beavers, D., Ackerman, M. J., et al. (2014). Reduced junctional Na+/Ca^{2+}−exchanger activity contributes to sarcoplasmic reticulum Ca^{2+} leak in junctophilin-2-deficient mice. *Am. J. Physiol. Heart Circ. Physiol.* 307, H1317–H1326. doi: 10.1152/ajpheart.00413.2014

Weber, M., Leutenegger, M., Stoldt, S., Jakobs, S., Mihaila, T. S., Butkevich, A. N., et al. (2021). MINSTED fluorescence localization and nanoscopy. *Nat. Photonics* 15, 361–366. doi: 10.1038/s41566-021-00774-2

Wei, S., Guo, A., Chen, B., Kutschke, W., Xie, Y. P., Zimmerman, K., et al. (2010). T-tubule remodeling during transition from hypertrophy to heart failure. *Circ. Res.* 107, 520–531. doi: 10.1161/CIRCRESAHA.109.212324

Weisenberg, R. C. (1972). Microtubule formation in vitro in solutions containing low calcium concentrations. *Science* 177, 1104–1105. doi: 10.1126/science.177.4054.1104

Westhoff, M., and Dixon, R. E. (2021). Mechanisms and regulation of cardiac CaV1.2 trafficking. *Int. J. Mol. Sci.* 22:5927. doi: 10.3390/ijms22115927

White, M., Roden, R., Minobe, W., Khan, M. F., Larrabee, P., Wollmering, M., et al. (1994). Age-related changes in beta-adrenergic neuroeffector systems in the human heart. *Circulation* 90, 1225–1238. doi: 10.1161/01.CIR.90.3.1225

Wu, T., and Baumgart, T. (2014). BIN1 membrane curvature sensing and generation show autoinhibition regulated by downstream ligands and PI(4,5) P2. *Biochemistry* 53, 7297–7309. doi: 10.1021/bi501082r

Wu, H. D., Xu, M., Li, R. C., Guo, L., Lai, Y. S., Xu, S. M., et al. (2012). Ultrastructural remodelling of Ca(2+) signalling apparatus in failing heart cells. *Cardiovasc. Res.* 95, 430–438. doi: 10.1093/cvr/cvs195

Wu, J., Yan, Z., Li, Z., Qian, X., Lu, S., Dong, M., et al. (2016). Structure of the voltage-gated calcium channel CaV1.1 at 3.6 A resolution. *Nature* 537, 191–196. doi: 10.1038/nature19321

Wu, J., Yan, Z., Li, Z., Yan, C., Lu, S., Dong, M., et al. (2015). Structure of the voltage-gated calcium channel Cav1.1 complex. *Science* 350:aad2395. doi: 10.1126/science.aad2395

Xiao, R. P., Spurgeon, H. A., O'Connor, F., and Lakatta, E. G. (1994). Age-associated changes in beta-adrenergic modulation on rat cardiac excitation-contraction coupling. *J. Clin. Invest.* 94, 2051–2059. doi: 10.1172/JCI117559

Xiao, R. P., Tomhave, E. D., Wang, D. J., Ji, X., Boluyt, M. O., Cheng, H., et al. (1998). Age-associated reductions in cardiac beta1- and beta2-adrenergic responses without changes in inhibitory G proteins or receptor kinases. *J. Clin. Invest.* 101, 1273–1282. doi: 10.1172/JCI1335

Xie, Y., Yang, Y., Galice, S., Bers, D. M., and Sato, D. (2019). Size matters: ryanodine receptor cluster size heterogeneity potentiates calcium waves. *Biophys. J.* 116, 530–539. doi: 10.1016/j.bpj.2018.12.017

Xu, L., and Brink, M. (2016). mTOR, cardiomyocytes and inflammation in cardiac hypertrophy. *Biochim Biophys Acta* 1863, 1894–1903. doi: 10.1016/j.bbamcr.2016.01.003

Yue, D. T., Herzig, S., and Marban, E. (1990). Beta-adrenergic stimulation of calcium channels occurs by potentiation of high-activity gating modes. *Proc. Natl. Acad. Sci. U. S. A.* 87, 753–757.

Zamponi, G. W., Striessnig, J., Koschak, A., and Dolphin, A. C. (2015). The physiology, pathology, and pharmacology of voltage-gated calcium channels and their future therapeutic potential. *Pharmacol. Rev.* 67, 821–870. doi: 10.1124/pr.114.009654

Zhang, L., Kelley, J., Schmeisser, G., Kobayashi, Y. M., and Jones, L. R. (1997). Complex formation between junctin, triadin, calsequestrin, and the ryanodine receptor. Proteins of the cardiac junctional sarcoplasmic reticulum membrane. *J. Biol. Chem.* 272, 23389–23397. doi: 10.1074/jbc.272.37.23389

Zhang, H. B., Li, R. C., Xu, M., Xu, S. M., Lai, Y. S., Wu, H. D., et al. (2013). Ultrastructural uncoupling between T-tubules and sarcoplasmic reticulum in human heart failure. *Cardiovasc. Res.* 98, 269–276. doi: 10.1093/cvr/cvt030

Zhang, T., Maier, L. S., Dalton, N. D., Miyamoto, S., Ross, J. Jr., Bers, D. M., et al. (2003). The deltaC isoform of CaMKII is activated in cardiac hypertrophy and induces dilated cardiomyopathy and heart failure. *Circ. Res.* 92, 912–919. doi: 10.1161/01.RES.0000069686.31472.C5

Zhou, Y. Y., Lakatta, E. G., and Xiao, R. P. (1998). Age-associated alterations in calcium current and its modulation in cardiac myocytes. *Drugs Aging* 13, 159–171. doi: 10.2165/00002512-199813020-00007

Zhu, Y., Zhang, C., Chen, B., Chen, R., Guo, A., Hong, J., et al. (2016). Cholesterol is required for maintaining T-tubule integrity and intercellular connections at intercalated discs in cardiomyocytes. *J. Mol. Cell. Cardiol.* 97, 204–212. doi: 10.1016/j.yjmcc.2016.05.013

Zidovetzki, R., and Levitan, I. (2007). Use of cyclodextrins to manipulate plasma membrane cholesterol content: evidence, misconceptions and control strategies. *Biochim. Biophys. Acta* 1768, 1311–1324. doi: 10.1016/j.bbamem.2007.03.026

Zima, A. V., Bovo, E., Bers, D. M., and Blatter, L. A. (2010). Ca^{2+} spark-dependent and -independent sarcoplasmic reticulum Ca(2)+ leak in normal and failing rabbit ventricular myocytes. *J. Physiol.* 588, 4743–4757. doi: 10.1113/jphysiol.2010.197913

Ziman, A. P., Gomez-Viquez, N. L., Bloch, R. J., and Lederer, W. J. (2010). Excitation-contraction coupling changes during postnatal cardiac development. *J. Mol. Cell. Cardiol.* 48, 379–386. doi: 10.1016/j.yjmcc.2009.09.016

Conflict of Interest: The author declares that the research was conducted in the absence of any commercial or financial relationships that could be construed as a potential conflict of interest.

ORIGINAL RESEARCH
published: 25 January 2022
doi: 10.3389/fphys.2021.805956

Magnesium Ions Moderate Calcium-Induced Calcium Release in Cardiac Calcium Release Sites by Binding to Ryanodine Receptor Activation and Inhibition Sites

Bogdan Iaparov, Iuliia Baglaeva, Ivan Zahradník and Alexandra Zahradníková*

Department of Cellular Cardiology, Institute of Experimental Endocrinology, Biomedical Research Center of the Slovak Academy of Sciences, Bratislava, Slovakia

Ryanodine receptor channels at calcium release sites of cardiac myocytes operate on the principle of calcium-induced calcium release. *In vitro* experiments revealed competition of Ca^{2+} and Mg^{2+} in the activation of ryanodine receptors (RyRs) as well as inhibition of RyRs by Mg^{2+}. The impact of RyR modulation by Mg^{2+} on calcium release is not well understood due to the technical limitations of *in situ* experiments. We turned instead to an *in silico* model of a calcium release site (CRS), based on a homotetrameric model of RyR gating with kinetic parameters determined from *in vitro* measurements. We inspected changes in the activity of the CRS model in response to a random opening of one of 20 realistically distributed RyRs, arising from Ca^{2+}/Mg^{2+} interactions at RyR channels. Calcium release events (CREs) were simulated at a range of Mg^{2+}-binding parameters at near-physiological Mg^{2+} and ATP concentrations. Facilitation of Mg^{2+} binding to the RyR activation site inhibited the formation of sparks and slowed down their activation. Impeding Mg-binding to the RyR activation site enhanced spark formation and speeded up their activation. Varying Mg^{2+} binding to the RyR inhibition site also dramatically affected calcium release events. Facilitation of Mg^{2+} binding to the RyR inhibition site reduced the amplitude, relative occurrence, and the time-to-end of sparks, and vice versa. The characteristics of CREs correlated dose-dependently with the effective coupling strength between RyRs, defined as a function of RyR vicinity, single-channel calcium current, and Mg-binding parameters of the RyR channels. These findings postulate the role of Mg^{2+} in calcium release as a negative modulator of the coupling strength among RyRs in a CRS, translating to damping of the positive feedback of the calcium-induced calcium-release mechanism.

Keywords: cardiac myocyte, cardiac dyad, calcium spark, ryanodine receptor, calcium release site

Edited by:
Niall Macquaide,
Glasgow Caledonian University,
United Kingdom

Reviewed by:
Christian Soeller,
University of Exeter, United Kingdom
William E. Louch,
University of Oslo, Norway
Yohannes Castro Shiferaw,
California State University, Northridge,
United States
Wayne Rodney Giles,
University of Calgary, Canada

Correspondence:
Alexandra Zahradníková
alexandra.zahradnikova@savba.sk

Specialty section:
This article was submitted to
Cardiac Electrophysiology,
a section of the journal
Frontiers in Physiology

Received: *31 October 2021*
Accepted: *21 December 2021*
Published: *25 January 2022*

Citation:
Iaparov B, Baglaeva I, Zahradník I and Zahradníková A (2022) Magnesium Ions Moderate Calcium-Induced Calcium Release in Cardiac Calcium Release Sites by Binding to Ryanodine Receptor Activation and Inhibition Sites. Front. Physiol. 12:805956. doi: 10.3389/fphys.2021.805956

INTRODUCTION

Magnesium ions, as the most abundant divalent cations in the cell cytoplasm, take part in many cellular processes including the contraction-relaxation cycle and excitation-contraction coupling of cardiac myocytes. They often act in antagonism to the activating function of calcium. In excitation-contraction coupling, the Mg/Ca antagonism arises from the direct and indirect interactions of

Mg^{2+} with the ryanodine receptor (RyR). Since the cytosolic concentration of free Mg^{2+} is by several orders of magnitude over that of Ca^{2+}, magnesium ions compete effectively with calcium ions for binding to the RyR calcium-activation site despite their relatively low affinity (Rousseau et al., 1986; Xu et al., 1996; Laver et al., 1997; Copello et al., 2002; Zahradnikova et al., 2003). Additionally, the ability to bind polyphosphates makes Mg^{2+} an important regulator of ATP-dependent processes through buffering the free ATP concentration and thus plays indirectly a role in the priming of RyRs by ATP to activation by Ca^{2+} (Xu et al., 1996; Tencerova et al., 2012).

In dyads of cardiac myocytes, the activation of RyR channels causes efflux of Ca^{2+} ions to the cytosol that can be observed as a transient and localized increase of Ca^{2+} concentration, dubbed calcium spark (Cheng and Lederer, 2008). In the absence of external activating stimulus, the activation of RyRs may happen by chance due to the non-zero RyR open probability at the resting cytosolic Ca^{2+} concentration and lead to the production of spontaneous calcium sparks (Cheng and Lederer, 2008; Zahradnikova et al., 2010) as well as of the non-spark (invisible) calcium release flux (Niggli and Shirokova, 2007; Bovo et al., 2011; Shang et al., 2014). Both the sparks and non-sparks are of small amplitude and duration and thus many of them are buried in the background noise. Still, the relationship between the frequency, amplitude, and time course of calcium release events (CREs) and the activity of RyR channels *in situ* has not been determined due to experimental difficulties. Analysis of observable calcium sparks indicated simultaneous activation of many (Bridge et al., 1999; Lukyanenko et al., 2000) or only a few RyRs (Wang et al., 2004; Janicek et al., 2012). These findings are inconsistent with the calcium-induced calcium-release mechanism of cardiac excitation-contraction coupling (Fabiato, 1983; Stern, 1992). The reason is most likely in the complex regulation of RyR activity that depends on many cytosolic factors (Meissner, 1994, 2004). Among these, the Ca/Mg antagonism is likely to play a central role.

The allosteric nature of the interaction between the activation sites of the RyR and the closed-open transition (Zahradnik et al., 2005; Zahradnikova et al., 2010) has been inferred from single-channel data of mutant RyR2 (Li and Chen, 2001) and the calcium dependence of calcium spark frequency (Lukyanenko and Gyorke, 1999). The allosteric mechanism was confirmed by the effect of ligands on the structure of RyR channels (des Georges et al., 2016; Chi et al., 2019). It was found that the conformation of the Ca^{2+} binding site affects the closed - open transition of the pore: the conformation with a low affinity for Ca^{2+} promotes the closed state of the pore, while the conformation with a high affinity for Ca^{2+} promotes the open state of the pore (Dashti et al., 2020).

Mechanisms by which Mg^{2+} affects RyR open probability were revealed by single-channel experiments. Inhibition of RyR activity by Mg^{2+} partially persisted at high cytosolic Ca^{2+} concentration, indicating the presence of a RyR inhibitory site (Laver et al., 1997; Zahradnikova et al., 2003). At the same time, the inhibition could be partially overcome by elevated Ca^{2+} levels, indicating competition between Ca^{2+} and Mg^{2+} binding at the RyR activation site (Laver et al., 1997; Zahradnikova et al., 2003).

The inhibitory effect of Mg^{2+} on ryanodine receptors was observed also in cardiac myocytes as a transient decrease of the frequency of sparks upon an increase in cytosolic free Mg^{2+} concentration (Lukyanenko et al., 2001; Gusev and Niggli, 2008). This process could not be studied in more detail because of rapid changes in the SR calcium load occurring in response to changes in calcium release,

A partial insight into the dynamics of RyR activation *in situ* was provided by two recent models of the calcium release site (CRS) based on RyRs with the same, realistic calcium dependence of the steady-state open probability in the presence of Mg^{2+} but with different kinetic assumptions. Postulating binding of Ca^{2+} ions to the RyR activation site as instantaneous and unbinding of Mg^{2+} from the calcium activation site as slow predicted 2-3 simultaneously open RyR channels at the peak of a spark (Zahradnikova and Zahradnik, 2012). Considering the equilibration between Ca^{2+} and Mg^{2+} on the RyR activation site as instantaneous predicted three types of calcium release events differing in the number of open RyRs (Iaparov et al., 2021): CREs consisting of only a single RyR opening that did not activate nearby RyRs in a CRS (quarks); CREs that involved activation of a small subset of RyRs and simultaneous opening of 2-3 RyRs in a CRS (blip); and CREs that involved sequential activation of all RyRs in the CRS and simultaneous opening of about half of the RyRs in the CRS (sparks). This *in silico* study indicated the role of dynamic Ca^{2+} and Mg^{2+} interaction with RyRs of a calcium release site that can be solved only by a RyR model explicitly incorporating the respective rate constants.

The need for a better understanding of the role of Mg^{2+} in the behavior of cardiac dyads is underlined by the findings that the aberrant behavior of RyRs in diseased myocytes may be in part due to a changed interaction of RyRs with Mg^{2+}. Several central domain RyR mutations causing calcium handling-related catecholaminergic polymorphic ventricular tachycardia (CPVT) showed a decreased inhibition of RyR activity by Mg^{2+} ions (Lehnart et al., 2004; Guo et al., 2020). Aberrant interaction with Mg^{2+} in the skeletal muscle isoform RyR1 due to mutations has been also postulated as an important cause of malignant hyperthermia, the skeletal muscle analog of CPVT (Steele and Duke, 2007). However, it is not known whether the changes in Mg^{2+}-RyR interaction are due to a decreased competition between Mg^{2+} and Ca^{2+} on the calcium activation site, due to a weaker Mg^{2+} interaction with the inhibition site, or both. Moreover, in heart failure of various etiologies, RyR2 hyper-phosphorylation has been observed in parallel with increased RyR open probability, calcium sensitivity, spark frequency, or diastolic calcium release (Marx et al., 2000; Okuda et al., 2018), and these effects were at least in part caused by changes in Mg^{2+} regulation of RyRs (Li et al., 2013).

Cardiac diseases and RyR mutations induce a variety of changes in calcium release. In heart failure (HF), increased non-spark leak, increased spark size, and decreased spark frequency were observed (Kolstad et al., 2018); in atrial fibrillation (AF), increased duration, frequency, and time to peak of sparks were observed (Macquaide et al., 2015). The changes observed at the

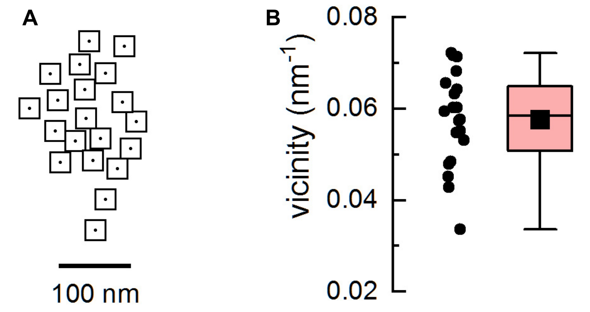

FIGURE 1 | The geometric model of the calcium release site. **(A)** The arrangement of ryanodine receptors (RyRs) in the model CRS. The empty squares with dots represent RyRs with a central ion channel, the gated point source of Ca2+ current. **(B)** The distribution of RyR vicinities in the model CRS. The box diagram shows the 25% and 75% percentile, whiskers show minimum and maximum, the black square depicts the mean, and the horizontal line represents the median.

cellular level might stem not only from changes in RyR gating but also from a changed structure of the calcium release sites that occurred in some (Macquaide et al., 2015; Kolstad et al., 2018) but not all models of cardiac disease (Munro et al., 2021). It is not known whether the changes observed in diseased cardiac myocytes are due to changes in the action of Mg^{2+}, but the RyR inhibitor dantrolene, which requires Mg^{2+} to exert its effect (Choi et al., 2017), was shown to have beneficial effects in AF (Hartmann et al., 2017). Thus, the relationship between the RyR sensitivity to Mg^{2+} and the resulting behavior of CRSs needs to be estimated. However, due to the complex relationship between RyR activity and activity of calcium release sites, this task would require complex and expensive experiments with an uncertain outcome. Instead, *in silico* modeling can provide useful insights by tests of working hypotheses, comparison of data obtained by different approaches and laboratories, and/or execution of virtual experiments that are not experimentally feasible yet.

In this study, we used a model of the calcium release site (**Figure 1**) based on a quantitative description of RyR gating (**Figure 2**), calcium diffusion, and ligand binding to analyze the dependence of simulated calcium release events on parameters relevant to Mg^{2+} binding. The explored parametric space of the CRS model included the description of stochastic RyR gating that allowed binding of Mg^{2+} to the RyR magnesium inhibitory site, Mg^{2+}/Ca^{2+} competitive binding to the RyR calcium-activation site, and allosteric regulation of RyR opening by Ca^{2+} and Mg^{2+} binding to the activation site. The simulated CRS activity in response to a random opening of a single RyR was analyzed for the fractions of generated quarks, blips, and sparks, as well as for the amplitudes and time courses of generated CREs. Inclusion of the kinetics of Ca- and Mg-binding to the RyR gating model allowed us to redefine the role of magnesium ions in the CRS function.

METHODS

Simulations and Analysis

The program for performing simulations was written in C++ and run on a PC with CPU AMD Ryzen 9 3900X (12 cores, 24 threads), 32 GB RAM. Individual calcium release events were

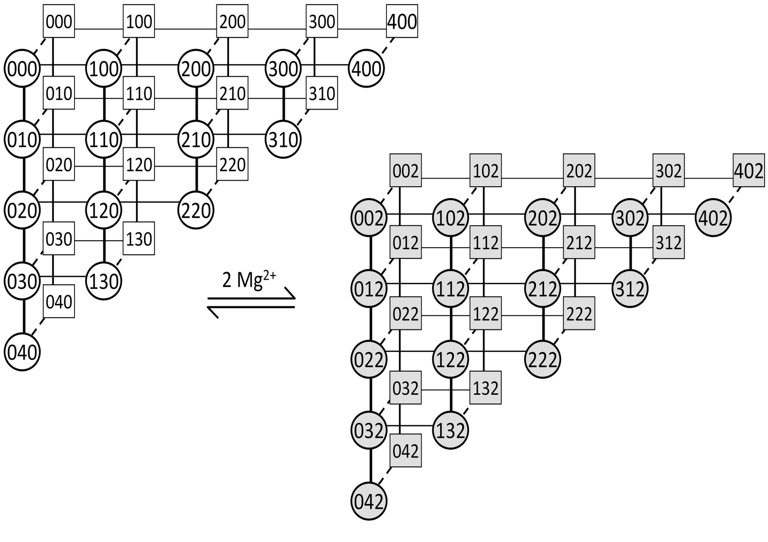

FIGURE 2 | The gating scheme of the MWC-Ca/Mg RyR model. The scheme depicts transitions of four allosterically coupled monomeric activation sites and one common inhibitory site of the RyR channel. The competitive binding of Ca^{2+} and Mg^{2+} ions to RyR activation sites is shown by horizontal (thin lines) and vertical (thick lines) transitions, respectively. The RyR open/close transitions (dashed lines) are independent of ion binding/unbinding. The RyR inhibitory site binds two Mg^{2+} ions simultaneously and switches the RyR channel to a non-conducting state without affecting the activation sites. Squares – closed states; Circles – open states; Gray – inhibited states. The three numerals in the symbols denote (from left to right): the number of Ca^{2+} ions bound to the activation site; the number of Mg^{2+} ions bound to the activation site; and the number of Mg^{2+} ions bound to the inhibition site. All RyR transitions between states are reversible and obey the principle of detailed balance.

simulated in parallel using the OpenMP API[1]. Parallel generation of random numbers was performed using OMPRNG (Bognar, 2013). The program consumed up to 6 GB of RAM during simulations. Cytosolic calcium signals were calculated using CalC (Matveev et al., 2002). Simulated records of RyR activity were analyzed in Python using the libraries NumPy (Harris et al., 2020), pandas (McKinney, 2010), SciPy (Virtanen et al., 2020), scikit-learn (Pedregosa et al., 2011), and lmfit (Newville et al., 2014). Figures were prepared using OriginPRO Ver. 2020b (OriginLab, United States).

Kinetic Parameters of the Ryanodine Receptor Gating Model

Nine of the 14 independent kinetic parameters of the RyR gating model (**Table 1**) were determined by approximating the published RyR single-channel characteristics obtained in bilayer experiments either from steady-state records of RyR activity (open probabilities, mean open times) or from responses of RyR activity to a laser pulse-induced stepwise [Ca^{2+}] increase (activation times). These experiments were performed on RyRs in isolated cardiac microsomal vesicles incorporated into lipid bilayers. RyR single-channel activity was recorded using Cs^{+} or Cs^{2+} ions as charge carriers in the presence of variable concentrations of total ATP (0 – 3 mM), free Mg^{2+} (0 – 1.3 mM), and free Ca^{2+} (0.1 – 100 μM) at the cytosolic side and 1 mM free Ca^{2+} at the luminal side (Zahradnikova et al., 1999, 2003; Tencerova et al., 2012; Cannell et al., 2013). The corresponding kinetic parameters (**Table 1**) were fitted and the standard errors of the fit were estimated using the differential evolution method (Storn and Price, 1997) from lmfit (Newville et al., 2014). The remaining kinetic parameters in **Table 1** were either taken directly from the literature (two parameters), or set according to known estimates (one parameter), or set to zero according to a reasonable guess (two parameters).

Kinetic Equations of the Ryanodine Receptor Gating Model

The RyR gating model was represented by a transition rate matrix **Q** with n states defined as follows:

$$Q_{ij} = \begin{cases} q_{ij}, & i \neq j \\ -\sum_j q_{ij}, & i = j \end{cases}, \tag{1}$$

where q_{ij} is the transition rate between states i and j. The transition rates between RyR states are given in **Supplementary Table 1** as functions of model parameters. The Q-matrix was used to calculate the mean open times and activation times of the model (Colquhoun and Hawkes, 1995). The mean open and closed times, t_O and t_C, were calculated from the multi-exponential distributions of open and closed times (Colquhoun and Hawkes, 1995):

$$t_O = \sum_{i=1}^{n_0} a_i \tau_i, \; t_C = \sum_{j=1}^{n_C} a_j \tau_j, \tag{2}$$

where n_O and n_C are the numbers of open and closed states and a_i, a_j and τ_i, τ_j are the areas and the time constants of individual exponentials. To calculate a_i and τ_i, the Q-matrix was partitioned into blocks:

$$\mathbf{Q} = \begin{bmatrix} \mathbf{Q}_{CC} & \mathbf{Q}_{CO} \\ \mathbf{Q}_{OC} & \mathbf{Q}_{OO} \end{bmatrix}, \tag{3}$$

where C and O correspond to closed and open states, respectively; $\tau_i = 1/\lambda_i$, where λ_i is the i^{th} eigenvalue of $-\boldsymbol{Q}_{OO}$; and $a_i = -\tau_i \Phi_0 \boldsymbol{A}_i \boldsymbol{Q}_{OO} \boldsymbol{u}_O$, where Φ_0 is the initial vector, $\boldsymbol{A}_i$ is the spectral matrix corresponding to eigenvalue λ_i, $\boldsymbol{u}_O$ is a column vector of ones with length equal to the number of open states. The values of a_j and τ_j were calculated analogously using the submatrix $\boldsymbol{Q}_{CC}$.

The time courses of open probability P_O in response to a step change of [Ca^{2+}] from the basal concentration $[\mathrm{Ca}^{2+}]_b$ to the end concentration $[\mathrm{Ca}^{2+}]_e$ were calculated from the system of Kolmogorov equations:

$$\frac{d\boldsymbol{P}(t)}{dt} = \mathbf{P}(t)\,\mathbf{Q}\left(\left[\mathrm{Ca}^{2+}\right]_e\right), \tag{4}$$

where $\boldsymbol{P}(t)$ is the vector of probabilities of individual RyR states, as the sum of the time-dependent probabilities of all open states. The initial vector $\mathbf{P}(0)$ was calculated from the Q-matrix at $[\mathrm{Ca}^{2+}]_b$ as the solution of the system of equations (Colquhoun and Hawkes, 1995):

$$\boldsymbol{P}(0)\,\boldsymbol{Q}\left(\left[\mathrm{Ca}^{2+}\right]_b\right) = \mathbf{0}, \tag{5}$$

where **0** is a zero-vector with a length equal to the number of states. The activation time was defined as the time when open probability reaches 63.2%, i.e., (1– 1/e)-th part of the interval between open probabilities at $[\mathrm{Ca}^{2+}]_b$ and $[\mathrm{Ca}^{2+}]_e$.

Calcium Buffers, Diffusion, Ryanodine Receptor State Transitions, and Fluorescence

The description of Ca^{2+} diffusion in the CRS assumed open RyRs as a source of constant single-channel calcium current i_{Ca}, flowing into calcium buffers that do not saturate (Naraghi and Neher, 1997). It also assumed instantaneous formation of free [Ca^{2+}] gradients upon opening or closing RyR channels. The components and parameters of the calcium buffers in the CRS model (**Table 2**) correspond to published data and should represent the minimal requirements for proper RyR function under near-physiological conditions (**Table 1**; section "Kinetic Parameters of the Ryanodine Receptor Gating Model"). Concentrations of divalent ions binding to RyRs were calculated using constant 1 mM free [Mg^{2+}] (**Table 2**), and basal 100 nM free [Ca^{2+}] that was changed by calcium release. The released calcium equilibrated with Mg-unbound ATP, calmodulin, and the fluorescent dye Fluo-4 (**Table 2**). New Ca^{2+} concentration profiles were recalculated for each change in the RyR open state (see below).

The above assumptions allowed the use of the Naraghi-Neher approximation for calculations of free calcium concentrations during Ca flux in the cytosolic half-space delimited by the plane of the CRS (Naraghi and Neher, 1997) and the event-based Gillespie

---

[1] https://www.openmp.org

TABLE 1 | Parameters of the ryanodine receptor (RyR) model and their reference values.

Parameter	Value	Unit	References
K_{ACa}	4.18 ± 0.13	μM	k_{AoffCa}/k_{AonCa}
k_{AonCa}	0.71	$\mu M^{-1}\ ms^{-1}$	Zahradnikova et al., 1999
k_{AoffCa}	2.97 ± 0.09	ms^{-1}	Fitted, this study.
K_{AMg}	92.3 ± 3.5	μM	k_{AoffMg}/k_{AonMg}
k_{AonMg}	0.0071	$\mu M^{-1}\ ms^{-1}$	0.01 × k_{AonCa}, Eigen and Wilkins, 1965
k_{AoffMg}	0.66 ± 0.025	ms^{-1}	Fitted, this study.
f_{Ca}	0.0058 ± 0.00015		Fitted, this study.
f_{Mg}	3.25 ± 0.052		Fitted, this study.
λ_{onCa}	0		Postulated, this study
λ_{onMg}	0		Postulated, this study
K_{O00}	10800		Zahradnik et al., 2005
k_{CO}	0.0011 ± 2.09E-05	ms^{-1}	Fitted, this study.
k_{OC}	11.9 ± 0.23	ms^{-1}	Fitted, this study.
λ_{CO}	0.671 ± 0.0015		Fitted, this study.
K_{IMg}	546 ± 54	μM	$(k_{IoffMg}/k_{IonMg})^{1/2}$
k_{IonMg}	5.9E-07 ± 2.6E-07	$\mu M^{-2}\ ms^{-1}$	Fitted, this study.
k_{IoffMg}	0.176 ± 0.084	ms^{-1}	Fitted, this study.

K_{ACa} – k_{AoffCa}/k_{AonCa}; Ca^{2+} dissociation constant of the RyR activation site in the closed state C00.
k_{AonCa} – Ca^{2+} binding rate constant of the RyR activation site in the closed state C00.
k_{AoffCa} – Ca^{2+} unbinding rate constant of the RyR activation site in the closed state C00.
K_{AMg} – k_{AoffMg}/k_{AonMg}; Mg^{2+} dissociation constant of the RyR activation site in the closed state C00.
k_{AonMg} – Mg^{2+} binding rate constant of the RyR activation site in the closed state C00.
k_{AoffMg} – Mg^{2+} unbinding rate constant of the RyR activation site in the closed state C00.
f_{Ca} – allosteric factor coupling Ca^{2+} binding to channel opening.
f_{Mg} – allosteric factor coupling Mg^{2+} binding to channel opening.
λ_{onCa} – partition contribution due to allosteric coupling on k_{AonCa}.
λ_{onMg} – partition contribution due to allosteric coupling on k_{AonMg}.
K_{O00} – k_{CO}/k_{OC}; dissociation constant of the ion-free open state O00.
k_{CO} – rate constant of the C00 → O00 transition.
k_{OC} – rate constant of the O00 → C00 transition.
λ_{CO} – partition contribution due to allosteric coupling on k_{CO}.
K_{IMg} – $(k_{IoffMg}/k_{IonMg})^{1/2}$; dissociation constant of Mg^{2+} ions at the RyR inhibitory site.
k_{IonMg} – Mg^{2+} binding rate constant of the RyR inhibition site.
k_{IoffMg} – Mg^{2+} unbinding rate constant of the RyR inhibition site.
The value of k_{AonMg} was set to 0.01 × k_{AonCa}, based on the generally accepted theory according to which the rate-limiting factor in ion binding to a ligand is the exchange rate of a water molecule in the hydration complex of an ion. The water exchange rate of Mg^{2+} is two orders of magnitude slower than that of the Ca^{2+} ion (Eigen and Wilkins, 1965).
*Values of λ_{onCa} and λ_{onMg} were set to zero since Ca^{2+} binding to the ion-free closed state C00 is diffusion-limited (Zahradnikova et al., 1999). This means that the binding of Ca^{2+} and Mg^{2+} at the activation site of one monomer does not affect the on-rate constants but only the off-rate constants of these ligands binding to other monomers (see **Supplementary Table 1**).*

algorithm (Gillespie, 1977) for simulations. Briefly, each CRE was started by an opening of the selected RyR. The starting open state for the selected RyR was chosen from all possible open states based on their conditional probabilities $P(i \mid \text{channel is open})$ at basal concentrations of free Ca^{2+} (100 nM) and free Mg^{2+} (1 mM), i.e., probabilities of the states given that the channel is open:

$$P\left(i|\text{channel is open}\right) = \frac{P_i S_i}{\sum_{i=1}^{n} P_i S_i}, \tag{6}$$

where $S_i = 1$ if the state i corresponds to an open state and 0 otherwise. The initial state of the closed channels was chosen based on the calculated probabilities from Eq. 6 but using $(1 - S_i)$ instead of S_i. Calcium influx upon the first channel opening changed the calcium distribution in the CRS and, correspondingly, the Q-matrix of individual RyRs. The index of the RyR that would change its state was sampled from the distribution of probabilities of state transitions of individual RyRs, which was for the j^{th} RyR equal to the ratio of its transition rate of leaving the microstate $M(j)$, equal to $-Q_{M(j)M(j)}$, to the sum of leaving rates over all the RyRs, $-\sum_{j=1}^{n} Q_{M(j)M(j)}$. The time of the next transition was sampled from the exponential distribution of waiting times with the rate $-\sum_{j=1}^{n} Q_{M(j)M(j)}$. If the transition changed the macrostate of the channel, i.e., opened a closed channel or closed an open channel, the transition would lead to a new distribution of $[Ca^{2+}]$ in the CRS and a new corresponding set of RyR transition rate constants. The algorithm was repeated until the end of the simulation. From each RyR in the CRS, a dataset of 500 CREs was collected at each set of tested parameters.

The fluorescence signals of CREs were calculated from the time course of calcium release flux $(N_O(t) \cdot i_{Ca})$ as if emanating symmetrically from a virtual spherical source of 100 nm radius and binding to cytosolic buffers, including the calcium selective fluorophore Fluo-4 and the non-diffusible buffers troponin, sarcolemma, and SR membrane (**Table 2**), in a sphere of 10 μm radius. The intensity of fluorescence is directly proportional to the concentration of calcium-bound Fluo-4 $[Ca^{2+}\text{-Fluo4}]$, thus the change of fluorescence was reported as $\Delta F/F_0$. The calculated spatial profile of $[Ca^{2+}\text{-Fluo4}]$ was convolved with a Gaussian point spread function with FWHM = 400, 400, and 800 nm for the X, Y, and Z coordinate, respectively, to approximate the image observed by fluorescent microscopy (Smith et al., 1998; Iaparov et al., 2021).

Parameter Space of the Simulations

To study how changes in Mg-RyR interactions affect the characteristics of CREs, the parameters of Mg^{2+} binding and unbinding were varied in a wide range relative to the reference values (**Table 1**). All values of Mg-binding parameters used in simulations are in **Supplementary Table 2**. The rate constants of the activation site were varied in the range [0.000596, 0.0271] $\mu M^{-1} ms^{-1}$ (k_{AonMg}, 9 unique values) and [0.055, 2.5] ms^{-1} (k_{AoffMg}, 9 unique values), resulting in 81 combinations that had K_{AMg} in the range [2.03, 4194] μM. The allosteric coefficient of Mg^{2+} at the RyR activation site was varied from 0.5 to 500, i.e., from 0.15× to 154× the reference value (**Table 1**) in 17 steps. The rate constants of the inhibition site were varied in the range between $[1.84, 16.75] \cdot 10^{-7}$ $\mu M^{-2} ms^{-1}$ (k_{IonMg}, 9 unique values) and between [0.055, 0.5] ms^{-1} (k_{IoffMg}, 9 unique values),

TABLE 2 | Calcium buffers used for calculation of Ca^{2+} concentrations and diffusion.

Components of the Ca buffer	$k_{on,Ca}$ (μM^{-1} ms^{-1})	$k_{off,Ca}$ (ms^{-1})	Concentration (μM)	D (μm^{-2} ms^{-1})	References
ATP (apparent total)	0.225	45	400*	0.14	Valent et al., 2007
Fluo-4	0.1	0.11	50	0.042	Hake et al., 2012
Calmodulin	0.023	0.238	24	0.025	
Troponin (cytosol only)	0.039	0.02	70	0	
Sarcolemma (cytosol only)	0.115	1	1124	0	Zahradnikova et al., 2007
SR membrane (cytosol only)	0.115	0.1	47	0	

Basal free [Ca^{2+}] was set to 100 nM.

**The apparent total ATP represents the ATP concentration used to calculate free Ca^{2+} during calcium release. This value was calculated for a total ATP of 5 mM, total Mg of 5.6 mM, free [Mg^{2+}] of 1 mM, and K$_{d,MgATP}$ of 87 μM (Valent et al., 2007). We used a constant apparent total ATP to simplify calculations of [Ca^{2+}] during calcium release, since the free Mg concentration stayed constant as well, and the released Ca^{2+} ions equilibrated effectively only with the apparent total ATP. The "cytosol only" components were used for calculation of the fluorescence signal in the cell cytosol volume.*

resulting in 81 combinations that had K_{IMg} in the range [181.23, 1647.56] μM.

Calcium Release Site and Calcium Release Events

Calcium release sites containing 20 RyRs with the geometric arrangement corresponding to a typical RyR cluster in cardiac dyads (**Figure 1**) were generated according to Jayasinghe et al. (2018). In brief, the first channel was placed on the coordinates (0, 0). The placement of further channels was defined by the distance from the preceding channel and the direction angle. The distance was sampled from a normal distribution with a mean of 40.1 nm and a standard deviation of 7.4 nm with a cutoff at 29 nm. The angle was sampled from the uniform distribution (0, 2π). To avoid overlap, a distance between RyRs of less than 29 nm was not allowed.

For quantitative characterization of the geometrical arrangement of RyRs, we used the concept of vicinity (Iaparov et al., 2021), an extension of the concept of adjacency (Walker et al., 2015) to arbitrary RyR-RyR distances. The RyR vicinities v_i and the group vicinity v were determined according to Iaparov et al. (2021) as:

$$v_i = \frac{\sum_{j,j\neq i} v_{ij}}{N_{RyR}-1} = \frac{\sqrt{N_{RyR}}\sum_{j,j\neq i} C_{ij}}{N_{RyR}-1} \text{ and } v = \frac{\sum_i v_i}{N_{RyR}}, \qquad (7)$$

where N_{RyR} is the number of RyRs in the CRS, and C_{ij} is the reciprocal value of the distance between the i^{th} and the j^{th} RyR (Iaparov et al., 2021). Out of 100 generated release sites, the one that showed the highest range of RyR vicinities was selected for simulations (**Figure 1**). The group vicinity of the CRS used in this study was v = 0.058 and the RyR vicinities spanned the range 0.034 - 0.072.

The simulation of a calcium release event was started by the opening of one of the RyRs and proceeded for 200 ms. Individual records of CREs were characterized by the number of RyRs open at the peak (N_O^{peak}), the time-to-peak (TTP), the time-to-end (TTE) of RyR activity, and the molar amount of Ca^{2+} released during the event (n_{Ca}). Calcium release events were classified as quarks, blips, and sparks as previously described (Iaparov et al., 2021). Events consisting of one channel opening were defined as quarks. Blips and sparks were discerned by their N_O^{peak} using the nadir of the amplitude histogram of CREs obtained with the reference set of CRS parameters. The nadir value for the reference model, determined by using the method of K-Means (MacQueen, 1967) implemented in scikit-learn (Pedregosa et al., 2011), was 6.2, thus CREs with 6 or fewer simultaneously open RyRs were classified as blips, and CREs with 7 and more simultaneously open RyRs were classified as sparks. The data were averaged for each dataset of 500 CREs that occurred in response to activation of one RyR under identical conditions.

Coupling Strength

To understand the effect of magnesium more deeply, the quantitative relationship between the characteristics of CREs and determinants of CRSs, such as RyR placement, calcium current, and Mg^{2+} binding would be instrumental. Previously (Iaparov et al., 2021), we have introduced the coupling strength φ as a descriptor of CREs that weights the vicinity of RyRs and the calcium current through individual RyRs:

$$\varphi_i = v_i (i_{Ca})^{\alpha}, \qquad (8)$$

where the index i enumerates individual RyRs of the CRS and the exponent α weights the contribution of i_{Ca} relative to vicinity v_i. It should be noted that v_i values are calculated from RyR coordinates in the CRS (section "Calcium Release Site and Calcium Release Events"), i_{Ca} is defined in the model, so the respective coupling strength can be directly evaluated for each CRS model if the weight factor α can be found. As shown in Iaparov et al. (2021), the relation between either v_i or i_{Ca} and the measured characteristics of the corresponding simulated calcium release events was suboptimal, which could be misinterpreted as if the CREs were not fully controlled by the determinants of CRS, at odds with current understanding of local calcium release. Optimization of the weight factor allowed to find coupling strength values that correlated with the measured CRE characteristics according to Hill function for the whole parameter range of inspected CRS determinants (Iaparov et al., 2021).

To account for the effect of Mg-RyR binding parameters on the coupling strength among RyRs, we included terms for allosteric coupling ($1/f_{Mg}$), activation (k_{AoffMg}, k_{AonMg}), and inhibition (k_{IoffMg}, k_{IonMg}) and defined the effective coupling strength as

$$\varphi_i^{effF} = \nu_i (i_{Ca})^{\alpha} \left(\frac{1}{f_{Mg}}\right)^{\beta}, \tag{9a}$$

$$\varphi_i^{effA} = \nu_i (i_{Ca})^{\alpha} \frac{\left(k_{AoffMg}\right)^{\gamma_{off}}}{\left(k_{AonMg}\right)^{\gamma_{on}}}, \tag{9b}$$

$$\varphi_i^{effI} = \nu_i (i_{Ca})^{\alpha} \frac{\left(k_{IoffMg}\right)^{\delta_{off}}}{\left(k_{IonMg}\right)^{\delta_{on}}}, \tag{9c}$$

where the exponents β, γ_{off}, γ_{on}, δ_{off}, and δ_{on} are the weight factors that determine the contribution of the respective RyR kinetic parameters to CRS activity relative to the contribution of RyR vicinity, in analogy to the weight factor α of i_{Ca}. According to the above formulae, the effective coupling strength between RyRs increases with increasing parameters that promote activation of other RyRs by a RyR opening, i.e., the vicinity, calcium current, and off-rate constants of Mg^{2+} binding. The effective coupling strength decreases with increasing parameters that hinder activation of other RyRs by a RyR opening, i.e., the allosteric factor and on-rate constants of Mg^{2+} binding. However, since the reference values of $1/f_{Mg}$, k_{AoffMg}/k_{AonMg}, and k_{IoffMg}/k_{IonMg} differed from each other, the values of coupling strengths φ_i^{effF}, φ_i^{effA}, and φ_i^{effI} differed numerically from each other as well despite describing the same RyR model. To aid the comparison between the effect of Mg^{2+}-binding parameters at the activation and the inhibition site, we normalized Mg^{2+}-dependent parameters to the respective parameters of the reference RyR model (reported in **Table 1**), resulting in the effective coupling strength in the form:

$$\varphi_i^{effF} = \nu_i (i_{Ca})^{\alpha} \left(\frac{1}{f_{Mg}^{rel}}\right)^{\beta}, \tag{10a}$$

$$\varphi_i^{effA} = \nu_i (i_{Ca})^{\alpha} \frac{\left(k_{AoffMg}^{rel}\right)^{\gamma_{off}}}{\left(k_{AonMg}^{rel}\right)^{\gamma_{on}}}, \tag{10b}$$

$$\varphi_i^{effI} = \nu_i (i_{Ca})^{\alpha} \frac{\left(k_{IoffMg}^{rel}\right)^{\delta_{off}}}{\left(k_{IonMg}^{rel}\right)^{\delta_{on}}}, \tag{10c}$$

where the superscript *rel* stays for a value relative to the reference value, and the remaining parameters have been already defined.

Determination of Weight Factors of the Effective Coupling Strength

Finding the effective coupling strength function (Eqs. 8-10) requires evaluation of the weight factors of individual components, namely, the RyR vicinity, single-channel current, and kinetic parameters of the activation and inhibition processes. The values of weight factors can be found by optimizing the effective coupling strength function to the distribution of measured CRE characteristics ($\bar{N}_O^{peak}$, F_q, and F_s). Iaparov et al. (2021) determined the values of weight factors by using the Hill function to optimize the relationships between coupling strength (Eq. 8) on the one hand, and the relative amplitudes of CREs (A_{rel}) and frequency of quarks and sparks (F_q and F_s) on the other hand by a proper weight factor. In the present case, however, it would not be appropriate to optimize the functional relationships between the effective coupling strength and CRE characteristics N_O^{peak}, F_q, and F_s using the Hill function, since the Mg-binding parameters do not characterize the state of the CRS but kinetic processes in the RyR molecule. Defining an *a priori* relational function could lead to a mutual dependence of the fitted parameters and a potential bias in weight factor estimates. To avoid this, we approached this problem using information theory as follows:

For a random variable (X) equal to the effective coupling strength, there is a dependent variable (Y) representing the CRE characteristics. The information content of a random variable X is quantified by its entropy $H(X)$ (Shannon, 1948) that is calculated based on the probability density function *P(X)* of the variable. For a discrete variable,

$$H(X) = -\sum_{i=1}^{n} P(x_i) \cdot \log P(x_i), \tag{11}$$

where n is the number of possible values of X. The entropy $H(X)$ defines the uncertainty of the random variable. A large value of H indicates a large number of states with low probabilities and the measurement of such a variable provides a large amount of information, while $H = 0$ means a deterministic outcome and the measurement of such a variable will not provide any information because its value is exactly known.

We have calculated the mutual information between the effective coupling strength and the CRE characteristics. Mutual information (MI) between random variables X and Y, $I(X, Y)$ is the amount of information obtained when X is known and vice versa (Shannon, 1948), defined through entropies:

$$I(X, Y) = H(X) + H(Y) - H(X, Y), \tag{12}$$

where $H(X, Y) = -\sum_{i=1}^{n}\sum_{j=1}^{m} P(x_i, y_i) \cdot \log P(x_i, y_i)$ is called the joint entropy. Mutual information is a non-negative number being zero when X and Y are independent variables. This definition indicates that when the maximal MI between the effective coupling strength and the CRE characteristics is reached, the effective coupling strength provides the most certain prediction for CRE characteristics.

We maximized the average MI estimated between effective coupling strengths and CRE characteristics $\bar{N}_O^{peak}$, F_q, and F_s (9 in total). MI was calculated using a non-parametric method based on entropy estimation from k-nearest neighbor distances (Kraskov et al., 2004) implemented in scikit-learn (Pedregosa et al., 2011). Average MI was maximized using the differential evolution implemented in scipy (Virtanen et al., 2020). The estimated maximal average MI was 2.6 bits. The parameters with their estimated standard deviations are summarized in **Table 3** of Results. The standard deviations were calculated using the bootstrap method from 100 bootstrap samples because of the

TABLE 3 | Parameters and weight factors of the effective coupling strength.

Parameter	Weight factor		Fold change of φ_i^{eff}	
	Name	**Value**	**Reference value × 0.5**	**Reference value × 2**
i_{Ca}	α	0.934 ± 0.016	0.52	1.91
f_{Mg}	β	0.146 ± 0.004	1.11	0.9
k_{Aoff}	γ_{off}	1.41 ± 0.01	0.38	2.66
k_{Aon}	γ_{on}	1.014 ± 0.0002	2.02	0.5
k_{Ioff}	δ_{off}	0.663 ± 0.014	0.63	1.58
k_{Ion}	δ_{on}	1.444 ± 0.022	2.72	0.37

Data are given as the mean and SE of the fit.

high computational complexity of the MI estimation. For each bootstrap sample, new weights were found using the Nelder-Mead method implemented in scipy (Virtanen et al., 2020).

Frequency of Calcium Release Events

The frequency of all spontaneous RyR openings in a group of N_{RyR} channels was calculated according to Kunze et al. (1985):

$$f = N_{RyR}/((t_O)_b + (t_C)_b), \tag{13}$$

where $(t_O)_b$ and $(t_C)_b$ are the values of the RyR open and closed time at basal [Ca^{2+}].

RESULTS

To study the role of Mg^{2+} ions in the activation of calcium release we turned to *in silico* experiments to overcome the complexities and uncertainties related to real experiments. We used the model of a calcium release site (CRS) based on a quantitative description of RyR gating that accounted for Ca^{2+} and Mg^{2+} binding kinetics, RyR distribution in a typical CRS, and the cytosolic Ca^{2+} buffer near RyRs and around the CRS. The reference parameter set of RyR gating was obtained by fitting the available experimental data of RyR open probability, open time, and activation time at a range of cytosolic concentrations of free Ca^{2+} and free Mg^{2+} that encompassed the physiological values (section "Kinetic Parameters of the Ryanodine Receptor Gating Model"). Then we analyzed the characteristics of simulated calcium release events generated at the physiological free [Mg^{2+}] concentration (1 mM) with the reference RyR model (section "Characteristics of Simulated Calcium Release Events for the Calcium Release Site With the Monod-Wyman-Changeux-Ca/Mg Ryanodine Receptor Model"). The consequences of variation in parameters related to Mg^{2+} binding on the activity of RyR channels and the ensuing CREs were determined in sections "Effect of Mg-Binding Parameters on Calcium Dependence of Ryanodine Receptor Activation" and "Mg-Binding Parameters Affect Calcium Release Events." Finally, we solved the relationship between RyR activity and the characteristics of CREs on the grounds of the effective coupling strength that, in addition to RyR vicinity and calcium current, accounts also for magnesium binding to RyR, and determined the effect of Mg-binding parameters on the characteristics of CREs (sections "Effective Coupling Strength Tallies Ryanodine Receptor Vicinity, Calcium Current, and Mg-Binding Parameters" and "The Frequency of Spontaneous Calcium Release Events Depends on the Ryanodine Receptor Closed Time of at Basal [Ca2+]").

Construction and Validation of the Ryanodine Receptor Gating Model

We developed a new model of RyR gating based on RyR single-channel studies of Ca^{2+} activation and Mg^{2+} inhibition (Zahradnikova et al., 1999, 2003; Tencerova et al., 2012; Cannell et al., 2013) and on the allosteric homotetrameric gating RyR model (Zahradnik et al., 2005; Zahradnikova et al., 2010). To reduce computational costs we omitted the long-lived L- and I-mode states of the original aHTG RyR gating model since their frequency of occurrence was much less than once per 200 ms (the duration of simulations). The gating scheme of the resulting Monod-Wyman-Changeux type, Ca^{2+}- and Mg^{2+}-binding (MWC-Ca/Mg) RyR model has 60 states (**Figure 2**). The kinetics was characterized by on/off rate constants of competitive binding of Ca^{2+} and Mg^{2+} to the RyR activation site allosterically coupled to channel opening, and on/off rate constants of Mg^{2+} binding to the RyR inhibition site that renders the channel non-conductive upon Mg^{2+} binding (see **Supplementary Data**).

The steady-state open probability of the MWC-Ca/Mg RyR gating model was described by Eq. 14 derived in the **Supplementary Data**:

$$P_O\left(\left[Ca^{2+}\right],\left[Mg^{2+}\right]\right)=\frac{(K_{IMg})^2}{(K_{IMg})^2+\left[Mg^{2+}\right]^2}\cdot$$

$$\frac{\left(\left[Ca^{2+}\right]+K_{ACa}\cdot f_{Ca}\left(1+\frac{\left[Mg^{2+}\right]}{K_{AMg}\cdot f_{Mg}}\right)\right)^4}{\left(\left[Ca^{2+}\right]+K_{ACa}\cdot f_{Ca}\left(1+\frac{\left[Mg^{2+}\right]}{K_{AMg}\cdot f_{Mg}}\right)\right)^4+K_{O00}\cdot(f_{Ca})^4\left(Ca+K_{ACa}\left(1+\frac{\left[Mg^{2+}\right]}{K_{AMg}}\right)\right)^4}. \tag{14}$$

The meaning of the model parameters in Eq. 14 is provided in **Table 1** together with their values. The values were estimated by optimizing the global approximation of the experimental data shown in **Figure 3** with the respective functions (Eqs. 2, 4, and 14). The optimized model predicts the Ca^{2+}-dependences of the open probability, the open time, and the rate of activation by Ca^{2+} at different Mg^{2+} concentrations in a very good agreement with the available experimental data (**Figure 3**). We will refer to this set of optimized parameters as the reference RyR model or parameter set. Note that for the reference RyR model and the free [Mg^{2+}] of 1 mM (red lines in **Figure 3**), the maximum steady-state open probability $P_O{}^{max}$ was 0.23 and the open time $t_O{}^{max}$ was 1.66 ms.

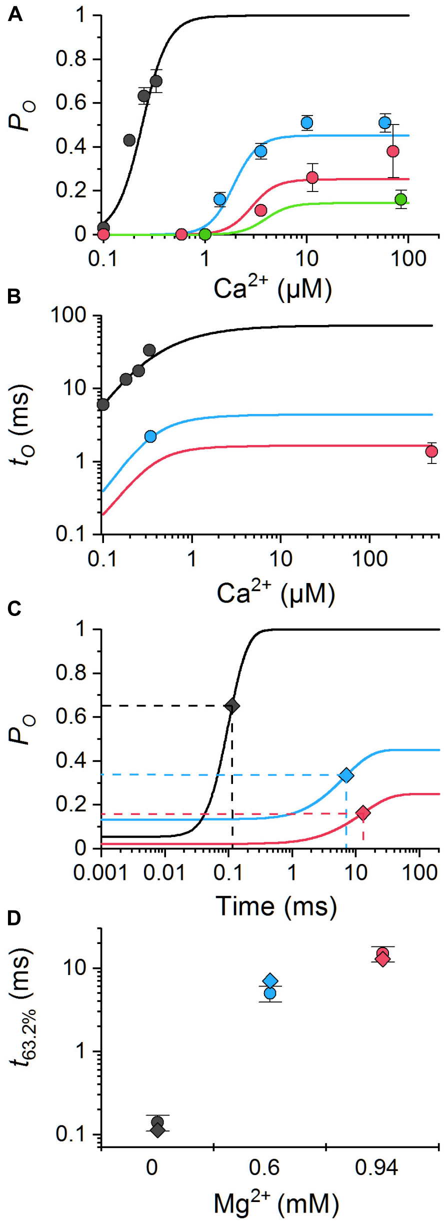

FIGURE 3 | Comparison of the MWC-Ca/Mg RyR model predictions with experimental data. The model predictions (lines) were calculated using Eqs. 14 **(A)**, 2 **(B)**, and 4 **(C)** and the reference set of parameter values (**Table 1**) for the same ion conditions as the experimental data (points). **(A)** The calcium dependence of open probability for 0 mM Mg^{2+} and 0.5 mM total ATP (Tencerova et al., 2012) (black), and for 0.6, 0.94, and 1.33 mM free Mg^{2+} (blue, red, and green, respectively) and 3 mM total ATP (Zahradnikova et al., 2003). **(B)** The calcium dependence of mean open time for 0 mM total Mg^{2+} and 0.5 mM ATP (Tencerova et al., 2012) (black), for 0.6 mM free Mg^{2+}, 3 mM total ATP (Zahradnikova et al., 2003) (blue), and for 1 mM free Mg^{2+} and 2 mM total ATP (Cannell et al., 2013) (red). **(C)** The simulated time course of RyR responses to a step Ca^{2+} increase from 100 nM to 20 μM in the absence of Mg^{2+} (black), and from 1.5 to 10 μM Ca^{2+} in the presence of 0.6 and 0.94 mM free Mg^{2+} and 3 mM total ATP (blue and red lines, respectively). The 63.2% activation time is indicated by diamonds. **(D)** Comparison of the calculated (diamonds) and experimental (dots with error bars) 63.2% activation times obtained under conditions shown in panel **(C)**; black - (Zahradnikova et al., 1999), red and blue - (Zahradnikova et al., 2003).

Characteristics of Simulated Calcium Release Events for the Calcium Release Site With the Monod-Wyman-Changeux-Ca/Mg Ryanodine Receptor Model

In the CRE simulations, we used the approximation of constant single-channel calcium current during RyR openings, which allowed us to analyze the effects of Mg^{2+} binding kinetics on the activation of calcium release without the multifaceted effects brought about by the inclusion of SR depletion in models of the CRS.

Calcium release events simulated with the reference parameter set of the MWC-Ca/Mg RyR model (**Figures 4A-C**) consisted of three event types as observed previously for CRSs constructed with the two-state Ca/Mg RyR model of Iaparov et al. (2021). Although the amplitude histograms of both models differed substantially in the relative fractions of CRE types, the nadir of histograms at ∼6 and the most frequent N_O^{peak} of sparks at ∼10 RyRs were the same in both models. The fraction of events with $N_O^{peak} \leq 6$ (quarks and blips) was much larger in the present model.

As shown in **Figure 4D**, the fraction of quarks decreased with the i_{Ca} value (93% at 0.15 pA and 72% at 0.6 pA). In comparison with CRSs based on the two-state RyR model of Iaparov et al. (2021), the decrease was much weaker. The fraction of blips increased with i_{Ca} (7% at 0.15 pA and 15% at 0.6 pA) on account of quarks, while in the two-state model it decreased with i_{Ca} since in the two-state model the fraction of sparks increased more steeply with i_{Ca} than in the MWC-Ca/Mg RyR model (0.06% of sparks at 0.15 pA and 13% of sparks at 0.6 pA in the present model). The time to peak of blips and sparks was curtailed at higher i_{Ca}, similar to the two-state model. However, the time to peak of sparks decreased with i_{Ca} in the present model while it increased in the two-state model. The time to end of quarks and blips shortened with i_{Ca}, as it did in the two-state model. In contrast to the two-state model, the time to end of sparks did not depend significantly on i_{Ca}. The amount of calcium released by CREs increased proportionally with i_{Ca}, less steeply than in the two-state model.

Effect of Mg-Binding Parameters on Calcium Dependence of Ryanodine Receptor Activation

Before characterization of calcium release events in the CRS, we inspected the single-channel RyR behavior of the MWC-Ca/Mg RyR model for a range of Mg-binding parameters at the physiological cytosolic free Mg^{2+} concentration of 1 mM. The calculated dependences of RyR characteristics on [Ca^{2+}] for the allosteric coefficient f_{Mg} at the RyR activation site and the on/off rate constants of Mg^{2+} at both the activation and the inhibition sites are summarized in **Figure 5**. These data confirm the validity of the RyR model and will be further used to analyze how the effect of a parameter change on RyR single-channel kinetics translates to its effect on calcium release events.

Mg-Binding Parameters of the Ryanodine Receptors Activation Site

As shown in **Figure 5A**, changes that facilitated Mg^{2+} binding to the RyR activation site, that is, a decrease of K_{AMg} by either an increase of k_{AonMg} (purple), or a decrease of k_{AoffMg} (light green), led to decreased calcium sensitivity (right shift) of the RyR open probability, open time, and closed time. At the basal calcium concentration, these changes decreased P_O and t_O but increased t_C. Vice versa, changes that impeded Mg^{2+} binding [a lower k_{AonMg} (pink) or a higher k_{AoffMg} (dark green)] had the opposite effect. A change of K_{AMg} led to a change of the apparent K_{Ca} in inverse proportion. Changing both on- and off-rate constants by the same fraction, that is, without changing K_{AMg} (light and dark blue), did not affect the calcium dependence of P_O, $t_{O,}$ and t_C.

Variation of the allosteric coefficient f_{Mg} relative to the reference value had a non-linear effect on the calcium dependence of RyR characteristics (orange and red; **Figure 5A**). It affected RyR open probability and closed time only at sub-micromolar $[Ca^{2+}]$ range (well below its apparent K_{Ca} of 3.02 μM at 1 mM Mg^{2+}), while it shifted the calcium dependence of open time in this $[Ca^{2+}]$ range but had no effect at low and high $[Ca^{2+}]$ range. Notably, at the lowest calcium concentration, a larger f_{Mg} decreased P_O and substantially increased t_C, while a smaller f_{Mg} increased P_O and decreased t_C. Variation of f_{Mg} exerted no effect on the maximal P_O, t_O, or minimal t_C, in agreement with Eqs. 2 and 14.

The rate of RyR activation by a step change of $[Ca^{2+}]$ was speeded up the most by an increased rate constant of Mg^{2+} unbinding from the RyR activation site, k_{AoffMg} (dark green), somewhat less by decreasing k_{AonMg} (pink), and even less when both rate constants were increased in proportion (dark blue). The RyR activation rate was slowed down the most by decreased k_{AoffMg} (light green) or increased k_{AonMg} (purple), but less when both on- and off-rate constants of Mg^{2+} binding decreased (light blue). Changes of f_{Mg} had negligible effects on the rate of RyR activation.

In other words, the changes of Mg-binding at the RyR activation site modify the calcium sensitivity and kinetics of RyR activation but do not influence the maximum mean open probability, the maximum mean open time, or the minimum closed time.

Mg-Binding Parameters of the Ryanodine Receptors Inhibition Site

By definition, changes of the on- and off-rate constants for Mg^{2+} binding at the RyR inhibition site do not affect the calcium sensitivity of RyR open probability (3.02 μM at 1 mM $[Mg^{2+}]$), but they had a profound effect on the maximum open probability (at 1 mM $[Mg^{2+}]$; **Figure 5B**). Increasing k_{IonMg} (purple) or decreasing k_{IoffMg} (light green) decreased P_O, while increasing k_{IoffMg} (dark green) or decreasing k_{IonMg} (pink) increased P_O. In effect, a change of K_{IMg} led to an almost proportional change of the maximum P_O. Changing both k_{IonMg} and k_{IoffMg} proportionally (light and dark blue; no change of K_{IMg}) did not affect P_O at any $[Ca^{2+}]$. On the other hand, the values of t_O were insensitive to changes of k_{IoffMg}. However, a change of k_{IonMg} or a proportional change of both k_{IonMg} and k_{IoffMg} affected the calcium sensitivity of t_O in the direction of the change but changed the maximum t_O in the opposite direction.

At the basal $[Ca^{2+}]$, the open time was not affected by rate constants of Mg^{2+} binding to the inhibition site. However, increasing k_{IonMg} or decreasing k_{IoffMg} increased the closed time, and decreasing k_{IonMg} or increasing k_{IoffMg} decreased it. Simultaneous equivalent changes in both k_{IonMg} and k_{IoffMg} did not affect t_C. At high $[Ca^{2+}]$, change of k_{IoffMg} or both k_{IonMg} and k_{IoffMg} in one direction changed the mean closed time in the opposite direction; however, changes of k_{IonMg} in either direction did not change it. The parameters of Mg^{2+} binding to the inhibition site did not affect the rate constant of RyR activation, as expected.

Notably, the Mg-RyR interaction at the inhibitory site transpires through RyR open time when the rate of Mg^{2+} binding is modulated, and through RyR closed time when the rate of Mg^{2+} unbinding is modulated. The changes of open and closed time evoked by RyR-Mg^{2+} interaction at the inhibitory site are not dependent on Ca^{2+} concentration.

Mg-Binding Parameters Affect Calcium Release Events

The relative occurrence of sparks steeply declined at lower i_{Ca} values (**Figure 4D**). Therefore, to assure an acceptable signal-to-noise ratio of the average sparks, we have used only the single-channel calcium current of 0.6 pA to analyze the effect of Mg-binding parameters on the time course of CREs.

Changes of the on- and off-rate constants of Mg^{2+} binding to the RyR activation site (**Figure 6A**) had a small effect on the decay rate of quarks. At a low allosteric coefficient f_{Mg} (orange) the quarks were shorter, and at a high f_{Mg} (red) they were longer than at the reference f_{Mg} (**Figure 6B**). Changes of the on- and off-rate constants of Mg^{2+} binding to the RyR inhibition site (**Figure 6C**) did not affect the time course of quarks substantially.

The amplitude and time course of blips were practically unaffected by changes of Mg-binding parameters of the RyR activation site (**Figure 6A**) or f_{Mg} (**Figure 6B**). Blips were strongly prolonged when k_{IoffMg} was decreased (light green) but the remaining changes of Mg^{2+}-binding parameters of the RyR inhibition site slightly curtailed them. Increased k_{IonMg} (purple) curtailed blips due to their rapid attrition, while decreased k_{IonMg} (pink) or increased k_{IoffMg} (dark green) due to the rapid formation of sparks (**Figure 6C**).

The amplitude of sparks was substantially affected by changes of Mg^{2+} binding to the RyR inhibition site (**Figure 6C**), while other parameters had only a marginal effect. Increasing k_{IonMg} (purple) or decreasing k_{IoffMg} (light green) decreased the peak number of open RyRs, while increasing k_{IoffMg} (dark green) or decreasing k_{IonMg} (pink) increased it. Spark activation was slowed down when Mg^{2+} binding to either the activation site or the inhibition site was facilitated by increased on-rates (purple;

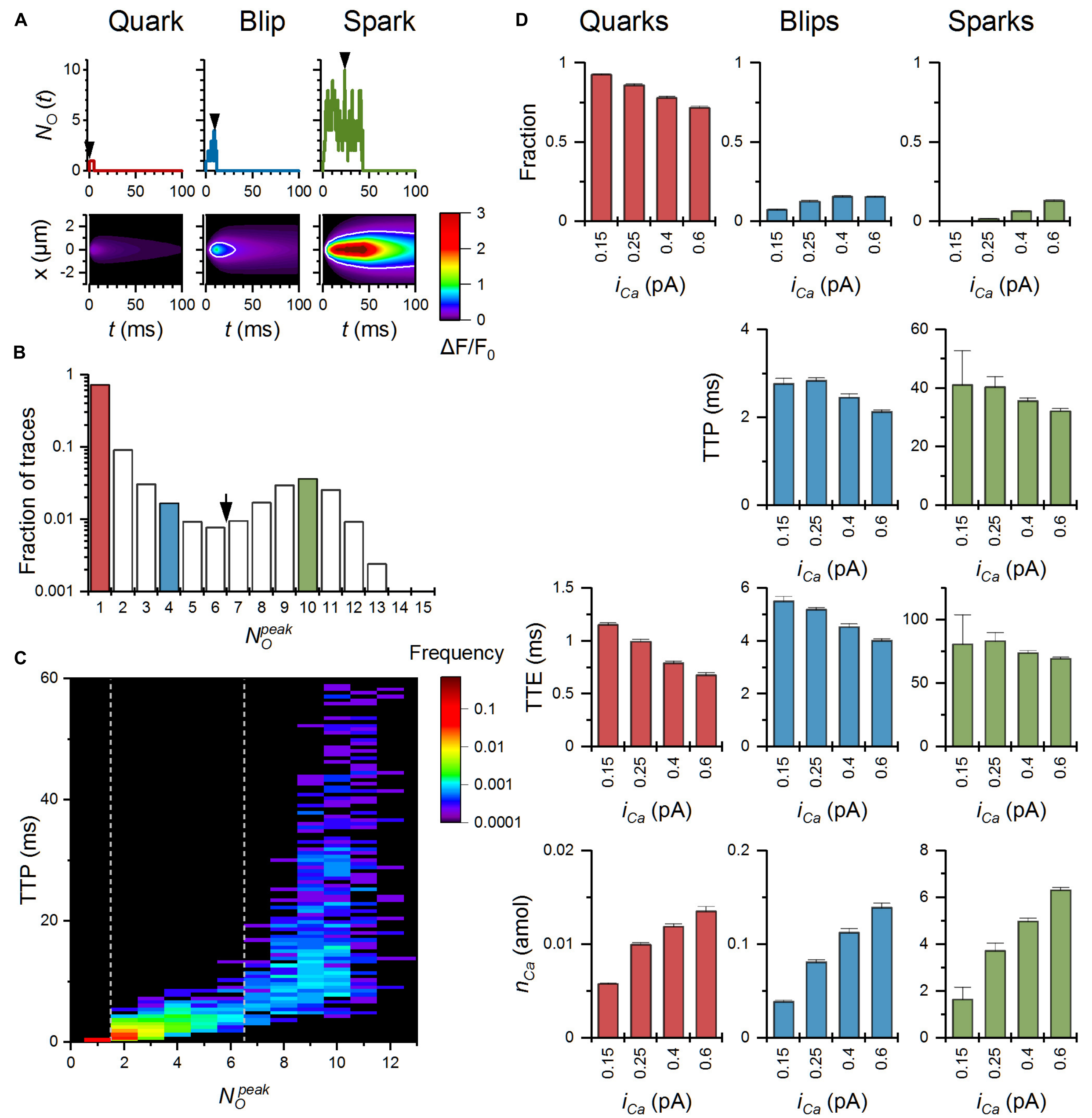

FIGURE 4 | Characteristics of calcium release events (CREs) simulated with the MWC-Ca/Mg RyR model and the reference set of parameters. **(A)** Top panel – the time courses of simulated CREs representing a typical quark, blip, and spark for i_{Ca} = 0.6 pA; Bottom panel – the fluorescence calcium signals emulating laser line-scan images in a confocal microscope corresponding to CREs in panel **(A)**. **(B)** The distribution of the peak number of open RyRs, N_O^{peak}, in the simulated calcium release events. The red, blue, and green columns correspond to peaks of respective traces shown in panel **(A)**. **(C)** The surface plot of the time to peak vs. N_O^{peak}; dotted lines indicate the N_O^{peak} values used for discrimination between quarks, blips, and sparks. **(D)** Relationships between i_{Ca} values and characteristics of simulated quarks, blips, and sparks; n_{Ca} – the amount of Ca^{2+} released *per* CRE.

Figures 6A,C) or decreased off-rates (light green; **Figures 6A,C**), or by an increased f_{Mg} (red; **Figure 6B**). It was speeded up when Mg^{2+} binding to either the activation site or the inhibition site was impeded by decreased on-rates (pink; **Figures 6A,C**) or increased off-rates (dark green; **Figures 6A,C**). Termination of sparks was virtually unaffected by the parameters of Mg^{2+} binding to the RyR activation site (**Figure 6A**). Increased Mg^{2+} binding to the RyR inhibition site curtailed sparks while decreased Mg^{2+} binding strongly prolonged them in addition to increasing their amplitude (**Figure 6C**).

The relative occurrence of CRE types (**Figures 6D-F**) was sensitive to the value of Mg-binding parameters as well. At the RyR activation site, the rate constants of Mg^{2+} binding/unbinding affected the relative fractions of quarks and

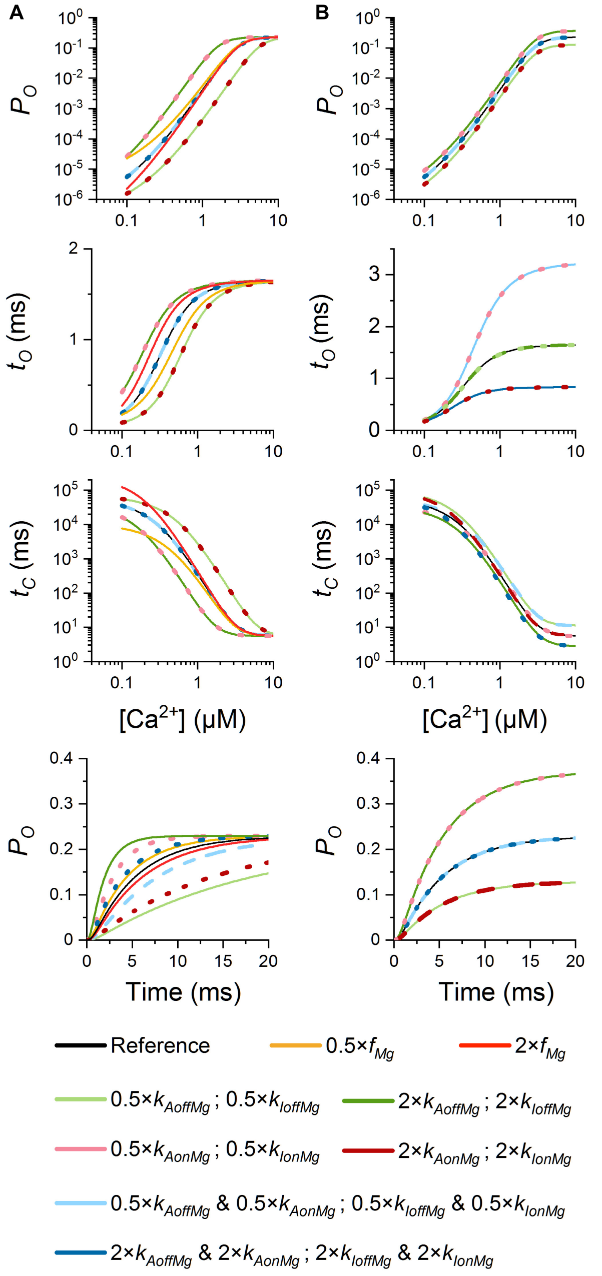

FIGURE 5 | Simulated dependence of RyR single-channel characteristics on Mg^{2+} binding. P_O([Ca^{2+}]), t_O([Ca^{2+}]), t_C([Ca^{2+}]), and $P_O(t)$ were calculated with Eqs. 14, 2, 2, and 4, respectively. **(A)** Variation of Mg-binding to the RyR activation site. **(B)** Variation of Mg-binding to the RyR inhibitory site. Bottom panels: time courses of P_O evolution after a stepwise increase of [Ca^{2+}] from 0.1 to 20 µM. Color-coding is described in the legend. The conditions that had the same effect are shown in solid, dashed, or dotted lines. Note the logarithmic scale of P_O and t_C.

sparks reciprocally, while the fraction of blips changed only slightly. Increased k_{AonMg} (light purple) and decreased k_{AoffMg} (light green) increased the fraction of quarks and reduced the fraction of sparks. Decreased k_{AonMg} (pink) and increased k_{AoffMg} (green) had the opposite effect. The decreased f_{Mg} (orange) did not affect the fractions of CREs but the increased f_{Mg} (red) strongly reduced the fraction of sparks and increased the fraction of quarks. At the RyR inhibition site, the parameters of Mg^{2+} binding, i.e., k_{IonMg} and k_{IoffMg}, affected the fractions of quarks and sparks similarly as k_{AonMg} and k_{AoffMg} did. While at the activation site the off-rate constant k_{AoffMg} had a stronger effect, at the inhibition site the on-rate constant k_{IonMg} had a stronger effect.

These findings can be summarized as follows: the interaction of Mg^{2+} with the RyR activation site predominantly affects the fraction of quarks, blips, and sparks and modulates the time to peak of sparks. On the other hand, the interaction of Mg^{2+} with the RyR inhibition site affects the recruitment of RyRs in sparks and thus modulates amplitudes of sparks, as well as the fractions of quarks, blips, and sparks.

Effective Coupling Strength Tallies Ryanodine Receptor Vicinity, Calcium Current, and Mg-Binding Parameters

We have shown above how the Mg-binding kinetics of RyR impacts the calcium dependence of single-channel activity and also how it influences the characteristics of calcium release events. Here we addressed how the kinetics of Mg^{2+} binding to RyRs combines with fundamental determinants of the calcium release site - RyR vicinity and single-channel calcium current. In other words, we evaluated their relative importance in shaping CRS activity. For this, we maximized mutual information between φ_i^{eff} and CRE characteristics (N_O^{peak}, F_q and F_s) evaluated for each RyR separately for all values of Mg-binding parameters (see **Supplementary Table 2**) and all values of i_{Ca}, and found the optimal values of weight factors (**Table 3**).

Weight factors for the calcium current and the on-rate of Mg-binding to the activation site are close to 1, so their effect is similar to that of the RyR vicinity. Factors for the off-rate constant of the activation site and the on-rate constant of the inhibition site have a stronger effect than RyR vicinity. Factors for the allosteric coefficient of Mg^{2+} and the off-rate constant of the inhibition site have a weaker effect than RyR vicinity.

The CRE characteristics evaluated for all RyR models obtained by variation of the Mg-binding kinetics and i_{Ca} are displayed against their effective coupling strength values (**Figure 7A**). Although all data are consistently united, there were diverging trends between the data related to the activation site and the inhibition site. This divergence suggests that the similar effect on the fractional occurrence of quarks, blips, and sparks caused by Mg^{2+} binding to either the activation sites or the inhibition site is caused by different molecular mechanisms (see below).

A closer inspection of **Figure 7A** (see pairs of symbols representing changes of individual Mg-binding parameters) revealed that characteristics of calcium release events react sensitively and specifically in proportion to the respective changes of the effective coupling strength. Changes at the activation site that increased the calcium sensitivity of P_O and t_O and speeded up the time course of activation had a strong activating

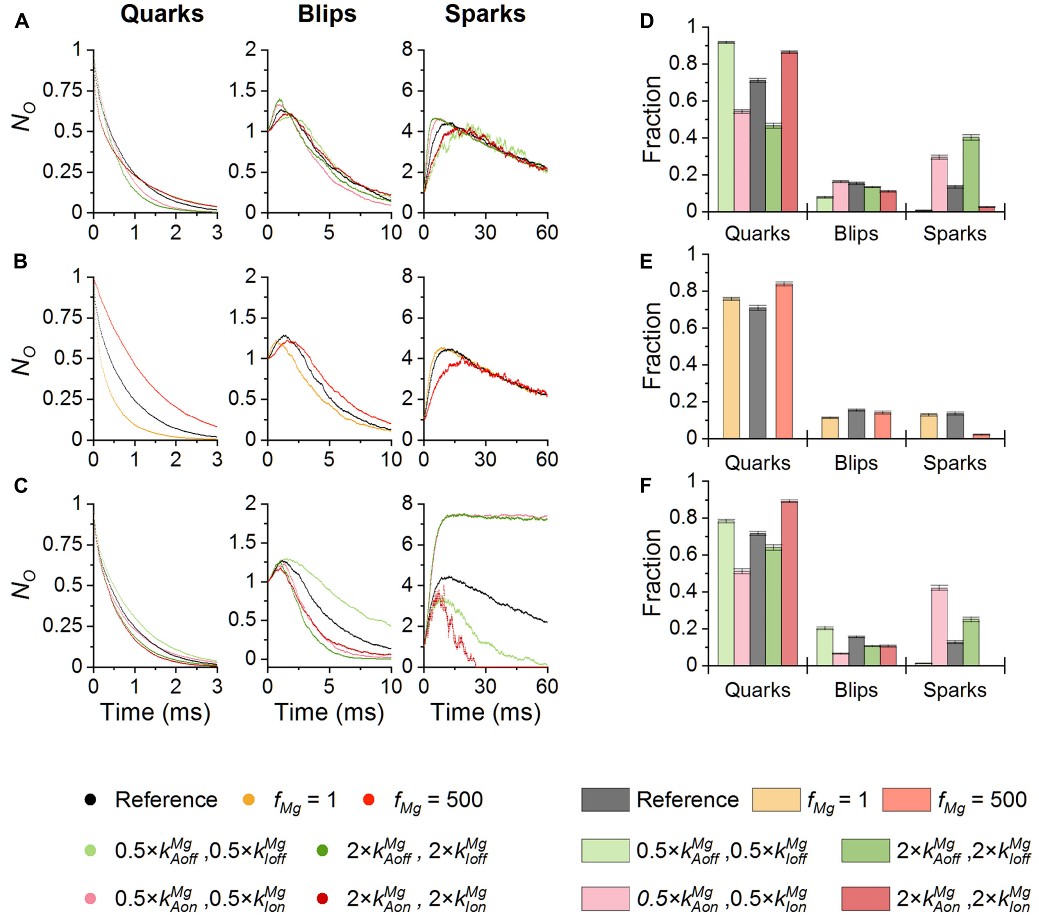

FIGURE 6 | The effect of Mg-binding parameters on CREs. Simulations were performed at 100 nM Ca^{2+} and i_{Ca} of 0.6 pA. **(A,D)** The effect of Mg-binding parameters at the activation site on the time course **(A)** and the fraction **(D)** of CREs. **(B,E)** The effects of the allosteric coefficient f_{Mg} on the time course **(B)** and the fraction **(E)** of CREs. **(C,F)** The effect of Mg-binding parameters at the inhibition site on the time course **(C)** and the fraction **(F)** of CREs. Individual conditions are color-coded as indicated in the legend.

effect on CREs, and those that decreased the calcium sensitivity of P_O and t_O and slowed down the time course of activation had an inhibitory effect. Comparably strong were the effects at the inhibition site that increased maximum P_O and maximum t_O, but did not change the calcium sensitivity of P_O and even decreased the calcium sensitivity of t_O and slowed down the time course of activation.

A concurrent increase of k_{IonMg} and k_{IoffMg}, that is, an unchanged equilibrium constant K_{IMg}, suppressed the fractional occurrence of sparks and promoted that of quarks and vice versa. These effects materialized at an unchanged P_O and activation rate. Thus, they could be only attributed to the change in RyR open and closed times. Similar effects materialized in the opposite direction for a concurrent change in k_{AonMg} and k_{AoffMg}, where a decrease of these parameters suppressed the fractional occurrence of sparks and promoted that of quarks (**Figure 7B**) but their increase had only a small effect. The effect of k_{AonMg} and k_{AoffMg} on CREs occurred in the absence of effects on P_O, t_O and t_C and thus could be only attributed to the change of the time course of P_O activation by increased $[Ca^{2+}]$. The changes of coupling strength and CRE properties evoked by changing both on- and off-rate constants can be attributed to the unequal weights of the on- and off-rates (**Table 3**). Biophysically they are due to the unequal effect of the on- and off-rates on the open and closed times and the activation rate constants (**Figure 5**).

The relationships between the effective coupling strength and the fractions of quarks, blips, and sparks upon changes in K_{IMg} evoked by changed on- or off-rate of Mg^{2+} binding to the inhibition site were of similar direction and extent as those evoked by changes of Mg^{2+} binding to the activation site. There were, however, pronounced changes in the amplitude characteristics of CREs caused by the dependence of maximum RyR open probability on K_{IMg}. As a result, the dependence of the peak number of open RyRs in all events (**Figure 7A**, blue symbols) sharply increased with φ_{eff}. In contrast to changes in Mg^{2+} binding to the RyR activation site, the amplitude of blips did not increase monotonously but showed a maximum at control values of k_{IonMg} and k_{IoffMg}, and the amplitudes of sparks increased with φ_{eff} due to the dependence between φ_{eff} and K_{IMg}.

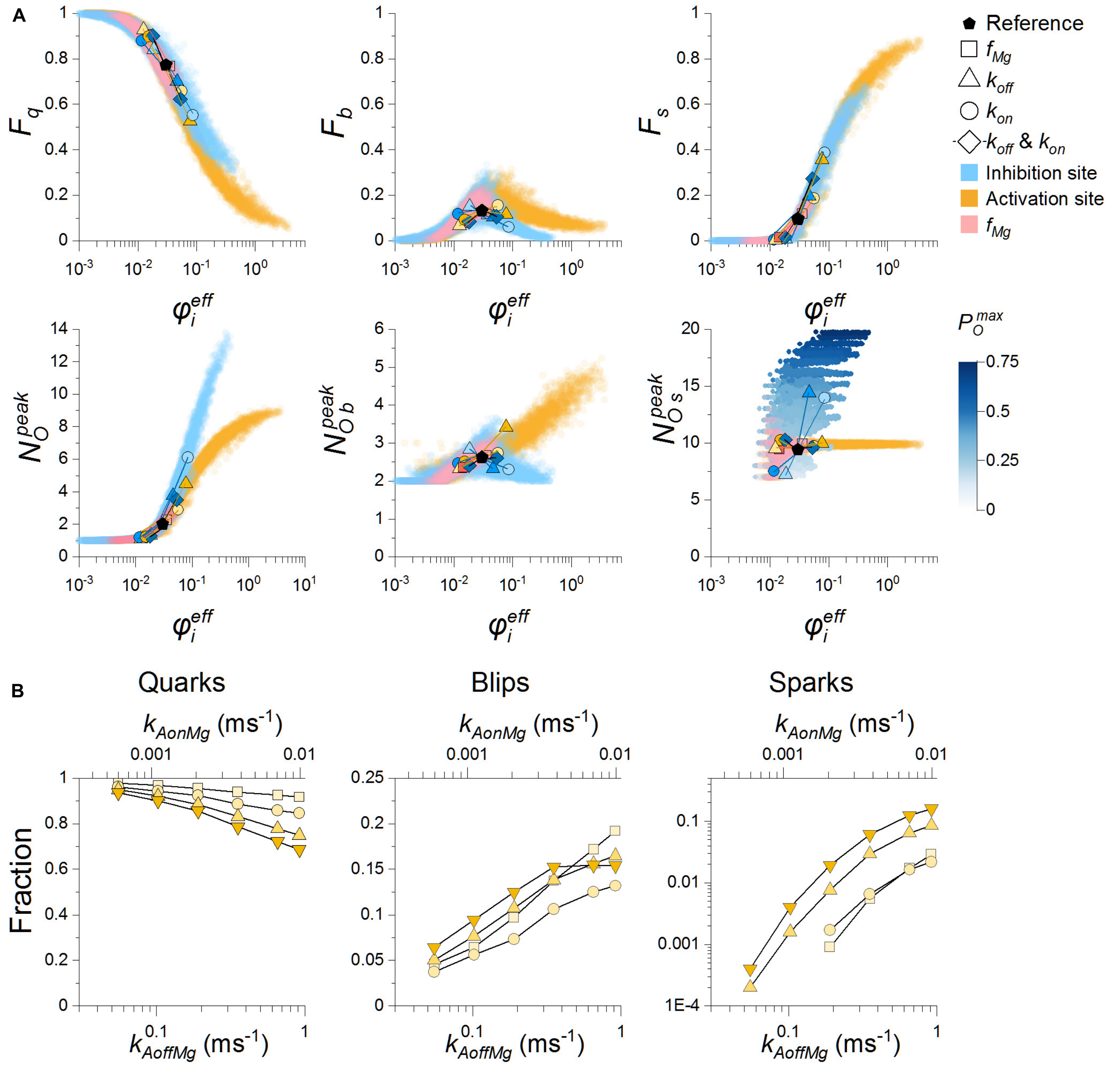

FIGURE 7 | Calcium release event characteristics related to the effective coupling strength. **(A)** The whole dataset (14240 points per panel) for various Mg-binding parameters of the RyR activation site (orange and pink) and the RyR inhibition site (blue), which were obtained for all RyR vicinities and all single-channel calcium currents (not indicated). The dots are semitransparent to better visualize the data. The circles, triangles, and diamonds mark results for decreased (×0.5; lighter color) or increased (×2; darker color) Mg-binding parameter values (see legend), relative to the reference parameter values (black pentagons). The P_O^{max} colormap refers solely to the N_{OS}^{peak} graph to indicate the relation of the N_{OS}^{peak} increase to P_O^{max} increase when varying Mg-binding at the inhibitory site, not present in the case of blips. **(B)** The dependence of the fraction of quarks, blips, and sparks on the reciprocally changed rate constants k_{AonMg} (top axis) and k_{AoffMg} (bottom axis), so that the equilibrium constant K_{AMg} stayed at the reference value of 92 μM. Squares, circles, up triangles and down triangles denote values of i_{Ca} = 0.15, 0.25, 0.4, and 0.6 pA, respectively.

The Frequency of Spontaneous Calcium Release Events Depends on the Ryanodine Receptor Closed Time at Basal [Ca^{2+}]

The last problem we addressed in this study was the impact of Mg-binding parameters of the RyR on the frequency of spontaneous occurrence of individual calcium release types at basal [Ca^{2+}]. The frequency of all events at the CRS was directly proportional to N_{RyR} and inversely proportional to the sum of t_C and t_O (Eq. 13 in section "Methods"). Since at basal [Ca^{2+}] $t_C >> t_O$, this effect, summarized in **Table 4** for the conditions examined in **Figure 5**, was chiefly due to changes in t_C. The event frequency was changed approximately in proportion (k_{AoffMg}, k_{IoffMg}) or inverse proportion (k_{AonMg}, k_{IonMg}, f_{Mg}) to the change of rate parameters. All parameters of Mg^{2+} binding affect the event frequency and the fraction of sparks in the same direction, and therefore they have a pronounced effect on the spontaneous spark frequency at the examined i_{Ca} of 0.6 pA. Since the fraction of blips is only weakly affected by Mg-binding parameters, the frequency of blips was changed only modestly.

DISCUSSION

The *in silico* model of the calcium release site was based on a novel model of RyR gating that incorporated Mg^{2+} binding kinetics (MWC-Ca/Mg RyR; **Figure 2**). Despite the complexity of the RyR model (60 states), the CRS model with 20 RyRs, written in C++ and Python, could be run fast on a generally available desktop computer, which allowed in-depth inspection of Mg^{2+} binding on the behavior of CRS.

Mg^{2+} Ions and Ryanodine Receptor Sensitivity to Calcium

The parameter values of the MWC-Ca/Mg RyR model (**Table 1**) were determined from RyR single-channel characteristics measured in independent bilayer experiments under conditions that included physiological concentrations of ATP (approx. 5 mM total) and Mg^{2+} ions (1 mM free; **Figure 3**). The close approximation of the experimental data by simulations of the MWC-Ca/Mg RyR model validated both the computational model as well as the best-fit parameter values used as the reference set for simulations. Nevertheless, the fitted set of experimental data, which was obtained at a limited range of Ca^{2+} and Mg^{2+} concentrations, has not been verified by others. Thus, the estimated reference parameter values may differ from the true values despite their high statistical agreement with the data. Therefore, we varied the Mg-binding parameters of the RyR model around their reference values at a constant Mg^{2+} concentration and calculated the RyR single-channel characteristics for a full scale of cytosolic Ca^{2+} concentrations (**Figure 5**).

TABLE 4 | The effect of Mg-binding parameters on the frequency of occurrence of spontaneous calcium release events.

Frequencies	**f_O (s^{-1})**		**f_Q (s^{-1})**		**f_B (s^{-1})**		**f_S (s^{-1})**	
Reference values	**0.57**		**0.409**		**0.089**		**0.072**	
Parameter	x ***0.5***	x ***2.0***	x ***0.5***	x ***2.0***	x ***0.5***	x ***2.0***	x ***0.5***	x ***2.0***
f_{Mg}	2.37	0.17	1.74	0.118	0.314	0.029	0.307	0.021
k_{AoffMg}	0.36	1.23	0.33	0.573	0.028	0.163	0.002	0.494
k_{AonMg}	1.23	0.36	0.668	0.311	0.199	0.040	0.363	0.009
k_{AoffMg} & k_{AonMg}	0.57	0.57	0.453	0.358	0.083	0.092	0.034	0.120
k_{IoffMg}	0.32	0.93	0.251	0.597	0.065	0.100	0.004	0.233
k_{IonMg}	0.88	0.36	0.45	0.321	0.059	0.038	0.371	0.001
k_{IoffMg} & k_{IonMg}	0.54	0.64	0.313	0.534	0.078	0.084	0.149	0.022

f_O, f_Q, f_B, f_S – the frequency of spontaneous RyR openings, quarks, blips, and sparks per CRS, respectively. CRS simulations were performed at 100 nM Ca^{2+} and i_{Ca} = 0.6 pA.

The tested RyR models showed a high sensitivity of RyR activation to parameters of Mg-binding. Increased Mg^{2+} affinity of the RyR activation site, achieved by variation of binding/unbinding rate constants, shifted the calcium dependence of the open probability, the open time, and the closed time of RyR models to higher Ca^{2+} concentrations. Decreased Mg^{2+} affinity had opposite effects. This is in line with the observed effect of Mg^{2+} on RyR calcium sensitivity (Laver et al., 1997; Gyorke and Gyorke, 1998; Zahradnikova et al., 2003). As originally revealed by Zahradnikova et al. (2010), the non-linear allosteric modulation of RyR activity by Mg^{2+} affected P_O and t_C significantly at sub-micromolar Ca^{2+} concentrations but did not influence RyR activity at the micromolar range. A change of f_{Mg}, which may result from metabolic regulation of the ryanodine receptor, may thus modulate the frequency of spontaneous RyR openings in diastolic myocytes by an order of magnitude without a change in the characteristics of calcium release events.

The kinetic description confirmed previous results of the equilibrium model of the RyR inhibition site (Zahradnikova et al., 2010) that the RyR open probability and the spark amplitude are shaped by modulation of Mg^{2+} affinity of the RyR inhibition site. Additionally, the kinetic description revealed substantial effects of rate constants (k_{IonMg} and k_{IoffMg}) of the RyR inhibition site on the RyR open and closed times and their relationships to the spark termination, CRE frequency, and relative occurrence of visible and invisible CREs (see below).

To sum up, the MWC-Ca/Mg RyR model predicts that at the physiological cytosolic concentration of 1 mM, Mg^{2+} ions influence the single-channel activity of RyRs considerably. Magnesium ions act through their allosteric competition with Ca^{2+} at the RyR activation site as well as through their binding at the RyR inhibition site. This means that modification of the Mg-binding properties of RyR channels by pharmacological, metabolic, or structural changes in RyR monomers may substantially affect the calcium release function of cardiac myocytes.

Calcium Release Events Generated by the Calcium Release Site Model With Monod-Wyman-Changeux-Ca/Mg Ryanodine Receptor Models

To assess the impact of Mg-modulation of RyR activity on cardiac calcium release, we applied the MWC-Ca/Mg RyR model to the model of the calcium release site developed previously (Iaparov et al., 2021). Interestingly, the three types of calcium release events that were observed in simulations of CRS models based on the two-state RyR model (Iaparov et al., 2021) occurred also in CRS models based on the MWC-Ca/Mg RyR model; however, the occurrence of sparks was much less frequent in the MWC-Ca/Mg RyR model. The difference between a two-state model and the full model tested in this work stems in part from the calcium-independent open time of the two-state model (Iaparov et al., 2021) and the calcium-dependent open time of the full model (**Figure 5**). Additionally, the probability that many RyRs would become active in a spark is low since the rate of Mg^{2+} unbinding from the calcium activation site is much slower than the rate of Ca^{2+} binding, in line with experiments (Zahradnikova et al., 2003) and simulations (Zahradnikova et al., 2010).

Simulations of the reference CRS model predict that a large fraction of spontaneous local calcium release events (quarks and blips) result from the activation of a subset of RyR channels in a CRS (**Figure 4**). When the i_{Ca} amplitude was small (0.15 or 0.25 pA), CRS models produced mostly quarks or blips. Individual records of blips were formed by 2 to 6 RyRs open at their peaks (at around 3 ms), and terminated fast, within 5 to 6 ms, by simple stochastic attrition (Stern and Cheng, 2004). When the i_{Ca} was higher (0.4 or 0.6 pA), CRS models produced similar quarks and blips as at lower i_{Ca} amplitudes but also a significant fraction of large sparks. With the reference parameter set, these sparks were formed by 7 to 13 RyRs (out of 20 in the CRS) open at their peaks (30 to 40 ms) and terminated very slowly (within 60 to 70 ms) by the attrition mechanism. However, the average rate of spark termination was very sensitive to the Mg-binding rate constants of the RyR inhibitory site (see below).

The RyR single-channel calcium current of 0.6 pA produced a higher amplitude of sparks but also a stronger calcium fluorescence signal (**Figure 4A**) so that blips were well over the detection threshold of intracellular calcium measurements and sparks were high ($\Delta F/F_0 > 3$) and prolonged. If real, such large calcium release flux would cause a rapid dissipation of the calcium gradient across SR membrane and fast termination of calcium release by a mechanism dubbed "induction decay" (Cannell et al., 2013) or "pernicious attrition" (Gillespie and Fill, 2013).

Effect of Mg^{2+} Binding Parameters on Calcium Release Events

Variation of the calcium sensitivity of RyRs by altering binding and unbinding of Mg^{2+} to/from the RyR activation site led to dramatic changes in the occurrence of spontaneous calcium release events and the relative proportions of quarks and sparks, while it had only a small effect on the relative occurrence of blips. In CRS simulations, the times to peak of both blips and sparks were very sensitive to the rates of Mg-binding and unbinding at the activation site. Changes that facilitated Ca^{2+} binding to the activation site, i.e., faster Mg-unbinding or slower Mg-binding, shortened the time-to-peak of blips and sparks, while the opposite changes prolonged it (**Figure 6A**). These findings indicate that Mg^{2+} ions modulate also the kinetics of the experimentally observable calcium sparks, although these changes may be blunted by the relatively slow kinetics of calcium indicators.

The allosteric coefficient f_{Mg} characterizes the change in the energy needed for the closed-open transition in the RyR homotetramer upon binding of Mg^{2+}. In the CRS simulations, the change of f_{Mg} markedly affected the closed time, not the open time, at low Ca^{2+} concentration but the fraction of blips changed only slightly while the fraction of sparks was strongly reduced at high f_{Mg}. As a result, the frequency of experimentally observable CREs (f_B and/or f_S, **Table 4**) would increase with decreasing f_{Mg}, and vice versa, while their time courses would be affected modestly (**Figure 6B**). The amplitude of the observed calcium fluorescence signals of CREs would be thus affected only slightly.

Variation of the Mg^{2+}-binding at the RyR inhibition site affected calcium release events profoundly (**Figures 6C,F**). Faster Mg-unbinding or slower Mg-binding, both of which increased the maximum P_O, increased the relative occurrence and the maximum N_O of sparks but also completely suppressed spontaneous spark termination. At the level of observed fluorescence signals, this would transpire as a large increase in the frequency and amplitude of the experimentally observable CREs, and thus as full reliance of spark termination on SR depletion. Slower Mg-unbinding or faster Mg-binding at the inhibition site, which both decreased the maximum P_O, suppressed the sparks almost completely and decreased their amplitude and duration substantially. Additionally, the blips became substantially longer, without a change in their amplitude, when Mg-unbinding was slower. It should be pointed out here that if Mg^{2+} inhibition was absent, activation of more than one RyR in the CRS always led to the activation of all RyRs (**Figure 7A**, lower right panel).

The Role of Mg^{2+} Binding in the Effective Coupling Strength Between Ryanodine Receptors

In a previous study (Iaparov et al., 2021) we characterized the interaction between ryanodine receptors through coupling strength - a weighted product of RyR vicinity and single-channel calcium current. The use of a more complex model of ryanodine receptor gating opened the question of whether the coupling strength is still applicable for the explanation of CRS activity. To this end, we introduced the effective coupling strength that accounted for variable RyR gating parameters (Eq. 10). This included weighing the parameters for Mg^{2+} binding to the activation site, the allosteric factor of Mg^{2+} binding to the activation site, or the parameters for Mg^{2+} binding to the inhibition site. Due to the multifactorial nature of the results (178 different parameter combinations), it was not possible to use fitting for the determination of the weight factors, since it was not *a priori* known whether they follow the same Hill equations, in contrast to our previous study (Iaparov et al., 2021). The weight factors were found by the original method of maximizing the mutual information between the effective coupling strength and CRE characteristics (see Methods). The weights enabled the comparison of CRS models differing in RyR Mg-binding parameter values.

As documented in **Figure 7**, the effective coupling strength consolidated the characteristics of simulated calcium release events into relationships of a dose-response type. The relative occurrence of quarks, blips, and sparks followed approximately the same relationship on the effective coupling strength, independently of RyR model parameters. However, the dependence of the average amplitude of all events differed markedly between models in which parameters of the activation site and the inhibition site were varied. This was mainly due to the steep dependence of RyR maximum open probability on K_{IMg}, leading to a steep increase of spark amplitude when

K_{IMg} was increased and inhibition of RyR activity by Mg^{2+} was reduced, independent of coupling strength.

Limitations

The CRS model used in this work does not account for the reduction of calcium gradient and the effect of depletion of SR calcium on the single-channel calcium current. This simplification was necessary to assess the effect of Mg–RyR interactions on the formation of calcium release events without the interference of parallel processes. Consequently, the simulated CREs differ from the real ones, especially in the case of large and prolonged sparks.

The CRS model also takes advantage of a simplified description of buffered calcium diffusion based on the instantaneous formation of the steady-state calcium gradient upon RyR opening (Naraghi and Neher, 1997). This approximation also assumes that calcium buffers do not saturate and therefore the build-up of calcium concentration at a RyR can be considered as additive in the case of multiple sources. More realistically, the free Ca^{2+} concentration in the dyadic gap temporarily reached higher values, which might locally saturate the buffers according to the reaction-diffusion models of narrow dyadic gaps (Soeller et al., 2007; Valent et al., 2007). Since the activation of RyRs is much slower than the build-up of calcium gradient (Soeller et al., 2007; Valent et al., 2007), the use of the Naraghi-Neher simplification should not weaken the conclusions of this study while allowing much faster calculations than the reaction-diffusion model of the dyadic gap (Valent et al., 2007).

The rate constant k_{AonMg} was set to $0.01 \times k_{AonCa}$, considering that the rate-limiting factor in ion binding to a ligand is the exchange rate of a water molecule in the hydration complex of the ion. The resulting value can be considered as the upper limit since other rate-limiting factors in Mg-RyR interaction could eventually slow down the reaction. Consequently, the corresponding unbinding rate constant k_{AoffMg} might have been overestimated by the fitting procedure to keep the equilibrium constant at the appropriate value.

We have previously estimated k_{AoffMg} in the range of 0.05 - 0.22 ms^{-1}, assuming instantaneous binding of Ca^{2+} to an Mg^{2+}-free RyR activation site (Zahradnikova et al., 2010). The known rate constants of Mg^{2+} unbinding from other calcium-binding proteins such as parvalbumin, its mutants, and troponin-C range widely between 0.001 ms^{-1} to 0.267 ms^{-1} (Rosenfeld and Taylor, 1985; Permyakov et al., 1987; Hou et al., 1993; Zhang et al., 2011), but are less than our estimate. We showed by permutation of Mg^{2+} binding/unbinding rates at a constant ratio that the lower rates (at no change in Mg^{2+} affinity) would have no effects on the calcium dependence of the steady-state P_O, t_O and t_C (**Figure 5**) and would only affect the time course of the response to a stepwise change in $[Ca^{2+}]$. This simultaneous and equivalent decrease of both rate constants would result in a still lower frequency of observable events (**Figure 7B** and **Table 4**).

In general, the rates of ligand-ion binding reactions are temperature dependent; however, the temperature coefficients of similar reaction systems are comparable but larger than that of passive diffusion, and smaller than that of enzymatic reactions. Therefore, their proportions should be expected to change with the temperature of the heart. Nevertheless, experiments at the cellular level are typically performed at room temperature, for which the presented results are pertinent.

Finally, our results point to the need for a more precise single-channel description of RyR activity at near-physiological conditions, especially at low cytosolic $[Ca^{2+}]$, in the presence of high ATP, and at a range of free Mg^{2+} concentrations. Such measurements would need very long recordings of single-channel activity to attain sufficient accuracy (Zahradnikova et al., 2020) but would be instrumental for a precise determination of K_{O0} and f_{Mg}.

Physiological Implications

The presented model provided a high fraction of quarks, i.e., initiating RyR openings that activated no other RyRs. In real experiments, quarks are not observable for their small calcium yield. To determine whether this finding is consistent with experimental data, we compared the predicted fraction of CREs of different types with the observed number of calcium release events in cardiac myocytes. The number of ryanodine receptors per volume unit of a myocyte has been estimated as 60 - 90 RyRs per μm^3 (Soeller et al., 2007; Hayashi et al., 2009). Assuming a confocal volume of $100 \times 1 \times 0.2 = 20\ \mu m^3$ per scanning line, this translates to 1250 - 1900 RyRs in the observation volume per 100 μm line length. Our reference value of mean closed time (35 s) and mean open time (0.2 ms) at 100 nM Ca^{2+} then corresponds to 36 - 54 RyR openings per second in this volume. Of these, there would be 2.7 - 8.4 blips per second and 0.02 - 7 sparks per second at a calcium current of 0.15 - 0.6 pA (see **Figure 4D** and **Table 4**). These can be compared with the experimental values of 0.2 - 4.6 sparks/(100 μm) (Lukyanenko and Gyorke, 1999; Guo et al., 2006; Parks and Howlett, 2012; Yin et al., 2021) in intact cells and 4 - 40 sparks/(100 μm) in skinned cardiac myocytes (Lukyanenko and Gyorke, 1999; Kubalova et al., 2005; Fernandez-Velasco et al., 2009; Ruiz-Hurtado et al., 2015). The values predicted by the model can be reconciled either with a lower i_{Ca} and a high predominance of blips or with a higher i_{Ca} and a comparable occurrence of both blips and sparks. However, our simplified calculations predict that blips cannot be detected when i_{Ca} is lower than 0.4 pA (Iaparov et al., 2021); thus a more realistic model of calcium diffusion in the dyadic gap and better estimates of Mg^{2+}-ATP binding kinetics are necessary to decide this point.

The Mg-binding parameters substantially affect the frequency of RyR openings by modulating the RyR closed time at the basal calcium concentration (**Table 4**). A similar conclusion was reached in our previous study of the effect of Mg^{2+} binding on spontaneous sparks and waves in a simplified kinetic model of the CRS (Petrovic et al., 2015). Additionally, here we observed a strong effect of Mg-binding parameters on the relative occurrence of quarks, blips, and sparks (**Figures 6D-F**). Such changes transposed to real experiments mean that a change in Mg-binding parameters due to RyR mutation, phosphorylation/dephosphorylation, or oxidation/reduction would affect the frequency of observed spontaneous calcium release events. An increase in the relative proportion of sparks would be associated with an increase of the mean amplitude of the observed CREs, due to the larger number of open RyRs at the peak of sparks than of blips, and a longer average duration of observed CREs, due to the longer duration of sparks than blips (**Figure 4D**).

CONCLUSION

The binding of Mg^{2+} to both the activation and the inhibition site negatively modulated the effective coupling strength in a qualitatively similar way. In other words, these findings reveal the role of Mg^{2+} ions as a damping agent that protects calcium release sites from uncontrolled activation at threshold calcium stimuli. This finding is of principal physiological importance since it helps to explain the graded behavior of calcium release at the level of ryanodine receptors, which impedes the positive feedback inherent to the calcium-induced calcium release mechanism.

DATA AVAILABILITY STATEMENT

The raw data supporting the conclusions of this article will be made available by the authors, without undue reservation.

AUTHOR CONTRIBUTIONS

BI, IZ, and AZ planned the research and wrote the manuscript. BI and AZ designed the simulations. BI wrote the software, derived mathematical expressions, and performed simulations. BI, JB, IZ, and AZ analyzed and interpreted the experimental and simulated data. All authors contributed to the article and approved the submitted version.

FUNDING

The research was supported by the SAV-TUBITAK project JRP/2019/836/RyRinHeart, by the project VEGA 2/0182/21, and by the Operational Programme Integrated Infrastructure for the project: Long-term strategic research of prevention, intervention, and mechanisms of obesity and its comorbidities, IMTS: 313011V344, co-financed by the European Regional Development Fund.

SUPPLEMENTARY MATERIAL

The Supplementary Material for this article can be found online at: https://www.frontiersin.org/articles/10.3389/fphys.2021.805956/full#supplementary-material

The derivation of the equations used in Methods is given in the **Supplementary Material**. The transition rates used for constructing the Q-matrix are summarized in **Supplementary Table 1**. The values of Mg-binding parameters used in this study are given in **Supplementary Table 2**.

REFERENCES

Bognar, M. (2013). *OMPRNG: A Parallel Statistical Random Number Generator for OpenMP*. Available online at: https://web.archive.org/web/20180125041447/http://homepage.divms.uiowa.edu/~mbognar/omprng/ (accessed December 29, 2021).

Bovo, E., Mazurek, S. R., Blatter, L. A., and Zima, A. V. (2011). Regulation of sarcoplasmic reticulum Ca(2)(+) leak by cytosolic Ca(2)(+) in rabbit ventricular myocytes. *J. Physiol.* 589(Pt 24), 6039–6050. doi: 10.1113/jphysiol.2011.214171

Bridge, J. H., Ershler, P. R., and Cannell, M. B. (1999). Properties of Ca2+ sparks evoked by action potentials in mouse ventricular myocytes. *J. Physiol.* 518, 469–478. doi: 10.1111/j.1469-7793.1999.0469p.x

Cannell, M. B., Kong, C. H., Imtiaz, M. S., and Laver, D. R. (2013). Control of sarcoplasmic reticulum Ca2+ release by stochastic RyR gating within a 3D model of the cardiac dyad and importance of 'induction decay' for CICR termination. *Biophys. J.* 104, 2149–2159. doi: 10.1016/j.bpj.2013.03.058

Cheng, H., and Lederer, W. J. (2008). Calcium sparks. *Physiol. Rev.* 88, 1491–1545.

Chi, X., Gong, D., Ren, K., Zhou, G., Huang, G., Lei, J., et al. (2019). Molecular basis for allosteric regulation of the type 2 ryanodine receptor channel gating by key modulators. *Proc. Natl. Acad. Sci. U.S.A.* 116, 25575–25582. doi: 10.1073/pnas.1914451116

Choi, R. H., Koenig, X., and Launikonis, B. S. (2017). Dantrolene requires Mg(2+) to arrest malignant hyperthermia. *Proc. Natl. Acad. Sci. U.S.A.* 114, 4811–4815. doi: 10.1073/pnas.1619835114

Colquhoun, D., and Hawkes, A. G. (1995). "A Q-matrix cookbook. How to write only one program to calculate the single-channel and macroscopic predictions for any kinetic mechanism," in *Single-Channel Recording*, second Edn, eds B. Sakmann and E. Neher (New York, NY: Plenum Press), 589–633. doi: 10.1007/978-1-4419-1229-9_20

Copello, J. A., Barg, S., Sonnleitner, A., Porta, M., Diaz-Sylvester, P., Fill, M., et al. (2002). Differential activation by Ca2+, ATP and caffeine of cardiac and skeletal muscle ryanodine receptors after block by Mg2+. *J. Membr. Biol.* 187, 51–64. doi: 10.1007/s00232-001-0150-x

Dashti, A., Mashayekhi, G., Shekhar, M., Ben Hail, D., Salah, S., Schwander, P., et al. (2020). Retrieving functional pathways of biomolecules from single-particle snapshots. *Nat. Commun.* 11:4734. doi: 10.1038/s41467-020-18403-x

des Georges, A., Clarke, O. B., Zalk, R., Yuan, Q., Condon, K. J., Grassucci, R. A., et al. (2016). Structural basis for gating and activation of RyR1. *Cell* 167, 145–157. doi: 10.1016/j.cell.2016.08.075

Eigen, M., and Wilkins, R. G. (eds) (1965). "The kinetics and mechanism of formation of metal complexes," in *Mechanisms of Inorganic Reactions*. (Washington, D.C: American Chemical Society), 55–80.

Fabiato, A. (1983). Calcium-induced release of calcium from the cardiac sarcoplasmic reticulum. *Am. J. Physiol.* 245, C1–C14.

Fernandez-Velasco, M., Rueda, A., Rizzi, N., Benitah, J. P., Colombi, B., Napolitano, C., et al. (2009). Increased Ca2+ sensitivity of the ryanodine receptor mutant RyR2R4496C underlies catecholaminergic polymorphic ventricular tachycardia. *Circ. Res.* 104, 201–209. doi: 10.1161/CIRCRESAHA.108.177493

Gillespie, D., and Fill, M. (2013). Pernicious attrition and inter-RyR2 CICR current control in cardiac muscle. *J. Mol. Cell Cardiol.* 58, 53–58. doi: 10.1016/j.yjmcc.2013.01.011

Gillespie, D. T. (1977). Exact stochastic simulation of coupled chemical reactions. *J. Phys. Chem.* 81, 2340–2391. doi: 10.1021/j100540a008

Guo, T., Zhang, T., Mestril, R., and Bers, D. M. (2006). Ca2+/Calmodulin-dependent protein kinase II phosphorylation of ryanodine receptor does affect calcium sparks in mouse ventricular myocytes. *Circ. Res.* 99, 398–406. doi: 10.1161/01.RES.0000236756.06252.13

Guo, W., Sun, B., Estillore, J. P., Wang, R., and Chen, S. R. W. (2020). The central domain of cardiac ryanodine receptor governs channel activation, regulation, and stability. *J. Biol. Chem.* 295, 15622–15635. doi: 10.1074/jbc.RA120.013512

Gusev, K., and Niggli, E. (2008). Modulation of the local SR Ca2+ release by intracellular Mg2+ in cardiac myocytes. *J. Gen. Physiol.* 132, 721–730. doi: 10.1085/jgp.200810119

Gyorke, I., and Gyorke, S. (1998). Regulation of the cardiac ryanodine receptor channel by luminal Ca2+ involves luminal Ca2+ sensing sites. *Biophys. J.* 75, 2801–2810. doi: 10.1016/S0006-3495(98)77723-9

Hake, J., Edwards, A. G., Yu, Z., Kekenes-Huskey, P. M., Michailova, A. P., McCammon, J. A., et al. (2012). Modelling cardiac calcium sparks in a three-dimensional reconstruction of a calcium release unit. *J. Physiol.* 590, 4403–4422. doi: 10.1113/jphysiol.2012.227926

Harris, C. R., Millman, K. J., van der Walt, S. J., Gommers, R., Virtanen, P., Cournapeau, D., et al. (2020). Array programming with NumPy. *Nature* 585, 357–362. doi: 10.1038/s41586-020-2649-2

Hartmann, N., Pabel, S., Herting, J., Schatter, F., Renner, A., Gummert, J., et al. (2017). Antiarrhythmic effects of dantrolene in human diseased cardiomyocytes. *Heart Rhythm.* 14, 412–419. doi: 10.1016/j.hrthm.2016.09.014

Hayashi, T., Martone, M. E., Yu, Z., Thor, A., Doi, M., Holst, M. J., et al. (2009). Three-dimensional electron microscopy reveals new details of membrane systems for Ca2+ signaling in the heart. *J. Cell Sci.* 122(Pt 7), 1005–1013. doi: 10.1242/jcs.028175

Hou, T. T., Johnson, J. D., and Rall, J. A. (1993). Role of parvalbumin in relaxation of frog skeletal muscle. *Adv. Exp. Med. Biol.* 332, 141–151. doi: 10.1007/978-1-4615-2872-2_13

Iaparov, B. I., Zahradnik, I., Moskvin, A. S., and Zahradnikova, A. (2021). In silico simulations reveal that RYR distribution affects the dynamics of calcium release in cardiac myocytes. *J. Gen. Physiol.* 153:e202012685. doi: 10.1085/jgp.202012685

Janicek, R., Zahradnikova, A. Jr., Polakova, E., Pavelkova, J., and Zahradnik, I. (2012). Calcium spike variability in cardiac myocytes results from activation of small cohorts of ryanodine receptor 2 channels. *J. Physiol.* 590, 5091–5106. doi: 10.1113/jphysiol.2012.234823

Jayasinghe, I., Clowsley, A. H., Lin, R., Lutz, T., Harrison, C., Green, E., et al. (2018). True molecular scale visualization of variable clustering properties of ryanodine receptors. *Cell Rep.* 22, 557–567. doi: 10.1016/j.celrep.2017.12.045

Kolstad, T. R., van den Brink, J., MacQuaide, N., Lunde, P. K., Frisk, M., Aronsen, J. M., et al. (2018). Ryanodine receptor dispersion disrupts Ca(2+) release in failing cardiac myocytes. *eLife* 7:e39427. doi: 10.7554/eLife.39427

Kraskov, A., Stogbauer, H., and Grassberger, P. (2004). Estimating mutual information. *Phys. Rev. E* 69:066138. doi: 10.1103/Physreve.69.066138

Kubalova, Z., Terentyev, D., Viatchenko-Karpinski, S., Nishijima, Y., Gyorke, I., Terentyeva, R., et al. (2005). Abnormal intrastore calcium signaling in chronic heart failure. *Proc. Natl. Acad. Sci. U.S.A.* 102, 14104–14109. doi: 10.1073/pnas.0504298102

Kunze, D. L., Lacerda, A. E., and Wilson, D. L. (1985). Cardiac Na currents and the inactivating, reopening, and waiting properties of single cardiac Na channels. *J. Gen. Physiol.* 86, 691–719. doi: 10.1085/jgp.86.5.691

Laver, D. R., Baynes, T. M., and Dulhunty, A. F. (1997). Magnesium inhibition of ryanodine-receptor calcium channels: evidence for two independent mechanisms. *J. Membr. Biol.* 156, 213–229. doi: 10.1007/s002329900202

Lehnart, S. E., Wehrens, X. H., Laitinen, P. J., Reiken, S. R., Deng, S. X., Cheng, Z., et al. (2004). Sudden death in familial polymorphic ventricular tachycardia associated with calcium release channel (ryanodine receptor) leak. *Circulation* 109, 3208–3214. doi: 10.1161/01.CIR.0000132472.98675.EC

Li, J., Imtiaz, M. S., Beard, N. A., Dulhunty, A. F., Thorne, R., vanHelden, D. F., et al. (2013). ss-Adrenergic stimulation increases RyR2 activity via intracellular Ca2+ and Mg2+ regulation. *PLoS One* 8:e58334. doi: 10.1371/journal.pone.0058334

Li, P., and Chen, S. R. (2001). Molecular basis of Ca(2)+ activation of the mouse cardiac Ca(2)+ release channel (ryanodine receptor). *J. Gen. Physiol.* 118, 33–44. doi: 10.1085/jgp.118.1.33

Lukyanenko, V., Gyorke, I., Subramanian, S., Smirnov, A., Wiesner, T. F., and Gyorke, S. (2000). Inhibition of Ca(2+) sparks by ruthenium red in permeabilized rat ventricular myocytes. *Biophys. J.* 79, 1273–1284. doi: 10.1016/S0006-3495(00)76381-8

Lukyanenko, V., and Gyorke, S. (1999). Ca2+ sparks and Ca2+ waves in saponin-permeabilized rat ventricular myocytes. *J. Physiol.* 521(Pt 3), 575–585. doi: 10.1111/j.1469-7793.1999.00575.x

Lukyanenko, V., Viatchenko-Karpinski, S., Smirnov, A., Wiesner, T. F., and Gyorke, S. (2001). Dynamic regulation of sarcoplasmic reticulum Ca(2+) content and release by luminal Ca(2+)-sensitive leak in rat ventricular myocytes. *Biophys. J.* 81, 785–798. doi: 10.1016/S0006-3495(01)75741-4

Macquaide, N., Tuan, H. T., Hotta, J., Sempels, W., Lenaerts, I., Holemans, P., et al. (2015). Ryanodine receptor cluster fragmentation and redistribution in persistent atrial fibrillation enhance calcium release. *Cardiovasc. Res.* 108, 387–398. doi: 10.1093/cvr/cvv231

MacQueen, J. (1967). "Some methods for classification and analysis of multivariate observations," in *Proceedings of the Fifth Berkeley Symposium on Mathematical Statistics and Probability*, eds L. M. Le Cam and J. Neyman (Berkeley: University of California Press).

Marx, S. O., Reiken, S., Hisamatsu, Y., Jayaraman, T., Burkhoff, D., Rosemblit, N., et al. (2000). PKA phosphorylation dissociates FKBP12.6 from the calcium release channel (ryanodine receptor): defective regulation in failing hearts. *Cell* 101, 365–376. doi: 10.1016/s0092-8674(00)80847-8

Matveev, V., Sherman, A., and Zucker, R. S. (2002). New and corrected simulations of synaptic facilitation. *Biophys. J.* 83, 1368–1373. doi: 10.1016/S0006-3495(02)73907-6

McKinney, W. (2010). "Data structures for statistical computing in python," in *Proceedings of the 9th Python in Science Conference*, Austin, TX.

Meissner, G. (1994). Ryanodine receptor/Ca2+ release channels and their regulation by endogenous effectors. *Annu. Rev. Physiol.* 56, 485–508. doi: 10.1146/annurev.ph.56.030194.002413

Meissner, G. (2004). Molecular regulation of cardiac ryanodine receptor ion channel. *Cell Calcium* 35, 621–628. doi: 10.1016/j.ceca.2004.01.015

Munro, M. L., van Hout, I., Aitken-Buck, H. M., Sugunesegran, R., Bhagwat, K., Davis, P. J., et al. (2021). Human atrial fibrillation is not associated with remodeling of ryanodine receptor clusters. *Front. Cell Dev. Biol.* 9:633704. doi: 10.3389/fcell.2021.633704

Naraghi, M., and Neher, E. (1997). Linearized buffered Ca2+ diffusion in microdomains and its implications for calculation of [Ca2+] at the mouth of a calcium channel. *J. Neurosci.* 17, 6961–6973. doi: 10.1523/JNEUROSCI.17-18-06961.1997

Newville, M., Stensitzki, T., Allen, D. B., and Ingargiola, A. (2014). *LMFIT: Non-Linear Least-Square Minimization and Curve-Fitting for Python*. San Francisco, CA: GitHub.

Niggli, E., and Shirokova, N. (2007). A guide to sparkology: the taxonomy of elementary cellular Ca2+ signaling events. *Cell Calcium* 42, 379–387. doi: 10.1016/j.ceca.2007.02.010

Okuda, S., Sufu-Shimizu, Y., Kato, T., Fukuda, M., Nishimura, S., Oda, T., et al. (2018). CaMKII-mediated phosphorylation of RyR2 plays a crucial role in aberrant Ca(2+) release as an arrhythmogenic substrate in cardiac troponin T-related familial hypertrophic cardiomyopathy. *Biochem. Biophys. Res. Commun.* 496, 1250–1256. doi: 10.1016/j.bbrc.2018.01.181

Parks, R. J., and Howlett, S. E. (2012). H-89 decreases the gain of excitation-contraction coupling and attenuates calcium sparks in the absence of beta-adrenergic stimulation. *Eur. J. Pharmacol.* 691, 163–172. doi: 10.1016/j.ejphar.2012.07.012

Pedregosa, F., Varoquaux, G., Gramfort, A., Michel, V., Thirion, B., Grisel, O., et al. (2011). Scikit-learn: machine learning in python. *J. Mach. Learn. Res.* 12, 2825–2830. doi: 10.1080/13696998.2019.1666854

Permyakov, E. A., Ostrovsky, A. V., and Kalinichenko, L. P. (1987). Stopped-flow kinetic studies of Ca(II) and Mg(II) dissociation in cod parvalbumin and bovine alpha-lactalbumin. *Biophys. Chem.* 28, 225–233. doi: 10.1016/0301-4622(87)80093-5

Petrovic, P., Valent, I., Cocherova, E., Pavelkova, J., and Zahradnikova, A. (2015). Ryanodine receptor gating controls generation of diastolic calcium waves in cardiac myocytes. *J. Gen. Physiol.* 145, 489–511. doi: 10.1085/jgp.201411281

Rosenfeld, S. S., and Taylor, E. W. (1985). Kinetic studies of calcium and magnesium binding to troponin C. *J. Biol. Chem.* 260, 242–251.

Rousseau, E., Smith, J. S., Henderson, J. S., and Meissner, G. (1986). Single channel and 45 Ca2+ flux measurements of the cardiac sarcoplasmic reticulum calcium channel. *Biophys. J.* 50, 1009–1014. doi: 10.1016/s0006-3495(86)83543-3

Ruiz-Hurtado, G., Li, L., Fernandez-Velasco, M., Rueda, A., Lefebvre, F., Wang, Y., et al. (2015). Reconciling depressed Ca2+ sparks occurrence with enhanced RyR2 activity in failing mice cardiomyocytes. *J. Gen. Physiol.* 146, 295–306. doi: 10.1085/jgp.201511366

Shang, W., Lu, F., Sun, T., Xu, J., Li, L. L., Wang, Y., et al. (2014). Imaging Ca2+ nanosparks in heart with a new targeted biosensor. *Circ. Res.* 114, 412–420. doi: 10.1161/CIRCRESAHA.114.302938

Shannon, C. E. (1948). A mathematical theory of communication. *Bell Syst. Tech. J.* 27, 379–423. doi: 10.1002/j.1538-7305.1948.tb01338.x

Smith, G. D., Keizer, J. E., Stern, M. D., Lederer, W. J., and Cheng, H. (1998). A simple numerical model of calcium spark formation and detection in cardiac myocytes. *Biophys. J.* 75, 15–32. doi: 10.1016/S0006-3495(98)77491-0

Soeller, C., Crossman, D., Gilbert, R., and Cannell, M. B. (2007). Analysis of ryanodine receptor clusters in rat and human cardiac myocytes. *Proc. Natl. Acad. Sci. U.S.A.* 104, 14958–14963. doi: 10.1073/pnas.0703016104

Steele, D. S., and Duke, A. M. (2007). Defective Mg2+ regulation of RyR1 as a causal factor in malignant hyperthermia. *Arch. Biochem. Biophys.* 458, 57–64. doi: 10.1016/j.abb.2006.03.001

Stern, M. D. (1992). Theory of excitation - contraction coupling in cardiac muscle. *Biophys. J.* 63, 497–517. doi: 10.1016/s0006-3495(92)81615-6

Stern, M. D., and Cheng, H. (2004). Putting out the fire: what terminates calcium-induced calcium release in cardiac muscle? *Cell Calcium* 35, 591–601. doi: 10.1016/j.ceca.2004.01.013

Storn, R., and Price, K. (1997). Differential evolution - A simple and efficient heuristic for global optimization over continuous spaces. *J. Glob. Optim.* 11, 341–359. doi: 10.1023/A:1008202821328

Tencerova, B., Zahradnikova, A., Gaburjakova, J., and Gaburjakova, M. (2012). Luminal Ca2+ controls activation of the cardiac ryanodine receptor by ATP. *J. Gen. Physiol.* 140, 93–108. doi: 10.1085/jgp.201110708

Valent, I., Zahradnikova, A., Pavelkova, J., and Zahradnik, I. (2007). Spatial and temporal Ca2+, Mg2+, and ATP2- dynamics in cardiac dyads during calcium release. *Biochim. Biophys. Acta* 1768, 155–166. doi: 10.1016/j.bbamem.2006.08.020

Virtanen, P., Gommers, R., Oliphant, T. E., Haberland, M., Reddy, T., Cournapeau, D., et al. (2020). SciPy 1.0: fundamental algorithms for scientific computing in Python. *Nat. Methods* 17, 261–272. doi: 10.1038/s41592-019-0686-2

Walker, M. A., Kohl, T., Lehnart, S. E., Greenstein, J. L., Lederer, W. J., and Winslow, R. L. (2015). On the adjacency matrix of RyR2 cluster structures. *PLoS Comput. Biol.* 11:e1004521. doi: 10.1371/journal.pcbi.1004521

Wang, S. Q., Stern, M. D., Rios, E., and Cheng, H. (2004). The quantal nature of Ca2+ sparks and in situ operation of the ryanodine receptor array in cardiac cells. *Proc. Natl. Acad. Sci. U.S.A.* 101, 3979–3984. doi: 10.1073/pnas.0306157101

Xu, L., Mann, G., and Meissner, G. (1996). Regulation of cardiac Ca2+ release channel (ryanodine receptor) by Ca2+, H+, Mg2+, and adenine nucleotides under normal and simulated ischemic conditions. *Circ. Res.* 79, 1100–1109. doi: 10.1161/01.res.79.6.1100

Yin, L., Zahradnikova, A. Jr., Rizzetto, R., Boncompagni, S., Rabesahala de Meritens, C., et al. (2021). Impaired binding to Junctophilin-2 and nanostructural alteration in CPVT mutation. *Circ. Res.* 129, e35–e52. doi: 10.1161/CIRCRESAHA.121.319094

Zahradnik, I., Gyorke, S., and Zahradnikova, A. (2005). Calcium activation of ryanodine receptor channels–reconciling RyR gating models with tetrameric channel structure. *J. Gen. Physiol.* 126, 515–527. doi: 10.1085/jgp.200509328

Zahradnikova, A. Jr., Polakova, E., Zahradnik, I., and Zahradnikova, A. (2007). Kinetics of calcium spikes in rat cardiac myocytes. *J. Physiol.* 578(Pt 3), 677–691. doi: 10.1113/jphysiol.2006.117796

Zahradnikova, A., Dura, M., Gyorke, I., Escobar, A. L., Zahradnik, I., and Gyorke, S. (2003). Regulation of dynamic behavior of cardiac ryanodine receptor by Mg2+ under simulated physiological conditions. *Am. J. Physiol.* 285, C1059–C1070. doi: 10.1152/ajpcell.00118.2003

Zahradnikova, A., Iaparov, B., and Zahradnik, I. (2020). The problem of accuracy in single-channel open probability measurements. *Prog. Biophys. Mol. Biol.* 157, 94–106. doi: 10.1016/j.pbiomolbio.2020.05.002

Zahradnikova, A., Valent, I., and Zahradnik, I. (2010). Frequency and release flux of calcium sparks in rat cardiac myocytes: a relation to RYR gating. *J. Gen. Physiol.* 136, 101–116. doi: 10.1085/jgp.200910380

Zahradnikova, A., and Zahradnik, I. (2012). Construction of calcium release sites in cardiac myocytes. *Front. Physiol.* 3:322. doi: 10.3389/fphys.2012.00322

Zahradnikova, A., Zahradnik, I., Gyorke, I., and Gyorke, S. (1999). Rapid activation of the cardiac ryanodine receptor by submillisecond calcium stimuli. *J. Gen. Physiol.* 114, 787–798. doi: 10.1085/jgp.114.6.787

Zhang, J., Shettigar, V., Zhang, G. C., Kindell, D. G., Liu, X., Lopez, J. J., et al. (2011). Engineering Parvalbumin for the Heart: optimizing the Mg binding properties of rat beta-Parvalbumin. *Front. Physiol.* 2:77. doi: 10.3389/fphys.2011.00077

Conflict of Interest: The authors declare that the research was conducted in the absence of any commercial or financial relationships that could be construed as a potential conflict of interest.

frontiers
in Physiology

REVIEW
published: 22 February 2022
doi: 10.3389/fphys.2022.841740

Tuning the Consonance of Microscopic Neuro-Cardiac Interactions Allows the Heart Beats to Play Countless Genres

Mauro Franzoso[1], Lolita Dokshokova[1], Libero Vitiello[2], Tania Zaglia[1] and Marco Mongillo[1]**

[1]Department of Biomedical Sciences, University of Padova, Padova, Italy, [2]Department of Biology, University of Padova, Padova, Italy

Edited by:
Nina D. Ullrich,
Heidelberg University, Germany

Reviewed by:
Crystal M. Ripplinger,
University of California,
Davis, United States
Nazareno Paolocci,
Johns Hopkins University,
United States

****Correspondence:***
Marco Mongillo
marco.mongillo@unipd.it
Tania Zaglia
tania.zaglia@unipd.it

Specialty section:
This article was submitted to
Striated Muscle Physiology,
a section of the journal
Frontiers in Physiology

Received: *22 December 2021*
Accepted: *01 February 2022*
Published: *22 February 2022*

Citation:
Franzoso M, Dokshokova L, Vitiello L, Zaglia T and Mongillo M (2022) Tuning the Consonance of Microscopic Neuro-Cardiac Interactions Allows the Heart Beats to Play Countless Genres. Front. Physiol. 13:841740. doi: 10.3389/fphys.2022.841740

Different from skeletal muscle, the heart autonomously generates rhythmic contraction independently from neuronal inputs. However, speed and strength of the heartbeats are continuously modulated by environmental, physical or emotional inputs, delivered by cardiac innervating sympathetic neurons, which tune cardiomyocyte (CM) function, through activation of β-adrenoceptors (β-ARs). Given the centrality of such mechanism in heart regulation, β-AR signaling has been subject of intense research, which has reconciled the molecular details of the transduction pathway and the fine architecture of cAMP signaling in subcellular nanodomains, with its final effects on CM function. The importance of mechanisms keeping the elements of β-AR/cAMP signaling in good order emerges in pathology, when the loss of proper organization of the transduction pathway leads to detuned β-AR/cAMP signaling, with detrimental consequences on CM function. Despite the compelling advancements in decoding cardiac β-AR/cAMP signaling, most discoveries on the subject were obtained in isolated cells, somehow neglecting that complexity may encompass the means in which receptors are activated in the intact heart. Here, we outline a set of data indicating that, in the context of the whole myocardium, the heart orchestra (CMs) is directed by a closely interacting and continuously attentive conductor, represented by SNs. After a roundup of literature on CM cAMP regulation, we focus on the unexpected complexity and roles of cardiac sympathetic innervation, and present the recently discovered Neuro-Cardiac Junction, as the election site of "SN-CM" interaction. We further discuss how neuro-cardiac communication is based on the combination of extra- and intra-cellular signaling micro/nano-domains, implicating neuronal neurotransmitter exocytosis, β-ARs and elements of cAMP homeostasis in CMs, and speculate on how their dysregulation may reflect on dysfunctional neurogenic control of the heart in pathology.

Keywords: cardiomyocytes, sympathetic neurons, neuro-cardiac junction, signaling nanodomains, β-adrenoceptor, neuro-cardiac junction

MULTIPLE ROLES OF NEURO-MUSCULAR INNERVATION

It is well-established that cardiac and skeletal muscles are "striated muscles," made for a large part of contractile cells [e.g., cardiomyocytes (CMs) and myofibers, respectively] which, although sharing the ability to contract, possess distinctive features. If we consider cell morphology, myofibers are tapered cells, with varied length depending on the muscle type (from about 7–40 mm), while CMs are smaller in size (average longitudinal and transversal diameters are about 150 and 30 mm, respectively), with a rod-shaped morphology (Adams and Schwartz, 1980). Additionally, while contraction is underlain, in both muscles, by the serial arrangement of sarcomeres along the cellular matrix, substrates of cell shortening, including sarcolemma, transverse-tubules (T-tubules), sarcoplasmic reticulum (SR), as well as mechanisms regulating contraction [mostly modulation of intracellular (Ca^{2+})], are muscle-type specific (Adams and Schwartz, 1980). Furthermore, it has been long known that, while skeletal muscles retain the ability to regenerate upon tissue damage, thanks to the presence of the satellite cells (Tedesco et al., 2010), the myocardium is a post-mitotic tissue and the irreversible exit of CMs from cell cycle makes the heart extremely vulnerable to damage (Lafontant and Field, 2006).

It is unquestioned that skeletal muscle contraction, finalized to voluntary movements, initiates upon the neurogenic input provided by the innervating motor neuron (MN), which releases acetylcholine at the Neuro-Muscular Junction (NMJ), a well-characterized neuromuscular synapse (Ruff, 2003). Differently, cardiac blood propulsion occurs independently from innervation, as the myocardium homes specialized cells, able to spontaneously generate repeated action potentials, which are organized into the conduction system and dictate the basal heart rhythm (His, 1949; DiFrancesco, 1995). Such difference is manifested by the continued rhythmic contractions of an explanted heart, when supplied with oxygen and nutrients, and well-exemplified by heart transplants which, although the organ is disconnected from central neurons, allow survival of many patients suffering from complex cardiovascular diseases (Scalco et al., 2021). In the physiologic heart, however, function is continuously modulated to meet the perfusional demands of the organism, both during daily activities and stresses, and such fundamental adaptation, encompassing both increased heart rate (i.e., chronotropic effect) and contractile force (i.e., inotropic effect), is mostly dependent on the activity of noradrenaline-releasing cardiac sympathetic neurons (Zaglia and Mongillo, 2017).

The roles of neurogenic components in skeletal and cardiac muscle physiology have somewhat settled with a simplified view, classifying MNs as the nervous activators of skeletal muscles, and autonomic neurons solely as heart modulators. Recent research, in both myology and cardiology, has, however, brought to light novel roles of sympathetic neurons (SNs) in both fields, blurring the divide between skeletal and cardiac muscle innervation. While SNs were identified several years ago, in anatomic studies, to account for a significant fraction of the neuronal types in nerves directed to hindlimb muscles (Straka et al., 2018; Di Bona et al., 2020), their initial role was restricted to the regulation of muscle blood vessel diameter, which is coherent with the adaptative response to physical exercise (Lombard and Cowley, 2012). Nonetheless, several recent reports, using refined imaging methods and pharmacologic approaches, have shown that SNs interact with muscle fibers and play initially unsuspected functions, ranging from the modulation of synaptic transmission between MNs and muscle cells, to the maintenance of morphological and functional stability of the NMJ (Khan et al., 2016; Straka et al., 2018, 2021). In addition, noradrenaline stimulation of muscle fibers leads to increase in contraction force, *via* PKA activation, and subsequent phosphorylation of downstream targets, involved in the mechanism of cell shortening (i.e., L-type Ca^{2+} channels; ryanodine receptors; Cairns and Dulhunty, 1993; Röder et al., 2009; Rudolf et al., 2013; Khan et al., 2016; Straka et al., 2021). Furthermore, noradrenaline release by muscle-innervating SNs regulates myocyte trophism, through activation of β2-adrenoceptors (β2-ARs), which modulate protein degradation, by negatively impinging on the expression of atrophic gene patterns (Navegantes et al., 2004; Rudolf et al., 2013). All of these effects, initially attributed to the trophic function of MNs, have brought light back to the sympathetic component of motor nerves, and established that skeletal muscle cells receive neurogenic input from two parallel and distinct systems, underlaying contraction (MNs), on the one hand, and functional and structural modulation (SNs), on the other.

Interestingly, parallel studies of neurogenic control of the heart have extended the role of sympathetic innervation beyond the confines of the stress response, coming into play only when more cardiac output is needed (i.e., fight-or-flight reaction, hemodynamic, or emotional stresses). Indeed, we and others have demonstrated that cardiac sympathetic innervation has additional constitutive functions, which include control of heart rate on a beat-to-beat basis (Zaza et al., 1991; Zaglia and Mongillo, 2017), and activation of signaling pathways regulating CM division, trophism and electrophysiological properties (Ogawa et al., 1992; Kanevskij et al., 2002; O'Connell et al., 2003; Zaglia et al., 2013; Kreipke and Birren, 2015; Pianca et al., 2019). As example, we identified that SN-dependent activation of CM β2-ARs is required to maintain the correct cardiac mass, by inhibiting protein degradation *via* the β2-AR/Akt/FOXO/ubiquitin ligase pathway, with a mechanism very similar to that active in skeletal muscles (Zaglia et al., 2013; Zaglia and Mongillo, 2017).

Such evidence supports that, while cardiac and skeletal muscles are unquestionably different for phenotypic and functional aspects, they are not so dissimilar with regards to the relationship with sympathetic nervous components. At this point, it is inevitable to think that a fundamental difference in the way skeletal and cardiac muscle interact with neurons is given by the structures underlaying such interactions. In fact, it has been known for a long time that MNs signal to

---

Abbreviations: β-AR, β-AdrenoReceptor; CM, CardioMyocyte; cSN, cardiac Sympathetic Neuron; GPCR, G-Protein Coupled Receptors; HF, Heart Failure; MN, Motor Neuron; NCJ, Neuro-Cardiac Junction; NMJ, Neuro-Muscular Junction; SN, Sympathetic Neuron; SR, Sarcoplasmic Reticulum; TH, Tyrosine Hydroxylase; T-tubules, Transverse-tubules.

the innervated fiber in a synaptic way, thanks to the NMJ (Acheson, 1948; Welsh, 1948; Del Castillo and Katz, 1956). The myocardium is instead considered orphan of synaptic contacts, and the common perception was that SNs activate CM β-ARs through noradrenaline which, once released, diffuses into the myocardial interstitium (Zaglia and Mongillo, 2017). In contrast with this model, our group recently demonstrated that also in the heart, neurogenic control of the myocardium is expressed thanks to the existence of structured intercellular interactions, called Neuro-Cardiac Junctions (NCJs), allowing SNs to communicate with target CMs in a synaptic fashion (Prando et al., 2018). Although the molecules building the NCJ are, at the time being, only scarcely identified, and may be different from those forming the NMJ (Shcherbakova et al., 2007; Prando et al., 2018), the final effect of both the NMJ and the NCJ is to ensure optimal efficiency in the neuro-muscular intercellular communication.

Starting from these base notes, this review will focus on the communication occurring between the single SN varicosity and the target CM, operating through intracellular and extracellular signaling microdomains, using the skeletal muscle and the NMJ as a benchmark. Furthermore, starting from the fine characterization of the NMJ structure, we will present a roundup of the literature identifying the molecular bricks which build the NCJ.

INTRACELLULAR COMPARTMENTATION OF β-ADRENOCEPTOR SIGNALING IN CARDIOMYOCYTES

As stated above, although the process of excitation-contraction coupling occurs in CMs independently from neuronal inputs, heart function is continuously adapted to precisely match the organism requests. Such adaptation results from the integration, by the central nervous system, of signals from peripheral sensors of homeostatic (i.e., blood pressure, pH, osmolarity, and temperature), sensory (environmental) and emotional (intrinsic) inputs, and routed to the heart through afferences of the autonomic nervous system (Scalco et al., 2021). Neurogenic release of noradrenaline activates adrenoreceptors (ARs), which, in CMs, are mostly the β-subtypes, increasing intracellular (cAMP) *via* receptor-associated Adenylyl Cyclases. Ignition of the β-AR/cAMP pathway is, by no doubts, the mainspring of cardiac "fight-or-flight" reaction, ultimately causing positive chronotropic, lusitropic and inotropic effects, mostly through PKA-dependent phosphorylation of sarcomeric proteins and molecular players regulating Ca^{2+} dynamics (Li et al., 2000; Bers, 2002; Eisner et al., 2017). While such mechanisms have been described few decades ago, and acknowledged thereafter, the notion that β-ARs belong to the large family of G-protein coupled receptors (GPCR), many of which share the same type of G-protein and second messenger, has soon opened the question (broadly applicable to signaling biology in any cell type) of specificity of receptor responses. In other words, "how can CMs activate the proper response to a selective receptor stimulation (e.g., β1- vs. β2-AR), if signaling is transduced by the same second messenger (i.e., cAMP) shared with many other receptor types, eliciting different, and sometimes opposed, biological responses?"

In this context, seminal studies elegantly showed that activation of β-ARs in one side of the cell led to local enhancement of cAMP sensitive Ca^{2+} currents on the same cell portion, demonstrating the concept of compartmentalization of β-AR/cAMP signaling (Jurevičius and Fischmeister, 1996). The initial view of signal transduction as a linear chain of biochemical events, initiated from the plasma membrane and reaching all intracellular effector(s), was thus gradually shifted to a model whereby membrane receptors signal to a fraction of selected intracellular targets in their proximity, or partitioned in defined cellular regions (Steinberg and Brunton, 2001). Progress in biotechnology soon allowed deeper insight into these mechanisms, thanks to the development of biosensors enabling to monitor changes of (cAMP) in real-time, with high spatial resolution, in living cells. Use of early-generation, genetically encoded, cAMP biosensors showed that β-AR activation led to cAMP elevations in multiple discrete microdomains in cultured CMs, displaying in the living cell the concept of compartmentalized signaling (Zaccolo and Pozzan, 2002; Surdo et al., 2017). Subsequent studies demonstrated that local regulation of the second messenger within the cell results from the combination of different factors, including the cellular localization and activity of specific families of cAMP degrading enzymes, i.e., phosphodiesterases, physical barriers to cAMP diffusion and its buffering by PKA, altogether shaping the spatial distribution and kinetics of cAMP fluctuations, and its access to the intracellular targets (Zaccolo and Pozzan, 2002; Mongillo et al., 2004, 2006; Fischmeister et al., 2006; Saucerman et al., 2006; Vandecasteele et al., 2006; Soto et al., 2009). A relevant example of how spatial organization of cAMP responses reflects the stimulation of a specific receptor subtype comes from the study of Nikolaev et al. showing, in murine CMs, that β1- or β2-AR agonism elicits increases in cAMP which spread throughout the entire cytoplasm, or remain localized at the level of T-tubuli, respectively (Nikolaev et al., 2006). In incremental developments, the now-accepted concept of compartmentalization of cAMP has been delved into with increasing precision and detail, thanks to an extended toolkit of diverse cAMP and PKA biosensors, with enhanced sensitivity, or targeted to specific subcellular compartments, and the combination with strategies for local delivery of extracellular stimuli, subcellular uncaging of cAMP analogs or targeted Adenylyl Cyclases (Schleicher and Zaccolo, 2018; Ghigo and Mika, 2019). It is now well appreciated that specifically distributed Adenylyl Cyclases (that make cAMP) and specific phosphodiesterase isoforms (that degrade cAMP) are selectively localized in different cellular domains (Bers et al., 2019), including the plasma membrane, SR, nucleus and mitochondria (Mongillo and Zaccolo, 2006; Leroy et al., 2008; Mika et al., 2012; Stangherlin and Zaccolo, 2012; Bedioune et al., 2018; Ghigo and Mika, 2019). Such molecular arrangement is an uttermost factor allowing the same signaling molecule (cAMP) to control both the thundering effect of the "fight-or-flight" reaction and, independently, gene expression, mitochondrial dynamics or other subdued homeostatic processes (Mongillo et al., 2004, 2006; Saucerman et al., 2006; Nikolaev et al., 2010; Sample et al., 2012; Tsvetanova and von Zastrow, 2014; Li et al., 2015; Bers et al., 2019; Naim et al., 2019; Zaccolo et al., 2021; **Figure 1**).

Collective evidence from the studies on cAMP is that the second messenger dynamics and intracellular targets are regulated in a way far more complex than initially expected. Studies using targeted versions of cAMP sensors suggest that selective modulation of cAMP signaling may take place in confined sub-microscopic domains. The tight spatial regulation of cAMP gradients, and the specific localization of intracellular targets (e.g., PKA, Epac) and signal regulators (e.g., phosphodiesterases, protein phosphatases) have been shown to impact on the downstream effect of receptor activation (Zakhary et al., 2000; Rehmann et al., 2006). Adding to such complexity, recent advances, based on the integration of *in vitro* experiments and numerical modeling, show that, in addition to the amplitude and localization of the cAMP signal, its kinetics may result in unexpected effects, not entirely correlated to the second messenger concentration (Bers et al., 2019). In detail, activation of PKA, at precise subcellular compartments, reflects the potency and duration of β-AR stimulation with a non-linear dose/effect relationship, so that at lower level of β-AR activation, inotropy is enhanced, while recruitment of additional lusitropic benefit only occurs at higher β-AR activation levels (Bers et al., 2019). Of note, subsynaptic and sarcomeric cAMP/PKA microdomains have been described also in the skeletal muscle, where noradrenaline mainly activates β2-ARs with a predominant effect on gene activation (Röder et al., 2009; Rudolf et al., 2013).

Given the complex and meticulous regulation of the β-AR signaling pathway, which holds a fundamental role in heart physiology, it is not surprising that disruption of the fine space–time organization of the cAMP signal impacts on the adequate CM response to β-AR stimulation. Consistently, results from several studies, in both human and rodents, demonstrate that CMs from failing hearts feature dysregulation in β-AR/cAMP signaling, characterized by desensitization/downregulation of β-ARs, reduced cAMP synthesis and altered phosphorylation of the main PKA targets (Lohse et al., 2003; Zaccolo and Movsesian, 2007; Ghigo and Mika, 2019). In addition, by using Scanning Ion Conductance Microscopy, Gorelik and colleagues identified that submicroscopic alterations of cAMP regulation take place in failing heart cells, as result of structural CM changes, i.e., loss of membrane T-tubules (Nikolaev et al., 2010). Data from this and other research groups consistently demonstrated that in failing CMs, βs2-ARs are "uncoupled" from the localized pools of PKA,leroy which are physiologically targeted within the β2-AR/cAMP signaling compartment and, consequently, activation of β2-AR leads, in failing cells, to a wide cAMP propagation pattern similar to that observed in normal CMs upon β1-AR stimulation (Calaghan et al., 2008; Mehel et al., 2013; Schobesberger et al., 2017; **Figure 2**). Given this evidence, molecular tools tailored to restore the normal cAMP nanodomains are expectedly promising therapeutic strategies, applicable in several cardiac pathologies associated to dysfunctional neurogenic control of heart function (Leroy and Fischmeister, 2018).

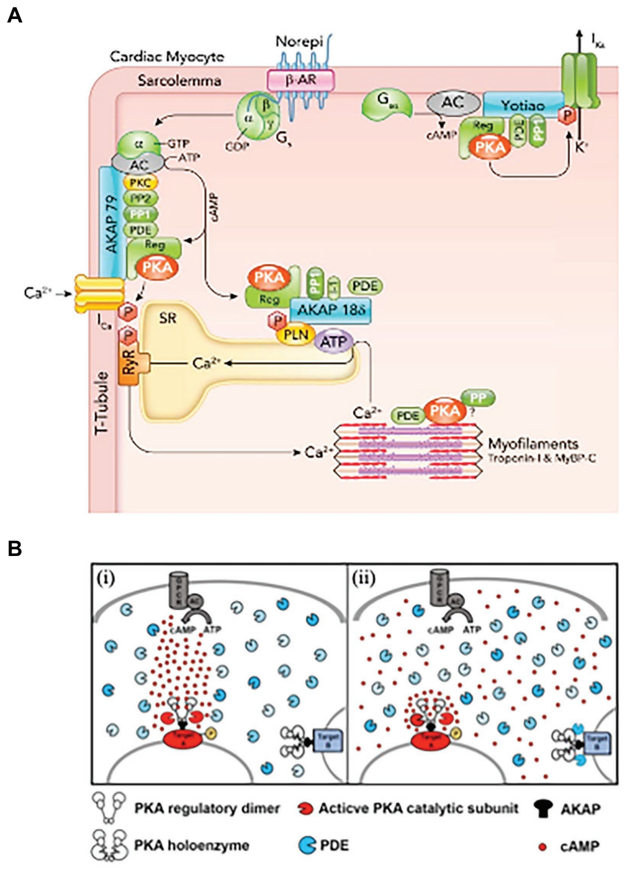

FIGURE 1 | Activation of cardiomyocyte β-adrenoceptors lead to compartmentalized increase in (cAMP). **(A)** β-AR, cAMP, and PKA signaling proteins in cardiomyocytes. β-AR activated by norepinephrine (Norepi) causes adenylyl cyclase (AC) to produce cAMP, which binds the PKA regulatory subunit. Activated PKA can selectively phosphorylate nearby target proteins including sarcolemmal L-type Ca channels, which increases I_{Ca}, SR phospholamban (PLN), which increases SR Ca-ATPase activity, and KCNQ1 to enhance delayed rectifier K^+ current I_{Ks}. PKA is anchored at these three targets by specific AKAPs (A-kinase anchoring proteins), namely AKAP150, AKAP18δ, and Yotiao. These AKAPs also bind additional cAMP-PKA modulators (PP1, PP2, PDEs, and PKC). **(B)** Hypotheses on the mechanisms underlying cAMP compartmentalization. (**i**) Restricted propagation model. On activation of the Gs protein-coupled receptor (GPCR), the adenylyl cyclase (AC) synthetizes cAMP. Phospodiesterases (PDEs), by degrading cAMP, limit its diffusion, directing propagation from the focal point of synthesis to a downstream PKA target (target A), leading to its selective phosphorylation. (**ii**) Nanodomain regulation model. cAMP freely propagates from the site of synthesis at the plasma membrane to the entire cell. PDEs anchored at specific subcellular sites act as a sink for cAMP, maintaining the level of the second messenger below the bulk cytosol and preventing activation of local PKA (exemplified by target B complex). At other sites, the absence of local PDEs and concomitant factors allow for cAMP to accumulate locally at levels higher than bulk cytosol, leading to selective phosphorylation (target A). According to this model, the functional outcome of the cAMP signal is dictated by the local levels of the second messenger in the extremely restricted environment immediately surrounding specific effector/target protein complexes. PDE, shown here in different shades of blue to illustrate the diversity of the multiple isoforms, localize to specific subcellular sites. **(A,B)** Modified with permission from Bers et al. (2019) and Chao et al. (2019).

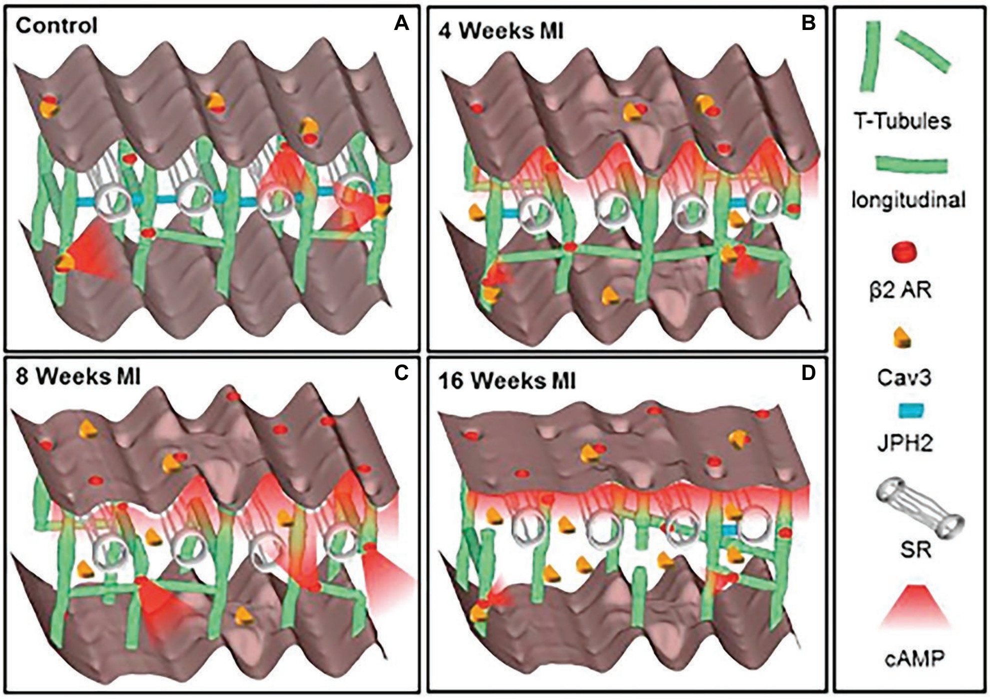

FIGURE 2 | Schematic of the changes in structure and location of β2-ARs during heart failure progression. **(A)** In control CMs the *external* surface structure (Z-grooves and crests) and the *internal* transverse and axial tubules (TAT) network, are intact, and β2-AR are located exclusively on T-tubules, connected with the SR through Junctophilin 2 (JPH2). cAMP does not diffuse far from the site of β2-AR activation, and Caveolin-3 (Cav3) is predominantly on the cell membrane. In heart failure the surface structure deteriorates progressively. **(B)** Four weeks after myocardial infarction, JPH2 is downregulated, and the density of longitudinal elements increases. β2-AR dependent cAMP responses appear at the crest, and cAMP is no longer confined to the site of β2-AR activation. **(C,D)** At later time, the CM surface elements and T-tubule structure further deteriorate, with decreased density of longitudinal element. Notably, inefficient β2-AR dependent AC activation leads to significant reduction in cAMP production. Adapted with permission from Schobesberger et al. (2017).

Altogether, the examples described above support that the spatial and temporal regulation of signaling of one specific GPCR is restricted to tightly organized compartments within the cell and may occur with singular kinetics. This may represent the receptor "signature," allowing its stimulation to distinctively activate the proper and specific biological responses in the target cell.

THE REAPPRAISAL OF THE IDEA OF A "CARDIAC SYMPATHETIC SYNAPSE"

While most studies on cAMP signaling, including those related to the fundamental mechanism underlying cardiac cell response to AR stimulation, have been conducted in cultured isolated cells, exposed to natural or artificial AR agonist, very few have aimed to replicate the conditions in which CMs are activated by SNs in the heart. Given that the complexity of cAMP responses, upon activation of β-ARs, depends on the cellular arrangement of the molecular partners of the signaling cascade, it is predictable that localization of the receptors throughout the heterogeneous cell membrane domains, the fraction—or specific subset—of receptors activated by the agonist, and the kinetics and potency of activation, are all critical players. As consequence, since SNs are the endogenous sources of noradrenaline triggering β-ARs in heart, to infer the implications of intracellular β-AR signaling compartmentation in neurocardiac physiology, the microanatomy of interactions between neurotransmitter-releasing neuronal varicosities and target cells, in the intact heart, must be taken into account.

Post-ganglionic SNs descend from sympathetic ganglia, located along the cervical and thoracic spine, and reach the epicardium along the great vessels, before entering the heart wall and distributing throughout the myocardial interstitium (Franzoso et al., 2016). We and others have shown that SN innervation of the mammalian heart is way denser than commonly expected (Franzoso et al., 2016; Zaglia and Mongillo, 2017; Prando et al., 2018; Pianca et al., 2019; Di Bona et al., 2020). Although the topology of heart innervation is species-specific, a common feature, only recently emerged from studies reconstructing the innervation network with high-resolution imaging, is that each CM is enveloped by multiple neuronal processes, which may belong to different branches of the same neuron, but also to different neurons (Zaglia and Mongillo, 2017; Pianca et al., 2019; **Figure 3A**). Furthermore, given the well-known pearl-necklace morphology of SNs, each process is constituted by regularly distributed enlargements—varicosities—where neurotransmitter vesicles are stored and released from, upon neuronal activation (**Figure 3**).

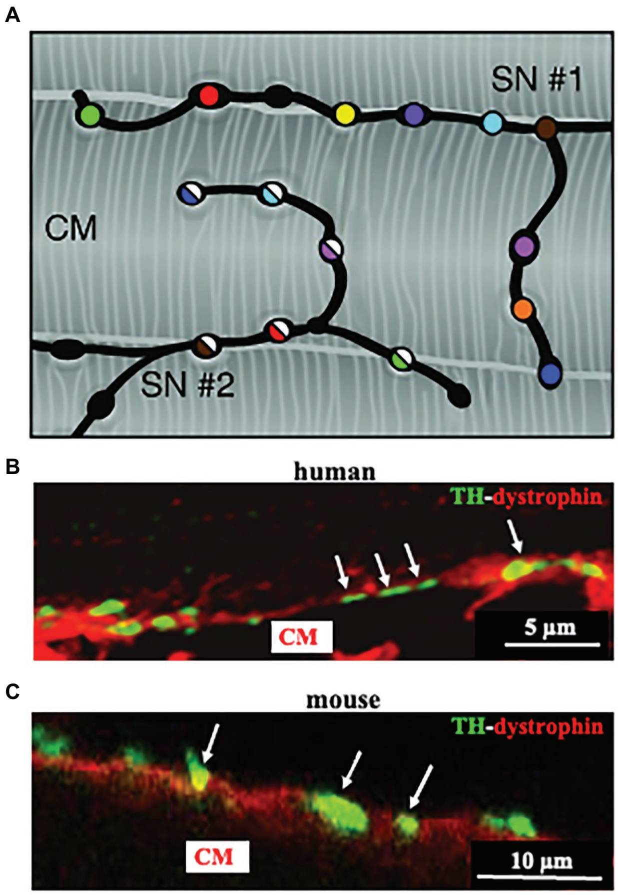

FIGURE 3 | Cardiac sympathetic neurons contact cardiomyocyte membrane at multiples sites. **(A)** Each CM is simultaneously innervated by different neuronal processes (two different processes in the picture are represented by filled or half-filled circles, respectively), all of which are characterized by regularly distributed varicosities, each highlighted by one color. **(B,C)** Confocal immunofluorescence imaging of a thin ventricular section of a normal mouse **(B)**, or human **(C)** heart, stained with antibodies to tyrosine hydroxylase (TH) and dystrophin. Modified with permission from Zaglia and Mongillo (2017) **(A)** Prando et al. (2018) **(B,C)**.

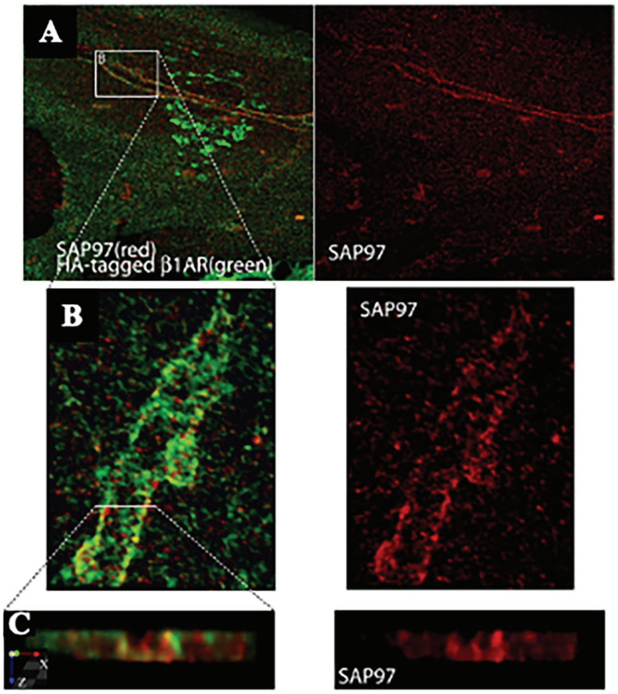

FIGURE 4 | SAP97 and β1-ARs localize to cardiac sympathetic synapses *in vitro*. **(A)** CMs were cocultured with SNs for 7 days, infected with recombinant adenovirus expressing HA-tagged β1-AR, and cultured for an additional 24 h before immunostaining for HA (green) and SAP97 (red). Two-photon image. **(B,C)** Enlargements of the boxed area in **(A)**. Modified with permission from Shcherbakova et al. (2007).

The idea that SN varicosities could establish specific contacts with CMs, structurally analogous to the well-known NMJ, dates back several years, but the initial studies failed to detect structured neuro-muscular contacts in the heart, thus endorsing the model whereby SN neurotransmitters "diffuse in wide gaps between nerve processes and cellular targets" (Fawcett and Selby, 1958; Kisch, 1961; Napolitano et al., 1965; Grillo, 1966). In contrast, other studies identified contacts between "unmyelinated SN processes and the CM surface, and the polarization of neurotransmitter vesicles on the side of neuronal varicosities facing the CM" [for a review on the topic see Di Bona et al. (2020)]. These latter studies surmised that neuromuscular transmission occurred at specific interaction sites, postulating that sympathetic neurotransmitters would therefore act on discrete pools of specialized sub-synaptic receptors, well before discovering the molecular identity of ARs (Baxter and Nisbet, 1963; Trautwein and Uchizono, 1963; Thaemert, 1969; Landis, 1976; Klemm et al., 1992; Choate et al., 1993; Di Bona et al., 2020). These conflicting results may be ascribed to the different species analyzed (amphibians vs. mammals), which show a completely different organization of the cardiac innervation network. Furthermore, the earlier studies suffered the lack of methodologies endowed with sufficient resolution and yield to resolve the relations between small, intermittently displaced parts of tortuous neurons and larger myocyte membranes, in thin heart slices.

Reappraisal of cardiac synapses started a decade ago, when Shcherbakova et al. (2007) using co-cultures between SNs and CMs, detected the formation of specialized cell–cell contacts between neuronal varicosities and CM membranes, characterized by specific organization of the post-junctional cell membrane. Remarkably, such sarcolemmal reorganization included membrane invaginations, accumulation of cadherin-catenin complexes [previously shown to have a critical role in stabilization of central synaptic contacts (Bamji et al., 2003), enrichment in β1-ARs and of the scaffold proteins SAP97 and AKAP79/150 (**Figures 4, 5**; Shcherbakova et al., 2007)]. Some of these aspects were confirmed in intact murine hearts (Shcherbakova et al., 2007). While this evidence supported the existence of a specific junction between SNs and CMs, the differences with the NMJ structural properties were also delineated, including the absence of MuSK, a key player in the organization of the post-synaptic membrane, at the NMJ (Bowen et al., 1998), suggesting therefore

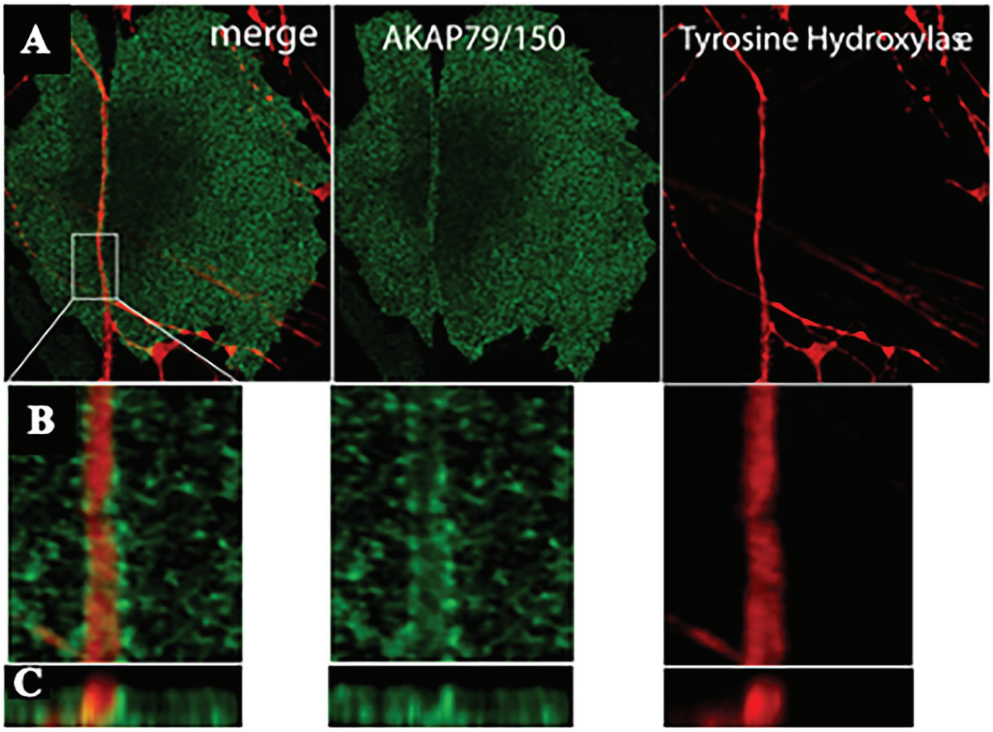

FIGURE 5 | AKAP79/150 accumulates at cardiac sympathetic synapses *in vitro*. **(A)** Colocalization of AKAP79/150 and tyrosine hydroxylase. CMs and SNs were cultured for 7 days and immunostained for tyrosine hydroxylase (red) and AKAP79/150 (green); two-photon image. **(B)** 3D-reconstructed enlarged fragment of the boxed area in **(A)**. **(C)** X-z cross section of the 3D reconstruction. Modified with permission from Shcherbakova et al. (2007).

that sympathetic synapse formation does not involve agrin-MuSK signaling.

Based on these results, the authors speculated that specific signaling domain on the myocyte plasma membrane, underscored by accumulation of the scaffolding components AKAP79/150 and SAP97, would be required for physiologic signaling of ARs in cardiac tissue. Interestingly, such post-synaptic organization has been described to be depauperated of β2-ARs, which are internalized upon neuronal noradrenaline discharge, thus supporting that "the subtype-specific distribution of β1- and β2-ARs relative to sympathetic synapses" could contribute to signaling specificity (Shcherbakova et al., 2007).

About 10 years later, we combined advanced biotechnologies, including cAMP imaging in "SN-CM" co-cultures, and sympathetic neuron optogenetics *in vivo*, to address neuro-cardiac communication and determine whether the effects of direct synaptic contacts, between neurons and CMs, could be addressed functionally. In line with the previous speculations, by monitoring cAMP, we demonstrated that the tight connection between the neuron and CM membrane enables neuro-cardiac communication to occur *via* specific extracellular signaling microdomains, with several implications on cardiac β-AR activation. First, the tight assembly of the NCJ minimizes extra-synaptic noradrenaline diffusion, rendering the neuronal varicosity a point source of noradrenaline, suited to activate therefore a subset of β-ARs, as shown by the formation of intracellular cAMP gradients, in the CM, originating from the neuronal contact site (Prando et al., 2018). Thus, our data supports the concept whereby spatial cAMP regulation is a downstream effect of the activation of a fraction of β-ARs, located in the limited portion of CM membrane, directly innervated by the neuronal varicosity (**Figure 6**). Secondly, the low-volume extracellular signaling domain allows (noradrenaline) to activate the receptor at its k_d with the number of vesicles released even by a single action potential, as demonstrated by the effect on cAMP elevations in culture. This result was consistent with numerical modeling predictions, previously elaborated using geometrical parameters for the synaptic cleft volume and intermembrane space, in accord with the experimentally determined dimensions (Šćepanović, 2011). Together, these experiments support that the establishment of structured contacts, in which neuro-cardiac communication occurs in a synaptic fashion, is functional for the efficiency of neurogenic regulation of heart function, as predicted by Shcherbakova et al. (2007), and confirmed by the rapid and potent effect of SN photostimulation *in vivo* (Prando et al., 2018; **Figure 7**).

Furthermore, with the notion that NCJs represent the fundamental "signaling units" of neuro-cardiac interaction, summation (integration) of inputs from an increasing number of simultaneously activated NCJs may allow heart regulation through a wide range of tones, spanning from the acute activation, during the stressful "fight-or-flight" reaction, to long-lasting effects, crucial for the maintenance of heart homeostasis (Tao et al., 2011; Zaglia et al., 2013; Zaglia and

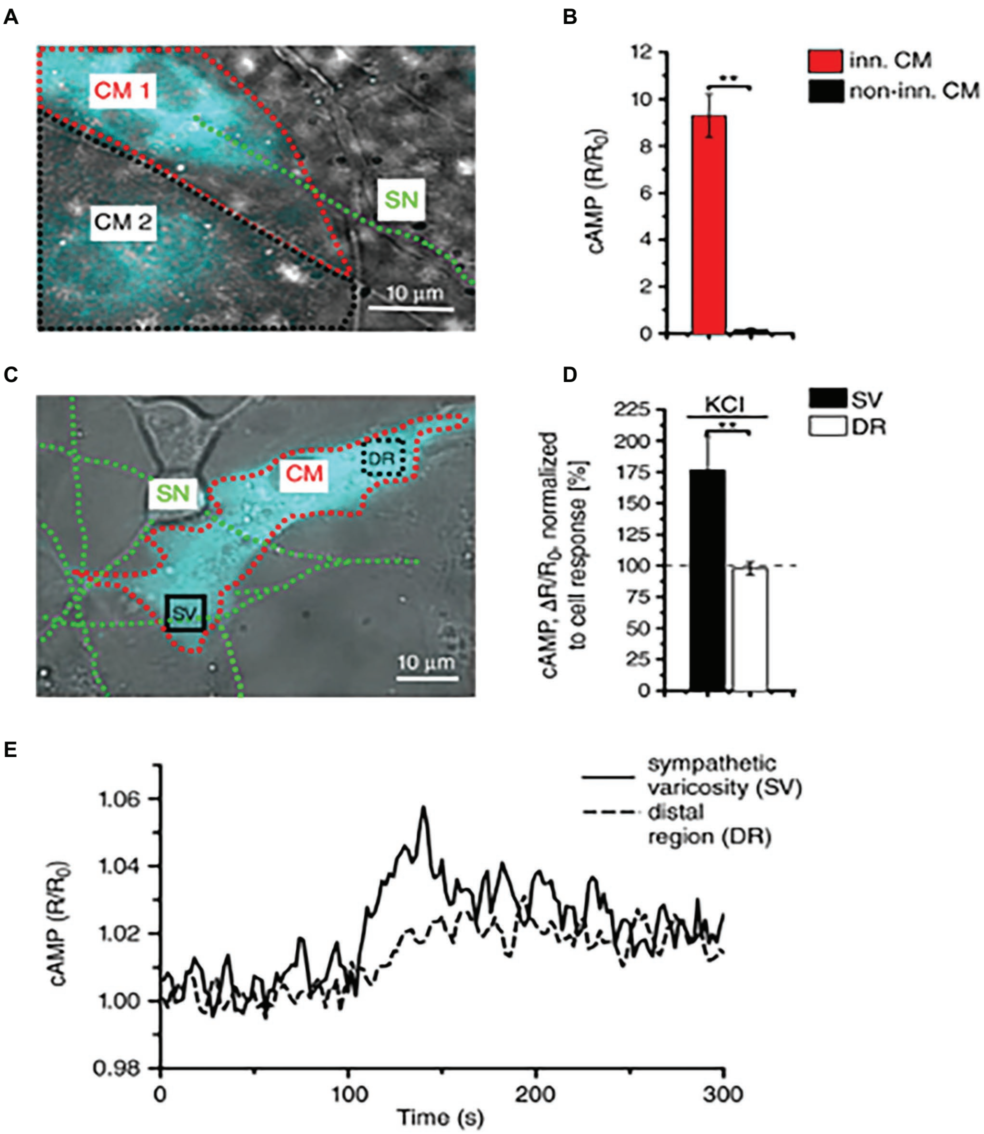

FIGURE 6 | Local activation of cardiomyocytes by innervating neurons. **(A)** Fluorescence image of two adjacent H187-expressing CMs, one of which (CM1, red line) is in direct interaction with a SN (green line), while CM2, highlighted by a black line, is not innervated. **(B)** Statistics of cAMP responses to KCl stimulation of SNs, in innervated vs. non-innervated CMs. Bars indicate SEM (**$p < 0.01$; $n = 70$ CM per group). **(C)** Fluorescence image of a H187-expressing CM innervated by SN processes. cAMP variations were evaluated in the CM delineated by a red line, in regions close to (SV) or far from (DR, distal region) the neurocardiac interaction site. Green line highlights the innervating neuron. **(D)** Statistics of subcellular cAMP variations elicited by neuronal activation in the SV and DR of $n = 36$ CMs with similar neurocardiac arrangements as in **(C)**; bars indicate SEM (**$p < 0.01$). **(E)** Representative trace of cAMP changes calculated in the SV and DR regions of the CM shown in **(C)**. Modified with permission from Prando et al. (2018).

Mongillo, 2017; Bardsley et al., 2018; Prando et al., 2018; Pianca et al., 2019; Burton et al., 2020; Scalco et al., 2021; **Figure 8**). In other words, as each CM forms several junctional sites with SNs, and may therefore receive noradrenaline simultaneously from multiple point sources (a varicosity every 1 or 2 mm), it is tempting to speculate that the number of neurons releasing noradrenaline to the same target CM may determine the degree of adrenergic responses across the wide latitude of physiologic regulation (Zaglia and Mongillo, 2017; **Figures 3A**, **8**).

The picture emerging is that, in intact hearts, neuro-cardiac communication involves extra-cellular (first-messenger) signaling microdomains and intracellular (second messenger) micro/nanodomains which combine to control, with exquisite precision and flexibility, CM responses to SN activation. The appreciation that neuro-cardiac communication occurs in defined extra-cellular spaces, that it involves the stimulation of defined receptor pools, each with singular and dynamic distribution on the cell membrane, and that it reflects on a tightly organized series of specific intracellular actions, allows new inference

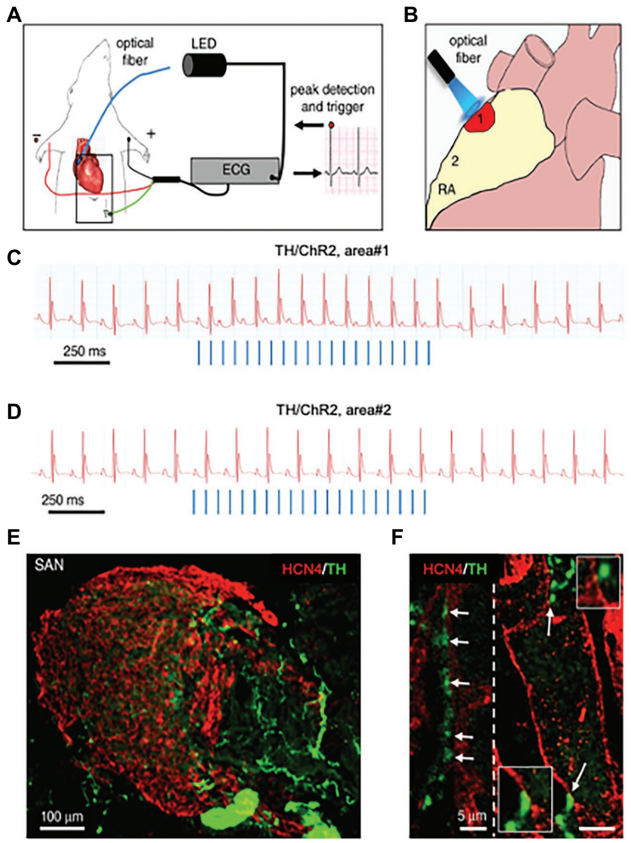

FIGURE 7 | Optogenetic control of cardiac sympathetic neurons *in vivo*. **(A)** Schematic illustration of the neuronal optogenetic set up used for right atrium illumination in open-chest anaesthetized mice. **(B)** Representation of the different photostimulated atrial regions (areas#1–2). **(C)** Representative ECG trace of the optogenetic experiment, showing positive chronotropic response upon photoactivation (blue lines) of the right atrial area#1 in TH/ChannelRhodopsin2 (TH/ChR2) mice. **(D)** Representative trace showing unchanged HR upon illumination of area#2. Behavior of experiments **(C,D)** was observed in $n = 15$ mice. **(E,F)**, area#1 was analyzed with double immunofluorescence with SAN (HCN4) and SN (TH) markers. The magnified image **(F)** highlights the close interaction between SN varicosities and SAN myocytes (left) and an example of multiple neuronal processes interacting with the same myocyte (right). Modified with permission from Prando et al. (2018).

based on experimental data which were, thus far, lacking explanation. This relates to the opening question of the current manuscript: "how can CMs maintain specificity of response to—say—β1- and b2-ARs, even if they are activated from the same extra-cellular agonist and transduced, intracellularly, by the same second messenger?"

To give an example, as discussed above, we have previously demonstrated that the presence of cSN is required to maintain correct CM mass, through constitutive stimulation of β2-AR signaling. However, it has to be taken into account that β1-ARs have higher affinity for noradrenaline than β2-ARs (Devic et al., 2001), and it is thus unlikely that activation of the β2-AR trophic signaling axis is mediated by increased resting levels of noradrenaline in the myocardial interstitium, as this would constitutively activate, and downregulate, the abundant β1-AR isotype. On the other hand, when considering that β2-AR stimulation initiates long-lasting downstream effects (mediated by either cAMP–Epac, PI3K–Akt, or β-arrestin pathways), constitutive control of gene transcription may develop from short repeated neuronal discharges, such as those occurring during normal daily activities (i.e., postural changes, movement; Paula-Gomes et al., 2013; Zaglia and Mongillo, 2017).

Furthermore, the different receptor dynamics may have a role, and in particular, given that β2-ARs, present in correspondence of the NCJ, are internalized upon noradrenaline binding and extruded from the junctional site (Devic et al., 2001; Shcherbakova et al., 2007), we might speculate that the time for reappearance of the receptor, underneath the SN, might represent the limiting factor for neurogenic activation of β2-AR signalling, upon repeated noradrenaline discharges. This mechanism would thus implicate the post-synaptic receptor dynamics in the limitation of receptor activation upon elevated neuronal firing rates, introducing, in other words, a *lowpass* filter in β2-AR dependent signaling (Zaglia and Mongillo, 2017).

This working model may also explain how heart stimulation by SNs is rapidly and simultaneously received by all CMs, with such direct "wired" connection protecting the heart, in physiologic conditions, from heterogeneous adrenergic stimulation which the organ would be exposed to, were the source of NE at variable distance to myocardial targets. The existence of a structured "cardiac synapse", underscoring the effects of sympathetic stimulation of the heart, has implications in cardiac physiology as well as on the pathophysiology of common cardiovascular diseases, such as heart failure (HF), one of the main causes of death in Europe.

In cardiac physiology, while it is commonly appreciated that catecholamine (norephinephrine, epinephrine) incretion occurs by both sympathetic efferences and the adrenal medulla, the effects of such distinct mechanisms of cardiovascular regulation have not been fully agreed upon. It is tempting to speculate that local neurogenic input, and diffuse stimulation by circulating catecholamines, would activate qualitatively different intracellular signaling compartments, with molecular and functionally different effects. This question is still awaiting answer, which we now have the tools to provide.

In cardiac pathology, it is well understood that HF features alterations in autonomic control of cardiac function, including decreased responsiveness to β-AR agonists, reduced noradrenaline content in sympathetic endings, increased venous spillover of neuronal noradrenaline and its accumulation in the myocardial interstitium (Liang, 2007; de Lucia et al., 2018; Prando, 2018; Ramchandra et al., 2018). Interestingly, most of these features would be explained by structural changes in the NCJ causing the loss of the low-volume intercellular cleft, thus reducing the efficiency of intercellular signaling (Prando et al., 2018), and local neurotransmitter reuptake. In further support of this, our data shows that changes in the NCJ function parallel with post-synaptic membrane disarrangement, SN degeneration and a reduction in the number of neuro-cardiac contacts (Prando et al., 2018). In the context of the complex organization of cAMP signaling in CMs, this scenario would likely impinge on the degree of adrenergic stimulation, and might result in

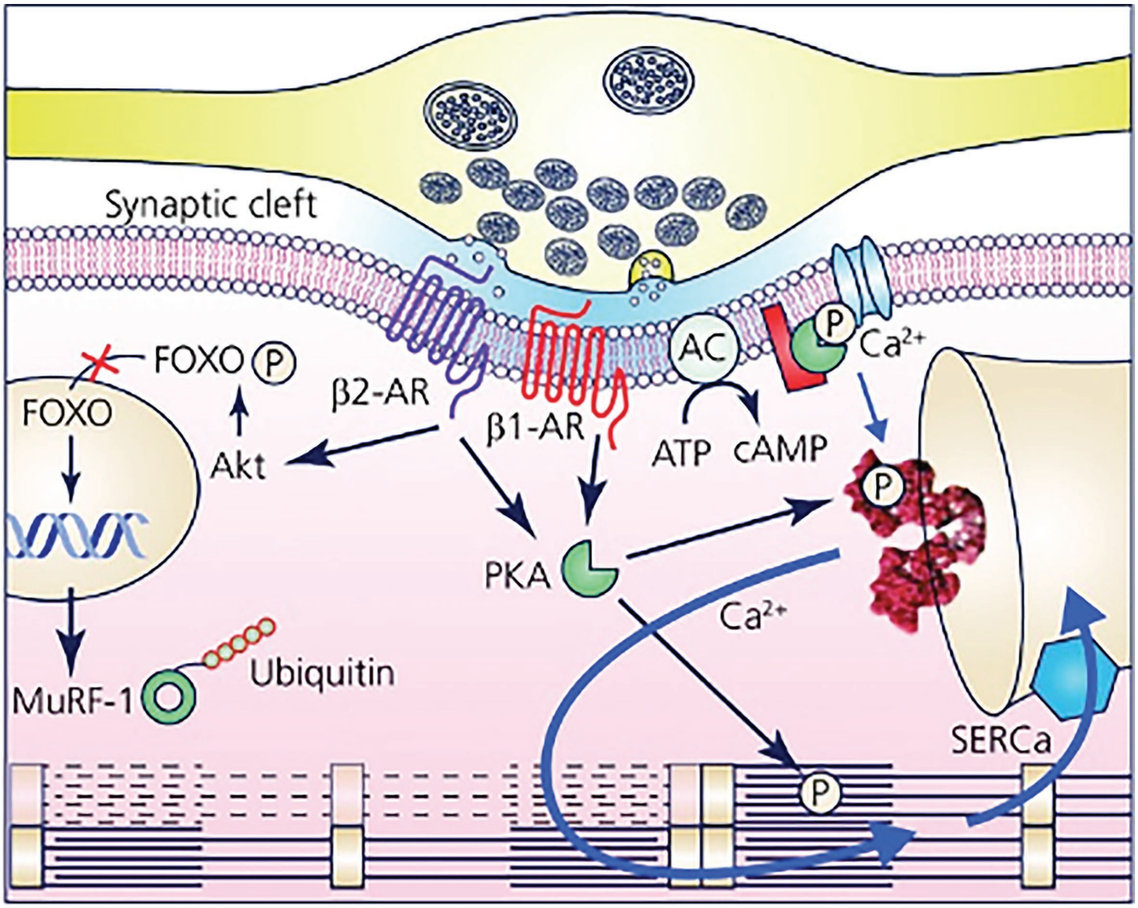

FIGURE 8 | The Neuro-Cardiac Junction is the functional unit of sympathetic neuron-to-cardiomyocytes communication. Schematic of the elements of neuro-cardiac interaction at the varicosity/CM interface. The elements of β-AR dependent signaling activated by noradrenaline released into the synaptic cleft are represented with reference to the β1-AR and β2-AR isotypes. The main downstream targets, respectively, associated with gene regulation of trophic genes (β2-AR) and Ca^{2+} homeostasis (β1-AR) are shown. Modified with permission from Zaglia and Mongillo (2017).

uneven activation of cAMP signaling in different subcellular domains (for reference see **Figures 1, 2**).

IS DYSTROPHIN A STRUCTURAL COMPONENT OF THE NEURO-CARDIAC CONNECTION?

Our data surmises that the molecular architecture of the cell–cell interaction site may influence the efficiency of neuro-cardiac communication. At the time being, while the components of the NCJ are still partially unresolved, the observation that in culture, the interaction between SNs and CMs is stable in time, as opposed to that SNs establish with, e.g., cardiac fibroblasts (Pianca et al., 2019), suggests that CM-specific structures may play a role at the intercellular contact site. With reference to the well-described NMJ, we made the hypothesis that dystrophin, which is a central organizer of the post-synaptic skeletal muscle membrane, functional for intercellular communication between MNs and myocytes, may also play a role in the NCJ (Rudolf et al., 2014). Consistently, cardiac fibroblasts, as opposed to CMs, do not express dystrophin (Mezzano et al., 2007). In line with the hypothesis that dystrophin may have a role in building the NCJ and tightening, in a strong bond, neurons and CMs, we observed, in co-cultures, that dystrophin and molecular players of the dystroglycan complex were enriched on the CM membrane, at the interaction site with sympathetic processes (Mongillo et al., 2020). Altogether, this data supports the dystroglycan complex, as a component of the NCJ, might have a role in the functional "SN-CM" communication. Interestingly, it has recently been demonstrated that lack of dystrophin, by affecting the subplasmalemmal cytoskeletal organization, leads to disarray of cAMP compartments, reflecting on the efficiency of β-AR stimulation (Brescia et al., 2020). While this was observed in cultured CMs, together with our observations, these results prompt the idea that absence of dystrophin may lead to profound alteration in the local nature of β-AR activators (neurons) and signaling, thus reflecting on neuro-cardiac fidelity.

In line with this, hearts of *mdx* mice, a model characterized by the absence of dystrophin expression (Hoffman et al., 1987), had reduced sympathetic innervation density. Most interesting results came from the analysis of hearts from female *mdx* carriers, in which clusters of dystrophin-expressing CMs co-exist with dystrophin-negative ones (**Figures 9A,B**). In all hearts analyzed, SN processes had lower density in dystrophin-negative regions, compared to the dystrophin-positive ones, identified with immunofluorescence staining (**Figure 9C**). In addition, the few processes contacting dystrophin-negative CMs had smaller varicosities, compared to those in contact with dystrophin-positive cells (Mongillo et al., 2020).

It is well-appreciated, in several organs innervated by SNs, that the target tissue provides the necessary neurotrophic factors to sustain neuronal survival. In the heart, that CMs could impact on neuronal viability was suggested years ago, although direct demonstration is still lacking. To test whether NCJs, in addition to their role on anterograde (SN-CM) communication, could also impact neurotrophic signaling from CMs to SNs, we set up co-cultures of mixed CMs and SNs from control

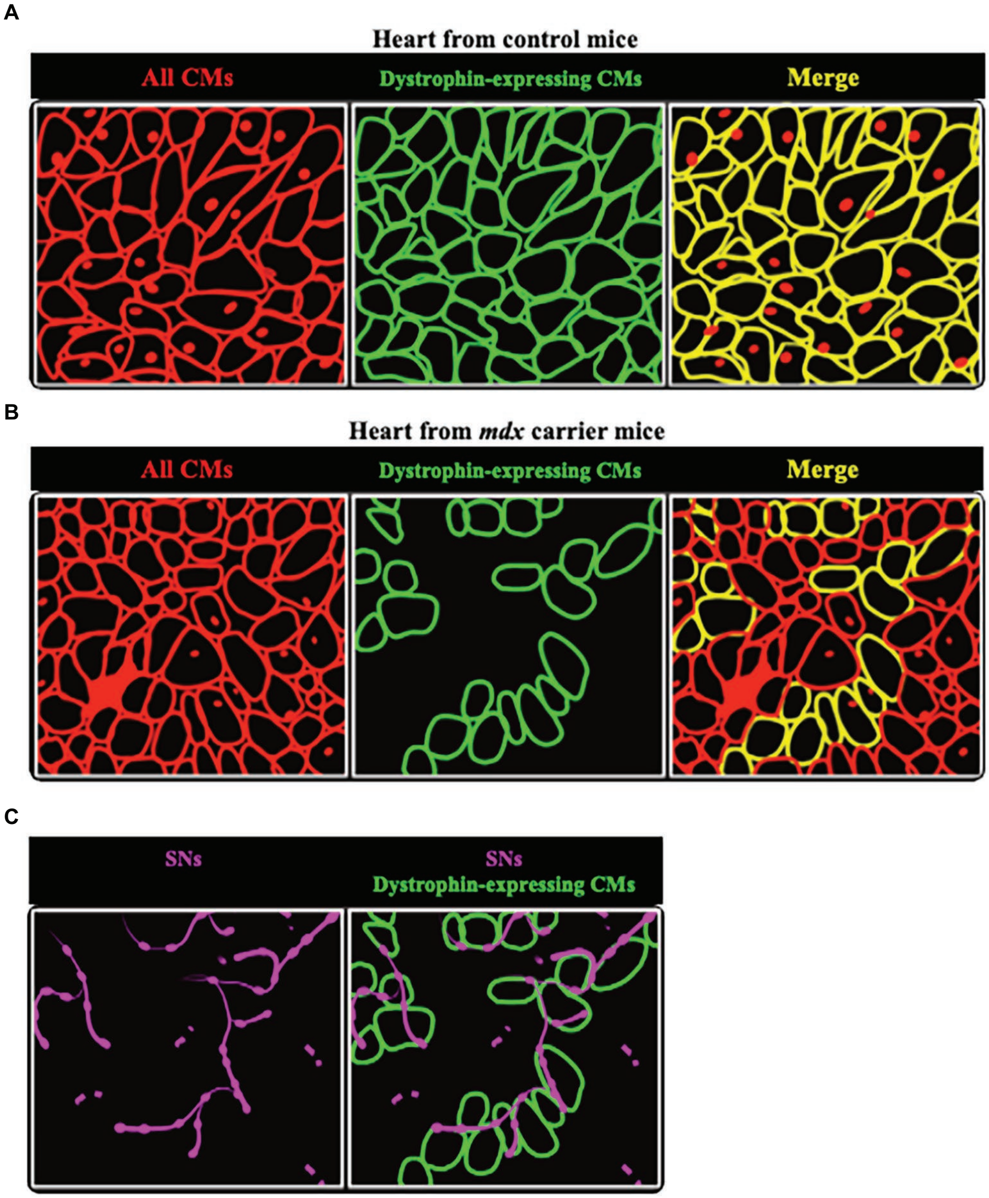

FIGURE 9 | Sympathetic neurons are found selectively in dystrophin-positive areas in hearts from female *mdx* carrier mice. **(A,B)** Representative cartoons showing the comparison between hearts from normal **(A)** and *mdx* carrier **(B)** female mice. While in the former dystrophin is homogeneously expressed by all CMs (identified by red lines), in hearts from *mdx* carriers clusters of dystrophin positive cells (identified by green lines) are intermingled with others lacking dystrophin. **(C)** Areas occupied by dystrophin negative CMs are less innervated, as compared to the positive ones, with neuronal processes (in purple) appear fragmented.

and *mdx* neonatal mice. In the presence of Nerve Growth Factor in the culture medium, both *mdx* and control neurons extended and branched their processes, developing contacts with CMs, irrespective of the cell genotype. Consistent with the role of CM dystrophin in sustaining "SN-CM" contact, survival of control SNs in co-culture with *mdx* CMs was significantly reduced (Mongillo et al., 2020). Altogether, this data further supports that dystrophin has a key role in bidirectional "SN-CM" communication, and that its ablation reflects on SN trophism and, consequently, on the cardiac innervation pattern.

At this point, one can object that what we observed was in a condition far from that of intact heart, and that previous studies failed to detect accumulation of dystrophin in the portion of the CM membrane innervated by the neuron (as occurring at the NMJ). It has to be noted, however, that while each skeletal muscle fiber establishes a single NMJ, with the MN terminal contacting the cell membrane in a well-defined point, the CM membrane is interspersed by repeating contacts with multiple SN varicosities. This implies that, although dystrophin accumulation may occur in the CM portion contacted by the SN varicosity, differences in dystrophin density along the sarcolemma may be less distinct for the overlap of neighboring postsynaptic membrane portions. Furthermore, we cannot exclude that the dystroglycan complex may contribute to stabilize intercellular contacts independent from selective accumulation at the site of the nervously touched CM membrane.

CONCLUDING REMARKS

The independence of contractions from innervation does not imply that in physiologic conditions the heart beats solo. While neurons, which densely innervate the myocardium, do not ignite contractions, research summarized in this review demonstrates that the finely-built interaction with cardiomyocytes, centered at the NCJ, allows neurons to precisely control multiple cell functions, ranging from contractility, electrophysiology to gene expression. Innervation serves as conductor of the cardiac cellular orchestra, setting the tempo, unifying performers, and shaping the beats of the ensemble. Like a conductor controls interpretation and pace of the music, with gaze and gestures to the performers, neurons do so through direct communication to the cardiomyocytes, guaranteeing the melody and harmony of heartbeats. When diseases break communication between the conductor and the musicians, the orchestra plays out of tune or synchrony, and heartbeats sound turbulent or noisy.

AUTHOR CONTRIBUTIONS

MF and LD contributed to manuscript and figure preparation. LV critically discussed data and the review layout. TZ and MM drafted and wrote the manuscript. All authors approved the final version of the manuscript and agree to be accountable for all aspects of the work, in ensuring that questions related to the accuracy or integrity of any part of the work are appropriately investigated and resolved, and that all persons designated as authors qualify for authorship and have been listed.

FUNDING

This work was supported by STARS-miniheartwork (UNIPD) to MM and STARS-SKoOP (UNIPD) to TZ.

ACKNOWLEDGMENTS

The authors thank the collaborators who have, in time, contributed to define the dynamics of neuro-cardiac communication and to identify the NCJ: Francesca Da Broi, Anna Pia Plazzo, Nicola Pianca, and Valentina Prando. The authors are also grateful to the late Gilberto Benetton and Corvallis Srl for supporting MM and TZ laboratories, respectively. Due to the numerous aspects of neuro-cardiology touched in this manuscript, the authors apologize to the many colleagues who contributed to the field, but have not been cited.

REFERENCES

Acheson, G. H. (1948). Physiology of neuro-muscular junctions; chemical aspects. *Fed. Proc.* 7, 447–457.

Adams, R. J., and Schwartz, A. (1980). Comparative mechanisms for contraction of cardiac and skeletal muscle. *Chest* 78, 123–139. doi: 10.1378/CHEST.78.1_SUPPLEMENT.123

Bamji, S. X., Shimazu, K., Kimes, N., Huelsken, J., Birchmeier, W., Lu, B., et al. (2003). Role of beta-catenin in synaptic vesicle localization and presynaptic assembly. *Neuron* 40, 719–731. doi: 10.1016/S0896-6273(03)00718-9

Bardsley, E. N., Davis, H., Buckler, K. J., and Paterson, D. J. (2018). Neurotransmitter switching coupled to β-adrenergic signaling in sympathetic neurons in prehypertensive states. *Hypertension* 71, 1226–1238. doi: 10.1161/HYPERTENSIONAHA.118.10844

Baxter, M. I., and Nisbet, R. H. (1963). Features of the nervous system and heart of Archachatina revealed by the electron microscope and by electrophysiological recording. *J. Molluscan Stud.* 35, 167–177. doi: 10.1093/oxfordjournals.mollus.a064915

Bedioune, I., Lefebvre, F., Lechêne, P., Varin, A., Domergue, V., Kapiloff, M. S., et al. (2018). PDE4 and mAKAPβ are nodal organizers of β2-ARs nuclear PKA signalling in cardiac myocytes. *Cardiovasc. Res.* 114, 1499–1511. doi: 10.1093/cvr/cvy110

Bers, D. M. (2002). Cardiac excitation–contraction coupling. *Nature* 415, 198–205. doi: 10.1038/415198a

Bers, D. M., Zaccolo, M., Xiang, Y. K., and Zaccolo, M. (2019). Whole-cell cAMP and PKA activity are epiphenomena, nanodomain signaling matters. *Physiology* 34, 240–249. doi: 10.1152/physiol.00002.2019

Bowen, D. C., Park, J. S., Bodine, S., Stark, J. L., Valenzuela, D. M., Stitt, T. N., et al. (1998). Localization and regulation of MuSK at the neuromuscular junction. *Dev. Biol.* 199, 309–319. doi: 10.1006/dbio.1998.8936

Brescia, M., Chao, Y. C., Koschinski, A., Tomek, J., and Zaccolo, M. (2020). Multi-compartment, early disruption of cGMP and cAMP Signalling in cardiac myocytes from the mdx model of Duchenne muscular dystrophy. *Int. J. Mol. Sci.* 21, 1–19. doi: 10.3390/IJMS21197056

Burton, R. A. B., Tomek, J., Ambrosi, C. M., Larsen, H. E., Sharkey, A. R., Capel, R. A., et al. (2020). Optical interrogation of sympathetic neuronal effects on macroscopic cardiomyocyte network. *Dynamics* 23:101334. doi: 10.1016/j.isci.2020.101334

Cairns, S. P., and Dulhunty, A. F. (1993). Beta-adrenergic potentiation of E-C coupling increases force in rat skeletal muscle. *Muscle Nerve* 16, 1317–1325. doi: 10.1002/mus.880161208

Calaghan, S., Kozera, L., and White, E. (2008). Compartmentalisation of cAMP-dependent signalling by caveolae in the adult cardiac myocyte. *J. Mol. Cell. Cardiol.* 45, 88–92. doi: 10.1016/j.yjmcc.2008.04.004

Chao, Y. C., Surdo, N. C., Pantano, S., and Zaccolo, M. (2019). Imaging cAMP nanodomains in the heart. *Biochem. Soc. Trans.* 47, 1383–1392. doi: 10.1042/BST20190245

Choate, J. K., Klemm, M., and Hirst, G. D. S. (1993). Sympathetic and parasympathetic neuromuscular junctions in the guinea-pig sino-atrial node. *J. Auton. Nerv. Syst.* 44, 1–15. doi: 10.1016/0165-1838(93)90374-4

de Lucia, C., Eguchi, A., and Koch, W. J. (2018). New insights in cardiac β-adrenergic signaling during heart failure and aging. *Front. Pharmacol.* 9:904. doi: 10.3389/fphar.2018.00904

Del Castillo, J., and Katz, B. (1956). Biophysical aspects of neuro-muscular transmission. *Prog. Biophys. Biophys. Chem.* 6, 121–170. doi: 10.1016/S0096-4174(18)30106-9

Devic, E., Xiang, Y., Gould, D., and Kobilka, B. (2001). β-Adrenergic receptor subtype-specific signaling in cardiac myocytes from beta(1) and beta(2) adrenoceptor knockout mice. *Mol. Pharmacol.* 60, 577–583.

Di Bona, A., Vita, V., Costantini, I., and Zaglia, T. (2020). Towards a clearer view of sympathetic innervation of cardiac and skeletal muscles. *Prog. Biophys. Mol. Biol.* 154, 80–93. doi: 10.1016/j.pbiomolbio.2019.07.003

DiFrancesco, D. (1995). The onset and autonomic regulation of cardiac pacemaker activity: relevance of the f current. *Cardiovasc. Res.* 29, 449–456. doi: 10.1016/S0008-6363(96)88518-X

Eisner, D. A., Caldwell, J. L., Kistamás, K., and Trafford, A. W. (2017). Calcium and excitation-contraction coupling in the heart. *Circ. Res.* 121, 181–195. doi: 10.1161/CIRCRESAHA.117.310230

Fawcett, D. W., and Selby, C. C. (1958). Observations on the fine structure of the turtle atrium. *J. Biophys. Biochem. Cytol.* 4, 63–72. doi: 10.1083/jcb.4.1.63

Fischmeister, R., Castro, L. R. V., Abi-Gerges, A., Rochais, F., Jurevičius, J., Leroy, J., et al. (2006). Compartmentation of cyclic nucleotide signaling in the heart: the role of cyclic nucleotide phosphodiesterases. *Circ. Res.* 99, 816–828. doi: 10.1161/01.RES.0000246118.98832.04

Franzoso, M., Zaglia, T., and Mongillo, M. (2016). Putting together the clues of the everlasting neuro-cardiac liaison. *Biochim. Biophys. Acta* 1863, 1904–1915. doi: 10.1016/j.bbamcr.2016.01.009

Ghigo, A., and Mika, D. (2019). cAMP/PKA signaling compartmentalization in cardiomyocytes: lessons from FRET-based biosensors. *J. Mol. Cell. Cardiol.* 131, 112–121. doi: 10.1016/j.yjmcc.2019.04.020

Grillo, M. A. (1966). Electron microscopy of sympathetic tissues. *Pharmacol. Rev.* 18, 387–399.

His, W. (1949). The activity of the embryonic human heart and its significance of the understanding of the heart movement in the adult. *J. Hist. Med. Allied Sci.* 4, 289–318. doi: 10.1093/jhmas/iv.3.289

Hoffman, E. P., Brown, R. H., and Kunkel, L. M. (1987). Dystrophin: the protein product of the duchenne muscular dystrophy locus. *Cell* 51, 919–928. doi: 10.1016/0092-8674(87)90579-4

Jurevičius, J., and Fischmeister, R. (1996). cAMP compartmentation is responsible for a local activation of cardiac Ca2+ channels by beta-adrenergic agonists. *Proc. Natl. Acad. Sci.* 93, 295–299. doi: 10.1073/PNAS.93.1.295

Kanevskij, M., Taimor, G., Schäfer, M., Piper, H. M., and Schlüter, K. D. (2002). Neuropeptide Y modifies the hypertrophic response of adult ventricular cardiomyocytes to norepinephrine. *Cardiovasc. Res.* 53, 879–887. doi: 10.1016/S0008-6363(01)00517-X

Khan, M. M., Lustrino, D., Silveira, W. A., Wild, F., Straka, T., Issop, Y., et al. (2016). Sympathetic innervation controls homeostasis of neuromuscular junctions in health and disease. *Proc. Natl. Acad. Sci.* 113, 746–750. doi: 10.1073/pnas.1524272113

Kisch, B. (1961). Electronmicroscopy of the frog's heart. *Exp. Med. Surg.* 19, 104–142.

Klemm, M., Hirst, G. D. S., and Campbell, G. (1992). Structure of autonomic neuromuscular junctions in the sinus venosus of the toad. *J. Auton. Nerv. Syst.* 39, 139–150. doi: 10.1016/0165-1838(92)90054-K

Kreipke, R. E., and Birren, S. J. (2015). Innervating sympathetic neurons regulate heart size and the timing of cardiomyocyte cell cycle withdrawal. *J. Physiol.* 593, 5057–5073. doi: 10.1113/JP270917

Lafontant, P. J. E., and Field, L. J. (2006). The cardiomyocyte cell cycle. Novartis Foundation symposium 274, 196. Available at: /PMC/articles/PMC2628757/ (Accessed October 21, 2021).

Landis, S. C. (1976). Rat sympathetic neurons and cardiac myocytes developing in microcultures: correlation of the fine structure of endings with neurotransmitter function in single neurons. *Proc. Natl. Acad. Sci.* 73, 4220–4224. doi: 10.1073/pnas.73.11.4220

Leroy, J., Abi-Gerges, A., Nikolaev, V. O., Richter, W., Lechêne, P., Mazet, J. L., et al. (2008). Spatiotemporal dynamics of β-adrenergic cAMP signals and L-type Ca2+ channel regulation in adult rat ventricular myocytes: role of phosphodiesterases. *Circ. Res.* 102, 1091–1100. doi: 10.1161/CIRCRESAHA.107.167817

Leroy, J., and Fischmeister, R. (2018). Inhibit a phosphodiesterase to treat heart failure? *Circulation* 138, 2003–2006. doi: 10.1161/CIRCULATIONAHA.118.036325

Li, L., Desantiago, J., Chu, G., Kranias, E. G., and Bers, D. M. (2000). Phosphorylation of phospholamban and troponin I in beta-adrenergic-induced acceleration of cardiac relaxation. *Am. J. Phys. Heart Circ. Phys.* 278, H769–H779. doi: 10.1152/ajpheart.2000.278.3.H769

Li, L., Gervasi, N., and Girault, J. A. (2015). Dendritic geometry shapes neuronal cAMP signalling to the nucleus. *Nat. Commun.* 6, 6319–6315. doi: 10.1038/ncomms7319

Liang, C. S. (2007). Cardiac sympathetic nerve terminal function in congestive heart failure. *Acta Pharmacol. Sin.* 28, 921–927. doi: 10.1111/j.1745-7254.2007.00585.x

Lohse, M. J., Engelhardt, S., and Eschenhagen, T. (2003). What is the role of beta-adrenergic signaling in heart failure? *Circ. Res.* 93, 896–906. doi: 10.1161/01.RES.0000102042.83024.CA

Lombard, J. H., and Cowley, A. W. (2012). "Neural control of blood vessels," in *Primer on the Autonomic Nervous System*. eds. D. Robertson, I. Biaggioni, G. Burnstock, P. A. Low and J. F. R. Paton (Cambridge, MA: Academic Press), 187–191.

Mehel, H., Emons, J., Vettel, C., Wittköpper, K., Seppelt, D., Dewenter, M., et al. (2013). Phosphodiesterase-2 is up-regulated in human failing hearts and blunts β-adrenergic responses in cardiomyocytes. *J. Am. Coll. Cardiol.* 62, 1596–1606. doi: 10.1016/J.JACC.2013.05.057

Mezzano, V., Cabrera, D., Vial, C., and Brandan, E. (2007). Constitutively activated dystrophic muscle fibroblasts show a paradoxical response to TGF-β and CTGF/CCN2. *J. Cell Commun. Signal.* 1, 205–217. doi: 10.1007/s12079-008-0018-2

Mika, D., Leroy, J. Ô., Vandecasteele, G., and Fischmeister, R. (2012). PDEs create local domains of cAMP signaling. *J. Mol. Cell. Cardiol.* 52, 323–329. doi: 10.1016/j.yjmcc.2011.08.016

Mongillo, M., Franzoso, M., Prando, V., Dokshokova, L., Di Bona, A., Basso, C., et al. (2020). The neuro-cardiac junction defines an extracellular microdomain required for neurotrophic signaling. *Eur. Heart J.* 41:S2. doi: 10.1093/ehjci/ehaa946.3589

Mongillo, M., McSorley, T., Evellin, S., Sood, A., Lissandron, V., Terrin, A., et al. (2004). Fluorescence resonance energy transfer-based analysis of cAMP dynamics in live neonatal rat cardiac myocytes reveals distinct functions of compartmentalized phosphodiesterases. *Circ. Res.* 95, 67–75. doi: 10.1161/01.RES.0000134629.84732.11

Mongillo, M., Tocchetti, C. G., Terrin, A., Lissandron, V., Cheung, Y. F., Dostmann, W. R., et al. (2006). Compartmentalized phosphodiesterase-2 activity blunts beta-adrenergic cardiac inotropy via an NO/cGMP-dependent pathway. *Circ. Res.* 98, 226–234. doi: 10.1161/01.RES.0000200178.34179.93

Mongillo, M., and Zaccolo, M. (2006). A complex phosphodiesterase system controls beta-adrenoceptor signalling in cardiomyocytes. *Biochem. Soc. Trans.* 34, 510–511. doi: 10.1042/BST0340510

Naim, N., White, A. D., Reece, J. M., Wankhede, M., Zhang, X., Vilardaga, J. P., et al. (2019). Luminescence-activated nucleotide cyclase regulates spatial and temporal cAMP synthesis. *J. Biol. Chem.* 294, 1095–1103. doi: 10.1074/jbc.AC118.004905

Napolitano, L. M., Willman, V. L., Hanlon, C. R., and Cooper, T. (1965). Intrinsic innervation of the heart. *Am. J. Phys.* 208, 455–458. doi: 10.1152/ajplegacy.1965.208.3.455

Navegantes, L. C., Resano, N. M., Baviera, A. M., Migliorini, R. H., and Kettelhut, I. C. (2004). Effect of sympathetic denervation on the rate of protein synthesis in rat skeletal muscle. *Am. J. Physiol. Endocrinol. Metab.* 286, E642–E647. doi: 10.1152/AJPENDO.00371.2003

Nikolaev, V. O., Bünemann, M., Schmitteckert, E., Lohse, M. J., and Engelhardt, S. (2006). Cyclic AMP imaging in adult cardiac myocytes reveals far-reaching β1-adrenergic but locally confined β2-adrenergic receptor-mediated signaling. *Circ. Res.* 99, 1084–1091. doi: 10.1161/01.RES.0000250046.69918.d5

Nikolaev, V. O., Moshkov, A., Lyon, A. R., Miragoli, M., Novak, P., Paur, H., et al. (2010). β2-adrenergic receptor redistribution in heart failure changes cAMP compartmentation. *Science* 327, 1653–1657. doi: 10.1126/science.1185988

O'Connell, T. D., Ishizaka, S., Nakamura, A., Swigart, P. M., Rodrigo, M. C., Simpson, G. L., et al. (2003). The α1A/C- and α1B-adrenergic receptors are required for physiological cardiac hypertrophy in the double-knockout mouse. Journal of clinical investigation 111. Available at: /PMC/articles/PMC156101/ (Accessed December 21, 2021).

Ogawa, S., Barnett, J. V., Sen, L., Galper, J. B., Smith, T. W., and Marsh, J. D. (1992). Direct contact between sympathetic neurons and rat cardiac myocytes in vitro increases expression of functional calcium channels. *J. Clin. Invest.* 89, 1085–1093. doi: 10.1172/JCI115688

Paula-Gomes, S., Gonçalves, D. A. P., Baviera, A. M., Zanon, N. M., Navegantes, L. C. C., and Kettelhut, I. C. (2013). Insulin suppresses atrophy- and autophagy-related genes in heart tissue and cardiomyocytes through AKT/FOXO signaling. *Horm. Metab. Res.* 45, 849–855. doi: 10.1055/s-0033-1347209

Pianca, N., Di Bona, A., Lazzeri, E., Costantini, I., Franzoso, M., Prando, V., et al. (2019). Cardiac sympathetic innervation network shapes the myocardium by locally controlling cardiomyocyte size through the cellular proteolytic machinery. *J. Physiol.* 597, 3639–3656. doi: 10.1113/JP276200

Prando, V. (2018). Neuroeffector coupling in the heart: determinants of function and survival of cardiac sympathetic neurons. Available at: http://paduaresearch.cab.unipd.it/10690/2/Valentina_Prando_Tesi.pdf (Accessed November 11, 2021).

Prando, V., Da Broi, F., Franzoso, M., Plazzo, A. P., Pianca, N., Francolini, M., et al. (2018). Dynamics of neuroeffector coupling at cardiac sympathetic synapses. *J. Physiol.* 596, 2055–2075. doi: 10.1113/JP275693

Ramchandra, R., Hood, S. G., Xing, D., Lambert, G. W., and May, C. N. (2018). Mechanisms underlying the increased cardiac norepinephrine spillover in heart failure. *Am. J. Physiol. Heart Circ. Physiol.* 315, H340–H347. doi: 10.1152/ajpheart.00069.2018

Rehmann, H., Das, J., Knipscheer, P., Wittinghofer, A., and Bos, J. L. (2006). Structure of the cyclic-AMP-responsive exchange factor Epac2 in its auto-inhibited state. *Nature* 439, 625–628. doi: 10.1038/nature04468

Röder, I. V. I. V., Lissandron, V., Martin, J., Petersen, Y., Di Benedetto, G., Zaccolo, M., et al. (2009). PKA microdomain organisation and cAMP handling in healthy and dystrophic muscle in vivo. *Cell. Signal.* 21, 819–826. doi: 10.1016/j.cellsig.2009.01.029

Rudolf, R., Khan, M. M., Labeit, S., and Deschenes, M. R. (2014). Degeneration of neuromuscular junction in age and dystrophy. *Front. Aging Neurosci.* 6:99. doi: 10.3389/fnagi.2014.00099

Rudolf, R., Khan, M. M., Lustrino, D., Labeit, S., Kettelhut, Í. C., Navegantes, L. C. C., et al. (2013). Alterations of cAMP-dependent signaling in dystrophic skeletal muscle. *Front. Physiol.* 4:290. doi: 10.3389/fphys.2013.00290

Ruff, R. L. (2003). Neurophysiology of the neuromuscular junction: overview. *Ann. N. Y. Acad. Sci.* 998, 1–10. doi: 10.1196/ANNALS.1254.002

Sample, V., Dipilato, L. M., Yang, J. H., Ni, Q., Saucerman, J. J., and Zhang, J. (2012). Regulation of nuclear PKA revealed by spatiotemporal manipulation of cyclic AMP. *Nat. Chem. Biol.* 8, 375–382. doi: 10.1038/nchembio.799

Saucerman, J. J., Zhang, J., Martin, J. C., Peng, L. X., Stenbit, A. E., Tsien, R. Y., et al. (2006). Systems analysis of PKA-mediated phosphorylation gradients in live cardiac myocytes. *Proc. Natl. Acad. Sci.* 103, 12923–12928. doi: 10.1073/PNAS.0600137103

Scalco, A., Moro, N., Mongillo, M., and Zaglia, T. (2021). Neurohumoral cardiac regulation: optogenetics gets Into the groove. *Front. Physiol.* 12:726895. doi: 10.3389/fphys.2021.726895

Šćepanović, D. (2011). A model of sinoatrial node cell regulation by the autonomic nervous system. Available at: https://dspace.mit.edu/handle/1721.1/68457 (Accessed November 9, 2021).

Schleicher, K., and Zaccolo, M. (2018). Using cAMP sensors to study cardiac nanodomains. *J. Cardiovasc. Dev. Dis.* 5:17. doi: 10.3390/jcdd5010017

Schobesberger, S., Wright, P., Tokar, S., Bhargava, A., Mansfield, C., Glukhov, A. V., et al. (2017). T-tubule remodelling disturbs localized β2-adrenergic signalling in rat ventricular myocytes during the progression of heart failure. *Cardiovasc. Res.* 113, 770–782. doi: 10.1093/cvr/cvx074

Shcherbakova, O. G., Hurt, C. M., Xiang, Y., Dell'Acqua, M. L., Zhang, Q., Tsien, R. W., et al. (2007). Organization of β-adrenoceptor signaling compartments by sympathetic innervation of cardiac myocytes. *J. Cell Biol.* 176, 521–533. doi: 10.1083/jcb.200604167

Soto, D., De Arcangelis, V., Zhang, J., and Xiang, Y. (2009). Dynamic protein kinase a activities induced by β-adrenoceptors dictate signaling propagation for substrate phosphorylation and myocyte contraction. *Circ. Res.* 104, 770–779. doi: 10.1161/CIRCRESAHA.108.187880

Stangherlin, A., and Zaccolo, M. (2012). Phosphodiesterases and subcellular compartmentalized cAMP signaling in the cardiovascular system. *Am. J. Physiol. Heart Circ. Physiol.* 302, H379–H390. doi: 10.1152/ajpheart.00766.2011

Steinberg, S., and Brunton, L. (2001). Compartmentation of G protein-coupled signaling pathways in cardiac myocytes. *Annu. Rev. Pharmacol. Toxicol.* 41, 751–773. doi: 10.1146/annurev.pharmtox.41.1.751

Straka, T., Schröder, C., Roos, A., Kollipara, L., Sickmann, A., Williams, M. P. I., et al. (2021). Regulatory function of sympathetic innervation on the endo/lysosomal trafficking of acetylcholine receptor. *Front. Physiol.* 12:626707. doi: 10.3389/fphys.2021.626707

Straka, T., Vita, V., Prokshi, K., Hörner, S. J., Khan, M. M., Pirazzini, M., et al. (2018). Postnatal development and distribution of sympathetic innervation in mouse skeletal muscle. *Int. J. Mol. Sci.* 19:1935. doi: 10.3390/ijms19071935

Surdo, N. C., Berrera, M., Koschinski, A., Brescia, M., MacHado, M. R., Carr, C., et al. (2017). FRET biosensor uncovers cAMP nano-domains at β-adrenergic targets that dictate precise tuning of cardiac contractility. *Nat. Commun.* 8, 1–14. doi: 10.1038/ncomms15031

Tao, T., Paterson, D. J., and Smith, N. P. (2011). A model of cellular cardiac-neural coupling that captures the sympathetic control of sinoatrial node excitability in normotensive and hypertensive rats. *Biophys. J.* 101, 594–602. doi: 10.1016/j.bpj.2011.05.069

Tedesco, F. S., Dellavalle, A., Diaz-Manera, J., Messina, G., and Cossu, G. (2010). Repairing skeletal muscle: regenerative potential of skeletal muscle stem cells. *J. Clin. Invest.* 120, 11–19. doi: 10.1172/JCI40373

Thaemert, J. C. (1969). Fine structure of neuromuscular relationships in mouse heart. *Anat. Rec.* 163, 575–585. doi: 10.1002/ar.1091630409

Trautwein, W., and Uchizono, K. (1963). Electron microscopic and electrophysiologic study of the pacemaker in the sino-atrial node of the rabbit heart. *Z. Zellforsch. Mikrosk. Anat.* 61, 96–109. doi: 10.1007/BF00341523

Tsvetanova, N. G., and von Zastrow, M. (2014). Spatial encoding of cyclic AMP signaling specificity by GPCR endocytosis. *Nat. Chem. Biol.* 10, 1061–1065. doi: 10.1038/nchembio.1665

Vandecasteele, G., Rochais, F., Abi-Gerges, A., and Fischmeister, R. (2006). Functional localization of cAMP signalling in cardiac myocytes. *Biochem. Soc. Trans.* 34, 484–488. doi: 10.1042/BST0340484

Welsh, J. H. (1948). Physiology of neuro-muscular junctions. *Fed. Proc.* 7:435.

Zaccolo, M., and Movsesian, M. A. (2007). cAMP and cGMP signaling cross-talk: role of phosphodiesterases and implications for cardiac pathophysiology. *Circ. Res.* 100, 1569–1578. doi: 10.1161/CIRCRESAHA.106.144501

Zaccolo, M., and Pozzan, T. (2002). Discrete microdomains with high concentration of cAMP in stimulated rat neonatal cardiac myocytes. *Science* 295, 1711–1715. doi: 10.1126/science.1069982

Zaccolo, M., Zerio, A., and Lobo, M. J. (2021). Subcellular organization of the cAMP signaling pathway. *Phamacol. Rev.* 73, 278–309. doi: 10.1124/pharmrev.120.000086

Zaglia, T., Milan, G., Franzoso, M., Bertaggia, E., Pianca, N., Piasentini, E., et al. (2013). Cardiac sympathetic neurons provide trophic signal to the heart via beta2-adrenoceptor-dependent regulation of proteolysis. *Cardiovasc. Res.* 97, 240–250. doi: 10.1093/cvr/cvs320

Zaglia, T., and Mongillo, M. (2017). Cardiac sympathetic innervation, from a different point of (re)view. *J. Physiol.* 595, 3919–3930. doi: 10.1113/JP273120

Zakhary, D. R., Moravec, C. S., and Bond, M. (2000). Regulation of PKA binding to AKAPs in the heart. *Circulation* 101, 1459–1464. doi: 10.1161/01.CIR.101.12.1459

Zaza, A., Malfatto, G., and Schwartz, P. J. (1991). Sympathetic modulation of the relation between ventricular repolarization and cycle length. *Circ. Res.* 68, 1191–1203. doi: 10.1161/01.RES.68.5.1191

Conflict of Interest: The authors declare that the research was conducted in the absence of any commercial or financial relationships that could be construed as a potential conflict of interest.

frontiers
in Physiology

REVIEW
published: 08 March 2022
doi: 10.3389/fphys.2022.834211

Image-Driven Modeling of Nanoscopic Cardiac Function: Where Have We Come From, and Where Are We Going?

William E. Louch*[1,2], *Harmonie Perdreau-Dahl*[1,2] and *Andrew G. Edwards*[3]

[1] Institute for Experimental Medical Research, Oslo University Hospital and University of Oslo, Oslo, Norway, [2] K.G. Jebsen Centre for Cardiac Research, University of Oslo, Oslo, Norway, [3] Simula Research Laboratory, Lysaker, Norway

Complementary developments in microscopy and mathematical modeling have been critical to our understanding of cardiac excitation–contraction coupling. Historically, limitations imposed by the spatial or temporal resolution of imaging methods have been addressed through careful mathematical interrogation. Similarly, limitations imposed by computational power have been addressed by imaging macroscopic function in large subcellular domains or in whole myocytes. As both imaging resolution and computational tractability have improved, the two approaches have nearly merged in terms of the scales that they can each be used to interrogate. With this review we will provide an overview of these advances and their contribution to understanding ventricular myocyte function, including exciting developments over the last decade. We specifically focus on experimental methods that have pushed back limits of either spatial or temporal resolution of nanoscale imaging (e.g., DNA-PAINT), or have permitted high resolution imaging on large cellular volumes (e.g., serial scanning electron microscopy). We also review the progression of computational approaches used to integrate and interrogate these new experimental data sources, and comment on near-term advances that may unify understanding of the underlying biology. Finally, we comment on several outstanding questions in cardiac physiology that stand to benefit from a concerted and complementary application of these new experimental and computational methods.

Keywords: excitation contraction coupling (ECC), ryanodine receptor (RyR), super resolution microscopy, calcium induced calcium release, mathematical modeling

Edited by:
Fabien Brette,
Institut National de la Santé et de la Recherche Médicale (INSERM), France

Reviewed by:
Julio Altamirano,
Tecnológico de Monterrey, Mexico
Jerome Leroy,
INSERM U1180 Signalisation et Physiopathologie Cardiovasculaire, France

****Correspondence:***
Andrew G. Edwards
andy@simula.no

Specialty section:
This article was submitted to Cardiac Electrophysiology, a section of the journal Frontiers in Physiology

Received: *13 December 2021*
Accepted: *31 January 2022*
Published: *08 March 2022*

Citation:
Louch WE, Perdreau-Dahl H and Edwards AG (2022) Image-Driven Modeling of Nanoscopic Cardiac Function: Where Have We Come From, and Where Are We Going? Front. Physiol. 13:834211. doi: 10.3389/fphys.2022.834211

THE COMPLEMENTARY HISTORY OF IMAGING AND COMPUTATION IN CARDIAC EXCITATION-CONTRACTION COUPLING

As in many fields of physiology, experimental and *in silico* approaches have each contributed elements critical to unraveling cardiac excitation–contraction coupling (ECC) during the past 60 years. However, it is only rarely that studies of both types have been designed in a coordinated manner, with one providing essential information to the other. Experimental approaches have always provided the foundation of the field, but as our understanding has developed it has repeatedly required investigation of structures and function that were unobservable via available methods. At those points, mathematical approaches have often been applied to crystalize the prevailing arguments and assumptions, and to provide clear, quantitative, and actionable postulates that have sometimes reoriented the field. These contributions of the subdisciplines are depicted in **Figure 1**, along with key (preceding) technological advances, and the resulting shifts in the working paradigm. Over the past decade, a number of major advances in microscopy have been applied to cardiac ECC, and provided a basis for entirely new approaches to coordinating experimental and computational studies. In this review, we describe key moments in the broader history of the discipline, and discuss how these new and burgeoning technologies may change the nature of investigation in the coming years. It is an exciting period for the field, as these new approaches promise to reconcile old controversies, and permit a degree of common understanding among modelers and experimentalists that has thus far largely been limited to the neurosciences.

Structure as the Basis of Function

Transmission electron microscopy (TEM) provided the earliest foundation for our understanding of nanoscale ECC in both cardiac ventricle and skeletal muscle. These studies were among the first applications of electron microscopy in biology and part of extensive structural characterizations performed by Porter and Palade (1957). Their work established the existence and basic structure of the sarcoplasmic reticulum (SR) in striated muscle, and specifically identified the "diad" structures ("triad" in skeletal muscle) as sites of possible importance in ECC. These structures were formed by bulbous projections of the SR several hundred nanometers in diameter termed "terminal sacs" or "terminal cisternae," which enwrapped a central tubular membrane that was later shown to be continuous with the sarcolemma (Franzini-Armstrong and Porter, 1964a,b). Together these elements provided a basis for sarcolemmal excitation to trigger Ca^{2+} release deep in the interior of the cell, thus verifying A F Huxley's remarkable local stimulation experiments in skeletal muscle, which had pointed to their existence nearly a decade earlier (Huxley and Taylor, 1958). Oxalate and Ca^{2+} labeling of TEM sections established that the SR cisternae were indeed a major intracellular Ca^{2+} depot, at least in resting tissue (Huxley and Taylor, 1958; Constantin et al., 1965; Winegrad, 1965a). Winegrad's (1965b) elegant follow-up study then put the final nail in the coffin by demonstrating transfer of Ca^{2+} from the cisternal structures to the myofilaments after K^{+}-induced depolarization. At this point (the late 1960s), most aspects of the ECC mechanisms in cardiac and skeletal muscle remained to be established, but the fundamental membrane structures were more-or-less clear.

The "Fuzzy" Foundation of Ca^{2+}-Induced Ca^{2+} Release

Our basic concept of how these nanoscopic structures participated in cardiac ECC was introduced in the 1970s (Endo et al., 1970; Fabiato and Fabiato, 1972, 1975a,b, 1977, 1978; Endo, 1977), well before modern nano-scale optical methods had been developed. As such, none of these early studies employed advanced imaging or computation, and many predated relatively straightforward measurement of intracellular Ca^{2+} via fluorescent dyes (Fabiato, 1981; Cobbold and Bourne, 1984). Still, through careful experimental design and interpretation, they laid out the framework of molecular events underlying cardiac ECC that endures today. It should be noted that, while the majority of these early findings hold for both ventricular and atrial myocardium, the ultrastructural differences between the chambers impart major differences in the subcellular dynamics of Ca^{2+}-induced Ca^{2+} release (CICR). Unless otherwise noted, we focus on the nanoscale structure-function relationships in ventricular tissue throughout this manuscript.

By the early 1980s a number of characteristics of cardiac ECC function were clear. It was well known that the majority of Ca^{2+} that drives cardiac contraction is released from the cardiac SR at the terminal cisternae (now commonly known as the junctional SR, jSR). In intact myocytes, cardiac ECC clearly required Ca^{2+} influx during the action potential (Näbauer et al., 1989). However, the meticulous studies of Fabiato and Fabiato (1972, 1975b,c) showed that this could be recapitulated by rapidly increasing free $[Ca^{2+}]$ around the SR in skinned (sarcolemma removed) preparations (Szent-Gyorgyi, 1949; Endo, 2011). This CICR was subject to a number of modulators including cytosolic $[Mg^{2+}]$ and ATP, and importantly, it was proportional to the rate at which the "trigger" $[Ca^{2+}]$ was introduced to stimulate SR Ca^{2+} release. In the early to mid 1980's the plant alkaloid ryanodine (a known inhibitor of SR Ca^{2+} release) was used to great effect for isolating, and reconstituting Ca^{2+} release function (Cannell et al., 1985; Fabiato, 1985; Fleischer et al., 1985; Maurer et al., 1985; Hymel et al., 1988). This established the ryanodine receptor (RyR) family as SR Ca^{2+} release channels, and recapitulated (at the single channel level) the important sensitivities of macroscopic CICR to cytosolic Ca^{2+}, ATP, and Mg^{2+}. Prior EM observations (in skeletal muscle) of these gigantic channels at the cytosolic face of the terminal cisternae suggested that they clustered together in an ensemble (Inui et al., 1987; Lai and Meissner, 1989), and most likely also operated in a coordinated fashion during SR Ca^{2+} release.

Together, this information suggested that CICR was the dominant mechanism of cardiac ECC, wherein Ca^{2+} influx via sarcolemmal L-type Ca^{2+} channels (LTCCs) during the action potential drives Ca^{2+} release from RyRs in the junctional SR. This conceptual model differed from skeletal muscle ECC, which occurred in very similar structures but was far less dependent on Ca^{2+} influx (Rios and Pizarro, 1988; Näbauer et al., 1989). Thus, at the beginning of the 1990's a wealth of functional studies had established the basic macroscopic properties of CICR in cardiac tissue, and given rise to a series of hypothetical nanoscale mechanisms (Stern, 1992). However, due to shortcomings in functional imaging resolution, these mechanisms could not be directly probed at the time, and it was mathematical

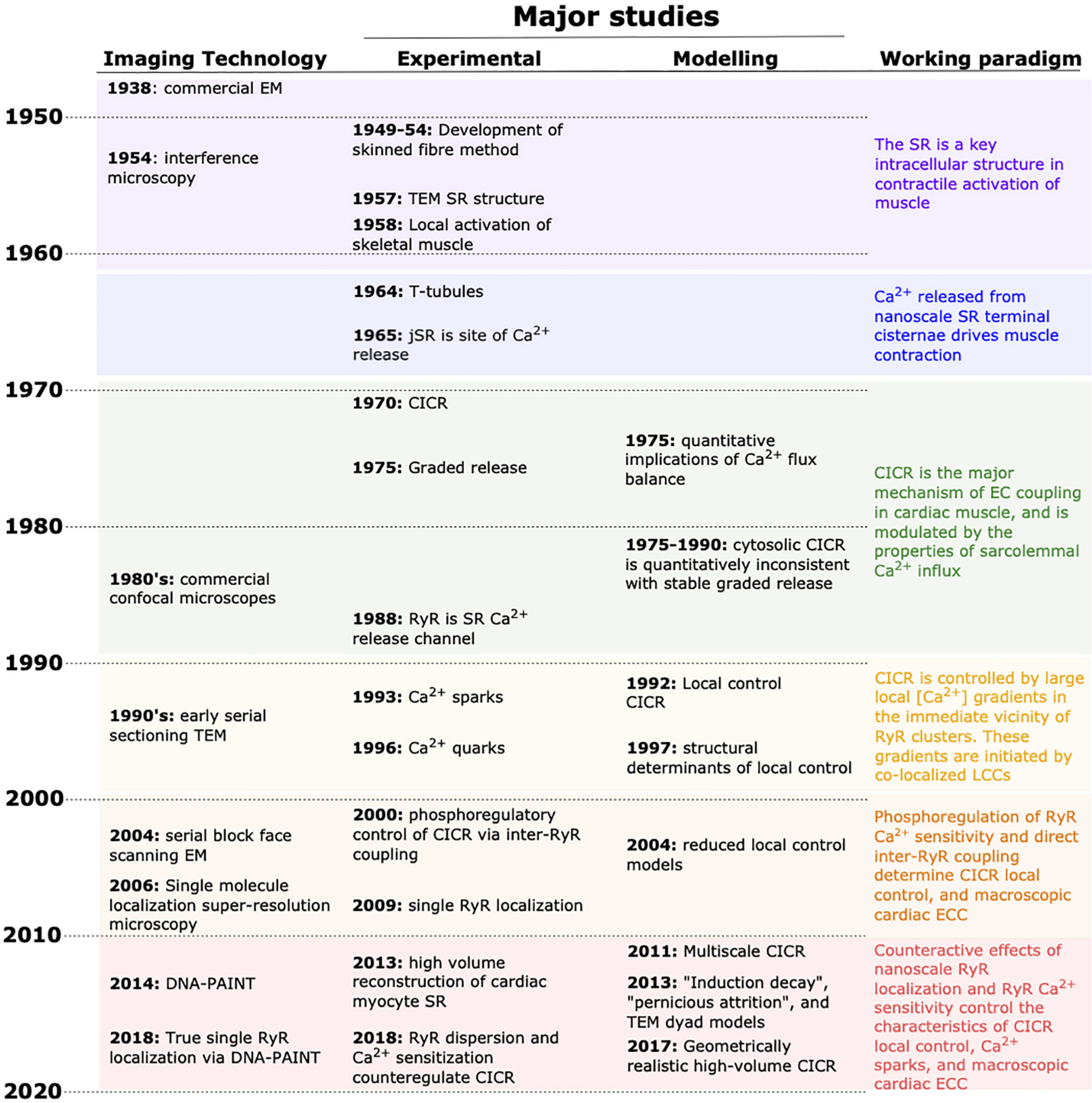

Major studies

	Imaging Technology	Experimental	Modelling	Working paradigm
	1938: commercial EM			The SR is a key intracellular structure in contractile activation of muscle
1950	**1954**: interference microscopy	**1949-54:** Development of skinned fibre method **1957:** TEM SR structure **1958:** Local activation of skeletal muscle		
1960		**1964:** T-tubules **1965:** jSR is site of Ca^{2+} release		Ca^{2+} released from nanoscale SR terminal cisternae drives muscle contraction
1970		**1970:** CICR **1975:** Graded release	**1975:** quantitative implications of Ca^{2+} flux balance	CICR is the major mechanism of EC coupling in cardiac muscle, and is modulated by the properties of sarcolemmal Ca^{2+} influx
1980	**1980's:** commercial confocal microscopes	**1988:** RyR is SR Ca^{2+} release channel	**1975-1990:** cytosolic CICR is quantitatively inconsistent with stable graded release	
1990	**1990's:** early serial sectioning TEM	**1993:** Ca^{2+} sparks **1996:** Ca^{2+} quarks	**1992:** Local control CICR **1997:** structural determinants of local control	CICR is controlled by large local [Ca^{2+}] gradients in the immediate vicinity of RyR clusters. These gradients are initiated by co-localized LCCs
2000	**2004:** serial block face scanning EM **2006:** Single molecule localization super-resolution microscopy	**2000:** phosphoregulatory control of CICR via inter-RyR coupling **2009:** single RyR localization	**2004:** reduced local control models	Phosphoregulation of RyR Ca^{2+} sensitivity and direct inter-RyR coupling determine CICR local control, and macroscopic cardiac ECC
2010	**2014:** DNA-PAINT **2018:** True single RyR localization via DNA-PAINT	**2013:** high volume reconstruction of cardiac myocyte SR **2018:** RyR dispersion and Ca^{2+} sensitization counteregulate CICR	**2011:** Multiscale CICR **2013:** "Induction decay", "pernicious attrition", and TEM dyad models **2017:** Geometrically realistic high-volume CICR	Counteractive effects of nanoscale RyR localization and RyR Ca^{2+} sensitivity control the characteristics of CICR local control, Ca^{2+} sparks, and macroscopic cardiac ECC
2020				

FIGURE 1 | Progress in unraveling cardiac EC coupling based on experimental imaging and mathematical modeling. Continual advancement of imaging technologies **(left column)** has provided the tools for critical experimental insight during the last decades. Complementary advancements in mathematical modeling have contributed to shifting the paradigm in our understanding of EC coupling **(right column)**. In recent years, experimental and modeling developments have allowed a near merging of the spatial and temporal scales that each can be used to investigate. EM, electron microscopy; TEM, transmission EM; CICR, calcium-induced calcium release; SR, sarcoplasmic reticulum.

modeling that made the first critical strides in interrogating these hypotheses.

Early Quantitative Modeling and the Birth of Local Control

In the period leading up to the early 1990s, computational investigations focused on reconstituting observable macroscopic ECC by integrating known characteristics of cardiac membrane ultrastructure with our understanding of Ca^{2+} transporter function. A number of early models managed to recapitulate dynamic ECC properties driven by Ca^{2+} flux balance, most prominently force-frequency relationships and staircase phenomena (Bassingthwaighte et al., 1973; Kaufmann et al., 1974; Adler et al., 1985; Hilgemann and Noble, 1987). However, these models were necessarily simplified, and all involved Ca^{2+} release mechanisms that were not solely tied to intracellular Ca^{2+}. The necessity for such phenomenological approaches was due to one major quantitative shortcoming of the central tenet of CICR—*when the Ca^{2+} released by the SR is assumed to* *contribute to the same pool as the trigger Ca^{2+}, SR release becomes a fully regenerative "all-or-none" phenomenon.* This was in stark contrast to Fabiato's (and others') clear observations that SR Ca^{2+} release was a graded phenomenon that depended on both the magnitude and velocity of triggering Ca^{2+} influx (Fabiato and Fabiato, 1975a, 1977). In 1992, Stern (1992) provided a critical theoretical study that crystalized this paradox and made crucial postulates for how nanoscale function and dynamics in CICR could overcome the issue. That paper was directive for the field and the formal birthplace of our 'local control' understanding of cardiac ECC.

In essence, local control quantitatively formalizes the concept that individual Ca^{2+} release sites must operate at least semi-independently, as they respond to their own local Ca^{2+} concentration. With this consideration, graded and stable SR Ca^{2+} release becomes an intrinsic property of the system across a much broader range of triggering fluxes and SR Ca^{2+} loads than if Ca^{2+} release is driven by the bulk cytosolic pool of Ca^{2+}. As part of his treatise, Stern formulated several key characteristics required for a local control system to operate in this way: (1) the Ca^{2+} released by an RyR into its own local environment must diffuse away from the channel with approximately the same (or faster) kinetics than those with which the RyR channels close—a reasonable assertion based on available evidence, and one that has held the test of time; (2) when the number of RyRs at a release site is more than one (best estimates at the time suggested an average of ~10), there must be a separate mechanism (e.g., RyR inactivation, or local jSR Ca^{2+} depletion) to terminate the Ca^{2+} release. If such a mechanism does not exist, the local [Ca^{2+}] that drives channel opening remains high and the various RyRs "trade off" in their opening over time, resulting in "latched" release. In part because of these clear postulates, one major direction that both experimental and computational efforts have pursued in the decades since has been to more accurately quantify the number of RyRs that participate at a release site. As Stern demonstrated, the interaction between this number and the local SR Ca^{2+} dynamics critically determines several micro- and macroscopic properties of cardiac ECC, notably including the mechanism of local Ca^{2+} release termination. With these fundamental functional characteristics becoming more clear, the terminology used to describe the structures involved in CICR also became more precise. The collection of RyRs at a single jSR terminal (thought to operate as a single coordinated functional unit), together with that local jSR volume and its releasable Ca^{2+}, became known as a Ca^{2+} release unit (CRU). Stern himself coined the term "couplon" to describe the CRU together with the local LTCCs that control Ca^{2+} release. Below we describe how super-resolution imaging has since added some subtlety to these definitions by identifying geometric subsets of RyRs within the CRU that likely behave semi-autonomously depending on conditions (e.g., SR load, RyR modulation). Such subsets are often termed "clusters."

In 1992, the simulations that Stern (1992) had implemented involving stochastically operating collections of RyRs were at the limit of computational tractability, even without solving for local diffusion of Ca^{2+}. However, it was clear that if local control was indeed the core mechanism of CICR, there were broad implications for how these nanoscopic local events were integrated over the whole cell, and how they both depended on and determined the macroscopic properties of cardiac ECC. With this seed, and parallel developments in both computing and imaging power, a second major direction for ensuing work has been to develop an integrated understanding of the interdependencies between locally controlled CICR and macroscopic cardiac ECC.

Ca^{2+}-Induced Ca^{2+} Release in the Age of Ca^{2+} Sparks and Quarks

By the early 1990s it was presumed that, given suitable optical conditions, local spontaneous Ca^{2+} release events (resulting from probabilistic opening of RyRs) should be observable in cardiac muscle. Interestingly, it was also at this time that the technology required to detect these elementary events had begun to become widely available. Laser scanning confocal microscopy (LSCM) critically enabled separation of in-focus and out-of-focus fluorescence, and built upon the basic concept for confocal optical sectioning developed and patented by Marvin Minsky in the late 1950s. At the time of Minsky's patent, critical complementary technologies involving light collection, data processing and storage, and visualization were not yet available. Thus, it wasn't until the late 1980s that commercial confocal microscopes began making their mark on biology, and could be applied to discerning these small localized Ca^{2+} release events. Only one year after Stern's paper, Heping Cheng working with Jon Lederer and Mark Cannell, published the first measurements of these spontaneous Ca^{2+} release events that many had envisaged (Cheng et al., 1993). In that classic study, they utilized LSCM to visualize and characterize the events, naming them Ca^{2+} *sparks*, and the paradigm of CICR quickly shifted to focus on Ca^{2+} signaling in the dyadic nanodomain. It is particularly noteworthy that Cheng's sparks exhibited a range of morphologies that closely reflected the various dynamic regimes predicted by Stern's computations, including the non-terminating events reflecting "latched" release. Since 1993 many studies have been conducted to extend our understanding of spark dynamics. In particular, considerable efforts have been made to establish the similarities and differences in Ca^{2+} release dynamics for these spontaneous local sparks versus cell-wide CICR driven by the action potential and opening of LTCCs ("triggered" CICR).

A technical aspect of spark measurements that remains significant today, is that signal-to-noise characteristics for modern Ca^{2+} fluorophores in conventional LSCM imaging volumes are typically not high. As a result, discernible sparks are often only those events that involve a relatively large regenerative Ca^{2+} release centered within the imaging volume. Many smaller or out-of-focus events simply contribute to the background fluorescence and noise. Recognizing this, experimentalists have since sought to observe and characterize these smaller events, and modelers have focused on understanding their contribution to triggered CICR and importance to macroscopic ECC. Ca^{2+} signals resulting from the opening of single RyRs were first suggested by Peter Lipp and Ernst Niggli, and named quarks for their presumed quantal underpinnings (Lipp and Niggli, 1996; Niggli, 1999). While those clever studies required decidedly indirect approaches to measuring these events, more recent work involving simultaneous monitoring of cytosolic and SR Ca^{2+} has established that sub-spark events are both measurable and frequent in cardiac cells (Brochet et al., 2010). While it is unclear from this work if these events reflected the opening of single RyRs or small RyR clusters, it is noteworthy that these small release events are relatively heterogeneous, both in size and kinetics. This variability may reflect differences in both local Ca^{2+}-mediated gating of RyRs and the geometric configuration of the RyR ensemble in the CRU.

In addition to an evolving understanding of RyR participation in Ca^{2+} sparks, experimental studies combining patch-clamp and confocal microscopy were providing new quantitative insight into triggered CICR. These studies reported the "gain" of this process in intact (non-permeabilized) myocytes, i.e., the quantitative relationship between LTCC-mediated sarcolemmal Ca^{2+} influx and RyR-mediated SR Ca^{2+} release, at the whole-cell level (Wier et al., 1994; Cannell et al., 1995). These studies brought forward a number of questions surrounding the efficiency of single LTCCs to trigger activation of the juxtaposed RyR ensemble—a property often described as ECC "fidelity." However, due largely to inadequacies of LTCC antibody labeling, confocal imaging studies in this era struggled to identify the degree of LTCC and RyR colocalization, which limited the certainty with which these relationships could be established. A classic study from the Franzini-Armstrong group then managed to address this issue at far higher resolution. Using EM freeze fracture, they reported that RyR "feet" were indeed in close proximity to dimples in the membrane attributed to L-type Ca^{2+} channels (Sun et al., 1995). But how closely localized must these two channels be, and how many LTCCs must contribute Ca^{2+} to the dyadic cleft to enable high fidelity functional coupling? To investigate these fundamental geometric and quantitative requirements of CICR, Cannell and Soeller (1997) and Soeller and Cannell (1997) developed an idealized computational model of electrodiffusion in the dyad. They were particularly interested in understanding how very brief openings (mean open time ∼0.2 ms) of sarcolemmal LTCCs could trigger nearby RyRs (for which opening latencies are on the order of ∼1–2 ms). This required a comprehensive reaction-diffusion simulation framework and meticulous attention to the RyR dynamic model. Through these efforts, they established a number of principles that continue to guide CICR concepts and modeling today. First, the width of the dyad (the distance between the sarcolemmal and jSR surfaces) is critically important to the efficiency and fidelity of coupling. This is now a ubiquitous model finding, but one which had not been addressed in a comprehensive way by prior studies. Second, even within such a constrained space, the distance of individual RyRs from an open LTCC was crucial for determining their probability of opening, suggesting that LTCCs and RyRs must be tightly arranged in the dyad. It was also remarkable that, in the context of the very restricted dyadic space, opening of a single LTCC could dramatically increase the effective $[Ca^{2+}]$ in the immediate vicinity of adjacent RyR binding sites on the microsecond time-scale, thus allowing measured LTCC kinetics to reliably trigger its accompanying CRU. Having noted those key findings, Soeller and Cannell also readily acknowledged the lack of certainty surrounding aspects of RyR dynamics that made their precision somewhat more fortuitous than it may have appeared. Indeed, it is now clear that RyR gating kinetics, dyadic $[Ca^{2+}]$ sensitivity, and unitary current all importantly determine the ability for opening of either an LTCC or RyR to trigger regenerative release. Thus, there is a growing appreciation that *in vivo* coupling fidelity is a plastic property. Indeed, RyR dynamics and Ca^{2+} sensitivity are strongly sensitive to modulation by Mg^{2+}, ATP, Calmodulin, and a host of post-translational modifications. RyR unitary current is also dynamic during the spark (due to jSR depletion), and important for determining the threshold for spark termination and inter-CRU CICR (Ca^{2+} waves) at high SR Ca^{2+} load (Guo et al., 2012). As these characteristics of single RyR function have become more clear (Fill and Copello, 2002; Guo et al., 2012), and SR Ca^{2+} dynamics somewhat more measurable (Zima et al., 2010), various models have been developed to fully capture both spark initiation and termination (Cannell et al., 2013; Gillespie and Fill, 2013; Laver et al., 2013). Virtually all of these studies have reinforced the roles of dyadic width, and radial position of RyRs in determining spark activation. All have also emphasized a critical role for the size of the depletable local SR Ca^{2+} pool (jSR Ca^{2+} content) for determining spark termination. These characteristics appear to be the most fundamental for enabling reproducible CICR resulting from LTCC or spontaneous RyR opening. However, a range of dynamic factors also exert important physiological modulation of CICR. For example, voltage-dependent enhancement of unitary LTCC current potentiates CICR (Cordeiro et al., 2004; Hund and Rudy, 2004; Harris et al., 2005). This is best established in the canine epicardium, where rapid early repolarization (prominent epicardial notch) increases unitary LTCC current and potentiates whole-cell CICR in a manner that is important for achieving transmurally synchronous contraction (Cordeiro et al., 2004; Hund and Rudy, 2004).

The determinants of spark characteristics described by those earlier studies have generally been supported by more recent experiments employing either simultaneous SR and cytosolic Ca^{2+} monitoring (Zima et al., 2008; Picht et al., 2011), or strong cytosolic buffering to constrain the released Ca^{2+} (yielding "Ca^{2+} spikes") (Song et al., 1998). As a result, it has become clear that local Ca^{2+} release dynamics are quite different during triggered whole-cell CICR compared to spontaneous sparks. In turn, the roles of intra-SR Ca^{2+} diffusion and the local SR geometry have been brought into clearer focus as critical counterparts to RyR gating dynamics in determining the major aspects of sparks and macroscopic CICR. Significant modeling efforts have since been made to dissect the contribution of each to observable Ca^{2+} release dynamics. In particular, Hake et al. (2012), constructed a finite element model of a single jSR terminal (with associated regional network SR) from a 3D TEM tomogram to determine the role that geometry likely played in determining local SR Ca^{2+} depletion during a spark. An important immediate observation was that substantial Ca^{2+} must flow into the jSR from adjacent network SR regions to permit sparks of realistic duration and amplitude, even with considerable local calsequestrin buffering. Unfortunately, the scale of the dataset used to build the geometry was not sufficient to allow fully realistic intra-SR diffusion from outside of the imaged SR structures, and the speed of Ca^{2+} diffusion within the SR remains both contentious for experimentalists and a problematic uncertainty for modelers (Swietach et al., 2008; Picht et al., 2011). For that model, Hake et al. (2012) chose a simple and phenomenological model of RyR dynamics, in part to avoid another debated topic among experimentalists—the potential for luminal Ca^{2+} to promote RyR activation independent of cytosolic Ca^{2+}. Several of the key modeling studies noted above found that such a mechanism was not necessary to observe major characteristics of a spark in reasonable geometries (for which jSR Ca^{2+} was depletable). However, a range of evidence had also suggested that luminal regulation is a feature of RyR function, and may be crucial for both normal and pathologic RyR behavior (Jiang et al., 2004, 2005; Priori and Chen, 2011; Tang et al., 2012; Chen et al., 2014; Peng et al., 2016). Most recently, Fill and Gillespie (2018) and Gillespie (2019) have provided an elegant pair of studies that appear to at least partially reconcile this argument. By analyzing the full closed and open time distributions (and correlations between paired events), they noticed that open time is both negatively related to the preceding closed time, and that the triple exponential open time distribution is qualitatively quite different to those of the 2-state RyR models used previously. By implementing these characteristics in a new model of RyR gating they observed that sparks spontaneously terminated at a critically low single RyR flux (and thus SR Ca^{2+} threshold), even when the SR is not depleted (Gillespie, 2019). This has provided an important basis for understanding many of the observations thought to support the role of SR Ca^{2+}-sensing in RyR function and dysfunction, as well as a number of more general characteristics of RyR gating in CICR.

As a final note related to these studies of dyadic function, experimental data emerging in the 1990's indicated that LTCCs need not be the sole triggers for RyR Ca^{2+} release. The Na^{+}-Ca^{2+} exchanger (NCX), which predominantly functions in "forward" mode to extrude Ca^{2+} from the cell, reverses during the early repolarization of the action potential, due to the brief rise in cytosolic Na^{+} concentration and membrane depolarization. Various groups (Leblanc and Hume, 1990; Sipido et al., 1997) showed that Ca^{2+} influx by NCX can serve as at least a weak trigger for CICR. However, it was simultaneously noted that realistic unitary flux for reverse-mode I_{NCX} imposes a major quantitative constraint on the ability of intra-dyadic NCX to provide trigger Ca^{2+}. Still, confocal imaging studies also appeared to confirm that a substantial proportion of NCX proteins were co-localized with RyRs, thus providing some structural support for this mechanism (Jayasinghe et al., 2009). To more comprehensively interrogate the quantitative constraints of this process, Lines et al. (2006) employed a mathematical model of the dyad accounting for diffusion of both Na^{+} and Ca^{2+}. Their simulations indicated that, in addition to closely colocalized NCX and RyRs, CICR between the two proteins requires nearby placement of a Na^{+} channel and extremely slow Na^{+} diffusion. While ionic diffusion speeds within the dyad remain the subject of debate, this experimental and modeling work highlighted a growing appreciation for the complexity of the CICR process.

A Fiery Start to Understanding Regulation of Ca^{2+}-Induced Ca^{2+} Release

Given the clear importance of individual RyR gating dynamics and local interaction among RyRs, LTCCs, NCX, and SR Ca^{2+} load, it was natural for questions about control of those characteristics to take center stage for CICR research at the start of the new millennium. The particular topics that forged this new direction focused strongly on phosphoregulation of the RyR channel, and its implications for both physical and functional interaction of RyRs within the dyad. Those topics also became some of the most controversial in the field and stimulated heated debate that continues to smolder. While a proper treatment of this history is beyond the scope of this review, the most contentious aspects revolved around a line of work from the lab of Andrew Marks at Columbia. At the beginning of the 2000s, Marks' group proposed that phosphorylation of RyR2 at Serine-2808 caused dissociation of the accessory protein, FK506-binding protein 12.6 (FKBP12.6) from the RyR ensemble, and that this in turn destabilized the RyR closed conformation causing more frequent unitary RyR openings (Marx et al., 2000; Gaburjakova et al., 2001; Huang et al., 2006; Lehnart et al., 2008). These findings constituted an exciting development because they implied that phosphoregulation of RyR may be critical to the acute cardioregulatory effects of β-adrenergic stimulation, particularly contributing to enhanced contractile function and arrhythmogenicity. No less, they provided a plausible and detailed mechanism, as RyRs were proposed to become hyperactive, even near resting cytosolic Ca^{2+} concentration, and thus "leaky." However, along with those details, Marks had made the relatively bold claim that this particular phosphorylation may represent a nexus for a range of CICR dysfunction in disease, based largely on the observation that RyR was hyperphosphorylated at this site in heart failure. Together these claims triggered a vigorous response, and for the next decade (and more) most of the assertions in the original work have been subjected to intense scrutiny and counterarguments—see Eschenhagen's excellent commentary for a comprehensive review (Eschenhagen, 2010). While the field has now mostly accepted that the original claim overemphasized the role of that particular phosphorylation site, and likely also FKBP12.6, other aspects of the original findings have stood the test of time. Perhaps most importantly, the boldness of the proposal and the resulting scrutiny have themselves served to considerably extend our knowledge of CICR and its regulation.

One of the most initially challenging concepts in Marks' regulatory model was that a single phosphorylation could so markedly alter function of the giant RyR protein, and in turn lead to the myriad observed outcomes. While such a potent role for S2808 has since been largely rejected (Bers, 2012), clinically meaningful potency has been clearly established for the family of RyR point mutations underlying catecholaminergic polymorphic tachycardia (CPVT) (Jiang et al., 2004, 2005; Priori and Chen, 2011; Tang et al., 2012), and indeed for Ca^{2+}/Calmodulin-dependent protein kinase II (CaMKII) phosphorylation of the nearby S2814 site. It is now broadly accepted that CaMKII phosphorylation at S2814 is capable of conferring the majority of outcomes originally claimed by Marks for protein kinase A-mediated phosphorylation of S2808 (Guo et al., 2006; Kohlhaas et al., 2006; Curran et al., 2010; Hashambhoy et al., 2010; Gonano et al., 2011). Specifically, S2814 is recognized to be hyperphosphorylated in many disease states, notably including heart failure, and is thought to contribute to disease etiology by increasing SR Ca^{2+} leak and promoting arrhythmia. Mice harboring phosphomimetic and phosphodeficient substitutions at S2814 recapitulate most of these outcomes (Oort et al., 2010). Finally, because CaMKII is a Ca^{2+} activated kinase, its activity is strongly evoked by the enhanced Ca^{2+} cycling elicited by β-adrenergic stimulation, and perhaps by Ca^{2+}-independent interactions (Pereira et al., 2007, 2013; Ogrodnik and Niggli, 2010). For this reason, distinguishing the impacts of PKA versus CaMKII in the purely acute setting has largely been the domain of a somewhat blunt set of pharmacological tools.

Following these phosphoregulatory studies, a range of other post-translational modifications have been shown to alter RyR function and contribute to regulation of cardiac ECC. Earlier work focused on the role of disulfide oxidation (Terentyev et al., 2008; Belevych et al., 2009) and nitrosylation (Xu et al., 1998; Sun et al., 2008; Bellinger et al., 2009), both of which increase RyR open probability under conditions of oxidative stress, again notably during heart failure (Terentyev et al., 2008). The effects of disulfide oxidation appear to rely on enhanced luminal Ca^{2+} sensitivity (Terentyev et al., 2008) whereas S-nitrosylation may involve enhanced sensitivity to cytosolic Ca^{2+} (Sun et al., 2008). More recently, a line of studies from Ben Prosser and Jon Lederer have established a role for localized stretch-induced ROS signaling that modulates RyR activity on a beat-to-beat basis (Prosser et al., 2011, 2013a,b; Limbu et al., 2015). The contention of this work is that stretch-induced activation of NADPH oxidase in the vicinity of RyR permits ROS-mediated activation of RyR, and may define a physiologic role for RyR redox status in myocytes.

Beyond these regulatory impacts on single RyR function, it is also possible that the nanoscale organization of RyRs within the dyad is subject to acute regulatory signaling. Fu et al. (2016) have observed that RyRs phosphorylated at S2808 more readily colocalize with LTCCs, and in a manner that requires bridging integrator 1 (BIN1). This intriguing finding suggests that S2808-phosphorylated RyR molecules are recruited to the dyad; an observation that appears to be supported by higher resolution imaging studies that have tracked phosphorylated and dephosphorylated RyR (Sheard et al., 2019; Hurley et al., 2021).

In sum, the strong debates and vigorous effort that has ensued from Marks original studies has added a great deal to our understanding of regulatory influences in cardiac CICR. For the purposes of discussing how these regulatory effects impact structure-function relationships in CICR, it is true that the mechanisms generally converge upon either enhanced or reduced RyR Ca^{2+}-sensitivity (observed as both cytosolic and luminal sensitivity). While the effects of regulation on other aspects of single RyR function need to be more comprehensively studied, this form of modulation has been a prominent finding in studies to date, and can be readily incorporated into modeling frameworks.

THE CHANGING INTERACTION OF EXPERIMENT AND SIMULATION IN THE ERA OF SINGLE MOLECULE IMAGING AND SERIAL SECTIONING ELECTRON MICROSCOPY

Single Molecule Localization Microscopy and Our Evolving Understanding of CRU Structure and Function

As noted in previous sections, it has long been realized that Ca^{2+} release occurs at discrete sites (i.e., CRUs), where cooperating RyRs generate Ca^{2+} sparks. Early estimates of CRU dimensions stemmed largely from 2D EM studies, using counts of RyR "feet" within the dyadic cleft (**Figure 2A**). These data were extended to 3D based on assumptions of dyadic shape, leading to the calculation that typical CRUs contained >100 RyRs, which were assumed to be densely packed in a single contiguous ensemble (Franzini-Armstrong et al., 1999). Data from studies employing confocal imaging coupled with deconvolution analysis appeared to support these estimates (Soeller et al., 2007), and led to the incorporation of such large, densely packed RyR arrays into mathematical models (Koh et al., 2006; Restrepo et al., 2008). Within these arrangements, RyRs were thought to be present in a "crystalline array," based on data from both *in situ* and *in vitro* imaging showing RyRs oriented in a corner-to-corner, grid-like arrangement (Franzini-Armstrong and Protasi, 1997; Yin et al., 2005). However, emerging imaging techniques have now directly challenged these assumptions. In this section we highlight how these advances have triggered broad reconsideration of dyadic structure and function.

With the advent of super-resolution imaging (Betzig et al., 2006) came an unprecedented opportunity to investigate dyadic structure at the nanoscale. The two more commonly used techniques of single molecule light microscopy (SMLM) are photoactivatable and photoconvertible localization microscopy (PALM) and stochastic optical reconstruction microscopy (STORM) (Nieves et al., 2018). Both techniques employ the stochastic sampling of permanently bound fluorescent molecules switching between an on and off state, and subsequent reconstruction of an image with a spatial resolution on the order of 30 nm. Thus, these techniques offer an impressive (nearly 10-fold) improvement in resolution over traditional light microscopy techniques such as LSCM, and the ability to discern tiny dyadic components. To this end, the first cardiac application of SMLM was a dSTORM-based analysis of RyR organization within dyads at the cell surface of rat cardiomyocytes (**Figure 3A**; Baddeley et al., 2009). In contrast to the prevailing assumption at the time, these investigators

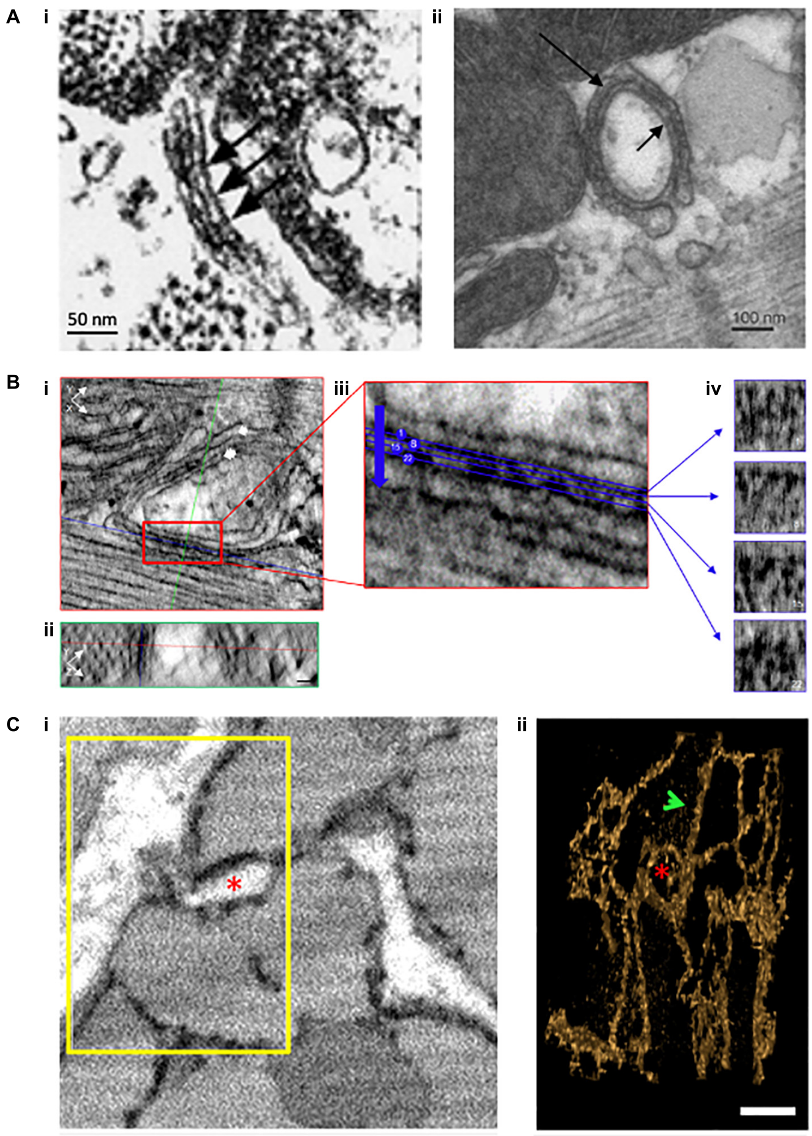

FIGURE 2 | Evolving understanding of dyadic structure from electron microscopy (EM) studies. Visualization of dyads was first enabled by EM, as early as the 1960s. Even with 2D applications of this technique **(A)**, dyadic junctions between the jSR and the cell surface [**(i)**, chick myocardium, (Franzini-Armstrong et al., 1998)] or t-tubules [**(ii)**, rat ventricular myocyte, (Novotová et al., 2020)] were readily apparent, and highlighted the tight geometry of the dyadic cleft. Electron dense "feet" visible in the cleft (arrows) were attributed to the cytosolic portion of the RyR. With the advent of tomography techniques and enhanced contrast agents, it became possible to assess the 3D orientation of individual RyRs within dyads (**B**, scale bars = 30 nm, Asghari et al., 2020). XY **(i)** and YZ **(ii)** orthagonal views are presented for a representative dyad (single arrow = jSR, double arrow = t-tubule). Indicated planes are positioned on a single RyR (red line = XY, blue line = XZ, and green line = YZ plane). **(iii)** A magnified view of the boxed region in **ii** illustrates selected sections (4 of 28 illustrated) taken across the dyadic cleft. Each of these four sections is presented in **(iv)**, allowing identification of the position and orientation of individual RyRs. Full 3D rendering of cardiomyocytes has been made possible by serial block face imaging coupled with scanning EM (**C**, Colman et al., 2017). **(i)** The presented 2D image from a sheep cardiomyocyte illustrates dyadic junctions between t-tubules (white) and the electron dense SR (black). Reconstruction of the boxed region in 3D **(ii)** illustrates both network SR (arrow) and the jSR encircling a t-tubule (asterisk). Copyright permission was obtained for the reproduction of Panel **(Ai)** (Franzini-Armstrong et al., 1998). Copyright permission was not required to reproduce the other figures.

reported that RyRs were not present in large ensembles, but rather in multiple small, neighboring clusters of a broad variety of shapes and sizes. Using a crystalline-array based filling of the identified cluster regions, Baddeley et al. (2009) calculated that the maximum occupancy of an average RyR cluster was only sufficient to hold approximately 14 channels, although many isolated single-channels were also observed. This insight required a major refinement of CICR models based on large (>100 RyRs), single-cluster CRUs. Xie et al. (2010) proposed that neighboring RyR clusters could coordinate the generation of a Ca^{2+} spark if their edge-to-edge distances were <100 nm. At these short distances, it was hypothesized that Ca^{2+} released from one

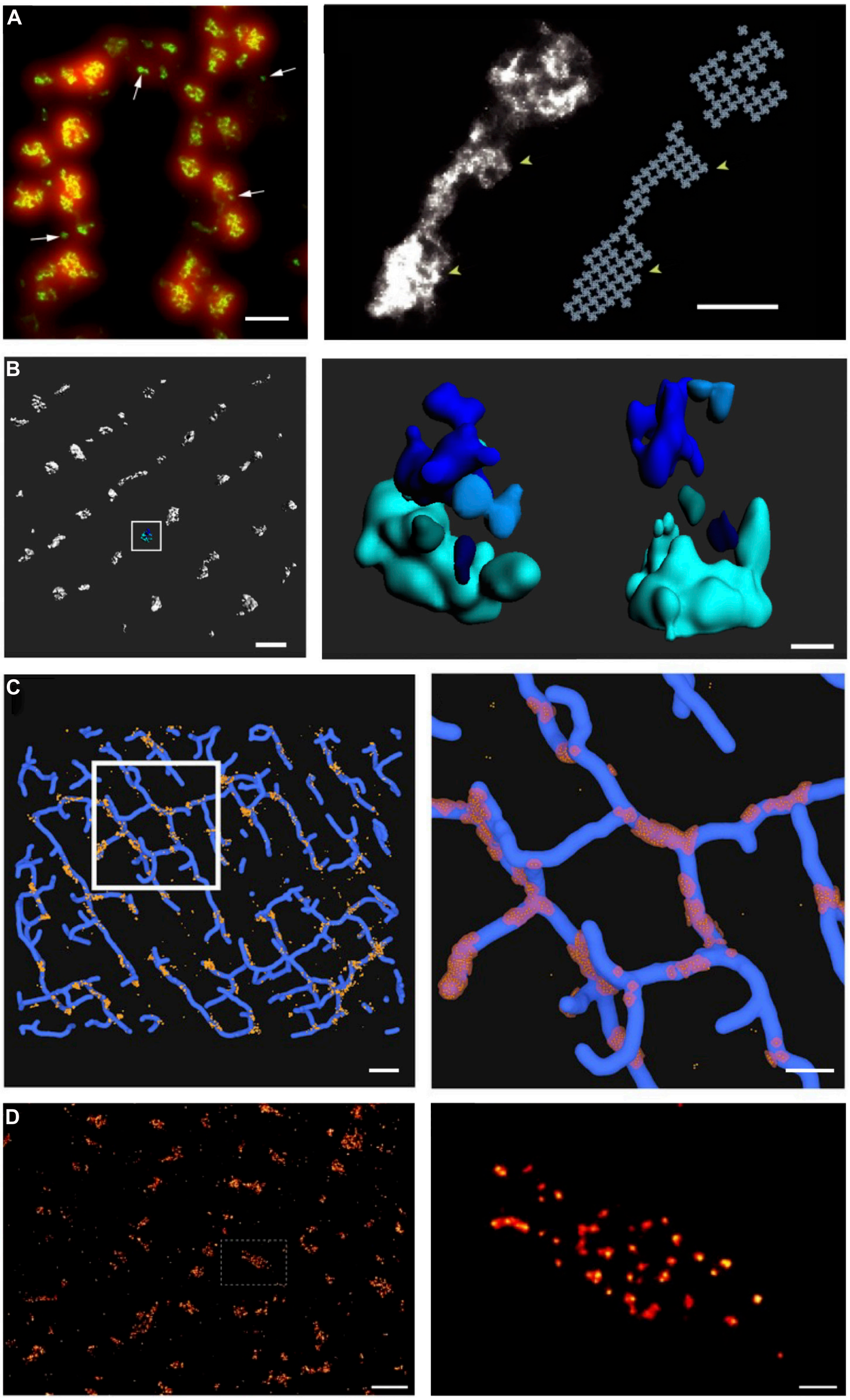

FIGURE 3 | Advances in super-resolution imaging provide novel insight into RyR organization. Although previous work had suggested that RyRs are present in large clusters, dSTORM super-resolution imaging of RyRs has shown that the channels are rather present in multiple small, neighboring clusters. On the cell surface, these arrangements are present in double rows, on either side of z-lines [**(A, left panel)**, (Baddeley et al., 2009)]. The increased resolution of RyR imaging by dSTORM (green) is noted in comparison with diffraction-limited imaging (red). Maximal occupancy of imaged clusters was calculated based on an assumed grid-link arrangement of channels **(A, right panel)**. Quantitative assessment of more complex RyR arrangements within the cell interior requires high-resolution in 3D. Using 3D dSTORM, internal Ca^{2+} release units (CRUs) containing multiple RyR clusters with diverse configurations were observed [**(B)**, enlargement of indicated region at right; (Shen et al., 2019)]. To gain insight into the orientation of RyRs within dyads, correlative 3D dSTORM imaging of RyRs was combined with confocal t-tubule imaging, and the channels were localized at the interfaces of the two signals [**(C)**, enlargement of indicated region at right, (Shen et al., 2019)]. Even higher resolution imaging using the DNA-PAINT technique revealed that RyRs exhibit irregular packing within clusters [**(D)**, (Jayasinghe et al., 2018)], in contrast to grid-based assumptions. Scale bars in left, right panels: A = 500 nm, 100 nm; B = 500 nm, 100 nm; C = 1 µm, 500 nm; D = 1 µm, 100 nm. Copyright permission was not required to reproduce the figures. **(A)** Copyright 2009, National Academy of Sciences.

cluster could jump to a nearby cluster, triggering its activation. Thus, according to this model, the basic unit of Ca^{2+} release in cardiomyocytes is a multi-cluster CRU or "super-cluster" of cooperating RyRs.

Of note, the seminal work of Baddeley et al. (2009) was conducted at the cell surface, where RyR arrangement was assumed to be roughly planar, enabling straight-forward estimation of channel numbers. The internal dyadic arrangements were expected to be far more complex, as the junctional SR curves around t-tubules (TTs) to form dyads, creating an arrangement where RyRs are super-imposed in the z axis. As with other optical imaging modalities, the resolution of dSTORM is considerably lower in the z axis than in the xy plane, meaning that it is not possible to discern vertically-aligned channels with 2D imaging. To circumvent this problem, Shen et al. (2019) employed phase-ramp dSTORM imaging to enable 3D imaging deep within rat cardiomyocytes (**Figure 3B**). In that study, we exploited an observed linear relationship between the number of fluorescent events (blinks) and the number of RyRs in images taken at the cell surface. Using this relationship for calibration, we estimated the numbers of RyRs within internal clusters and CRUs. These analyses showed that internal CRUs contain a highly variable number of rather small clusters (**Figure 3B**). While we found that many clusters contained only a single RyR, the average cluster (a fully contiguous RyR ensemble) contained 13 channels, and the average CRU (an RyR ensemble for which separation between individual channels did not exceed 100 nm) contained 23 channels (Shen et al., 2019). These estimates are significantly smaller than earlier estimates based on 2D EM (Franzini-Armstrong et al., 1999) or dSTORM of interior RyRs (Hou et al., 2015). However, they are in better alignment with EM tomography studies, which also further supported a complex, multi-cluster arrangement of internal CRUs (Hayashi et al., 2009). Of note, while the calibration-based approach to 3D imaging employed in Shen et al. (2019) enabled tallying of RyR numbers, it did not reveal the actual orientation of RyRs within clusters. Thus, correlative 3D dSTORM/confocal imaging of RyRs and t-tubules was employed to create an interface between the opposing jSR and TT membranes where the RyRs were arranged based on grid-based occupancy (**Figure 3C**). This analysis revealed that most RyRs are present in dyads in healthy cardiomyocytes, and that non-dyadic, "orphaned" or "rogue" RyRs are present in very small clusters. This latter observation supports that non-dyadic RyRs contribute to non-spark based "silent" RyR leak, since the released Ca^{2+} is of too low magnitude for detection by standard confocal techniques.

The novel, imaging-driven insights into CRU morphology described above have inspired new directions in mathematical modeling over the past decade. Based on the realization that RyR clusters are of irregular shapes, Walker et al. (2014) simulated the efficacy of Ca^{2+} spark generation with differing CRU configurations. They observed that more regular RyR cluster geometries exhibited higher spark fidelity than irregular shapes, in which individual RyRs have on average fewer neighboring channels. Cooperative "saltatory" Ca^{2+} release between clusters has also been studied in a number of mathematical models, based on both idealized (Nivala et al., 2012; Louch et al., 2013) and super-resolution defined CRU geometries (**Figure 4**; Macquaide et al., 2015; Kolstad et al., 2018). These analyses support the concept of super-cluster functionality; a paradigm that is somewhat analogous to the inter-CRU coordination that occurs at the micrometer scale during Ca^{2+} waves (Cheng et al., 1996; Keizer and Smith, 1998). These studies further indicated that the degree of cooperation between CRU sub-clusters also has significant implications for spark magnitude and kinetics (Louch et al., 2013; Macquaide et al., 2015; Kolstad et al., 2018). Of course, these aspects of CRU substructure interact strongly with RyR Ca^{2+} dependence and unitary current (as mentioned above) to determine local RyR interaction and release dynamics. The quantitative hierarchy of importance of structural versus RyR regulatory subtleties remains to be established, but it is clear that both are capable of markedly altering local control of CICR.

The dSTORM studies highlighted above estimated a maximum occupancy of each imaged RyR cluster based on a crystalline, lattice arrangement of the RyR channels reported in earlier work (Franzini-Armstrong and Protasi, 1997; Yin et al., 2005). However, with xy resolution very close to the actual size of the RyR (30 nm), it was not possible to assess intra-CRU packing in these dSTORM studies. Insight at that level (intra-CRU) has thus required the advancement of techniques with even higher resolution. Using tilt-EM tomography, Asghari et al. (2014, 2020) have shown that RyRs do not form an ordered pattern, but instead exhibit a more scattered arrangement even within clusters (**Figure 2B**). Similar results have been provided by a newer technique called DNA-PAINT. This approach was developed to achieve transient binding of fast-diffusing fluorescent DNA oligomers ("imager") to a target of interest ("docker") conjugated to antibodies (Sharonov and Hochstrasser, 2006; Jungmann et al., 2010). The repeated, transient binding events produce fluorescence blinking, allowing stochastic imaging at a resolution of <10 nm. Employing this technique, Jayasinghe et al. (2018) recently confirmed that RyR clusters exhibit irregular packing (**Figure 3D**). But what implications does this hold for function? Until recently, few modeling studies had interrogated the effects of RyR packing. Walker et al. (2014) observed that less dense RyR clusters exhibit lower Ca^{2+} spark fidelity, and Louch et al. (2013) reported that when sparks are successfully generated, the Ca^{2+} release is of reduced magnitude and slowed kinetics. Thus, by 2015, and thanks to the application of SMLM and structurally-defined modeling approaches, it was clear that CRU function (and even CRU definition) is critically dependent on the local arrangement of individual RyRs.

Extending the Horizon: High Volume Membrane Mapping Through Serial Sectioning Scanning Electron Microscopy

While the development of SMLM has provided enormous power by mapping RyR cluster structures in large sections of a myocyte, these methods are not sufficient in-and-of-themselves to constrain models of structure-function relationships in CICR. This is because, as described above, RyR cluster size interacts

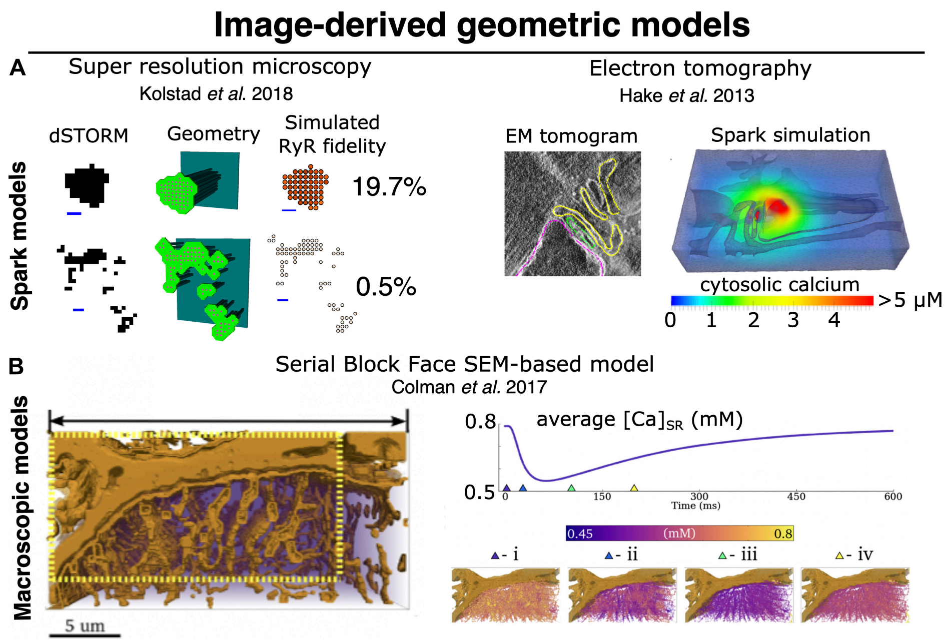

FIGURE 4 | Image-derived approaches to geometric modeling of CRU and whole-cell cardiac ECC. **(A)** Image-driven models of single dyad (and CRU) structures have been implemented beginning with both super resolution light microscopy (dSTORM), (left) (Walker et al., 2014; Kolstad et al., 2018), and tilt-section tomography from high voltage TEM imaging (right) (Hake et al., 2012; Edwards et al., 2018). To date, no correlative light/EM datasets visualizing both protein and membrane localization have been employed for this purpose, although such approaches would be highly desirable. **(B)** High-volume EM methods, particularly SBF-SEM, have recently been used as a basis for constructing image-driven geometries for much larger subsections of a cardiac myocyte (Colman et al., 2017; Colman, 2019). Simulations in these geometries can be used to interrogate the interaction of local Ca^{2+} release with uncertain (and difficult-to-measure) physiological properties, such as intra-SR Ca^{2+} diffusion. At right, spatially distributed intra-SR Ca^{2+} concentration is shown at various times during the evoked macroscopic SR Ca^{2+} release. Models of this type will likely provide the basis for bridging between the stochastic dynamics of single CRUs (and single RyRs) and pseudo-continuous dynamics of macroscopic CICR, thereby allowing us to better deconvolve the multitude of factors known to influence both. Copyright permission was not required to reproduce the figures.

with the local jSR Ca^{2+} pool to determine the dynamic regime of Ca^{2+} release. That is, the relationship between RyR cluster size and the local jSR size, and thus Ca^{2+} content, is critically important. When SMLM-defined RyR locations are used to build computational structures, one must make important assumptions about these relationships (Kolstad et al., 2018), none of which are well-constrained at this time. EM methods provide a means of imposing this constraint, because they can be used to map the jSR membrane structure, which yields the local depletable SR volume. However, until recently, technical challenges prevented this type of membrane mapping in volumes comparable to those now accessible via SMLM.

The EM studies described in earlier sections involved transmission EM performed on thin cryotome sections or freeze fractured surfaces (Sun et al., 1995; Franzini-Armstrong et al., 1999), occasionally with tilt tomography to assess 3D membrane structures within the section plane (Hayashi et al., 2009). While these methods provided the bulk of our early understanding of the cardiac membrane structures in cardiac ECC, they are also limited to assessing those structures in the relatively small volumes imposed by the thinness of the individual sections. Neuroscientists have had long-standing interest in mapping membrane structures in full 3D volumes to reconstruct neural microcircuits. Until the early 2000s, this had been achieved via the same thin-sectioning approach performed serially (and manually) through a tissue block. This was both extraordinarily laborious and challenging to achieve high-quality registration of the manually collected sections. Shortly into the new millennium, a new range of techniques began appearing involving a variety of automated approaches to serially section a fixed tissue block and then record a scanning EM image of the freshly exposed tissue plane. These sectioning approaches include automated serial block-face SEM (SBF-SEM) (Denk and Horstmann, 2004), focused ion-beam milling SEM (FIB-SEM) (Heymann et al., 2006), and automated tape-collecting ultramicrotomy SEM (ATUM-SEM) (Hayworth et al., 2006).

The unprecedented ability for these methods to map membrane structures at resolution of a few nanometers (zeptoliter voxels) (Pinali et al., 2013; Pinali and Kitmitto, 2014; Morgan et al., 2016), but in total tissue volumes approaching ~ 1 mm^3, have provided a new foundation for simulating multiscale dynamics in cardiac ECC. Importantly, the scale constraints applying to experiments of this type should not be underestimated. At this resolution and tissue volume, the duration of the sectioning and imaging alone is measured in weeks, and the final retrieved dataset approaches petabyte storage scales. Those challenges notwithstanding, the first study to apply these techniques in cardiac myocytes was performed by Pinali et al. (2013) and imaged voxels of ∼ 11 zL over 5–8 cells (∼150–240 pL) per tissue block via SBF-SEM. This study provided the first cell-wide mapping of cardiac SR structure, verifying it as a diffuse but entirely continuous depot for storage and transport of Ca^{2+} (**Figure 2C**). Their work additionally provided new understanding of the complexity of dyadic junctions between jSR terminals and an intricately branched t-tubule system. While these findings were not entirely unexpected, the depth of detail available via these datasets has provided the first basis for modeling and simulation adhering to full geometric realism of the intracellular Ca^{2+} handling machinery. The first follow-up simulation efforts have demonstrated both the power and challenges of applying data that span such a range of spatial scales. In order for simulations to remain tractable, Colman et al. (2017) were forced to construct their simulation geometry from a myocyte subsection (∼1/12th of the cell volume), considerably down-sample the model from the full imaging resolution, and apply homogeneous jSR sizes at all positions where the SR and TTs were observed to form dyads (**Figure 4**). In this way, the model likely captured dynamics that depend on the spatial distribution of the dyads within the cell, but failed to incorporate the nanoscale CRU dynamics described in the previous section, and which should (in principle) be accessible at the raw imaging resolution.

Nevertheless, with future improvements in computational power and efficient modeling approaches, high volume SEM imaging promises to provide a key platform for constraining our understanding of critical properties of cardiac ECC. In particular, simulations involving such realistic and large SR geometries could provide clear constraint on the rates of intra-SR Ca^{2+} diffusion and jSR Ca^{2+} refilling, which at this time remain poorly understood. This is noteworthy because these properties are central to aspects of macroscopic frequency dependence in cardiac ECC, and for the pathologic dynamics underlying Ca^{2+} waves, and electrical and mechanical alternans (Gaeta et al., 2009, 2010; Gaeta and Christini, 2012; Groenendaal et al., 2014; Colman, 2019).

Plasticity of CRU Structure and Function in Health and Disease

Based on the above discussions, the impression may be that while CRU organization is very complex, it is at least static. However, a wealth of data indicate that, in fact, there is remarkable plasticity of dyadic structure and function. Even basic confocal imaging studies have long established that TT organization is highly malleable, as these structures appear gradually during development and are significantly reorganized during disease (reviewed in Setterberg et al., 2021). This structural reorganization leaves functionally "orphaned" RyRs, which are no longer present in dyads, and these sites exhibit delayed Ca^{2+} release during the action potential only after diffusion of trigger Ca^{2+} from intact dyads (Louch et al., 2006; Song et al., 2006). Thus, the overall pattern of Ca^{2+} release across the cell is desynchronized and slowed. More recently, high-resolution imaging studies have provided even greater detail in examining nanoscale TT structure in health and disease. Using SMLM, non-SMLM techniques such as STED microscopy, and EM, several studies have reported that there is considerable variation in t-tubule diameter and in the extent of folding of their luminal membranes (Wagner et al., 2012; Hong et al., 2014; Jayasinghe et al., 2014; Crossman et al., 2017; Frisk et al., 2021). Importantly, t-tubules dilate during heart failure, and the intricate folding structure is lost (Hong et al., 2014; Crossman et al., 2017; Frisk et al., 2021). While it is possible that t-tubule dilation may result in misalignment of LTCCs and RyRs (Jones et al., 2018), modeling studies have indicated that loss of inner membrane folding increases the rate of solute exchange between the t-tubule lumen and extracellular space, in a pro-arrhythmic manner (Hong et al., 2014).

Sarcoplasmic reticulum structure is also known to be malleable, as classic EM studies revealed that jSR geometry differentiates gradually in the developing heart with initial appearance of jSR at the cell surface, prior to the later introduction of cisternae at t-tubule sites (Franzini-Armstrong et al., 2005). As mentioned above, SBF-SEM imaging has provided fantastic 3D detail of SR structure (**Figure 2C**), and indicated that there is an overall loss of SR during heart failure, including local lesions where structure is markedly disrupted (Pinali et al., 2013). Coincident with changes in SR structure, are alterations in the nanoscale arrangements of RyRs during disease. Indeed, several studies have reported that RyR clusters are broken apart in heart failure (Kolstad et al., 2018; Sheard et al., 2019) and atrial fibrillation (Macquaide et al., 2015). We have, with the help of mathematical modeling, linked this "dispersion" of RyR clusters and CRUs to slowing of spark kinetics during heart failure, as Ca^{2+} release spreads between sequentially activated clusters (Louch et al., 2013; Kolstad et al., 2018), desynchronization of the Ca^{2+} transient, and slowing of cardiomyocyte contraction (Bøkenes et al., 2008). Interestingly, Macquaide et al. (2015) linked similar rearrangements of RyRs to the generation of pro-arrhythmic Ca^{2+} waves, enabled by an increased appearance of fragmented CRUs extending between z-lines. The drivers of this RyR reorganization are as yet unclear. However, even in the healthy heart Asghari et al. (2020) observed that RyR position and orientation are sensitive to phosphorylation status, Mg^{2+} concentrations, and the presence or absence of accessory proteins such as FKBP12.6. We anticipate that unraveling these mechanisms and their consequences for Ca^{2+} homeostasis in the normal and diseased cardiomyocyte will be an important topic of future experimental and modeling analyses.

Addressing Remaining Experimental Limitations

An exciting time is upon us, as experimentalists and modelers now find themselves nearly aligned in terms of the spatial scale that can be investigated. However, there remain significant experimental hurdles in directly linking nanoscale CRU structure and function, and this in turn leaves computational scientists without definitive validation data for their models. Specifically, the super-resolution imaging techniques described above generally require fixed cardiomyocytes, which has precluded directly pairing Ca^{2+} recordings to cellular substructure. One recent study attempted this feat in a correlative manner, with sparks recorded first in live cells, prior to fixation, and subsequent super-resolution imaging of the same CRUs (Hurley et al., 2021). However, it should be noted that with complex protocols for fixation, labeling, and imaging, there is considerable risk for disrupting cell geometry and alignment between imaging modalities. Another option is to use super-resolution imaging in live cells expressing a photo-activated fluorophore affixed to a protein of interest. Recent work has employed this approach to examine LTCC positions together with "sparklets"; i.e., Ca^{2+}-dependent fluorescence events corresponding to single channel openings (Ito et al., 2019). Similar approaches could be envisioned to allow pairing of RyR localization and Ca^{2+} spark measurements in the same, living cell. This would enable direct investigation of RyR cooperativity within and between clusters, and definition of CRUs based on function rather than assumptions based solely on knowledge of RyR positions.

While there have been impressive recent strides taken in the advancement of light microscopy, the above discussion has made clear that SMLM techniques like dSTORM and PALM cannot adequately resolve the arrangement of proteins within clusters. Indeed, these techniques routinely yield an xy resolution of 30–40 nm which, even in the case of a large protein like the RyR (width ∼27 nm), is sufficient only for defining an area occupied by the channel. For insight into intra-cluster, real-time RyR location, the increased resolution of a technique like DNA-PAINT would be needed (**Figure 3D**), but with suitability for live cell experiments. By definition, live cells cannot provide the immobile "docking" strands that DNA-PAINT requires, and DNA "imager" strands may be rapidly degraded and/or associate with cellular DNA or RNA. Thus, live-cell applications of DNA-PAINT have so far been very limited, and only employed for imaging molecules on cell surfaces (Strauss et al., 2018). A very recent study surmounted the latter challenge by designing "docker" and 'imager' probes with left-handed DNA (L-DNA) which do not hybridize with endogenous nucleic acids (Geertsema et al., 2021). Still, it seems clear that continued refinement of these techniques will be necessary to gain further experimental insight into dynamic changes in CRU structure and function at the length scale of single RyRs.

Although much of this review has focused on developments in improving the spatial scale of imaging, it should be noted that the temporal scale of measurements is also a critical experimental limitation. While events such as RyR openings are quite brief (∼5 ms, given best estimates of simultaneous changes in jSR and cytosolic [Ca^{2+}]), the frame time for recording Ca^{2+} release events is limited to approximately 2 ms with even the latest cMOS cameras. Thus, recorded Ca^{2+} signals are near the limit of Nyquist discrimination for single channel openings, and generally represent a complex integration of releases from multiple RyRs. One approach to addressing this issue was developed by the Lipp group (Tian et al., 2017). Termed "CaCLEAN," this technique removes the Ca^{2+} released in previous frames (and its expected diffusion) to reveal only the newly released Ca^{2+} signal. It is hoped that this type of approach, together with the further development of camera technology (sufficient signal:noise performance despite high frame rates), will shed further light into the true nature of RyR functional dynamics.

The above discussion has indicated that there remain substantial limits in attaining adequate spatial and temporal resolution to discern CRU structure and function based on experiments alone. Surely, this is good news for mathematical modelers, but will modelers be side-lined when technology eventually enables imaging of individual dyadic proteins and their Ca^{2+} signals in live cells in real time? This seems highly unlikely because protein organization is only one determinant of function. Post-translational modifications such as phosphorylation add yet another layer of complexity, and impose an additional level of difficulty in terms of imaging. Still, this integration of single protein regulation and structural dynamics is a very high priority for the field. If experimental and modeling frameworks can be devised to discriminate the contributions of each, it will open the door to being able to truly understand how each class of mechanism influences a broad range of disease phenotypes. This in turn would have important implications for effective therapeutic targeting of those diseases. Interestingly, emerging data indicate that phosphorylation of RyRs need not occur uniformly across clusters (Sheard et al., 2019), suggesting that channels at different positions in the CRU may have different Ca^{2+} sensitivities. However, modeling work to date has assumed the same Ca^{2+} sensitivity for all channels ("blanket phosphorylation"). We thus expect that including the regulation of individual channels in mathematical models will be essential for fully describing CRU channel behavior, even as imaging techniques continue to advance. Perhaps more importantly, the manner in which RyR localization and regulation contribute to whole-cell function will likely require an entirely different level of integration across the spatial scales of cardiac ECC—from CRU to cell. In the following section we deal specifically with the challenges to developing modeling approaches that may be capable of that level of integration.

THE COMING CHALLENGES OF INTERDISCIPLINARY DESIGN IN STUDYING CARDIAC ECC—A COMPUTATIONAL SCIENTIST'S PERSPECTIVE

The Unique Challenges of Modeling the Biology of Cardiac ECC

As described above, the characteristics of unitary SR Ca^{2+} release events (sparks and spikes) exhibit a range of dynamic regimes, such as latched release and stochastic attrition, which depend critically on the number and proximity of RyR channels in a local CRU domain. These shifts in dynamics represent the direct influence of stochastic properties of individual channels on the local ensemble dynamics. Furthermore, as mentioned, modern imaging has made it abundantly clear that the number of RyRs present in many CRUs (from <4 to >200 colocalized channels) spans a range that crosses these transitions in ensemble dynamics. Finally, spatial gradients in [Ca^{2+}] resulting from continuum diffusion in both the cytosol and SR also clearly contribute to determining those dynamic transitions. In combination, these characteristics enforce several basic requirements for accurately modeling cardiac CICR. Specifically, the scales covered by the model should allow for the stochastic operation of single RyRs to interact with realistic variability in the size and spatial organization of RyR clusters, as well as diffusive transport of Ca^{2+} in the cytosol and SR. As we discuss below, these requirements impose a substantial computational burden when simulating CICR among multiple CRUs up to subcellular scales. Thus, while the local studies of Stern (1992), Cannell and Soeller (1997), Soeller and Cannell (1997), Hake et al. (2012), and many others have already provided critical insights to single CRU function, the scale-up of these models to interrogate data arising from serial sectioning EM and other modern imaging methods (see **Figure 4**) will meet major technical challenges.

The Ideal Model of Cardiac Myocyte Ca^{2+}-Induced Ca^{2+} Release

To discuss these challenges in concrete terms it first helps to construct the hypothetical "ideal" model. Given the recent advances in serial sectioning EM and SMLM described above, it seems plausible to expect that existing or near-term datasets could yield: (1) the spatial distributions and geometric sizes of all jSR terminals in an average cardiac myocyte [via serial sectioning scanning electron microscopy (SS-SEM)], (2) the total volume and regional volume densities of the network SR in an average cardiac myocyte (via SS-SEM), and (3) the variation in RyR cluster sizes and their spatial distribution in a representative (perhaps 20 μm^3) region of an average cardiac myocyte (via SMLM). In principle, these datasets should be collected in similar cells. That is, for example, from the same species, same cardiac chamber, or otherwise similar in terms of any variable known to impart systematic differences in membrane ultrastructure or RyR localization. From these datasets it will be possible to construct representative distributions of the quantities (1–3), as well as many others, e.g., the volumetric density of jSR terminals that are not coupled to t-tubules. Of course, the characteristics of the membrane and RyR cluster geometries will not be spatially correlated because they will be collected in different cells. However, given sufficient data, some form of registration between the distributions should allow for assigning reasonable cluster sizes to individual jSR geometries. This approximation could be made considerably more precise with correlative SMLM-EM datasets. Still, to continue with our thought experiment; presuming these essential data (1–3 above) are available, it is in principle possible to construct a model with full geometric detail of all jSR terminals incorporating realistic RyR cluster sizes and inter-cluster distances for an intact myocyte. It is another matter entirely to determine if such a model could be simulated with fully stochastic RyR dynamics and local diffusive coupling.

Computational Requirements of the Ideal Model

The most costly dynamics for simulating such an expansive model of CICR will certainly occur in the ~20,000 dyads of the average ventricular myocyte. To reliably solve the local reaction-diffusion dynamics in the dyadic space during a Ca^{2+} spark, a spatial resolution (mesh edge length) of 12–15 nm is typically required (Hake et al., 2012; Kolstad et al., 2018). Recent data suggest that the dyadic width may be even narrower (~10 nm) than has been presumed in the past, and thus further refinement may be required (Rog-Zielinska et al., 2021; Setterberg et al., 2021). Presuming 12 nm is approximately correct, the volume of each mesh block would be approximately 1.7×10^{-9} pL. In the most conservative simulation strategy, involving a homogeneous finite volume integration, this would amount to some 1.7×10^{10} mesh blocks. The dynamics, particularly of the local RyR release current are also relatively stiff in the dyad, and require time discretization $\Delta t \sim 0.1\ \mu s$ using operator splitting solution schemes, even with analytic solution for the current itself. This also ignores the cost of implementing local electrodiffusion (as opposed to conventional Fickian diffusion), which generally requires considerably finer temporal resolution. Of course, the scale of the problem can be reduced by employing finite element approaches involving larger mesh blocks (thus fewer computational nodes) in regions where the transporter gating dynamics are less stiff and gradients are less severe. Still, this problem represents a substantial computational effort. To date, very large cardiac simulations involving both classical and more recent electrodiffusion models (Tveito et al., 2017; Jæger et al., 2021a) have been performed at a similar scale (several billion computational nodes), albeit using powerful compute resources and for very brief simulation times (Jæger et al., 2021b). As such, approaching this computational problem is likely to require similarly substantial computational resources, thoroughly optimized numerical implementations, and well-designed simulations of relatively short duration.

Approximating the Problem

The computational challenges imposed by simulating detailed stochastic dynamics across the comparatively large volume of a myocyte have been appreciated for some time. Some of the earliest efforts to perform this type of multiscale integration were begun by Ray Winslow's group at Hopkins, and Robert Hinch at Oxford. Initially, Greenstein and Winslow (2002) implemented a whole myocyte with 12,500 CRUs, each with 4 coupled dyadic subspaces (to represent the intracellular compartment for each of 4 LTCCs) and a single local jSR (**Figure 5B**). These 12,500 CRUs were coupled to single compartments for the network SR and the cytosol. In 2002 this was a substantial computational effort even though it did not implement genuine continuum diffusion throughout these compartments. Hinch followed up by cleverly reducing the scale of the problem (**Figure 5D**; Hinch et al., 2004). He recognized that very rapid intradyadic Ca^{2+} diffusion implied that it was only the state of the channels (open or closed) that dictated the cleft $[Ca^{2+}]$ at any point in time. Thus, he was able to reduce the dyadic dynamics to a set of equations, the size of which was determined by the number of channels (both LTCCs and RyRs) assumed to be in each dyad. This in turn allowed grouping of the rate constants that applied at similar timescales to each channel

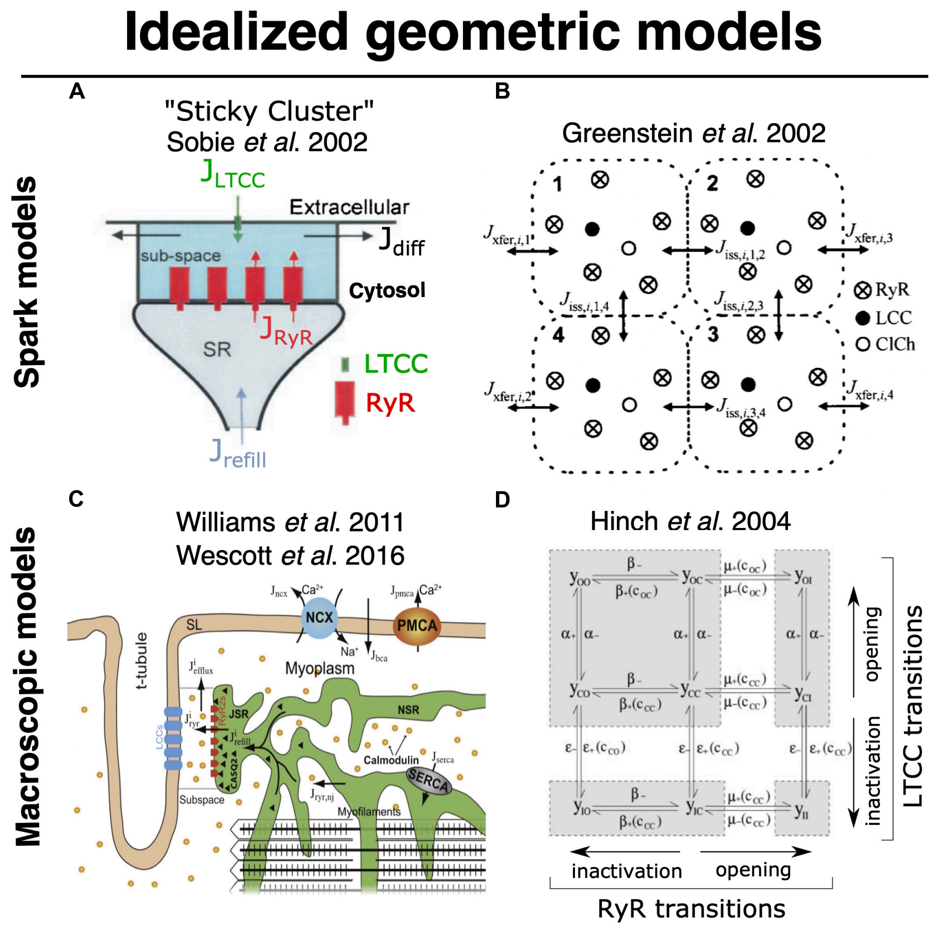

FIGURE 5 | Foundational models for idealized geometric modeling of cardiac ECC. **(A)** Two important early dyadic structure models involving stochastic RyR dynamics were provided by Sobie's sticky cluster (Sobie et al., 2002) **(A)**, and the 4-couplon model of Greenstein and Winslow (2002) **(B).** These two average dyadic models were each then extended to simulate whole-cell ECC by instantiating the 12,500–20,000 stochastically operating CRUs in the average ventricular myocyte Williams et al. (2011) and Wescott et al. (2016) **(C)**. Implemented models that solved stochastic RyR dynamics across these many identical sticky-cluster-derived CRUs, whereas Hinch et al. (2004) and Hinch (2004) performed a clever timescale decomposition to markedly reduce the scale of the problem **(D)**. Both families of model have been successful in replicating and/or interrogating a number of important macroscopic properties of ECC. However, neither is readily capable of assessing the impact of local RyR dispersion, and they do not implement known heterogeneities in CRU structure and function (see Section 2). Copyright permission to reproduce the figures.

species and permitted a 9-state (and even 4-state) model of each dyad. This strategy recapitulated the essential properties of local control, while markedly reducing computational cost. Unfortunately, this approach still assumes a single spatially homogeneous dyadic [Ca^{2+}], which from the more recent super resolution studies described above seems unlikely to reflect the nanoscale reality.

More recent studies that have attempted to bridge the scales in a manner similar to what would be achievable via the ideal model (see previous section) have used a variety of simplifications to maintain tractability. Notably, the proof-of-principle work from Colman et al. (2017) described above used a range of approximations that prevented modulation of CRU size and avoided any potential for CRU fragmentation (i.e., dispersion of RyRs on the dyadic surface of the jSR), **Figure 4B**. Another range of computational studies from George Williams, Eric Sobie and Saleet Jafri has explicitly sought to simulate the whole-cell manifestations of dynamics that may be attributed to RyR dispersion in the single CRU studies described earlier (see **Figure 5C**) (Williams et al., 2011; Wescott et al., 2016; Sobie et al., 2017). Specifically, they investigated the role of changes in functional coupling between RyRs to explore the determinants of visible and "silent" SR Ca^{2+} leak (which represents sub-spark release events such as quarks) in a whole cell model involving distributed dyads. These clever studies diffusively coupled their 20,000 jSR terminals to a common network SR and employed thorough mass conservation and reuptake-release balance. Their dyadic model utilizes a modified version of the well-known "sticky-cluster" model developed by Sobie (**Figure 5A**; Sobie et al., 2002). This formulation implements an arbitrary number of RyRs at each dyad, each of which senses a common dyadic Ca^{2+} concentration, but for which an inter-RyR coupling term reflects the ability for opening and closing events in each RyR to trigger analogous events in other members of the cluster. By updating the original Ca^{2+} sensitivity of the RyR model, Wescott et al. (2016) were able to completely relax this coupling term and assess the effect of RyR mutations present in catecholaminergic polymorphic ventricular tachycardia (CPVT) on whole myocyte silent leak and ECC. In principle, through its inter-RyR coupling term, this model provides a phenomenological approach capable of recapitulating changes in inter-RyR coupling due either to dispersion or presumed inter-RyR interactions accompanying phosphorylation.

Discriminating the Roles of RyR Regulation and Localization

The above approximations are important first steps toward simulating whole-myocyte CICR while retaining the critical stochastic characteristics of RyR gating. However, their ability to simultaneously discriminate regulatory effects (e.g., phosphorylation) that impact RyR Ca^{2+} sensitivity from changes in RyR cluster morphology or other disease-associated structural changes can only be described as phenomenological. To fully simulate the interaction of these changes, which are generally observed simultaneously in disease, will provide a key foundation for understanding whether individual changes in dyadic structure and single channel function contribute to the pathology, or if either is in fact compensatory in nature. As mentioned above, the ability to integrate these effects over an entire cell will allow us to begin these interrogations. This can be considered one of the major goals of the new modeling frameworks that can now be developed based on state-of-the art SSEM and SMLM imaging.

Looking Forward to Image-Driven Multiscale Simulation of Cardiac ECC

In 1960, Wigner (1960) discussed the almost mystic efficiency of mathematics in physics; "the enormous usefulness of mathematics in the natural sciences is something bordering on the mysterious and there is no rational explanation for it." Forty-five years later, Cohen (2004) expressed similar—or even stronger sentiments—regarding the application of mathematics in Biology. Cardiac physiology has a history rich with successful integration of experimentation and mathematics. The storied work of Hodgkin and Huxley (1952a,b,c,d) and Hodgkin et al. (1952) gave every reason for optimism, and the same methods were quickly applied to understand cardiac electrical activation (Noble, 1962). From these formalisms, continuum mathematical representations were developed to understand many aspects of macroscopic cardiac function (Plonsey and Barr, 1987; Henriquez, 1993, 2014; Henriquez et al., 2004; Roberts et al., 2008; Tveito et al., 2017; Jæger et al., 2021a). As many of the imaging methods described above have developed, it has become apparent that nanometer scale structures and their functional dynamics make critical contributions to cardiac electrophysiology and contractile function. Specifically in cardiac ECC, the value of mathematical methods in earlier years developed around their ability to address these nanoscale mechanisms. This type of modeling has been built upon studies of patch clamp electrophysiology and protein biochemistry, which have provided, and will continue to provide, our understanding of the functional building blocks of cardiac ECC. However, it is likely that mathematical approaches will become even more important for integrating experimental observations across the range of accessible scales. To achieve this will require development of efficient and automated handling of large SSEM and SMLM datasets, carefully designed heuristics to simulate CICR across at least 3 spatial orders of magnitude, and efficient but robust numerical approaches to solving the underlying systems of equations. These constitute major computational challenges, but appear to be within reach.

CONCLUDING REMARKS

Over the history of cardiac ECC there have been many instances in which technological or methodological advances have permitted step-changes in the progression of knowledge and shifts in the working paradigm. Rarely, however, has there been a period in which a range of major and complementary technical developments have occurred in such quick succession, as has been the case over the past decade. Like many others, we are eager to see what these developments yield for the field. We particularly expect data sources that are now becoming available to provide a foundation for reconciling multiple levels of investigation and postulates from past decades. We hope this, in turn, will provide new tools and approaches for understanding the relationship between dynamic nanoscale changes and whole-cell function, and new insight to mechanisms of disease that span these scales. Perhaps more than any other aspect, we expect this period to require integrated design of experiments and simulations to fully leverage the power of these new technologies and methods.

AUTHOR CONTRIBUTIONS

WL and AE co-designed, wrote, edited, and developed figures for manuscript. HP-D wrote, edited, and developed figures for manuscript. All authors contributed to the article and approved the submitted version.

FUNDING

This work was financially supported by the Norwegian Research Council (grant #287395), the South-Eastern Norway Regional Health Authority, the K.G. Jebsen Centre for Cardiac Research, and the University of Oslo.

REFERENCES

Adler, D., Wong, A. Y. K., Mahler, Y., and Klassen, G. A. (1985). Model of calcium movements in the mammalian myocardium: interval-strength relationship. *J. Theor. Biol.* 113, 379–394. doi: 10.1016/s0022-5193(85)80233-2

Asghari, P., Scriven, D. R., Ng, M., Panwar, P., Chou, K. C., van Petegem, F., et al. (2020). Cardiac ryanodine receptor distribution is dynamic and changed by auxiliary proteins and post-translational modification. *Elife* 9:e51602. doi: 10.7554/eLife.51602

Asghari, P., Scriven, D. R., Sanatani, S., Gandhi, S. K., Campbell, A. I., Moore, E. D., et al. (2014). Nonuniform and variable arrangements of ryanodine receptors within mammalian ventricular couplons. *Circ. Res.* 115, 252–262. doi: 10.1161/CIRCRESAHA.115.303897

Baddeley, D., Jayasinghe, I. D., Lam, L., Rossberger, S., Cannell, M. B., Soeller, C., et al. (2009). Optical single-channel resolution imaging of the ryanodine receptor distribution in rat cardiac myocytes. *Proc. Natl. Acad. Sci.* 106, 22275–22280. doi: 10.1073/pnas.0908971106

Bassingthwaighte, J. B., Beeler, G. W., Sidell, P. M., Reuter, H., and Safford, R. E. A. (1973). Model for calcium movements and excitation-contraction coupling in cardiac cells. *IFAC Proc. Volumes* 6, 36–38.

Belevych, A. E., Terentyev, D., Viatchenko-Karpinski, S., Terentyeva, R., Sridhar, A., Nishijima, Y., et al. (2009). Redox modification of ryanodine receptors underlies calcium alternans in a canine model of sudden cardiac death. *Cardiovasc. Res.* 84, 387–395. doi: 10.1093/cvr/cvp246

Bellinger, A. M., Reiken, S., Carlson, C., Mongillo, M., Liu, X., Rothman, L., et al. (2009). Hypernitrosylated ryanodine receptor calcium release channels are leaky in dystrophic muscle. *Nat. Med.* 15, 325–330. doi: 10.1038/nm.1916

Bers, D. M. (2012). Ryanodine receptor S2808 phosphorylation in heart failure. *Circ. Res.* 110, 796–799.

Betzig, E., Patterson, G. H., Sougrat, R., Lindwasser, O. W., Olenych, S., Bonifacino, J. S., et al. (2006). Imaging intracellular fluorescent proteins at nanometer resolution. *Science* 313, 1642–1645. doi: 10.1126/science.1127344

Bøkenes, J., Aronsen, J. M., Birkeland, J. A., Henriksen, U. L., Louch, W. E., Sjaastad, I., et al. (2008). Slow contractions characterize failing rat hearts. *Basic Res. Cardiol.* 103, 328–344. doi: 10.1007/s00395-008-0719-y

Brochet, D. X. P., Xie, W., Yang, D., Cheng, H., and Lederer, W. J. (2010). Quarky calcium release in the heart. *Circ. Res.* 108, 210–218. doi: 10.1161/CIRCRESAHA.110.231258

Cannell, M. B., Cheng, H., and Lederer, W. J. (1995). The control of calcium release in heart muscle. *Science* 268, 1045–1049. doi: 10.1126/science.7754384

Cannell, M. B., Kong, C. H. T., Imtiaz, M. S., and Laver, D. R. (2013). Control of sarcoplasmic reticulum Ca^{2+} release by stochastic RyR gating within a 3D model of the cardiac dyad and importance of induction decay for CICR termination. *Biophys. J.* 104:2159. doi: 10.1016/j.bpj.2013.03.058

Cannell, M. B., and Soeller, C. (1997). Numerical analysis of ryanodine receptor activation by L-type channel activity in the cardiac muscle diad. *Biophys. J.* 73, 112–122. doi: 10.1016/S0006-3495(97)78052-4

Cannell, M. B., Vaughan-Jones, R. D., and Lederer, W. J. (1985). Ryanodine block of calcium oscillations in heart muscle and the sodium-tension relationship. *Fed. Proc.* 44, 2964–2969.

Chen, W., Wang, R., Chen, B., Zhong, X., Kong, H., Bai, Y., et al. (2014). The ryanodine receptor store-sensing gate controls Ca^{2+} waves and Ca^{2+}-triggered arrhythmias. *Nat. Med.* 20, 184–192. doi: 10.1038/nm.3440

Cheng, H., Lederer, M. R., Lederer, W. J., and Cannell, M. B. (1996). Calcium sparks and $[Ca^{2+}]_i$ waves in cardiac myocytes. *Am. J. Physiol.* 270, C148–C159. doi: 10.1152/ajpcell.1996.270.1.C148

Cheng, H., Lederer, W., and Cannell, M. (1993). Calcium sparks: elementary events underlying excitation-contraction coupling in heart muscle. *Science* 262, 740–744. doi: 10.1126/science.8235594

Cobbold, P. H., and Bourne, P. K. (1984). Aequorin measurements of free calcium in single heart cells. *Nature* 312, 444–446. doi: 10.1038/312444a0

Cohen, J. E. (2004). Mathematics is biology's next microscope, only better; biology is mathematics' next physics, only better. *PLoS Biol.* 2:e439. doi: 10.1371/journal.pbio.0020439

Colman, M. A. (2019). Arrhythmia mechanisms and spontaneous calcium release: bi-directional coupling between re-entrant and focal excitation. *PLoS Comput. Biol.* 15:e1007260. doi: 10.1371/journal.pcbi.1007260

Colman, M. A., Pinali, C., Trafford, A. W., Zhang, H., and Kitmitto, A. (2017). A computational model of spatio-temporal cardiac intracellular calcium handling with realistic structure and spatial flux distribution from sarcoplasmic reticulum and t-tubule reconstructions. *PLoS Comput. Biol.* 13:e1005714. doi: 10.1371/journal.pcbi.1005714

Constantin, L., Franzini-Armstrong, C., and Podolsky, R. J. (1965). Localization of calcium-accumulating structures in striated muscle fibers. *Science* 147, 158–160. doi: 10.1126/science.147.3654.158

Cordeiro, J. M., Greene, L., Heilmann, C., Antzelevitch, D., and Antzelevitch, C. (2004). Transmural heterogeneity of calcium activity and mechanical function in the canine left ventricle. *Am. J. Physiol.* 286, H1471–H1479. doi: 10.1152/ajpheart.00748.2003

Crossman, D. J., Shen, X., Jüllig, M., Munro, M., Hou, Y., Middleditch, M., et al. (2017). Increased collagen within the transverse tubules in human heart failure. *Cardiovasc. Res.* 113, 879–891. doi: 10.1093/cvr/cvx055

Curran, J., Brown, K. H., Santiago, D. J., Pogwizd, S., Bers, D. M., Shannon, T. R., et al. (2010). Spontaneous Ca waves in ventricular myocytes from failing hearts depend on Ca^{2+}-calmodulin-dependent protein kinase II. *J. Mol. Cell. Cardiol.* 49, 25–32. doi: 10.1016/j.yjmcc.2010.03.013

Denk, W., and Horstmann, H. (2004). Serial block-face scanning electron microscopy to reconstruct three-dimensional tissue nanostructure. *PLoS Biol.* 2:e329. doi: 10.1371/journal.pbio.0020329

Edwards, A. G., Hake, J., Michailova, A. P., Hoshijima, M., and McCulloch, A. D. (2018). *Cardiac Electrophysiology: From Cell to Bedside. Part V*. Amsterdam: Elsevier, 314–324. doi: 10.1016/b978-0-323-44733-1.00033-x

Endo, M. (1977). Calcium release from the sarcoplasmic reticulum. *Physiol. Rev.* 57, 71–108.

Endo, M. (2011). Reiji natori, setsuro ebashi, and excitation–contraction coupling. *Prog. Biophys. Mol. Biol.* 105, 129–133. doi: 10.1016/j.pbiomolbio.2010.12.002

Endo, M., Tanaka, M., and Ogawa, Y. (1970). Calcium induced release of calcium from the sarcoplasmic reticulum of skinned skeletal muscle fibres. *Nature* 228, 34–36. doi: 10.1038/228034a0

Eschenhagen, T. (2010). Is ryanodine receptor phosphorylation key to the fight or flight response and heart failure? *J. Clin. Invest.* 120, 4197–4203. doi: 10.1172/JCI45251

Fabiato, A. (1981). Myoplasmic free calcium concentration reached during the twitch of an intact isolated cardiac cell and during calcium-induced release of calcium from the sarcoplasmic reticulum of a skinned cardiac cell from the adult rat or rabbit ventricle. *J. Gen. Physiol.* 78, 457–497. doi: 10.1085/jgp.78.5.457

Fabiato, A. (1985). Effects of ryanodine in skinned cardiac cells. *Fed. Proc.* 44, 2970–2976.

Fabiato, A., and Fabiato, F. (1972). Excitation-contraction coupling of isolated cardiac fibers with disrupted or closed sarcolemmas: calcium-dependent cyclic and tonic contractions. *Circ. Res.* 31, 293–307. doi: 10.1161/01.res.31.3.293

Fabiato, A., and Fabiato, F. (1975a). Contractions induced by a calcium-triggered release of calcium from the sarcoplasmic reticulum of single skinned cardiac cells. *J. Physiol.* 249, 469–495. doi: 10.1113/jphysiol.1975.sp011026

Fabiato, A., and Fabiato, F. (1975b). Effects of magnesium on contractile activation of skinned cardiac cells. *J. Physiol.* 249, 497–517. doi: 10.1113/jphysiol.1975.sp011027

Fabiato, A., and Fabiato, F. (1975c). Relaxing and inotropic effects of cyclic AMP on skinned cardiac cells. *Nature* 253, 556–558. doi: 10.1038/253556b0

Fabiato, A., and Fabiato, F. (1977). Calcium release from the sarcoplasmic reticulum. *Circ. Res.* 40, 119–129.

Fabiato, A., and Fabiato, F. (1978). Myofilament-generated tension oscillations during partial calcium activation and activation dependence of the sarcomere length-tension relation of skinned cardiac cells. *J. Gen. Physiol.* 72, 667–699. doi: 10.1085/jgp.72.5.667

Fill, M., and Copello, J. A. (2002). Ryanodine receptor calcium release channels. *Physiol. Rev.* 82, 893–922.

Fill, M., and Gillespie, D. (2018). Ryanodine receptor open times are determined in the closed state. *Biophys. J.* 115, 1160–1165. doi: 10.1016/j.bpj.2018.08.025

Fleischer, S., Ogunbunmi, E. M., Dixon, M. C., and Fleer, E. A. (1985). Localization of Ca^{2+} release channels with ryanodine in junctional terminal cisternae of sarcoplasmic reticulum of fast skeletal muscle. *Proc. Natl. Acad. Sci.* 82, 7256–7259. doi: 10.1073/pnas.82.21.7256

Franzini-Armstrong, C., and Porter, K. R. (1964a). Sarcolemmal imaginations and the t-system in fish skeletal muscle. *Nature* 202, 355–357.

Franzini-Armstrong, C., and Porter, K. R. (1964b). Sarcolemmal invaginations constituting the T system in fish muscle fibers. *J. Cell Biol.* 22, 675–696. doi: 10.1083/jcb.22.3.675

Franzini-Armstrong, C., and Protasi, F. (1997). Ryanodine receptors of striated muscles: a complex channel capable of multiple interactions. *Physiol. Rev.* 77, 699–729. doi: 10.1152/physrev.1997.77.3.699

Franzini-Armstrong, C., Protasi, F., and Ramesh, V. (1999). Shape, size, and distribution of Ca^{2+} release units and couplons in skeletal and cardiac muscles. *Biophys. J.* 77, 1528–1539. doi: 10.1016/S0006-3495(99)77000-1

Franzini-Armstrong, C., Protasi, F., and Ramesh, V. (1998). Comparative ultrastructure of Ca^{2+} release units in skeletal and cardiac muscle. *Ann. N.Y.Acad. Sci.* 853, 20–30. doi: 10.1111/j.1749-6632.1998.tb08253.x

Franzini-Armstrong, C., Protasi, F., and Tijskens, P. (2005). The assembly of calcium release units in cardiac muscle. *Ann. N.Y.Acad. Sci.* 1047, 76–85. doi: 10.1196/annals.1341.007

Frisk, M., Le, C., Shen, X., Røe, ÅT., Hou, Y., Manfra, O., et al. (2021). Etiology-dependent impairment of diastolic cardiomyocyte calcium homeostasis in heart failure with preserved ejection fraction. *J. Am. Coll. Cardiol.* 77, 405–419. doi: 10.1016/j.jacc.2020.11.044

Fu, Y., Shaw, S. A., Naami, R., Vuong, C. L., Basheer, W. A., Guo, X., et al. (2016). Isoproterenol promotes rapid ryanodine receptor movement to bridging integrator 1 (bin1)–organized dyads. *Circulation* 133, 388–397. doi: 10.1161/CIRCULATIONAHA.115.018535

Gaburjakova, M., Gaburjakova, J., Reiken, S., Huang, F., Marx, S. O., Rosemblit, N., et al. (2001). FKBP12 binding modulates ryanodine receptor channel gating. *J. Biol. Chem.* 276, 16931–16935. doi: 10.1074/jbc.M100856200

Gaeta, S. A., Bub, G., Abbott, G. W., and Christini, D. J. (2009). Dynamical mechanism for subcellular alternans in cardiac myocytes. *Circ. Res.* 105, 335–342. doi: 10.1161/CIRCRESAHA.109.197590

Gaeta, S. A., and Christini, D. J. (2012). Non-linear dynamics of cardiac alternans: subcellular to tissue-level mechanisms of arrhythmia. *Front. Physiol.* 3:157. doi: 10.3389/fphys.2012.00157

Gaeta, S. A., Krogh-Madsen, T., and Christini, D. J. (2010). Feedback-control induced pattern formation in cardiac myocytes: a mathematical modeling study. *J. Theor. Biol.* 266, 408–418. doi: 10.1016/j.jtbi.2010.06.041

Geertsema, H. J., Aimola, G., Fabricius, V., Fuerste, J. P., Kaufer, B. B., Ewers, H., et al. (2021). Left-handed DNA-PAINT for improved super-resolution imaging in the nucleus. *Nat. Biotechnol.* 39, 551–554. doi: 10.1038/s41587-020-00753-y

Gillespie, D. (2019). Recruiting ryrs to open in a Ca^{2+} release unit: single-ryr gating properties make ryr group dynamics. *Biophys. J.* 118, 232–242. doi: 10.1016/j.bpj.2019.11.021

Gillespie, D., and Fill, M. (2013). Pernicious attrition and inter-ryr2 cicr current control in cardiac muscle. *J. Mol. Cell. Cardiol.* 58, 53–58. doi: 10.1016/j.yjmcc.2013.01.011

Gonano, L. A., Sepúlveda, M., Rico, Y., Kaetzel, M., Valverde, C. A., Dedman, J., et al. (2011). Calcium-calmodulin kinase ii mediates digitalis-induced arrhythmias. *Circ. Arrhythmia Electrophysiol.* 4, 947–957. doi: 10.1161/CIRCEP.111.964908

Greenstein, J. L., and Winslow, R. L. (2002). An integrative model of the cardiac ventricular myocyte incorporating local control of Ca^{2+} release. *Biophys. J.* 83, 2918–2945. doi: 10.1016/S0006-3495(02)75301-0

Groenendaal, W., Ortega, F. A., Krogh-Madsen, T., and Christini, D. J. (2014). Voltage and calcium dynamics both underlie cellular alternans in cardiac myocytes. *Biophys. J.* 106, 2222–2232. doi: 10.1016/j.bpj.2014.03.048

Guo, T., Gillespie, D., and Fill, M. (2012). Ryanodine receptor current amplitude controls Ca^{2+} sparks in cardiac muscle. *Circ. Res.* 111, 28–36. doi: 10.1161/CIRCRESAHA.112.265652

Guo, T., Zhang, T., Mestril, R., and Bers, D. M. (2006). Ca^{2+}/calmodulin-dependent protein kinase ii phosphorylation of ryanodine receptor does affect calcium sparks in mouse ventricular myocytes. *Circ. Res.* 99, 398–406. doi: 10.1161/01.RES.0000236756.06252.13

Hake, J., Edwards, A. G., Yu, Z., Kekenes-Huskey, P. M., Michailova, A. P., McCammon, J. A., et al. (2012). Modelling cardiac calcium sparks in a three-dimensional reconstruction of a calcium release unit. *J. Physiol.* 590, 4403–4422. doi: 10.1113/jphysiol.2012.227926

Harris, D. M., Mills, G. D., Chen, X., Kubo, H., Berretta, R. M., Votaw, V. S., et al. (2005). Alterations in early action potential repolarization causes localized failure of sarcoplasmic reticulum Ca^{2+} release. *Circ. Res.* 96, 543–550. doi: 10.1161/01.RES.0000158966.58380.37

Hashambhoy, Y. L., Greenstein, J. L., and Winslow, R. L. (2010). Role of CaMKII in RyR leak, EC coupling and action potential duration: a computational model. *J. Mol. Cell. Cardiol.* 49, 617–624. doi: 10.1016/j.yjmcc.2010.07.011

Hayashi, T., Martone, M. E., Yu, Z., Thor, A., Doi, M., Holst, M. J., et al. (2009). Three-dimensional electron microscopy reveals new details of membrane systems for Ca^{2+} signaling in the heart. *J. Cell Sci.* 122, 1005–1013. doi: 10.1242/jcs.028175

Hayworth, K., Kasthuri, N., Schalek, R., and Lichtman, J. (2006). Automating the collection of ultrathin serial sections for large volume tem reconstructions. *Microsc. Microanal.* 12, 86–87. doi: 10.1017/s1431927606066268

Henriquez, C. S. (1993). Simulating the electrical behavior of cardiac tissue using the bidomain model. *Crit. Rev. Biomed. Eng.* 21, 1–77.

Henriquez, C. S., Tranquillo, J. V., Weinstein, D., Hsu, E. W., and Johnson, C. R. (2004). *Cardiac Electrophysiology (Fourth Edition). Part V*. Amsterdam: Elsevier, 273–281. doi: 10.1016/b0-7216-0323-8/50033-6

Henriquez, C. S. (2014). A brief history of tissue models for cardiac electrophysiology. *IEEE Trans. Biomed. Eng.* 61, 1457–1465. doi: 10.1109/TBME.2014.2310515

Heymann, J. A. W., Hayles, M., Gestmann, I., Giannuzzi, L. A., Lich, B., Subramaniam, S., et al. (2006). Site-specific 3D imaging of cells and tissues with a dual beam microscope. *J. Struct. Biol.* 155, 63–73. doi: 10.1016/j.jsb.2006.03.006

Hilgemann, D. W., and Noble, D. (1987). Excitation-contraction coupling and extracellular calcium transients in rabbit atrium: reconstruction of basic cellular mechanisms. *Proc. R. Soc. Lond. Ser. B Biol. Sci.* 230, 163–205. doi: 10.1098/rspb.1987.0015

Hinch, R., Greenstein, J. L., Tanskanen, A. J., Xu, L., and Winslow, R. L. (2004). A simplified local control model of calcium-induced calcium release in cardiac ventricular myocytes. *Biophys. J.* 87, 3723–3736. doi: 10.1529/biophysj.104.049973

Hinch, R. A. (2004). Mathematical analysis of the generation and termination of calcium sparks. *Biophys. J.* 86, 1293–1307. doi: 10.1016/S0006-3495(04)74203-4

Hodgkin, A. L., and Huxley, A. F. (1952a). A quantitative description of membrane current and its application to conduction and excitation in nerve. *J. Physiol.* 117, 500–544. doi: 10.1113/jphysiol.1952.sp004764

Hodgkin, A. L., and Huxley, A. F. (1952b). Currents carried by sodium and potassium ions through the membrane of the giant axon of Loligo. *J. Physiol.* 116, 449–472. doi: 10.1113/jphysiol.1952.sp004717

Hodgkin, A. L., and Huxley, A. F. (1952c). The dual effect of membrane potential on sodium conductance in the giant axon of Loligo. *J. Physiol.* 116, 497–506. doi: 10.1113/jphysiol.1952.sp004719

Hodgkin, A. L., and Huxley, A. F. (1952d). The components of membrane conductance in the giant axon of Loligo. *J. Physiol.* 116, 473–496. doi: 10.1113/jphysiol.1952.sp004718

Hodgkin, A. L., Huxley, A. F., and Katz, B. (1952). Measurement of current-voltage relations in the membrane of the giant axon of Loligo. *J. Physiol.* 116, 424–448. doi: 10.1113/jphysiol.1952.sp004716

Hong, T., Yang, H., Zhang, S. S., Cho, H. C., Kalashnikova, M., Sun, B., et al. (2014). Cardiac BIN1 folds T-tubule membrane, controlling ion flux and limiting arrhythmia. *Nat. Med.* 20, 624–632. doi: 10.1038/nm.3543

Hou, Y., Jayasinghe, I., Crossman, D. J., Baddeley, D., and Soeller, C. (2015). Nanoscale analysis of ryanodine receptor clusters in dyadic couplings of rat cardiac myocytes. *J. Mol. Cell. Cardiol.* 80, 45–55. doi: 10.1016/j.yjmcc.2014.12.013

Huang, F., Shan, J., Reiken, S., Wehrens, X. H. T., and Marks, A. R. (2006). Analysis of calstabin2 (FKBP12.6)-ryanodine receptor interactions: rescue of heart failure by calstabin2 in mice. *Proc. Natl. Acad. Sci. U.S.A.* 103:3461. doi: 10.1073/pnas.0511282103

Hund, T. J., and Rudy, Y. (2004). Rate dependence and regulation of action potential and calcium transient in a canine cardiac ventricular cell model. *Circulation* 110, 3168–3174. doi: 10.1161/01.CIR.0000147231.69595.D3

Hurley, M. E., Sheard, T. M. D., Norman, R., Kirton, H. M., Shah, S. S., Pervolaraki, E., et al. (2021). A correlative super-resolution protocol to visualise structural underpinnings of fast second-messenger signalling in primary cell types. *Methods* 193, 27–37. doi: 10.1016/j.ymeth.2020.10.005

Huxley, A. F., and Taylor, R. E. (1958). Local activation of striated muscle fibres. *J. Physiol.* 144, 426–441. doi: 10.1113/jphysiol.1958.sp006111

Hymel, L., Inui, M., Fleischer, S., and Schindler, H. (1988). Purified ryanodine receptor of skeletal muscle sarcoplasmic reticulum forms Ca^{2+}-activated oligomeric Ca^{2+} channels in planar bilayers. *Proc. Natl. Acad. Sci.* 85, 441–445. doi: 10.1073/pnas.85.2.441

Inui, M., Saito, A., and Fleischer, S. (1987). Purification of the ryanodine receptor and identity with feet structures of junctional terminal cisternae of sarcoplasmic reticulum from fast skeletal muscle. *J. Biol. Chem.* 262, 1740–1747. doi: 10.1016/s0021-9258(19)75701-9

Ito, D. W., Hannigan, K. I., Ghosh, D., Xu, B., Del Villar, S. G., Xiang, Y. K., et al. (2019). β-adrenergic-mediated dynamic augmentation of sarcolemmal CaV1.2 clustering and co-operativity in ventricular myocytes. *J. Physiol.* 597, 2139–2162. doi: 10.1113/jp277283

Jayasinghe, I., Clowsley, A. H., Lin, R., Lutz, T., Harrison, C., Green, E., et al. (2018). True molecular scale visualization of variable clustering properties of ryanodine receptors. *Cell Rep.* 22, 557–567. doi: 10.1016/j.celrep.2017.12.045

Jayasinghe, I. D., Cannell, M. B., and Soeller, C. (2009). Organization of ryanodine receptors, transverse tubules, and sodium-calcium exchanger in rat myocytes. *Biophys. J.* 97, 2664–2673. doi: 10.1016/j.bpj.2009.08.036

Jayasinghe, I. D., Clowsley, A. H., Munro, M., Hou, Y., Crossman, D. J., Soeller, C., et al. (2014). Revealing t-tubules in striated muscle with new optical super-resolution microscopy techniques. *Eur. J. Transl. Myol.* 25, 15–26. doi: 10.4081/ejtm.2015.4747

Jiang, D., Wang, R., Xiao, B., Kong, H., Hunt, D. J., Choi, P., et al. (2005). Enhanced store overload–induced Ca^{2+} release and channel sensitivity to luminal Ca^{2+} activation are common defects of ryr2 mutations linked to ventricular tachycardia and sudden death. *Circ. Res.* 97, 1173–1181. doi: 10.1161/01.RES.0000192146.85173.4b

Jiang, D., Xiao, B., Yang, D., Wang, R., Choi, P., Zhang, L., et al. (2004). RyR2 mutations linked to ventricular tachycardia and sudden death reduce the threshold for store-overload-induced Ca^{2+} release (SOICR). *Proc. Natl. Acad. Sci. U.S.A.* 101, 13062–13067. doi: 10.1073/pnas.0402388101

Jones, P. P., MacQuaide, N., and Louch, W. E. (2018). Dyadic plasticity in cardiomyocytes. *Front. Physiol.* 9:1773. doi: 10.3389/fphys.2018.01773

Jungmann, R., Steinhauer, C., Scheible, M., Kuzyk, A., Tinnefeld, P., Simmel, F. C., et al. (2010). Single-molecule kinetics and super-resolution microscopy by fluorescence imaging of transient binding on DNA origami. *Nano Lett.* 10, 4756–4761. doi: 10.1021/nl103427w

Jæger, K. H., Edwards, A. G., Giles, W. R., and Tveito, A. (2021a). From millimeters to micrometers; re-introducing myocytes in models of cardiac electrophysiology. *Front. Physiol.* 12:763584. doi: 10.3389/fphys.2021.763584

Jæger, K. H., Hustad, K. G., Cai, X., and Tveito, A. (2021b). Efficient numerical solution of the emi model representing the extracellular space (e), cell membrane (m) and intracellular space (i) of a collection of cardiac cells. *Front. Phys.* 8:579461. doi: 10.3389/fphy.2020.579461

Kaufmann, R., Bayer, R., Fürniss, T., Krause, H., and Tritthart, H. (1974). Calcium-movement controlling cardiac contractility. II. Analog computation of cardiac excitation-contraction coupling on the basis of calcium kinetics in a multi-compartment model. *J. Mol. Cell. Cardiol.* 6, 543–559. doi: 10.1016/0022-2828(74)90035-2

Keizer, J., and Smith, G. D. (1998). Spark-to-wave transition: saltatory transmission of calcium waves in cardiac myocytes. *Biophys. Chem.* 72, 87–100. doi: 10.1016/s0301-4622(98)00125-2

Koh, X., Srinivasan, B., Ching, H. S., and Levchenko, A. (2006). A 3D monte carlo analysis of the role of dyadic space geometry in spark generation. *Biophys. J.* 90, 1999–2014. doi: 10.1529/biophysj.105.065466

Kohlhaas, M., Zhang, T., Seidler, T., Zibrova, D., Dybkova, N., Steen, A., et al. (2006). Increased sarcoplasmic reticulum calcium leak but unaltered contractility by acute CaMKII overexpression in isolated rabbit cardiac myocytes. *Circ. Res.* 98, 235–244. doi: 10.1161/01.RES.0000200739.90811.9f

Kolstad, T. R., van den Brink, J., MacQuaide, N., Lunde, P. K., Frisk, M., Aronsen, J. M., et al. (2018). Ryanodine receptor dispersion disrupts Ca^{2+} release in failing cardiac myocytes. *Elife* 7:e39427. doi: 10.7554/eLife.39427

Lai, F. A., and Meissner, G. (1989). The muscle ryanodine receptor and its intrinsic Ca^{2+} channel activity. *J. Bioenerg. Biomembr.* 21, 227–246. doi: 10.1007/BF00812070

Laver, D. R., Kong, C. H. T., Imtiaz, M. S., and Cannell, M. B. (2013). Termination of calcium-induced calcium release by induction decay: an emergent property of stochastic channel gating and molecular scale architecture. *J. Mol. Cell. Cardiol.* 54, 98–100. doi: 10.1016/j.yjmcc.2012.10.009

Leblanc, N., and Hume, J. R. (1990). Sodium current-induced release of calcium from cardiac sarcoplasmic reticulum. *Science* 248, 372–376. doi: 10.1126/science.2158146

Lehnart, S. E., Mongillo, M., Bellinger, A., Lindegger, N., Chen, B. X., Hsueh, W., et al. (2008). Leaky Ca^{2+} release channel/ryanodine receptor 2 causes seizures and sudden cardiac death in mice. *J. Clin. Invest.* 118, 2230–2245. doi: 10.1172/JCI35346

Limbu, S., Hoang-Trong, T. M., Prosser, B. L., Lederer, W. J., and Jafri, M. S. (2015). Modeling local X-ROS and calcium signaling in the heart. *Biophys. J.* 109, 2037–2050. doi: 10.1016/j.bpj.2015.09.031

Lines, G. T., Sande, J. B., Louch, W. E., Mørk, H. K., Grøttum, P., Sejersted, O. M., et al. (2006). Contribution of the Na^{+}/Ca^{2+} exchanger to rapid Ca^{2+} release in cardiomyocytes. *Biophys. J.* 91, 779–792. doi: 10.1529/biophysj.105.072447

Lipp, P., and Niggli, E. (1996). Submicroscopic calcium signals as fundamental events of excitation–contraction coupling in guinea-pig cardiac myocytes. *J. Physiol.* 492, 31–38. doi: 10.1113/jphysiol.1996.sp021286

Louch, W. E., Hake, J., Mørk, H. K., Hougen, K., Skrbic, B., Ursu, D., et al. (2013). Slow Ca^{2+} sparks de-synchronize Ca^{2+} release in failing cardiomyocytes: evidence for altered configuration of Ca^{2+} release units? *J. Mol. Cell. Cardiol.* 58, 41–52. doi: 10.1016/j.yjmcc.2013.01.014

Louch, W. E., Mørk, H. K., Sexton, J., Strømme, T. A., Laake, P., Sjaastad, I., et al. (2006). T-tubule disorganization and reduced synchrony of Ca^{2+} release in murine cardiomyocytes following myocardial infarction. *J. Physiol.* 574, 519–533. doi: 10.1113/jphysiol.2006.107227

Macquaide, N., Tuan, H. T., Hotta, J., Sempels, W., Lenaerts, I., Holemans, P., et al. (2015). Ryanodine receptor cluster fragmentation and redistribution in persistent atrial fibrillation enhance calcium release. *Cardiovasc. Res.* 108, 387–398. doi: 10.1093/cvr/cvv231

Marx, S. O., Reiken, S., Hisamatsu, Y., Jayaraman, T., Burkhoff, D., Rosemblit, N., et al. (2000). PKA phosphorylation dissociates FKBP12.6 from the calcium release channel (ryanodine receptor) defective regulation in failing hearts. *Cell* 101, 365–376. doi: 10.1016/s0092-8674(00)80847-8

Maurer, A., Tanaka, M., Ozawa, T., and Fleischer, S. (1985). Purification and crystallization of the calcium binding protein of sarcoplasmic reticulum from skeletal muscle. *Proc. Natl. Acad. Sci.* 82, 4036–4040.

Morgan, J. L., Berger, D. R., Wetzel, A. W., and Lichtman, J. W. (2016). The fuzzy logic of network connectivity in mouse visual thalamus. *Cell* 165, 192–206. doi: 10.1016/j.cell.2016.02.033

Näbauer, M., Callewaert, G., Cleemann, L., and Morad, M. (1989). Regulation of calcium release is gated by calcium current, not gating charge, in cardiac myocytes. *Science* 244, 800–803. doi: 10.1126/science.2543067

Nieves, D. J., Gaus, K., and Baker, M. A. B. D. N. A. - (2018). Based super-resolution microscopy: DNA-paint. *Genes* 9:621. doi: 10.3390/genes9120621

Niggli, E. (1999). Localized intracellular calcium signaling in muscle: calcium sparks and calcium quarks. *Annu. Rev. Physiol.* 61, 311–335. doi: 10.1146/annurev.physiol.61.1.311

Nivala, M., Ko, C. Y., Nivala, M., Weiss, J. N., and Qu, Z. (2012). Criticality in intracellular calcium signaling in cardiac myocytes. *Biophys. J.* 102, 2433–2442. doi: 10.1016/j.bpj.2012.05.001

Noble, D. (1962). A modification of the Hodgkin—Huxley equations applicable to Purkinje fibre action and pacemaker potentials. *J. Physiol.* 160, 317–352. doi: 10.1113/jphysiol.1962.sp006849

Novotová, M., Zahradníková, A., Nichtová, Z., Kováč, R., Kráľová, E., Stankovičová, T., et al. (2020). Structural variability of dyads relates to calcium release in rat ventricular myocytes. *Sci. Rep.* 10:8076. doi: 10.1038/s41598-020-64840-5

Ogrodnik, J., and Niggli, E. (2010). Increased Ca^{2+} leak and spatiotemporal coherence of Ca^{2+} release in cardiomyocytes during β-adrenergic stimulation. *J. Physiol.* 588, 225–242.

Oort, R. J., McCauley, M. D., Dixit, S. S., Pereira, L., Yang, Y., Respress, J. L., et al. (2010). Ryanodine receptor phosphorylation by calcium/calmodulin-dependent protein kinase II promotes life-threatening ventricular arrhythmias in mice with heart failure. *Circulation* 122, 2669–2679. doi: 10.1161/CIRCULATIONAHA.110.982298

Peng, W., Shen, H., Wu, J., Guo, W., Pan, X., Wang, R., et al. (2016). Structural basis for the gating mechanism of the type 2 ryanodine receptor RyR2. *Science* 354:aah5324. doi: 10.1126/science.aah5324

Pereira, L., Cheng, H., Lao, D. H., Na, L., van Oort, R. J., Brown, J. H., et al. (2013). Epac2 mediates cardiac β1-adrenergic–dependent sarcoplasmic reticulum Ca^{2+} leak and arrhythmia. *Circulation* 127, 913–922. doi: 10.1161/CIRCULATIONAHA.12.148619

Pereira, L., Métrich, M., Fernández-Velasco, M., Lucas, A., Leroy, J., Perrier, R., et al. (2007). The cAMP binding protein Epac modulates Ca^{2+} sparks by a Ca^{2+}/calmodulin kinase signalling pathway in rat cardiac myocytes. *J. Physiol.* 583, 685–694. doi: 10.1113/jphysiol.2007.133066

Picht, E., Zima, A. V., Shannon, T. R., Duncan, A. M., Blatter, L. A., Bers, D. M., et al. (2011). Dynamic calcium movement inside cardiac sarcoplasmic reticulum during release. *Circ. Res.* 108, 847–856. doi: 10.1161/CIRCRESAHA.111.240234

Pinali, C., Bennett, H., Davenport, J. B., Trafford, A. W., and Kitmitto, A. (2013). Three-dimensional reconstruction of cardiac sarcoplasmic reticulum reveals a continuous network linking transverse-tubules: this organization is perturbed in heart failure. *Circ. Res.* 113, 1219–1230. doi: 10.1161/CIRCRESAHA.113.301348

Pinali, C., and Kitmitto, A. (2014). Serial block face scanning electron microscopy for the study of cardiac muscle ultrastructure at nanoscale resolutions. *J. Mol. Cell. Cardiol.* 76, 1–11. doi: 10.1016/j.yjmcc.2014.08.010

Plonsey, R., and Barr, R. C. (1987). Mathematical modeling of electrical activity of the heart. *J. Electrocardiol.* 20, 219–226. doi: 10.1016/s0022-0736(87)80019-5

Porter, K. R., and Palade, G. E. (1957). Studies on the endoplasmic reticulum. III. Its form and distribution in striated muscle cells. *J. Biophys. Biochem. Cytol.* 3, 269–300. doi: 10.1083/jcb.3.2.269

Priori, S. G., and Chen, S. R. W. (2011). Inherited dysfunction of sarcoplasmic reticulum Ca^{2+} handling and arrhythmogenesis. *Circ. Res.* 108, 871–883. doi: 10.1161/CIRCRESAHA.110.226845

Prosser, B. L., Khairallah, R. J., Ziman, A. P., Ward, C. W., and Lederer, W. J. (2013a). X-ROS signaling in the heart and skeletal muscle: stretch-dependent local ROS regulates $[Ca^{2+}]_i$. *J. Mol. Cell. Cardiol.* 58, 172–181. doi: 10.1016/j.yjmcc.2012.11.011

Prosser, B. L., Ward, C. W., and Lederer, W. J. (2013b). X-ROS signalling is enhanced and graded by cyclic cardiomyocyte stretch. *Cardiovasc. Res.* 98, 307–314. doi: 10.1093/cvr/cvt066

Prosser, B. L., Ward, C. W., and Lederer, W. J. (2011). X-ROS signaling: rapid mechano-chemo transduction in heart. *Science* 333, 1440–1445. doi: 10.1126/science.1202768

Restrepo, J. G., Weiss, J. N., and Karma, A. (2008). Calsequestrin-mediated mechanism for cellular calcium transient alternans. *Biophys. J.* 95, 3767–3789.

Rios, E., and Pizarro, G. (1988). Voltage sensors and calcium channels of excitation-contraction coupling. *Physiology* 3, 223–227.

Roberts, S. F., Stinstra, J. G., and Henriquez, C. S. (2008). Effect of nonuniform interstitial space properties on impulse propagation: a discrete multidomain model. *Biophys. J.* 95, 3724–3737. doi: 10.1529/biophysj.108.137349

Rog-Zielinska, E. A., Moss, R., Kaltenbacher, W., Greiner, J., Verkade, P., Seemann, G., et al. (2021). Nano-scale morphology of cardiomyocyte t-tubule/sarcoplasmic reticulum junctions revealed by ultra-rapid high-pressure freezing and electron tomography. *J. Mol. Cell. Cardiol.* 153, 86–92. doi: 10.1016/j.yjmcc.2020.12.006

Setterberg, I. E., Le, C., Frisk, M., Perdreau-Dahl, H., Li, J., Louch, W. E., et al. (2021). The physiology and pathophysiology of T-tubules in the heart. *Front. Physiol.* 12:718404. doi: 10.3389/fphys.2021.718404

Sharonov, A., and Hochstrasser, R. M. (2006). Wide-field subdiffraction imaging by accumulated binding of diffusing probes. *Proc. Natl. Acad. Sci.* 103, 18911–18916. doi: 10.1073/pnas.0609643104

Sheard, T. M. D., Hurley, M. E., Colyer, J., White, E., Norman, R., Pervolaraki, E., et al. (2019). Three-dimensional and chemical mapping of intracellular signaling nanodomains in health and disease with enhanced expansion microscopy. *ACS Nano* 13, 2143–2157. doi: 10.1021/acsnano.8b08742

Shen, X., van den Brink, J., Hou, Y., Colli, D., Le, C., Kolstad, T. R., et al. (2019). 3D dSTORM imaging reveals novel detail of ryanodine receptor localization in rat cardiac myocytes. *J. Physiol.* 597, 399–418. doi: 10.1113/JP277360

Sipido, K. R., Maes, M., and Werf, F. V. de (1997). Low efficiency of Ca^{2+} entry through the Na^{+}-Ca^{2+} exchanger as trigger for Ca^{2+} release from the sarcoplasmic reticulum: a comparison between L-type Ca^{2+} current and reverse-mode Na^{+}-Ca^{2+} exchange. *Circ. Res.* 81, 1034–1044. doi: 10.1161/01.res.81.6.1034

Sobie, E. A., Dilly, K. W., Cruz, J., dos, S., Lederer, W. J., and Jafri, M. S. (2002). Termination of cardiac Ca^{2+} sparks: an investigative mathematical model of calcium-induced calcium release. *Biophys. J.* 83, 59–78. doi: 10.1016/s0006-3495(02)75149-7

Sobie, E. A., Williams, G. S. B., and Lederer, W. J. (2017). Ambiguous interactions between diastolic and SR Ca^{2+} in the regulation of cardiac Ca^{2+} release. *J. Gen. Physiol.* 149, 847–855. doi: 10.1085/jgp.201711814

Soeller, C., and Cannell, M. B. (1997). Numerical simulation of local calcium movements during L-type calcium channel gating in the cardiac diad. *Biophys. J.* 73, 97–111. doi: 10.1016/S0006-3495(97)78051-2

Soeller, C., Crossman, D., Gilbert, R., and Cannell, M. B. (2007). Analysis of ryanodine receptor clusters in rat and human cardiac myocytes. *Proc. Natl. Acad. Sci.* 104, 14958–14963. doi: 10.1073/pnas.0703016104

Song, L., Sham, J. S. K., Stern, M. D., Lakatta, E. G., and Cheng, H. (1998). Direct measurement of SR release flux by tracking 'Ca^{2+} spikes' in rat cardiac myocytes. *J. Physiol.* 512, 677–691. doi: 10.1111/j.1469-7793.1998.677bd.x

Song, L.-S., Sobie, E. A., McCulle, S., Lederer, W. J., Balke, C. W., Cheng, H., et al. (2006). Orphaned ryanodine receptors in the failing heart. *Proc. Natl. Acad. Sci. U.S.A.* 103, 4305–4310. doi: 10.1073/pnas.0509324103

Stern, M. D. (1992). Theory of excitation-contraction coupling in cardiac muscle. *Biophys. J.* 63, 497–517.

Strauss, S., Nickels, P. C., Strauss, M. T., Jimenez Sabinina, V., Ellenberg, J., Carter, J. D., et al. (2018). Modified aptamers enable quantitative sub-10-nm cellular DNA-PAINT imaging. *Nat. Methods* 15, 685–688. doi: 10.1038/s41592-018-0105-0

Sun, J., Yamaguchi, N., Xu, L., Eu, J. P., Stamler, J. S., Meissner, G., et al. (2008). Regulation of the cardiac muscle ryanodine receptor by O_2 tension and s-nitrosoglutathione. *Biochemistry* 47, 13985–13990.

Sun, X. H., Protasi, F., Takahashi, M., Takeshima, H., Ferguson, D. G., Franzini-Armstrong, C., et al. (1995). Molecular architecture of membranes involved in excitation-contraction coupling of cardiac muscle. *J. Cell Biol.* 129, 659–671. doi: 10.1083/jcb.129.3.659

Swietach, P., Spitzer, K. W., and Vaughan-Jones, R. D. (2008). Ca^{2+}-mobility in the sarcoplasmic reticulum of ventricular myocytes is low. *Biophys. J.* 95, 1412–1427. doi: 10.1529/biophysj.108.130385

Szent-Gyorgyi, A. (1949). Free-energy relations and contraction of actomyosin. *Biol. Bull.* 96, 140–161.

Tang, Y., Tian, X., Wang, R., Fill, M., and Chen, S. R. W. (2012). Abnormal termination of Ca^{2+} release is a common defect of ryr2 mutations associated with cardiomyopathies. *Circ. Res.* 110, 968–977. doi: 10.1161/CIRCRESAHA.111.256560

Terentyev, D., Györke, I., Belevych, A. E., Terentyeva, R., Sridhar, A., Nishijima, Y., et al. (2008). Redox modification of ryanodine receptors contributes to sarcoplasmic reticulum Ca^{2+} leak in chronic heart failure. *Circ. Res.* 103, 1466–1472. doi: 10.1161/CIRCRESAHA.108.184457

Tian, Q., Kaestner, L., Schröder, L., Guo, J., and Lipp, P. (2017). An adaptation of astronomical image processing enables characterization and functional 3D mapping of individual sites of excitation-contraction coupling in rat cardiac muscle. *Elife* 6:e30425. doi: 10.7554/eLife.30425

Tveito, A., Jæger, K. H., Kuchta, M., Mardal, K.-A., and Rognes, M. E. A. (2017). Cell-based framework for numerical modeling of electrical conduction in cardiac tissue. *Front. Phys.* 5:48. doi: 10.3389/fphy.2017.00048

Wagner, E., Lauterbach, M. A., Kohl, T., Westphal, V., Williams, G. S., Steinbrecher, J. H., et al. (2012). Stimulated emission depletion live-cell super-resolution imaging shows proliferative remodeling of t-tubule membrane structures after myocardial infarction. *Circ. Res.* 111, 402–414. doi: 10.1161/CIRCRESAHA.112.274530

Walker, M. A., Williams, G. S. B., Kohl, T., Lehnart, S. E., Jafri, M. S., Greenstein, J. L., et al. (2014). Superresolution modeling of calcium release in the heart. *Biophys. J.* 107, 3018–3029. doi: 10.1016/j.bpj.2014.11.003

Wescott, A. P., Jafri, M. S., Lederer, W. J., and Williams, G. S. B. (2016). Ryanodine receptor sensitivity governs the stability and synchrony of local calcium release during cardiac excitation-contraction coupling. *J. Mol. Cell. Cardiol.* 92, 82–92. doi: 10.1016/j.yjmcc.2016.01.024

Wier, W. G., Egan, T. M., López-López, J. R., and Balke, C. W. (1994). Local control of excitation-contraction coupling in rat heart cells. *J. Physiol.* 474, 463–471. doi: 10.1113/jphysiol.1994.sp020037

Wigner, E. P. (1960). The unreasonable effectiveness of mathematics in the natural sciences. Richard courant lecture in mathematical sciences delivered at New York University, May 11, 1959. *Commun Pure Appl. Math.* 13, 1–14. doi: 10.1002/cpa.3160130102

Williams, G. S. B., Chikando, A. C., Tuan, H. T., Sobie, E. A., Lederer, W. J., Jafri, M. S., et al. (2011). Dynamics of calcium sparks and calcium leak in the heart. *Biophys. J.* 101, 1287–1296. doi: 10.1016/j.bpj.2011.07.021

Winegrad, S. (1965a). Autoradiographic studies of intracellular calcium in frog skeletal muscle. *J. Gen. Physiol.* 48, 455–479. doi: 10.1085/jgp.48.3.455

Winegrad, S. (1965b). The location of muscle calcium with respect to the myofibrils. *J. Gen. Physiol.* 48, 997–1002. doi: 10.1085/jgp.48.6.997

Xie, W., Brochet, D. X. P., Wei, S., Wang, X., and Cheng, H. (2010). Deciphering ryanodine receptor array operation in cardiac myocytes. *J. Gen. Physiol.* 136, 129–133. doi: 10.1085/jgp.201010416

Xu, L., Eu, J. P., Meissner, G., and Stamler, J. S. (1998). Activation of the cardiac calcium release channel (ryanodine receptor) by poly-s-nitrosylation. *Science* 279, 234–237. doi: 10.1126/science.279.5348.234

Yin, C.-C., Han, H., Wei, R., and Lai, F. A. (2005). Two-dimensional crystallization of the ryanodine receptor Ca^{2+} release channel on lipid membranes. *J. Struct. Biol.* 149, 219–224. doi: 10.1016/j.jsb.2004.10.008

Zima, A. V., Bovo, E., Bers, D. M., and Blatter, L. A. (2010). Ca^{2+} spark-dependent and -independent sarcoplasmic reticulum Ca^{2+} leak in normal and failing rabbit ventricular myocytes. *J. Physiol.* 588, 4743–4757. doi: 10.1113/jphysiol.2010.197913

Zima, A. V., Picht, E., Bers, D. M., and Blatter, L. A. (2008). Termination of cardiac Ca^{2+} sparks. *Circ. Res.* 103, e105–e115.

Conflict of Interest: The authors declare that the research was conducted in the absence of any commercial or financial relationships that could be construed as a potential conflict of interest.

frontiers
in Physiology

REVIEW
published: 09 March 2022
doi: 10.3389/fphys.2022.836622

Multi-Scale Computational Modeling of Spatial Calcium Handling From Nanodomain to Whole-Heart: Overview and Perspectives

***Michael A. Colman*[1]*, *Enrique Alvarez-Lacalle*[2], *Blas Echebarria*[2], *Daisuke Sato*[3], *Henry Sutanto*[4,5] *and Jordi Heijman*[5]**

[1] School of Biomedical Sciences, University of Leeds, Leeds, United Kingdom, [2] Departament de Fisica, Universitat Politècnica de Catalunya-BarcelonaTech, Barcelona, Spain, [3] Department of Pharmacology, School of Medicine, University of California, Davis, Davis, CA, United States, [4] Department of Physiology and Pharmacology, State University of New York Downstate Health Sciences University, Brooklyn, NY, United States, [5] Department of Cardiology, Cardiovascular Research Institute Maastricht, Maastricht University, Maastricht, Netherlands

Edited by:
Niall Macquaide,
Glasgow Caledonian University,
United Kingdom

Reviewed by:
Mohsin Saleet Jafri,
George Mason University,
United States
Wayne Rodney Giles,
University of Calgary, Canada
Glenn Terje Lines,
Simula Research Laboratory, Norway

***Correspondence:**
Michael A. Colman
m.a.colman@leeds.ac.uk

Specialty section:
This article was submitted to
Cardiac Electrophysiology,
a section of the journal
Frontiers in Physiology

Received: 15 December 2021
Accepted: 31 January 2022
Published: 09 March 2022

Citation:
Colman MA, Alvarez-Lacalle E, Echebarria B, Sato D, Sutanto H and Heijman J (2022) Multi-Scale Computational Modeling of Spatial Calcium Handling From Nanodomain to Whole-Heart: Overview and Perspectives.
Front. Physiol. 13:836622.
doi: 10.3389/fphys.2022.836622

Regulation of intracellular calcium is a critical component of cardiac electrophysiology and excitation-contraction coupling. The calcium spark, the fundamental element of the intracellular calcium transient, is initiated in specialized nanodomains which co-locate the ryanodine receptors and L-type calcium channels. However, calcium homeostasis is ultimately regulated at the cellular scale, by the interaction of spatially separated but diffusively coupled nanodomains with other sub-cellular and surface-membrane calcium transport channels with strong non-linear interactions; and cardiac electrophysiology and arrhythmia mechanisms are ultimately tissue-scale phenomena, regulated by the interaction of a heterogeneous population of coupled myocytes. Recent advances in imaging modalities and image-analysis are enabling the super-resolution reconstruction of the structures responsible for regulating calcium homeostasis, including the internal structure of nanodomains themselves. Extrapolating functional and imaging data from the nanodomain to the whole-heart is non-trivial, yet essential for translational insight into disease mechanisms. Computational modeling has important roles to play in relating structural and functional data at the sub-cellular scale and translating data across the scales. This review covers recent methodological advances that enable image-based modeling of the single nanodomain and whole cardiomyocyte, as well as the development of multi-scale simulation approaches to integrate data from nanometer to whole-heart. Firstly, methods to overcome the computational challenges of simulating spatial calcium dynamics in the nanodomain are discussed, including image-based modeling at this scale. Then, recent whole-cell models, capable of capturing a range of different structures (such as the T-system and mitochondria) and cellular heterogeneity/variability are discussed at two different levels of discretization. Novel methods to integrate the models and data across the scales and simulate stochastic dynamics in tissue-scale models are then discussed, enabling elucidation of the mechanisms by which nanodomain remodeling underlies arrhythmia and contractile dysfunction. Perspectives on model differences and future directions are provided throughout.

Keywords: cardiac electrophysiology, calcium handling in cardiomyocytes, excitation-contraction coupling, computational modeling methods, multi-scale model

INTRODUCTION

Intracellular calcium (Ca^{2+}) handling is a critical component of cardiac electrophysiology (Cheng et al., 1993; Bers, 2002; Song et al., 2015): it governs excitation-contraction coupling (ECC), is involved in multiple signaling pathways, and its impairment has been causally linked to both mechanical and electrical dysfunction of the heart (Eisner et al., 2009; Voigt et al., 2014; Clarke et al., 2015). Elucidating the fundamental mechanisms of Ca^{2+} homeostasis and the perturbations of the system in disease is therefore vital for understanding the electrophysiology of the heart and identifying better diagnostic and treatment strategies for multiple cardiovascular diseases.

One major challenge of dissecting the specific roles and contributions of the many components of intracellular Ca^{2+} handling to observed (dys)function is the complex, non-linear and multi-scale properties of the system in space and time. Spatially, Ca^{2+} sparks, the fundamental element of Ca^{2+}-induced-Ca^{2+}-release (CICR; see next sub-section), are controlled at the nanometer-scale in localized nanodomains referred to as dyads or couplons, yet Ca^{2+} homeostasis occurs inherently at the cellular-scale where flux balance through the membrane and subcellular transporters determines the total Ca^{2+} levels in the cell and in the Sarcoplasmic Reticulum (SR, the intracellular Ca^{2+} store). Homeostatic conditions of cardiomyocytes at the cell-level are integrated in the heterogeneous syncytium of cardiac muscle tissue where individual myocytes do not function as isolated entities. Temporally, the gating of Ca^{2+} channels occurs on sub-millisecond time-frames (Zahradníková et al., 1999); the heartbeat itself occurs on the order of a second; signaling and regulation, such as sympathetic stimulation, can occur over minutes (Heijman et al., 2011); and transcription and circadian rhythms can influence dynamics over hours or even days (Black et al., 2019; D'Souza et al., 2021). Thus, structure-function relationships from the nanometer- to the whole-heart-scales and dynamics occurring over nanoseconds to hours all contribute to the macroscopic behavior of the heartbeat.

Recent advances in experimental imaging modalities and image-analysis are enabling the super-resolution reconstruction of the structures responsible for regulating Ca^{2+} homeostasis at the nanometer scale (Baddeley et al., 2009; Crossman et al., 2011; Macquaide et al., 2015; Jayasinghe et al., 2018b; Sheard et al., 2019). Extrapolating functional and imaging data from the dyad to the whole-heart is non-trivial due to multi-scale systems interactions; it is therefore a substantial challenge using experimental techniques alone to employ integrative approaches which aim to understand how macroscopic cardiac function arises from these fundamental building blocks. Computational modeling therefore has important roles to play in helping to dissect these structure-function relationships at multiple scales and elucidate the mechanisms by which cellular phenomena translate to the whole-heart.

Over the last decade in particular there have been substantial advances in the complexity and sophistication of computational models of spatial intracellular Ca^{2+} handling. Due to the variety of independently developed models and range of contexts in which they have been applied, it can be a challenging field to get into and understand, whether one is a computational modeler wanting to use and develop these models, or an experimental researcher hoping to understand the models' limitations and where they can be used to support one's research. This review aims to provide an accessible entry-point for those not already familiar with these models and a useful reference for those who are. We focus on methods and approaches, in particular those for image-based and multi-scale modeling, how these differ between models, and the implications of these model differences. Applications of the models will be discussed primarily within this context; the reader is referred to previous reviews for more extensive descriptions of the role of computational modeling in elucidating the Ca^{2+}-mediated mechanisms of cardiac (dys)function (Heijman et al., 2016; Maleckar et al., 2017; Vagos et al., 2018; Sutanto et al., 2020).

Structure–Function Relationships in Ca^{2+} Homeostasis: Local Control of Ca^{2+}-Induced-Ca^{2+}-Release

Excitation-contraction coupling is mediated by CICR (Cheng et al., 1993; Bers, 2002), illustrated in **Figure 1**: **(1)** Ca^{2+} enters the cell through the L-type Ca^{2+} channels (LTCC) during electrical excitation (the action potential, AP); **(2)** This local rise in Ca^{2+} activates the ryanodine receptors (RyRs) to trigger a large release of Ca^{2+} (triggered Ca^{2+} spark) from the SR; **(3)** Ca^{2+} diffuses throughout the myocyte, binds with the contractile apparatus, and initiates cellular contraction; **(4)** Peak contraction occurs when Ca^{2+} has diffused sufficiently throughout the cell to permit substantial binding with the contractile apparatus; Ca^{2+} influx has largely terminated at this point; intracellular Ca^{2+} is removed into the extracellular space through the sodium-Ca^{2+} exchanger (NCX) and the plasmalemmal Ca^{2+} pump, and SR-Ca^{2+} is restored through the SR-Ca^{2+} pump (SERCA); **(5)** As NCX and SERCA reduce the Ca^{2+} concentration in the intracellular volume, myofilaments release Ca^{2+} from their binding sites and cellular relaxation occurs; **(6)** NCX and SERCA continue to act to restore resting Ca^{2+} levels, ready for the next cycle.

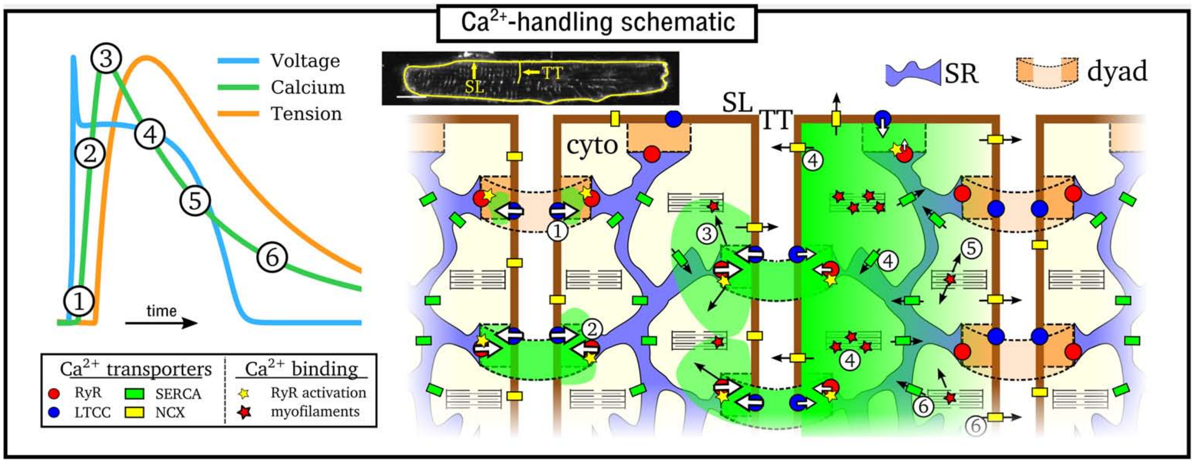

FIGURE 1 | Simplified illustration of the intracellular Ca^{2+}-handling cycle in ventricular myocytes. Left: illustration of an action potential (voltage), calcium transient (CaT), and developed tension, with the different stages broadly labeled on the CaT. Right: cartoon schematic of the different stages of Ca^{2+} cycling in the intracellular volume. High Ca^{2+} concentration is indicated by the green areas; SL refers to the sarcolemmal membrane and TT to a transverse tubule, illustrated on a real cell image (modified from Gadeberg et al., 2016). Numbered stages correspond to those in the main text and are illustrated at different spatial locations of the schematic for brevity – it should be clarified that all stages occur throughout the cell volume.

The rise and decay of Ca^{2+} in the intracellular volume is referred to as the intracellular Ca^{2+} transient (CaT), and broadly follows the AP (**Figure 1**). Rather than being a whole-cell, homogeneous event, the CaT is the summation of many thousands of locally controlled Ca^{2+} sparks, conferred in the specialized nanodomains called dyads or couplons which co-localize the RyRs on the SR membrane with the LTCCs on the sarcolemma membrane. Cardiomyocytes therefore feature an intracellular structure which facilitates whole-cell contraction mediated by this local control of CICR: the SR forms a cell-wide network coupling the spatially distributed dyads throughout the intracellular volume; the surface sarcolemma (SL) membrane contains multiple invaginations into the cell interior, consisting of the transverse-tubule (TT) and axial-tubule (AT) system (T-system), harboring LTCCs, NCX, and other ion channels (Dibb et al., 2022) which enables dyads to be formed throughout the cellular volume. The reader is referred to the previous works and reviews by Cannell and Kong (2012, 2017) and Laver et al. (2013) for discussion about the importance of local control to explain the properties of CICR in the heart.

Although the Ca^{2+}-handling system is conceptually similar and involves the same machinery in all regions of the heart, there are functional and structural differences between myocytes from the pacemaker regions, cardiac conduction system, atria and ventricles that are important for normal physiology as well as the genesis of cardiac arrhythmias (Sutanto et al., 2020). For example, atrial myocytes do not have as robust and dense a T-system as ventricular myocytes (Richards et al., 2011), featuring more orphaned RyR clusters (those without associated LTCCs); in the pacemaker cells of the sinoatrial and atrioventricular nodes, the Ca^{2+} handling system forms the Ca^{2+}-clock which is involved in the generation of APs and does not function primarily to initiate cellular contraction (Maltsev and Lakatta, 2013; Yaniv et al., 2015; Maltsev et al., 2017). Discussing models of pacemaker and conduction system myocytes is beyond the scope of the current review, which will focus on the working myocardium of the ventricles and atria.

Multi-Scale Dynamics of Ca^{2+} Handling

The inherently multi-scale nature of cardiac Ca^{2+}-handling is perhaps best illustrated by considering the mechanisms of spontaneous Ca^{2+} release events (SCRE) and their involvement in proarrhythmogenic premature focal excitations (**Figure 2**).

One consequence of local control is that each dyad contains only small numbers of channels, with typical values thought to be 5–15 LTCCs and 5–200 RyRs (Baddeley et al., 2009; Jayasinghe et al., 2018a,b), located within a very small volume of order $< 10^{-3}$ μm^3 (Scriven et al., 2013). Stochastic oscillations of single RyR channels can result in small-scale intracellular Ca^{2+}-release (Ca^{2+} quarks), potentially inducing the nanodomain-wide event of a spontaneous Ca^{2+} spark by recruiting further RyRs within the dyad to sustain a release flux. The specific mechanism for this recruitment is either a large flux of Ca^{2+} through the pore of a channel that stochastically opens, which raises the local Ca^{2+} sufficiently to trigger the opening of adjacent RyRs, or a cascade of events where a single channel opening increases the probability of opening of a second round of receptors, which triggers more rounds of receptors opening (Asfaw et al., 2013). Irrespective of the specific mechanism, once a reasonably large spark is originated, spatial-diffuse coupling provides a substrate for the propagation of Ca^{2+}-sparks throughout the cell as a spark-induced-spark mediated Ca^{2+}-wave (**Figure 2**).

These SCRE are potentially pro-arrhythmic cellular phenomena: Ca^{2+} release can activate NCX which results in a transient inward current when Ca^{2+} is extruded, depolarizing the cell membrane potential as a delayed-after-depolarization (DAD) or, if of sufficient magnitude,

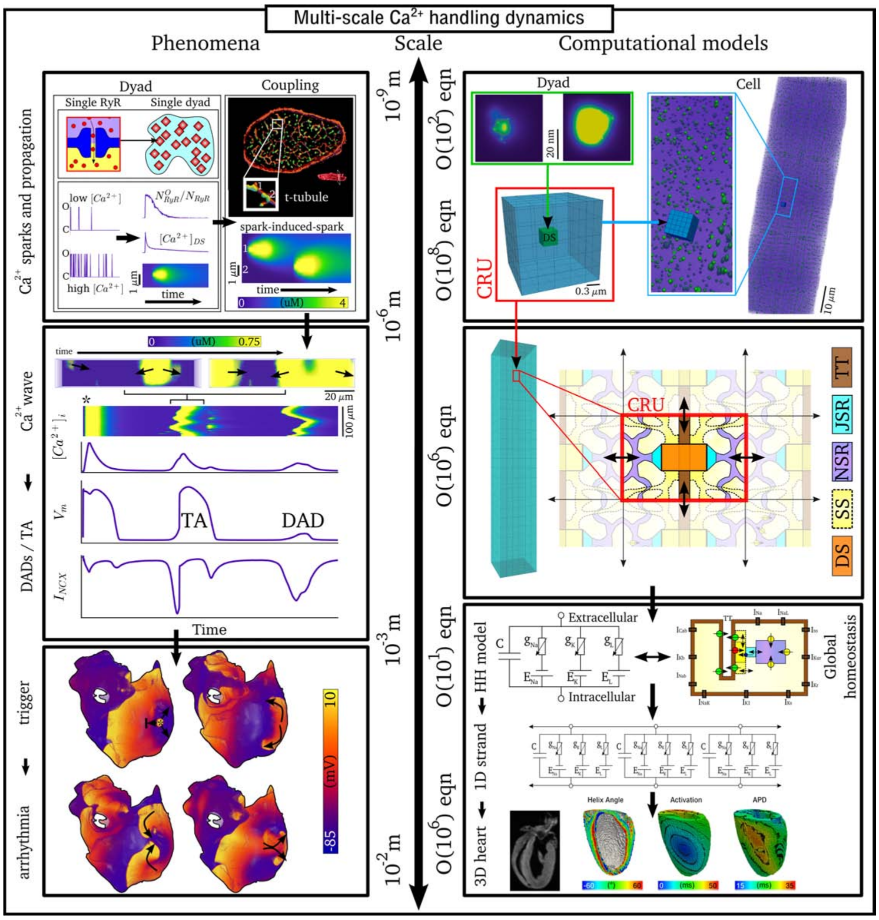

FIGURE 2 | Illustration of the scales involved in cardiac Ca^{2+}-handling electrophysiology. Left, upper: illustration of a single RyR and the distribution of RyRs in a dyad, RyR channel function at low and high local Ca^{2+}, and propagation of a Ca^{2+}-spark between dyads. Cell-structure image re-rendered using data from Jayasinghe et al. (2018a). Left, middle: Illustration of an intracellular Ca^{2+}-wave and the impact of the spontaneous Ca^{2+}-transient on NCX and the action potential (AP), demonstrating both a delayed-after-depolarization (DAD) and triggered AP (TA). Left, lower: illustration of a focal excitation in tissue which degenerates into a re-entrant excitation pattern. Simulation data from Colman et al. (2013). Right, upper: spatial model of a single dyad (model as presented in Sheard et al., 2019) and illustration of a sub-micron full-cell model with dyads distributed therein. Right, middle: illustration of a coarse-grained 3D cell model with different intracellular and SR compartments labeled. Right, lower: illustration of standard, non-spatial Hodgkin-Huxley electric circuit models of cardiac electrophysiology, their coupling in a 1D strand, and implementation in 3D whole-heart models based on imaging data, reproduced using data from Benson et al. (2011).

a full triggered AP (TA; **Figure 2**). Multiple cells must undergo some degree of synchronization of these TA in order for them to overcome electrotonic load and manifest in tissue as a focal excitation (Xie et al., 2010; Campos et al., 2015; Liu et al., 2015; Colman, 2019). Similar considerations apply for many sub-cellular Ca^{2+} handling phenomena, from rate-dependence to arrhythmogenic CaT alternans; the fundamental pumping function itself ultimately depends on these multi-scale interactions and can thusly be potentially perturbed by random, stochastic oscillations at the nanometer-scale. Ca^{2+}-dependent regulation of the membrane potential is one of the key factors in understanding arrhythmogenesis. Elucidating these mechanisms is, alongside ECC and contractile function, a primary motivation for the development of biophysically detailed models of intracellular Ca^{2+} handling. For a comprehensive overview of the multi-scale implications of Ca^{2+} handling in normal and abnormal cardiac function, the reader is referred to, for example, the reviews of Eisner et al. (2009, 2017).

Multi-Scale Computational Models of Spatial Ca^{2+} Handling

Due to the importance of local control, common-pool models of the cell – that is, those which treat the intracellular space as single homogenized volumes – fail to properly capture the underlying mechanisms and dynamics of Ca^{2+} handling. For example, Sato et al. (2013) demonstrated that stochasticity in Ca^{2+} cycling is necessary to explain the emergence of discordant alternans, which cannot be reproduced with deterministic, common-pool cell models. Models which explicitly account for the spatial nature of the cardiomyocyte as well as stochastic dynamics of the RyRs and LTCCs are therefore much better suited to detailed analyses of Ca^{2+}-handling phenomena. However, these models are also computationally more intensive than common-pool models, by a factor of $>10^5$, and less suitable for tissue-scale and especially whole-heart simulations. Therefore, different models need to be considered at different spatial scales (**Figure 2**).

This review will discuss models of spatial Ca^{2+} handling at the multiple scales of the single nanodomain, the cardiomyocyte, and the whole-heart. Models describing the kinetics of the RyRs will first be discussed, followed by spatial models of the single nanodomain. Approaches to whole-cell modeling will then be discussed, with a particular focus on mechanisms of spatial Ca^{2+} coupling. This discussion will then be expanded to approaches for modeling variable and heterogeneous sub-cellular structure and the integration of experimental imaging data. Finally, approaches to develop simplified, computationally efficient models which still capture important features of spatial and stochastic Ca^{2+} handling will be discussed, in both the context of providing generalizable mechanistic explanations and for performing tissue-scale simulations of many thousands or millions of coupled cells. Overall clarity is prioritized over providing substantial details of all available models and investigations; thus, this review should not be considered exhaustive. The reader is also referred to the extensive overview of multi-scale mathematical and computational modeling methods presented in Qu et al. (2014).

MODELING Ca^{2+}-INDUCED-Ca^{2+}-RELEASE: DESCRIPTIONS OF RYANODINE RECEPTORS' KINETICS

There are multiple descriptions of RyR kinetics which have been used in computational modeling. The simplest form are two-state models, which have only a closed/inactivated state and an open/activated state. Most frequently used are four-state models, which have more details of refractoriness and inactivation (which may or may not physiologically occur, discussed in the later sub-section "Perspectives on model differences") and can simulate different potential mechanisms of these behaviors. The model structure of the RyR is directly related to the type of behavior that is considered to be behind the appearance of local sparks. In two-state models, refractoriness is not considered relevant in the dynamics of initiation and termination of sparks, whereas refractoriness and more complex gating, that may play critically important roles in the regulation of spark dynamics, can be included in four-state and other models. Previous studies and reviews have compared fundamentally different models of the RyR regarding their ability to reproduce different features of the physiology and/or assess the ability of different proposed mechanisms to explain these features. For example, Stern et al. (1999) evaluated different Markov-chain model constructions for reproducing CICR, and Cannell and Kong (2012, 2017) assessed different mechanisms of Ca^{2+}-spark termination.

This section aims to provide a clear indication of the models used in various studies by different groups and explain what the major features of these models' differences are, in order to guide the reader through the many studies. The focus is primarily on those models which are utilized in whole-cell simulations, rather than those designed specifically to evaluate RyR function in isolation or in bilayers, such as Zahradníková et al. (1999).

Model Structure

The four-state Markov chain RyR model (**Figure 3**) which forms the basis for the majority of modeling studies, originally presented in Stern et al. (1999), is governed by the following state-equations:

$$\frac{dC}{dt} = O \cdot K_{O-C} + C^* \cdot K_{C^*-C} - C \cdot (K_{C-O} + K_{C-C^*}) \qquad (1)$$

$$\frac{dO}{dt} = C \cdot K_{C-O} + O^* \cdot K_{O^*-O} - O \cdot (K_{O-C} + K_{O-O^*}) \qquad (2)$$

$$\frac{dC^*}{dt} = O^* \cdot K_{O^*-C^*} + C \cdot K_{C-C^*} - C^* \cdot (K_{C^*-O^*} + K_{C^*-C}) \qquad (3)$$

And by definition/conservation:

$$O^* = 1 - (C + O + C^*) \qquad (4)$$

Where O, O*, C, and C* represent the four states of the model and correspond to different physical conditions dependent on the specific model implemented (e.g., active; refractory; inactivated; buffer binding state). The release flux, J_{rel}, is generally given by:

$$J_{rel} = J_{rel}^{\max} \cdot O \cdot \left(\left[Ca^{2+} \right]_{SR} - \left[Ca^{2+} \right]_i \right) \qquad (5)$$

Where ${J_{rel}}^{max}$ is the maximal flux rate and the subscripts SR and i denote the SR and intracellular Ca^{2+} concentrations. The models have the following symmetries (some of which are broken in further model developments):

$$K_{C-O} = K_{C^*-O^*} \qquad (6)$$

$$K_{O-C} = K_{O^*-C^*} \qquad (7)$$

$$K_{C-C^*} = K_{O-O^*} \qquad (8)$$

$$K_{C^*-C} = K_{O^*-O} \qquad (9)$$

If all of these symmetries are preserved, the description becomes equivalent to a Hodgkin-Huxley model with two independent gating variables.

The functional form of these transition rates, including the variables that they depend on and which states correspond to release flux, differ between the different implementations. In the original study by Stern et al. (1999), and henceforth referred to as the "Stern-like" models, one single state (O) corresponds to the release flux [equation (5)]; transitions from the closed-to-open states, which are symmetric for C-O and C^*–O^*, are dependent on the square of local cytosolic Ca^{2+} ("Ca_i" from herein for brevity and to avoid confusion with notation of

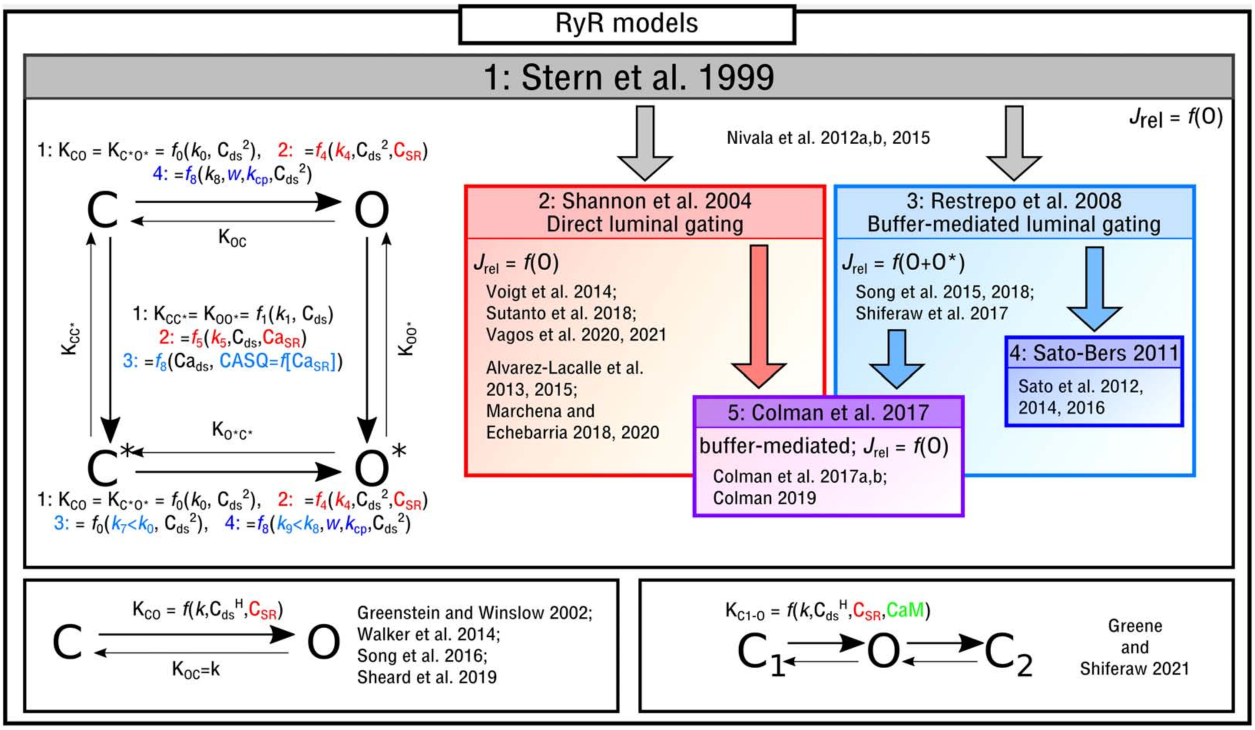

FIGURE 3 | Illustration of RyR Markov-chain models. The four-state, two-state and three-state models are illustrated with the different features highlighted and a selection of publications in which they are used listed. Block arrows indicate model inheritance.

powers); transitions from the top-to-bottom, also symmetric, are linearly dependent on the local Ca_i:

$$K_{C-O} = K_{C^*-O^*} = f_0(Ca_i^2) = k_0 Ca_i^2 \tag{10}$$

$$K_{C-C^*} = K_{O-O^*} = f_1(Ca_i) = k_1 Ca_i \tag{11}$$

$$K_{O-C} = K_{O^*-C^*} = k_2 \tag{12}$$

$$K_{C^*-C} = K_{O^*-O} = k_3 \tag{13}$$

Where k_{0-3} are constants. This model is directly used in, for example, Nivala et al. (2012a,b, 2015).

Shannon et al. (2004) updated this formulation to introduce the SR-Ca^{2+} (Ca_{SR} for brevity) as a gating variable, which will be referred to here as "direct luminal gating." The transition rates from the closed-to-open states are now functions of Ca_{SR} as well as $Ca_i{}^2$, and the transitions from active to inactive (top-to-bottom) are dependent on both Ca_{SR} and Ca_i:

$$K_{C-O} = K_{C^*-O^*} = f_4(Ca_i^2, Ca_{SR}) = \left(\frac{k_4}{k_{CaSR}}\right) Ca_i^2 \tag{14}$$

$$K_{C-C^*} = K_{O-O^*} = f_5(Ca_i, Ca_{SR}) = k_5 k_{CaSR} Ca_i \tag{15}$$

Where

$$k_{CaSR} = SR^{\max} - \left(SR^{\max} - SR^{\min}\right) . \left[1 + \left(\frac{EC_{50}^{SR}}{Ca_{SR}}\right)^H\right]^{-1} \tag{16}$$

This formulation is one of the most-commonly used (Alvarez-Lacalle et al., 2013, 2015; Voigt et al., 2014; Marchena and Echebarria, 2018, 2020; Sutanto et al., 2018; Vagos et al., 2020, 2021).

Whereas the above model introduced direct luminal gating, many models include "buffer-mediated luminal gating," wherein the Ca_{SR} influences gating of the RyRs not directly but rather mediated through the SR-Ca^{2+} buffer calsequestrin (CASQ), as introduced by Restrepo et al. (2008) and similar to that of Gaur and Rudy (2011). The closed-to-open transition rates have the same form as the original Stern formulation and the top-to-bottom rates are now dependent on CASQ. Two major differences are: (1) There are now two open states (O and O* in the illustration) with the formulation for J_{rel} [equation (5)] updated accordingly [equation (21)]; (2) The constant for the open transition rate for the lower portion of the model (which now corresponds to CASQ-bound) is smaller than that of the top, breaking one of the symmetries in the previous models [equation (6) is no longer true]:

$$K_{C-O} = f_6(Ca^2) = k_6 Ca_i^2 \tag{17}$$

$$K_{C^*-O^*} = f_7(Ca^2) = k_7 Ca_i^2 \tag{18}$$

Where

$$k_6 > k_7 \tag{19}$$

And CASQ determines the unbound-bound transition rates:

$$K_{C-C^*} = K_{O-O^*} = f_8(Ca_i, CASQ) \tag{20}$$

The release flux is now given by:

$$J_{rel} = J_{rel}^{\max} \cdot \left(O + O^*\right) .(Ca_{SR} - Ca_i) \tag{21}$$

The reader is referred to the work of Restrepo et al. (2008) for details of the CASQ buffering and gating equations [equation (20)]. Models which use this formulation include Song et al. (2015, 2017, 2018) and Shiferaw et al. (2017).

In Sato and Bers (2011) and subsequent studies (Sato et al., 2012, 2014, 2016), this model was updated in order to reduce the number of RyRs open during a Ca^{2+} spark:

$$K_{C-O} = f_8(Ca_i^2) = \frac{k_8 Ca_i^2}{k_{cp}^2 + Ca_i^2} + w \tag{22}$$

$$K_{C^*-O^*} = f_9(Ca_i^2) = \frac{k_9 Ca_i^2}{k_{cp}^2 + Ca_i^2} + w \tag{23}$$

Where k_{cp} and w are further constants. The majority of the models presented in the field – especially those of whole-cells – implement an RyR model which falls into one of these three broad categories. It is worth noting that the relatively simple functional forms of the transition rates given for the different models above may be modified in studies which aim to fit to experimental data describing RyR open probability, e.g., Voigt et al. (2014), Sutanto et al. (2018), and Vagos et al. (2020); these studies contain further parameters and more complex functions, but their Ca_i and Ca_{SR} dependence is still captured in the general forms of the model given above. Further alternatives and updates exist of these baseline models. In Colman et al. (2016, 2017a,b) and Colman (2019), a functionally motivated hybrid was developed wherein only one state corresponds to the open condition but the luminal dependence is buffer-mediated rather than direct.

One feature of the models, which is independent of the fundamental model structure but nonetheless important for model behavior, is the Hill coefficient, H, to which Ca_i is raised by for the closed-to-open (left-to-right) transition rates. Many of the models use a simple coefficient of $H = 2$. However, single-channel and single-nanodomain studies (Sobie et al., 2005; Cannell et al., 2013) indicate that H is species-dependent and varies in the range 2–2.8 which may be implemented in some studies.

Alternative Models of the Ryanodine Receptors

There are alternative formulations to describe RyR kinetics which either: (1) are not of the form of a four-state model or (2) introduce further environmental variables to control gating. In Song et al. (2016), a reduced two-state approximation of the four-state RyR model was introduced in a study focused on elucidating long-lasting Ca^{2+} sparks. A reduced, or minimal, two-state model (**Figure 3**) was used in studies of single nanodomains (Greenstein and Winslow, 2002; Walker et al., 2014; Sheard et al., 2019). In Greene and Shiferaw (2021) a three-state RyR model (**Figure 3**) was implemented which does not correspond directly to a reduction of the four-state model. The model included a second closed state after the open state, which was introduced to reproduce “flicker” based on Mukherjee et al. (2012), as well as containing regulation of the RyRs by Calmodulin (CaM). CaM was also included in the deterministic model presented in Wei et al. (2021).

There is also the question of whether allosteric interactions/cooperativity play a role in RyR gating, with Marx et al. (2001) demonstrating that the regulatory subunit FK506-binding protein could functionally couple neighboring RyRs to underlie coordinated gating. These interactions are included in many works (Stern et al., 1999; Sobie et al., 2002; Chen et al., 2009; Greene and Shiferaw, 2021) and have been proposed as one explanation for self-termination of the Ca^{2+} spark, as discussed in Cannell and Kong (2017), although as argued in that review, unlikely to be a major contributor to this phenomenon.

Numerical Solutions to the Ryanodine Receptors Model

In common-pool models of the cardiomyocyte, the solutions to the RyR/LTCC models are typically numerically approximated using deterministic algorithms such as the forward-Euler method. These numerical solutions correspond to tracking only the average state of the system, i.e., the proportion of open RyRs/LTCCs across the whole-cell; information on the state of individual channels or channel clusters is not preserved in such an approximation. One motivation for the development of detailed spatial models of the dyad or cardiomyocyte is to capture the stochastic (random) nature of individual RyRs/LTCCs as well as their local control, due to the relevance of both of these features for both CICR and more complex emergent dynamics such as Ca^{2+}-waves. Thus, deterministic solutions are no longer suitable. Instead, stochastic algorithms that explicitly account for randomness and track individual channels are required.

The most straight-forward method is to implement the Monte-Carlo approach: the state of each individual channel is tracked directly, and state-transitions are determined based on random numbers and the probability of transition. For example, for a two-state RyR model corresponding to only closed (C) and open (O) states, the algorithm at each time-step (Δt) might look like:

```
Loop over all RyRs:
    RAND = generate random number between 0 and 1
    IF state is equal to C:
        IF RAND < $K_{C-O} \times \Delta t$: state becomes O
        ELSE state remains C
    ELSE IF state is equal to O:
        IF RAND < $K_{O-C} \times \Delta t$: state becomes C
        ELSE state remains O
```

The release flux is then given by the sum of the open channels in each dyad. This approach is ideally suited to cases where each individual channel is required to be tracked, for example in spatial models of the single nanodomain (Mesa et al., 2021). However, in larger models, e.g., of the whole-cell, this then requires the state of ∼50 RyRs + ∼15 LTCCs per dyad × ∼20,000 dyads to be tracked individually, with random numbers generated to determine state transitions for each one, which can be computationally intensive. There are more sophisticated approaches that can capture these same dynamics but at a reduced computational cost, such as a modified Gillespie's algorithm (Gillespie, 1976; Rathinam et al., 2003; Nivala et al., 2012a; Song et al., 2019), or the Fokker-Planck or Langevin equations (Herzel, 1991; Wang et al., 2015), which can be briefly summarized as the addition of noise to a deterministic solution. Further approaches to capture the stochastic nature of RyR dynamics at a reduced computational cost, suitable for large-scale tissue simulations, are described in the final section of this review: "Simplified, minimal and tissue models."

Perspectives on Model Differences

The disparity between the gating mechanisms of the different models could have important implications for model dynamics and thus mechanistic conclusions drawn from these simulations. Due to inter-model differences in the setup of the whole-cell (see section "Spatial models of the whole cardiomyocyte"), it is not necessarily trivial to directly evaluate RyR function, as dynamics are intricately linked with other model parameters such as dyadic cleft volume, LTCC formulation/magnitude, local Ca^{2+} buffering, and spatial Ca^{2+} coupling; an RyR model often cannot simply be "dropped in" or "swapped out" in a whole-cell model. One major difference in model function is the typical number (or proportion) of RyRs that open in a given cluster during a triggered Ca^{2+} spark, as directly addressed in the reformulation presented in Sato and Bers (2011). A similar model structure (e.g., the same four states and functional dependence on local Ca^{2+} concentrations) but with different parameters governing the transition rates and maximal Ca^{2+}-flux rate may lead to very different outcomes in adaptive function regarding Ca^{2+}-spark dynamics and homeostasis.

Another difference is the description of RyR inactivation and refractoriness, corresponding to the multiple approaches discussed above (e.g., no inactivation, luminal gating, buffer-mediated gating). One reason for the disparities between the model structures is the current debate regarding the fundamental physiological relevance of RyR inactivation (Cannell and Kong, 2017), where there is no strong evidence that significant inactivation occurs under physiological conditions. However, there are strong indications of interactions between CaM binding sites and opening properties of the RyR that may be relevant for mathematically equivalent states to inactivation: Wei et al. (2021), for example, demonstrate that inactivation may be mediated by CaM-Ca^{2+} binding to the RyR and that this plays a significant role in CaT alternans. An important implication of the model choice to either include or omit significant RyR inactivation is the degree to which the junctional SR depletes during a triggered Ca^{2+}-spark: models which do not include RyR inactivation (e.g., Hake et al., 2012; Cannell et al., 2013) exhibit substantially greater depletion of local SR-Ca^{2+} concentrations than those which do include inactivation (e.g., Restrepo et al., 2008; Colman et al., 2017b; Sutanto et al., 2018). This further highlights the challenge of evaluating RyR models under the same environmental cell conditions: the extent of junctional SR depletion will have large implications on homeostasis when combined with the specific formulations and parameterization of the Ca^{2+} buffers, SERCA and NCX, which primarily control the balance of SR-Ca^{2+}-refilling and cellular Ca^{2+} efflux. Recent studies have also highlighted the direct importance of SERCA function for Ca^{2+} homeostasis and the dynamics of Ca^{2+} sparks (Hake et al., 2012; Sato et al., 2016, 2021; Holmes et al., 2021).

A further factor, which has recently been included in Berti et al. (2017), is the role of other ions such as K^+, Mg^{2+}, Cl^-, and the counter-ion fluxes they facilitate during SR-Ca^{2+} release which help to maintain the trans-SR membrane driving force, especially at rapid pacing rates. It is possible that these dynamics could also influence RyR refractoriness by modulating this driving force.

Considerations of further complexity, such as the inclusion/omission of regulation by CaM (or other potential RyR and Ca^{2+} signaling modulators) can be directly motivated by the aim of the specific study; it is generally the perspective that additional complexity should only be included where specifically required, in order to reduce the influence of the propagation of unknown errors. However, it could also be argued that a non-linear, multi-scale complex system such as this presents the possibility for unpredictable emergent phenomena, which may depend on the interaction of factors such as CaM with other variables. In this case, it can be argued that one should aim to include as many (rigorously derived) components of the system as is feasible. Perspectives on this are ultimately philosophical and it would be unwise to disregard either argument.

Whereas the original study of Stern et al. (1999) compared multiple formulations of the RyR, this necessarily did not include the more recent updates described above (Shannon et al., 2004; Restrepo et al., 2008; Sato and Bers, 2011; Song et al., 2016; Greene and Shiferaw, 2021). Thus, a comprehensive benchmarking study which determines the implications of these model differences in relation to multiple dynamic Ca^{2+}-handling-mediated phenomena would be hugely beneficial. Previous reviews and studies, such as Cannell et al. (2013), have performed this in specific contexts such as in the evaluation of the mechanism of termination of Ca^{2+} sparks, but a more holistic benchmarking study which considers RyR function in the context of multiple relevant factors simultaneously (such as CICR, Ca^{2+} spark termination, spatial Ca^{2+} coupling, spontaneous Ca^{2+} spark dynamics, responses to changes in pacing rate and cell environment, reproduction of alternans or after-depolarization) has yet to be performed. Such a study, requiring the whole-cell models described later in this review, could be hugely valuable in understanding the features of the different models and revealing fundamental insight into the physiology of cardiac Ca^{2+} handling.

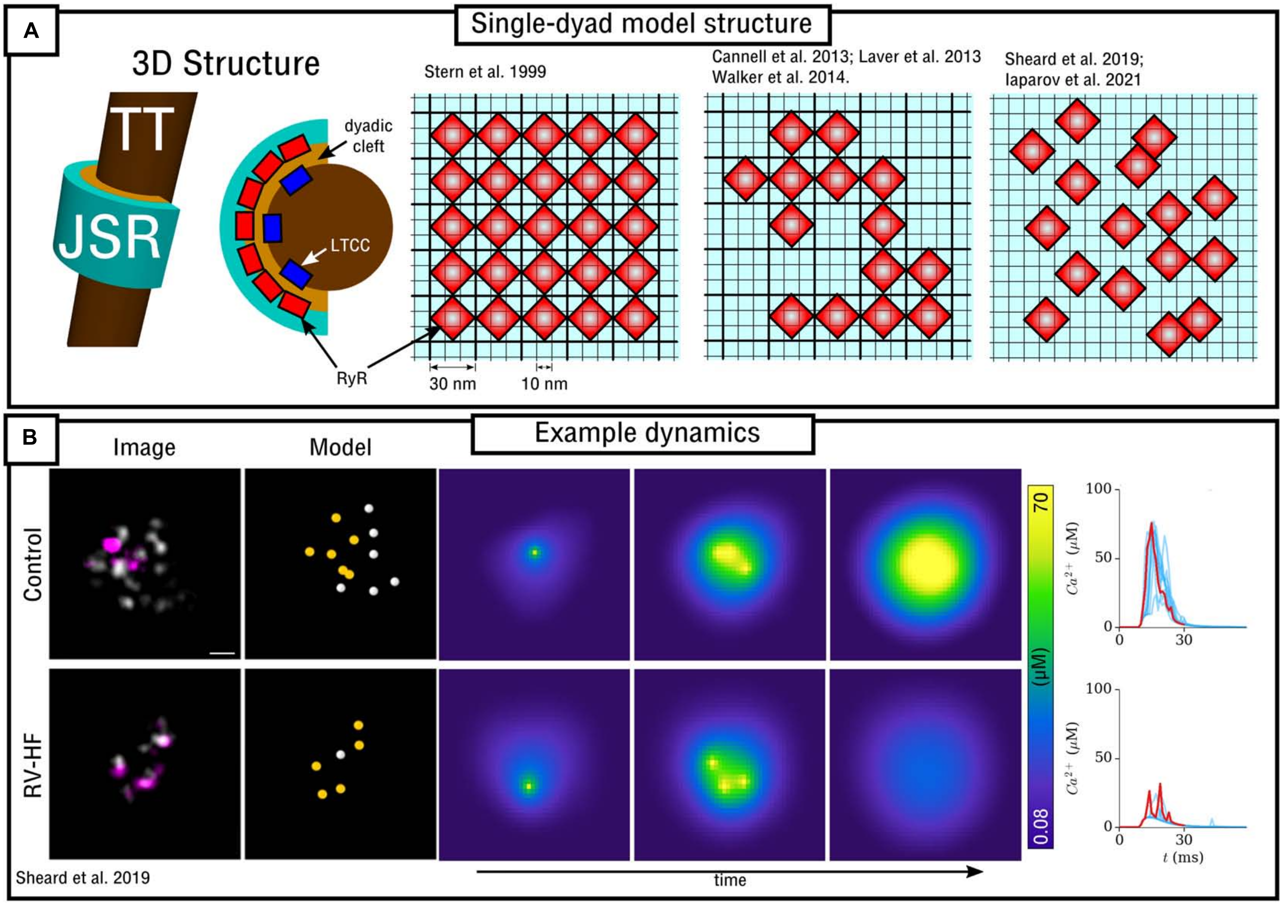

FIGURE 4 | Spatial models of the dyad. **(A)** Illustration of model structure (left) and different approaches to RyR arrangement (right), ranging from regular lattice through irregular lattice to free-placement. **(B)** Illustration of a triggered Ca^{2+} spark occurring in two different RyR arrangements, corresponding to control and right-ventricular heart failure (RV-HF) directly reconstructed from imaging data. Scale bar corresponds to 50 nm. Reproduced with data from Sheard et al. (2019).

SPATIAL MODELS OF THE SINGLE DYAD/NANODOMAIN

Only recently have experimental imaging techniques been able to resolve individual RyRs (Protasi et al., 1998; Baddeley et al., 2009; Crossman et al., 2011; Macquaide et al., 2015; Jayasinghe et al., 2018b; Sheard et al., 2019), enabling the structure of dyads (including number and arrangement of RyRs) to be described in detail. However, it is still challenging to correlate local Ca^{2+} concentration to RyR activity and quantify the specific fractional opening of RyRs during a typical spark in imaging data, and optical methods are limited to the close proximity of the cell surface. Thus, computational models of the single, spatially distributed dyad are useful to understand the mechanisms of Ca^{2+} sparks and their dependence on RyR number and arrangement.

In the original paper by Stern et al. (1999), which evaluated multiple RyR Markov-chain structures including the four-state model described in detail in the previous section, dynamics were evaluated using a spatial model of the nanodomain. The 2D model was discretized at a resolution of 10 nm, with RyRs being arranged in a regular lattice with spacing 30 nm (i.e., each RyR of size 30 nm occupies a 3 × 3 grid at dx = 10 nm; **Figure 4A**). Dynamics were evaluated using different numbers of RyRs in the dyad. Whereas Ca^{2+} could diffuse within the dyadic space, the rapid equilibrium approximation was generally implemented in order to improve computational efficiency, a far more pressing constraint in 1999 than presently.

In Louch et al. (2010) a 3D cylinder model of the dyad was employed to assess the causes of dyssynchronous Ca^{2+} release in heart failure. The model was combined with AP recordings from control and heart failure myocytes. They observed that whereas AP prolongation reduces the driving force for Ca^{2+} entry through the LTCCs, this is balanced by the increase in RyR sensitivity which results from steady-state increased SR-Ca^{2+}. Thus, they conclude that other factors (such as T-system disruption, see section "Modelling variability in sub-cellular structure and function") underlie the loss of spatial synchrony in the CaT.

A detailed 3D model of multiple structures surrounding a dyad, reconstructed from electron tomograms of a mouse ventricular myocyte, was presented by Hake et al. (2012).

Whereas not focusing on RyR distribution, the model included a substantial level of detail in the structures of the junctional SR (which was split into three parts of the back, release, and rim locations) and local T-tubules. The model implemented a phenomenological description of RyR gating as well as local buffers (including CASQ) and fluxes (including SERCA and NCX), and revealed the substantial gradients in local Ca^{2+} in the cytosol which emphasized the importance of the location of SERCA and its role in facilitating long-lasting Ca^{2+} sparks.

Walker et al. (2014) developed a 3D model of the dyad, junctional SR and TT based on the previous work of Sobie et al. (2002) and Williams et al. (2011). Whereas Ca^{2+} could diffuse in 3D, the RyRs were arranged on a 2D pancake (**Figure 4A**). Similar to the Stern et al. (1999) model, the spatial resolution was ∼10 nm with minimum RyR-spacing of ∼30 nm; RyRs were arranged on this regular lattice but now in irregular patterns. This study demonstrated the importance of specific RyR arrangement – not just total number – on Ca^{2+} spark dynamics and therefore highlighted the importance of Ca^{2+} diffusion within the dyad.

A similar model was also presented in Cannell et al. (2013) and Laver et al. (2013), which included a network SR with SERCA and its associated intracellular uptake flux. The RyR model was specifically fit to Ca^{2+} concentrations corresponding to CICR and thus not suitable for quiescent/spontaneous spark analysis. These models supported the mechanism of induction-decay for Ca^{2+}-spark termination, described mathematically by Hinch (2004) and referring to the mechanism by which reduced release flux as the SR depletes results in increased closed-times of adjacent RyRs and thus an increase in the probability of spontaneous spark termination, as a direct consequence of the steep relationship between local Ca^{2+} and the closed-to-open transition rate for the RyRs. This work also demonstrated that other more complex mechanisms (such as inactivation of the RyRs, discussed earlier) were not necessary to explain experimental observations, although they do state that they likely still play a role facilitating multiple points of control.

In Sheard et al. (2019) a 2D model was presented based directly on super-resolution imaging data. The model was also discretized at a resolution of 10 nm with minimum RyR-spacing of 30 nm. In this case, RyR positions were not arranged in a lattice, but were freely placed, directly determined by experimental images of multiple dyads in both control and right-ventricular heart failure (RV-HF) conditions (**Figure 4**). This model also included differentiation between non-phosphorylated and phosphorylated RyRs (modeled as a simple increase in sensitivity to Ca^{2+}), and results support the conclusions of both Cannell et al. (2013) and Walker et al. (2014) regarding the importance of both number and specific arrangement of RyRs for triggered Ca^{2+} spark dynamics and fidelity. Mesa et al. (2021) also investigated the functional impact of selected phosphorylated RyRs within a cluster, indicating that they can play a compensatory role in recovering healthy spark dynamics which had been lost through cluster disruption. Iaparov et al. (2021) developed a 2D model which included further possibilities for RyR arrangement and spacing (including both approaches outlined above), number, and dyad extent. They found that Ca^{2+} spark occurrence varied with the spatial arrangement, but did not consistently correlate with total RyR number, the magnitude of Ca^{2+} current or the surface density. This model included allosteric interactions and the authors found RyR coupling strength to be a major factor underlying sparks.

Challenges and Future Directions; Importance of Spatial Ca^{2+} Coupling

As the experimental structural data improves in resolution and quality it will become more feasible and important to develop models based directly on these data, requiring semi-automated image processing pipelines to produce these geometries in both 2D and 3D. This will enable the models to be applied to more specific conditions including disease states, with many pathologies producing complex and heterogeneous subcellular remodeling. However, there are still numerous challenges in regards to model validation of Ca^{2+} spark spatio-temporal functional properties. Because of the difficulty in measuring Ca^{2+} function and underlying sub-cellular structure simultaneously, computational modeling can be useful to help fill in the gaps to relate structure to function, but for the same reasons, challenging to directly validate. It is worth highlighting that the models of single nanodomains do not reproduce well experimentally measured values for the full width half maximum (FWHM) of Ca^{2+}, generally resulting in values of ∼1 μm which are below the 1.8–2.2 μm in experiment. Hoang-Trong et al. (2021) for example did simulate a realistic feature of 1.85 μm, but this required using a large RyR cluster combined with two smaller satellite clusters. However, due to spatio-temporal limits on the resolution of functional imaging experiments, sparks smaller than given sizes are not detected experimentally with any given accuracy. This generates an arbitrary experiment-dependent cut-off that affects the spark distribution and thus makes comparisons between simulation and experiment non-trivial.

A potential limitation of these models is the high spatial-resolution (and thus small voxel/element volumes) required to model RyR distribution: whereas this does not pose a problem during CICR, in which local Ca^{2+} concentration is relatively large, it does pose a problem at resting/quiescent Ca^{2+} levels, where the low Ca^{2+}concentration of ∼0.1 μM in small volumes of 10^{-21}–10^{-18}L (Scriven et al., 2013) corresponds to the presence of countable numbers of Ca^{2+} ions (i.e., ion distribution is discrete and the notion of a well-defined concentration is debatable); similar considerations may also apply in the junctional SR during CICR when its Ca^{2+} load has been depleted (Hake et al., 2012; Cannell et al., 2013). Continuous approximations may therefore no longer be valid, and simulations of spontaneous Ca^{2+}-sparks, in particular, may be non-trivial to implement and analyze. Hybrid schemes which implement spatial stochastic methods to capture the trajectories of individual particles, such as presented in skeletal muscle simulations implementing the Mcell framework (Kerr et al., 2008; Holash and MacIntosh, 2019), may offer solutions to this challenge.

These spatial nanodomain models have demonstrated the importance of specific RyR arrangement – and not just the total number – in determining Ca^{2+} spark dynamics. This presents a challenge for the translation to whole-cell modeling, as it is not feasible to simulate ~20,000 spatially distributed dyads in a whole cell at resolutions of ~10 nm, even if this high resolution is only adaptively applied in the local dyadic space. Therefore, in order to understand how a heterogeneous system of dyads with different RyR numbers and spatial arrangements coordinates in a whole-cell, coarse-graining methods will need to be developed which capture the features of this dyad heterogeneity at a reduced computational cost.

SPATIAL MODELS OF THE WHOLE CARDIOMYOCYTE

Spatial models of the cardiomyocyte describe the cell as a 2D area / 3D volume throughout which dyads are distributed and within which Ca^{2+} can diffuse in both the cytosolic and SR spaces. It is useful now to bring in the terminology of a Ca^{2+}-release-unit (CRU). Whereas some studies use this to refer to the dyad or individual RyRs, cellular-scale modeling studies commonly refer to all of the intracellular and SR compartments associated with a single dyad as a CRU, i.e., it can be thought of as the entire volume of cell surrounding each dyad. Typically, this will contain the network SR (NSR), bulk cytoplasmic space (cyto), and the restricted volume of the dyad (treated as a common-pool). It is also common to include a distinct junctional SR compartment (JSR), as well as other optional sub-spaces, such as the sub-sarcolemma volume just below the surface or T-system membrane, included in order to preserve the higher local Ca^{2+} concentration close to a dyad in regions where the membrane fluxes are located. A major focus of this section is to discuss the various approaches to modeling sub-cellular structure in regards to spatial Ca^{2+} coupling.

Fundamental Model Equations of Ca^{2+} Transport and Homeostasis

Calcium homeostasis in the compartments is described by:

$$\frac{d[Ca^{2+}]_{cyto}}{dt} = \beta_{cyto}\left(\mathbf{D}\nabla^2[Ca^{2+}]_{cyto} + \phi_{cyto} + \left(v_{ss}/v_{cyto}\right)J_{ss}\right) \tag{24}$$

$$\frac{d[Ca^{2+}]_{SS}}{dt} = \beta_{SS}\left(\mathbf{D}\nabla^2[Ca^{2+}]_{SS} + \phi_{SS} - J_{ss} + \left(v_{ds}/v_{ss}\right)J_{ds}\right) \tag{25}$$

$$\frac{d[Ca^{2+}]_{nSR}}{dt} = \beta_{nSR}\left(\mathbf{D}\nabla^2[Ca^{2+}]_{nSR} + \phi_{nSR} - \left(v_{jsr}/v_{nsr}\right)J_{jSR}\right) \tag{26}$$

$$\frac{d\left[Ca^{2+}\right]_{ds}}{dt} = \mathbf{D}\nabla^2[Ca^{2+}]_{ds} + \phi_{ds} - J_{ds} \tag{27}$$

$$\frac{d\left[Ca^{2+}\right]_{JSR}}{dt} = \beta_{jSR}\left(\phi_{JSR} + J_{jSR}\right) \tag{28}$$

Transfer between compartments is given by:

$$J_{ss} = \left(\left[Ca^{2+}\right]_{SS} - \left[Ca^{2+}\right]_{cyto}\right)\tau_{ss}^{-1} \tag{29}$$

$$J_{ds} = \left(\left[Ca^{2+}\right]_{ds} - \left[Ca^{2+}\right]_{SS}\right)\tau_{ds}^{-1} \tag{30}$$

$$J_{jSR} = \left(\left[Ca^{2+}\right]_{nSR} - \left[Ca^{2+}\right]_{jSR}\right)\tau_{jSR}^{-1} \tag{31}$$

And the general form for the reaction terms are:

$$\phi_{cyto} = J_{NaCa} + J_{pCa} + J_{Cab} - \left(J_{up} - J_{leak}\right) - J_{trpn} \tag{32}$$

$$\phi_{nSR} = \left(J_{up} - J_{leak}\right)\left(v_i/v_{nsr}\right) \tag{33}$$

$$\phi_{ss} = J_{NaCa\_SS} + J_{pCa\_SS} + J_{Cab\_SS} \tag{34}$$

$$\phi_{ds} = J_{rel} + J_{CaL} \tag{35}$$

$$\phi_{JSR} = -J_{rel}\left(v_{ds}/v_{jSR}\right) \tag{36}$$

Where *cyto*, *SS*, *nSR*, *ds*, and *JSR* refer to the Ca^{2+} concentrations in each of the (sometimes optional) compartments, β refers to the instantaneous buffering term, ϕ refers to a general reaction term in each compartment, J_x refers to transfer flux between compartments, ∇^2 is the spatial Laplacian operator in 2D or 3D, describing coupling between CRUs, D is the diffusion constant, v refers to the volumes of the compartments, and τ to the time constants of diffusion. The concentration in the dyadic space can be described by a quasi-steady-state approximation, motivated by the rapid equilibration of Ca^{2+} in this small volume. By setting:

$$\frac{d\left[Ca^{2+}\right]_{ds}}{dt} = 0 \tag{37}$$

An approximation for equation (27) can be obtained as in Hinch (2004):

$$\left[Ca^{2+}\right]_{ds} = \left[Ca^{2+}\right]_{SS} + \frac{\tau_{ds}.\left(k_{rel}.\left[Ca^{2+}\right]_{jSR} + J_{CaL}\right)}{\left(1 + \tau_{ds}.k_{rel}\right)} \tag{38}$$

Where k_{rel} is defined by $J_{rel} = k_{rel}(Ca_{SR}\text{-}Ca_{ds})$ and therefore corresponds to:

$$k_{rel} = n_{RyR\_O} \cdot g_{RyR}.v_{ds}^{-1} \tag{39}$$

Where g_{RyR} is the conductance of a single RyR channel and n_{RyR_O} is the number of open RyRs in the dyad (corresponding to states O or O+O*, dependant on the RyR model implemented). This approximation enables less constraint on the time-step for the simulation, allowing faster simulations to be performed. A limitation of this approximation is that the introduction of this type of equation leads to a lack of ionic Ca^{2+} conservation in the models; similar issues arise with the implementation of the rapid buffering approximations [β terms in equations (24) – (28)]. Models that try to analyze homeostatic properties require that the computing algorithm conserves ions at all orders (Conesa et al., 2020).

Ca^{2+}-Voltage Coupling; Incorporation With an Action Potential Model

In general, it is only the Ca^{2+} concentrations and Ca^{2+}-handling channels which are described spatially, with the membrane voltage (V_m) and other ion-currents/concentrations assumed to be homogeneous throughout the cell. This is justified by the fast diffusion of V_m along the cell membrane, indicating that it is valid to assume all channels "see" the same global voltage, at least, in the time-frames considered by the models; moreover, the Debye length in cardiac cells is approximately 1 nm (Mori et al., 2008). Detailed electro-diffusion models, such as implemented in simulations of neurons (Pods et al., 2013), are therefore not generally used or required for cardiomyocytes. The spatial description of the Ca^{2+} handling system can simply replace the equivalent components of common-pool models and can therefore be integrated with either simplified descriptions of the AP (such as assuming it follows a simple, analytical form) or biophysically detailed models of the primary ion currents and global ionic concentrations.

The Ca^{2+} and voltage systems are coupled through the influence of V_m on the activity of the LTCCs and NCX (and any other voltage-dependent Ca^{2+} channel), and feedback of Ca^{2+} into the voltage is captured if a biophysically detailed model of the AP is included, wherein I_{CaL} and I_{NaCa} directly influence V_m. Thus, the interaction between global voltage and local Ca^{2+} dynamics can be described in these models, enabling study of the mechanisms of, for example, Ca^{2+}-induced AP duration (APD) alternans and afterdepolarizations (Eisner et al., 2009, 2017; Qu et al., 2014).

Whereas explicit diffusion of V_m along the membrane of a single-cell has generally not been included in the described models, this has been simulated in models presented by Crocini et al. (2014) and Scardigli et al. (2018). These studies simulated the impact of disruption of the T-system in disease on the ability of the AP to propagate along the T-system into the interior of the cell, indicating that AP propagation failure can directly contribute to a loss of intracellular Ca^{2+} synchronization.

Model Discretization

Numerical solutions to the spatio-temporal reaction-diffusion equations above require the cell to be described in a discretized space. Models can be broadly categorized as being one of two approaches (**Figure 5A**):

(1) "**CRU-grid**" or "**compartmentalized**" models, wherein the spatial resolution is ~ 1 μm × 1 μm × 2 μm and each pixel/voxel corresponds to a single CRU;
(2) "**Sub-micron**" or "**free-diffusion**" models, wherein the volumes of the SR and cytoplasm, and SS if present, are discretized *within* each CRU.

Details of each approach are described below. In general, the CRU-grid approach is more computationally efficient and consequently suitable for statistical simulations and high-throughput, population-cohort models of spatial structure and heterogeneity. Its simplified structure also facilitates the dissection of the mechanisms by which various components contribute to macroscopic function. The advantages of the sub-micron approach are that one can more precisely control aspects such as heterogeneous inter-dyad spacing and co-localization of different channels, they have a more accurate recapitulation of Ca^{2+} diffusion and cellular geometry, and are better suited to direct incorporation of experimental imaging data.

Ca^{2+}-Release-Unit-Grid Models

In these models, each voxel contains all of the compartments contained within a CRU. Spatial coupling is described using the isotropic finite-difference method (FDM), or approximations thereof. Each CRU is coupled to its four or six nearest-neighbors (for 2D or 3D, respectively) along the principal axes:

$$\mathbf{D}\nabla^2[Ca^{2+}]_{c=cyto,nSR,(SS)}$$
$$\approx \frac{\beta D}{{}^{e_i}dx^2}\sum_{i=1}^{i=3}\left({}^{e_i+1}[Ca^{2+}]_c + {}^{e_i-1}\,[Ca^{2+}]_c - 2^{e_i}[Ca^{2+}]_c\right) \quad (40)$$

Where e_i refers to the three dimensions (x,y,z), the subscript c refers to any compartment which is spatially coupled (i.e., the bulk cyto and NSR spaces and any coupled sub-space), D is the diffusion coefficient and dx is the spatial step (i.e., the resolution). The diffusion term (D/dx^2) is often approximated with a time-constant of diffusion between spatially coupled compartments ($\tau_{c,ei}$):

$$\mathbf{D}\nabla^2[Ca^{2+}]_c \approx J_{Ca\_diff\_c}$$
$$= \sum_{i=1}^{i=3}\left(\frac{{}^{e_i+1}[Ca^{2+}]_c + {}^{e_i-1}\,[Ca^{2+}]_c - 2^{e_i}[Ca^{2+}]_c}{\tau_{c,e_i}}\right) \quad (41)$$

Note that whereas these approximations are derived from the isotropic FDM, the models are often discretized at a larger resolution in the longitudinal direction than the transverse, reflecting the larger spacing of dyads along the cell compared to along a TT. Thus, dx^2 in equation (40) or τ in equation (41) can be larger in the longitudinal (z) direction compared to the transverse. This therefore introduces an anisotropy (preferential propagation along the transverse direction) despite the model equations being derived from isotropic approximations.

Sub-Micron Models

In these models, each CRU is further discretized into voxels or elements. Not every voxel necessarily contains all compartments. For example, nanodomains/jSR will only be present in a small subset of voxels, and in some models, the T-system or even nSR may also only be present in a subset of voxels. Spatial coupling is solved using FDM [equation (40)] on regular structured grids or using the more complex finite element method (FEM) on structured or unstructured meshes. They can be discretized at different choices of resolution, generally between 0.05 and 0.2 μm

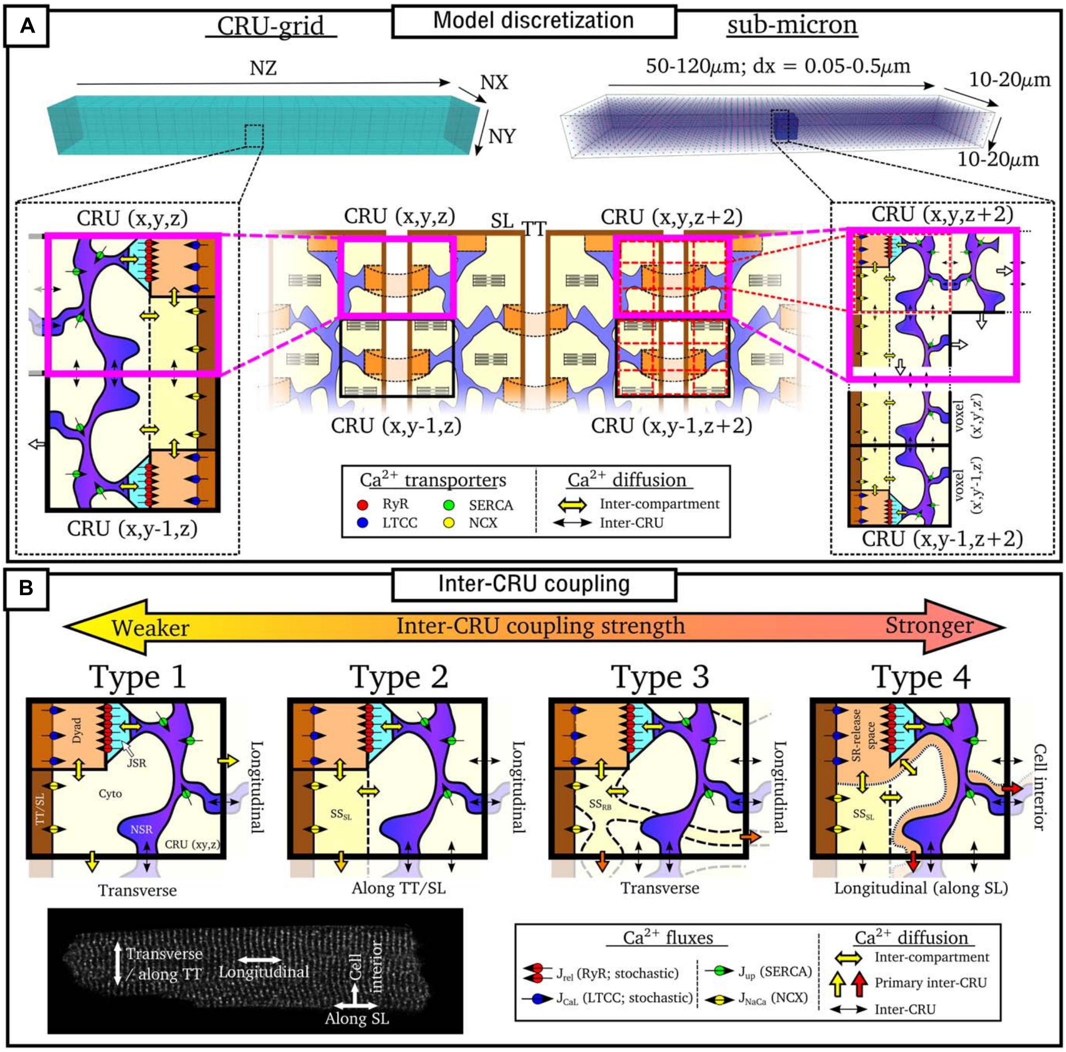

FIGURE 5 | Discretization and CRU coupling of whole-cell models of spatial Ca^{2+} handling. **(A)** Illustration of the CRU-grid and sub-micron approaches to model discretisation. Top panels illustrate the whole-cell whereas bottom panels demonstrate the discretisation of the cell into either CRUs or sub-CRU voxels. **(B)** Illustration of different model structures for inter-CRU coupling. The primary pathway of CRU coupling in the intracellular space is shown by the colored-block arrows. Note that within the cell, coupling is symmetric in the ±-axes directions; a single direction only is shown for the purpose of clarity. Cell image for illustration provided by Dr. Izzy Jayasinghe, The University of Sheffield.

(Nivala et al., 2012a, 2015; Colman et al., 2017b; Marchena and Echebarria, 2018, 2020; Hoang-Trong et al., 2021), although there are other intermediary approaches, such as Sutanto et al. (2018) which uses the CRU-grid approach in the transverse direction but is discretized at half-CRU distance in the longitudinal direction.

Model Compartment Structure: Inter-Ca^{2+}-Release-Unit Coupling

In addition to model discretization, there are important differences in underlying model structure, notably regarding the mechanisms of inter-CRU coupling. Different structures of inter-CRU coupling lead to variable strengths of spatial Ca^{2+} coupling, in part due to the variable peak Ca^{2+} concentrations in the compartments selected for coupling: compartments which have a smaller volume and are more directly coupled to the dyad exhibit larger CaTs and thus stronger inter-CRU coupling compared to larger compartments which are less directly coupled to the dyad. In this context, coupling strength refers only to the intracellular space, not the SR, the spatial coupling of which is independently controlled. Broadly, there can be considered four different structures which the models follow (**Figure 5B** and **Table 1**):

Type 1

The simplest model structure comprises of the four compartments of the bulk cytoplasm and dyadic space and network and junctional SR. The bulk cytoplasm and network SR spaces are the only ones which are spatially coupled throughout the cell. These models contain the weakest coupling due to

TABLE 1 | Summary of properties of whole-cell models of spatio-temporal Ca^{2+} handling.

Publication	CRU-coupling	Discretisation	T-system	Celltype
Alvarez-Lacalle et al., 2015	Type 2	CRU-grid	Full	Ventricle
Colman, 2019	Type 3	CRU-grid	Full	Generic
Colman et al., 2016	Type 3	CRU-grid	Variable	Atria
Colman et al., 2017a	Type 3	CRU-grid	Full	Ventricle
Colman et al., 2017b	Type 3	Sub-micron	Realistic	Ventricle
Conesa et al., 2020	Type 2	CRU-grid	Full	Ventricle
Gaur and Rudy, 2011	Type 4	CRU-grid	Full	Ventricle
Hoang-Trong et al., 2021	Type 1	Sub-micron	Detailed	Ventricle
Greene and Shiferaw, 2021	Type 2	CRU-grid	Variable	Atria
Marchena and Echebarria, 2018, 2020	Type 1	Sub-micron	Variable	Atria
Nivala et al., 2015	Type 1	Sub-micron	Variable	Ventricle
Nivala et al., 2012a,b	Type 1	Sub-micron	Full	Ventricle
Restrepo et al., 2008	Type 2	CRU-grid	Full	Ventricle
Sato et al., 2016	Type 2	CRU-grid	Full	Ventricle
Shiferaw et al., 2017, 2018, 2020	Type 2	CRU-grid	Variable	Atria
Singh et al., 2017	Type 2	CRU-grid	Variable	Ventricle
Song et al., 2015, 2016, 2017	Type 2	CRU-grid	Full	Ventricle
Song et al., 2018	Type 2	CRU-grid	Variable	Generic/Ventricle
Song et al., 2019	Type 2	CRU-grid	Variable	Ventricle
Sutanto et al., 2018	Type 4	Hybrid	Variable	Atria
Vagos et al., 2020, 2021	Type 4	CRU-grid	None	Atria
Voigt et al., 2014	Type 4	CRU-grid	None	Atria
Williams et al., 2011	Type 1	CRU-grid	Full	Generic/Ventricle

the coupling of bulk cytoplasm only, which contains Ca^{2+} concentrations of the same order of magnitude as the whole-cell average. Models using this include Nivala et al. (2012a,b, 2015).

Type 2

Many models also include a sub-sarcolemmal subspace from/into which the other membrane fluxes (NCX and the plasmalemmal Ca^{2+} pump) act. This subspace has a smaller volume and higher Ca^{2+} concentrations at peak than the bulk cytoplasm. This sub-space is generally coupled between CRUs in the transverse direction only, i.e., along the TTs. Longitudinal coupling of this sub-space may be present where ATs are modeled, but does not by default occur for every CRU throughout the cell. Coupling strength is higher than the simplest type 1 models due to the larger CaT in this sub-space. Models of this type include Song et al. (2015, 2016, 2018).

Type 3

Other models implement a sub-space which couples CRUs in both transverse and longitudinal directions independently of the presence or absence of T-system/SL. Introduced in Colman et al. (2017a,b) and Colman (2019), this sub-space contains fewer buffers and represents potential pathways between dyads around the intracellular buffers. Given the reduced buffering (higher CaT peaks) and coupling in all directions, these models have stronger inter-CRU coupling than those which contain a sub-sarcolemmal subspace only.

Type 4

Finally, other models have more direct inter-CRU coupling between dyads, or SR-release spaces (Gaur and Rudy, 2011; Voigt et al., 2014; Sutanto et al., 2018; Vagos et al., 2020). Due to this direct spatial coupling of the compartment into which release occurs, these models have the strongest spatial coupling.

This classification is simplified, but captures the major features of the various approaches. For example, the Heijman-lab models (type 4) were originally designed to represent atrial cells with no T-system: interior compartments did not contain the SL fluxes or associated sub-space. However, models of type 1–3 can be generalized to match this structure by removing these same SL fluxes and associated sub-space (where present) from interior CRUs, e.g., as in Colman et al. (2016), Shiferaw et al. (2017), Song et al. (2018), and Marchena and Echebarria (2020). Similarly, the Heijman-lab models can also be generalized to incorporate a T-system by the inclusion of the SL fluxes and sub-space in interior CRUs, e.g., as was performed in Sutanto et al. (2018). Thus, the above types represent four fundamentally different approaches to inter-CRU coupling, and can be generalized to any cell structure, containing, for example, full, no, or variable T-system density (see next section "Modeling variability in sub-cellular structure and function").

Implications of Model Structures

One major feature of the differences between these models is the relationship between RyR sensitivity, inter-CRU coupling strength and the size of the CaT in normal pacing, which has significant implications for the robustness of inter-CRU Ca^{2+} propagation. Broadly, models with weaker inter-CRU Ca^{2+} coupling (type 1–2 above) tend to contain either a physiologically sized CaT and operate at the threshold of Ca^{2+} propagation, or contain a substantially larger CaT ($>$2–8 μM) with more robust Ca^{2+} propagation (Nivala et al., 2015; Song et al., 2015; Marchena and Echebarria, 2020). Alternatively, widespread initiation of CICR (reflecting an extensive T-system bringing LTCC close to RyR throughout the cardiomyocyte) contributes to robust, synchronized Ca^{2+} release in some of these models. Models with stronger inter-CRU coupling (type 3–4 above) tend to contain more robust Ca^{2+} propagation while maintaining physiologically sized CaTs (i.e., below 1 μM), as in Voigt et al. (2014), Colman et al. (2017a), Colman (2019), and Vagos et al. (2020). Such robust propagation is particularly relevant when simulating cells without an extensive T-system that rely more heavily on fire-diffuse-fire mechanisms for Ca^{2+}-wave propagation, such as in the atria. The implications of these differences are far-reaching: Ca^{2+} propagation is relevant for graded release of CICR, the dynamics of CaT alternans, success or failure of triggered Ca^{2+} wave propagation into regions without T-system, and the dynamics of spontaneous Ca^{2+} sparks and waves.

These features and limitations, generally discussed openly in the original papers, do not detract from the ambitions of the various studies nor question their analyses, as model choices are motivated by the focus of the specific study. It is important to note that all approaches are capable of reproducing all of the phenomena described above, including properties such as the statistics of SCRE and dynamics of alternans, although various model parameters are likely to be substantially different in order to reproduce these same macroscopic features. Nevertheless, it is still important to carefully consider the motivations of the study for model selection. As an oversimplified example, if the ambition is to study Ca^{2+}-voltage interactions during SCRE or alternans, it may be best to prioritize CaT magnitude (as this will determine the degree of Ca^{2+}-induced inactivation of I_{CaL} and the magnitude of I_{NCX} which feedback into the voltage) and use a more "functional" description of inter-CRU coupling (types 3–4) in order to maintain robust Ca^{2+} propagation. However, if the focus of the study is on the mechanisms and implications of inter-CRU coupling then the simpler and (potentially) more physiologically justified inter-CRU coupling structures (types 1–2) may be prioritized. These considerations may be particularly relevant for the development of atrial cell models and those with variable T-system density, and will be discussed in this context in more detail in the next section.

These disparities and compromises indicate that there are fundamental properties of the CaT and inter-CRU coupling which we do not fully understand, and these gaps in our understanding and model differences reflect the large degree of uncertainty in the experimental data on which the models are based. There is an important possibility that different internal structures need different behavior at the dyadic level since weaker coupling generally requires stronger transients to reproduce wave-like propagation. This might lead to important model-dependent conclusions on new research issues. As models become more sophisticated, getting closer to genuine cell- and species- specificity (indeed as more data become available), and are applied in more complex and clinically oriented studies, it will become imperative to solve these issues and develop models which include fully physiologically justified descriptions of RyRs and spatial Ca^{2+} coupling. Further to this, it is these authors' opinion that future studies would do well to implement multiple, disparate models in order to navigate the limitation of model-dependent conclusions.

MODELING VARIABILITY IN SUB-CELLULAR STRUCTURE AND FUNCTION

Cardiomyocytes demonstrate a large degree of inter-cellular, inter-subject and inter-species heterogeneity in properties such as ion-channel expression and sub-cellular structure, and recent studies have highlighted the importance of including such variabilities in, for example, predictive models of pharmacology (Muszkiewicz et al., 2016; Passini et al., 2017). This section will describe how heterogeneity in sub-cellular structure can be captured using models of spatial Ca^{2+} cycling.

T-System Variability: Models of Atrial and Remodeled Ventricular Myocytes

The structure and density of the T-system is one of the most important factors which determines sub-cellular dynamics. In healthy ventricular myocytes the T-system is generally robust and dense throughout the volume of the cell. However, in atrial myocytes and diseased ventricular myocytes the T-system can be substantially sparser and more variable (Lyon et al., 2009; Richards et al., 2011; Gadeberg et al., 2016; Singh et al., 2017). This reduction in T-system density is generally correlated with alterations to the CaT (primarily, a prolonged time-to-peak, reduced spatial synchronization, and often a small, sometimes large, reduction in magnitude) and possibly linked to an increased vulnerability to pro-arrhythmic dynamics (Trafford et al., 2013; Gadeberg et al., 2016; Shiferaw et al., 2017, 2018). In these conditions, triggered Ca^{2+} sparks will occur only in regions of the cell where LTCCs are closely coupled to RyRs [although even these regions may not exhibit triggered sparks if the AP fails to reach them (Crocini et al., 2014)]. Ca^{2+} may then propagate into regions without the T-system, i.e., where orphaned RyRs are found without coupling to the LTCCs, through spark-induced-spark triggered Ca^{2+} waves, resulting in "u" or "w" shaped linescan images (**Figure 6**). However, Ca^{2+} may also fail to propagate as a triggered wave, leading to regions of the cell which do not undergo substantial Ca^{2+}-release which consequently underlies a substantially smaller whole-cell CaT. The conditions which either enable or inhibit triggered Ca^{2+}-wave propagation, which may be species-, cell-, disease-, and environment-dependent, are unclear from experimental studies alone, and these analyses form the focus of many computational studies which implement variable T-system density and structure.

Implementation of variable T-system structure is relatively straight-forward in these spatial models of Ca^{2+} handling, for both the CRU-grid and sub-micron approaches. The inclusion or omission of a TT or AT from a CRU or voxel/element can be trivially implemented by either the inclusion or omission of the membrane Ca^{2+} fluxes (LTCCs, NCX, Ca^{2+} pump) and any associated sub-sarcolemma sub-space. Thus, one needs only create a map which describes which CRUs or voxels/elements contain a TT or AT. Creation of this map could be through random selection, a T-system generating algorithm, or directly based on experimental imaging data.

Modeling Atrial Cardiomyocytes

Atrial cells exhibit variable T-system density in both control and disease conditions (Richards et al., 2011; Park et al., 2020), and thus computational models of atrial cells tend to either not include the T-system or explicitly model its variability. Koivumäki et al. (2011) developed a simplified, 1D model of the atrial myocyte which captured the propagation of Ca^{2+} waves from the surface to the interior. The deterministic model contained four sub-cellular compartments as a coarse-grained discretisation of the transversal direction of the cell.

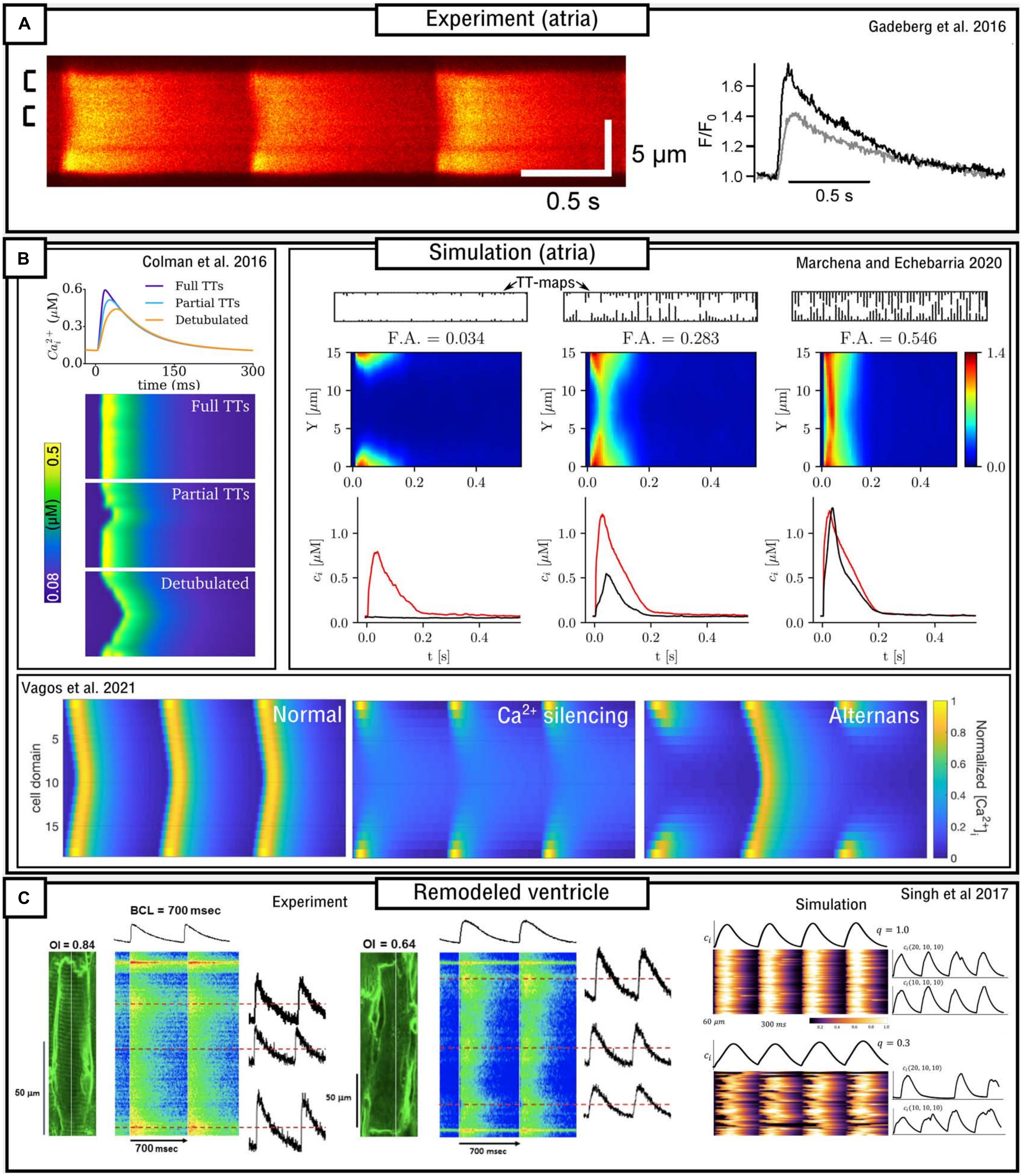

FIGURE 6 | Models of variable T-system density in atrial and remodeled ventricular myocytes. **(A)** Experimental data demonstrating "u" waves in pig atrial myocytes, and the corresponding local CaTs at the surface (black) and interior (gray) of the cell. Data is from Gadeberg et al. (2016). **(B)** Dynamics in different computational models of atrial cells, illustrating recapitulation of "u" waves, dependence on T-system density, and Ca^{2+} silencing and CaT alternans. Data from Colman et al. (2016); Marchena and Echebarria (2020), and Vagos et al. (2021). **(C)** Experimental and simulation data from remodeled ventricular myocytes (Singh et al., 2017), demonstrating a loss of T-system density and associated loss of spatial synchrony of the CaT, in relation to the Organizational index (OI; experiment) and the proportion of CRUs associated with LTCCs (q; simulation).

Colman et al. (2016) implemented an atrial cell model with variable T-system density in a "type 3," 3D CRU-grid model. Variable T-system structure was crudely implemented by removing patches of the T-system of variable and controllable size within the cell, based on randomly generated seeds. This model demonstrated "u" and "w" linescans during normal pacing (**Figure 6**), a delay in the time-to-peak, and a small reduction in the magnitude of the CaT as T-system density decreased. CaT alternans and SCRE were found to increase as T-system density decreased and the specific dynamics were highly controlled by the structure: alternans involved alternating between successful and failed Ca^{2+} propagation into the non-T-system regions, and spontaneous Ca^{2+} waves preferentially emerged from regions without a TT or AT.

The atrial models developed in the Heijman-lab (Voigt et al., 2014; Vagos et al., 2020) contained no T-system by default. These models, of type 4 structure, demonstrate generally robust Ca^{2+} propagation into the cell interior, the mechanisms and sensitivity of which were investigated in detail in Vagos et al. (2020) and further expanded on in Vagos et al. (2021). A mechanism of CaT alternans similar to that described in Colman et al. (2016) was observed (**Figure 6**). Sutanto et al. (2018) expanded the approach by incorporating RyR/LTCC expression/distribution based on experimental imaging data (see later sub-section "Pipelines for image-based modeling"), as well as the inclusion of variable T-system in the interior of the cell, demonstrating the important role of both TTs and ATs in facilitating Ca^{2+} propagation.

In a series of studies which integrated computational modeling with experimental functional measurements of atrial cell dynamics Shiferaw et al. (2017, 2018, 2020) comprehensively investigated the mechanisms and sensitivity of triggered Ca^{2+} wave propagation using a model of heterogeneous T-system density, in combination with other factors such as β-adrenergic stimulation. In brief, these studies demonstrated rate-dependent triggered Ca^{2+} waves emerging in SR-Ca^{2+} overload conditions. It is argued that the emergence and dynamics of triggered Ca^{2+} waves exhibit a highly non-linear dependence on SR-Ca^{2+} load and that this feature of atrial cells contributes to dynamic instabilities which may be pro-arrhythmic.

Marchena and Echebarria (2018, 2020) also developed models of the atrial cell using a type 1 sub-micron approach. A comprehensive analysis of the relationship between the fractional area occupied by the T-system and the magnitude and morphology of the whole-cell CaT was provided (**Figure 6**). These studies indicated that SR-Ca^{2+} load was unaffected by T-system density and that reduced CaTs were a consequence of failure of Ca^{2+}-wave to fully propagate from the cell periphery into the interior; however, Ca^{2+}-release gain was increased in detubulated cells as a consequence of the activation of at least some orphaned RyRs. No significant differences in spontaneous Ca^{2+} spark dynamics were found, indicating that experimental observations of heterogeneous spark dynamics (Hüser et al., 1996; Kirk et al., 2003; Brette et al., 2005) could be explained by different kinetics or regulation of RyRs in membrane and non-membrane regions, not captured in the models. This is consistent with Brandenburg et al. (2016) and Sutanto et al. (2018) which show, in experiment and modeling, that RyR hyperphosphorylation contributed to these regional differences.

Modeling Ventricular Cardiomyocytes With Disease-Related T-System Remodeling

In a combined experimental-computational study, Wagner et al. (2012) characterized the remodeling of sub-cellular structure (T-system properties and other related proteins such as junctophilin) post myocardial-infarction (MI). They observed a progressive, time-dependent post-MI increase in the cross-sectional area of individual T-tubules, a decreased expression of junctophilin, an orphaning of RyR clusters, and uncoupling of CICR. Simulations were performed using the previously presented model of Williams et al. (2011), which implemented the simplest type 1 structure at CRU-grid resolution. Remodeling was incorporated by an increased spacing between TTs and RyRs in a subset of the model's compartments. Simulation results demonstrated that RyR orphaning contributed to post-MI associated AP prolongation, especially when combined with remodeling of NCX and SERCA, as well as reduced SR-Ca^{2+} load and increased Ca^{2+}-leak, potentially contributing toward arrhythmogenic afterdepolarizations. However, the changes to TT cross-sectional area were not captured in this model and require more detailed models, discussed in the later sub-section: "Toward realistic sub-cellular structure."

Nivala et al. (2015) implemented a loss of the T-system representing remodeled ventricular myocytes using a sub-micron, type 1 model. Voxels containing LTCCs (i.e., dyads) were randomly selected for removal of the membrane components. This study demonstrated that disruption of the T-system led to perturbed spatial Ca^{2+} handling (delay in the time-to-peak and slightly reduced magnitude of the CaT) which was more pronounced when combined with remodeling of whole-cell parameters associated with heart failure.

Song et al. (2018) expanded on the work of Nivala et al. (2015) using a type 2 CRU-grid model. In this study, an algorithm was developed to generate more realistic variable T-system structures. Results were largely concurrent with the previous studies, with the major differences that: (1) a more substantial reduction in CaT amplitude was observed in detubulated cells; (2) a biphasic relationship between T-system density and arrhythmogenic dynamics was observed, wherein intermediate densities demonstrate the most instabilities.

Singh et al. (2017) combined experimental measurements and computational modeling to explore the relationship between T-system density and the features of the CaT in a rat ventricular model of the progression of heart failure (**Figure 6C**). Experimental measurements, in agreement with their previous study (Shah et al., 2014), demonstrate that the CaT exhibits a slower upstroke and reduced magnitude associated with substantial loss of the T-system, but Ca^{2+} propagation is not silenced. The computational (type 2) model was in strong agreement with these observations, revealing a non-linear relationship on both distribution of release units and separation between LTCCs and RyRs.

Model Parameterization

Differences in the dynamics and sensitivity of triggered wave propagation observed in the models can be largely related to the underlying model structure (type 1–4 as described in the previous section). The development of models of atrial myocytes presents a major challenge in this context, i.e., in obtaining robust triggered Ca^{2+} wave propagation with physiologically sized CaTs but without an over-propensity for spontaneous activity. In the Colman-lab and Heijman-lab models, stronger inter-CRU coupling (type 3–4) was implemented for this purpose, as it facilitated triggered Ca^{2+} wave propagation with physiologically sized CaTs. Without this strong inter-CRU coupling, it was not possible to reproduce stable Ca^{2+} homeostasis during regular pacing while maintaining robust Ca^{2+} wave propagation and physiological CaTs without also observing highly arrhythmogenic spontaneous activity – either the spontaneous spark rate or Ca^{2+}-wave rate was too high. Type 3–4 models somewhat solve this through the inclusion of these stronger coupling mechanisms, but also tend to exhibit low spontaneous spark rates and a higher probability for a spark to develop into a full wave. This indicates the possible physiological relevance of stronger coupling (e.g., pathways between buffers and/or along the SR membrane), but this has not been supported with imaging experiments.

It is generally assumed triggered waves should propagate in normal conditions in healthy atrial myocytes, but the validity of this assumption and whether it also translates to remodeled ventricular myocytes is not clear. It is worth noting that different experimental observations cover the range of behavior exhibited by these models, with some experiments observing generally robust triggered Ca^{2+}-wave propagation with "u" or "w" waves and only a small reduction in the magnitude of the CaT in cells with low T-system density (Louch et al., 2010; Trafford et al., 2013; Crocini et al., 2014; Gadeberg et al., 2016; Setterberg et al., 2021), whereas others demonstrate more variability and sensitivity of triggered Ca^{2+} waves in many different pacing conditions, associated with substantially smaller CaTs in detubulated cells in normal pacing conditions (Brette et al., 2005; Shiferaw et al., 2017).

Toward Realistic Sub-Cellular Structure

Modeling Cellular Contraction, Mitochondria and Energetics

Two components of the structure-function relationships governing cardiac cellular electrophysiology which have not yet been discussed in detail are the myofilaments (and related contractile apparatus) and the mitochondria (and associated localized buffering and energetics). Okada et al. (2005) developed a FEM-based model of cellular contraction associated with intracellular Ca^{2+} waves, enabling investigation of the impact of cell shortening on Ca^{2+}-wave velocity. The model also revealed the potential for spiral Ca^{2+} waves which could maintain arrhythmicity. Hatano et al. (2011, 2012) expanded this model to include realistic local mitochondrial Ca^{2+} buffering and ATP production, T-tubules, SR structure, and myofilaments. These models revealed slow changes in the average mitochondrial Ca^{2+} during the cardiac cycle and that asynchronous contraction caused by a large detubulated region can lead to impairment of myocyte contractile efficiency. Recently, Xie et al. (2018), Song et al. (2019), and Pandey et al. (2021) developed CRU-grid spatial models which also explicitly accounted for local buffering and dynamics of the mitochondria. These mitochondria were assigned to alternating CRUs in the transverse direction (but every CRU in the longitudinal direction) and the models were applied to study the role mitochondria may play in proarrhythmogenic dynamics including afterdepolarizations.

Heterogeneous Channel Distribution

Beyond the T-system, the distribution and local density of different Ca^{2+}-handling transporters is also important for governing Ca^{2+} homeostasis through effects on local Ca^{2+}-flux balance. Sub-micron models are ideal for controlling the fine details of channel distribution and co-localization between different channels, but CRU-grid models remain suitable for investigating heterogeneous channel/transporter expression in different regions of the myocyte.

The number of RyRs and LTCCs per dyad, as well as dyad volume, are commonly heterogeneous in the default implementations of many models (assigned by scaling the expression or volume by numbers randomly sampled from a normalized Gaussian or other distribution). These heterogeneous properties have been shown to be important for capturing the features of graded intracellular Ca^{2+}-release (Greenstein and Winslow, 2002; Shiferaw et al., 2003; Restrepo et al., 2008). In principle, heterogeneous expression of any transporter or component (e.g., SERCA, NCX, buffer concentration) could be implemented in the same manner by sampling scale-factors from a defined statistical distribution. However, determining heterogeneous structure based on experimental data and with constraints on the spatial variation/correlation provide more powerful and physiologically relevant approaches.

Pipelines for Image-Based Modeling

In Sutanto et al. (2018) a pipeline was developed which enabled the expression of RyRs and LTCCs (and in principle any desired Ca^{2+}-handling component) observed in experimental imaging studies to be processed to align with the modified CRU-grid model (**Figure 7A**). Thus, RyR or LTCC expression in each dyad was determined by the intensity of immunofluorescence image labeling for each of these channels. The method involved processing the real cellular data so that it could be registered on the idealized cellular geometry of the computational model.

In an alternative approach, a method was presented in Colman et al. (2020) which involved the development of image-analysis techniques to extract parameters describing the spatial correlation and distribution of the channels (**Figure 7A**). This involved calculating the length-scale which describes the distance over which expression is correlated. This parameter can be used to generate Gaussian random fields which produce expression maps with the same spatial correlations, but not limited to the specifics of the imaging data.

The above approaches enable efficient and high-throughput simulations of variable cellular structure to be performed, which

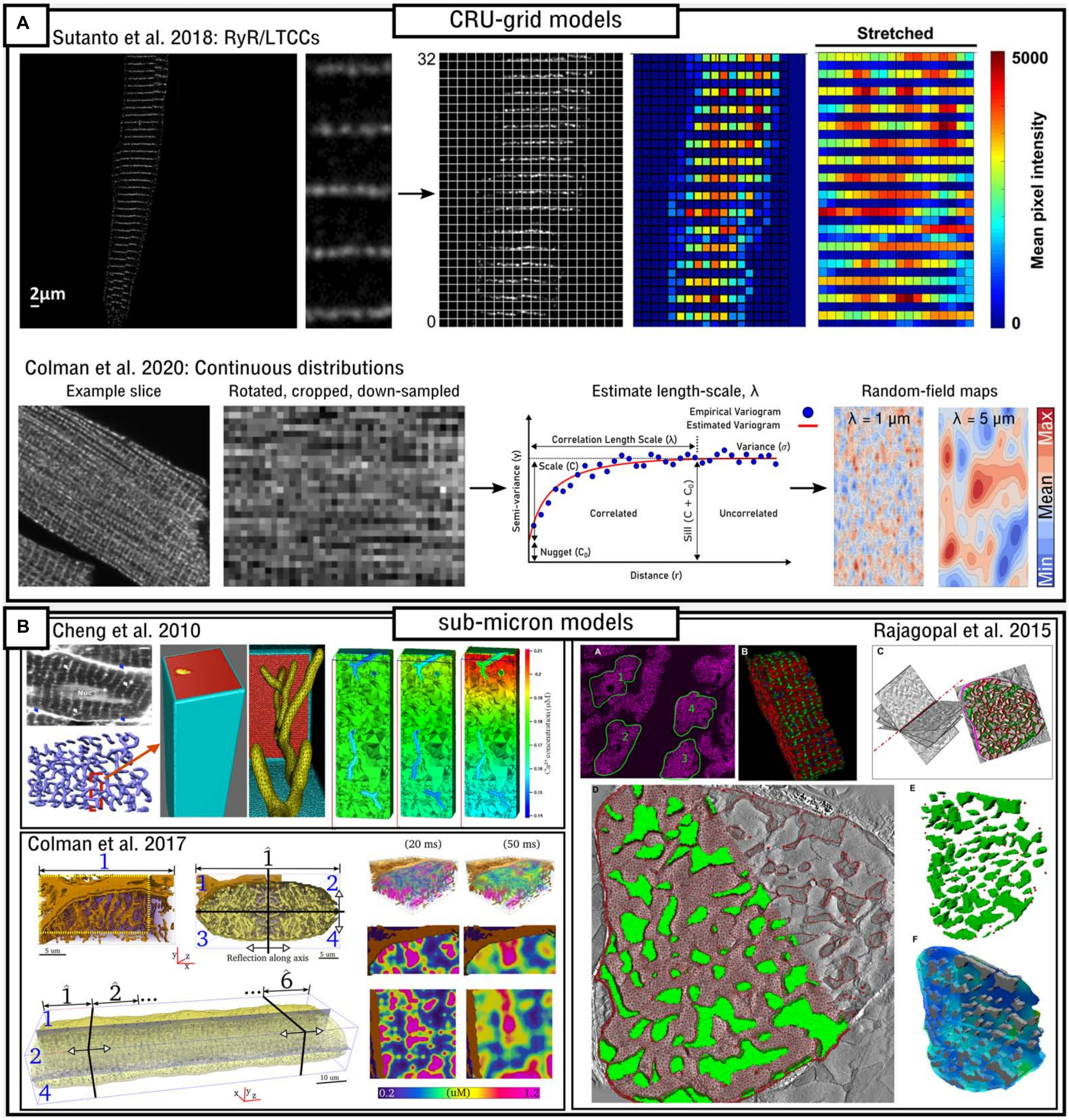

FIGURE 7 | Image-based modeling approaches. **(A)** Approaches for image-based modeling in idealized, CRU-grid cell models. The top panel illustrates the processing of LTCC/RyR image data so that it can be aligned and registered on an idealized grid computational model, as presented in Sutanto et al. (2018). The lower panel illustrates the method of calculating the correlation length-scale (λ) in order to generate Gaussian-random field maps which match these parameters in order to describe sub-cellular heterogeneity, as presented in Colman et al. (2020). **(B)** Approaches for directly incorporating imaging data into realistic, sub-micron cell models. The top-left panel demonstrates processing of ultra-structural data describing T-system structure into a mesh for simulations, and illustrates the large Ca^{2+} gradients that can occur under different flux-distributions, as presented in Cheng et al. (2010). Lower panel illustrates processing of data describing the T-system and SR in a portion of a cell, approaches to tesselate the cell portion into a whole-cell, and the substantial Ca^{2+}-gradients observed in this model also, as presented in Colman et al. (2017b). Right panel illustrates the semi-automated pipeline for segmenting multiple structures, including the myofibrils and mitochondria, into a 3D structurally-detailed representation of a sarcomere, as presented in Rajagopal et al. (2015).

are ideally suited to statistical analysis and the extraction of fundamental mechanisms of homeostasis. However, sub-micron models, which are substantially more computationally intensive, provide more possibilities for the direct inclusion of experimental imaging data. In a series of studies (Cheng et al., 2010; Kekenes-Huskey et al., 2012; Hake et al., 2014) an ultra-structure model of a realistic single TT and its surrounding half-sarcomeres was developed (**Figure 7B**), extending their previous work which implemented an idealistic TT (Lu et al., 2009). The local cellular geometry was reconstructed from light-and electron-microscopy images of a rat ventricular myocyte and the studies investigated the impact of the distribution of Ca^{2+}-flux channels and buffers. They observed substantial and rapid spatial gradients in local Ca^{2+} concentration in the sub-sarcolemmal sub-space (**Figure 7B**) and their analyses demonstrate the importance of accounting for T-system ultra-structure and Ca^{2+} flux distribution. These detailed models present the possibility for features of T-tubule ultrastructural remodeling to be included, such as observed in Wagner et al. (2012) and Crocini et al. (2014), and could also potentially be extended to account for other local ionic concentrations and the counter-ion fluxes relevant for SR-Ca^{2+} release, such as presented in Berti et al. (2017).

In Colman et al. (2017b) a sub-micron, whole-cell model was developed which directly incorporated imaging data describing the structure of the T-system, SR and distribution of the dyads (**Figure 7B**). A semi-automatic pipeline was developed in which the images were processed and down-sampled to create simulation-ready geometries. Whereas only a portion of the cellular geometry was reconstructed, the model was tessellated to construct a whole-cell, exploiting the periodic structure of cardiac myocytes. This model also observed substantial intracellular Ca^{2+} gradients which emerged only in the realistic geometries, in agreement with Cheng et al. (2010). The imaging data was based on electron-microscopy (Pinali et al., 2013) and thus channel distribution was not captured in the data. However, future studies could use advances in correlative light-electron microscopy to integrate T-system and SR structure with immunofluorescence-based protein levels associated with each membrane, enabling the possibility to directly impose local relative channel expression on these structures.

This model also indicated the importance of realistic (and variable) dyad distribution on the specific dynamics of both CaT alternans and SCRE, providing spatial constraints on the randomness of both. These results are further supported by the recent sub-micron, type 1 model of Hoang-Trong et al. (2021) which included experimentally influenced spatial distributions of multiple Ca^{2+}-flux channels, explicit modeling of transverse- and axial-tubules, and Ca^{2+}-CaM interactions. This study highlighted the importance of CRU distribution and the presence of rogue (non-junctional or orphaned) RyRs on Ca^{2+}-spark propagation and wave dynamics. The model was able to reproduce regenerative Ca^{2+} waves at high Ca^{2+}-overload conditions, emerging from the same location on subsequent instances, and the implementation employed several techniques to reduce computational load and memory requirements, enabling efficient implementation of GPU solvers.

Rajagopal et al. (2015, 2018), Ghosh et al. (2018), and Hussain et al. (2018) present a rather different approach and focus to the other whole-cell computational models so-far described, with a higher level of structural detail accounted for **Figure 7B**. The 3D computational model is generated from images of the myofibrils, mitochondria and RyR clusters; Data from different sources and of different resolutions (e.g., 3D electron microscopy and high-contrast confocal) were fused through spatial statistics techniques (Illian et al., 2008; Theakston et al., 2010). These models focus on many more details of the structure of myocytes and their impact on local Ca^{2+} buffering and regulation, including that of the contractile apparatus and mitochondria, and simulations focus more on the upstroke of the CaT than on long-term homeostasis. The methods for processing high resolution imaging data to generate meshes for simulation are the most advanced in the field, and the potential of these models to understand the super-resolution features of channel distribution, co-localization and Ca^{2+} regulation is currently unparalleled. It would be a significant achievement to develop computational models which account for this level of structural detail that are also sufficiently efficient to simulate long-term dynamics, homeostasis, and Ca^{2+}-voltage coupling in a whole-cell.

SIMPLIFIED, MINIMAL, AND TISSUE MODELS

The complexity of the spatio-temporal models described above hinders ease of analysis and extraction of fundamental mechanisms, and also precludes the efficient cellular simulations required to model hundreds, thousands or millions of cells in cardiac tissue, due to the high computational load of these detailed models. Thus, approaches are required to simplify these complex descriptions into easily analyzable systems and/or efficient computational models while preserving the underlying stochastic dynamics and the emergent phenomena therein. Almost 20-years ago, Shiferaw et al. (2003) presented a number of simplifications to describe spatial Ca^{2+} handling which underlie many of the developments since. Various different approaches have been used including those which explicitly model the cell as a spatial structure but with simplified components of Ca^{2+} release and propagation, and those which develop entirely non-spatial descriptions (**Figure 8A**). This section focuses primarily on theoretical and numerical approaches which enable large-scale tissue simulations. Analytical and statistical descriptions have also been presented but are not described in detail here; the reader is referred to Rovetti et al. (2007) and Asfaw et al. (2013), for example, where a mean first-passage-time approach was used to demonstrate how Ca^{2+}-release depends on local properties within microdomains and to quantify measures of how events synchronize in tissue.

Spatial Simplified Models

Williams et al. (2007, 2008) pioneered methods for efficient simulation of stochastic Ca^{2+} dynamics while preserving the importance of local control and features such as graded release. The first study (Williams et al., 2007) developed a probability density approach for modeling local control of CICR and compared results to a Monte-Carlo simulation regarding both validation and computational efficiency. As a simplification based on the "all-or-nothing" response of RyRs within a CRU, the RyRs in each CRU were described as a single "megachannel" i.e., treating them as a single channel which can only occupy a single state at once. Describing this megachannel with a simple two-state model enabled combination with a two-state model of the LTCCs to develop a four-state, minimal model of the state of

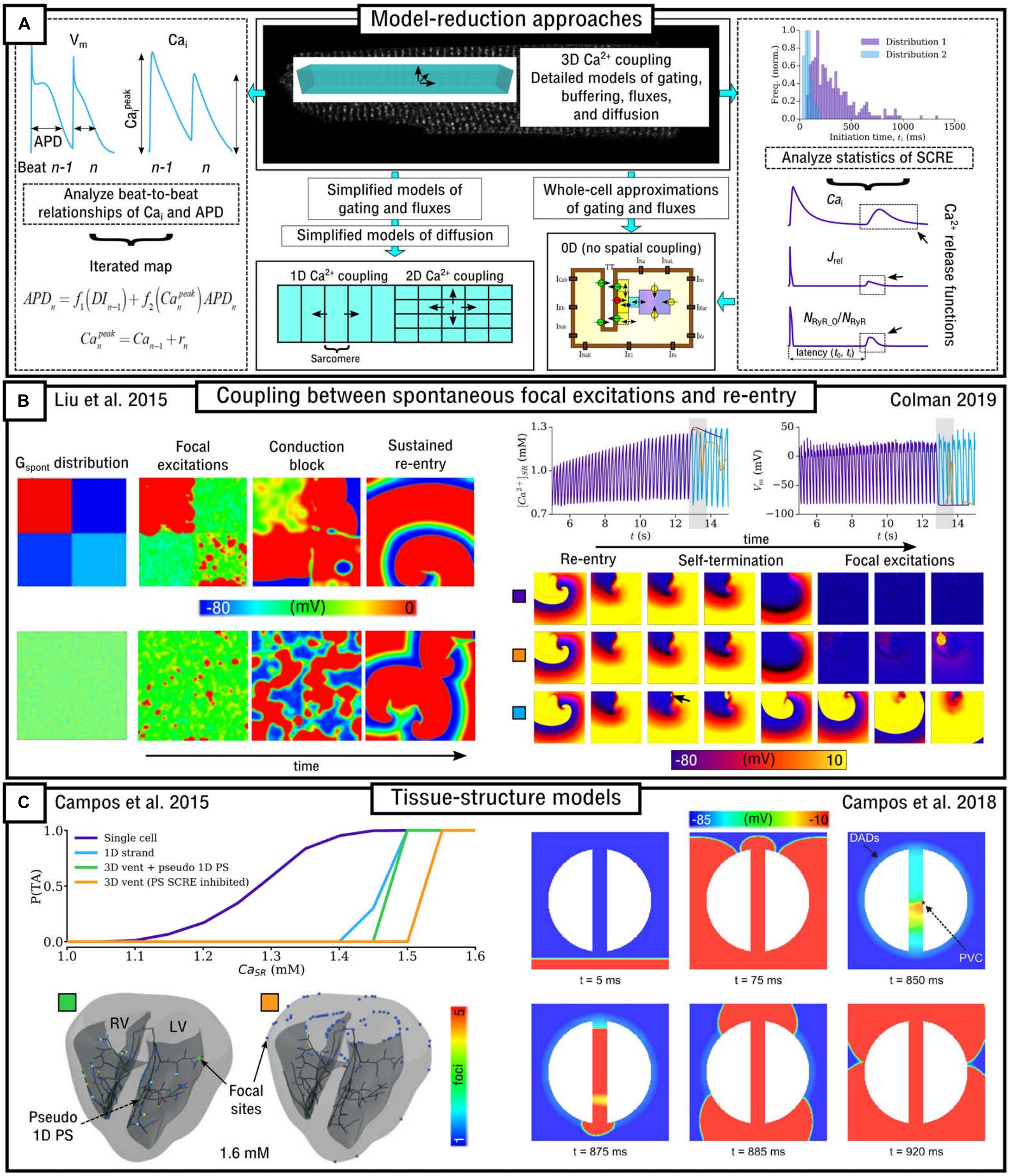

FIGURE 8 | Multi-scale modeling approaches. **(A)** Illustration of different approaches for reducing the computational intensity of models of sub-cellular Ca^{2+} handling. The center, upper panel illustrates a fully detailed 3D cell model, with biophysically detailed descriptions of gating, fluxes and diffusion. Below this panel are illustrated mathematical approaches for model reduction, either resulting in simplified spatial models (left) or non-spatial models (right). The left-most panel indicates how analysis of AP and CaT dynamics on a beat-to-beat basis can lead to the development of a non-spatial, iterated map model. The right-most panel illustrates how analysis of SCRE statistics enables the parameterization of analytical Ca^{2+} release functions which can be imposed in a traditional, non-spatial cell model. **(B)** Illustration of bi-directional coupling between focal excitations and re-entry. Left: spontaneous excitations interact with each-other to cause conduction block and re-entry, modified from Liu et al. (2015). Right: illustration of the emergence of focal excitations following self-termination after a period of re-entry, from Colman (2019). **(C)** Structurally detailed tissue models imeplementing SCRE. Left: probability of SCRE as a function of SR-Ca^{2+} in single-cell and 1D, 2D, and 3D with or without the pseudo-1D Purkinje System (PS), with the locations of focal exictations shown in the lower panel, modified from Campos et al. (2015); right: demonstration of a focal excitation emerging within the isthmus of an infarct borderzone, modified from Campos et al. (2018).

the CRU. The probability density approach was then applied in the limit that the number of CRUs in the myocyte is sufficiently large ($>$5,000, which is less than the ~20,000 observed in cardiomyocytes) by describing the probability that one would find a randomly sampled CRU in a specific state (S), associated with local dyadic Ca^{2+} (Ca$_{ds}$) and Ca$_{\mathrm{SR}}$ concentrations:

$$\rho^i(Ca_{ds}, Ca_{SR}, t)dCa_{ds}dCa_{SR} = \begin{array}{c} \Pr\{Ca_{ds} < \tilde{C}a_{ds}(t) < Ca_{ds} + dCa_{ds} \text{ and} \\ Ca_{SR} < \tilde{C}a_{SR}(t) < Ca_{SR} + dCa_{SR} \text{ and} \\ \tilde{S}(t) = i\} \end{array} \tag{42}$$

Where i is an index that runs over the four CRU states and tildes indicate random quantities. This must satisfy advection-reaction equations in order to make it equivalent to the Monte-Carlo approach. This approximation was combined with a deterministic solution to the bulk concentrations and a high resolution FDM approximation of spatial dynamics. The authors also derived a univariate approximation to the model based on the marginal density of Ca$_{\mathrm{SR}}$ jointly distributed with the CRU state, although the reader is referred to the original publication for further details beyond the scope of this overview. Importantly, they demonstrated that the approximation agreed strongly with the Monte-Carlo approach, which converges to this result so long as it contains a realistically large number of CRUs. The resulting method is ~500 times more computationally efficient than the Monte-Carlo approach.

Subsequently, the approach was generalized to describe situations where the dynamics of Ca$_{ds}$ are much faster than Ca$_{\mathrm{SR}}$ (Williams et al., 2008). The minimal four-state model of the CRU (two states for the RyR megachannel and two for the LTCCs) was expanded to a 12-state model, by extending the two-state RyR model to a six-state model that includes highly cooperative opening and an SR-Ca^{2+} dependence such that depletion of the SR-Ca^{2+} reduces the open probability. The model builds on the univariate approximation presented in the previous study, employing a moment-closure approach truncated at the second-order. The resulting method similarly agrees with the Monte-Carlo approach but with a substantial increase in computational efficiency by a factor of ~10,000.

Chen et al. (2011) developed a simplified spatial model by imposing a number of reductions to a full description of spatial Ca^{2+} handling. The following two-assumptions drove model development: (1) Whereas Ca^{2+}-waves nucleate at some location within the cell and propagate rapidly in the transverse direction, the greater length of the cell compared to its width implies that most Ca^{2+}-wave propagation is approximately planar in the longitudinal direction; and (2) in general during a Ca^{2+}-wave, all CRUs within a sarcomere are activated at approximately the same time. These assumptions enable a 1D lattice model to be constructed where each node represents a sarcomere (**Figure 8A**). The state of each sarcomere can be simplified into either being in a non-spark or spark condition [represented by 0 and 1 respectively and conceptually similar to the use of a single RyR megachannel as described in Williams et al. (2007, 2008) above]. The rate of spark recruitment was defined by:

$$R(t) = R_{ICaL}(t) + R_{SCRE}(t) \tag{43}$$

Where R_{ICaL}(t) is the recruitment rate due to activation by I_{CaL}, and R_{SCRE}(t) is the rate of recruitment via spontaneous sparks and waves. Assuming the release flux (J_{rel}) associated with each spark is approximately exponential, the spark-rate, R(t), can be associated with J_{rel} via the following differential equation:

$$\frac{dJ_{rel}(t)}{dt} = g{\cdot}Ca_{SR}(t){\cdot}R(t) - \frac{J_{rel}(t){\cdot}\left(1 - \tau_d\left[dCa_{SR}/dt\right]/Ca_{SR}\right)}{\tau_d} \tag{44}$$

Where τ_d is the time-constant of the exponential function assumed to describe the spark flux. The rates of spontaneous spark initiation and a transmission-time and -probability [i.e., the components of R_{SCRE}(t)] are primarily regulated by Ca$_{\mathrm{SR}}$ and were fit to experimental data to describe Ca^{2+}-wave velocity, enabling many features of whole-cell SCRE to be captured at a significantly reduced cost.

In Hernandez-Hernandez et al. (2015) a similar model was constructed in 2D (**Figure 8A**). The state of each CRU (0 or 1 for non-spark or spark, respectively) was described by the following simple reaction:

$$0 \underset{\beta}{\overset{\alpha=f(Ca_i)}{\rightleftharpoons}} 1 \tag{45}$$

Inter-CRU coupling was described using a spatially exponential function such that the influence of one CRU on its neighbors decays rapidly as distance increases:

$$h_{ij} = r_j e^{-|x_i - x_j|^2/l^2} \tag{46}$$

Where r_j is the Ca^{2+} released at site j, x_{i}, and x_j are the locations of the two coupled CRUs and l is the diffusive length-scale. This model was used to evaluate the influence of CRU connectivity on Ca^{2+}-wave nucleation and propagation.

In Romero et al. (2019) a 2D model was developed where the dynamics of each CRU were described by a non-linear map which relates Ca^{2+} concentrations from one beat to the next (rather than solving concentrations on a small time-step within each beat). This is a spatial analog of the iterative-map approach described in the next sub-section. Concentrations for beat n+1 are functions of concentrations and fluxes during beat n:

$$Ca^x_{SR}(n+1) = Ca^x_{SR}(n) - R^x(n) + U^x(n) \tag{47}$$

$$Ca^x_i(n+1) = Ca^x_i(n) + R^x(n) - U^x(n) \tag{48}$$

Where Ca$_{\mathrm{SR}}{}^x$ and Ca$_{\mathrm{i}}{}^x$ are the SR and intracellular Ca^{2+} concentrations at the spatial point x (=i,j in 2D), R^x(n) is the total Ca^{2+} released from the SR at point x during beat n and U^x(n) is the total Ca^{2+} pumped back into the SR at point x during beat n. As a simplification, it is assumed that the total Ca^{2+} is conserved (Ca$_{\mathrm{SR}}$ + Ca$_{\mathrm{i}}$ = C) and can be thusly normalized to 1 (arbitrary units). The stochastic dependence of intracellular Ca^{2+} release (R^x) on voltage can be incorporated by accounting for the probability of release, and intracellular uptake is given as a function of the CaT peak. Ca^{2+} diffusion was then described by accounting for the average Ca^{2+} over the nearest neighbors in the 2D lattice of CRUs.

In Cantalapiedra et al. (2017) a spatial model was developed which included simplified descriptions of the LTCCs and RyRs through exploiting symmetries and other factors to substantially reduce the number of equations/parameters governing these dynamics; spatial coupling was described explicitly as in a CRU-grid fully spatial model. The model was used to study the influence of SR-Ca^{2+} load and RyR refractoriness on the dynamics of CaT alternans.

Non-spatial Simplified Models

Further simplification can be achieved by developing non-spatial (or "0D") approximations, which have no explicit description of spatial diffusion in the sub-cellular volume and present the opportunity for the largest increases in computational efficiency. Several different techniques have been proposed.

Reduction to (Semi-)deterministic Models

In Chen et al. (2012) a model was developed which describes single-cell SCRE dynamics using a single simple two-state reaction scheme that is able to capture the statistics of SCRE timing and magnitude. This is the same basic scheme as presented by Hernandez-Hernandez et al. (2015) and equation (45), but is now solved in the deterministic limit describing the whole-cell (**Figure 8A**). This was applied in a 1D model of tissue to analyze the relationship between the statistics of single-cell SCRE (pertaining to timing, magnitude and duration) and the emergence of spontaneous focal (or ectopic) excitation in tissue.

In studies by Shiferaw et al. (2018, 2020) a phenomenological, population-dynamics-like model of spark recruitment was developed that matched behavior of the 3D cell model. Here, rather than modeling CRU dynamics explicitly, the number of active CRUs (or number of sparks) were tracked and dynamically evolves dependent on the number of sparks initiated (Δn^{+}) and extinguished (Δn^{-}) at each time-step (Δt):

$$n_i(t + \triangle t) = n_i(t) + \triangle n_i^{+} - \triangle n_i^{-} \tag{49}$$

The number of sparks initiated was determined by the rate at which sparks are recruited (either spontaneous or triggered) and stochasticity was maintained through the use of random number sampling. This used a similar approach to individual CRU recruitment to that of Chen et al. (2012) and Hernandez-Hernandez et al. (2015) but now included distinction between junctional and non-junctional sparks [both described by equation (45) but with different values for the transition rates], enabling the impact of heterogeneous and variable atrial T-systems to be captured in this reduced model. The approximation could reproduce both CaT alternans and SCRE. The model was used to study synchronization of SCRE in atrial tissue, developing focal excitations, conduction-block, and non-stable re-entrant-like excitation patterns.

Iterated-Map Models

Qu et al. (2007) developed an iterated-map model of CRU activity, relating Ca^{2+} and voltage properties on a beat-to-beat basis (**Figure 8A**), a whole-cell equivalent to the more recent approach presented in Romero et al. (2019). The approach can be briefly summarized by the following equations. Firstly, the APD can depend on both the diastolic interval (DI) and peak of the CaT (Ca^{peak}). Thus, the APD at the current cycle (n) depends on the previous cycle (n-1) and is given by:

$$APD_n = f_1\left(DI_{n-1}\right) + f_2\left(Ca_n^{peak}\right) APD_n \tag{50}$$

Where the functions of DI and intracellular Ca^{2+} have been separated: f_1 is the APD restitution function and f_2 accounts for the coupling strength between Ca^{2+} and APD (which can be positive or negative). The peak Ca^{2+} concentration at cycle n can be given by the sum of the diastolic Ca^{2+} from the previous cycle (Ca_{n-1}) and the total Ca^{2+} released from the SR in the current cycle (r_n):

$$Ca_n^{peak} = Ca_{n-1} + r_n \tag{51}$$

The total Ca^{2+} released from the SR, r_n, is given by:

$$r_n = f_3\left(DI_{n-1}\right) f_4\left(CaSR_{n-1}^{load}\right) \tag{52}$$

Where f_3 describes the restitution properties of SR-Ca^{2+} release (e.g., RyR refractoriness) and f_4 describes the dependence of Ca^{2+} release on the SR-Ca^{2+} load. The reader is referred to the original publication for full details on the parameters and functions involved. This model reproduced the non-linear dynamics of Ca^{2+} handling including CaT alternans, and this simplification helped to develop a unified theory of CaT alternans in cardiac cells (Qu et al., 2016). Furthermore, this vast simplification in both space and time produces exceptionally efficient simulations, computationally less intense than standard, non-spatial common-pool models of cardiac cellular electrophysiology.

Models of Imposed, Stochastic Spontaneous Ca^{2+} Release Functions

As an alternative to the above approaches, it is also possible to control spontaneous CaTs in otherwise deterministic cell models by imposing (or clamping) SCRE waveforms (**Figure 8A**). In Xie et al. (2010), the intracellular release flux (J_{rel}) associated with SCRE was controlled by imposing a waveform defined by two sigmoidal functions, the parameters of which determined the timing, duration and magnitude of SCRE:

$$\begin{aligned} J_{rel}^{spont} &= G_{spont}\left(1 + e^{-(t-t_0)/\tau_1}\right)^{-1} \\ &\left(1 + e^{(t-t_0)/\tau_2}\right)^{-1}\left(\frac{v_{ds}}{v_{jsr}} Ca_{SR} - Ca_{ds}\right) \end{aligned} \tag{53}$$

Where G_{spont} is a rate constant (set to 0.0674 ms^{-1} in the original study), t_0 was set to 425 ms and τ_1 = 10 ms and τ_2 = 30 ms. The model was used to determine the minimum number of cells undergoing DADs in various tissue conditions in order for this to manifest as a focal excitation. Whereas not performed in the original study, the timing and duration parameters (t_0, τ_1, τ_2) could be randomly sampled from distributions to reproduce stochasticity in independent cellular SCRE. This approach was used in Liu et al. (2015), sampling from Gaussian distributions, in order to study the dynamics of independently timed DADs in tissue, revealing mechanisms of synchronization into focal excitation and DAD-mediated conduction block (e.g., **Figure 8B**). Liu et al. (2016) and Ko et al. (2017) used a similar but further simplified approach in which the Ca_i associated with SCRE was directly controlled, described by a Gaussian-shaped function with equivalent parameters to control timing, magnitude and duration:

$$Ca_i^{spont} = Ae^{-(t-t_0)^2/2\sigma^2} \tag{54}$$

Where A sets the maximum amplitude, t_0 sets the latency (timing) and σ sets the duration. In Colman et al. (2017a) and Colman (2019) an approach was developed which used sigmoidal functions to control the RyR-state directly, reproducing different shapes of long- and short-release waveforms. For short (spike-like) waveforms:

$$N_{RyR\_O} = N_{RyR\_O}^{peak}\left(1+e^{-(t-t_1)/k_1}\right)^{-1}\left(1+e^{(t-t_2)/k_2}\right)^{-1} \tag{55}$$

$$t_1 = t_i + 0.5\left(t_p - t_i\right) \tag{56}$$

$$t_2 = t_p + 0.5\left(t_f - t_p\right) \tag{57}$$

$$k_1 = 0.1689(t_p - t_i) + 0.00255 \tag{58}$$

$$k_2 = 0.1689\left(t_f - t_p\right) + 0.00255 \tag{59}$$

where t_i is the initiation time (equivalent to latency, t_0, in the above models) of the SCRE, t_f is the end time (duration, λ, thus = t_f-t_i), t_p is the time of the peak of the waveform and $N_{RyR\_O}{}^{peak}$ is the peak proportion of open RyRs. In this model, N_{RyR_O} [equation (55)] replaces the "O" in the J_{rel} equation [equation (5)] and so J_{rel} and the CaT are allowed to dynamically evolve according to their deterministic functions; the magnitude of the CaT associated with the SCRE is therefore dependent on $N_{RyR\_O}{}^{peak}$, the SR-Ca^{2+} and J_{rel} maximal flux rate. This model demonstrated feedback between re-entry and focal excitation in which the rapid activation during re-entry loads the SR-Ca^{2+} to promote focal excitations following re-entry termination (**Figure 8B**).

In all implementations, the parameters defining the distributions which describe SCRE statistics could be set as a function of environmental variables, such as SR-Ca^{2+}, enabling the simplified cell model to respond to pacing with variable SCRE statistics in congruence with the dynamics of spatial Ca^{2+} cell models. All of these models employ an algorithm to determine if Ca_i, J_{rel} or RyR-state is controlled by the deterministic cell model or undergoes the imposed SCRE clamped waveform, enabling integration with dynamically evolving deterministic cell models in both single-cell and tissue simulations. The computational efficiency of these models is comparable to that of standard common-pool models of cardiac electrophysiology; the largest computational cost is the generation of random numbers (where one must indeed be careful with implementations of parallelization in tissue simulations), but the cost of this inclusion is smaller than the typical differences in computational efficiency between common-pool models which feature a different number of components and governing equations.

Estimating Probabilities of Rare Events

Walker et al. (2017) implemented a study in which 3D cell models were coupled in a 1D tissue strand (or fiber). They investigated the mediators of Ca^{2+} waves and DADs in single cells, and used the 1D fiber model to translate these features to tissue activity. From this, they developed a spatial-average filtering model which aimed to estimate V_m from intracellular release fluxes, enabling the estimation of the probabilities of "extreme" (i.e., rare) events in which multiple cells synchronously undergo large-scale SCRE, i.e., the requirements for focal excitations. This type of approach is powerful and important because the generation of a serious arrhythmia in an individual is often a very rare event that cannot be robustly or consistently captured in simulations of a generally normally functioning heart. In agreement with other studies (Liu et al., 2016; Campos et al., 2017; Colman, 2019), they found reduced I_{K1} and inter-cellular coupling to be important for enabling SCRE to overcome electrotonic load and promote focal excitations.

Whole-Heart Models; Integration With Tissue Imaging

A few studies have integrated these reduced models of stochastic sub-cellular Ca^{2+} handling into models of the whole atria or ventricle in order to study the interaction between cellular function and tissue structure in controlling the emergence and dynamics of arrhythmogenic triggers. This is perhaps taken the furthest in a series of papers by Campos et al. (2015, 2017, 2018, 2019). The initial study (Campos et al., 2015) combined the phenomenological model of SCRE as proposed in Chen et al. (2011) with a full bi-ventricular 3D model which included a description of the Purkinje network. This model demonstrated that focal excitations were preferentially located to the Purkinje network due to the reduced electrotonic load in these pseudo-1D-strands, with focal excitations increasingly repressed as dimensionality increased from 1D to 3D (**Figure 8C**). Campos et al. (2017) subsequently incorporated a description of sodium-channel dysfunction, which promoted focal excitations and conduction block leading to re-entry. The two more recent studies (Campos et al., 2018, 2019) now combined these analyses with structural remodeling associated with infarcts in both idealized 2D sheets (**Figure 8C**) and realistic geometries in the 3D bi-ventricular model, demonstrating that the macroscopic and microscopic anatomy of the infarct region could promote both focal excitation and re-entry and highlighting the mechanisms by which fibrosis could increase the probability of focal excitations in these conditions.

These studies demonstrate structural features which can co-localize both focal excitation and re-entrant excitation. In

Colman (2019) a purely functional mechanism which can co-locate focal and re-entrant excitation was revealed: the in-excited core of re-entrant excitation lead to substantially longer latency times in this region, enabling focal excitation to preferentially emerge from this same location (**Figure 8B**); interaction of focal excitation with the tail of the previous re-entrant excitation could lead to highly asymmetric focal excitations which themselves may degenerate back into re-entry with a core in the same approximate location. Thus, these studies are revealing both structural and functional mechanisms which spatially relate focal and re-entrant excitation.

Drawing on Physical Analogies for Mechanistic Explanation

Other works have used detailed or simplified models to make analogies that relate cardiac Ca^{2+}-handling phenomena to other physical phenomena, which may offer further insight into fundamental underlying mechanisms or provide more predictive power.

Alvarez-Lacalle et al. (2015) used both a 2D sub-cellular spatial model and simplified descriptions in order to analyze the dynamics of CaT alternans. Through scaling analysis of correlations near the transition to alternans it was demonstrated that CaT alternans could be described as an order-disorder phase transition, leading to an analogy to the Ising model of ferromagnetism in statistical mechanics. This was further generalized to describe more features of Ca^{2+} dynamics, including coupling with voltage, in Romero et al. (2019), where the analogy was extended to the more general Potts model. Both discontinuous first-order phase transitions and second-order continuous phase transitions (alternans) were observed to emerge under different conditions in cardiac cellular dynamics, further supporting the idea that statistical mechanics tools may be valuable for understanding cardiac function.

Conesa et al. (2020) presented a novel approach to understanding steady-state activity through analysis of a single beat which is not in homeostatic balance, by reduction to two-variable general equilibrium conditions in analogy to models of macro-economics. Such an approach can help to explain the complex and often counter-intuitive features of Ca^{2+}-handling and offers substantial predictive power without the requirement for computer-intensive simulations.

SUMMARY AND CONCLUSION

Recent advances in the robustness, complexity and sophistication of computational models of spatial Ca^{2+}-handling from the nanometer-scale to the whole-heart scale are enabling advanced simulations to be performed to reveal fundamental properties of cardiac ECC in both health and disease. Multiple different approaches have been explored to describe nanodomain dynamics, model inter-CRU coupling, implement experimental imaging data, and translate models to the whole-heart scale. There are fundamental differences in the approaches and structure of these models, and in some cases model behavior can differ substantially (e.g., in triggered Ca^{2+} wave propagation). Nevertheless, the general agreement between models is encouraging and the availability of multiple different models provides the opportunity to comprehensively test hypotheses and explore fundamental theories. As computational power increases, experimental imaging data improves, and more powerful coarse-graining techniques are developed, the relevance, scope and power of these models will only continue to increase.

There are a number of challenges and avenues for future development and innovation. Robust validation of the models remains a major difficulty, not-least because of the challenges in obtaining sufficient and congruent experimental data to validate the many interacting model components and emergent functional phenomena. Validation of the governing RyR models themselves, in isolation and in the context of the spatial-nanodomain, is non-trivial - important features of Ca^{2+} sparks, such as the spatial FWHM, do not necessarily match experimental observations. This is not the only difficulty associated with obtaining a realistic and well-validated description of RyR gating: Integration of spark properties in the context of whole-cell homeostasis is also highly challenging due to the interaction with the wider model system and further constraints on model stability and long-term dynamics.

At the whole-cell scale, many approaches have been implemented to describe spatial Ca^{2+} coupling, corresponding to fundamentally different underlying model structures. Each approach has associated features of the CaT and Ca^{2+}-handling dynamics, such as the robustness of Ca^{2+}-wave propagation; certainly, not all of these structures and parameter combinations can simultaneously accurately describe real myocytes, and there are therefore fundamental questions about the mechanisms of inter-CRU Ca^{2+} diffusion which remain to be resolved. Nevertheless, the success of these models to explain and provide interpretations into experimental results is highly encouraging, especially in the more recent studies which combine experiment and simulation and are indeed beginning to resolve some of these issues.

One of the most exciting and challenging prospects is true multi-scale model integration. The recent spatial models of single nanodomains highlight the importance of specific RyR arrangement and microstructure of the dyad; incorporating these features into a whole-cell model containing tens of thousands of heterogeneous dyads is far from trivial. The detailed models of the local regions of a single T-tubule reveal important features of local Ca^{2+} gradients and channel distribution – combining these models with detailed representations of RyR arrangement in nanodomains, models of counter-ion fluxes, and the electrophysiology of the T-tubule membrane itself presents exciting prospects for powerful and highly accurate models of local control; again, translating these to the whole-cell scale is associated with a number of challenges. Initial success has been achieved in models attempting to preserve the impact of stochastic spatial Ca^{2+} dynamics in reduced, computationally efficient cell models suitable for tissue simulations, revealing the mechanisms of ectopic excitation, its interaction with re-entry, and dependence on tissue structure. Generalizing these models to naturally capture the dynamics of heterogenous populations of cells, themselves depending on heterogeneous sub-cellular structure, remains a major goal.

Finally, there have been substantial advances in approaches for image-based modeling, both for high-throughput, population-cohort simulations, and for direct integration of experimental structures. Closely related to advances in experimental imaging modalities, this is occurring at multiple spatial scales including the nanodomain, localized sub-cellular regions, whole-cells, and whole-heart. The further development and automation of these experimental-simulation frameworks presents exciting prospects for the true mechanistic analysis of structure-function relationships underlying cardiac electrophysiology from the nanometer to the whole-heart.

AUTHOR CONTRIBUTIONS

MC conceived the review, drafted and edited the manuscript, and prepared the illustrations. All the authors drafted and edited the manuscript.

FUNDING

This work was supported by a Medical Research Council, United Kingdom, Strategic Skills Fellowship (Grant Number MR/M014967/1) and Career Development Award (Grant Number MR/V010050/1) awarded to MC, by the Netherlands Organization for Scientific Research NWO/ZonMW Vidi 09150171910029 awarded to JH, by MICINN/AEI through research grants SAF-2017-88019-C3-2-R and PID2020-116927RB-C22 awarded to BE and EA-L, and by the National Institutes of Health (Grant Numbers R01-HL149349 and P01-HL141084) awarded to DS.

ACKNOWLEDGMENTS

The authors would like to thank the following for helpful conversations and perspectives on this topic: Yohannes Shiferaw (California State University, Northridge), Zhen Song and Zhilin Qu (University of California, Los Angeles), Fernando Campos and Martin Bishop (King's College London), and Izzy Jayasinghe (The University of Sheffield).

REFERENCES

Alvarez-Lacalle, E., Cantalapiedra, I. R., Peñaranda, A., Cinca, J., Hove-Madsen, L., and Echebarria, B. (2013). Dependency of calcium alternans on ryanodine receptor refractoriness. *PLoS One* 8:e55042. doi: 10.1371/journal.pone.0055042

Alvarez-Lacalle, E., Echebarria, B., Spalding, J., and Shiferaw, Y. (2015). Calcium alternans is due to an order-disorder phase transition in cardiac cells. *Phys. Rev. Lett.* 114:108101. doi: 10.1103/PhysRevLett.114.108101

Asfaw, M., Alvarez-Lacalle, E., and Shiferaw, Y. (2013). The timing statistics of spontaneous calcium release in cardiac myocytes. *PLoS One* 8:e62967. doi: 10.1371/journal.pone.0062967

Baddeley, D., Jayasinghe, I. D., Lam, L., Rossberger, S., Cannell, M. B., and Soeller, C. (2009). Optical single-channel resolution imaging of the ryanodine receptor distribution in rat cardiac myocytes. *Proc. Natl. Acad. Sci. U. S. A.* 106, 22275–22280. doi: 10.1073/pnas.0908971106

Benson, A. P., Bernus, O., Dierckx, H., Gilbert, S. H., Greenwood, J. P., Holden, A. V., et al. (2011). Construction and validation of anisotropic and orthotropic ventricular geometries for quantitative predictive cardiac electrophysiology. *Interface Focus* 1, 101–116. doi: 10.1098/rsfs.2010.0005

Bers, D. M. (2002). Cardiac excitation–contraction coupling. *Nature* 415, 198–205. doi: 10.1038/415198a

Berti, C., Zsolnay, V., Shannon, T. R., Fill, M., and Gillespie, D. (2017). Sarcoplasmic reticulum Ca2+, Mg2+, K+, and Cl- concentrations adjust quickly as heart rate changes. *J. Mol. Cell. Cardiol.* 103, 31–39. doi: 10.1016/j.yjmcc.2016.10.018

Black, N., D'Souza, A., Wang, Y., Piggins, H., Dobrzynski, H., Morris, G., et al. (2019). Circadian rhythm of cardiac electrophysiology, arrhythmogenesis, and the underlying mechanisms. *Heart Rhythm* 16, 298–307. doi: 10.1016/j.hrthm.2018.08.026

Brandenburg, S., Kohl, T., Williams, G. S. B., Gusev, K., Wagner, E., Rog-Zielinska, E. A., et al. (2016). Axial tubule junctions control rapid calcium signaling in atria. *J. Clin. Invest.* 126, 3999–4015. doi: 10.1172/JCI88241

Brette, F., Despa, S., Bers, D. M., and Orchard, C. H. (2005). Spatiotemporal characteristics of SR Ca2+ uptake and release in detubulated rat ventricular myocytes. *J. Mol. Cell. Cardiol.* 39, 804–812. doi: 10.1016/j.yjmcc.2005.08.005

Campos, F. O., Shiferaw, Y., Prassl, A. J., Boyle, P. M., Vigmond, E. J., and Plank, G. (2015). Stochastic spontaneous calcium release events trigger premature ventricular complexes by overcoming electrotonic load. *Cardiovasc. Res.* 107, 175–183. doi: 10.1093/cvr/cvv149

Campos, F. O., Shiferaw, Y., Vigmond, E. J., and Plank, G. (2017). Stochastic spontaneous calcium release events and sodium channelopathies promote ventricular arrhythmias. *Chaos* 27:093910. doi: 10.1063/1.4999612

Campos, F. O., Shiferaw, Y., Weber dos Santos, R., Plank, G., and Bishop, M. J. (2018). Microscopic Isthmuses and Fibrosis Within the Border Zone of Infarcted Hearts Promote Calcium-Mediated Ectopy and Conduction Block. *Front. Phys.* 6:57. doi: 10.3389/fphy.2018.00057

Campos, F. O., Whitaker, J., Neji, R., Roujol, S., O'Neill, M., Plank, G., et al. (2019). Factors promoting conduction slowing as substrates for block and reentry in infarcted hearts. *Biophys. J.* 117, 2361–2374. doi: 10.1016/j.bpj.2019.08.008

Cannell, M. B., and Kong, C. H. T. (2012). Local control in cardiac E-C coupling. *J. Mol. Cell. Cardiol.* 52, 298–303. doi: 10.1016/j.yjmcc.2011.04.014

Cannell, M. B., and Kong, C. H. T. (2017). Quenching the spark: termination of CICR in the submicroscopic space of the dyad. *J. Gen. Physiol.* 149, 837–845. doi: 10.1085/jgp.201711807

Cannell, M. B., Kong, C. H. T., Imtiaz, M. S., and Laver, D. R. (2013). Control of Sarcoplasmic Reticulum Ca2+ Release by Stochastic RyR Gating within a 3D Model of the Cardiac Dyad and Importance of Induction Decay for CICR Termination. *Biophys. J.* 104, 2149–2159. doi: 10.1016/j.bpj.2013.03.058

Cantalapiedra, I. R., Alvarez-Lacalle, E., Peñaranda, A., and Echebarria, B. (2017). Minimal model for calcium alternans due to SR release refractoriness. *Chaos* 27:093928. doi: 10.1063/1.5000709

Chen, W., Aistrup, G., Wasserstrom, J. A., and Shiferaw, Y. (2011). A mathematical model of spontaneous calcium release in cardiac myocytes. *Am. J. Physiol.-Heart Circ. Physiol.* 300, H1794–H1805. doi: 10.1152/ajpheart.01121.2010

Chen, W., Asfaw, M., and Shiferaw, Y. (2012). The Statistics of Calcium-Mediated Focal Excitations on a One-Dimensional Cable. *Biophys. J.* 102, 461–471. doi: 10.1016/j.bpj.2011.12.045

Chen, W., Wasserstrom, J. A., and Shiferaw, Y. (2009). Role of coupled gating between cardiac ryanodine receptors in the genesis of triggered arrhythmias. *Am. J. Physiol.-Heart Circ. Physiol.* 297, H171–H180. doi: 10.1152/ajpheart.00098.2009

Cheng, H., Lederer, W. J., and Cannell, M. B. (1993). Calcium sparks: elementary events underlying excitation-contraction coupling in heart muscle. *Science* 262, 740–744. doi: 10.1126/science.8235594

Cheng, Y., Yu, Z., Hoshijima, M., Holst, M. J., McCulloch, A. D., McCammon, J. A., et al. (2010). Numerical Analysis of Ca2+ Signaling in Rat Ventricular Myocytes with Realistic Transverse-Axial Tubular Geometry and Inhibited Sarcoplasmic Reticulum. *PLoS Comput. Biol.* 6:e1000972. doi: 10.1371/journal.pcbi.1000972

Clarke, J. D., Caldwell, J. L., Horn, M. A., Bode, E. F., Richards, M. A., Hall, M. C. S., et al. (2015). Perturbed atrial calcium handling in an ovine model of heart failure: potential roles for reductions in the L-type calcium current. *J. Mol. Cell. Cardiol.* 79, 169–179. doi: 10.1016/j.yjmcc.2014.11.017

Colman, M. A. (2019). Arrhythmia mechanisms and spontaneous calcium release: Bi-directional coupling between re-entrant and focal excitation. *PLoS Comput. Biol.* 15:e1007260. doi: 10.1371/journal.pcbi.1007260

Colman, M. A., Aslanidi, O. V., Kharche, S., Boyett, M. R., Garratt, C., Hancox, J. C., et al. (2013). Pro-arrhythmogenic effects of atrial fibrillation-induced electrical remodelling: insights from the three-dimensional virtual human atria. *J. Physiol.* 591, 4249–4272. doi: 10.1113/jphysiol.2013.254987

Colman, M. A., Holmes, M., Whittaker, D. G., Jayasinghe, I., and Benson, A. P. (2020). Multi-scale approaches for the simulation of cardiac electrophysiology: I - Sub-cellular and stochastic calcium dynamics from cell to organ. *Methods* 185, 49–59. doi: 10.1016/j.ymeth.2020.02.011

Colman, M. A., Perez Alday, E. A., Holden, A. V., and Benson, A. P. (2017a). Trigger vs. Substrate: multi-Dimensional Modulation of QT-Prolongation Associated Arrhythmic Dynamics by a hERG Channel Activator. *Front. Physiol.* 8:757. doi: 10.3389/fphys.2017.00757

Colman, M. A., Pinali, C., Trafford, A. W., Zhang, H., and Kitmitto, A. (2017b). A computational model of spatio-temporal cardiac intracellular calcium handling with realistic structure and spatial flux distribution from sarcoplasmic reticulum and t-tubule reconstructions. *PLoS Comput. Biol.* 13:e1005714. doi: 10.1371/journal.pcbi.1005714

Colman, M. A., Sarathy, P. P., MacQuiaide, N., and Workman, A. J. (2016). "A new model of the human atrial myocyte with variable T-tubule organization for the study of atrial fibrillation," in *2016 Computing in Cardiology Conference (CinC)*, (Vancouver), 221–224. doi: 10.23919/CIC.2016.7868719

Conesa, D., Echebarria, B., Peñaranda, A., Cantalapiedra, I. R., Shiferaw, Y., and Alvarez-Lacalle, E. (2020). Two-variable nullcline analysis of ionic general equilibrium predicts calcium homeostasis in ventricular myocytes. *PLoS Comput. Biol.* 16:e1007572. doi: 10.1371/journal.pcbi.1007572

Crocini, C., Coppini, R., Ferrantini, C., Yan, P., Loew, L. M., Tesi, C., et al. (2014). Defects in T-tubular electrical activity underlie local alterations of calcium release in heart failure. *Proc. Natl. Acad. Sci. U. S. A.* 111, 15196–15201. doi: 10.1073/pnas.1411557111

Crossman, D. J., Ruygrok, P. N., Ruygrok, P. R., Soeller, C., and Cannell, M. B. (2011). Changes in the organization of excitation-contraction coupling structures in failing human heart. *PLoS One* 6:e17901. doi: 10.1371/journal.pone.0017901

Dibb, K. M., Louch, W. E., and Trafford, A. W. (2022). Cardiac Transverse Tubules in Physiology and Heart Failure. *Annu. Rev. Physiol.* 84. doi: 10.1146/annurev-physiol-061121-040148

D'Souza, A., Wang, Y., Anderson, C., Bucchi, A., Baruscotti, M., Olieslagers, S., et al. (2021). A circadian clock in the sinus node mediates day-night rhythms in Hcn4 and heart rate. *Heart Rhythm* 18, 801–810. doi: 10.1016/j.hrthm.2020.11.026

Eisner, D. A., Caldwell, J. L., Kistamás, K., and Trafford, A. W. (2017). Calcium and Excitation-Contraction Coupling in the Heart. *Circ. Res.* 121, 181–195. doi: 10.1161/CIRCRESAHA.117.310230

Eisner, D. A., Kashimura, T., Venetucci, L. A., and Trafford, A. W. (2009). From the ryanodine receptor to cardiac arrhythmias. *Circ. J.* 73, 1561–1567. doi: 10.1253/circj.cj-09-0478

Gadeberg, H. C., Bond, R. C., Kong, C. H. T., Chanoit, G. P., Ascione, R., Cannell, M. B., et al. (2016). Heterogeneity of T-Tubules in Pig Hearts. *PLoS One* 11:e0156862. doi: 10.1371/journal.pone.0156862

Gaur, N., and Rudy, Y. (2011). Multiscale modeling of calcium cycling in cardiac ventricular myocyte: macroscopic consequences of microscopic dyadic function. *Biophys. J.* 100, 2904–2912. doi: 10.1016/j.bpj.2011.05.031

Ghosh, S., Tran, K., Delbridge, L. M. D., Hickey, A. J. R., Hanssen, E., Crampin, E. J., et al. (2018). Insights on the impact of mitochondrial organisation on bioenergetics in high-resolution computational models of cardiac cell architecture. *PLoS Comput. Biol.* 14:e1006640. doi: 10.1371/journal.pcbi.1006640

Gillespie, D. T. (1976). A general method for numerically simulating the stochastic time evolution of coupled chemical reactions. *J. Comput. Phys.* 22, 403–434. doi: 10.1016/0021-9991(76)90041-3

Greene, D., and Shiferaw, Y. (2021). Mechanistic link between CaM-RyR2 interactions and the genesis of cardiac arrhythmia. *Biophys. J.* 120, 1469–1482. doi: 10.1016/j.bpj.2021.02.016

Greenstein, J. L., and Winslow, R. L. (2002). An integrative model of the cardiac ventricular myocyte incorporating local control of Ca2+ release. *Biophys. J.* 83, 2918–2945. doi: 10.1016/S0006-3495(02)75301-0

Hake, J., Edwards, A. G., Yu, Z., Kekenes-Huskey, P. M., Michailova, A. P., McCammon, J. A., et al. (2012). Modelling cardiac calcium sparks in a three-dimensional reconstruction of a calcium release unit. *J. Physiol.* 590, 4403–4422. doi: 10.1113/jphysiol.2012.227926

Hake, J., Kekenes-Huskey, P. M., and McCulloch, A. D. (2014). Computational modeling of subcellular transport and signaling. *Curr. Opin. Struct. Biol.* 25, 92–97. doi: 10.1016/j.sbi.2014.01.006

Hatano, A., Okada, J., Hisada, T., and Sugiura, S. (2012). Critical role of cardiac t-tubule system for the maintenance of contractile function revealed by a 3D integrated model of cardiomyocytes. *J. Biomech.* 45, 815–823. doi: 10.1016/j.jbiomech.2011.11.022

Hatano, A., Okada, J., Washio, T., Hisada, T., and Sugiura, S. (2011). A Three-Dimensional Simulation Model of Cardiomyocyte Integrating Excitation-Contraction Coupling and Metabolism. *Biophys. J.* 101, 2601–2610. doi: 10.1016/j.bpj.2011.10.020

Heijman, J., Erfanian Abdoust, P., Voigt, N., Nattel, S., and Dobrev, D. (2016). Computational models of atrial cellular electrophysiology and calcium handling, and their role in atrial fibrillation. *J. Physiol.* 594, 537–553. doi: 10.1113/JP271404

Heijman, J., Volders, P. G. A., Westra, R. L., and Rudy, Y. (2011). Local control of β-adrenergic stimulation: effects on ventricular myocyte electrophysiology and Ca2+-transient. *J. Mol. Cell. Cardiol.* 50, 863–871. doi: 10.1016/j.yjmcc.2011.02.007

Hernandez-Hernandez, G., Alvarez-Lacalle, E., and Shiferaw, Y. (2015). Role of connectivity and fluctuations in the nucleation of calcium waves in cardiac cells. *Phys. Rev. E Stat. Nonlin. Soft Matter Phys.* 92:052715. doi: 10.1103/PhysRevE.92.052715

Herzel, H. (1991). Risken, H., The Fokker-Planck-Equation. Methods of Solution and Applications. Second edition. Berlin etc., Springer-Verlag 1989. XIV, 472 pp., 95 figs., DM 98,—. ISBN3-540-50498-2 (Springer Series in Synergetics 18). *ZAMM - J. Appl. Math. Mech. Z. Für Angew. Math. Mech.* 71, 67–67. doi: 10.1002/zamm.19910710128

Hinch, R. (2004). A mathematical analysis of the generation and termination of calcium sparks. *Biophys. J.* 86, 1293–1307. doi: 10.1016/S0006-3495(04)74203-4

Hoang-Trong, T. M., Ullah, A., Lederer, W. J., and Jafri, M. S. (2021). A Stochastic Spatiotemporal Model of Rat Ventricular Myocyte Calcium Dynamics Demonstrated Necessary Features for Calcium Wave Propagation. *Membranes* 11:989. doi: 10.3390/membranes11120989

Holash, R. J., and MacIntosh, B. R. (2019). A stochastic simulation of skeletal muscle calcium transients in a structurally realistic sarcomere model using MCell. *PLoS Comput. Biol.* 15:e1006712. doi: 10.1371/journal.pcbi.1006712

Holmes, M., Hurley, M., Sheard, T., Benson, A., Jayasinghe, I., and Colman, M. (2021). Increased SERCA2a sub-cellular heterogeneity in right-ventricular heart failure inhibits excitation-contraction coupling and modulates arrhythmogenic dynamics. *Philos. Trans. R. Soc. B Biol. Sci.* (in press). doi: 10.1098/rstb.2021-0317 [Epub ahead of print].

Hüser, J., Lipsius, S. L., and Blatter, L. A. (1996). Calcium gradients during excitation-contraction coupling in cat atrial myocytes. *J. Physiol.* 494, 641–651. doi: 10.1113/jphysiol.1996.sp021521

Hussain, A., Ghosh, S., Kalkhoran, S. B., Hausenloy, D. J., Hanssen, E., and Rajagopal, V. (2018). An automated workflow for segmenting single adult cardiac cells from large-volume serial block-face scanning electron microscopy data. *J. Struct. Biol.* 202, 275–285. doi: 10.1016/j.jsb.2018.02.005

Iaparov, B. I., Zahradnik, I., Moskvin, A. S., and Zahradníková, A. (2021). In silico simulations reveal that RYR distribution affects the dynamics of calcium release in cardiac myocytes. *J. Gen. Physiol.* 153:e202012685. doi: 10.1085/jgp.202012685

Illian, J., Penttinen, A., Stoyan, H., and Stoyan, D. (2008). *Statistical Analysis and Modelling of Spatial Point Patterns*. Chichester: John Wiley & Sons Ltd, doi: 10.1002/9780470725160

Jayasinghe, I., Clowsley, A. H., Lin, R., Lutz, T., Harrison, C., Green, E., et al. (2018b). True Molecular Scale Visualization of Variable Clustering Properties of Ryanodine Receptors. *Cell Rep.* 22, 557–567. doi: 10.1016/j.celrep.2017.12.045

Jayasinghe, I., Clowsley, A. H., de Langen, O., Sali, S. S., Crossman, D. J., and Soeller, C. (2018a). Shining New Light on the Structural Determinants of Cardiac Couplon Function: insights From Ten Years of Nanoscale Microscopy. *Front. Physiol.* 9:1472. doi: 10.3389/fphys.2018.01472

Kekenes-Huskey, P., Cheng, Y., Hake, J., Sachse, F., Bridge, J., Holst, M., et al. (2012). Modeling Effects of L-Type Ca2+ Current and Na+-Ca2+ Exchanger on Ca2+ Trigger Flux in Rabbit Myocytes with Realistic T-Tubule Geometries. *Front. Physiol.* 3:351. doi: 10.3389/fphys.2012.00351

Kerr, R. A., Bartol, T. M., Kaminsky, B., Dittrich, M., Chang, J.-C. J., Baden, S. B., et al. (2008). Fast Monte Carlo Simulation Methods for Biological Reaction-Diffusion Systems in Solution and on Surfaces. *SIAM J. Sci. Comput.* 30, 3126–3149. doi: 10.1137/070692017

Kirk, M. M., Izu, L. T., Chen-Izu, Y., McCulle, S. L., Wier, W. G., Balke, C. W., et al. (2003). Role of the Transverse-Axial Tubule System in Generating Calcium Sparks and Calcium Transients in Rat Atrial Myocytes. *J. Physiol.* 547, 441–451. doi: 10.1113/jphysiol.2002.034355

Ko, C. Y., Liu, M. B., Song, Z., Qu, Z., and Weiss, J. N. (2017). Multiscale Determinants of Delayed Afterdepolarization Amplitude in Cardiac Tissue. *Biophys. J.* 112, 1949–1961. doi: 10.1016/j.bpj.2017.03.006

Koivumäki, J. T., Korhonen, T., and Tavi, P. (2011). Impact of Sarcoplasmic Reticulum Calcium Release on Calcium Dynamics and Action Potential Morphology in Human Atrial Myocytes: a Computational Study. *PLoS Comput. Biol.* 7:e1001067. doi: 10.1371/journal.pcbi.1001067

Laver, D. R., Kong, C. H. T., Imtiaz, M. S., and Cannell, M. B. (2013). Termination of calcium-induced calcium release by induction decay: an emergent property of stochastic channel gating and molecular scale architecture. *J. Mol. Cell. Cardiol.* 54, 98–100. doi: 10.1016/j.yjmcc.2012.10.009

Liu, M. B., de Lange, E., Garfinkel, A., Weiss, J. N., and Qu, Z. (2015). Delayed afterdepolarizations generate both triggers and a vulnerable substrate promoting reentry in cardiac tissue. *Heart Rhythm* 12, 2115–2124. doi: 10.1016/j.hrthm.2015.06.019

Liu, M. B., Ko, C. Y., Song, Z., Garfinkel, A., Weiss, J. N., and Qu, Z. (2016). A Dynamical Threshold for Cardiac Delayed Afterdepolarization-Mediated Triggered Activity. *Biophys. J.* 111, 2523–2533. doi: 10.1016/j.bpj.2016.10.009

Louch, W. E., Hake, J., Jølle, G. F., Mørk, H. K., Sjaastad, I., Lines, G. T., et al. (2010). Control of Ca2+ Release by Action Potential Configuration in Normal and Failing Murine Cardiomyocytes. *Biophys. J.* 99, 1377–1386. doi: 10.1016/j.bpj.2010.06.055

Lu, S., Michailova, A., Saucerman, J., Cheng, Y., Yu, Z., Kaiser, T., et al. (2009). Multi-Scale Modeling in Rodent Ventricular Myocytes: contributions of structural and functional heterogeneities to excitation-contraction coupling. *IEEE Eng. Med. Biol. Mag. Q. Mag. Eng. Med. Biol. Soc.* 28, 46–57. doi: 10.1109/MEMB.2009.931787

Lyon, A. R., MacLeod, K. T., Zhang, Y., Garcia, E., Kanda, G. K., Lab, M. J., et al. (2009). Loss of T-tubules and other changes to surface topography in ventricular myocytes from failing human and rat heart. *Proc. Natl. Acad. Sci. U. S. A.* 106, 6854–6859. doi: 10.1073/pnas.0809777106

Macquaide, N., Tuan, H.-T. M., Hotta, J., Sempels, W., Lenaerts, I., Holemans, P., et al. (2015). Ryanodine receptor cluster fragmentation and redistribution in persistent atrial fibrillation enhance calcium release. *Cardiovasc. Res.* 108, 387–398. doi: 10.1093/cvr/cvv231

Maleckar, M. M., Edwards, A. G., Louch, W. E., and Lines, G. T. (2017). Studying dyadic structure–function relationships: a review of current modeling approaches and new insights into Ca2+ (mis)handling. *Clin. Med. Insights Cardiol.* 11:1179546817698602. doi: 10.1177/1179546817698602

Maltsev, A. V., Maltsev, V. A., and Stern, M. D. (2017). Stabilization of diastolic calcium signal via calcium pump regulation of complex local calcium releases and transient decay in a computational model of cardiac pacemaker cell with individual release channels. *PLoS Comput. Biol.* 13:e1005675. doi: 10.1371/journal.pcbi.1005675

Maltsev, V. A., and Lakatta, E. G. (2013). Numerical models based on a minimal set of sarcolemmal electrogenic proteins and an intracellular Ca2+ clock generate robust, flexible, and energy-efficient cardiac pacemaking. *J. Mol. Cell. Cardiol.* 59, 181–195. doi: 10.1016/j.yjmcc.2013.03.004

Marchena, M., and Echebarria, B. (2018). Computational Model of Calcium Signaling in Cardiac Atrial Cells at the Submicron Scale. *Front. Physiol.* 9:1760. doi: 10.3389/fphys.2018.01760

Marchena, M., and Echebarria, B. (2020). Influence of the tubular network on the characteristics of calcium transients in cardiac myocytes. *PLoS One* 15:e0231056. doi: 10.1371/journal.pone.0231056

Marx, S. O., Gaburjakova, J., Gaburjakova, M., Henrikson, C., Ondrias, K., and Marks, A. R. (2001). Coupled Gating Between Cardiac Calcium Release Channels (Ryanodine Receptors). *Circ. Res.* 88, 1151–1158. doi: 10.1161/hh1101.091268

Mesa, M. H., van den Brink, J., Louch, W. E., McCabe, K. J., and Rangamani, P. (2021). Nanoscale organization of ryanodine receptor distribution and phosphorylation pattern determines the dynamics of calcium sparks. *bioRxiv* [Preprint] doi: 10.1101/2021.10.19.465028

Mori, Y., Fishman, G. I., and Peskin, C. S. (2008). Ephaptic conduction in a cardiac strand model with 3D electrodiffusion. *Proc. Natl. Acad. Sci. U. S. A.* 105, 6463–6468. doi: 10.1073/pnas.0801089105

Mukherjee, S., Thomas, N. L., and Williams, A. J. (2012). A mechanistic description of gating of the human cardiac ryanodine receptor in a regulated minimal environment. *J. Gen. Physiol.* 140, 139–158. doi: 10.1085/jgp.201110706

Muszkiewicz, A., Britton, O. J., Gemmell, P., Passini, E., Sánchez, C., Zhou, X., et al. (2016). Variability in cardiac electrophysiology: using experimentally-calibrated populations of models to move beyond the single virtual physiological human paradigm. *Prog. Biophys. Mol. Biol.* 120, 115–127. doi: 10.1016/j.pbiomolbio.2015.12.002

Nivala, M., de Lange, E., Rovetti, R., and Qu, Z. (2012a). Computational Modeling and Numerical Methods for Spatiotemporal Calcium Cycling in Ventricular Myocytes. *Front. Physiol.* 3:114. doi: 10.3389/fphys.2012.00114

Nivala, M., Ko, C. Y., Nivala, M., Weiss, J. N., and Qu, Z. (2012b). Criticality in intracellular calcium signaling in cardiac myocytes. *Biophys. J.* 102, 2433–2442. doi: 10.1016/j.bpj.2012.05.001

Nivala, M., Song, Z., Weiss, J. N., and Qu, Z. (2015). T-tubule disruption promotes calcium alternans in failing ventricular myocytes: mechanistic insights from computational modeling. *J. Mol. Cell. Cardiol.* 79, 32–41. doi: 10.1016/j.yjmcc.2014.10.018

Okada, J., Sugiura, S., Nishimura, S., and Hisada, T. (2005). Three-dimensional simulation of calcium waves and contraction in cardiomyocytes using the finite element method. *Am. J. Physiol.-Cell Physiol.* 288, C510–C522. doi: 10.1152/ajpcell.00261.2004

Pandey, V., Xie, L.-H., Qu, Z., and Song, Z. (2021). Mitochondrial Contributions in the Genesis of Delayed Afterdepolarizations in Ventricular Myocytes. *Front. Physiol.* 12:744023. doi: 10.3389/fphys.2021.744023

Park, S. H., Kim, A., An, J., Cho, H. S., and Kang, T. M. (2020). Nanoscale imaging of rat atrial myocytes by scanning ion conductance microscopy reveals heterogeneity of T-tubule openings and ultrastructure of the cell membrane. *Korean J. Physiol. Pharmacol.* 24, 529–543. doi: 10.4196/kjpp.2020.24.6.529

Passini, E., Britton, O. J., Lu, H. R., Rohrbacher, J., Hermans, A. N., Gallacher, D. J., et al. (2017). Human In Silico Drug Trials Demonstrate Higher Accuracy than Animal Models in Predicting Clinical Pro-Arrhythmic Cardiotoxicity. *Front. Physiol.* 8:668. doi: 10.3389/fphys.2017.00668

Pinali, C., Bennett, H., Davenport, J. B., Trafford, A. W., and Kitmitto, A. (2013). Three-dimensional reconstruction of cardiac sarcoplasmic reticulum reveals a continuous network linking transverse-tubules: this organization is perturbed in heart failure. *Circ. Res.* 113, 1219–1230. doi: 10.1161/CIRCRESAHA.113.301348

Pods, J., Schönke, J., and Bastian, P. (2013). Electrodiffusion Models of Neurons and Extracellular Space Using the Poisson-Nernst-Planck Equations—Numerical Simulation of the Intra- and Extracellular Potential for an Axon Model. *Biophys. J.* 105, 242–254. doi: 10.1016/j.bpj.2013.05.041

Protasi, F., Franzini-Armstrong, C., and Allen, P. D. (1998). Role of Ryanodine Receptors in the Assembly of Calcium Release Units in Skeletal Muscle. *J. Cell Biol.* 140, 831–842. doi: 10.1083/jcb.140.4.831

Qu, Z., Hu, G., Garfinkel, A., and Weiss, J. N. (2014). Nonlinear and stochastic dynamics in the heart. *Phys. Rep.* 543, 61–162. doi: 10.1016/j.physrep.2014.05.002

Qu, Z., Liu, M. B., and Nivala, M. (2016). A unified theory of calcium alternans in ventricular myocytes. *Sci. Rep.* 6:35625. doi: 10.1038/srep35625

Qu, Z., Shiferaw, Y., and Weiss, J. N. (2007). Nonlinear dynamics of cardiac excitation-contraction coupling: an iterated map study. *Phys. Rev. E Stat. Nonlin. Soft Matter Phys.* 75:011927. doi: 10.1103/PhysRevE.75.011927

Rajagopal, V., Bass, G., Ghosh, S., Hunt, H., Walker, C., Hanssen, E., et al. (2018). Creating a Structurally Realistic Finite Element Geometric Model of a Cardiomyocyte to Study the Role of Cellular Architecture in Cardiomyocyte Systems Biology. *JoVE J. Vis. Exp.* 134:e56817. doi: 10.3791/56817

Rajagopal, V., Bass, G., Walker, C. G., Crossman, D. J., Petzer, A., Hickey, A., et al. (2015). Examination of the Effects of Heterogeneous Organization of RyR Clusters, Myofibrils and Mitochondria on Ca2+ Release Patterns in Cardiomyocytes. *PLoS Comput. Biol.* 11:e1004417. doi: 10.1371/journal.pcbi.1004417

Rathinam, M., Petzold, L. R., Cao, Y., and Gillespie, D. T. (2003). Stiffness in stochastic chemically reacting systems: the implicit tau-leaping method. *J. Chem. Phys.* 119, 12784–12794. doi: 10.1063/1.1627296

Restrepo, J. G., Weiss, J. N., and Karma, A. (2008). Calsequestrin-mediated mechanism for cellular calcium transient alternans. *Biophys. J.* 95, 3767–3789. doi: 10.1529/biophysj.108.130419

Richards, M. A., Clarke, J. D., Saravanan, P., Voigt, N., Dobrev, D., Eisner, D. A., et al. (2011). Transverse tubules are a common feature in large mammalian atrial myocytes including human. *Am. J. Physiol. - Heart Circ. Physiol.* 301, H1996–H2005. doi: 10.1152/ajpheart.00284.2011

Romero, L., Alvarez-Lacalle, E., and Shiferaw, Y. (2019). Stochastic coupled map model of subcellular calcium cycling in cardiac cells. *Chaos Interdiscip. J. Nonlin. Sci.* 29:023125. doi: 10.1063/1.5063462

Rovetti, R., Das, K. K., Garfinkel, A., and Shiferaw, Y. (2007). Macroscopic consequences of calcium signaling in microdomains: a first-passage-time approach. *Phys. Rev. E Stat. Nonlin. Soft Matter Phys.* 76:051920. doi: 10.1103/PhysRevE.76.051920

Sato, D., Bartos, D. C., Ginsburg, K. S., and Bers, D. M. (2014). Depolarization of Cardiac Membrane Potential Synchronizes Calcium Sparks and Waves in Tissue. *Biophys. J.* 107, 1313–1317. doi: 10.1016/j.bpj.2014.07.053

Sato, D., and Bers, D. M. (2011). How Does Stochastic Ryanodine Receptor-Mediated Ca Leak Fail to Initiate a Ca Spark? *Biophys. J.* 101, 2370–2379. doi: 10.1016/j.bpj.2011.10.017

Sato, D., Bers, D. M., and Shiferaw, Y. (2013). Formation of spatially discordant alternans due to fluctuations and diffusion of calcium. *PLoS One* 8:e85365. doi: 10.1371/journal.pone.0085365

Sato, D., Despa, S., and Bers, D. M. (2012). Can the Sodium-Calcium Exchanger Initiate or Suppress Calcium Sparks in Cardiac Myocytes? *Biophys. J.* 102, L31–L33. doi: 10.1016/j.bpj.2012.03.051

Sato, D., Shannon, T. R., and Bers, D. M. (2016). Sarcoplasmic Reticulum Structure and Functional Properties that Promote Long-Lasting Calcium Sparks. *Biophys. J.* 110, 382–390. doi: 10.1016/j.bpj.2015.12.009

Sato, D., Uchinoumi, H., and Bers, D. M. (2021). Increasing SERCA function promotes initiation of calcium sparks and breakup of calcium waves. *J. Physiol.* 599, 3267–3278. doi: 10.1113/JP281579

Scardigli, M., Ferrantini, C., Crocini, C., Pavone, F. S., and Sacconi, L. (2018). Interplay Between Sub-Cellular Alterations of Calcium Release and T-Tubular Defects in Cardiac Diseases. *Front. Physiol.* 9:1474. doi: 10.3389/fphys.2018.01474

Scriven, D. R. L., Asghari, P., and Moore, E. D. W. (2013). Microarchitecture of the dyad. *Cardiovasc. Res.* 98, 169–176. doi: 10.1093/cvr/cvt025

Setterberg, I. E., Le, C., Frisk, M., Li, J., and Louch, W. E. (2021). The Physiology and Pathophysiology of T-Tubules in the Heart. *Front. Physiol.* 12:718404. doi: 10.3389/fphys.2021.718404

Shah, S. J., Aistrup, G. L., Gupta, D. K., O'Toole, M. J., Nahhas, A. F., Schuster, D., et al. (2014). Ultrastructural and cellular basis for the development of abnormal myocardial mechanics during the transition from hypertension to heart failure. *Am. J. Physiol. Heart Circ. Physiol.* 306, H88–H100. doi: 10.1152/ajpheart.00642.2013

Shannon, T. R., Wang, F., Puglisi, J., Weber, C., and Bers, D. M. (2004). A Mathematical Treatment of Integrated Ca Dynamics within the Ventricular Myocyte. *Biophys. J.* 87, 3351–3371. doi: 10.1529/biophysj.104.047449

Sheard, T. M. D., Hurley, M. E., Colyer, J., White, E., Norman, R., Pervolaraki, E., et al. (2019). Three-Dimensional and Chemical Mapping of Intracellular Signaling Nanodomains in Health and Disease with Enhanced Expansion Microscopy. *ACS Nano* 13, 2143–2157. doi: 10.1021/acsnano.8b08742

Shiferaw, Y., Aistrup, G. L., Louch, W. E., and Wasserstrom, J. A. (2020). Remodeling Promotes Proarrhythmic Disruption of Calcium Homeostasis in Failing Atrial Myocytes. *Biophys. J.* 118, 476–491. doi: 10.1016/j.bpj.2019.12.012

Shiferaw, Y., Aistrup, G. L., and Wasserstrom, J. A. (2017). Mechanism for Triggered Waves in Atrial Myocytes. *Biophys. J.* 113, 656–670. doi: 10.1016/j.bpj.2017.06.026

Shiferaw, Y., Aistrup, G. L., and Wasserstrom, J. A. (2018). Synchronization of Triggered Waves in Atrial Tissue. *Biophys. J.* 115, 1130–1141. doi: 10.1016/j.bpj.2018.08.015

Shiferaw, Y., Watanabe, M. A., Garfinkel, A., Weiss, J. N., and Karma, A. (2003). Model of intracellular calcium cycling in ventricular myocytes. *Biophys. J.* 85, 3666–3686. doi: 10.1016/S0006-3495(03)74784-5

Singh, J. K., Barsegyan, V., Bassi, N., Marszalec, W., Tai, S., Mothkur, S., et al. (2017). T-tubule remodeling and increased heterogeneity of calcium release during the progression to heart failure in intact rat ventricle. *Physiol. Rep.* 5:e13540. doi: 10.14814/phy2.13540

Sobie, E. A., Dilly, K. W., dos Santos Cruz, J., Lederer, W. J., and Jafri, M. S. (2002). Termination of cardiac Ca(2+) sparks: an investigative mathematical model of calcium-induced calcium release. *Biophys. J.* 83, 59–78. doi: 10.1016/s0006-3495(02)75149-7

Sobie, E. A., Song, L.-S., and Lederer, W. (2005). Local recovery of Ca2+ release in rat ventricular myocytes. *J. Physiol.* 565, 441–447. doi: 10.1113/jphysiol.2005.086496

Song, Z., Karma, A., Weiss, J. N., and Qu, Z. (2016). Long-Lasting Sparks: multi-Metastability and Release Competition in the Calcium Release Unit Network. *PLoS Comput. Biol.* 12:e1004671. doi: 10.1371/journal.pcbi.1004671

Song, Z., Ko, C. Y., Nivala, M., Weiss, J. N., and Qu, Z. (2015). Calcium-voltage coupling in the genesis of early and delayed afterdepolarizations in cardiac myocytes. *Biophys. J.* 108, 1908–1921. doi: 10.1016/j.bpj.2015.03.011

Song, Z., Liu, M. B., and Qu, Z. (2018). Transverse tubular network structures in the genesis of intracellular calcium alternans and triggered activity in cardiac cells. *J. Mol. Cell. Cardiol.* 114, 288–299. doi: 10.1016/j.yjmcc.2017.12.003

Song, Z., Qu, Z., and Karma, A. (2017). Stochastic initiation and termination of calcium-mediated triggered activity in cardiac myocytes. *Proc. Natl. Acad. Sci. U. S. A.* 114, E270–E279. doi: 10.1073/pnas.1614051114

Song, Z., Xie, L.-H., Weiss, J. N., and Qu, Z. (2019). A Spatiotemporal Ventricular Myocyte Model Incorporating Mitochondrial Calcium Cycling. *Biophys. J.* 117, 2349–2360. doi: 10.1016/j.bpj.2019.09.005

Stern, M. D., Song, L.-S., Cheng, H., Sham, J. S. K., Yang, H. T., Boheler, K. R., et al. (1999). Local Control Models of Cardiac Excitation–Contraction Coupling. *J. Gen. Physiol.* 113, 469–489.

Sutanto, H., Lyon, A., Lumens, J., Schotten, U., Dobrev, D., and Heijman, J. (2020). Cardiomyocyte calcium handling in health and disease: insights from in vitro and in silico studies. *Prog. Biophys. Mol. Biol.* 157, 54–75. doi: 10.1016/j.pbiomolbio.2020.02.008

Sutanto, H., van Sloun, B., Schönleitner, P., van Zandvoort, M. A. M. J., Antoons, G., and Heijman, J. (2018). The Subcellular Distribution of Ryanodine Receptors and L-Type Ca2+ Channels Modulates Ca2+-Transient Properties and Spontaneous Ca2+-Release Events in Atrial Cardiomyocytes. *Front. Physiol.* 9:1108. doi: 10.3389/fphys.2018.01108

Theakston, E., Walker, C., O'Sullivan, M., and Rajagopal, V. (2010). Stochastic modelling of cardiac cell structure. *Annu. Int. Conf. IEEE Eng. Med. Biol. Soc.* 2010, 3257–3260. doi: 10.1109/IEMBS.2010.5627229

Trafford, A. W., Clarke, J. D., Richards, M. A., Eisner, D. A., and Dibb, K. M. (2013). Calcium signalling microdomains and the t-tubular system in atrial mycoytes: potential roles in cardiac disease and arrhythmias. *Cardiovasc. Res.* 98, 192–203. doi: 10.1093/cvr/cvt018

Vagos, M., van Herck, I. G. M., Sundnes, J., Arevalo, H. J., Edwards, A. G., and Koivumäki, J. T. (2018). Computational Modeling of Electrophysiology and Pharmacotherapy of Atrial Fibrillation: recent Advances and Future Challenges. *Front. Physiol.* 9:1221. doi: 10.3389/fphys.2018.01221

Vagos, M. R., Arevalo, H., Heijman, J., Schotten, U., and Sundnes, J. (2020). A Novel Computational Model of the Rabbit Atrial Cardiomyocyte With Spatial Calcium Dynamics. *Front. Physiol.* 11:556156. doi: 10.3389/fphys.2020.556156

Vagos, M. R., Arevalo, H., Heijman, J., Schotten, U., and Sundnes, J. (2021). A Computational Study of the Effects of Tachycardia-Induced Remodeling on Calcium Wave Propagation in Rabbit Atrial Myocytes. *Front. Physiol.* 12:651428. doi: 10.3389/fphys.2021.651428

Voigt, N., Heijman, J., Wang, Q., Chiang, D. Y., Li, N., Karck, M., et al. (2014). Cellular and molecular mechanisms of atrial arrhythmogenesis in patients with paroxysmal atrial fibrillation. *Circulation* 129, 145–156. doi: 10.1161/CIRCULATIONAHA.113.006641

Wagner, E., Lauterbach, M. A., Kohl, T., Westphal, V., Williams, G. S. B., Steinbrecher, J. H., et al. (2012). Stimulated Emission Depletion Live-Cell Super-Resolution Imaging Shows Proliferative Remodeling of T-Tubule Membrane Structures After Myocardial Infarction. *Circ. Res.* 111, 402–414. doi: 10.1161/CIRCRESAHA.112.274530

Walker, M. A., Gurev, V., Rice, J. J., Greenstein, J. L., and Winslow, R. L. (2017). Estimating the probabilities of rare arrhythmic events in multiscale computational models of cardiac cells and tissue. *PLoS Comput. Biol.* 13:e1005783. doi: 10.1371/journal.pcbi.1005783

Walker, M. A., Williams, G. S. B., Kohl, T., Lehnart, S. E., Jafri, M. S., Greenstein, J. L., et al. (2014). Superresolution Modeling of Calcium Release in the Heart. *Biophys. J.* 107, 3018–3029. doi: 10.1016/j.bpj.2014.11.003

Wang, X., Weinberg, S. H., Hao, Y., Sobie, E. A., and Smith, G. D. (2015). Calcium homeostasis in a local/global whole cell model of permeabilized ventricular myocytes with a Langevin description of stochastic calcium release. *Am. J. Physiol.-Heart Circ. Physiol.* 308, H510–H523. doi: 10.1152/ajpheart.00296.2014

Wei, J., Yao, J., Belke, D., Guo, W., Zhong, X., Sun, B., et al. (2021). Ca2+-CaM Dependent Inactivation of RyR2 Underlies Ca2+ Alternans in Intact Heart. *Circ. Res.* 128, e63–e83. doi: 10.1161/CIRCRESAHA.120.318429

Williams, G. S. B., Chikando, A. C., Tuan, H.-T. M., Sobie, E. A., Lederer, W. J., and Jafri, M. S. (2011). Dynamics of calcium sparks and calcium leak in the heart. *Biophys. J.* 101, 1287–1296. doi: 10.1016/j.bpj.2011.07.021

Williams, G. S. B., Huertas, M. A., Sobie, E. A., Jafri, M. S., and Smith, G. D. (2007). A Probability Density Approach to Modeling Local Control of Calcium-Induced Calcium Release in Cardiac Myocytes. *Biophys. J.* 92, 2311–2328. doi: 10.1529/biophysj.106.099861

Williams, G. S. B., Huertas, M. A., Sobie, E. A., Jafri, M. S., and Smith, G. D. (2008). Moment Closure for Local Control Models of Calcium-Induced Calcium Release in Cardiac Myocytes. *Biophys. J.* 95, 1689–1703. doi: 10.1529/biophysj.107.125948

Xie, A., Song, Z., Liu, H., Zhou, A., Shi, G., Wang, Q., et al. (2018). Mitochondrial Ca2+ Influx Contributes to Arrhythmic Risk in Nonischemic Cardiomyopathy. *J. Am. Heart Assoc.* 7:e007805. doi: 10.1161/JAHA.117.007805

Xie, Y., Sato, D., Garfinkel, A., Qu, Z., and Weiss, J. N. (2010). So little source, so much sink: requirements for afterdepolarizations to propagate in tissue. *Biophys. J.* 99, 1408–1415. doi: 10.1016/j.bpj.2010.06.042

Yaniv, Y., Lakatta, E. G., and Maltsev, V. A. (2015). From two competing oscillators to one coupled-clock pacemaker cell system. *Front. Physiol.* 6:28. doi: 10.3389/fphys.2015.00028

Zahradníková, A., Zahradník, I., Györke, I., and Györke, S. (1999). Rapid Activation of the Cardiac Ryanodine Receptor by Submillisecond Calcium Stimuli. *J. Gen. Physiol.* 114, 787–798. doi: 10.1085/jgp.114.6.787

Conflict of Interest: The authors declare that the research was conducted in the absence of any commercial or financial relationships that could be construed as a potential conflict of interest.

frontiers in Physiology

ORIGINAL RESEARCH
published: 11 March 2022
doi: 10.3389/fphys.2022.834220

Aldosterone-Induced Sarco/Endoplasmic Reticulum Ca^{2+} Pump Upregulation Counterbalances $Ca_v1.2$-Mediated Ca^{2+} Influx in Mesenteric Arteries

Rogelio Salazar-Enciso[1,2], Agustín Guerrero-Hernández[1], Ana M. Gómez[2], Jean-Pierre Benitah[2] and Angélica Rueda[1]*

[1] Departamento de Bioquímica, Centro de Investigación y de Estudios Avanzados del IPN, Mexico City, Mexico, [2] Signaling and Cardiovascular Pathophysiology - UMR-S 1180, Inserm, Université Paris-Saclay, Châtenay-Malabry, France

OPEN ACCESS

Edited by:
Manuel F. Navedo,
University of California, Davis,
United States

Reviewed by:
Thomas J. Heppner,
University of Vermont, United States
Sean Michael Wilson,
Loma Linda University, United States

***Correspondence:**
Angélica Rueda
arueda@cinvestav.mx

Specialty section:
This article was submitted to
Vascular Physiology,
a section of the journal
Frontiers in Physiology

Received: 13 December 2021
Accepted: 08 February 2022
Published: 11 March 2022

Citation:
Salazar-Enciso R,
Guerrero-Hernández A, Gómez AM,
Benitah J-P and Rueda A (2022)
Aldosterone-Induced
Sarco/Endoplasmic Reticulum Ca^{2+}
Pump Upregulation Counterbalances
$Ca_v1.2$-Mediated Ca^{2+} Influx
in Mesenteric Arteries.
Front. Physiol. 13:834220.
doi: 10.3389/fphys.2022.834220

In mesenteric arteries (MAs), aldosterone (ALDO) binds to the endogenous mineralocorticoid receptor (MR) and increases the expression of the voltage-gated L-type $Ca_v1.2$ channel, an essential ion channel for vascular contraction, sarcoplasmic reticulum (SR) Ca^{2+} store refilling, and Ca^{2+} spark generation. In mesenteric artery smooth muscle cells (MASMCs), Ca^{2+} influx through $Ca_v1.2$ is the indirect mechanism for triggering Ca^{2+} sparks. This process is facilitated by plasma membrane-sarcoplasmic reticulum (PM-SR) nanojunctions that drive Ca^{2+} from the extracellular space into the SR via Sarco/Endoplasmic Reticulum Ca^{2+} (SERCA) pump. Ca^{2+} sparks produced by clusters of Ryanodine receptors (RyRs) at PM-SR nanodomains, decrease contractility by activating large-conductance Ca^{2+}-activated K^+ channels (BK_{Ca} channels), which generate spontaneous transient outward currents (STOCs). Altogether, $Ca_v1.2$, SERCA pump, RyRs, and BK_{Ca} channels work as a functional unit at the PM-SR nanodomain, regulating intracellular Ca^{2+} and vascular function. However, the effect of the ALDO/MR signaling pathway on this functional unit has not been completely explored. Our results show that short-term exposure to ALDO (10 nM, 24 h) increased the expression of $Ca_v1.2$ in rat MAs. The depolarization-induced Ca^{2+} entry increased SR Ca^{2+} load, and the frequencies of both Ca^{2+} sparks and STOCs, while $[Ca^{2+}]_{cyt}$ and vasoconstriction remained unaltered in Aldo-treated MAs. ALDO treatment significantly increased the mRNA and protein expression levels of the SERCA pump, which counterbalanced the augmented $Ca_v1.2$-mediated Ca^{2+} influx at the PM-SR nanodomain, increasing SR Ca^{2+} content, Ca^{2+} spark and STOC frequencies, and opposing to hyperpolarization-induced vasoconstriction while enhancing Acetylcholine-mediated vasorelaxation. This work provides novel evidence for short-term ALDO-induced upregulation of the functional unit comprising Ca$_V$1.2, SERCA2 pump, RyRs, and BK$_{Ca}$ channels; in which the SERCA pump buffers ALDO-induced upregulation of Ca^{2+} entry at the superficial SR-PM nanodomain of MASMCs, preventing ALDO-triggered depolarization-induced vasoconstriction and enhancing vasodilation. Pathological conditions that lead to SERCA pump downregulation, for instance, chronic exposure to ALDO, might favor the development of ALDO/MR-mediated augmented vasoconstriction of mesenteric arteries.

Keywords: calcium sparks, aldosterone (ALDO), ryanodine receptor, STOCs, Ca$_V$1.2 Ca^{2+} channel, SERCA pump, mesenteric artery (MA), vascular smooth muscle cell

INTRODUCTION

Aldosterone (ALDO) is a steroid hormone that regulates the balance of water and electrolytes in the body and acts primarily through the mineralocorticoid receptor (MR), a transcription factor activated by ligand (Mangelsdorf et al., 1995). Clinical trials have evidenced the participation of MR in blood pressure (BP) regulation by showing the beneficial effects of MR blockers in the treatment of high BP; including mild, moderate and resistant hypertension (Weinberger et al., 2002; Acelajado et al., 2019). The MR is mainly expressed in kidney epithelial cells, but it is also found in several vascular tissues, including small, resistance-sized (150–300 μm in lumen diameter) mesenteric arteries (MAs) (Lombès et al., 1992; Salazar-Enciso et al., 2018), which supply blood to the gastrointestinal tract and contribute to the hypertensive process under pathological exposure to ALDO (Schiffrin, 1992). Whereas, MR, aldosterone synthase, and 11-beta hydroxysteroid dehydrogenase type 2 (11-BHSD2), key proteins of the local ALDO system, are expressed in rat MAs (Takeda et al., 1993, 1997); the impact of the ALDO/MR signaling pathway on Ca^{2+} handling proteins in mesenteric artery smooth muscle cells (MASMCs) has not been fully evaluated.

In the heart, aorta, coronary and MAs, the activation of the ALDO/MR signaling pathway increases voltage-gated L-type Ca$_V$1.2 channel (LTCCs) expression (Bénitah and Vassort, 1999; Lalevée et al., 2005; Mesquita et al., 2018), resulting in enhanced vascular contraction of coronary arteries (Mesquita et al., 2018). In experimental animal models of chronic hypertension such as the spontaneously hypertensive rat (SHR), LTCCs are upregulated, Ca^{2+} influx is increased, vascular reactivity is enhanced, and receptor-stimulated contractile responses are higher than in arteries of control rats (Cox and Lozinskaya, 1995; Matsuda et al., 1997; Pratt et al., 2002; Xavier et al., 2008). However, it has been also shown that when LTCCs are activated via K$^+$-mediated membrane depolarization maneuvers, vasoconstriction responses are unaffected in MAs of SHR and Wistar-Kyoto rats treated with ALDO (Xavier et al., 2008); in deoxycorticosterone (DOCA)-salt hypertensive rats (Suzuki et al., 1994); or in the young transgenic mouse with smooth muscle cell (SMC)-specific MR deficiency (SMC-MR-KO mouse) (McCurley et al., 2012); and in cerebral arteries of ALDO-treated mice (Chrissobolis et al., 2014). These studies support the notion that in some types of vascular tissues, the activation of the ALDO/MR signaling pathway enhances receptor-mediated vasoconstriction responses (for instance, α-adrenoceptor-mediated contraction) but not vasoconstriction responses induced by KCl (Suzuki et al., 1994; Xavier et al., 2008; Chrissobolis et al., 2014); and the molecular mechanisms that underlie this discrepancy are elusive.

L-type voltage-dependent Ca^{2+} channels are the primary route of Ca^{2+} entry in the vasculature (Ghosh et al., 2017). For instance, Ca^{2+} entry via LTCCs is the principal mediator of myogenic response, vascular contraction, sarcoplasmic reticulum (SR) Ca^{2+} refilling, Ca^{2+} spark generation and blood pressure in resistance-sized MAs (Nelson and Worley, 1989; Moosmang et al., 2003; Ghosh et al., 2017; Fan et al., 2018). Ca^{2+} entering the cytoplasm is captured to the SR Ca^{2+} stores by the SERCA pump at the superficial or junctional SR, which occupies a vast subcellular area with multiple plasma membrane-sarcoplasmic reticulum (PM-SR) junctions in vascular smooth muscle cells (VSMCs). In fact, LTCC-mediated subcellular Ca^{2+} signals, named Ca^{2+} sparklets, coincide with junctional SR expressing SERCA pumps and Ryanodine receptors (RyRs), demonstrating the close association of these proteins in the subplasmalemmal nanodomain (Takeda et al., 2011). In addition, the SERCA pump tightly regulates Ca^{2+} influx and as a result, indirectly controls Ca^{2+} spark ignition (Chen and van Breemen, 1993; Van Breemen et al., 1995; Essin and Gollasch, 2009). Ca^{2+} sparks, which are local Ca^{2+} signals produced by the simultaneous activation of clusters of Ca^{2+} release channels/Ryanodine receptors (RyRs), are involved in vasorelaxation (Nelson et al., 1995; Essin and Gollasch, 2009; Krishnamoorthy et al., 2014). Ca^{2+} sparks activate large-conductance Ca^{2+}-activated K$^+$ channels (BK$_{Ca}$ channels) that generate spontaneous transient

---

Abbreviations: ALDO, aldosterone; MA, mesenteric arteries; MASMC, mesenteric artery smooth muscle cell; LTCC, L-type voltage-dependent Ca^{2+} channels; SMC, smooth muscle cell; ACh, acetylcholine; ALDO, aldosterone; BK$_{Ca}$ channel, large-conductance Ca^{2+}-activated K$^+$ channel; CASQ2, calsequestrin-2; DMEM, Dulbecco's Modified Eagle Medium; FKBP12.6, 12.6 kDa FK506-binding protein; GAPDH, glyceraldehyde-3-phosphate dehydrogenase; LTCC, voltage-gated L-type Ca$_V$1.2 channel; MA, mesenteric artery; MASMC, mesenteric artery smooth muscle cell; MR, mineralocorticoid receptor; Nif, Nifedipine; *Orai1*, calcium release-activated calcium channel protein 1; PM-SR, plasma membrane-sarcoplasmic reticulum; PSS, physiological saline solution; RyR, ryanodine receptor; *Rpl32*, 60S ribosomal protein L32; *sm22*, smooth muscle protein 22-alpha; SERCA, Sarco/Endoplasmic reticulum Ca^{2+} pump; *Sgk1*, serum/glucocorticoid regulated kinase 1; SMC, smooth muscle cell; *Stim1*, stromal interaction molecule 1; SOCE, store-operated calcium entry; STOC, spontaneous transient outward current; TGN, thapsigargin; VSMC, vascular smooth muscle cell; *Ywhaz*, 14-3-3 protein zeta/delta; 11-BHSD2, 11-beta-hydroxysteroid dehydrogenase type 2.

outward currents (STOCs) (Nelson et al., 1995; Pérez et al., 1999; Essin and Gollasch, 2009). STOCs have a key role in the control of arterial myogenic tone by shifting the plasma membrane potential toward less positive values (which limits Ca^{2+} influx through LTCCs), diminishing global cytoplasmic Ca^{2+} concentration ($[Ca^{2+}]_{cyt}$), and opposing vasoconstriction (Ganitkevich and Isenberg, 1990; Krishnamoorthy et al., 2014). Therefore, altogether $Ca_v1.2$, SERCA2 pump, RyRs, and BK_{Ca} channels comprise a functional unit at the PM-SR nanodomain that regulates vascular function favoring vasorelaxation (Jaggar et al., 1998; Essin et al., 2007; Essin and Gollasch, 2009; Van Breemen et al., 2013).

Accessory proteins of RyRs (for instance, FKBP12.6, sorcin, and calsequestrin-2) (Wang et al., 2004; Rueda et al., 2006; Esfandiarei et al., 2013), might also participate in regulating this functional unit, but whether ALDO treatment alters their expression and activity in MAs is unknown.

In this work, we determined the effect of a short-term (24 h) exposure to aldosterone (ALDO) in the expression and activity of $Ca_v1.2$, SERCA2 pump, RyR, and BK_{Ca} channels, proteins that regulate intracellular Ca^{2+} handling and vascular function of mesenteric arteries.

MATERIALS AND METHODS

All procedures were performed according to the ethical guidelines of the Mexican Official Norm (NOM-062-ZOO-1999) and the National Institutes of Health Guide for the Care and Use of Laboratory Animals (NIH publication updated in 2011). The animal protocol was approved by the Institutional Bioethical Committee for Care and Handling of Laboratory Animals at the Cinvestav-IPN (approved CICUAL Protocol No. 0100-14). Unless specified, all reagents were purchased from Sigma–Aldrich Quimica, S. de RL. de C.V., Toluca, Mexico.

Dissection of Mesenteric Arteries and Aldosterone Treatment

Twelve-week-old male Wistar rats (250–300 g of body weight) were anesthetized by intraperitoneal injection of sodium pentobarbital solution (100 mg/Kg of body weight. Pisabental® PISA agropecuaria S.A. de C.V. Tula, Hidalgo, Mexico). To rule out the effects of chronic ALDO-mediated maladaptive vessel changes, and to avoid unsought Angiotensin II-induced vascular MR activation (Jaffe and Mendelsohn, 2005); MAs were isolated and *ex vivo* exposed to 10 nM ALDO for 24 h, as previously described (Mesquita et al., 2018). Briefly, third-order, resistance-sized MAs were dissected under the microscope in ice-cold HEPES-buffered dissection solution (in mM: 80 Na-Glutamate, 55 NaCl, 6 KCl, 2 $MgCl_2$, 10 glucose, 10 HEPES; pH 7.4 with NaOH). Arteries were cleaned of fat and connective tissue and transferred to free-serum Dulbecco's Modified Eagle Medium (DMEM, Gibco^{TM} Cat# 11885084, Thermo Fisher Scientific Inc., Waltham, MA, United States) supplemented with penicillin and streptomycin as previously described (Mesquita et al., 2018). Artery segments were cultured in a humidified atmosphere of 5% CO_2 at 37°C for 24 h in the presence of 10 nM aldosterone (ALDO group) or in its absence (control group). After incubation, MAs were used for vascular reactivity experiments or stored at −80°C for Western Blots and real-time qPCR experiments.

Vascular Reactivity Assays

Vascular reactivity was assessed in third-order, resistance-sized MAs using a wire myograph for small vessels (Danish Myotechnology, Aarhus, Denmark) as previously described (Mesquita et al., 2018) with some modifications. After treatment, MAs were cut into 1.5–2.0 mm rings, cannulated with two 40 μm diameter stainless steel wires and mounted in an organ bath, warmed at 37°C with physiological saline solution (PSS) containing (in mM): 119 NaCl, 4.7 KCl, 2.5 $CaCl_2$, 1.17 $MgSO_4$, 1.18 KH_2PO_4, 25 $NaHCO_3$, 11 glucose and continuously gassed with carbogen (95% O_2, 5% CO_2) to maintain pH at 7.4. The MA rings were stabilized at a tension equivalent to that generated at 0.9× the diameter of the vessel at 100 mmHg for 45 min before experimentation. To determine the ring viability and achieve the maximal contractile response, MA rings were challenged with 60 mM KCl-containing PSS solution (equimolar substitution with NaCl to maintain constant ionic strength) twice before the beginning of concentration-response curves (KCl, from 10 to 60 mM). Endothelium integrity was tested using an endothelium-dependent agonist, Acetylcholine (ACh). The vasorelaxation response was determined by concentration-response curves (ACh, from 10^{-9} to 10^{-5} M) in pre-contracted MA rings with 60 mM KCl. Each vasoconstriction or vasorelaxation experiment was performed in duplicate, with the mean used as a single experimental value. Data are shown as the percentage of maximal contractile response elicited by 60 mM KCl-containing solution, which was considered 100%.

Preparation of Mesenteric Artery Homogenates, Sodium Dodecyl Sulfate-Polyacrylamyde Gel Electrophoresis and Immunoblot Analyses

Protein expression levels were assessed by immunoblotting as previously reported (Rueda et al., 2013; Mesquita et al., 2018) with some modifications. Briefly, 3–4 MA segments pooled from three rats were pulverized in liquid N_2 and homogenized on ice with a glass tissue grinder (Potter-Elvehjem) containing 200 μl cold homogenization buffer (composition in mM: 20 HEPES, 20 NaF, 300 sucrose, plus 0.5% sodium deoxycholate, and 0.1% SDS, pH 7.2 with NaOH) supplemented with protease inhibitors (1 μg/ml aprotinin, 500 μM benzamidine, 12 μM leupeptin, 100 μM PMSF). Homogenates were centrifuged at 2,000 × *g* for 10 min at 4°C and the supernatant was collected. Protein concentration was determined by the Bradford method. Supernatants were fractionated on 4–12% discontinuous gradient SDS-PAGE gel (20 μg of protein per well, for 2 h at 90 V). Separated proteins were transferred onto nitrocellulose or PVDF membrane for 2 h, 100 V at 4°C and blocked from non-specific binding with 5% non-fat dried milk in phosphate buffered saline-Tween 20 (0.1%) (PBS-T) for 1 h, before the incubation with commercial primary antibodies previously used at indicated publications, against $Ca_v1.2$ (1:200, Cat# AB10515, Millipore, Merck KGaA, Darmstadt, Germany) (Mesquita et al., 2018); SERCA2 pump (1:4,000, Cat# ab2861, Abcam, Cambridge, MA, United States) (Romero-García et al., 2020); Ryanodine receptor (RyR, 1:5000, Cat# ab2868, Abcam, Cambridge, MA, United States) (Rueda et al., 2006); calsequestrin (CSQ2, 1:4,000, Cat# ab108289, Abcam, Cambridge, MA, United States) (de Alba-Aguayo et al., 2017); sorcin (1:1,000, a kind gift from Héctor H. Valdivia laboratory, University of Wisconsin, Madison, WI, United States) (Rueda et al., 2006); FKBP12.6 (1:2,000, Cat# sc-376135, Santa Cruz Biotechnology, Inc., Dallas, TX, United States) (Gómez et al., 2009); MR (1:200; Cat# MRN2 2B7, DSHB, University of Iowa, Iowa City, IA, United States) (Gomez-Sanchez et al., 2006); BK_{Ca} α subunit (1:200, Cat# APC-009, Alomone Labs, Jerusalem, Israel) (Rueda et al., 2013), BK_{Ca} β1 subunit (1:5000, Cat# APC-036, Alomone Labs, Jerusalem, Israel) (Rueda et al., 2013), Orai1 (1:200, Cat# O8264, Sigma–Aldrich Química, S.L. Toluca, Mexico) (Bartoli et al., 2020) and GAPDH (1:100,000 Cat# AM4300, Ambion®, Thermo Fisher Scientific Inc., Waltham, MA, United States) (Romero-García et al., 2020) for 2 h at room temperature (RT). Membranes were incubated for 1 h at 37°C with horseradish peroxidase-conjugated anti-rabbit y/or anti-mouse in PBS-T with 1% non-fat dried milk. Signal was detected by chemiluminescence on radiograph film. The density of immunoreactive bands was measured on KODAK Image Station. GAPDH was used as loading control.

Total RNA Isolation and Real-Time Quantitative Polymerase Chain Reaction

Total RNA was extracted from pools of MAs from 3 to 4 animals by TRIzol reagent® according to the manufacturer's protocol. Total RNA was digested for 20 min at 37°C with 0.5 μL DNase (Roche, Mannheim, Germany). The reverse transcription was performed with Superscript II Reverse Transcriptase KIT (Invitrogen). The resulting DNA samples were amplified by real-time qPCR using the QuantiTect SYBR ®Green PCR Kits (QIAGEN) in a Rotor-Gene cycler (Corbett Research, Sydney, NSW, Australia). mRNA levels were normalized to the geometric mean of three housekeeping genes, 60S ribosomal protein L32 (*Rpl32*), 14-3-3 protein zeta/delta (*Ywhaz*), and transgelin (*Sm22*) (Mesquita et al., 2018). All samples were quantified in triplicate. The values were expressed as a relative expression using the Pfaffl equation (Pfaffl, 2001). The specific primers sequences are listed in **Table 1**.

Mesenteric Artery Smooth Muscle Cell Isolation

Single smooth muscle cells from mesenteric arteries (MASMCs) were enzymatically isolated following as previously described (Rueda et al., 2013) with some modifications. Briefly, MAs were cut into small segments and transferred to a 1-ml aliquot of PSS containing (in mg/ml): 1 papain, 1 bovine serum albumin (BSA), 1 dithiothreitol for 16 min at 37°C. The digested tissue was transferred to a 1 ml PSS supplemented with collagenase type F (1 mg/ml) plus 100 μM $CaCl_2$ for 8 min at 37°C. The digestion was stopped by three washes with cold PSS. Individual cells were dissociated from vessels by gentle trituration with a fire polish glass pipette. The resulting cell suspension was stored at 4°C for up 1 h and was used on the same day. Only long, smooth, and optically refractive cells were used.

Cytoplasmic Ca^{2+} Concentration Measurements in Single Mesenteric Artery Smooth Muscle Cells

The global cytoplasmic Ca^{2+} concentration ($[Ca^{2+}]_{cyt}$) and the amplitude of caffeine-induced Ca^{2+} transients were estimated as previously described (Rueda et al., 2002) with some modifications. Briefly, isolated MASMCs were loaded with 8 μM Fura 2-AM in 20 mM K^+-physiological saline solution (PSS-20K, composition in mM: 122 NaCl, 20 KCl, 2 $CaCl_2$, 1 $MgCl_2$, 10 glucose, 10 HEPES, pH 7.4 with NaOH) for 25 min at RT and washed. An aliquot of 20 μL of Fura 2-loaded cells was placed in a 1-mL-volume recording chamber (homemade) filled with PSS-20K at RT. Cells were allowed to adhere to the chamber's glass bottom for at least 5 min. Fura-2 fluorescence excitation ratios (F_{340}/F_{380}) were determined in individual cells each 50 ms within a 100-μm^2 recording window in an inverted microscope (Nikon Diaphot, Japan) coupled to a PTI microfluorometry system (Ratio-Master^{TM} PTI Technologies Inc., South Brunswick, NJ, United States). A single and brief pulse (10 s) of 10 mM caffeine (Caff) was locally applied by a pneumatic pump (PV830 PicoPump, WPI, Sarasota, FL, United States) using a TW100F-4 borosilicate micropipette placed above the cell. Data acquisition and analyses were performed in FeliX32 software (PTI Technologies Inc., South Brunswick, NJ, United States). The Fura-2 fluorescence ratio values (F_{340}/F_{380}) were converted to $[Ca^{2+}]$ with the Grynkiewicz equation: $[Ca^{2+}] = K_d{*}\beta\ (R-R_{min}/R_{max}-R)$ (Grynkiewicz et al., 1985); where R is the ratio (F_{340}/F_{380}) after background subtraction. Values of 0.21, 6.25, and 9.7 obtained from Fura-2 *in situ* calibration were used for R_{min}, R_{max}, and β, respectively; R_{min} and R_{max} were obtained in the presence of 2 mM EGTA and 2.5 mM extracellular Ca^{2+}, respectively. K_d used was 282 nM.

Determination of Ca^{2+} Influx

Fluo 4-loaded MASMCs were kept in a Na^+ and Ca^{2+} free solution (in mM: 136 LiCl, 6 KCl, 2 $MgCl_2$, 10 glucose, 10 HEPES, 1 EGTA; pH 7.4 with LiOH), and incubated with either thapsigargin (TGN, 100 nM) or Nifedipine (1 μM) for 10 min at RT. Subsequently, cells were perfused with a Na^+ free solution containing 1.8 mM Ca^{2+}. Changes in cytoplasmic Ca^{2+} were recorded with a laser scanning confocal microscope (Zeiss, LSM 700) equipped with an ×63 oil immersion objective (N.A. 1.2). Fluo-4 was excited at 488 nm with a diode laser of 488 nm (5% intensity), and emitted light was directed onto a main dichroic beam splitter (MDBS) to separate the emission from the excitation light. The emitted light was diverted to a secondary dichroic (VSD) beam splitter which in combination with a long pass filter (LP515) allowed the collection of light by the photomultiplier (PMT) above 510 nm. After subtracting background fluorescence (calculated outside of the cell), Fluo 4 fluorescence signals were normalized by dividing the fluorescence intensity of each pixel (F) by the average basal fluorescence intensity inside the cell (F_0). Fluo 4 fluorescence signals corresponding to the response after the reintroduction of external Ca^{2+} were reported as $\Delta F/F_0$.

Ca^{2+} Sparks Recordings

The local Ca^{2+} release events were recorded as previously described (Rueda et al., 2013) with some modifications. Intact MA segments were loaded with the Ca^{2+} indicator Fluo 4-AM (10 μM final concentration, 40 min) prepared in PSS-20K. The MA segments were allowed to adhere to the bottom of a glass coverslip in a perfusion chamber and were perfused with PSS-20K at RT. Ca^{2+} sparks were recorded with a laser scanning confocal microscope (Zeiss, LSM 700, Carl Zeiss de México, S.A. de C.V.) equipped with an ×63 oil immersion objective (N.A. 1.2) in *line scan* mode (five images per cell of 1000 lines each, at speed of 1.92 ms/line). Fluo-4 was excited at 488 nm with a diode laser (3% intensity) and emitted light was directed onto a MDBS to separate the emission from the excitation light. The emitted light was diverted to a VSD beam splitter which in combination with a LP515 allowed the collection of light by the PMT above 510 nm. Images of Ca^{2+} sparks were normalized by dividing the fluorescence intensity of each pixel (F) by the average basal fluorescence intensity (F_0) inside the cell to generate an F/F_0 image. Ca^{2+} spark frequency was reported as the number of events recorded per cell in five *line-scan* images. Ca^{2+} spark properties of amplitude (F/F_0), duration (FDHM, full duration at half maximum, in ms), and width (FWHM, full width at half maximum, in μm) were measured with a custom-made program running in IDL 5.5 software (Research Systems Inc.) (Rueda et al., 2013).

Spontaneous Transient Outward Currents Recordings

Spontaneous transient outward currents (STOCs) were recorded with the patch-clamp technique in whole-cell configuration, as previously reported (Rueda et al., 2013). Polish fire patch pipettes (3–5 MΩ) were filled with internal solution containing (in mM): 80 K-glutamate, 5 NaCl, 40 KCl, 2 $MgCl_2$, 2 Mg_2-ATP, 0.1 Na-GTP, 0.05 K-EGTA, 20 HEPES, pH 7.2 with KOH. MASMCs were perfused with PSS and voltage-clamped from −60 to 0 mV to record STOCs. Membrane capacitance (Cm) was determined from the current amplitude elicited in response to a hyperpolarizing pulse from a holding potential at −60 mV (duration, 10 ms; amplitude, 10 mV). Currents were filtered at 500 Hz and digitalized at 2 kHz (500 μs/point). STOCs analysis was performed offline, using the event detection tool of Clampfit 9.2 (Axon Instruments, Inc.). All experiments were done at RT. Only smooth, elongated, spindle shape and optically refractive cells were used for patch experiments.

Statistical Data Analysis

Data are presented as the mean ± standard error of the mean (M ± SEM). The number of animals for each experiment was indicated by "*N*," while the number of vessels, cells, or independent experiments was indicated as "*n*." All analyses were performed using Origin Pro v.8 software (Origin Lab Corporation, Northampton, MA, United States) or Sigma Plot v11.0 (Systat Software Inc., San Jose, CA, United States). After checking for normal distribution of data with the Shapiro–Wilk test, statistical significance was evaluated by either Student's *t*-test or one-way RM Analysis of Variance (ANOVA) followed by Bonferroni *post-hoc* test. When data sets failed the normality distribution test, statistical significance

TABLE 1 | List of primer sequences for real-time qPCR.

Target gene	Sequence accession number	Primer	Tm (◦C)	Sequence	Product length (pb)
Atp2a2	NM_001110139.2	F	59.0	5′- ACCTGGAAGATTCTGCGAAC -3′	86
		R	59.1	5′- AATCCTGGGAGGGTCCAG -3′	
Sgk1	NM_019232.3	F	60.3	5′- CTGCTCGAAGTACCCTCACC -3′	128
		R	58.4	5′- GCATGCATAGGAGTTGTTGG -3′	
Orai1 Stim1	NM_001013982.1	F	59.49	5′- ATCGTCTTTGCCGTTCACTT -3′	131
	NM_001108496.2	R	59.88	5′- AGAGAATGGTCCCCTCTGTG -3′	112
		F	59.54	5′- TCTCTGAGTTGGAGGATGAGTAGA -3′	
		R	59.63	5′- CAATATAGGGGAGCAGAGGTAAGA -3′	
Tagln	NM_031549.2	F	60.5	5′- GTTTGGCCGTGACCAAGAAC -3′	129
		R	62.2	5′- GGAGGCCAATGACGTGCTTC -3′	
Rpl32	NM_013226.2	F	58.6	5′- GCTGCTGATGTGCAACAAA -3′	115
		R	58.9	5′- GGGATTGGTGACTCTGATGG -3′	
Ywhaz	NM_013011.3	F	60.3	5′- AGACGGAAGGTGCTGAGAAA -3′	127
		R	54.7	5′- GAAGCATTGGGGATCAAGA -3′	

Atp2a2, ATPase sarcoplasmic/endoplasmic reticulum Ca^{2+} transporting 2 or SERCA pump; Sgk1, serum/glucocorticoid-regulated kinase; Orai1, calcium release-activated calcium channel protein 1; Stim1, stromal interaction molecule 1; Tagln, transgelin also known as smooth muscle cell 22 alpha; Rpl32, ribosomal protein L32; Ywaz, tyrosine 3-monooxygenase/tryptophan 5-monooxygenase activation protein, zeta; F, forward; R, reverse; Tm, melting temperature; pb, pair bases. Information obtained from MFEprimer 3.1 (Wang et al., 2019).

was evaluated by either Mann–Whitney rank sum test or Kruskal–Wallis one-way ANOVA on ranks followed by Bonferroni *post-hoc* test. A *P*-value of ≤0.05 was considered statistically significant.

RESULTS

Increased Expression of Ca$_{\mathrm{V}}$1.2 Does Not Enhance Depolarization-Induced Vasoconstriction in Aldosterone-Treated Mesenteric Arteries

We have reported previously that ALDO-induced MR activation increased Ca$_{\mathrm{v}}$1.2 expression in rat vascular tissues, including resistance MAs (Mesquita et al., 2018). However, the functional outcome of the ALDO-induced Ca$_{\mathrm{v}}$1.2 increased expression remained uncharacterized in MAs. Herein, we first evaluate the effect of depolarization-induced vasoconstriction in MAs isolated from male *Wistar* rats treated or not with ALDO (10 nM, 24 h). **Figure 1A** shows representative KCl-induced contractile responses of MA rings treated or untreated with ALDO. The vasoconstriction response of ALDO-treated MA was similar to those of control MAs (EC$_{50}$ for vasoconstriction in mM: 28.87 ± 0.62, n = 7 control arteries vs. 29.64 ± 0.45, n = 7 ALDO-treated arteries; P = 0.9534). This result contrasts with previous data, that ALDO increased the depolarization-induced vasoconstriction response of coronary arteries (Mesquita et al., 2018). This observation prompted us to measure the endogenous expression of MR and its functional activity in resistance MAs. As reported previously (Takeda et al., 1993, 1997), we corroborate the constitutive expression of MR in rat MAs (**Supplementary Figure 1**). Furthermore, ALDO treatment induced the expression of the serum and glucocorticoid-induced kinase 1 (*Sgk1*), an enzyme that increases its expression in response to ALDO-MR activation in MAs (Briet et al., 2016). Our results demonstrate that the endogenous MR is functional in *ex vivo*-treated MAs.

In addition, we confirmed the specificity of MR activation for inducing the expression of Ca$_{\mathrm{v}}$1.2 in MAs treated with ALDO. **Figure 1B** shows representative immunoblots of Ca$_{\mathrm{v}}$1.2 and GAPDH (as the loading control) from ALDO-treated (10 nM, 24 h) and untreated MAs. Dispersion data graph (*below*) showed a 1.8-fold increase in Ca$_{\mathrm{v}}$1.2 expression in MAs incubated with ALDO. Importantly, the addition of 1 μM RU28318, a selective MR antagonist (Kim et al., 1998), blocked the effect of ALDO on Ca$_{\mathrm{v}}$1.2 expression.

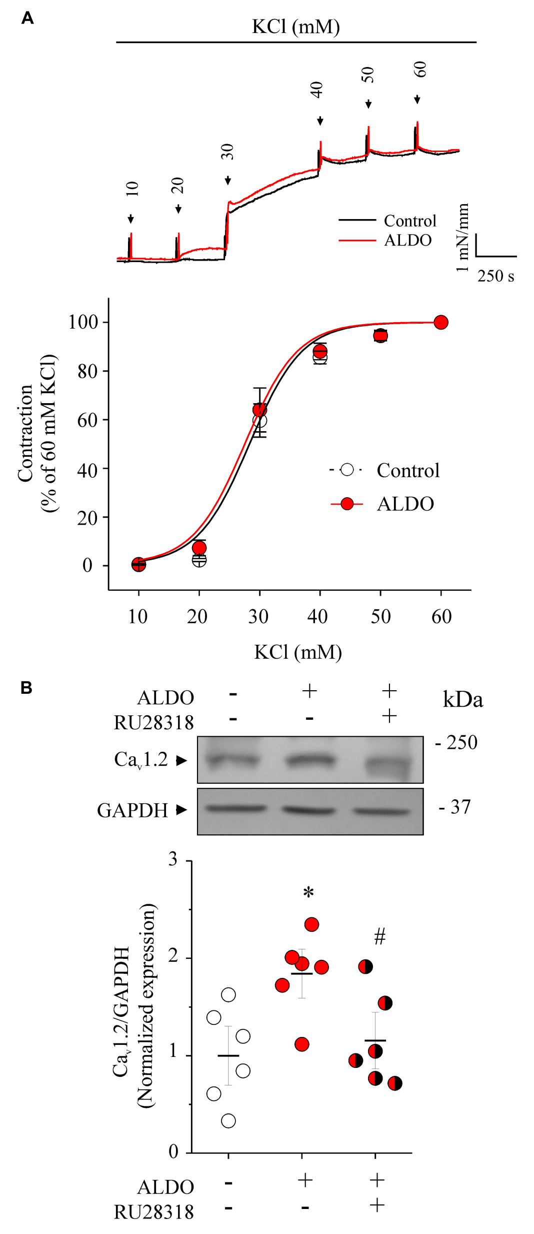

FIGURE 1 | Aldosterone treatment increases Ca$_{\mathrm{V}}$1.2 expression but does not change depolarization-induced vasoconstriction responses of rat mesenteric arteries. **(A)** Representative traces of tension changes (*top recordings*) in response to potassium chloride (KCl) additions (from 10 to 60 mM KCl) of rat MA rings treated with aldosterone (ALDO 10 nM, 24 h, *red trace*) or without it (Control, *black trace*). The concentration-response graph (*below*) shows vasoconstriction responses of MA rings treated (*red circles*) or not (*empty circles*) with ALDO (10 nM, 24 h). Depolarization-induced contraction was expressed as a percentage of maximal contractile response induced by 60 mM KCl. Data are shown as mean ± SEM of n = 7 MA rings from N = 7 rats for each experimental group. **(B)** Representative immunoblot image and scatterplot with mean ± SEM (*below*) of Ca$_{\mathrm{V}}$1.2 protein expression from homogenates of control MAs (*empty circles*), ALDO-treated MAs (*red circles*), and ALDO-treated MAs co-incubated with RU 28318, a selective MR antagonist (1 μM, *red/black circles*). Data are shown as mean ± SEM of n = 6 independent experiments for each group. Each experiment was performed with a pool of 3–4 MA segments from three rats. $^{*}P < 0.01$ vs. untreated MAs. $^{\#}P < 0.05$ vs. ALDO-treated MAs.

Aldosterone Increases Sarcoplasmic Reticulum Ca^{2+} Content but Does Not Elevate Global Cytoplasmic Ca^{2+} Concentration in Mesenteric Artery Smooth Muscle Cells

Previous evidence suggests a dual role of Ca$_{\mathrm{v}}$1.2-mediated Ca^{2+} entry in VSMCs by contributing to increase global [Ca^{2+}]$_{\mathrm{cyt}}$ and vasoconstriction (Moosmang et al., 2003), and to refill SR Ca^{2+} stores, supporting Ca^{2+} sparks and vascular relaxation

(Essin et al., 2007; Fan et al., 2018). The lack of ALDO effect in enhancing depolarization-induced vasoconstriction of MAs, despite inducing an augmented $Ca_V1.2$ expression (**Figure 1**), prompted us to hypothesize that $Ca_V1.2$ might provide Ca^{2+} primarily for loading SR Ca^{2+} stores. To determine whether the increase in $Ca_V1.2$ expression had an impact on the intracellular Ca^{2+} levels, we evaluated the effect of ALDO on global $[Ca^{2+}]_{cyt}$ and SR Ca^{2+} content. The latter with a challenge of caffeine (Caff, 10 mM) in Fura 2-loaded MASMCs. **Figure 2A** shows that global $[Ca^{2+}]_{cyt}$ was similar in ALDO-treated and untreated, controls cells, even under mild depolarizing conditions (bath solution containing 20 mM K^+). Therefore, Ca^{2+} influx due to depolarization-induced $Ca_V1.2$ activation did not increase global $[Ca^{2+}]_{cyt}$ significantly. Then, we evaluated the SR Ca^{2+} content by a single caffeine challenge. **Figure 2B** shows representative Caff-evoked Ca^{2+} transients in MASMCs treated or not with ALDO. Summarized data show a significantly higher amplitude of the caffeine-induced Ca^{2+} transient in MASMCs treated with ALDO with respect to control cells (**Figure 2C**). In addition, the area-under-the-curve (AUC) of the Caff-induced Ca^{2+} transient was significantly larger in the ALDO-treated MASMCs (AUC in arbitrary units: 7,564 ± 775 in ALDO-treated group vs. 5,448 ± 630 in CONTROL group; $P \leq 0.05$; $n = 15$ cells for each experimental condition). These results suggest that mild depolarizing conditions activate $Ca_V1.2$-mediated Ca^{2+} influx, which mainly contributes to increasing SR Ca^{2+} stores instead of increasing global $[Ca^{2+}]_{cyt}$. In the presence of the SERCA pump inhibitor thapsigargin (TGN, 100 nM) no increase in $[Ca^{2+}]_{cyt}$ was produced by an additional caffeine challenge (**Supplementary Figure 2**). Therefore, when SR Ca^{2+} stores are empty, the application of solution with the puffer pipette is neither releasing more Ca^{2+} from other Ca^{2+} storage organelles nor activating transient receptor potential (TRP) channels involved in mechanosensitive-mediated Ca^{2+} entry (for instance, TRPC6 and TRPP2) (Ghosh et al., 2017).

Aldosterone Treatment Increases $Ca_v1.2$-Mediated Ca^{2+} Entry but the Sarco/Endoplasmic Reticulum Ca^{2+} Pump Impedes Ca^{2+} Reaching the Bulk of the Cytoplasm of Mesenteric Artery Smooth Muscle Cells

Sarco/Endoplasmic reticulum Ca^{2+} pump transports Ca^{2+} ions from the cytoplasm into the SR and contributes to maintaining luminal SR Ca^{2+} levels (Flores-Soto et al., 2013). The augmented SR Ca^{2+} load in ALDO-treated cells suggests that SERCA pump was involved in buffering Ca^{2+} coming from the extracellular space, preventing the increase in global $[Ca^{2+}]_{cyt}$. To unmask the effect of the SERCA pump, we measured Ca^{2+} entry in MASMCs preincubated with thapsigargin (TGN 100 nM, 10 min) or in its absence. **Figure 3A** shows representative recordings of Ca^{2+} entry in Fluo 4-loaded MASMCs under all experimental conditions. After maintaining cells in the Na^+ and Ca^{2+} free solution, the reintroduction of extracellular Ca^{2+} increased cytoplasmic Ca^{2+} in both CTRL and ALDO-treated

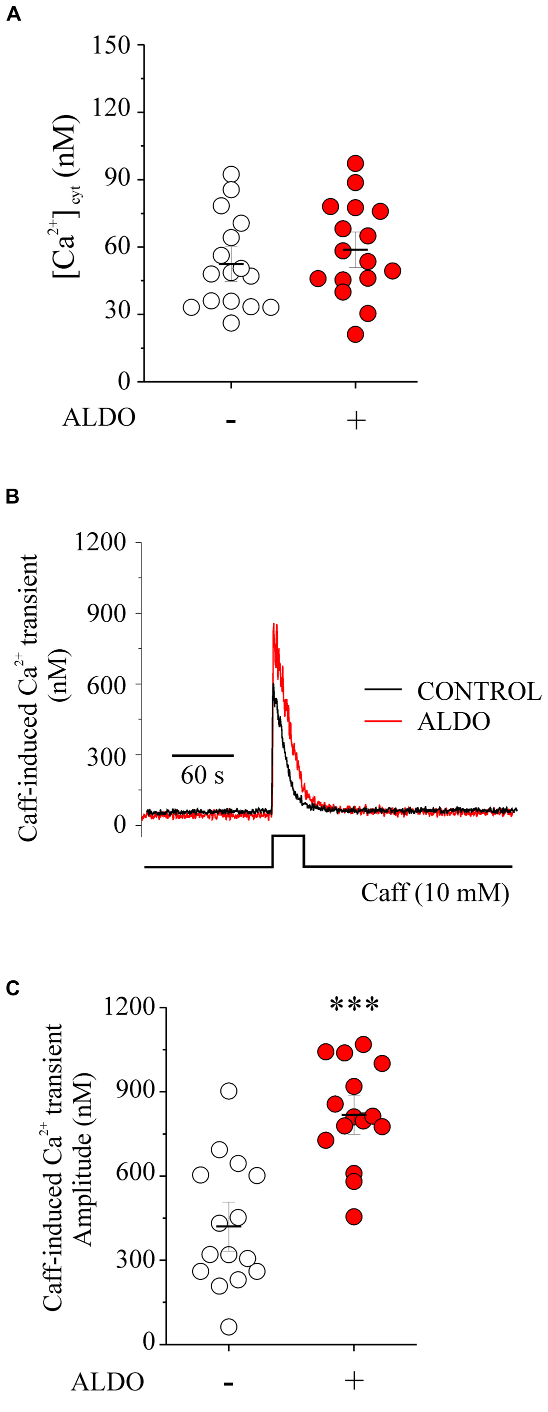

FIGURE 2 | Aldosterone treatment increases SR Ca^{2+} content and does not change global $[Ca^{2+}]_{cyt}$ in Fura 2-loaded MASMCs. **(A)** Scatterplot with mean ± SEM illustrates basal $[Ca^{2+}]_{cyt}$ before caffeine challenge determined in Fura 2-loaded MASMCs, treated (*red circles*, $n = 16$ cells/$N = 5$ rats) or not (*empty circles*, $n = 16$ cells/$N = 5$ rats) with aldosterone (ALDO 10 nM, 24 h). **(B)** Representative recordings of caffeine-induced $[Ca^{2+}]$ transients in Fura 2-loaded MASMCs treated (ALDO, *red trace*) or not (CONTROL, *black trace*) with aldosterone (10 nM, 24 h). **(C)** Scatterplot with mean ± SEM of caffeine-induced Ca^{2+} transient amplitude recorded at the peak of the Ca^{2+} transient in MASMCs treated (*red circles*, $n = 16$ cells/$N = 5$ rats) or not (*empty circles*, $n = 16$ cells/$N = 5$ rats) with ALDO. $^{***}P < 0.001$ vs. control MASMCs.

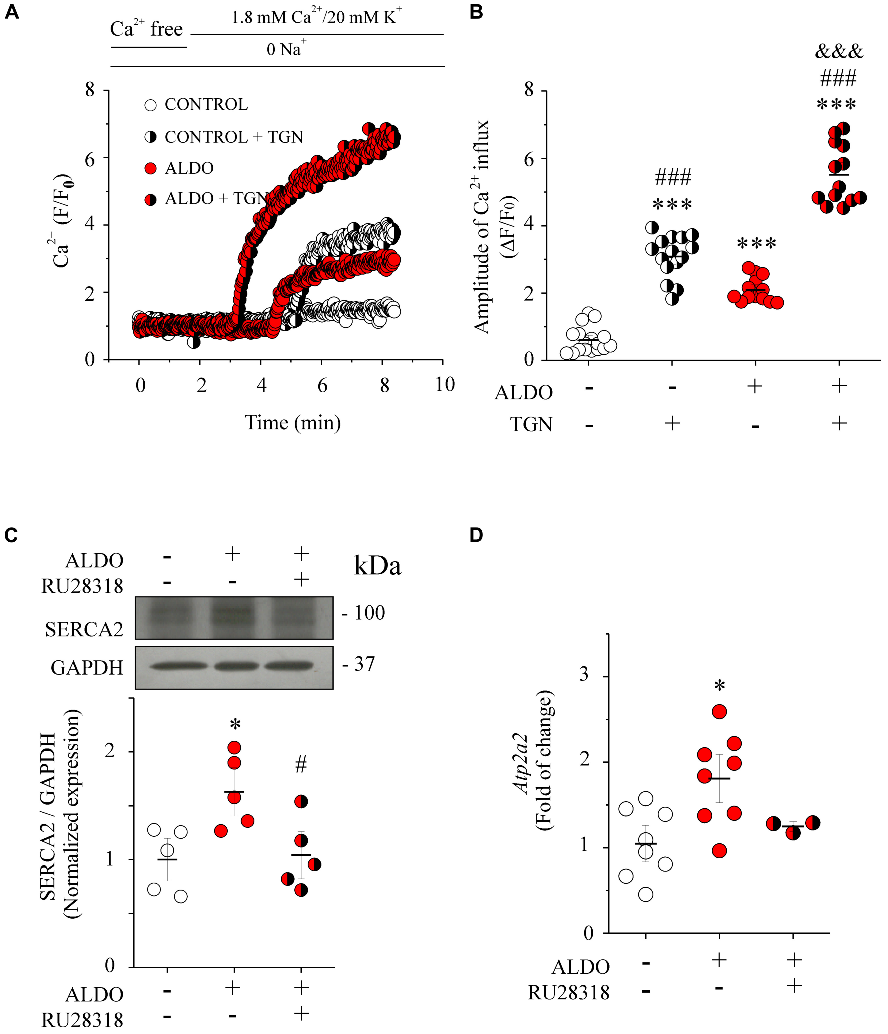

FIGURE 3 | SERCA pump counterbalances depolarization-induced Ca^{2+} entry in ALDO-treated MASMCs. **(A)** Representative Ca^{2+} influx recordings (F/F_0) of Fluo 4-loaded MASMCs from control (*empty circles*) or ALDO-treated (*red circles*) cells preincubated with thapsigargin (TGN) 100 nM for 10 min (*white/black* and *red/black circles*, respectively) to block SERCA pump activity, or in its absence. Cells were kept in Na^+ and Ca^{2+} free solution. After 2-min of *frame-scan* recording, cells were perfused with Na^+ free solution (to block Na^+/Ca^{2+} exchanger activity) containing 1.8 mM $CaCl_2$ plus 20 mM KCl to induce LTCC-mediated Ca^{2+} influx. Changes in cytoplasmic Ca^{2+} were recorded with a laser scanning confocal microscope (Zeiss, LSM 700) equipped with an ×63 oil immersion objective (N.A. 1.2). **(B)** Scatterplot with mean ± SEM illustrates the amplitude of depolarization-induced Ca^{2+} entry ($\Delta F/F_0$) of Fluo 4-loaded MASMCs under the different experimental conditions. The amplitude of Ca^{2+} influx was determined at minute 8 of the recording in control MASMCs (n = 17 cells/N = 4 rats, *empty circles*), ALDO-treated MASMCs (n = 13 cells/N = 5 rats, *empty circles*), control MASMCs + TGN (n = 15 cells/N = 6 rats, *white/black circles*) and ALDO-treated MASMCs + TGN (n = 13 cells/N = 5 rats, *red/black circles*), respectively. $^{***}P < 0.001$ vs. control cells; $^{\#\#\#}P < 0.001$ vs. ALDO-treated cells; $^{\&\&\&}P < 0.001$ vs. control + TGN cells. **(C)** Representative immunoblot image and scatterplot with mean ± SEM (*below*) of SERCA pump protein expression from homogenates of control MAs (*empty circles*), ALDO-treated MAs (*red circles*), and ALDO-treated MAs co-incubated with 1 μM RU28318, a selective MR antagonist (*red/black circles*). Data are shown as mean ± SEM of n = 5 experiments for each group. Each experiment was performed with a pool of 3–4 MA segments from three rats. SERCA pump expression levels were normalized to the expression of GAPDH for each independent experiment. $^{*}P < 0.05$ vs. control group. $^{\#}P < 0.05$ vs. ALDO-treated group. **(D)** Scatterplot with mean ± SEM of *Atp2a2* relative mRNA levels determined by real-time qPCR from control MAs (*empty circles*, n = 8), ALDO-treated MAs (*red circles*, n = 8), and ALDO-treated MAs co-incubated with 1 μM RU28318 (*red/black circles, n* = 3). $^{*}P < 0.05$ vs. control group.

cells with respect to basal Ca^{2+} levels. Importantly, the increase in cytoplasmic Ca^{2+} level was larger in ALDO-treated cells preincubated with TGN (5 min) than in cells without the SERCA inhibitor ($\Delta F/F_0$: 0.6 ± 0.1, n = 15 control cells, vs. 3.1 ± 0.2, n = 17 control + TGN cells; and 2.1 ± 0.1, n = 13 ALDO-treated MASMCs vs. 5.5 ± 0.1, n = 13 ALDO-treated + TGN cells. **Figure 3B**), unmasking SERCA buffering activity. We measured the protein and mRNA levels of the SERCA pump by Western blot and qPCR, respectively (**Figures 3C,D**). Both were significantly increased in the ALDO group (1.7 and 1.8 folds, respectively), and blunted in the presence of RU28318 (**Figures 3C,D**). Given that TGN diminishes luminal SR Ca^{2+} load and stimulates store-operated Ca^{2+} entry (SOCE) (Leung et al., 2008; Trebak and Putney, 2017); and also that ALDO

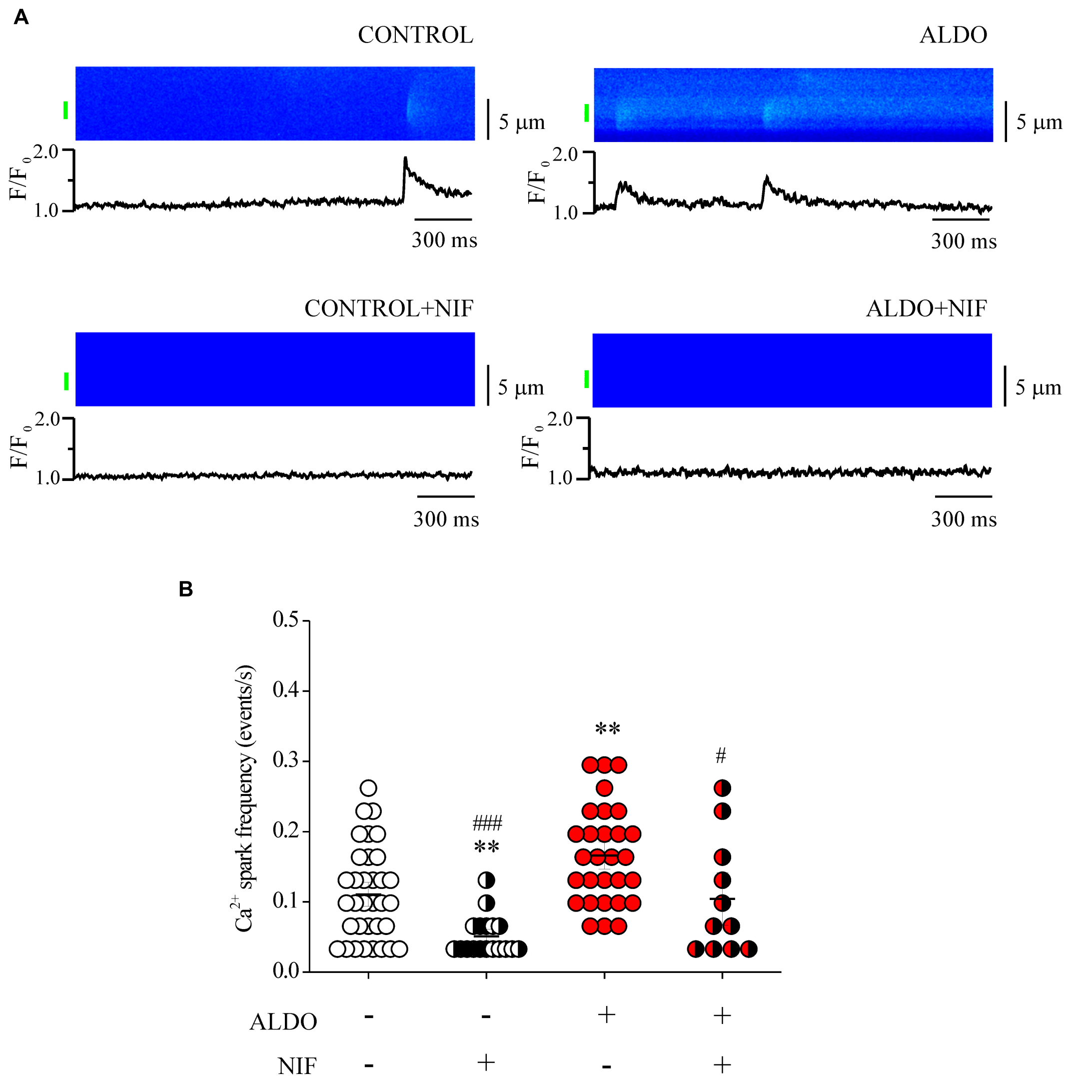

FIGURE 4 | Aldosterone treatment increases Ca^{2+} spark frequency in MASMCs. **(A)** Representative pseudo-colored confocal images of Ca^{2+} sparks (*top*) and normalized (F/F_0) fluorescence profiles (*bottom*) from Fluo 4-loaded MASMCs treated or not with aldosterone (ALDO 10 nM, 24 h) and preincubated or not with Nifedipine (1 µM, 10 min). The fluorescence profile was calculated in the region indicated by the green bar. **(B)** Scatterplot with mean ± SEM illustrates Ca^{2+} spark frequency in Fluo 4-loaded MASMCs from control (*empty circles*, $n = 35$ cells/$N = 5$ rats); ALDO-treated arteries (*red circles*, $n = 29$ cells/$N = 4$ rats); pre-incubated with Nifedipine (NIF, *white/black circles*, $n = 18$ cells/$N = 4$ rats; and *red/black circles,* $n = 11$ cells/$N = 3$ rats, respectively). $^{**}P < 0.01$ vs. control cells.$^{\#}P < 0.05$ and $^{\#\#\#}P < 0.001$ vs. ALDO-treated group.

treatment increases SOCE and Orai1 expression in neonatal rat ventricular cardiomyocytes (Sabourin et al., 2016); we measured Orai1 protein expression by immunoblotting. Our results show that Orai1 protein expression was similar in both experimental conditions (**Supplementary Figure 3**). Considering that the stromal interaction molecule (STIM)/Orai system is involved in SOCE (Trebak and Putney, 2017), we determined the mRNA levels of both proteins. However, no changes in mRNA levels of *Orai1* and *Stim1* were observed in ALDO-treated arteries (normalized *Orai1* mRNA levels: 1.0 ± 0.16, $n = 4$ control vs. 0.72 ± 0.11, $n = 4$ ALDO-treated samples, $P = 0.2084$; normalized *Stim1* mRNA levels: 1.0 ± 0.08, in $n = 4$ control vs. 1.15 ± 0.16, $n = 4$ ALDO-treated samples, $P = 0.4217$). These results do not rule out the participation of additional mechanisms of Ca^{2+} entry (for instance, $Ca_v3.2$ and TRP channels) (Evans, 2017; Trebak and Putney, 2017; Fan et al., 2018) which might be altered by ALDO treatment and deserve further studies. Taken together, these data support the conclusion that $Ca_v1.2$ contributes to refilling intracellular Ca^{2+} stores in MASMCs via SERCA pump activity. To rule out the possibility that changes in SR Ca^{2+} load were associated with ALDO-induced modifications in the expression of calsequestrin-2 (CSQ2), a key SR Ca^{2+} buffering protein (Dagnino-Acosta and Guerrero-Hernández, 2009; Esfandiarei et al., 2013), we measured CSQ2 expression in Aldo-treated and untreated MAs. No differences were found in the expression of CSQ2 (Normalized CSQ2/GAPDH expression:

TABLE 2 | Characteristics of Ca^{2+} spark recorded in untreated (Control) and aldosterone-treated (ALDO) mesenteric artery smooth muscle cells in the absence and presence of Nifedipine (1 μ M).

			+ Nifedipine	
	Control	**ALDO**	**Control**	**ALDO**
Cells (*n*)	**35**	**29**	**18**	**11**
Basal fluorescence (F_0)	5.81 ± 0.52	5.90 ± 0.53	3.58 ± 0.25$^{\#\#}$	5.78 ± 0.56
Frequency (events/s)	0.11 ± 0.01	0.17 ± 0.01**	0.05 ± 0.01$^{**,\#\#\#}$	0.10 ± 0.02$^{\#}$
Amplitude (F/F_0)	1.89 ± 0.05	1.77 ± 0.03	2.10 ± 0.09	1.91 ± 0.07
FWHM (μm)	1.88 ± 0.07	1.89 ± 0.06	2.05 ± 0.15	1.87 ± 0.12
FDHM (ms)	45.97 ± 2.36	50.25 ± 2.09	42.62 ± 4.88$^{\#}$	37.55 ± 6.10$^{*,\#\#\#}$
Rising time (ms)	21.80 ± 1.40	23.67 ± 1.14	18.37 ± 1.73	19.12 ± 2.48
Decay time (ms)	84.82 ± 16.83	79.91 ± 9.43	70.63 ± 23.22	35.29 ± 4.53

Values are mean ± SEM of indicated recorded cells (n) for each experimental condition. Confocal images of Ca^{2+} sparks were recorded with a laser scanning confocal microscope in line scan mode (five images per cell of 1000 lines each, at speed of 1.92 ms/line). Basal fluorescence intensity (F_0) was calculated inside the cell as the average fluorescence intensity of those pixels without sparks. Ca^{2+} spark data were obtained from nCTL = 191 events, nCTL + Nif = 35 events, nALDO = 315 events, and nALDO + Nif = 50 events.$P \leq 0.05$, and **$P \leq 0.01$ vs. control condition. $^{\#}P \leq 0.05$, $^{\#\#}P \leq 0.01$, and $^{\#\#\#}P \leq 0.001$ vs. ALDO-treated cells. FDHM, full duration at half maximum, FWHM, full width at half maximum.*

1.00 ± 0.09 in the control group vs. 1.14 ± 0.26 in the ALDO-treated group; $P = 0.6$; $N = 5$ for each experimental condition. **Supplementary Figure 4**).

Aldosterone Treatment Increases Ca^{2+} Spark Frequency in Mesenteric Artery Smooth Muscle Cells

Mesenteric artery smooth muscle cells exhibit Ca^{2+} sparks reflecting localized Ca^{2+} release through type 2 RyR, the predominant isoform of RyRs in these cells (Krishnamoorthy et al., 2014; Matsuki et al., 2018). Given that $Ca_v1.2$-mediated Ca^{2+} influx contributes to increase SR Ca^{2+} load in MASMCs, and that Ca^{2+} spark ignition is tightly regulated by SR Ca^{2+} load due to a spatial coupling between LTCCs and RyRs, in which SERCA pump must have a role (Cheranov and Jaggar, 2002; Essin et al., 2007; Takeda et al., 2011; Fan et al., 2018), we measured Ca^{2+} sparks. We previously showed that ALDO modified spatio-temporal properties of Ca^{2+} sparks in cardiomyocytes (Gómez et al., 2009); therefore, we analyzed the frequency and spatial properties of Ca^{2+} sparks in Fluo 4-loaded MASMCs by confocal microscopy. **Figure 4A** shows representative confocal images and fluorescence profiles of Ca^{2+} sparks recorded in ALDO-treated MASMCs and control cells, with and without Nifedipine (1 μM) to block $Ca_v1.2$-mediated Ca^{2+} entry. We have found a significant increase in Ca^{2+} spark frequency in MASMCs treated with ALDO (**Figure 4B** and **Table 2**) an effect blocked in presence of Nifedipine (**Figure 4B** and **Table 2**). In-depth analysis of Ca^{2+} sparks characteristics revealed a Nifedipine-dependent reduction of basal fluorescence (F_0) in control MASMCs, an effect that has been previously observed with diltiazem, a benzothiazepine class of LTCC channel blocker (Cheranov and Jaggar, 2002). In ALDO-treated and untreated cells, Nifedipine also reduced the duration of Ca^{2+} sparks (**Table 2**). The coincubation of MASMCs with ALDO and the selective MR inhibitor RU28318 prevented the increase in Ca^{2+} spark frequency induced by ALDO treatment alone (Ca^{2+} spark frequency in events/s: 0.16 ± 0.1, $n = 29$ ALDO-treated cells/$N = 4$ rats vs. 0.11 ± 0.01, $n = 30$ ALDO + RU28318-treated cells/$N = 3$ rats, $P < 0.001$). These data suggest a direct link between the MR signaling pathway activation, SR Ca^{2+} load and RyR activity in MASMCs. Changes in RyR protein expression or the expression of RyR accessory proteins might alter Ca^{2+} spark frequency and properties in VSMCs (Fernández-Velasco et al., 2014). Moreover, in ALDO-treated cardiac cells the alterations in frequency and properties of Ca^{2+} sparks were associated with downregulation of immunophilin FK506-binding proteins (FKBP12 and 12.6), which regulate RyR activity (Gómez et al., 2009); therefore, we also determined the protein expression levels of three key regulatory proteins of RyR activity in VSMCs: FKBP12.6, sorcin, and calsequestrin (Wang et al., 2004; Rueda et al., 2006; Esfandiarei et al., 2013). Immunoblot results showed a similar expression of RyR2 and its regulatory proteins in both experimental groups (**Supplementary Figure 4**).

Aldosterone Treatment Increases Spontaneous Transient Outward Current Frequency in Mesenteric Artery Smooth Muscle Cells

In VSMCs, Ca^{2+} sparks exert a negative feedback effect on contractility by decreasing LTCC-mediated Ca^{2+} entry due to the activation of BK_{Ca} channel and STOCs generation (Gollasch et al., 1998). Particularly, in resistance-sized MAs, spark-activated BK_{Ca} channels oppose vasoconstriction (Krishnamoorthy et al., 2014), an effect also observed in cerebral arteries (Knot et al., 1998; Jaggar et al., 2000). In addition, BK_{Ca} channels have been recognized as targets of ALDO-induced MR activation in vascular cells (Liu et al., 1995; Ambroisine et al., 2007). Firstly, to assess the effect of ALDO treatment on cell size, we measured cell capacitance to estimate membrane surface area of MASMCs, as an indirect index of cell dimension. No difference in membrane capacitance was found in MASMCs of both experimental groups (in pF: 13.0 ± 1.1, $n = 12$ control cells vs. 12.38 ± 0.54, $n = 12$

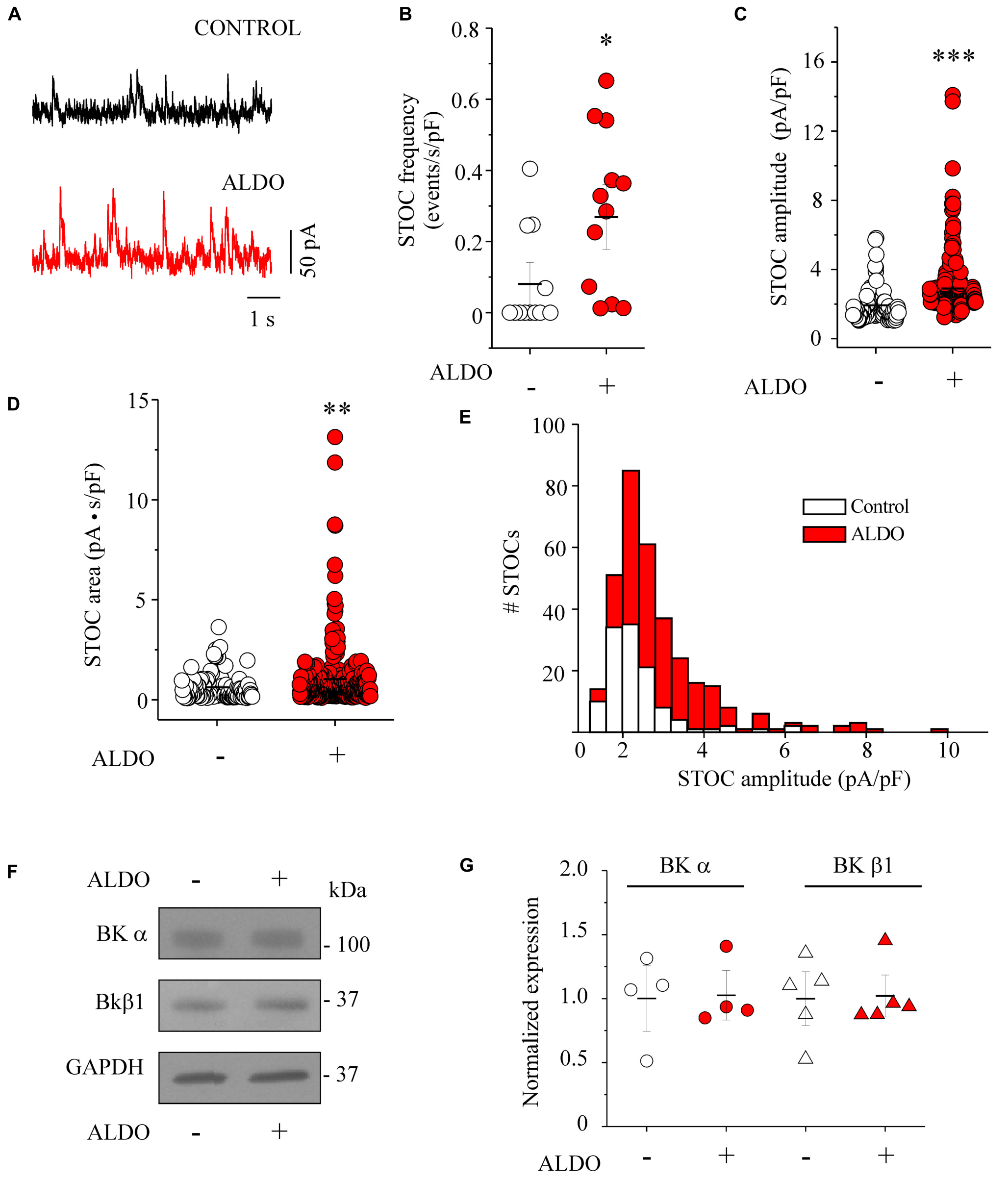

FIGURE 5 | Aldosterone treatment increases the frequency and the amplitude of STOCs in MASMCs without modifying BK channel subunit expression. **(A)** Representative traces of STOCs recorded at a holding potential of –40 mV from MASMCs in the absence (CONTROL, *black trace*) or after 24 h-treatment with aldosterone 10 nM (ALDO, *red trace*). Scatterplots with mean ± SEM illustrate STOC frequency (**B**, normalized with respect to cell capacitance, in events/s/pF), STOC amplitude (**C**, normalized with respect to cell capacitance, in pA/pF), and STOC area-under-the-curve (**D**, in pA.s) in control MASMCs ($n = 119$ events/$n = 12$ cells/$N = 4$ animals, *empty circles*) and ALDO-treated cells ($n = 333$ events/$n = 12$ cells/$N = 5$ animals, *red circles*). $^*P < 0.05$, $^{**}P < 0.01$, and $^{***}P < 0.001$ vs. control group. **(E)** Histogram distribution of normalized STOC amplitudes in control ($n = 119$ events/$n = 12$ cells/$N = 4$ rats, *white bars*) and ALDO-treated MASMCs ($n = 333$ events/$n = 12$ cells/$N = 5$ rats, *red bars*) indicates the increase in the amplitude of STOCs above 3.6 pA/pF in ALDO-treated cells. **(F,G)** Representative immunoblot images and scatterplot with mean ± SEM of BK_{Ca} channel α subunit expression ($n = 4$ control samples, *empty circles*; $n = 4$ ALDO-treated samples, *red circles*), and β1 subunit expression ($n = 5$ control samples, *empty triangles*; $n = 5$ ALDO-treated samples, *red triangles*). Each sample was prepared with a pool of 3–4 MA segments from three rats. Values were normalized with respect to GAPDH expression.

ALDO-treated cells). Thus, we studied whether the increase in Ca^{2+} spark frequency in ALDO-treated MASMCs could have an impact on BK_{Ca} channel activity by analyzing STOC frequency and amplitude at near resting membrane potential (−40 mV) in PSS. **Figure 5A** shows representative STOC recordings in MASMCs elicited at −40 mV. The STOC frequency was higher in ALDO-treated MASMCs than in control cells (**Figure 5B**). Moreover, STOC amplitude (**Figure 5C**) and area-under-the-curve (**Figure 5D**) were significantly increased in ALDO-treated MASMCs. **Figure 5E** shows a histogram distribution of STOC amplitudes. Aldosterone promoted the increase of STOC events with amplitudes of >3.6 pA/pF. Considering that membrane depolarization of MASMCs increased the frequency and amplitude of STOCs (Pucovský and Bolton, 2006), we measured the voltage dependence of STOC frequency and amplitude in MASMCs of both experimental groups. In ALDO-treated cells, STOC properties were significantly augmented at depolarizing holding potentials of −40 mV, −20 mV, and 0 mV, with respect to control MASMCs (**Supplementary Figure 5**). Because STOCs result from BK$_{Ca}$ channel activation (Pérez et al., 1999; Krishnamoorthy et al., 2014), we determined the effect of ALDO treatment on BK channel subunit expression. **Figure 5F** shows representative immunoblots of both the pore-forming α subunit and the β1 accessory subunit of BK$_{Ca}$ channels. Protein expression of both BK$_{Ca}$ channel subunits was similar between ALDO-treated and control MAs (**Figure 5G**). Therefore, the augmented STOC activity was not due to changes in BK$_{Ca}$ channel expression and could be attributed to the increase of Ca^{2+} spark frequency and SR Ca^{2+} load in ALDO-treated cells.

Aldosterone Enhances Acetylcholine-Induced Vasorelaxation of Mesenteric Arteries

Large-conductance Ca^{2+}-activated K^{+} channels through STOCs play an important role in the regulation of vascular tone by hyperpolarizing MASMCs and inducing vasorelaxation (Krishnamoorthy et al., 2014). The functional coupling between Ca^{2+} sparks and STOCs promotes vasorelaxation by decreasing LTCC-mediated Ca^{2+} entry. Thus, we determine whether vasorelaxation was enhanced in our experimental model. As shown in **Figure 6**, in 60 mM KCl-precontracted MA rings the vasorelaxation response to ACh was augmented in ALDO-treated MA rings compared to control arteries (EC$_{50}$ for ACh-induced relaxation in mM: 0.69 ± 0.10, $n = 6$ control arteries vs. 0.37 ± 0.04, $n = 6$ ALDO-treated arteries; $P \leq 0.05$). However, the maximal relaxation response to ACh showed a tendency to be higher in ALDO-treated MA rings with respect to control arteries; though, this tendency was not significant as illustrated by the P value (Maximal relaxation in %: 28.3 ± 4.8, $n = 6$ control arteries vs. 40.8 ± 5.4, $n = 6$ ALDO-treated arteries, $P = 0.1162$); These data suggest that ALDO treatment increased the sensitivity to ACh, but not the maximal relaxation response to this agonist.

DISCUSSION

In this study, we describe the crucial role of the SERCA pump in buffering Ca$_V$1.2-mediated Ca^{2+} entry in ALDO-treated MASMCs. Our work shows that a short-term (24 h) *ex vivo* exposure to 10 nM ALDO of resistance MAs: (1) increased both Ca$_V$1.2 and SERCA pump protein expressions; (2) increased depolarization-induced Ca^{2+} influx, luminal SR Ca^{2+} load, and Ca^{2+} spark and STOC frequencies; in consequence, (3) depolarization-induced vasoconstriction was unaffected as well global [Ca^{2+}]$_{cyt}$; and (4) ACh-mediated vasorelaxation was enhanced. In the presence of TGN, the reintroduction of extracellular Ca^{2+} induced a significant increase in cytoplasmic Ca^{2+} levels, unmasking the key participation of the SERCA pump in counterbalancing Ca^{2+} influx and avoiding undesired increments of global [Ca^{2+}]$_{cyt}$. All these data allow us to propose the model depicted in **Figure 7**. Under physiological conditions (Control, *left side*), Ca$_V$1.2-mediated Ca^{2+} influx is directed by SERCA pump to the SR Ca^{2+} stores; this, in turn, promotes the ignition of Ca^{2+} sparks (*via* clusters of RyRs) and STOCs (through BK$_{Ca}$ channel activation). Therefore, Ca$_V$1.2, SERCA pump, RyRs and BK$_{Ca}$ channels are actively working as a functional unit at the PM-SR nanodomain, regulating [Ca^{2+}]$_{cyt}$, luminal SR Ca^{2+} levels, and opposing to vasoconstriction. The exposure to 10 nM aldosterone (ALDO, *right side*) increases Ca$_V$1.2 protein expression and induces higher Ca$_V$1.2-mediated Ca^{2+} influx in MASMCs. However, the depolarization-induced vascular contraction is not enhanced because of SERCA pump upregulation, which efficiently counterbalances Ca^{2+} entry at the PM-SR nanodomain, increasing SR Ca^{2+} content, Ca^{2+} spark and STOC frequencies, and enhancing ACh-mediated vasorelaxation. The net result of this new steady-state is higher Ca^{2+} cycling at the PM-SR nanodomain, dampening unsought elevations of [Ca^{2+}]$_{cyt}$. However, higher luminal SR Ca^{2+} levels might also participate in enhancing receptor-mediated Ca^{2+} release and promote abnormal vasoconstriction, a hallmark feature of overactive ALDO/MR signaling pathway in chronic pathological conditions.

Cumulative evidence supports the physiological role of MR signaling in MAs. Highly specific binding of [^{3}H]-aldosterone has been observed in rat mesenteric vascular arcade

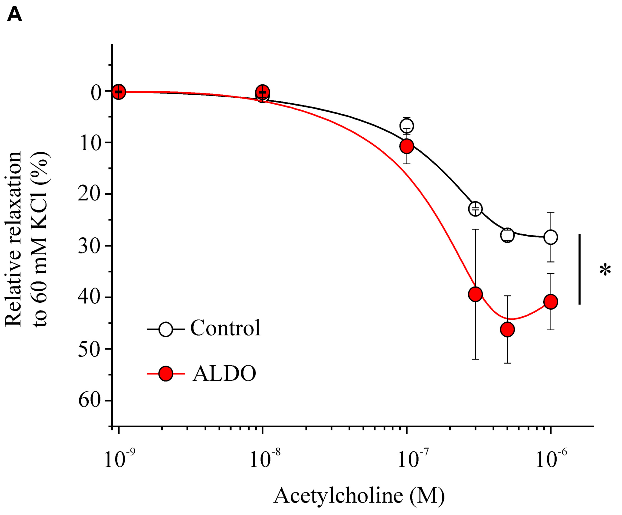

FIGURE 6 | Enhanced acetylcholine-mediated vasorelaxation of ALDO-treated MAs. Relaxation responses of MAs treated (ALDO, *red circles*) or not (CONTROL, *empty circles*) with aldosterone (10 nM, 24 h) to increasing concentrations of acetylcholine (ACh, from 0.001 to 1 μM). MA rings were pre-contracted with KCl 60 mM and exposed to cumulative ACh concentrations (n = 6 MA rings/N = 6 rats, for each experimental condition). Relaxation is shown as a percentage with respect to the contraction response produced by 60 mM KCl, which was taken as 100%. Data are shown as mean ± SEM. *$P < 0.05$ vs. non-linear data fit of control arteries.

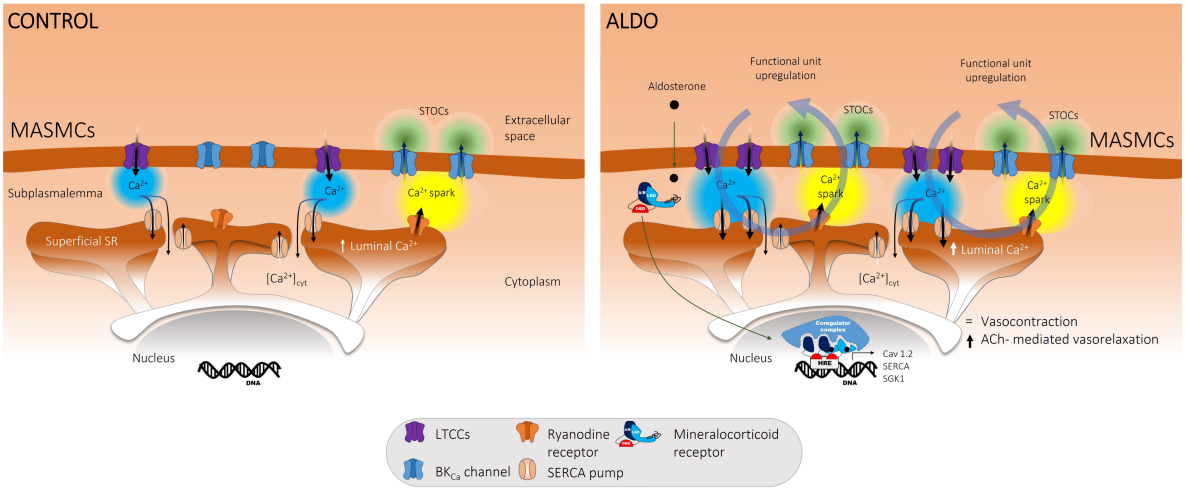

FIGURE 7 | Proposed model for ALDO-mediated upregulation of the functional unit that controls Ca^{2+} dynamics at the SR-PM nanodomain of MASMCs. In normal conditions (CONTROL, *left*) K^+-mediated membrane depolarization induces a Ca^{2+} influx via $Ca_V1.2$ (LTCCs). This Ca^{2+} entry is buffered by the SERCA pump toward the luminal SR Ca^{2+} reservoirs activating RyRs (Ca^{2+} sparks) and BK_{Ca} channels (STOCs). $Ca_V1.2$, SERCA pump, RyRs and BK_{Ca} channels work as a functional unit in the PM-SR nanodomain regulating $[Ca^{2+}]_{cyt}$, luminal SR Ca^{2+} levels, and opposing vasoconstriction. The treatment of MAs with aldosterone (ALDO, *right*) increases $Ca_V1.2$ protein expression and induces higher Ca^{2+} entry in MASMCs. However, the depolarization-induced vascular contraction was not enhanced because of the upregulation of this functional unit, which involves increased expression and activity of SERCA pump controlling abnormal Ca^{2+} influx at the PM-SR nanodomain, increasing SR Ca^{2+} content, Ca^{2+} spark and STOC frequencies, opposing to depolarization-induced vasoconstriction and enhancing ACh-mediated vasorelaxation.

(Funder et al., 1989). In addition, MR, aldosterone synthase and 11-BHSD2 activity, key proteins of the local ALDO system are found in MAs (Takeda et al., 1993, 1997). Because over-activation of the MR/ALDO signaling pathway has been associated with vascular dysfunction (Schiffrin, 2006); it is thus reasonable to consider that either the chronic exposure to pathological levels of ALDO or the increased expression of vascular MR might promote vascular damage, endothelial dysfunction, and altered vasorelaxation (Virdis et al., 2002; Pu et al., 2003; Schiffrin, 2006; Nguyen Dinh Cat et al., 2010). More recent evidence from our laboratories has shown that the activation of the ALDO/RM pathway upregulates $Ca_V1.2$ expression in MAs (Mesquita et al., 2018); however, the effect of ALDO-induced MR activation on key Ca^{2+} handling proteins of the PM-SR nanodomain, such as SERCA pump, RyRs, and BK_{Ca} channels has remained elusive; and this work demonstrates that the compensatory increased expression of SERCA pump counterbalanced the higher activity of $Ca_V1.2$ channels.

Increased vascular resistance and vascular reactivity could be attributable to the thickening of the vascular walls as part of the maladaptive vessel changes in hypertension (Folkow, 1978). Therefore, to rule out the effects of chronic ALDO-mediated maladaptive vessel changes; and to avoid unsought Angiotensin II-induced vascular MR activation (Jaffe and Mendelsohn, 2005); we studied the effects of ALDO in rat MAs *ex vivo* following a previously described protocol (Mesquita et al., 2018) and our results demonstrate that short-term treatment with ALDO induced changes involving SERCA pump upregulation which precedes all the chronic maladaptive effects in MAs.

The precise control of $[Ca^{2+}]_{cyt}$ in MASMCs is crucial for regulating their physiological activity; and LTCCs have a prominent role in Ca^{2+} entry, regulating myogenic tone, arterial diameter, and BP (Moosmang et al., 2003; Fan et al., 2018). In spontaneous hypertensive rats (SHR), the chronic elevation of ALDO induces the upregulation of LTCCs in MAs, which has been associated with increased Ca^{2+} influx and vascular reactivity (Cox and Lozinskaya, 1995; Matsuda et al., 1997; Pratt et al., 2002). However, contrary to what might have been expected, we found no increase in depolarization-induced vasoconstriction, as previously reported in coronary arteries exposed to ALDO under similar experimental conditions (Mesquita et al., 2018). One explanation for this discrepancy could be distinct molecular targets activated by the ALDO/MR signaling pathway between vascular tissues. For instance, SERCA pump expression is augmented in mesenteric arteries but, to our knowledge, there is no data available about SERCA pump expression in coronary arteries exposed to ALDO in similar conditions used in this work (10 nM, 24 h). Therefore, we propose that SERCA efficiently counterbalances abnormal Ca^{2+} influx in some types of arteries (i.e., mesenteric arteries) but probably not in others (i.e., coronary arteries). This idea is further supported by reports showing that when LTCCs are activated through K^+-mediated membrane depolarization maneuvers, vasoconstriction responses of mesenteric and cerebral arteries are unaffected even in conditions of ALDO/MR signaling pathway over-activation (Suzuki et al., 1994; Xavier et al., 2008; Chrissobolis et al., 2014).

Once membrane depolarization is initiated, several processes act in concert to control $[Ca^{2+}]_{cyt}$ elevation, including (1) negative feedback mechanisms that decrease Ca^{2+} influx; for instance, Ca^{2+}-dependent inactivation of LTTCs, and BK_{Ca} channel activation which induces membrane hyperpolarization and decreases the open probability of LTCCs; (2) cytosolic Ca^{2+} buffering by proteins such as sorcin and calmodulin; and (3) Ca^{2+} removal mechanisms at the PM-SR nanodomain which include the SERCA pump, the Na^+/Ca^{2+} exchanger, and the plasma membrane Ca^{2+} ATPase (Kamishima and McCarron, 1996; Van Breemen et al., 2013; Evans, 2017). Our data support the notion that SERCA pump, RyR2, and BK_{Ca} channels act simultaneously to control abnormal $Ca_v1.2$-mediated Ca^{2+} influx in MAs treated with ALDO. Importantly, our data also highlight the crucial role of the superficial buffer barrier in SMCs in controlling Ca^{2+} influx. Van Breemen et al. (1995) have postulated the existence of a superficial and fenestrated surface of the SR separated from the plasma membrane by a narrow space that generates a barrier to Ca^{2+} entry *via* $Ca_v1.2$ channels. Then, extracellular Ca^{2+} is effectively captured toward the luminal SR Ca^{2+} stores by the SERCA pump limiting its access to the bulk myoplasm (Chen and van Breemen, 1993; Van Breemen et al., 1995; Van Breemen et al., 2013). Because SMC contraction relies on the increment of $[Ca^{2+}]_{cyt}$ due to Ca^{2+} influx and Ca^{2+} release from SR Ca^{2+} stores (Flores-Soto et al., 2013); and occurs only when actin-myosin myofilaments are activated by Ca^{2+} reaching the deep myoplasm, not by Ca^{2+} localized in the space between the plasma membrane and the superficial SR (Van Breemen et al., 1995), it is possible to reduce the force of contraction when the rate of Ca^{2+} influx is controlled (Casteels and Droogmans, 1981). Interestingly, vasoconstriction response to α-adrenoceptor is augmented in MAs of DOCA-salt rats but not depolarization-induced contraction (Perry and Webb, 1991; Suzuki et al., 1994) supporting the idea that contraction is related more to the rate than to the extent of Ca^{2+} entry (Casteels and Droogmans, 1981).

L-type voltage-dependent Ca^{2+} channels also contribute to refilling luminal SR Ca^{2+} load via SERCA pump activity and are involved in the formation of Ca^{2+} sparks, which induce vasorelaxation (Cheranov and Jaggar, 2002; Krishnamoorthy et al., 2014; Fan et al., 2018). In fact, the tight coupling between $Ca_v1.2$ and RyR is not required for $Ca_v1.2$ to initiate Ca^{2+} sparks in MASMCs. Instead, the $Ca_v1.2$ channel contributes to $[Ca^{2+}]_{cyt}$, which in turn activates the SERCA pump, increases SR Ca^{2+} load, and triggers Ca^{2+} sparks (Essin et al., 2007; Fan et al., 2018). Interestingly, the $Ca_v3.2$ channel is also involved in the ignition of Ca^{2+} sparks, though by a direct mechanism in which its localization in caveolae and close apposition to RyRs is crucial to trigger Ca^{2+} sparks in MASMCs. Despite $Ca_v3.2$ channel has a smaller participation in the generation of Ca^{2+} sparks with respect to $Ca_v1.2$ channel (Fan et al., 2018); additional work is required to delineate its specific contribution to Ca^{2+} spark ignition in ALDO-treated MASMCs.

Thus, in our experimental model, we hypothesize that $Ca_v1.2$ is the predominant pathway to provide Ca^{2+} for loading SR Ca^{2+} stores; and that the SERCA pump has a crucial role in the control of $Ca_v1.2$-mediated Ca^{2+} influx. In agreement with this idea, we demonstrate that blocking Ca^{2+} entry with Nifedipine significantly reduced Ca^{2+} spark frequency, suggesting that the SERCA pump mediates Ca^{2+} store refilling and, in consequence, Ca^{2+} spark generation.

Reports about ALDO effects on the expression and activity of the SERCA pump are scarce. In this regard, a study has shown that the treatment of human aortic SMCs with ALDO decreased SERCA2a transcription (Chou et al., 2015). Specifically, this work demonstrated that 48-h ALDO exposure (10 nM and 100 nM) reduced SERCA2 protein expression and SERCA2a mRNA levels. Aldosterone inhibited the expression of SERCA2a through MR-dependent mitochondrial DNA-specific transcription factors TFAM and TFB2M (Chou et al., 2015). Our work also provides evidence for an MR-mediated genomic pathway inducing the increase of SERCA pump mRNA levels. However, we did not examine the transcription factor involved in this response. An alternative mechanism could be that increased intracellular Ca^{2+} levels promote SERCA pump expression in VSMCs (Wu et al., 2001). Previous works have shown that resting $[Ca^{2+}]_{cyt}$ is augmented (1.6-fold over controls) in aortic SMCs of ALDO-salt hypertensive rats (Liu et al., 1995), which might increase SERCA pump expression (Levitsky et al., 1993). However, our results demonstrate that $[Ca^{2+}]_{cyt}$ is not elevated in ALDO-treated MASMCs, arguing against this mechanism. Moreover, an MR antagonist blocked the ALDO-mediated increase in SERCA pump mRNA and protein expression; therefore, an MR-mediated, tissue-specific genomic pathway is involved. Given that rat MAs express SERCA2a and SERCA2b isoforms (Lagaud et al., 1999), our data do not clarify whether one or both isoforms responded to ALDO treatment. We think that SERCA2a might be sensitive to ALDO because this isoform increases the rate of Ca^{2+} store refilling in VSMCs, maintaining a high SR Ca^{2+} concentration (Bobe et al., 2011). However, this hypothesis awaits further studies.

Regarding ALDO effects on RyR expression and activity, this work is the first to report that short-term treatment with ALDO increases Ca^{2+} spark frequency in MASMCs. Previously, we have demonstrated that ALDO/MR signaling pathway activation augmented Ca^{2+} spark frequency and altered Ca^{2+} spark properties in cardiomyocytes, which was associated with the downregulation of FKBP12 and FKBP12.6, accessory proteins of the RyR macromolecular complex (Gómez et al., 2009). Likely, we found an increase in Ca^{2+} spark frequency of ALDO-treated MASMCs but FKBP12.6 expression remained unchanged; therefore, this does not explain the change in Ca^{2+} spark frequency. In our hands, the increase in Ca^{2+} spark frequency was associated with the increased SR Ca^{2+} load in ALDO-treated MAs, because the addition of Nifedipine, an LTCC blocker, effectively reduced the frequency of these local Ca^{2+} events, even in ALDO-treated cells. This result agrees with previous publications (Cheranov and Jaggar, 2002; Fan et al., 2018). Diltiazem belongs to the benzothiazepine subclass of Ca^{2+} channel antagonists and blocks $Ca_v1.2$ in resting state, but membrane depolarization enhances its inhibitory effect (Tang et al., 2019). This attribute explains the inhibitory effect on Ca^{2+} sparks in VSMC under resting, non-depolarizing conditions (bath solution containing

6 mM K^+) (Cheranov and Jaggar, 2002). Nifedipine belongs to the dihydropyridine subclass of LTCC blockers and exhibits prominent a voltage-dependent antagonism, according to which its potency increases with the level of depolarization. This justifies, in part, the general vascular selectivity of Nifedipine over other Ca^{2+} channel blockers (Triggle, 1991). Consistent with this feature, in the present work, Nifedipine reduced the frequency and duration of Ca^{2+} sparks in both experimental groups under mild-depolarized conditions (PSS-20K).

Depolarization of MASMCs increased the frequency and amplitude of STOCs and elicited Ca^{2+} sparks from Ca^{2+} discharge regions (Pucovský and Bolton, 2006). Moreover, in VSMCs of the transgenic mouse with VSMC-specific $Ca_v1.2$ channel gene inactivation (SMAKO mouse), both frequency and amplitude of STOCs were reduced, together with decreased cytosolic Ca^{2+} levels and SR Ca^{2+} load (Essin et al., 2007). Accordingly, we observed an increase in STOC and spark activities associated with higher $Ca_v1.2$ and SERCA pump protein expressions. Although, Ca^{2+} influx through $Ca_v1.2$ channels is the primary source of Ca^{2+} for triggering Ca^{2+} sparks (70–80%) in MASMCs; an additional Ca^{2+} source is provided by $Ca_v3.2$ channels (20–30%) (Fan et al., 2018). Besides, higher micromolar concentrations of Nifedipine may interfere with T-type Ca^{2+} channel activity (Abd El-Rahman et al., 2013). Therefore, future work is needed to delineate the specific contribution of $Ca_v1.2$ and $Ca_v3.2$ to Ca^{2+} spark generation in ALDO-treated MASMCs.

Existing evidence shows an association between ALDO/MR signaling pathway, vascular BK_{Ca} channel expression, and activity. In a mouse model with cardiomyocyte-specific overexpression of the aldosterone synthase gene (MAS mice), an impairment in ACh-induced vasorelaxation, associated with decreased mRNA expression of α and β1 subunits of BK_{Ca} channels in coronary arteries has been reported (Ambroisine et al., 2007). Although BK_{Ca} channel protein expression levels were not determined, the β1 subunit of the BK_{Ca} channel showed a similar expression in immunostainings of freshly isolated coronary arteries (Ambroisine et al., 2007). In contrast, in the SMC-MR-KO mouse no difference was found in mRNA expression of α and β1 subunits of BK_{Ca} channel in aorta (McCurley et al., 2012); similarly to our results in coronary arteries treated with ALDO (Mesquita et al., 2018). Further experiments with the SMC-MR-KO mouse will be helpful to corroborate our results.

In contrast with previous results in coronary arteries (Mesquita et al., 2018), we found a higher sensitivity of ACh-mediated vasorelaxation after 24-h ALDO treatment. This result can be explained by the increased SERCA-mediated SR Ca^{2+} load, and augmented Spark-STOC activity. On the other hand, chronic effects of ALDO can lead to an impairment of endothelium-dependent vasorelaxation of MAs (Xavier et al., 2008). The pre-treatment of chronically exposed MAs to ALDO with indomethacin (a cyclooxygenase inhibitor), resulted in a recovery of the sensitivity to ACh without modification of the ACh-mediated maximal vasodilation response (Xavier et al., 2008). The latter similar to our results, suggesting the lack of endothelial damage in our experimental conditions. Rapid vasodilator action of ALDO has been described to depend on MR receptor activation, enhancing the production of nitric oxide (NO) (Davel et al., 2017). Therefore, endothelial MRs (EC-MR) could potentially contribute to ALDO effects in MAs. However, the EC-MR may not be involved in the enhanced ACh-induced vasorelaxation observed in our experimental model of ALDO-treated MAs, based on the following considerations. First, EC-MR-mediated vasodilator actions of ALDO occur in minutes after the mineralocorticoid application (Davel et al., 2017), while our study evaluates ALDO effects after 24-h treatment. Second, we have shown previously that the endothelial layer is not involved in ALDO effects on coronary and aorta vasoconstriction (Mesquita et al., 2018). Third, it has been suggested that EC-MR does not play a significant role in the control of vascular function in non-disease states (Mueller et al., 2015). Finally, NO-mediated relaxation of MAs from a mouse model over-expressing EC-MR was similar to control (Nguyen Dinh Cat et al., 2010). Interestingly, EC protection is lost when cardiovascular risk factors are present (Jaffe and Jaisser, 2014; Davel et al., 2017; DuPont and Jaffe, 2017). Therefore, the role of EC-MR in MAs deserves more studies, specifically under pathological conditions.

This work highlights the intricacies of tissue-specific MR signaling and the differential actors of MR signaling across vascular beds, contributing to ALDO-associated impairments of vascular functions and blood flow control. Initial functional changes induced by ALDO are adaptative, but in chronic pathological conditions will become maladaptive, leading to poor vascular function, vascular remodeling, and poor compliant arteries as observed in hypertension; thus, further delineation of the MR-induced molecular pathways that control vascular SERCA2 expression will require additional analysis.

New and Noteworthy

Cumulative evidence has shown that the mineralocorticoid receptor (MR) is found in vascular tissues where regulates expression and activity of ion channels that participate in Ca^{2+} handling of smooth muscle cells (SMCs), but none of these studies had evaluated the effect of ALDO/MR signaling pathway on the functional unit that regulates vascular function, comprising $Ca_v1.2$, SERCA pump, Ryanodine receptors, and BK_{Ca} channels, and we aimed to study it comprehensively. Our work provides novel evidence about ALDO-induced upregulation of this functional unit unveiling the crucial role of the SERCA pump in counterbalancing $Ca_v1.2$-mediated Ca^{2+} influx at the subplasmalemmal space of mesenteric artery SMCs. This work highlights the intricacies of tissue-specific MR signaling and the differential actors of the ALDO/MR signaling pathway across vascular beds, contributing to ALDO-associated impairments of vascular functions. Initial functional changes induced by ALDO are adaptative, but in chronic pathological conditions, they would become maladaptive leading to vascular dysfunction, vascular remodeling, and poor compliant arteries as observed in hypertension.

DATA AVAILABILITY STATEMENT

The raw data supporting the conclusions of this article will be made available by the authors, without undue reservation.

ETHICS STATEMENT

The animal study was reviewed and approved by COMITÉ INTERNO PARA EL CUIDADO Y USO DE LOS ANIMALES DE LABORATORIO (CICUAL) Cinvestav.

AUTHOR CONTRIBUTIONS

RS-E contributed to the conceptualization, methodology, data collecting, data analysis, and writing. AG-H contributed to the conceptualization, resources, review and editing. AG contributed to the conceptualization, resources, funding acquisition, and review and editing. J-PB contributed to the conceptualization, methodology, resources, funding acquisition, and review and editing. AR contributed to the conceptualization, methodology, data analysis, writing, resources, funding acquisition, and review and editing. All authors contributed to the article and approved the submitted version.

FUNDING

This work was supported by program Conacyt ECOS-Nord France (Evaluatio-orientation de la COopération Scientifique) project No. M13S01 to J-PB and AR. By Fundación Miguel Alemán A.C., by Fondo SEP-Cinvestav project No. 601410 FIDSC 2018/2; and by Fondo Sectorial de Investigación para la Educación de Conacyt (Project # A1-S-9082) to AR. By Agence National de la Recherche, ANR-19-CE-0031-01 to AG. RS-E was a CONACYT Ph.D. fellow.

ACKNOWLEDGMENTS

We are grateful to Dr. Beatriz Xoconostle (Department of Biotechnology, CINVESTAV-IPN, Mexico) for giving us access to a real-time qPCR equipment. We gratefully acknowledge the generosity and expert guidance of Dr. Boris Manoury with the wire myograph system. We also thank Dr. Thássio R. Mesquita Ribeiro and Dr. Nohemi A. Camacho Concha for their critical advice during the development of this project. We acknowledge the technical assistance of Martha Mercado Morales and Juan Carlos García Torres; and the invaluable help of the specialists at the Proteomic, Genomic, and Metabolomic Unit (LaNSE, Cinvestav-IPN). Anti-sorcin antibody was a generous gift from Dr. Héctor H. Valdivia (University of Wisconsin-Madison, Madison, WI, United States).

SUPPLEMENTARY MATERIAL

The Supplementary Material for this article can be found online at: https://www.frontiersin.org/articles/10.3389/fphys.2022.834220/full#supplementary-material

REFERENCES

Abd El-Rahman, R. R., Harraz, O. F., Brett, S. E., Anfinogenova, Y., Mufti, R. E., Goldman, D., et al. (2013). Identification of L- and T-type Ca2+ channels in rat cerebral arteries: role in myogenic tone development. *Am. J. Physiol. Heart Circ. Physiol.* 304, H58–H71. doi: 10.1152/AJPHEART.00476.2012

Acelajado, M. C., Hughes, Z. H., Oparil, S., and Calhoun, D. A. (2019). Treatment of resistant and refractory hypertension. *Circ. Res.* 124, 1061–1070. doi: 10.1161/CIRCRESAHA.118.31S2156

Ambroisine, M. L., Favre, J., Oliviero, P., Rodriguez, C., Gao, J., Thuillez, C., et al. (2007). Aldosterone-induced coronary dysfunction in transgenic mice involves the calcium-activated potassium (BKCa) channels of vascular smooth muscle cells. *Circulation* 116, 2435–2443. doi: 10.1161/CIRCULATIONAHA.107.722009

Bartoli, F., Bailey, M. A., Rode, B., Mateo, P., Antigny, F., Bedouet, K., et al. (2020). Orai1 channel inhibition preserves left ventricular systolic function and normal Ca2+ handling after pressure overload. *Circulation* 141, 199–216. doi: 10.1161/CIRCULATIONAHA.118.038891

Bénitah, J. P., and Vassort, G. (1999). Aldosterone upregulates Ca2+ current in adult rat cardiomyocytes. *Circ. Res.* 85, 1139–1145. doi: 10.1161/01.RES.85.12.1139

Bobe, R., Hadri, L., Lopez, J. J., Sassi, Y., Atassi, F., Karakikes, I., et al. (2011). SERCA2a controls the mode of agonist-induced intracellular Ca2+ signal, transcription factor NFAT and proliferation in human vascular smooth muscle cells. *J. Mol. Cell. Cardiol.* 50, 621–633. doi: 10.1016/J.YJMCC.2010.12.016

Briet, M., Barhoumi, T., Mian, M. O. R., Coelho, S. C., Ouerd, S., Rautureau, Y., et al. (2016). Aldosterone-induced vascular remodeling and endothelial dysfunction require functional angiotensin type 1a receptors. *Hypertension* 67, 897–905. doi: 10.1161/HYPERTENSIONAHA.115.07074

Casteels, R., and Droogmans, G. (1981). Exchange characteristics of the noradrenaline-sensitive calcium store in vascular smooth muscle cells or rabbit ear artery. *J. Physiol.* 317, 263–279. doi: 10.1113/jphysiol.1981.sp013824

Chen, Q., and van Breemen, C. (1993). The superficial buffer barrier in venous smooth muscle: sarcoplasmic reticulum refilling and unloading. *Br. J. Pharmacol.* 109, 336–343. doi: 10.1111/j.1476-5381.1993.tb13575.x

Cheranov, S. Y., and Jaggar, J. H. (2002). Sarcoplasmic reticulum calcium load regulates rat arterial smooth muscle calcium sparks and transient K Ca currents. *J. Physiol.* 544, 71–84. doi: 10.1113/jphysiol.2002.025197

Chou, C. H., Chen, Y. H., Hung, C. S., Chang, Y. Y., Tzeng, Y. L., Wu, X. M., et al. (2015). Aldosterone impairs vascular smooth muscle function: from clinical to bench research. *J. Clin. Endocrinol. Metab.* 100, 4339–4347. doi: 10.1210/jc.2015-2752

Chrissobolis, S., Drummond, G. R., Faraci, F. M., and Sobey, C. G. (2014). Chronic aldosterone administration causes Nox2-mediated increases in reactive oxygen species production and endothelial dysfunction in the cerebral circulation. *J. Hypertens.* 32, 1815–1821. doi: 10.1097/HJH.0000000000000259

Cox, R. H., and Lozinskaya, I. M. (1995). Augmented calcium currents in mesenteric artery branches of the spontaneously hypertensive rat. *Hypertension* 26, 1060–1064. doi: 10.1161/01.HYP.26.6.1060

Dagnino-Acosta, A., and Guerrero-Hernández, A. (2009). Variable luminal sarcoplasmic reticulum Ca(2$^+$) buffer capacity in smooth muscle cells. *Cell Calcium* 46, 188–196. doi: 10.1016/j.ceca.2009.07.005

Davel, A. P., Anwar, I. J., and Jaffe, I. Z. (2017). The endothelial mineralocorticoid receptor: mediator of the switch from vascular health to disease. *Curr. Opin. Nephrol. Hypertens.* 26, 97–104. doi: 10.1097/MNH.0000000000000306

de Alba-Aguayo, D. R., Pavón, N., Mercado-Morales, M., Miranda-Saturnino, M., López-Casamichana, M., Guerrero-Hernández, A., et al. (2017). Increased calcium leak associated with reduced calsequestrin expression in hyperthyroid cardiomyocytes. *Cell Calcium* 62, 29–40. doi: 10.1016/j.ceca.2017.01.009

DuPont, J. J., and Jaffe, I. Z. (2017). The role of the mineralocorticoid receptor in the vasculature. *J. Endocrinol.* 234, T67–T82. doi: 10.1530/JOE-17-0009

Esfandiarei, M., Fameli, N., Choi, Y. Y. H., Tehrani, A. Y., Hoskins, J. G., and van Breemen, C. (2013). Waves of calcium depletion in the sarcoplasmic reticulum of vascular smooth muscle cells: an inside view of spatiotemporal Ca2+ regulation. *PLoS One* 8:e55333. doi: 10.1371/journal.pone.0055333

Essin, K., and Gollasch, M. (2009). Role of ryanodine receptor subtypes in initiation and formation of calcium sparks in arterial smooth muscle: comparison with striated muscle. *J. Biomed. Biotechnol.* 2009:135249. doi: 10.1155/2009/135249

Essin, K., Welling, A., Hofmann, F., Luft, F. C., Gollasch, M., and Moosmang, S. (2007). Indirect coupling between Ca v 1.2 channels and ryanodine receptors to generate Ca2+ sparks in murine arterial smooth muscle cells. *J. Physiol.* 584, 205–219. doi: 10.1113/jphysiol.2007.138982

Evans, A. M. (2017). *Nanojunctions of the Sarcoplasmic Reticulum Deliver Site- and Function-Specific Calcium Signaling in Vascular Smooth Muscles*, 1st Edn. Amsterdam: Elsevier Inc, doi: 10.1016/bs.apha.2016.10.001

Fan, G., Kaßmann, M., Hashad, A. M., Welsh, D. G., and Gollasch, M. (2018). Differential targeting and signalling of voltage-gated T-type Cav3.2 and L-type Cav1.2 channels to ryanodine receptors in mesenteric arteries. *J. Physiol.* 596, 4863–4877. doi: 10.1113/JP276923

Fernández-Velasco, M., Ruiz-Hurtado, G., Gómez, A. M., and Rueda, A. (2014). Ca2+ handling alterations and vascular dysfunction in diabetes. *Cell Calcium* 56, 397–407. doi: 10.1016/j.ceca.2014.08.007

Flores-Soto, E., Reyes-García, J., Sommer, B., and Montaño, L. M. (2013). Sarcoplasmic reticulum Ca2+ refilling is determined by L-type Ca2+ and store operated Ca2+ channels in guinea pig airway smooth muscle. *Eur. J. Pharmacol.* 721, 21–28. doi: 10.1016/j.ejphar.2013.09.060

Folkow, B. (1978). Cardiovascular structural adaptation; its role in the initiation and maintenance of primary hypertension. *Clin. Sci.* 55, 3s–22s. doi: 10.1042/cs055003s

Funder, J. W., Pearce, P. T., Smith, R., and Campbell, J. (1989). Vascular type I aldosterone binding sites are physiological mineralocorticoid receptors. *Endocrinology* 125, 2224–2226. doi: 10.1210/endo-125-4-2224

Ganitkevich, V., and Isenberg, G. (1990). Isolated guinea pig coronary smooth muscle cells. *Circ. Res.* 67, 525–529. doi: 10.1161/01.res.67.2.525

Ghosh, D., Syed, A. U., Prada, M. P., Nystoriak, M. A., Santana, L. F., Nieves-Cintrón, M., et al. (2017). Calcium channels in vascular smooth muscle. *Adv. Pharmacol.* 78, 49–87. doi: 10.1016/bs.apha.2016.08.002

Gollasch, M., Wellman, G. C., Knot, H. J., Jaggar, J. H., Damon, D. H., Bonev, A. D., et al. (1998). Ontogeny of local sarcoplasmic reticulum Ca2+ signals in cerebral arteries: Ca2+ sparks as elementary physiological events. *Circ. Res.* 83, 1104–1114. doi: 10.1161/01.res.83.11.1104

Gómez, A. M., Rueda, A., Sainte-Marie, Y., Pereira, L., Zissimopoulos, S., Zhu, X., et al. (2009). Mineralocorticoid modulation of cardiac ryanodine receptor activity is associated with downregulation of FK506-binding proteins. *Circulation* 119, 2179–2187. doi: 10.1161/CIRCULATIONAHA.108.805804

Gomez-Sanchez, C. E., De Rodriguez, A. F., Romero, D. G., Estess, J., Warden, M. P., Gomez-Sanchez, M. T., et al. (2006). Development of a panel of monoclonal antibodies against the mineralocorticoid receptor. *Endocrinology* 147, 1343–1348. doi: 10.1210/EN.2005-0860

Grynkiewicz, G., Poenie, M., and Tsien, R. Y. (1985). A new generation of Ca2+ indicators with greatly improved fluorescence properties. *J. Biol. Chem.* 260, 3440–3450.

Jaffe, I. Z., and Jaisser, F. (2014). Endothelial cell mineralocorticoid receptors: turning cardiovascular risk factors into cardiovascular dysfunction. *Hypertens* 63, 915–917. doi: 10.1161/HYPERTENSIONAHA.114.01997

Jaffe, I. Z., and Mendelsohn, M. E. (2005). Angiotensin II and aldosterone regulate gene transcription via functional mineralocortocoid receptors in human coronary artery smooth muscle cells. *Circ. Res.* 96, 643–650. doi: 10.1161/01.RES.0000159937.05502.d1

Jaggar, J. H., Porter, V. A., Jonathan Lederer, W., and Nelson, M. T. (2000). Calcium sparks in smooth muscle. *Am. J. Physiol. Cell Physiol.* 278, C235–C256. doi: 10.1152/ajpcell.2000.278.2.c235

Jaggar, J. H., Wellman, G. C., Heppner, T. J., Porter, V. A., Perez, G. J., Gollasch, M., et al. (1998). Ca2+ channels, ryanodine receptors and Ca(2+)-activated K+ channels: a functional unit for regulating arterial tone. *Acta Physiol. Scand.* 164, 577–587. doi: 10.1046/j.1365-201X.1998.00462.x

Kamishima, T., and McCarron, J. G. (1996). Depolarization-evoked increases in cytosolic calcium concentration in isolated smooth muscle cells of rat portal vein. *J. Physiol.* 492(Pt 1), 61–74. doi: 10.1113/jphysiol.1996.sp021289

Kim, P. J., Cole, M. A., Kalman, B. A., and Spencer, R. L. (1998). Evaluation of RU28318 and RU40555 as selective mineralocorticoid receptor and glucocorticoid receptor antagonists, respectively: receptor measures and functional studies. *J. Steroid Biochem. Mol. Biol.* 67, 213–222. doi: 10.1016/s0960-0760(98)00095-8

Knot, H. J., Standen, N. B., and Nelson, M. T. (1998). Ryanodine receptors regulate arterial diameter and wall [Ca2+] in cerebral arteries of rat via Ca2+-dependent K+ channels. *J. Physiol.* 508, 211–221. doi: 10.1111/j.1469-7793.1998.211br.x

Krishnamoorthy, G., Sonkusare, S. K., Heppner, T. J., and Nelson, M. T. (2014). Opposing roles of smooth muscle BK channels and ryanodine receptors in the regulation of nerve-evoked constriction of mesenteric resistance arteries. *Am. J. Physiol. Hear. Circ. Physiol.* 306:H981. doi: 10.1152/ajpheart.00866.2013

Lagaud, G. J., Randriamboavonjy, V., Roul, G., Stoclet, J. C., and Andriantsitohaina, R. (1999). Mechanism of Ca2+ release and entry during contraction elicited by norepinephrine in rat resistance arteries. *Am. J. Physiol.* 276, H300–H308.

Lalevée, N., Rebsamen, M. C., Barrère-Lemaire, S., Perrier, E., Nargeot, J., Bénitah, J. P., et al. (2005). Aldosterone increases T-type calcium channel expression and *in vitro* beating frequency in neonatal rat cardiomyocytes. *Cardiovasc. Res.* 67, 216–224. doi: 10.1016/j.cardiores.2005.05.009

Leung, F. P., Yung, L. M., Yao, X., Laher, I., and Huang, Y. (2008). Store-operated calcium entry in vascular smooth muscle. *Br. J. Pharmacol.* 153, 846–857. doi: 10.1038/sj.bjp.0707455

Levitsky, D., Clergue, M., Lambert, F., Souponitskayas, V., Jemtelfl, T. H., Le Lecarpentier, Y., et al. (1993). Sarcoplasmic reticulum calcium transport and Ca2+ -ATPase gene expression in thoracic and abdominal aortas of normotensive and spontaneously hypertensive rats. *J. Biol. Chem.* 268, 8325–8331. doi: 10.1016/s0021-9258(18)53099-4

Liu, Y., Jones, A. W., and Sturek, M. (1995). Ca(2+)-dependent K+ current in arterial smooth muscle cells from aldosterone-salt hypertensive rats. *Am. J. Physiol.* 269, H1246–H1257.

Lombès, M., Oblin, M. E., Gasc, J. M., Baulieu, E. E., Farman, N., and Bonvalet, J. P. (1992). Immunohistochemical and biochemical evidence for a cardiovascular mineralocorticoid receptor. *Circ. Res.* 71, 503–510. doi: 10.1161/01.res.71.3.503

Mangelsdorf, D. J., Thummel, C., Beato, M., Herrlich, P., Schütz, G., Umesono, K., et al. (1995). The nuclear receptor superfamily: the second decade. *Cell* 83, 835–839. doi: 10.1016/0092-8674(95)90199-x

Matsuda, K., Lozinskaya, I., and Cox, R. H. (1997). Augmented contributions of voltage-gated Ca2+ channels to contractile responses in spontaneous hypertensive rat mesenteric arteries. *Am. J. Hypertens.* 7061, 1231–1239. doi: 10.1016/s0895-7061(97)00225-2

Matsuki, K., Kato, D., Takemoto, M., Suzuki, Y., Yamamura, H., Ohya, S., et al. (2018). Negative regulation of cellular ca2+ mobilization by ryanodine receptor type 3 in mouse mesenteric artery smooth muscle. *Am. J. Physiol. Cell Physiol.* 315, C1–C9. doi: 10.1152/ajpcell.00006.2018

McCurley, A., Pires, P. W., Bender, S. B., Aronovitz, M., Zhao, M. J., Metzger, D., et al. (2012). Direct regulation of blood pressure by smooth muscle cell mineralocorticoid receptors. *Nat. Med.* 18, 1429–1433. doi: 10.1038/nm.2891

Mesquita, T. R., Auguste, G., Falcón, D., Ruiz-Hurtado, G., Salazar-Enciso, R., Sabourin, J., et al. (2018). Specific activation of the alternative cardiac promoter of cacna1c by the mineralocorticoid receptor. *Circ. Res.* 122, e49–e61. doi: 10.1161/CIRCRESAHA.117.312451

Moosmang, S., Schulla, V., Welling, A., Feil, R., Feil, S., Wegener, J. W., et al. (2003). Dominant role of smooth muscle L-type calcium channel Cav1.2 for blood pressure regulation. *EMBO J.* 22, 6027–6034. doi: 10.1093/emboj/cdg583

Mueller, K. B., Bender, S. B., Hong, K., Yang, Y., Aronovitz, M., Jaisser, F., et al. (2015). Endothelial mineralocorticoid receptors differentially contribute to coronary and mesenteric vascular function without modulating blood pressure. *Hypertension* 66, 988–997. doi: 10.1161/HYPERTENSIONAHA.115.06172

Nelson, M. T., and Worley, J. F. (1989). Dihydropyridine inhibition of single calcium channels and contraction in rabbit mesenteric artery depends on voltage. *J. Physiol.* 412, 65–91. doi: 10.1113/jphysiol.1989.sp017604

Nelson, M. T., Cheng, H., Rubart, M., Santana, L. F., Bonev, A. D., Knot, H. J., et al. (1995). Relaxation of arterial smooth muscle by calcium sparks. *Science* 270, 633–637. doi: 10.1126/science.270.5236.633

Nguyen Dinh Cat, A., Griol-Charhbili, V., Loufrani, L., Labat, C., Benjamin, L., Farman, N., et al. (2010). The endothelial mineralocorticoid receptor regulates vasoconstrictor tone and blood pressure. *FASEB J.* 24, 2454–2463. doi: 10.1096/fj.09-147926

Pérez, G. J., Bonev, A. D., Patlak, J. B., and Nelson, M. T. (1999). Functional coupling of ryanodine receptors to KCa channels in smooth muscle cells from rat cerebral arteries. *J. Gen. Physiol.* 113, 229–238. doi: 10.1085/jgp.113.2.229

Perry, P. A., and Webb, R. C. (1991). Agonist-sensitive calcium stores in arteries from steroid hypertensive rats. *Hypertension* 17, 603–611. doi: 10.1161/01.HYP.17.5.603

Pfaffl, M. W. (2001). A new mathematical model for relative quantification in real-time RT-PCR. *Nucleic Acids Res.* 29:e45. doi: 10.1093/nar/29.9.e45

Pratt, P. F., Bonnet, S., Ludwig, L. M., Bonnet, P., and Rusch, N. J. (2002). Upregulation of L-type Ca2+ channels in mesenteric and skeletal arteries of SHR. *Hypertension* 40, 214–219. doi: 10.1161/01.HYP.0000025877.23309.36

Pu, Q., Neves, M. F., Virdis, A., Touyz, R. M., and Schiffrin, E. L. (2003). Endothelin antagonism on aldosterone-induced oxidative stress and vascular remodeling. *Hypertension* 42, 49–55. doi: 10.1161/01.HYP.0000078357.92682.EC

Pucovský, V., and Bolton, T. B. (2006). Localisation, function and composition of primary Ca(2+) spark discharge region in isolated smooth muscle cells from guinea-pig mesenteric arteries. *Cell Calcium* 39, 113–129. doi: 10.1016/J.CECA.2005.10.002

Romero-García, T., Landa-Galvan, H. V., Pavón, N., Mercado-Morales, M., Valdivia, H. H., and Rueda, A. (2020). Autonomous activation of CaMKII exacerbates diastolic calcium leak during beta-adrenergic stimulation in cardiomyocytes of metabolic syndrome rats. *Cell Calcium* 91:102267. doi: 10.1016/j.ceca.2020.102267

Rueda, A., Fernández-Velasco, M., Benitah, J.-P., and Gómez, A. M. (2013). Abnormal Ca2+ spark/STOC coupling in cerebral artery smooth muscle cells of obese type 2 diabetic mice. *PLoS One* 8:e53321. doi: 10.1371/journal.pone.0053321

Rueda, A., García, L., and Guerrero-Hernández, A. (2002). Luminal Ca2+ and the activity of sarcoplasmic reticulum Ca2+ pumps modulate histamine-induced all-or-none Ca2+ release in smooth muscle cells. *Cell. Signal.* 14, 517–527. doi: 10.1016/s0898-6568(01)00284-4

Rueda, A., Song, M., Toro, L., Stefani, E., and Valdivia, H. H. (2006). Sorcin modulation of Ca^{2+} sparks in rat vascular smooth muscle cells. *J. Physiol.* 576, 887–901. doi: 10.1113/jphysiol.2006.113951

Sabourin, J., Bartoli, F., Antigny, F., Gomez, A. M., and Benitah, J.-P. P. (2016). Transient Receptor Potential Canonical (TRPC)/Orai1-dependent Store-operated Ca2+ Channels: new targets of aldosterone in cardiomyocytes. *J. Biol. Chem.* 291, 13394–13409. doi: 10.1074/jbc.M115.693911

Salazar-Enciso, R., Camacho-Concha, N. A., Mesquita, T. R., Falcón, D., Benitah, J.-P., Gomez, A.-M., et al. (2018). "Mineralocorticoid receptor in calcium handling of vascular smooth muscle cells," in *Calcium and Signal Transduction*, eds J. Buchholz, et al. (London: InTech), 1–21.

Schiffrin, E. L. (1992). Reactivity of small blood vessels in hypertension: relation with structural changes. *Hypertension* 19, II1–II9. doi: 10.1161/01.HYP.19.2_Suppl.II1-a

Schiffrin, E. L. (2006). Effects of Aldosterone on the Vasculature. *Hypertension* 47, 312–318. doi: 10.1161/01.HYP.0000201443.63240.a7

Suzuki, S., Takata, Y., Kubota, S., Ozaki, S., and Kato, H. (1994). Characterization of the alpha-1 adrenoceptors in the mesenteric vasculature from deoxycorticosterone-salt hypertensive rats: studies on vasoconstriction, radioligand binding and postreceptor events. *J. Pharmacol. Exp. Ther.* 268, 576–583.

Takeda, Y., Miyamori, I., Inaba, S., Furukawa, K., Hatakeyama, H., Yoneda, T., et al. (1997). Vascular aldosterone in genetically hypertensive rats. *Hypertension* 29, 45–48.

Takeda, Y., Nystoriak, M. A., Nieves-Cintrón, M., Santana, L. F., and Navedo, M. F. (2011). Relationship between Ca2+ sparklets and sarcoplasmic reticulum Ca2+ load and release in rat cerebral arterial smooth muscle. *Am. J. Physiol. Hear. Circ. Physiol.* 301, H2285–H2294. doi: 10.1152/ajpheart.00488.2011

Takeda, Y., Yoneda, T., Miyamori, I., Gathiram, P., and Takeda, R. (1993). 11β−hidroxysteroid dehydrogenase activity in mesenteric arteries of spontaneously hypertensive rats. *Clin. Exp. Pharmacol. Physiol.* 20, 627–631. doi: 10.1111/j.1440-1681.1993.tb01644.x

Tang, L., Gamal El-Din, T. M., Lenaeus, M. J., Zheng, N., and Catterall, W. A. (2019). Structural basis for diltiazem block of a voltage-gated Ca 2+ channel. *Mol. Pharmacol.* 96, 485–492. doi: 10.1124/MOL.119.117531

Trebak, M., and Putney, J. W. (2017). ORAI calcium channels. *Physiology* 32, 332–342. doi: 10.1152/physiol.00011.2017

Triggle, D. J. (1991). Sites, mechanisms of action, and differentiation of calcium channel antagonists. *Am. J. Hypertens.* 4, 422S–429S. doi: 10.1093/ajh/4.7.422S

Van Breemen, C., Chen, Q., and Laher, I. (1995). Superficial buffer barrier function of smooth muscle sarcoplasmic reticulum. *Trends Pharmacol. Sci.* 16, 98–105. doi: 10.1016/S0165-6147(00)88990-7

Van Breemen, C., Fameli, N., and Evans, A. M. (2013). Pan-junctional sarcoplasmic reticulum in vascular smooth muscle: nanospace Ca2+ transport for site- and function-specific Ca2+ signalling. *J. Physiol.* 591, 2043–2054. doi: 10.1113/jphysiol.2012.246348

Virdis, A., Neves, M. F., Amiri, F., Viel, E., Touyz, R. M., and Schiffrin, E. L. (2002). Spironolactone improves angiotensin-induced vascular changes and oxidative stress. *Hypertension* 40, 504–510. doi: 10.1161/01.HYP.0000034738.79310.06

Wang, K., Li, H., Xu, Y., Shao, Q., Yi, J., Wang, R., et al. (2019). MFEprimer-3.0: quality control for PCR primers. *Nucleic Acids Res.* 47, W610–W613. doi: 10.1093/nar/gkz351

Wang, Y.-X., Zheng, Y.-M., Mei, Q.-B., Wang, Q.-S., Collier, M. L., Fleischer, S., et al. (2004). FKBP12.6 and cADPR regulation of Ca2+ release in smooth muscle cells. *Am. J. Physiol. Cell Physiol.* 286, C538–C546. doi: 10.1152/ajpcell.00106.2003

Weinberger, M. H., Roniker, B., Krause, S. L., and Weiss, R. J. (2002). Eplerenone, a selective aldosterone blocker, in mild-to-moderate hypertension. *Am. J. Hypertens.* 15, 709–716. doi: 10.1016/S0895-7061(02)02957-6

Wu, K. D., Bungard, D., and Lytton, J. (2001). Regulation of SERCA Ca2+ pump expression by cytoplasmic [Ca2+] in vascular smooth muscle cells. *Am. J. Physiol. Cell Physiol.* 280, 843–851. doi: 10.1152/ajpcell.2001.280.4.c843

Xavier, F. E., Aras-López, R., Arroyo-Villa, I., Del Campo, L., Salaices, M., Rossoni, L. V., et al. (2008). Aldosterone induces endothelial dysfunction in resistance arteries from normotensive and hypertensive rats by increasing thromboxane A 2 and prostacyclin. *Br. J. Pharmacol.* 154, 1225–1235. doi: 10.1038/bjp.2008.200

Conflict of Interest: The authors declare that the research was conducted in the absence of any commercial or financial relationships that could be construed as a potential conflict of interest.

frontiers | Frontiers in Physiology

ORIGINAL RESEARCH
published: 20 April 2022
doi: 10.3389/fphys.2022.805909

Aging Alters the Formation and Functionality of Signaling Microdomains Between L-type Calcium Channels and β2-Adrenergic Receptors in Cardiac Pacemaker Cells

Sabrina Choi[‡], *Oscar Vivas*[‡], *Matthias Baudot and Claudia M. Moreno* *[†]

Department of Physiology and Biophysics, University of Washington, Seattle, WA, United States

Heart rate is accelerated to match physiological demands through the action of noradrenaline on the cardiac pacemaker. Noradrenaline is released from sympathetic terminals and activates β1-and β2-adrenergic receptors (ARs) located at the plasma membrane of pacemaker cells. L-type calcium channels are one of the main downstream targets potentiated by the activation of β-ARs. For this signaling to occur, L-type calcium channels need to be located in close proximity to β-ARs inside caveolae. Although it is known that aging causes a slowdown of the pacemaker rate and a reduction in the response of pacemaker cells to noradrenaline, there is a lack of in-depth mechanistic insights into these age-associated changes. Here, we show that aging affects the formation and function of adrenergic signaling microdomains inside caveolae. By evaluating the β1 and β2 components of the adrenergic regulation of the L-type calcium current, we show that aging does not alter the regulation mediated by β1-ARs but drastically impairs that mediated by β2-ARs. We studied the integrity of the signaling microdomains formed between L-type calcium channels and β-ARs by combining high-resolution microscopy and proximity ligation assays. We show that consistent with the electrophysiological data, aging decreases the physical association between β2-ARs and L-type calcium channels. Interestingly, this reduction is associated with a decrease in the association of L-type calcium channels with the scaffolding protein AKAP150. Old pacemaker cells also have a reduction in caveolae density and in the association of L-type calcium channels with caveolin-3. Together the age-dependent alterations in caveolar formation and the nano-organization of β2-ARs and L-type calcium channels result in a reduced sensitivity of the channels to β2 adrenergic modulation. Our results highlight the importance of these signaling microdomains in maintaining the chronotropic modulation of the heart and also pinpoint the direct impact that aging has on their function.

Keywords: cardiac pacemaker, aging, L-type calcium channel, beta-adrenergic receptor, signaling microdomain, AKAP150, caveolin-3 (Cav-3), scaffolding proteins

Edited by:
Nina D. Ullrich,
Heidelberg University, Germany

Reviewed by:
Wayne Rodney Giles,
University of Calgary, Canada
Ivana Kuo,
Loyola University Chicago,
United States
Delphine Mika,
INSERM U1180 Signalisation et
Physiopathologie Cardiovasculaire,
France

Correspondence:
Claudia M. Moreno
morenocm@uw.edu

[†]ORCID:
Claudia M. Moreno
orcid.org/0000-0001-8397-3649

[‡]These authors have contributed equally to this work and share first authorship

Specialty section:
This article was submitted to Membrane Physiology and Membrane Biophysics,
a section of the journal Frontiers in Physiology

Received: *31 October 2021*
Accepted: *03 March 2022*
Published: *20 April 2022*

Citation:
Choi S, Vivas O, Baudot M and Moreno CM (2022) Aging Alters the Formation and Functionality of Signaling Microdomains Between L-type Calcium Channels and β2-Adrenergic Receptors in Cardiac Pacemaker Cells.
Front. Physiol. 13:805909.
doi: 10.3389/fphys.2022.805909

INTRODUCTION

Animals regulate their heart rate to match physiological demands and to respond to external challenges such as danger. The homeostatic regulation of heart rate is achieved through fine neural control of the cardiac pacemaker. Anatomically known as the sinoatrial node (SAN), the cardiac pacemaker is a specialized tissue located at the intercaval region (**Figure 1A**) and has the ability to spontaneously generate the electricity that initiates each heartbeat. Despite occupying less than 2% of the total volume of the heart, the SAN is the most innervated region in this organ (Csepe et al., 2016). Autonomic terminals innervate the pacemaker and regulate its firing rate through the release of neurotransmitters. Pacemaker rate is accelerated by the action of noradrenaline released from sympathetic terminals (Brown et al., 1979; DiFrancesco, 1986; Boyett et al., 2000; Mangoni and Nargeot, 2008). Noradrenaline activates beta-adrenergic receptors (β-ARs) expressed in the surface of pacemaker cells and triggers a signaling pathway that elevates cAMP levels and results in firing rate acceleration.

Mammals experience a natural slowdown of the intrinsic pacemaker rate throughout their lifespan (Yin et al., 1979; Di Gennaro et al., 1987; Marcus et al., 1990; Alings and Bouman, 1993; Ostchega et al., 2011). Pacemaker rate slowdowns linearly with age at a rate of ~0.8 bpm/year in humans (Tanaka et al., 2001) and ~4 bpm/month in mice (Larson et al., 2013). This slowdown is the main cause for the development of pathological SAN dysfunction and for the requirement of artificial pacemaker devices in humans. The slowdown of the pacemaker has been proposed to be caused by a combination of mechanisms including the reduction in the activation of HCN channels (Larson et al., 2013; Sharpe et al., 2017), the loss of pacemaker cells (Evans and

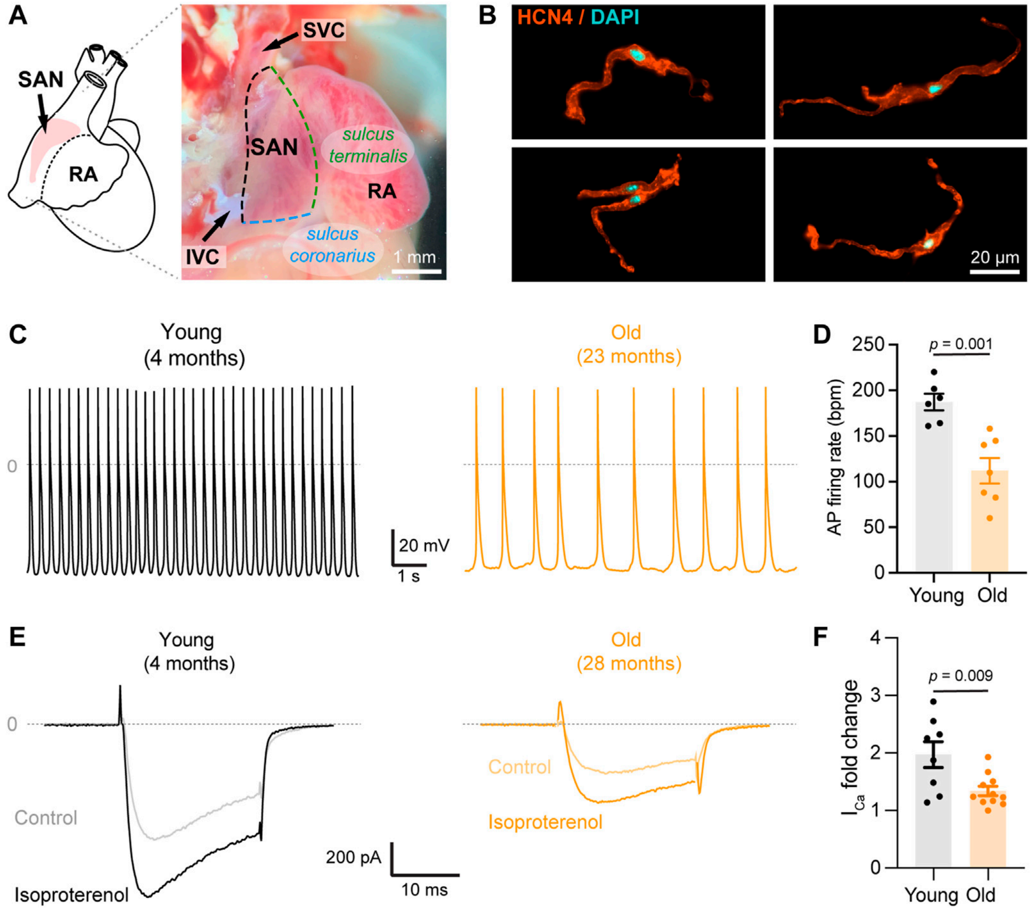

FIGURE 1 | Aging slows down action potential firing and decreases isoproterenol-mediated up regulation of calcium currents. **(A)** (*left*) Schematic representation of the position of the SAN pacemaker in the heart; (right) Image of the intercaval region of the mouse heart depicting the anatomical landmarks used to isolate the pacemaker explant. **(B)** Representative confocal images of isolated pacemaker cells immunostained against HCN4 (orange) and counterstained with DAPI (cyan). **(C)** Representative recordings of spontaneous firing of action potential from a young (gray) and old (orange) isolated pacemaker cell. **(D)** Comparison of the action potential firing rate in beats per minute (bpm) in young (n = 6, N = 3 animals) and old (n = 7, N = 4 animals) pacemaker cells. **(E)** Representative calcium currents from young (*left*, gray) and old (*right,* orange) cells, in the absence (light) or presence (dark) of 100 nM isoproterenol. **(F)** Fold-change of the calcium current peak after isoproterenol application in young (black, n = 10 cells, N = 3 animals) and old (orange, n = 12 cells, and N = 5 animals) pacemaker cells. Statistical comparison used an unpaired t-test with significance at $p < 0.05$.

Shaw, 1977; Thery et al., 1977; Shiraishi et al., 1992), and an increase in tissue fibrosis (Evans and Shaw, 1977; Thery et al., 1977; Shiraishi et al., 1992; Hao et al., 2011).

Interestingly, the age-associated slowdown of the pacemaker is accompanied by a reduction in its sensitivity to adrenergic stimulation (Yaniv et al., 2016; Alghamdi et al., 2020). It is estimated that about 17% of the age-associated decrease in maximum heart rate is explained by a loss of the absolute response of pacemaker cells to adrenergic modulation (Christou and Seals, 2008; Peters et al., 2020). However, our understanding of how aging affects adrenergic signaling in pacemaker cells is still incomplete. So far, we know that aging causes a reduction in the expression of some electrogenic proteins including HCN4, $Ca_V1.2$, $Na_V1.5$, and several K^+ channels (Jones et al., 2007; Tellez et al., 2011; Alghamdi et al., 2020). However, dialysis of a high concentration of exogenous cAMP into pacemaker cells completely restores action potential firing rate in old cells to the same levels observed in young cells (Sharpe et al., 2017), suggesting that in old cells, the machinery responsible for the adrenergic pathway retains its full potential to be activated. If these proteins are fully functional, then what prevents them from operating at full capacity? We explore the idea that aging disrupts the spatial organization of some components of the adrenergic signaling pathway.

The automaticity of the pacemaker relies on a spontaneous phase known as diastolic depolarization which brings the membrane potential to the required threshold to trigger the action potential (AP). This diastolic depolarization is sustained by the activation of HCN4 channels (Baruscotti et al., 2010), voltage-gated calcium channels (Furukawa et al., 1999; Wang et al., 2000), ryanodine receptors (RyR) (Vinogradova and Lakatta, 2009; MacDonald et al., 2020), and the calcium sodium exchanger (NCX) (Ebert and Taylor, 2006; Mangoni and Nargeot, 2008; Gordan et al., 2015). L-type calcium channels play an essential role in the normal function of the pacemaker (Christel et al., 2012). $Ca_V1.3$ channels contribute to the diastolic depolarization phase and the potentiation of calcium release from RyR (Torrente et al., 2016). The important role of $Ca_V1.3$ channels in the control of pacemaker rate is highlighted by the fact that knockout animals exhibit bradycardia (Mangoni et al., 2003; Baudot et al., 2020), and mutations of this channel are associated with sick sinus syndrome in humans (Milanesi et al., 2015). $Ca_v1.2$ channels are essential for sustaining the AP since pacemaker cells express very low amounts of voltage-gated sodium channels compared to atrial and ventricular cardiomyocytes (Mangoni and Nargeot, 2008; Christel et al., 2012).

Upregulation of L-type calcium channels is one of the crucial mechanisms by which noradrenaline accelerates the pacemaker rate (Zaza et al., 1996). The cAMP elevation caused by the activation of β-ARs increases L-type calcium channel activity through two known mechanisms: the first is direct PKA-mediated phosphorylation of the α subunit of the channel (Fu et al., 2014), and the second is the removal of the tonic inhibition of the channel mediated by the small GTPase Rad (Liu et al., 2020; Levitan et al., 2021). Pacemaker cells express β1-and β2-AR as other cardiac cells; however, the pacemaker is the region with the highest β2 expression in the heart (Brodde et al., 1982; Rodefeld et al., 1996). The expression ratio in the pacemaker is 51.6% ± 3.2 for β1-AR and 48.4% ± 3.2 for β2-AR (Saito et al., 1989) compared to the 70:30 observed in atrial and the 80:20 in ventricular cells (Brodde et al., 1982; Brodde et al., 2001). Evidence in ventricular cardiomyocytes shows that L-type calcium channels associate preferentially with β2-AR inside T-tubules (Nikolaev et al., 2006) and caveolae (Shibata et al., 2006; Harvey and Hell, 2013). Although pacemaker cells lack T-tubules, it has been proposed that in these cells, caveolae serve as the compartments for the signaling of β2-ARs with ion channels. Although evidence exists for the association of caveolin-3 with channels (Barbuti et al., 2007), no evidence for the association with LTCCs has been provided in pacemaker cells. Furthermore, whether the age-associated reduction in the sensitivity of the pacemaker to adrenergic stimulation involves changes in these signaling microdomains remains unknown.

Here, we tested the hypothesis that aging differentially affects the association of L-type calcium channels with β1 and β2-ARs and the upregulation mediated by each subtype. Our results reveal that aging specifically impairs the L-type calcium channel upregulation mediated by β2-ARs. This effect is accompanied by a reduction in caveolar density and in the association of L-type calcium channels with caveolin-3 and AKAP150. Our results highlight the importance of these signaling microdomains in maintaining the chronotropic modulation of the heart and unveil a new mechanism behind the age-associated loss of sensitivity to adrenergic modulation in pacemaker cells.

METHODS

Isolation of Pacemaker Cells

Pacemaker cells were freshly isolated from young (4–6 months, equivalent to ~20–30 years in humans) and old (20–24 months, equivalent to ~60–69 years in humans) C57BL/6 male mice. Animals were anesthetized with an intraperitoneal overdose of Euthasol (Virbac, 400 mg/ml), and their hearts were harvested according to a protocol approved by the UW Institutional Animal Care and Use Committee (IACUC). The harvested heart was dissected under the microscope in warm Tyrode's solution containing: 148 mM NaCl, 5.4 mM KCl, 5 mM HEPES, 5.5 mM glucose, 1 mM $MgCl_2$, and 1.8 mM $CaCl_2$, adjusted to pH 7.4 with NaOH. The sinoatrial node (SAN) region was identified as the region located within the superior vena cava, the *sulcus terminalis,* the *coronary sulcus,* and the inferior vena cava (**Figure 1A**). The SAN artery was also used as an anatomical landmark to identify the pacemaker. Pacemaker cells were isolated from the SAN tissue as described in Fenske et al. (2016). Briefly, the excised SAN tissue was immersed into a pre-heated 2 ml tube at 37°C containing 675 µl of Tyrode Low-Ca^{2+} pH 6.9 solution for 5 min. Then BSA was added to the tube to obtain a final concentration (Cf) of 1 mg/ml, followed by the addition of elastase (Cf = 18.87 U/ml, Millipore 3,24,682), protease (Cf = 1.79 U/ml, Sigma P5147), and collagenase B (Cf = 0.54 U/ml, Roche 11088807001). Digestion was carried out for 30 min at 37°C in a water bath along with a mechanical dissociation with a short fire-polished glass pipette every 10 min. To stop the digestion, the SAN was washed by centrifugation at 200 rfc for 2 min at 4°C. The supernatant was discarded and replaced twice with 1 ml of Tyrode's Low-Ca^{2+} solution containing: 140 mM NaCl, 5.4 mM KCl, 5 mM HEPES, 5.5 mM glucose, 1.2 mM KH_2PO_4, 50 mM taurine, 0.5 mM $MgCl_2$, and 0.2 mM $CaCl_2$, adjusted to pH 6.9 with NaOH. This process was repeated 2 more times with 1 ml of calcium-free KB solution containing: 80 mM L-glutamic acid, 25 mM KCl, 10 mM HEPES, 10 mM glucose, 10 mM KH_2PO_4, 20 mM taurine, 0.5 mM EGTA, and 3 mM $MgCl_2$, adjusted to pH 7.4 with KOH. The tissue was left resting in KB solution at 4°C for a minimum of 40 min before proceeding to mechanical dissociation. Single cells were dissociated by mechanical dissociation as aforementioned. The concentration and incubation times for the enzymes were slightly modified to obtain cells from old animals. In this case, the SAN explant was incubated for 20 min in Tyrode's Low-Ca^{2+} containing twice the concentration of collagenase B, followed by the same 30 min digestion with the three enzymes at the concentration used for young tissues. Mechanical dissociation for the old tissue was performed every 5–7 min for the duration of the incubation. Cells were plated on poly-L Lysine (PLL)-coated coverslips for immunocytochemistry or PLA assays. For electrophysiology experiments, to recover the automaticity of young and old pacemaker cells, Ca^{2+} was reintroduced into the KB cell's storage solution by the gradual addition of small amounts of Tyrode' solution (10, 50, and 100 μl at 5 min intervals).

Electrophysiology Recordings

Action potentials were recorded using perforated patch-clamp under gap-free acquisition. Borosilicate patch pipettes with resistances of 3–5 MΩ were filled with an intracellular solution containing 130 mM L-Aspartic acid K, 10 mM NaCl, 0.04 mM $CaCl_2$, 10 mM HEPES, 2 mM Mg-ATP, 0.1 mM Na-GTP, 6.6 mM phosphocreatine, and adjusted to pH 7.2 with KOH. Freshly prepared 25 μM β-Escin were added to the internal solution the day of the experiment. Cells were perfused at room temperature with Tyrode's solution containing 140 mM NaCl, 5.4 mM KCl, 1 mM $MgCl_2$, 1.8 mM $CaCl_2$, 5 mM HEPES, and 5.5 mM Glucose, adjusted to pH 7.4 with NaOH. Seal resistances were in the range of 2–5 GΩ, and no holding or transient current was applied. Data acquisition was performed using an Axoclamp 200B patch-clamp amplifier connected to a Digidata 1,500 interface (Molecular Devices).

Calcium currents were recorded using the whole-cell configuration of the patch-clamp technique in voltage-clamp mode. Isolated pacemaker cells were perfused with Tyrode's solution at room temperature before starting recordings. Borosilicate patch pipettes with resistances of 3–4 MΩ were filled with an internal solution containing: 50 mM CsCl, 10 mM HEPES, 70 mM L-Aspartic acid, 30 mM TEA-Cl, 5 mM EGTA, 5 mM Mg-ATP (added right before use), 1 mM MgCl2, and 0.7 mM CaCl2, adjusted to pH 7.2 with CsOH. Once the gigaseal was obtained, the bath solution was exchanged from Tyrode's to a solution without sodium, containing: 5 mM CsCl, 10 mM HEPES, 10 mM glucose, 110 mM N-methyl-D-glucamine, 30 mM TEA-Cl, 4 mM 4-Aminopyridine, 1 mM MgCl2, and 2 mM CaCl2, adjusted to pH 7.4 with HCl. Cells were then stimulated using a 20 ms square voltage pulse from a resting membrane potential of −70 mV to −20 mV. Currents were sampled at a frequency of 10 kHz and low-pass filtered at 2 kHz using an Axopatch 200B amplifier. To activate β2-ARs and β1-ARs in a sequential manner, we used the specific β2 agonist, formoterol, which is 330-fold more selective for β2 than for β1. An external solution with 100 nM of formoterol was perfused first (β2-AR activation), followed by a solution with 100 nM formoterol +100 nM isoproterenol (β2-AR + β1-AR activation). Upregulation induced by β1-AR was calculated by subtracting these two components. Lastly, a solution containing 10 μM of nifedipine was perfused at the end of the experiments to block the L-type calcium channels. Currents were analyzed using pCLAMP 11 (Molecular Devices).

Protein Extraction and Western Blot

SAN explants dissected using the landmarks shown in **Figure 1A** were homogenized in RIPA lysis buffer (Thermo Scientific, Cat # 89,900) and supplemented with Complete Mini protease inhibitor cocktail (Roche, Cat # 11836170001). After centrifugation (16,000g, 4°C, and 20 min), the concentration of protein lysates in the supernatant was determined using Pierce BCA Protein Assay Kit (Thermo Scientific, Cat # 23,225). 40 μg of total protein were loaded per line on 4–12% polyacrylamide Bis-Tris gels, run under reducing conditions for 1 h 15 min at 155 V, and transferred onto nitrocellulose membranes (Life Technologies, Cat # LC2000) using a Mini-Bolt system (A25977; Thermo Fisher Scientific). After 1 h of incubation at room temperature in TBS buffer supplemented with 0.05% Tween-20 (TBS–T) and 7% non-fat dry milk, membranes were exposed overnight at 4°C to rabbit monoclonal β2-AR antibody (Abcam Cat# ab182136, RRID: AB_2747383), goat polyclonal β1-AR antibody (Abcam Cat# ab77189, RRID: AB_1523202), rabbit polyclonal β1-AR antibody (Abcam Cat# ab3442), or mouse monoclonal GAPDH antibody (Abcam Cat# ab8245, RRID: AB_2107448). Membranes were washed in TBS-T and incubated for 1 h at room temperature with secondary antibodies. The secondary antibody against rabbit β1-AR and β2-AR were HRP-conjugated. Secondary antibodies against goat β1-AR and GAPDH were fluorescent. Fluorescent blotted bands were detected using fluorescent secondary antibodies donkey anti-goat 680RD (LI-COR Biosciences Cat# 925-68,074, RRID: AB_2650427) and donkey anti-mouse 800CW (LI-COR Biosciences Cat# 926-32212, RRID: AB_621847). Signals were detected using either an iBright imaging system (Thermo Fisher Scientific) for chemiluminescent or a Sapphire Gel Imager (Azure Biosystems) for fluorescent blots. ImageJ was used to calculate the fluorescence density of each band. β2-AR bands were normalized to total protein, while β1-AR bands were normalized to GAPDH (N = 2) or total protein (N = 5). Total protein was detected using the No-stain® reagent (A44449 ThermoFisher). Protein abundance was reported relative to the abundance in young pacemaker explants.

Proximity Ligation Assay

12 mm diameter round 1.5 glass coverslips were coated with PLL hydrobromide (Sigma P1524, MW ≥ 300,000) for 30 min at 37°C; then, thoroughly washed with water, and left to dry overnight. Isolated pacemaker cells were plated on these coverslips and left

to attach for 30 min at 37°C in a humidity chamber. Cells were fixed with 4% paraformaldehyde in PBS for 10 min at room temperature and washed with PBS. All the washing steps in this protocol, unless stated otherwise, consisted of 3 rinses with PBS followed by 3 × 5 min washes with PBS on a rocker. To quench any excess PFA, 50 mM Glycine in PBS was added for 15 min at room temperature and washed with PBS. Cells were then blocked with Duolink Blocking Solution (Sigma, DUO82007) for 30 min at 37°C in a humidity chamber. Primary antibodies were diluted in Duolink Antibody Diluent Solution (Sigma, DUO82008) to a concentration of 10 µg/ml (100 µl/coverslip) and incubated overnight at 4°C under gentle orbital agitation. We used the following antibodies: $Ca_V1.2$ and $Ca_V1.3$ (rabbit anti CNC1 and CND1, respectively; provided by Drs. William Catterall and Ruth Westenbroek, UW), mouse anti-β2-AR (Santa Cruz Biotechnology, sc-271322), goat anti-β1-ARs (Abcam, ab77189), rabbit anti-β1-ARs (Abcam, ab3442), mouse anti-caveolin-3 (BD Transduction Labs, 610420), and mouse anti-AKAP150 (BD Transduction Labs, A31320G). The following day, coverslips were washed with PBS and transferred to a parafilm-lined humid chamber for easier application of solutions. Coverslips were rinsed twice with 100 µl of Duolink Buffer A (Sigma, DUO82049) for 5 min under gentle orbital agitation. Rabbit-plus and mouse-minus or goat-minus Duolink *In Situ* PLA secondary probes (Sigma DUO92002; 92004; 92006) were added according to manufacturer's specifications and incubated for 1 h at 37°C in a humidity chamber. This was followed by the addition of 20 µl per coverslip of ligation solution consisting of 4 µl 5X ligation stock, 15.5 µl pure water, and 0.5 µl ligase (Duolink *In Situ* PLA Detection Reagents Orange, Sigma DUO92007) for 30 min at 37°C in a humidity chamber. 20 µl of amplification solution consisting of 4 µl 5X amplification stock, 15.75 µl pure water, and 0.25 µl polymerase (Duolink *In Situ* PLA Detection Reagents Orange, Sigma DUO92007), was then added to each coverslip and incubated for 100 min at 37°C in a humidity chamber, followed by two 10 min Duolink Buffer B (Sigma, DUO82049) washes and 1 min Duolink Buffer B (1%) wash under gentle orbital agitation. Coverslips were left to dry covered from light for a minimum of 30 min before mounting on microscope slides with Prolong Diamond Antifade Mountant (no DAPI, Invitrogen, P36961). Images were taken as described below but with these additional experimental details. Z-stacks with a step size of 0.5 µm were acquired to generate high-resolution images. Images were processed with ImageJ (NIH). Processing consisted of filtering with a Median 3D filter with a sigma of 1 for each axis, converting the stack into a maximum intensity projection, thresholding, and binarization. Finally, images were analyzed to calculate cell area and the number of particles from these Z-projections. Data is reported as particle density for each cell.

Immunocytochemistry and Expansion Microscopy

For HCN4 and caveolin-3 immunostaining, pacemaker cells plated on 12 mm PLL-coated coverslips were fixed in 4% PFA in PBS for 15 min. All the washing steps in this protocol, unless stated otherwise, consisted of 3 rinses with PBS followed by 3 × 5 min washes with PBS on a rocker. After washing with PBS, cells were incubated with 1 mg/ml $NaHB_4$ at room temperature for 5 min and washed again with PBS. Cells were blocked by incubating with 3% BSA and 0.25% v/v Triton X-100 in PBS (blocking solution) for 30 min. The cells were then incubated for 1 h at room temperature with mouse anti-caveolin-3 antibody (BD Transduction Labs, 6,10,420) or overnight at 4°C with rabbit anti-HCN4 (Sigma, AB5808) at 10 µg/ml in blocking solution. Cells were then washed with PBS, incubated for 1 h with Alexa Fluor 488-conjugated donkey anti-mouse or donkey anti-rabbit (2 µg/ml; Invitrogen, A32787/A32790) secondary antibodies, and washed again with PBS. For immunocytochemistry, coverslips were mounted using Prolong Diamond Antifade Mountant (with DAPI, Thermo Scientific, P36962).

For expansion microscopy, we closely followed the protocol published by Chozinski et al. (2016). Instead of mounting, the immunostained coverslips were incubated with 25 mM MA-NHS in PBS for 1 h at room temperature, followed by 3 washes with PBS. The coverslips were incubated in a monomer solution of 2 M NaCl, 2.5% (w/w) acrylamide, 0.15% (w/w) N, N′-methylenebisacrylamide, and 8.625% (w/w) sodium acrylate, for ~1 min at room temperature prior to gelation. Concentrated stocks of tetramethylethylenediamine (TEMED) and ammonium persulfate (APS) at 10% (w/w) in water were freshly prepared. TEMED and APS were quickly added to the monomer solution to achieve a final concentration of 0.2% (w/w). 70 µl of the gelation solution were placed on a Teflon flat surface and the coverslip was then placed on top of this solution with cells face down. Gelation was allowed to proceed at room temperature for 30 min. The coverslip and gel were removed with tweezers and placed in digestion buffer (1 × TAE buffer, 0.5% Triton X-100, 0.8 M guanidine HCl) containing 8 units/ml of freshly added Proteinase K (Thermo Scientific, EO0491). Gels were digested at 37°C overnight. The next day, the gels were placed in ~50 ml DI water to expand. Water was replaced every 30 min x 4 or until expansion was complete. Cells were expanded 2.5 times and the resolution was 50 nm.

High-Resolution Imaging

Cells were imaged using an inverted AiryScan microscope (Zeiss LSM 880) run by Zen black v2.3 and equipped with a plan apochromat 63X oil immersion lens with a 1.4 NA. Fluorescent dyes were excited with a 405 nm diode, 458–514 nm argon, 561 nm, or 633 nm laser. Emission light was detected using an Airyscan 32 GaAsP detector and appropriate emission filter sets. The point spread functions were calculated using ZEN black software and 0.1 µm fluorescent microspheres. After deconvolution, the point spread functions were: 124 nm in X-Y, and 216 nm in Z (488 nm excitation); 168 nm in X-Y and 212 nm in Z (594 nm excitation). The temperature inside the microscope housing was 27–30°C. Images were analyzed using a custom-made macro written in ImageJ (NIH). Processing consisted of thresholding and binarization of images to isolate labeled structures. Particles were analyzed to calculate the area and number of particles from these images.

RESULTS

Aging Slows Down Action Potential Firing and Decreases Adrenergic Up Regulation of Calcium Currents in Pacemaker Cells

It is known that aging reduces the adrenergic-mediated acceleration of heart rate and the sensitivity of pacemaker cells to the non-specific agonist, isoproterenol (Christou and Seals, 2008; Larson et al., 2013; Yaniv et al., 2016). Despite calcium channels being one of the main targets of β-adrenergic modulation, there are only a few studies on the effects of aging on the isoproterenol-induced upregulation of calcium currents (Dun et al., 2003; Larson et al., 2013). We tested the effect of isoproterenol in the upregulation of calcium-currents in pacemaker cells isolated from the SAN. Isolated cells presented the morphology reported for pacemaker cells and were positive for the pacemaker marker HCN4 (**Figure 1B**), confirming the identity of the cells. In addition, current-clamp recordings demonstrated the automaticity of the isolated pacemaker cells (**Figure 1C**). As previously reported, aging slowed the action potential firing rate (**Figure 1D**). While young cells fired action potentials (AP) at a rate of 187 ± 9 beats per minute (bpm, n = 6 cells), old cells fired AP at a rate of 112 ± 14 bpm (n = 7 cells). Moreover, old pacemaker cells exhibited different parameters of the action potentials. For example, the cycle length was 624 ± 97 ms in old cells compared to 324 ± 15 ms in the young, action potentials last for 260 ± 23 ms in old cells compared to 183 ± 24 ms in the young, and the diastolic depolarization lasted for 314 ± 73 ms in old cells compared to 127 ± 9 ms in the young. All quantified parameters, n number, and *p*-values are shown in **Supplementary Table S1**. We recorded time courses of calcium currents in isolated pacemaker cells from young and old animals before and during the application of 100 nM isoproterenol. The application of isoproterenol was efficient in upregulating the calcium current in young and old cells (**Figure 1E**). Isoproterenol upregulated the calcium current in the young group by 2-fold (n = 8), and by 1.3-fold in the old (n = 11, **Figure 1F**), suggesting that aging significantly reduces the isoproterenol-mediated upregulation of calcium currents in pacemaker cells ($p = 0.009$).

Aging Reduces β2-but Not β1-Mediated Upregulation of the L-type Calcium Current

As we mentioned before, pacemaker cells express in similar proportions β1 and β2-AR. We already showed that aging reduces the global adrenergic upregulation of calcium channels. However, whether the β1 and β2 components are differentially affected by aging is not known. We tested the hypothesis that aging has a differential effect on the upregulation of calcium currents triggered by the activation of either β1 or β2-AR. For this, we designed an experimental approach to study upregulation of the calcium current in pacemaker cells under a 5 min application of the β2-specific agonist formoterol (100 nM) followed by a 5 min simultaneous application of formoterol (100 nM) and isoproterenol (100 nM) to activate the remaining β1 component (**Figure 2A**). We stimulated the cells with a voltage step from −70 to −20 mV every 5 s and measured the change in peak of current density over time. As shown in the average temporal course in **Figure 2B** and in the representative examples in **Figure 2C**, calcium currents in both young and old cells were upregulated under the activation of the β2-ARs (phase 2) and further upregulated upon the activation of the β1-ARs (phase 3). The upregulation of the calcium current was completely reversed by washing off the agonists and the current amplitude was restored to basal levels (phase 4 in **Figures 2B,C**). The calcium current was mainly carried by L-type calcium channels as confirmed by the application of 10 μM nifedipine, which abolished about 80% of the current in both young and old cells (phase 5 in **Figures 2B,C**).

We quantified the change in the calcium current upon β2 and β1-AR activation. **Figure 2D** shows the change in the raw current density for each cell. β2-AR activation increased calcium current density in young and old cells, going from 7.8 ± 1.1 pA/pF to 15.4 ± 1.9 pA/pF in the young group ($p = 0.0007$) and from 5.4 ± 1.0 pA/pF to 8.7 ± 1.7 pA/pF in the old ($p = 0.006$, **Figure 2D**). Subsequent activation of β1-AR in the same cells led to a further upregulation reaching a maximal current density of 18.2 ± 2.5 pA/pF in the young ($p = 0.2$) and 10.7 ± 1.7 pA/pF in the old group ($p = 0.02$). To compare the regulation from each receptor, we calculated the fold-change relative to the peak of the current in control conditions. Interestingly, the β2-mediated upregulation was significantly reduced in old cells. The activation of β2-ARs increased the calcium current 2.0 ± 0.2 times relative to control levels in young cells (n = 9), whereas it only increased it 1.5 ± 0.1 times in old cells (n = 13) (**Figure 2E**). In contrast, the activation of β1-ARs increased the calcium current 1.5 ± 0.2 times in young (n = 9) and 1.6 ± 0.1 times in old (n = 13) (**Figure 2E**). These results suggest that aging causes a significant reduction in the sensitivity of the calcium current to the activation of β2-ARs, but not of β1-ARs.

Next, we assessed if old cells had a reduction in the expression of β2-ARs that could account for the observed reduction in the β2-mediated regulation. Using protein extracts from young and old pacemaker explants, we did not find any difference in β2-ARs expression (**Figures 2F,G**). The average fold change for β2-ARs in old compared to young pacemakers was 1.8 ± 0.5 (N = 7 animals per age) independent pacemaker isolations, $p = 0.4$). Expression of β1-ARs was also unchanged. The average fold change for β1-ARs in old compared to young pacemakers was 0.9 ± 0.05 (N = 7 animals per age). An important consideration regarding this experiment is that even though only the SAN explant was collected, the tissue contains different cell types (i.e., vascular cells, neurons, fibroblasts). As a consequence, the analyzed abundance of β-ARs reflected the expression in all cell types. These results suggest that aging reduces β2-mediated upregulation by a mechanism independent of receptor level changes.

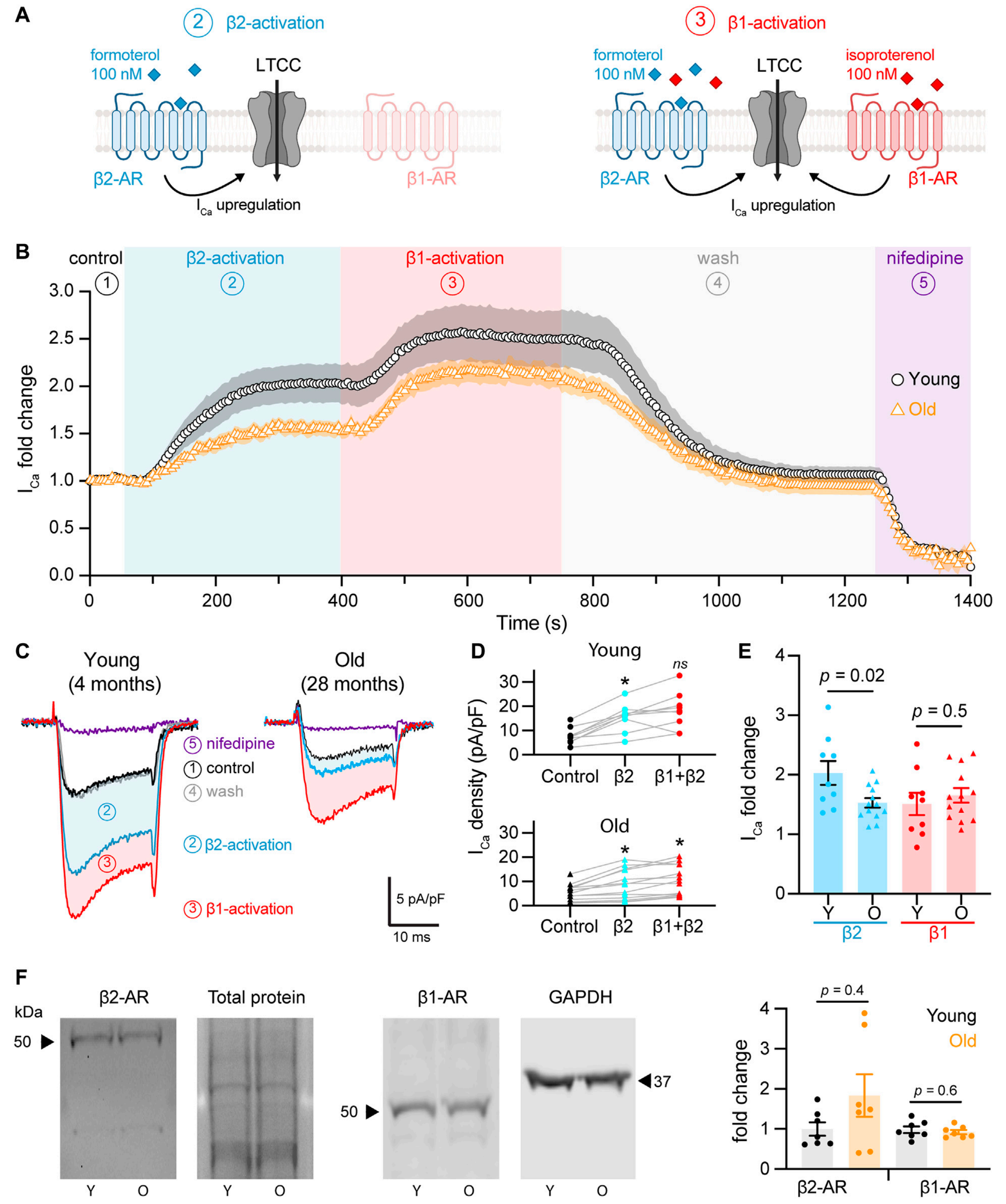

FIGURE 2 | Aging reduces β2-but not β1-mediated regulation of L-type calcium currents in pacemaker cells. **(A)** Diagrammatic representation summarizes the protocol used to isolate β2 from β1-AR upregulation of calcium currents, which consisted in the stimulation using 100 nM formoterol followed by the simultaneous stimulation with 100 nM formoterol +100 nM isoproterenol. Diagram created with BioRender.com. **(B)** Time course of calcium current fold change in control conditions (1) β2-specific activation (2) β1-activation (3), washout (4), and lastly with nifedipine to block LTCCs (5) in young (black circles, n = 10 cells, N = 3 animals) and old (orange triangles, n = 14 cells, N = 4 animals) pacemaker cells. **(C)** Representative calcium currents from the time course in B. **(D)** Calcium current density regulation after

(Continued)

FIGURE 2 | the activation of β2-and co-activation of β2 and β1-ARs relative to control and paired for individual cells isolated from young (top) and old (bottom) mice. Statistical comparison relative to the control condition used two independent paired t-tests with significance at $p < 0.05$. **(E)** Comparison of the fold-change of the calcium current peak after the activation of β2 and β1-ARs from the same cells presented in D. Statistical comparison used two independent unpaired t-tests with significance at $p < 0.05$. **(F)** Western blots testing for changes in the expression of β2 and β1-ARs from SAN explants. β2-AR expression was normalized to total protein (N = 7 independent pacemaker isolations per age, $p = 0.4$), while β1-AR expression was normalized to GAPDH in 2 of the 7 experiments and to total protein in 5 of the 7 experiments (N = 7 independent pacemaker isolations per age, $p = 0.6$).

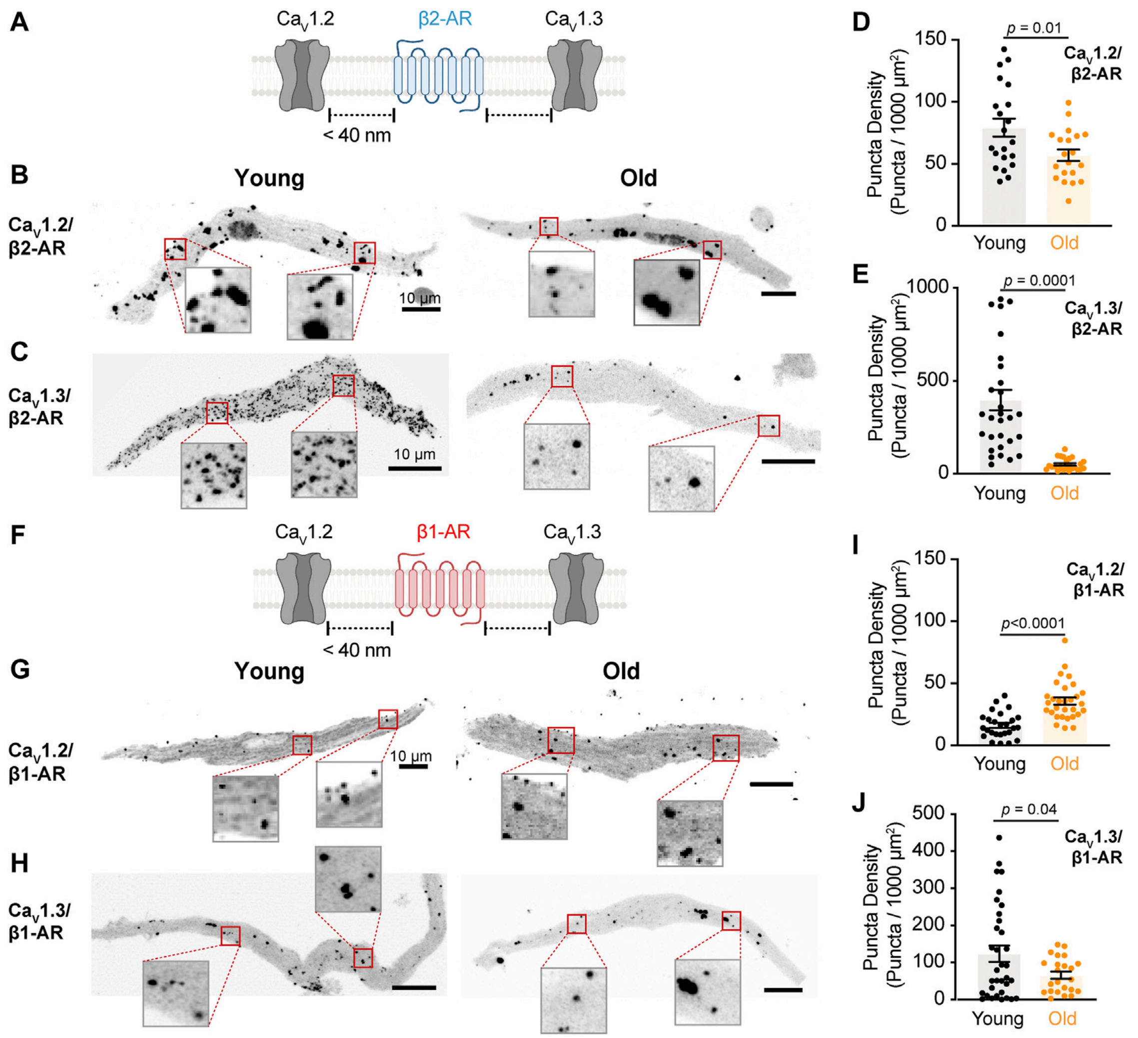

FIGURE 3 | The physical association between L-type calcium channels and β2-AR is reduced in old pacemaker cells. **(A)** Diagrammatic representation of the molecular association being tested between β2-AR and specific LTCCs. Diagram created with BioRender.com. **(B)** Representative pictures of proximity ligation assay (PLA) between β2-AR and Ca$_V$1.2 channels in young and old pacemaker cells. **(C)** Representative PLA pictures between β2-AR and Ca$_V$1.3 channels in young and old pacemaker cells. **(D)** Comparison of the puncta density formed by the association of β2-AR with Ca$_V$1.2 channels between young (n = 21 cells, N = 3 mice) and old (n = 20 cells, N = 3 mice). **(E)** Comparison of the puncta density formed by the association of β2-AR with Ca$_V$1.3 channels between young (n = 30 cells, N = 3 mice) and old (n = 24 cells, N = 3 mice). **(F)** Diagrammatic representation of the molecular association being tested between β1-AR and specific LTCCs. **(G)** Representative PLA pictures between β1-AR and Ca$_V$1.2 channels in young and old pacemaker cells. **(H)** Representative PLA pictures between β1-AR and Ca$_V$1.3 channels in young and old pacemaker cells. **(I)** Comparison of the puncta density formed by the association of β1-AR with Ca$_V$1.2 channels between young (n = 26 cells, N = 3 mice) and old (n = 30 cells, N = 3 mice). **(J)** Comparison of the puncta density formed by the association of β1-AR with Ca$_V$1.3 channels between young (n = 34 cells, N = 3 mice) and old (n = 23 cells, N = 3 mice). Statistical comparison used an unpaired t-test with significance at $p < 0.05$.

The Physical Association Between L-type Calcium Channels and β2-AR Is Reduced in Old Pacemaker Cells

As the expression of β-ARs did not change, we tested whether the molecular proximity between the two specific β-AR isoforms and L-type calcium channels were disrupted in old cells using Proximity Ligation Assay (PLA, **Figure 3A**). The formation of PLA fluorescent puncta between a specific pair of proteins (β2-AR/$Ca_V1.2$, β2-AR/$Ca_V1.3$, β1-AR/$Ca_V1.2$, and β1-AR/$Ca_V1.3$) was evaluated in isolated pacemaker cells from young and old mice. The formation of fluorescent puncta was interpreted as proximity below 40 nm between the two proteins of interest and it was quantified as the puncta number normalized by cell area (puncta/1,000 μm^2). PLA quantifications were expressed as puncta density regardless of puncta size since different factors can influence the size of the fluorescent puncta including variation in the ligation and amplification efficiency, antibody type, and the number of bound antibodies per protein. Negative controls, where one of the two primary antibodies was omitted, resulted in a low puncta density (**Supplementary Figure S1**), confirming that the pairs of secondary probes used do not bind close to each other non-specifically. We first tested the changes in the association between the β2-AR and $Ca_V1.2$ channels. Puncta density was significantly lower in old (56.9 ± 4.6, n = 20) compared to young cells (79.2 ± 7.2, n = 21) (**Figures 3B,D**). A more dramatic reduction was observed when comparing puncta density between β2-AR and $Ca_V1.3$ channels in young and old cells. In old pacemaker cells, the β2-AR/$Ca_V1.3$ puncta density was seven-fold smaller than in young cells (50.7 ± 6.6, n = 24 vs. 369.9 ± 54.5, and n = 30, **Figures 3C,E**). Next, we used PLA to assess the effect of aging on the molecular proximity between β1-ARs and L-type calcium channels (**Figure 3F**). In contrast to the reduction observed for the β2-ARs, pacemaker cells co-labeled with primary antibodies against β1-AR and $Ca_V1.2$ channels showed a significantly higher puncta density in old animals compared to that of young (35.8 ± 2.8, n = 30 vs. 16.1 ± 2.0, and n = 26, **Figures 3G,I**). A small reduction was observed when comparing the puncta density between β1-AR and $Ca_V1.3$ channels. For β1-AR/$Ca_V1.3$ the puncta density was 65.7 ± 9.8 (n = 23) in old cells, while in young cells, the puncta density was 123.7 ± 21.7 (n = 34, **Figures 3H,J**). The specific reduction in the proximity of β2-AR and L-type calcium channels observed in old cells correlates with the specific decrease in the calcium current upregulation mediated by the activation of β2-ARs with formoterol. Altogether, these results suggest that the β2-mediated regulation of L-type calcium channels is compromised in pacemaker cells of old animals due to loss of proximity between β2-AR and both $Ca_V1.2$ and $Ca_V1.3$ channels rather than a reduction in cellular β2-AR abundance.

Aging Reduces the Association of $Ca_V1.2$ and $Ca_V1.3$ Channels With the Scaffolding Protein AKAP150 in Pacemaker Cells

Scaffolding proteins play an important role in recruiting and maintaining the molecular components inside signaling microdomains. Little is known about what scaffolding proteins maintain β-adrenergic signaling microdomains in pacemaker cells. AKAP150 is perhaps the most studied scaffolding protein in the cardiovascular system. In ventricular cardiomyocytes (Cheng et al., 2011) and vascular smooth muscle cells (Navedo et al., 2008), AKAP150 has been shown to bind β-ARs and L-type calcium channels. The function of AKAP150 in pacemaker cells has yet to be studied. We used PLA in isolated pacemaker cells to determine if L-type calcium channels are associated with AKAP150 and determine whether aging changes this association (**Figure 4A**). We found that aging causes a dramatic reduction in the proximity between AKAP150 and both channels. AKAP150-$Ca_V1.2$ puncta density was reduced by 7-fold in old cells, from 520.0 ± 56.3 puncta in young (n = 15) to 68.4 ± 13.6 puncta in old (n = 17) (**Figures 4B,D**). The association between AKAP150 and the $Ca_V1.3$ channel was reduced even further, showing a 14-fold reduction in puncta density, going from 716.0 ± 63.1 puncta in young (n = 15) to 51.4 ± 6.7 puncta in old cells (n = 17) (**Figures 4C,E**). The observed strong association of AKAP150 with both L-type calcium channels suggests that AKAP150 plays an important role in anchoring these channels in pacemaker cells and that this association is susceptible to the deleterious effects of aging.

Aging Decreases Caveolar Density in Pacemaker Cells and the Recruitment of L-type Calcium Channels Into These Microdomains

Caveolae are abundant in pacemaker cells and enable the local signaling of β-ARs due to the compartmentalization of different effectors such as L-type calcium channels (Barbuti et al., 2007).

We assessed whether old cells exhibit less or disrupted caveolae by immunostaining against caveolin-3 and imaging with high-resolution microscopy. Young cells showed continuous caveolin-3 labeling along the plasma membrane, consistent with the high density of caveolae in these cells. However, in old cells, the membrane labeling of caveolin-3 had a discontinuous dash-like pattern (**Figure 5A**). To quantify this alteration, we set thresholds and binarized the signal to isolate the labeling at the plasma membrane of the equatorial planes of the cell. The size of caveolin-3 positive segments was significantly shorter in old (0.14 ± 0.01 μm^2, n = 8) compared to young cells (0.29 ± 0.04 μm^2, n = 8) (**Figure 5B**). The percentage area occupied by caveolin-3 was smaller in old (4.63 ± 0.46%, n = 8) compared to young cells (6.64 ± 0.70%, n = 8) (**Figure 5C**). As the external diameter of caveolae is only about 70 nm (Matthaeus and Taraska, 2020), we utilized expansion microscopy combined with high-resolution imaging to determine the differences in caveolae size between young and old cells. With this improved resolution, the reduction in caveolae density at the plasma membrane in old cells was even more evident (**Figure 5D**). The size of caveolin-3 positive structures in old cells was half of that observed in young cells (0.38 ± 0.04 μm^2, n = 13 vs. 0.76 ± 0.10 μm^2, and n = 10, **Figure 5E**). Moreover, the area occupied by caveolin-3 was also smaller in expanded old cells (4.8 ± 0.3%, n = 13) compared to expanded young cells (7.4 ± 0.6%, n = 10) (**Figure 5F**). The labeling of caveolin-3 at the cell footprint exhibited a bimodal pattern between punctuated and reticular (**Figure 5G**). By analyzing these images, we

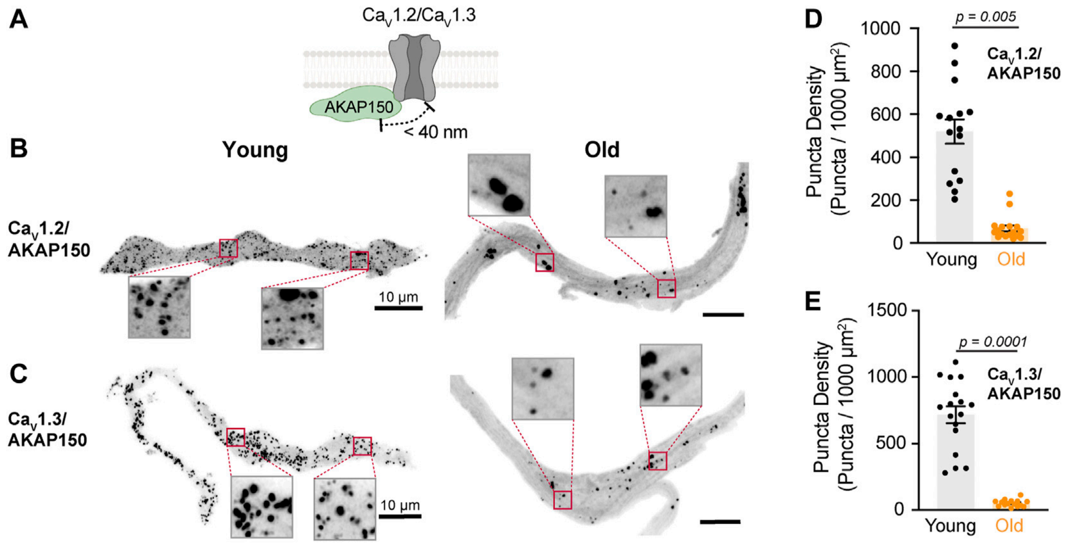

FIGURE 4 | Aging reduces the association between L-type calcium channels and AKAP150. **(A)** Diagrammatic representation of the molecular association being tested between AKAP150 and specific LTCCs. Diagram created with BioRender.com. **(B)** Representative PLA pictures between AKAP150 and $\mathrm{Ca_V}1.2$ channels in young and old pacemaker cells. **(C)** Representative PLA pictures between AKAP150 and $\mathrm{Ca_V}1.3$ channels in young and old pacemaker cells. **(D)** Comparison of the puncta density formed by the association of AKAP150 with $\mathrm{Ca_V}1.2$ between young (n = 15, N = 3 mice) and old (n = 17, N = 3 mice) pacemaker cells. **(E)** Comparison of the puncta density formed by the association of AKAP150 with $\mathrm{Ca_V}1.3$ channels between young (n = 15, N = 3 mice) and old (n = 17, N = 3 mice) pacemaker cells. Statistical comparison used an unpaired t-test with significance at $p < 0.05$.

confirmed that the caveolar size distribution was shifted toward smaller sizes in old compared to young cells (**Figure 5H**).

Although caveolae size (as reported by caveolin-3) was reduced in old cells, L-type calcium channels could still be strongly associated with these fragmented structures. Therefore, we decided to evaluate the association between caveolin-3 and L-type calcium channels (**Figure 6A**). We first used PLA in isolated pacemaker cells co-labeled with primary antibodies against caveolin-3 and $\mathrm{Ca_V}1.2$ channels. The PLA fluorescent puncta density was 2-times lower in old (45.08 ± 3.63, n = 12) compared to young (101.1 ± 10.4, n = 19) (**Figures 6B,D**). In pacemaker cells co-labeled with primary antibodies against caveolin-3 and $\mathrm{Ca_V}1.3$ channels, the PLA fluorescent puncta density was almost 3-times lower in old (143.5 ± 19.1, n = 15) compared to young (387 ± 47.9, n = 13) (**Figures 6C,D**). Altogether, these results suggest that in pacemaker cells, aging is associated with a reduction in caveolae and a loss of caveolar localization of L-type calcium channels.

DISCUSSION

Adrenergic modulation has two main effects on the heart: the first one is to increase ventricular contraction force, also known as the positive inotropic effect, and the second one is to accelerate pacemaker rate, known as the positive chronotropic effect. Studies in ventricular cardiomyocytes have revealed that the activation of β1 and β2-ARs play different roles in the positive inotropic effect induced by noradrenaline (Xiao and Lakatta, 1993; Altschuld et al., 1995; Kuschel et al., 1999). These differences rely on the compartmentalization of β-AR receptors into different signaling microdomains and their specific association with sub-pools of $\mathrm{Ca_V}1.2$ channels (Johnson and Antoons, 2018). While this has been extensively studied in the context of ventricular inotropy (Nikolaev et al., 2010; Wright et al., 2014; Schobesberger et al., 2017), the characteristics of this subtype-specific association in pacemaker cells and its role in the positive chronotropic effect is much less understood. The fact that pacemaker cells express a higher ratio of β2-AR compared to other cardiac regions has suggested that β2-ARs may have an important role in the chronotropic effect. Moreover, the fact that pacemaker cells express both $\mathrm{Ca_V}1.2$ and $\mathrm{Ca_V}1.3$ channels also opens the question of whether these channels associate preferentially to any of the β-AR subtypes or if they are differentially regulated by them. Our results show that in fact, in young pacemaker cells both L-type calcium channels are preferentially associated to β2-ARs. In contrast with previous results (Larson et al., 2013), when we simultaneously activated both β-ARs using the non-specific agonist isoproterenol, we observed that upregulation of the calcium current in old cells is significantly reduced compared to that of young cells. However, when we dissected the β1 and β2 components pharmacologically, we unveiled that aging specifically affects the L-type calcium current upregulation mediated by the β2-AR. No significant changes were observed for the upregulation mediated by the β1-AR. However, it would be interesting to measure dose-response curves for each receptor to determine if aging has any effect on the receptor sensitivity that is not evident at the saturating concentrations used in this study.

This reduction is in part explained by an age-associated reduction in the physical proximity between $\mathrm{Ca_V}1.2$ and $\mathrm{Ca_V}1.3$ channels and β2-ARs. Our results agree with the idea put forward by DiFrancesco's group that the

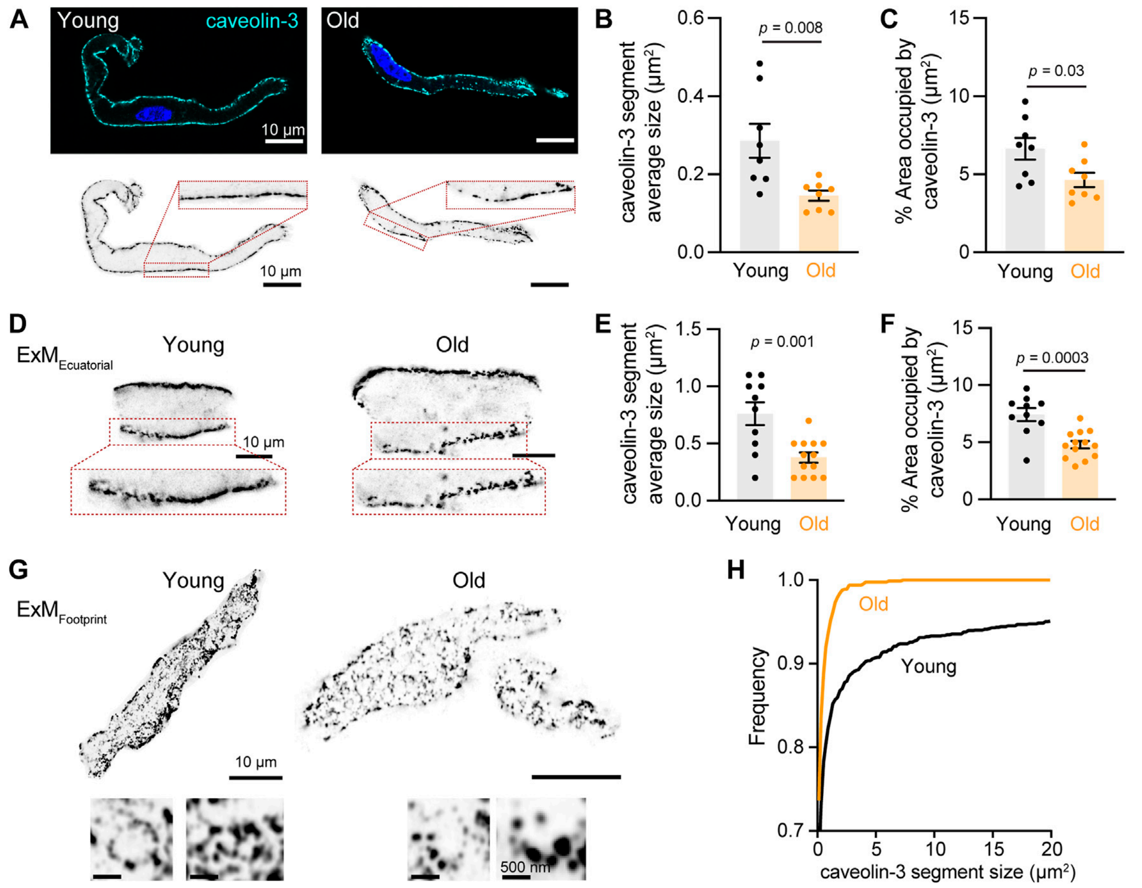

FIGURE 5 | Aging decreases the size and area occupied by caveolae. **(A)** Representative pictures of pacemaker cells labeled with antibody anti-caveolin-3 (cyan) and counterstained with DAPI to visualize the nucleus (blue). Same pictures in grayscale and inverted are shown at the bottom. **(B)** Comparison of the average segment size positive for caveolin-3 between young (n = 8, N = 3 mice) and old (n = 8, N = 3 mice) cells. **(C)** Comparison of percent area occupied by caveolin-3 structures between young (n = 8, N = 3 mice) and old (n = 8, N = 3 mice) cells. **(D)** Representative pictures of pacemaker cells expanded to improve the resolution of caveolin-3 segments. Only a region of the cell is shown. **(E)** Comparison of the average segment size positive for caveolin-3 between expanded young (n = 10, N = 3 mice) and old (n = 13, N = 3 mice) cells. **(F)** Comparison of percent area occupied by caveolin-3 structures between expanded young (n = 10, N = 3 mice) and old (n = 13, N = 3 mice) cells. Note a 2.5-fold increase in segment size between expanded and not expanded cells. Statistical comparison used an unpaired t-test with significance at $p < 0.05$. **(G)** Representative pictures of the footprint of expanded young and old pacemaker cells labeled with anti-caveolin-3. **(H)** Comparison of the cumulative frequency distribution of the size of caveolin-3 segments from expanded young (black, n = 10, N = 3 mice) and old (orange, n = 13, N = 3 mice) cells.

compartmentalization and the specific stimulation of β2-ARs are the main mechanisms by which heart rate is modulated (DiFrancesco, 1986). Interestingly, the association with β2-ARs and the age-associated reduction of this association was remarkably more robust for the $Ca_V1.3$ than for the $Ca_V1.2$ channel. It had been previously proposed that in pacemaker cells, the $Ca_V1.2$ channel was the one preferentially associated with β2-ARs (Balijepalli et al., 2006; Harvey and Hell, 2013), similar to what has been seen in ventricular cardiomyocytes (Lang and Glukhov, 2018). However, we show that this is not the case. This finding is relevant since $Ca_V1.3$ channels not only contribute to the action potential of the pacemaker but they also play a crucial role in the diastolic depolarization that drives pacemaker automaticity (Christel et al., 2012). Therefore, their close association with β2-ARs suggests that $Ca_V1.3$ channels are one of the main targets for the adrenergic control of pacemaker rate. It also shows that the reduction of $Ca_V1.3$ regulation is an important mechanism in the age-associated loss of responsivity to adrenergic stimulation.

Are other components of the β-AR and L-type calcium channel signaling microdomains disrupted by aging? In the case of β-adrenergic signaling in ventricular cardiomyocytes, scaffolding proteins play an important role in recruiting and organizing specific molecular components into these microdomains. AKAP150 (Cong et al., 2001; Liu et al., 2004; Tao and Malbon, 2008) and AKAP250 (Shih et al., 1999; Tao et al., 2003; Malbon et al., 2004) were initially identified as partners for the β2-ARs. The binding of β2-ARs and $Ca_V1.2$ channels to AKAP150 is essential for the localization of these molecules to T-tubules and the correct excitation-contraction coupling (Balijepalli et al., 2006; Nichols et al., 2010). In contrast, the association of β1-ARs and a different pool of $Ca_V1.2$ channels to AKAP150 outside T-tubules plays an important role in the generation of global cAMP elevations. Our results indicate that AKAP150 strongly associates with $Ca_V1.2$ and $Ca_V1.3$ channels

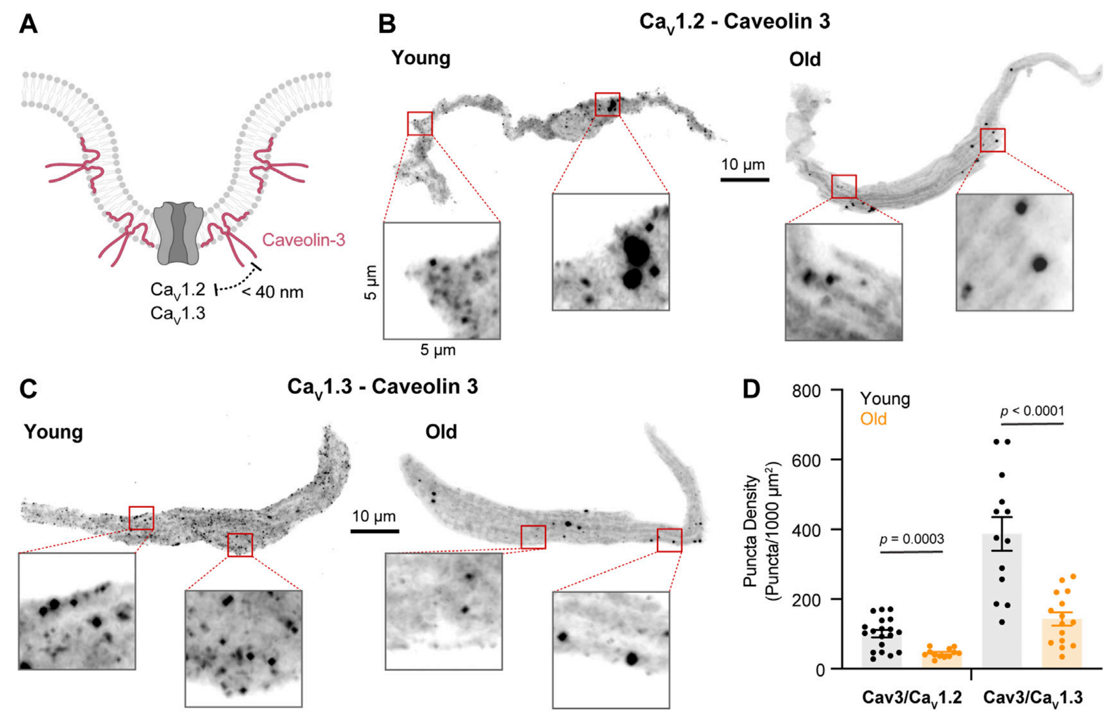

FIGURE 6 | Aging decreases the association between L-type calcium channels and caveolin-3. **(A)** Diagrammatic representation of the molecular association being tested between caveolin-3 and specific LTCCs. Diagram created with BioRender.com. **(B)** Representative PLA pictures between caveolin-3 and Ca$_V$1.2 channels in young and old pacemaker cells. **(C)** Representative PLA pictures between caveolin-3 and Ca$_V$1.3 channels in young and old pacemaker cells. **(D)** Comparison of the puncta density formed by the association of caveolin-3 with specific LTCCs in young (Ca$_V$1.2 n = 19 cells, Ca$_V$1.3 n = 13 cells, and N = 3 mice) and old (Ca$_V$1.2 n = 12 cells, Ca$_V$1.3 n = 15 cells, and N = 3 mice). Statistical comparison used an unpaired t-test with significance at $p < 0.05$.

in pacemaker cells and that aging causes a dramatic reduction in this association. However, whether these associations are happening preferentially inside or outside caveolar microdomains need to be further studied. It is unknown what specific scaffolding proteins organize β-ARs and L-type calcium channels in pacemaker cells. Mutations in different scaffolding proteins including AKAP10 (Tingley et al., 2007), ankyrin-B (Mohler et al., 2003; Le Scouarnec et al., 2008), and caveolin-3 (Campostrini et al., 2017) have been seen to cause bradycardia and other forms of pacemaker dysfunctions (Lang and Glukhov, 2018). Thus, future research should focus on systematically testing for the role of these scaffolding proteins in the formation of β-ARs/L-type calcium channels microdomains and their alterations in aging.

In ventricular cardiomyocytes, β2-AR are compartmentalized in close proximity to Ca$_V$1.2 channels inside caveolae and t-tubules. As a result, the cAMP elevations triggered by the activation of β2-AR are localized, and their main function is to precisely facilitate the calcium current without affecting other PKA-dependent processes (Kuschel et al., 1999; Xiao et al., 1999). Pacemaker cells lack T-tubules, and caveolae have been proposed to serve as compartments for the signaling between β2-ARs and L-type calcium channels. β2-AR receptors in pacemaker cells have been seen to localize preferentially inside caveolae in close proximity to HCN4 channels (Barbuti et al., 2012). Our results show that caveolae also facilitate the close proximity of β2-AR receptors to Ca$_V$1.3 and Ca$_V$1.2 channels. Interestingly, our results not only demonstrate that L-type calcium channels associate with caveolin-3 but that this association is reduced with age. We also show that aging causes a decrease in caveolae density in pacemaker cells. These findings are in line with reports in ventricular cardiomyocytes from patients with heart disease (Fridolfsson and Patel, 2013; Egorov et al., 2019). A limitation of our study is that it was not possible to test the changes in proximity between β-ARs and caveolin-3. More data is necessary to estimate the ratio of β2-ARs that locate inside and outside caveolae and the effect of aging on this ratio. The important role of caveolae in cardiac function has been highlighted by the fact that animal models lacking caveolin-1 and -3 display severe cardiomyopathy characterized by an increase in ventricular wall thickness, hypertrophy, and a decrease in fractional shortening. In addition, mutations in caveolin-3 are associated with long-QT congenital syndrome (Vatta et al., 2006). The importance of caveolin-3 in the specific function of the pacemaker has been shown in the caveolin-3 cardiac-specific KO mouse, where there is a significant beat-to-beat heart rate lability linked with suppressed pacemaker function (Lang and Glukhov, 2018). Here, we reveal that the age-associated disruption of caveolae is a newly identified mechanism that leads to a reduction in the compartmentalized β-adrenergic signaling and in the responsiveness of the pacemaker to this modulation.

Figure 7 summarizes our model for the age-associated impairment of β2-mediated L-type calcium current regulation. We propose that young pacemaker cells have a vast caveolar

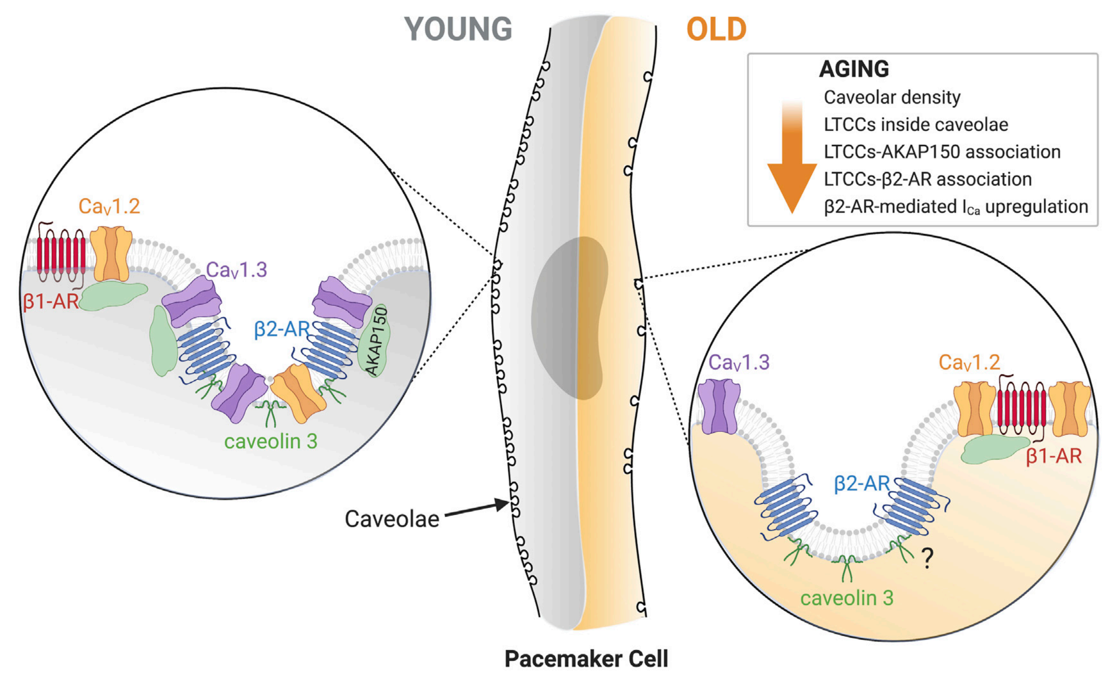

FIGURE 7 | Diagrammatic representation of the main changes in old pacemaker cells that lead to a reduction in L-type calcium current regulation. A global reduction in caveolar density is characteristic of old cells. Zoomed in on the left side represent the proposed architectural layout of associated proteins in young cells: β1-AR (red)/$Ca_V1.2$ (orange) outside of caveolae and β2-AR (blue)/$Ca_V1.2$ (orange)/$Ca_V1.3$ (purple)/Caveolin-3 (dark green)/AKAP150 (light green) inside caveolae. Zoomed in on the right side shows the proposed architectural changes of associated proteins in old cells: β1-AR (red)/$Ca_V1.2$ (orange) remain outside caveolae, and β2-AR (blue)/Caveolin-3 (dark green) remain inside caveolae, while $Ca_V1.3$ shift outside caveolae. If aging alters the proximity of β2-AR with caveolin-3 needs future testing. Created with BioRender.com.

network that allows efficient signaling between β2-ARs and L-type calcium channels. In these networks, L-type calcium channels are anchored through their binding to AKAP150. $Ca_V1.3$ channels are especially enriched inside these caveolar microdomains, while $Ca_V1.2$ channels can also associate with β1-ARs outside these microdomains. In contrast, old pacemaker cells exhibit a global reduction in caveolar density. This is accompanied by a reduction in the co-localization of $Ca_V1.3$ and $Ca_V1.2$ channels with β2-ARs inside caveolae. However, whether β2-ARs compartmentalization inside caveolae is reduced with age has yet to be tested. As HCN4 channels, NCX, and potassium channels are also localized inside caveolae and modulated by β2-ARs (Lang and Glukhov, 2018), future studies will have to evaluate the effects of the age-associated reduction in caveolar density over the function of these proteins to gain a more holistic view on how aging affects pacemaker dysfunction at the molecular level.

DATA AVAILABILITY STATEMENT

The raw data supporting the conclusion of this article will be made available by the authors, upon request.

ETHICS STATEMENT

The animal study was reviewed and approved by UW Institutional Animal Care and Use Committee.

AUTHOR CONTRIBUTIONS

SC, performed experiments, formal analysis, writing-original draft; OV, conceptualization, performed experiments, formal analysis, writing—original draft, funding acquisition; MB, performed experiments, formal analysis and writing-reviewing; CM, conceptualization, performed experiments, formal analysis, writing—original draft, reviewing and editing, funding acquisition, project administration.

FUNDING

This work was supported by Grants from the US National Institutes of Health/NIA (CMM: R00 AG056595), the AFAR-Glenn Foundation Junior Faculty Award (CMM), and the Sagol Geromics Award (OV).

SUPPLEMENTARY MATERIAL

The Supplementary Material for this article can be found online at: https://www.frontiersin.org/articles/10.3389/fphys.2022.805909/full#supplementary-material

REFERENCES

Alghamdi, A. M., Boyett, M. R., Hancox, J. C., and Zhang, H. (2020). Cardiac Pacemaker Dysfunction Arising from Different Studies of Ion Channel Remodeling in the Aging Rat Heart. *Front. Physiol.* 11, 546508. doi:10.3389/fphys.2020.546508

Alings, A. M. W., and Bouman, L. N. (1993). Electrophysiology of the Ageing Rabbit and Cat Sinoatrial Node - A Comparative Study. *Eur. Heart J.* 14 (9), 1278–1288. doi:10.1093/eurheartj/14.9.1278

Altschuld, R. A., Starling, R. C., Hamlin, R. L., Billman, G. E., Hensley, J., Castillo, L., et al. (1995). Response of Failing Canine and Human Heart Cells to β2 -Adrenergic Stimulation. *Circulation* 92 (6), 1612–1618. doi:10.1161/01.cir.92.6.1612

Balijepalli, R. C., Foell, J. D., Hall, D. D., Hell, J. W., and Kamp, T. J. (2006). Localization of Cardiac L-type Ca2+ Channels to a Caveolar Macromolecular Signaling Complex is Required for β2 -adrenergic Regulation. *Proc. Natl. Acad. Sci. U.S.A.* 103 (19), 7500–7505. doi:10.1073/pnas.0503465103

Barbuti, A., Terragni, B., Brioschi, C., and DiFrancesco, D. (2007). Localization of F-Channels to Caveolae Mediates Specific β2-adrenergic Receptor Modulation of Rate in Sinoatrial Myocytes. *J. Mol. Cell Cardiol.* 42 (1), 71–78. doi:10.1016/j.yjmcc.2006.09.018

Barbuti, A., Scavone, A., Mazzocchi, N., Terragni, B., Baruscotti, M., and Difrancesco, D. (2012). A Caveolin-Binding Domain in the HCN4 Channels Mediates Functional Interaction with Caveolin Proteins. *J. Mol. Cell Cardiol.* 53 (2), 187–195. doi:10.1016/j.yjmcc.2012.05.013

Baruscotti, M., Bottelli, G., Milanesi, R., DiFrancesco, J. C., and DiFrancesco, D. (2010). HCN-related Channelopathies. *Pflugers Arch. Eur. J. Physiol.* 460 (2), 405–415. doi:10.1007/s00424-010-0810-8

Baudot, M., Torre, E., Bidaud, I., Louradour, J., Torrente, A. G., Fossier, L., et al. (2020). Concomitant Genetic Ablation of L-type Cav1.3 (α1D) and T-type Cav3.1 (α1G) Ca2+ Channels Disrupts Heart Automaticity. *Sci. Rep.* 10 (1), 18906. doi:10.1038/s41598-020-76049-7

Boyett, M., Honjo, H., and Kodama, I. (2000). The Sinoatrial Node, a Heterogeneous Pacemaker Structure. *Cardiovasc. Res.* 47 (4), 658–687. doi:10.1016/s0008-6363(00)00135-8

Brodde, O.-E., Leifert, F.-J., and Krehl, H.-J. (1982). Coexistence of β1 and β2-Adrenoceptors in the Rabbit Heart. *J. Cardiovasc. Pharmacol.* 4 (1), 34–43. doi:10.1097/00005344-198201000-00007

Brodde, O.-E., Bruck, H., Leineweber, K., and Seyfarth, T. (2001). Presence, Distribution and Physiological Function of Adrenergic and Muscarinic Receptor Subtypes in the Human Heart. *Basic Res. Cardiol.* 96 (6), 528–538. doi:10.1007/s003950170003

Brown, H., Difrancesco, D., and Noble, S. (1979). Cardiac Pacemaker Oscillation and its Modulation by Autonomic Transmitters. *J. Exp. Biol.* 81, 175–204. doi:10.1242/jeb.81.1.175

Campostrini, G., Bonzanni, M., Lissoni, A., Bazzini, C., Milanesi, R., Vezzoli, E., et al. (2017). The Expression of the Rare Caveolin-3 Variant T78M Alters Cardiac Ion Channels Function and Membrane Excitability. *Cardiovasc. Res.* 113 (10), 1256–1265. doi:10.1093/cvr/cvx122

Cheng, E. P., Yuan, C., Navedo, M. F., Dixon, R. E., Nieves-Cintrón, M., Scott, J. D., et al. (2011). Restoration of Normal L-type Ca2+ Channel Function during Timothy Syndrome by Ablation of an Anchoring Protein. *Circ. Res.* 109 (3), 255–261. doi:10.1161/CIRCRESAHA.111.248252

Chozinski, T. J., Halpern, A. R., Okawa, H., Kim, H.-J., Tremel, G. J., Wong, R. O. L., et al. (2016). Expansion Microscopy with Conventional Antibodies and Fluorescent Proteins. *Nat. Methods* 13 (6), 485–488. doi:10.1038/nmeth.3833

Christel, C. J., Cardona, N., Mesirca, P., Herrmann, S., Hofmann, F., Striessnig, J., et al. (2012). Distinct Localization and Modulation of Cav1.2 and Cav1.3 L-type Ca2+channels in Mouse Sinoatrial Node. *J. Physiol.* 590 (24), 6327–6341. doi:10.1113/jphysiol.2012.239954

Christou, D. D., and Seals, D. R. (2008). Decreased Maximal Heart Rate with Aging Is Related to Reduced β-adrenergic Responsiveness but Is Largely Explained by a Reduction in Intrinsic Heart Rate. *J. Appl. Physiol. (1985)* 105 (1), 24–29. doi:10.1152/japplphysiol.90401.2008

Cong, M., Perry, S. J., Lin, F.-T., Fraser, I. D., Hu, L. A., Chen, W., et al. (2001). Regulation of Membrane Targeting of the G Protein-Coupled Receptor Kinase 2 by Protein Kinase A and its Anchoring Protein AKAP79. *J. Biol. Chem.* 276 (18), 15192–15199. doi:10.1074/jbc.M009130200

Csepe, T. A., Zhao, J., Hansen, B. J., Li, N., Sul, L. V., Lim, P., et al. (2016). Human Sinoatrial Node Structure: 3D Microanatomy of Sinoatrial Conduction Pathways. *Prog. Biophys. Mol. Biol.* 120 (1-3), 164–178. doi:10.1016/j.pbiomolbio.2015.12.011

Di Gennaro, M., Bernabei, R., Sgadari, A., Carosella, L., and Carbonin, P. U. (1987). Age-related Differences in Isolated Rat Sinus Node Function. *Basic Res. Cardiol.* 82 (6), 530–536. doi:10.1007/BF01907222

DiFrancesco, D. (1986). Characterization of Single Pacemaker Channels in Cardiac Sino-Atrial Node Cells. *Nature* 324 (6096), 470–473. doi:10.1038/324470a0

Dun, W., Yagi, T., Rosen, M. R., and Boyden, P. A. (2003). Calcium and Potassium Currents in Cells from Adult and Aged Canine Right Atria. *Cardiovasc. Res.* 58 (3), 526–534. doi:10.1016/s0008-6363(03)00288-8

Ebert, S., and Taylor, D. (2006). Catecholamines and Development of Cardiac Pacemaking: an Intrinsically Intimate Relationship. *Cardiovasc. Res.* 72 (3), 364–374. doi:10.1016/j.cardiores.2006.08.013

Egorov, Y. V., Lang, D., Tyan, L., Turner, D., Lim, E., Piro, Z. D., et al. (2019). Caveolae-Mediated Activation of Mechanosensitive Chloride Channels in Pulmonary Veins Triggers Atrial Arrhythmogenesis. *J. Am. Heart Assoc.* 8 (20), e012748. doi:10.1161/JAHA.119.012748

Evans, R., and Shaw, D. B. (1977). Pathological Studies in Sinoatrial Disorder (Sick Sinus Syndrome). *Heart* 39 (7), 778–786. doi:10.1136/hrt.39.7.778

Fenske, S., Pröbstle, R., Auer, F., Hassan, S., Marks, V., Pauza, D. H., et al. (2016). Comprehensive Multilevel *In Vivo* and *In Vitro* Analysis of Heart Rate Fluctuations in Mice by ECG Telemetry and Electrophysiology. *Nat. Protoc.* 11 (1), 61–86. doi:10.1038/nprot.2015.139

Fridolfsson, H. N., and Patel, H. H. (2013). Caveolin and Caveolae in Age Associated Cardiovascular Disease. *J. Geriatr. Cardiol.* 10 (1), 66–74. doi:10.3969/j.issn.1671-5411.2013.01.011

Fu, Y., Westenbroek, R. E., Scheuer, T., and Catterall, W. A. (2014). Basal and β-adrenergic Regulation of the Cardiac Calcium Channel Ca V 1.2 Requires Phosphorylation of Serine 1700. *Proc. Natl. Acad. Sci. U.S.A.* 111 (46), 16598–16603. doi:10.1073/pnas.1419129111

Furukawa, Y., Miyashita, Y., Nakajima, K., Hirose, M., Kurogouchi, F., and Chiba, S. (1999). Effects of Verapamil, Zatebradine, and E-4031 on the Pacemaker Location and Rate in Response to Sympathetic Stimulation in Dog Hearts. *J. Pharmacol. Exp. Ther.* 289 (3), 1334–1342.

Gordan, R., Gwathmey, J. K., and Xie, L.-H. (2015). Autonomic and Endocrine Control of Cardiovascular Function. *World J. Cardiol.* 7 (4), 204–214. doi:10.4330/wjc.v7.i4.204

Hao, X., Zhang, Y., Zhang, X., Nirmalan, M., Davies, L., Konstantinou, D., et al. (2011). TGF-β1-Mediated Fibrosis and Ion Channel Remodeling Are Key Mechanisms in Producing the Sinus Node Dysfunction Associated with SCN5A Deficiency and Aging. *Circ. Arrhythm Electrophysiol.* 4 (3), 397–406. doi:10.1161/CIRCEP.110.960807

Harvey, R. D., and Hell, J. W. (2013). CaV1.2 Signaling Complexes in the Heart. *J. Mol. Cell Cardiol.* 58, 143–152. doi:10.1016/j.yjmcc.2012.12.006

Johnson, D. M., and Antoons, G. (2018). Arrhythmogenic Mechanisms in Heart Failure: Linking β-Adrenergic Stimulation, Stretch, and Calcium. *Front. Physiol.* 9, 1453. doi:10.3389/fphys.2018.01453

Jones, S. A., Boyett, M. R., and Lancaster, M. K. (2007). Declining into Failure. *Circulation* 115 (10), 1183–1190. doi:10.1161/CIRCULATIONAHA.106.663070

Kuschel, M., Zhou, Y.-Y., Spurgeon, H. A., Bartel, S., Karczewski, P., Zhang, S.-J., et al. (1999). β2-Adrenergic cAMP Signaling is Uncoupled from Phosphorylation of Cytoplasmic Proteins in Canine Heart. *Circulation* 99 (18), 2458–2465. doi:10.1161/01.cir.99.18.2458

Lang, D., and Glukhov, A. V. (2018). Functional Microdomains in Heart's Pacemaker: A Step beyond Classical Electrophysiology and Remodeling. *Front. Physiol.* 9, 1686. doi:10.3389/fphys.2018.01686

Larson, E. D., St. Clair, J. R., Sumner, W. A., Bannister, R. A., and Proenza, C. (2013). Depressed Pacemaker Activity of Sinoatrial Node Myocytes Contributes to the Age-dependent Decline in Maximum Heart Rate. *Proc. Natl. Acad. Sci. U.S.A.* 110 (44), 18011–18016. doi:10.1073/pnas.1308477110

Le Scouarnec, S., Bhasin, N., Vieyres, C., Hund, T. J., Cunha, S. R., Koval, O., et al. (2008). Dysfunction in Ankyrin-B-dependent Ion Channel and Transporter

Targeting Causes Human Sinus Node Disease. *Proc. Natl. Acad. Sci. U.S.A.* 105 (40), 15617–15622. doi:10.1073/pnas.0805500105

Levitan, B. M., Ahern, B. M., Aloysius, A., Brown, L., Wen, Y., Andres, D. A., et al. (2021). Rad-GTPase Contributes to Heart Rate via L-type Calcium Channel Regulation. *J. Mol. Cell Cardiol.* 154, 60–69. doi:10.1016/j.yjmcc.2021.01.005

Liu, G., Shi, J., Yang, L., Cao, L., Park, S. M., Cui, J., et al. (2004). Assembly of a Ca2+-dependent BK Channel Signaling Complex by Binding to β2 Adrenergic Receptor. *EMBO J.* 23 (11), 2196–2205. doi:10.1038/sj.emboj.7600228

Liu, G., Papa, A., Katchman, A. N., Zakharov, S. I., Roybal, D., Hennessey, J. A., et al. (2020). Mechanism of Adrenergic CaV1.2 Stimulation Revealed by Proximity Proteomics. *Nature* 577 (7792), 695–700. doi:10.1038/s41586-020-1947-z

MacDonald, E. A., Rose, R. A., and Quinn, T. A. (2020). Neurohumoral Control of Sinoatrial Node Activity and Heart Rate: Insight from Experimental Models and Findings from Humans. *Front. Physiol.* 11, 170. doi:10.3389/fphys.2020.00170

Malbon, C. C., Tao, J., and Wang, H.-y. (2004). AKAPs (A-Kinase Anchoring Proteins) and Molecules that Compose Their G-Protein-Coupled Receptor Signalling Complexes. *Biochem. J.* 379 (Pt 1), 1–9. doi:10.1042/BJ20031648

Mangoni, M. E., and Nargeot, J. (2008). Genesis and Regulation of the Heart Automaticity. *Physiol. Rev.* 88 (3), 919–982. doi:10.1152/physrev.00018.2007

Mangoni, M. E., Couette, B., Bourinet, E., Platzer, J., Reimer, D., Striessnig, J., et al. (2003). Functional Role of L-type Cav1.3 Ca2+ Channels in Cardiac Pacemaker Activity. *Proc. Natl. Acad. Sci. U S A.* 100, 5543. doi:10.1073/pnas.0935295100

Marcus, B., Gillette, P. C., and Garson, A., Jr. (1990). Intrinsic Heart Rate in Children and Young Adults: An index of Sinus Node Function Isolated from Autonomic Control. *Am. Heart J.* 119 (4), 911–916. doi:10.1016/s0002-8703(05)80331-x

Matthaeus, C., and Taraska, J. W. (2020). Energy and Dynamics of Caveolae Trafficking. *Front. Cel Dev. Biol.* 8, 614472. doi:10.3389/fcell.2020.614472

Milanesi, R., Bucchi, A., and Baruscotti, M. (2015). The Genetic Basis for Inherited Forms of Sinoatrial Dysfunction and Atrioventricular Node Dysfunction. *J. Interv. Card. Electrophysiol.* 43 (2), 121–134. doi:10.1007/s10840-015-9998-z

Mohler, P. J., Schott, J.-J., Gramolini, A. O., Dilly, K. W., Guatimosim, S., duBell, W. H., et al. (2003). Ankyrin-B Mutation Causes Type 4 Long-QT Cardiac Arrhythmia and Sudden Cardiac Death. *Nature* 421 (6923), 634–639. doi:10.1038/nature01335

Navedo, M. F., Nieves-Cintro´n, M., Amberg, G. C., Yuan, C., Votaw, V. S., Lederer, W. J., et al. (2008). AKAP150 Is Required for Stuttering Persistent Ca2+ Sparklets and Angiotensin II-Induced Hypertension. *Circ. Res.* 102 (2), e1–e11. doi:10.1161/CIRCRESAHA.107.167809

Nichols, C. B., Rossow, C. F., Navedo, M. F., Westenbroek, R. E., Catterall, W. A., Santana, L. F., et al. (2010). Sympathetic Stimulation of Adult Cardiomyocytes Requires Association of AKAP5 with a Subpopulation of L-type Calcium Channels. *Circ. Res.* 107 (6), 747–756. doi:10.1161/CIRCRESAHA.109.216127

Nikolaev, V. O., Bünemann, M., Schmitteckert, E., Lohse, M. J., and Engelhardt, S. (2006). Cyclic AMP Imaging in Adult Cardiac Myocytes Reveals Far-Reaching β1-Adrenergic but Locally Confined β2-Adrenergic Receptor-Mediated Signaling. *Circ. Res.* 99 (10), 1084–1091. doi:10.1161/01.RES.0000250046.69918.d5

Nikolaev, V. O., Moshkov, A., Lyon, A. R., Miragoli, M., Novak, P., Paur, H., et al. (2010). β2-Adrenergic Receptor Redistribution in Heart Failure Changes cAMP Compartmentation. *Science* 327 (5973), 1653–1657. doi:10.1126/science.1185988

Ostchega, Y., Porter, K. S., Hughes, J., Dillon, C. F., and Nwankwo, T. (2011). Resting Pulse Rate Reference Data for Children, Adolescents, and Adults: United States, 1999-2008. *Natl. Health Stat. Rep.* (41), 1–16.

Peters, C. H., Sharpe, E. J., and Proenza, C. (2020). Cardiac Pacemaker Activity and Aging. *Annu. Rev. Physiol.* 82, 21–43. doi:10.1146/annurev-physiol-021119-034453

Rodefeld, M. D., Beau, S. L., Schuessler, R. B., Boineau, J. P., and Saffitz, J. E. (1996). Beta-adrenergic and Muscarinic Cholinergic Receptor Densities in the Human Sinoatrial Node: Identification of a High Beta 2-adrenergic Receptor Density. *J. Cardiovasc. Electrophysiol.* 7 (11), 1039–1049. doi:10.1111/j.1540-8167.1996.tb00479.x

Saito, K., Torda, T., Potter, W. Z., and Saavedra, J. M. (1989). Characterization of β1- and β2-adrenoceptor Subtypes in the Rat Sinoatrial Node and Stellate Ganglia by Quantitative Autoradiography. *Neurosci. Lett.* 96 (1), 35–41. doi:10.1016/0304-3940(89)90239-5

Schobesberger, S., Wright, P., Tokar, S., Bhargava, A., Mansfield, C., Glukhov, A. V., et al. (2017). T-tubule Remodelling Disturbs Localized β2-adrenergic Signalling in Rat Ventricular Myocytes during the Progression of Heart Failure. *Cardiovasc. Res.* 113 (7), 770–782. doi:10.1093/cvr/cvx074

Sharpe, E. J., Larson, E. D., and Proenza, C. (2017). Cyclic AMP Reverses the Effects of Aging on Pacemaker Activity and if in Sinoatrial Node Myocytes. *J. Gen. Physiol.* 149 (2), 237–247. doi:10.1085/jgp.201611674

Shibata, E. F., Brown, T. L. Y., Washburn, Z. W., Bai, J., Revak, T. J., and Butters, C. A. (2006). Autonomic Regulation of Voltage-Gated Cardiac Ion Channels. *J. Cardiovasc. Electrophysiol.* 17 (Suppl. 1), S34–S42. doi:10.1111/j.1540-8167.2006.00387.x

Shih, M., Lin, F., Scott, J. D., Wang, H.-y., and Malbon, C. C. (1999). Dynamic Complexes of β2-Adrenergic Receptors with Protein Kinases and Phosphatases and the Role of Gravin. *J. Biol. Chem.* 274 (3), 1588–1595. doi:10.1074/jbc.274.3.1588

Shiraishi, I., Takamatsu, T., Minamikawa, T., Onouchi, Z., and Fujita, S. (1992). Quantitative Histological Analysis of the Human Sinoatrial Node during Growth and Aging. *Circulation* 85 (6), 2176–2184. doi:10.1161/01.cir.85.6.2176

Tanaka, H., Monahan, K. D., and Seals, D. R. (2001). Age-predicted Maximal Heart Rate Revisited. *J. Am. Coll. Cardiol.* 37 (1), 153–156. doi:10.1016/s0735-1097(00)01054-8

Tao, J., and Malbon, C. C. (2008). G-protein-coupled Receptor-Associated A-Kinase Anchoring Proteins AKAP5 and AKAP12: Differential Signaling to MAPK and GPCR Recycling. *J. Mol. Signal.* 3, 19. doi:10.1186/1750-2187-3-19

Tao, J., Wang, H. Y., and Malbon, C. C. (2003). Protein Kinase A Regulates AKAP250 (Gravin) Scaffold Binding to the 2-adrenergic Receptor. *EMBO J.* 22 (24), 6419–6429. doi:10.1093/emboj/cdg628

Tellez, J. O., Mączewski, M., Yanni, J., Sutyagin, P., Mackiewicz, U., Atkinson, A., et al. (2011). Ageing-dependent Remodelling of Ion Channel and Ca2+clock Genes Underlying Sino-Atrial Node Pacemaking. *Exp. Physiol.* 96 (11), 1163–1178. doi:10.1113/expphysiol.2011.057752

Thery, C., Gosselin, B., Lekieffre, J., and Warembourg, H. (1977). Pathology of Sinoatrial Node. Correlations with Electrocardiographic Findings in 111 Patients. *Am. Heart J.* 93 (6), 735–740. doi:10.1016/s0002-8703(77)80070-7

Tingley, W. G., Pawlikowska, L., Zaroff, J. G., Kim, T., Nguyen, T., Young, S. G., et al. (2007). Gene-trapped Mouse Embryonic Stem Cell-Derived Cardiac Myocytes and Human Genetics Implicate AKAP10 in Heart Rhythm Regulation. *Proc. Natl. Acad. Sci. U.S.A.* 104 (20), 8461–8466. doi:10.1073/pnas.0610393104

Torrente, A. G., Mesirca, P., Neco, P., Rizzetto, R., Dubel, S., Barrere, C., et al. (2016). L-type Cav1.3 Channels Regulate Ryanodine Receptor-dependent Ca2+release during Sino-Atrial Node Pacemaker Activity. *Cardiovasc. Res.* 109 (3), 451–461. doi:10.1093/cvr/cvw006

Vatta, M., Ackerman, M. J., Ye, B., Makielski, J. C., Ughanze, E. E., Taylor, E. W., et al. (2006). Mutant Caveolin-3 Induces Persistent Late Sodium Current and Is Associated with Long-QT Syndrome. *Circulation* 114 (20), 2104–2112. doi:10.1161/CIRCULATIONAHA.106.635268

Vinogradova, T. M., and Lakatta, E. G. (2009). Regulation of Basal and reserve Cardiac Pacemaker Function by Interactions of cAMP-Mediated PKA-dependent Ca2+ Cycling with Surface Membrane Channels. *J. Mol. Cell Cardiol.* 47 (4), 456–474. doi:10.1016/j.yjmcc.2009.06.014

Wang, L., Swirp, S., and Duff, H. (2000). Age-dependent Response of the Electrocardiogram to K+ Channel Blockers in Mice. *Am. J. Physiol. Cell Physiol.* 278 (1), C73–C80. doi:10.1152/ajpcell.2000.278.1.C73

Wright, P. T., Nikolaev, V. O., O'Hara, T., Diakonov, I., Bhargava, A., Tokar, S., et al. (2014). Caveolin-3 Regulates Compartmentation of Cardiomyocyte Beta2-Adrenergic Receptor-Mediated cAMP Signaling. *J. Mol. Cell Cardiol.* 67, 38–48. doi:10.1016/j.yjmcc.2013.12.003

Xiao, R. P., and Lakatta, E. G. (1993). Beta 1-adrenoceptor Stimulation and Beta 2-adrenoceptor Stimulation Differ in Their Effects on Contraction, Cytosolic Ca2+, and Ca2+ Current in Single Rat Ventricular Cells. *Circ. Res.* 73 (2), 286–300. doi:10.1161/01.res.73.2.286

Xiao, R.-P., Cheng, H., Zhou, Y.-Y., Kuschel, M., and Lakatta, E. G. (1999). Recent Advances in Cardiac β 2 -Adrenergic Signal Transduction. *Circ. Res.* 85 (11), 1092–1100. doi:10.1161/01.res.85.11.1092

Yaniv, Y., Ahmet, I., Tsutsui, K., Behar, J., Moen, J. M., Okamoto, Y., et al. (2016). Deterioration of Autonomic Neuronal Receptor Signaling and Mechanisms Intrinsic to Heart Pacemaker Cells Contribute to Age-associated Alterations in Heart Rate Variability *In Vivo*. *Aging Cell* 15 (4), 716–724. doi:10.1111/acel.12483

Yin, F. C., Spurgeon, H. A., Greene, H. L., Lakatta, E. G., and Weisfeldt, M. L. (1979). Age-associated Decrease in Heart Rate Response to Isoproterenol in Dogs. *Mech. Ageing Dev.* 10 (1-2), 17–25. doi:10.1016/0047-6374(79)90067-8

Zaza, A., Robinson, R. B., and DiFrancesco, D. (1996). Basal Responses of the L-type Ca2+ and Hyperpolarization-Activated Currents to Autonomic Agonists in the Rabbit Sino-Atrial Node. *J. Physiol.* 491 (Pt 2), 347–355. doi:10.1113/jphysiol.1996.sp021220

Conflict of Interest: The authors declare that the research was conducted in the absence of any commercial or financial relationships that could be construed as a potential conflict of interest.

frontiers | Frontiers in Physiology

REVIEW
published: 22 June 2022
doi: 10.3389/fphys.2022.827334

Regulation of Cardiac Contractility by the Alpha 2 Subunit of the Na^+/ K^+-ATPase

Jonas Skogestad[1,2] *and Jan Magnus Aronsen*[1,2]*

[1]*Department of Molecular Medicine, Institute of Basic Medical Sciences, Faculty of Medicine, University of Oslo, Oslo, Norway,*
[2]*Department of Pharmacology, Oslo University Hospital, Oslo, Norway*

Cytosolic Na + concentrations regulate cardiac excitation-contraction coupling and contractility. Inhibition of the Na^+/K^+-ATPase (NKA) activity increases cardiac contractility by increasing cytosolic Ca^{2+} levels, as increased cytosolic Na^+ levels are coupled to less Ca^{2+} extrusion and/or increased Ca^{2+} influx from the Na^+/Ca^{2+}-exchanger. NKA consists of one α subunit and one β subunit, with α1 and α2 being the main α isoforms in cardiomyocytes. Substantial evidence suggests that NKAα2 is the primary regulator of cardiac contractility despite being outnumbered by NKAα1 in cardiomyocytes. This review will mainly focus on differential regulation and subcellular localization of the NKAα1 and NKAα2 isoforms, and their relation to the proposed concept of subcellular gradients of Na^+ in cardiomyocytes. We will also discuss the potential roles of NKAα2 in mediating cardiac hypertrophy and ventricular arrhythmias.

Keywords: NKA, sodium, calcium, ion gradients, NCX, Cardiomyocyte, EC-coupling

OPEN ACCESS

Edited by:
Niall Macquaide,
Glasgow Caledonian University,
United Kingdom

Reviewed by:
Sanda Despa,
University of Kentucky, United States
Thomas Friedrich,
Technical University of Berlin,
Germany

****Correspondence:***
Jan Magnus Aronsen
j.m.aronsen@medisin.uio.no

Specialty section:
This article was submitted to
Cardiac Electrophysiology,
a section of the journal
Frontiers in Physiology

Received: *01 December 2021*
Accepted: *16 May 2022*
Published: *22 June 2022*

Citation:
Skogestad J and Aronsen JM (2022)
Regulation of Cardiac Contractility by
the Alpha 2 Subunit of the Na^+/K^+-
ATPase.
Front. Physiol. 13:827334.
doi: 10.3389/fphys.2022.827334

INTRODUCTION

Cardiac contraction is initiated by the opening of voltage-gated Na^+ channels, leading to rapid Na^+ influx into cardiomyocytes and membrane depolarization. The membrane depolarization activates the L-type Ca^{2+} channels, and the resulting Ca^{2+} influx leads to the opening of the ryanodine receptors (RyRs), causing a substantial Ca^{2+} release from the sarcoplasmic reticulum (SR). The ensuing rise in cytosolic $[Ca^{2+}]$ eventually leads to cardiac contraction when free cytosolic Ca^{2+} binds troponin-C in the myofilaments, where the contraction's strength depends on the levels of cytosolic Ca^{2+} (Bers, 2002). For the cardiomyocyte to relax and re-lengthen, the Ca^{2+} entering the cytosol during the excitation-contraction coupling must be extruded from the cytosolic space. The Ca^{2+} extrusion is mainly executed by either the SR Ca^{2+} ATPase (SERCA2), which pumps Ca^{2+} into the SR, or the Na^+/Ca^{2+}- exchanger (NCX), which extrudes Ca^{2+} over the cell membrane in exchange for 3 Na^+ ions.

Because NCX exchanges Ca^{2+} for Na^+, NCX indirectly couples intracellular $[Na^+]$ to regulate cardiac contractility. NCX can operate in two modes: A forward mode with Ca^{2+} efflux and Na^+ influx and a reverse mode with Ca^{2+} influx and Na^+ efflux. Whether NCX operates in forward or reverse mode depends on the transmembrane gradients for Na^+ and Ca^{2+} and the membrane potential. Most of the time, NCX extrudes Ca^{2+} (forward mode), and Ca^{2+} entry through NCX (reverse mode) only occurs briefly during the early stages of a regular action potential, where increased $[Na^+]_i$ (due to the Na^+ influx in early phases of the action potential), low $[Ca^{2+}]_i$, and positive membrane potential all favors NCX-mediated Ca^{2+} influx (Bers, 2001).

During a regular contraction-relaxation cycle, a considerable amount of Na^+ enters the cell, mainly through the Na^+ channels and the NCX (Bers and Despa, 2009). To maintain equilibrium, all

Na^+ entering the cell must be transported out of the cell. The main Na^+ efflux route is the Na^+/K^+-ATPase (NKA), which uses the energy from ATP to extrude 3 Na^+ for 2 K^+. NKA is ubiquitously expressed in all cell types and contributes to a wide range of cellular tasks in addition to the regulation of cardiac contractility, including secondary active transport, volume regulation, and pH regulation (Kaplan, 2002). NKA is a protein complex consisting of an α subunit and a β subunit that form a "minimal functional unit" and a ϒ subunit (FXYD proteins) that regulates NKA function. Different subunit isoforms (α1-3 and β1-2) can form different αβ combinations in the heart. In humans, NKAα1-3 is expressed in all heart tissue (Sweadner et al., 1994), while β1 is the predominant β isoform (Liu et al., 2016). The α1β1-combination of NKA is the most abundant and has been extensively studied (McDonough et al., 1990; Blanco and Mercer, 1998). NKAα1 and NKAα2 are expressed in the left ventricle of adult rodents (Orlowski and Lingrel, 1988; Hensley et al., 1992; James et al., 1999), possibly with some expression of NKAα3 (Harada et al., 2006; Stanley et al., 2015). Protein levels, mRNA expression, and functional experiments suggest that NKAα1 is the most abundant cardiac isoform (70–95%) in humans, large animals, and rodents, with consistently lower expression and activity of NKAα2 (10–30%) (Sweadner et al., 1994; Gao et al., 1999; Berry et al., 2007; Swift et al., 2007). Despite being outnumbered by a factor of approximately 10:1, the existing evidence clearly suggests that NKAα2 and not NKAα1 is the primary regulator of cardiac contractility. We here aim to review the evidence of NKAα2 as regulator of cardiac contractility, and discuss possible underlying mechanisms and pathophysiological roles of NKAα2-mediated control of cardiac excitation-contraction coupling.

NKA/NCX Interaction as a Regulator of Intracellular [Ca^{2+}] and Cardiac Contractility

NKA indirectly regulates NCX activity through a functional interaction: NKA regulates cytosolic [Na^+], thereby modulating NCX activity and subsequently cytosolic [Ca^{2+}] and cardiac contractility. A key, unsolved question is whether NCX activity is regulated by the average [Na^+] and [Ca^{2+}] in the cytosol or whether NCX "senses" localized Na^+ pools, i.e., subdomains where the [Na^+] is higher or lower than the average [Na^+]. Such localized gradients are well documented for Ca^{2+} ions, particularly in the dyad, where repetitive Ca^{2+} influx causes standing and dynamic gradients of Ca^{2+} between the dyad and the bulk cytosol (Bers, 2008; Acsai et al., 2011).

The existence of localized Na^+ gradients in cardiomyocytes is more controversial and the evidence conflicting (Garcia et al., 2016; Lu and Hilgemann, 2017). The lack of methods allowing high-resolution measurements of intracellular Na^+ means that the proposed concept of localized Na^+ gradients is based mainly on indirect evidence. Perhaps most profound among these indirect lines of evidence is the large amount of data showing that NKAα2 preferentially regulates cardiac contractility without modulating global levels of Na^+.

NKAα2 Preferentially Regulates Ca^{2+} Cycling and Cardiac Contractility

Different cardiac NKAα isoforms are present in nearly all species, including humans and rodents (Hensley et al., 1992; Sweadner et al., 1994), suggesting differential functional roles in the heart, which is also supported by the fact that the isoform-defining regions are highly conserved through evolution (Baxter-Lowe et al., 1989; Pressley, 1992). Mice lacking both copies of the NKAα1 gene die during the embryonical stage, while mice without NKAα2 die immediately following birth (James et al., 1999; Barcroft et al., 2004; Dostanic-Larson et al., 2006). In a landmark paper, James *et al.* showed that heterozygous inactivation of NKAα2 (NKAα$2^{+/-}$) increased Ca^{2+} transients and cardiac contractility in mice, while NKAα$1^{+/-}$ mice were hypocontractile (James et al., 1999). Genetic analysis of the NKAα$1^{+/-}$ mice revealed alterations in several genes important for ion transport and cardiac contractility (Moseley et al., 2005), and the functional effects in NKAα1 deficient mice thus might be due to indirect effects. However, these initial findings suggesting a distinct role of NKAα2 in regulating NCX activity, intracellular [Ca^{2+}], and cardiac contractility has since been reproduced and elaborated by several groups (Yamamoto et al., 2005; Swift et al., 2007; Swift et al., 2010; Despa et al., 2012).

The glycoside ouabain has been an invaluable tool to evaluate functional roles of NKA α1 versus NKAα2. NKAα1 in rodents is less sensitive to the glycoside ouabain than NKAα2 due to two positively charged amino acids (arginine-111 and aspartic acid-122) in the extracellular region (Price and Lingrel, 1988; Price et al., 1990) of NKAα1. Ouabain does not alter the NKAα1 activity itself (Dostanic-Larson et al., 2006) or the coefficients towards Na^+ and K^+ (Periyasamy et al., 1983). In contrast, NKAα2 has a higher affinity towards ouabain (O'Brien et al., 1994; Ishizuka et al., 1996). A double-sigmoid affinity curve is seen in mice and rats (Swift et al., 2007; Despa et al., 2012), allowing specific inhibition of NKAα2 with a low dose of ouabain (300 nM), where only a small fraction of NKAα1 is inhibited. Specific inhibition of NKAα2 increases NCX-sensed [Na^+], increases Ca^{2+} transient amplitude and cardiac contractility without effects on global [Na^+] (Yamamoto et al., 2005; Swift et al., 2007; Despa et al., 2012).

Overexpression of NKAα1 and NKAα2 both lower intracellular [Ca^{2+}], but overexpression of NKAα1 reduces the expression of NKAα2 and *vice versa* (Correll et al., 2014). Generating SWAP mice has helped overcome these limitations of NKAα1 and NKAα2 overexpression. The SWAP mice have reversed NKAα isoform affinity towards ouabain, i.e., NKAα1 is ouabain-sensitive, and NKAα2 is ouabain-resistant, while the expression of both NKAα isoforms remains unaltered (Dostanic et al., 2003). This model has generated some apparently divergent findings. In contrast to many previous reports, Dostanic *et al.* found that NKAα1 interacted with NCX and regulated cardiac contractility when ~40% of NKAα1 was inhibited (Dostanic et al., 2004). On the other hand, a later study found that 25% NKA inhibition in the SWAP mice (i.e., NKAα1 inhibition) and 25% NKA inhibition in the WT mice (i.e., NKAα2 inhibition) gave a similar rise in intracellular [Na^+], but only WT mice with NKAα2

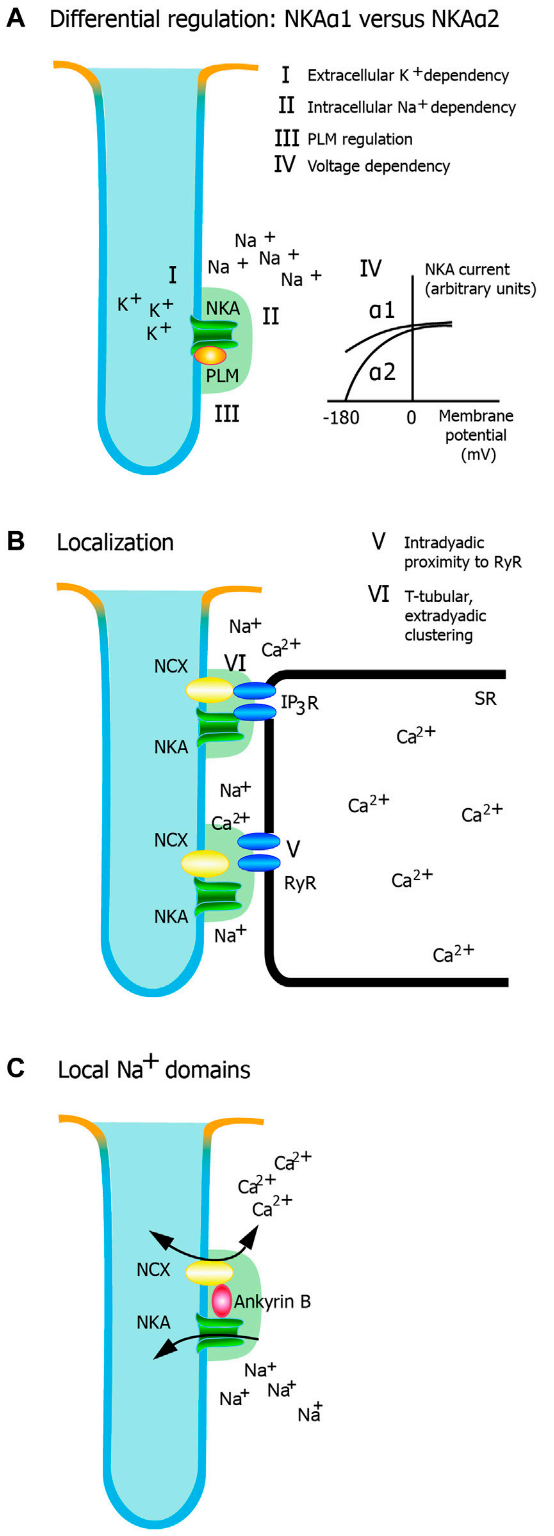

FIGURE 1 | Potential mechanisms for regulation of cardiac contractility by NKAα2. Different mechanisms have been proposed, and this figure highlights the most important hypotheses. **(A)** Differential regulation of α isoforms. NKA activity is regulated by **(I)** the extracellular K$^+$ dependency of NKA, ii) the intracellular Na$^+$ dependency of NKA, iii) beta-adrenergic *(Continued)*

FIGURE 1 | regulation mediated through phospholemman, and iv) voltage dependency. Only the extracellular K$^+$ dependency and the voltage dependency are markedly different between NKAα1 and NKA α2. **(B)** Localization. There is a relative clustering of NKAα2 in the t-tubules. v) Intradyadic proximity to RyR and vi) T-tubular, extradyadic clustering (potentially interacting with IP3 receptors) are two mechanisms that could have an impact on dyadic Ca^{2+} signaling. Whether one or both are important for NKAα2 regulation of Ca^{2+} and cardiac contractility remain to be established. c) Local Na$^+$ domains. AnkyrinB facilitates a macromolecular complex with NKA and NCX, characterized by tight regulation of Na$^+$ and Ca^{2+} in local domains.

inhibition exerted increased Ca^{2+} levels (Despa et al., 2012). While these results could seem contradictory, one should bear in mind that the question should be whether NKAα2 *preferentially* regulates Ca^{2+} cycling and contractility compared to NKAα1, and not whether NKAα1 inhibition is without any effect.

The affinity of the clinically used glycoside digoxin is up to four-fold higher towards human NKAα2 compared to NKAα1 (Katz et al., 2010), and glycoside-induced inotropy and hypertension have been shown to be mediated by NKAα2 in mice (Dostanic et al., 2003; Dostanic et al., 2005). Moreover, NKAα2 preferentially regulates Ca^{2+} cycling in both astrocytes (Golovina et al., 2003) and smooth muscles (Zhang et al., 2005). Overall, existing evidence clearly suggest that the more abundant NKAα1 has a "housekeeping" role, regulating global [Na$^+$] (Aronsen et al., 2013), whereas NKAα2 could specifically regulate Na$^+$ in distinct functional domains shared with NCX in cardiomyocytes.

Mechanisms for Regulation of Cardiac Contractility by NKAα2

While there is a paucity of conclusive evidence, several structural and molecular mechanisms have been proposed as to how NKAα2 preferentially regulates NCX activity and cytosolic Ca^{2+} fluxes in cardiomyocytes. An illustration of the main hypotheses are shown in **Figure 1**, and the different suggested mechanisms will be discussed in the next sections.

Differential Regulation of NKA α Isoforms

The primary regulators of NKA activity are extracellular [K$^+$], intracellular [Na$^+$], the inhibitory protein phospholemman, and the membrane potential, and we will here discuss each of these separately with focus on any differences NKAα2 versus NKAα1.

Intracellular [Na$^+$] and Extracellular [K$^+$] Affinity

There is a sigmoid relationship between intracellular [Na$^+$] and the NKA current in cardiomyocytes, where increasing concentrations of Na$^+$ lead to increased NKA currents (Nakao and Gadsby, 1989; Skogestad et al., 2019a). No differences in the Na$^+$ dependence between NKAα1 and NKAα2 have been found (Price et al., 1990; Berry et al., 2007; Bibert et al., 2008). In contrast, the extracellular [K$^+$] dependency differs between NKAα1 and NKAα2 (Crambert et al., 2002; Bibert et al., 2008; Han et al., 2009). NKAα1 has higher affinity towards extracellular [K$^+$] ($k_{0.5}$=1.5 mM) compared to NKAα2 ($k_{0.5}$=2.9 mM) (Han et al., 2009), meaning that NKAα1 is nearly maximally activated at physiological [K^+] (~4.5 mM). This could have some critical physiological and pathophysiological implications. Diffusion of K^+ could be restricted in the T-tubules (Swift et al., 2006), which could influence the regulation of NKAα2 activity more than NKAα1, especially considering the relative abundance of NKAα2 in the T-tubules (Berry et al., 2007; Despa and Bers, 2007), as discussed in the next section. The different extracellular [K^+] affinity could also be significant in hypokalemia, a common clinical condition that increases the risk of Ca^{2+}-induced triggered arrhythmias (Kjeldsen, 2010; Weiss et al., 2017). As discussed later, we have previously shown that hypokalemia-induced effects on Ca^{2+} cycling and arrhythmias are mainly mediated through NKAα2 (Aronsen et al., 2015).

Phospholemman

Phospholemman (PLM) is a member of the FXYD family of small, membrane-spanning proteins (Palmer et al., 1991) that associates with the α subunit of the NKA (Khafaga et al., 2012). PLM binding to NKA increases the apparent affinity for intracellular [Na^+] and extracellular [K^+] (Crambert et al., 2002; Despa et al., 2005; Han et al., 2009), which reduces NKA activity. PLM mediates the effects of β-adrenergic signaling on NKA, and it has two main phosphorylation sites: Serine (Ser)-63 and Ser-68 (Walaas et al., 1994; Song et al., 2005). A third phosphorylation site at Threonine (Thr)-69 has also been described (Fuller et al., 2009), but phosphorylation of Ser-63 and Ser-68 is sufficient to mediate all functional effects (Han et al., 2010) of beta-adrenergic activation. Ser-68 is the primary substrate for protein kinase A (PKA) (Silverman et al., 2005), while protein kinase C (PKC) phosphorylates both Ser-63 and Ser-68 (Han et al., 2006; Fuller et al., 2009). Following PLM phosphorylation, PKA phosphorylation at Ser-68 increases NKA activity by reducing the affinity of intracellular [Na^+] (Despa et al., 2005; Han et al., 2006; Bibert et al., 2008; Despa et al., 2008). Although PKC phosphorylation also consistently increases NKA activity, the evidence is equivocal on whether this is due to a reduction in the intracellular [Na^+] affinity, an increase in the maximal activity, or both (Han et al., 2006; Bibert et al., 2008; Han et al., 2010).

Two early reports found no effects of β-adrenergic stimulation on NKAα2 activity (Silverman et al., 2005; Berry et al., 2007). In these studies, the NKAα2 activity was calculated by subtracting ouabain-sensitive current from the total current, a strategy that could lead to large variation and in our opinion, a high risk of false-negative results. Later studies found that PLM interacted with both NKAα1 and NKAα2 (Feschenko et al., 2003; Bossuyt et al., 2005; Bossuyt et al., 2009), that PKA-mediated PLM phosphorylation increased the activities of both NKAα1 and NKAα2 (Bibert et al., 2008; Bossuyt et al., 2009). The same studies also found that PKC regulated the maximal activity of NKAα2, not NKAα1, whereas the dependency of intracellular [Na^+] was affected similarly in both isoforms (Bibert et al., 2008; Bossuyt et al., 2009).

Voltage-Dependence of NKAα2 and NKAα1

As NKA moves one positive charge out of the cell per pumping cycle (3 Na^+ ions out and 2 K^+ ions in), NKA activity becomes dependent on the membrane potential. The current-voltage relationship for NKAα2 is different compared to NKAα1. NKAα1 is activated over a broad range of physiological potentials, whereas NKAα2 is nearly inactive at resting membrane potentials, indicating that NKAα2 only is active during phases one to four of the action potential when the membrane potential is more positive (Swift et al., 2007; Stanley et al., 2015). Some suggest that NKAα2 might be acting as a "pump reserve", where increased Na^+ influx during the action potential are counteracted by more Na^+ extrusion during the same period (Stanley et al., 2015). Another possible (and not mutually exclusive) interpretation is that Na^+ influx during the contraction more readily accumulates in the NKAα2 compartment, rendering the baseline Na^+ levels higher in the NKAα2 compartment than in the NKAα1 compartment. Thus, the differences in the voltage dependence of NKAα1 and NKAα2 could contribute to a unique local ion environment. However, several studies have shown preferential NKAα2 regulation of NCX also at fixed membrane potential (usually in the range from -50 mv to 0 mV) (Yamamoto et al., 2005; Swift et al., 2007; Skogestad et al., 2019b), indicating that differences in voltage-dependence alone are not sufficient to explain the preferential regulatory role of NKAα2.

NKA Localization

Subcellular Localization

A prerequisite for an effective excitation-contraction coupling is the dyads, i.e., functional Ca^{2+}domains in the T-tubules where sarcolemmal L-type Ca^{2+} channels are located near ryanodine receptors (RyRs), allowing effective Ca^{2+}-induced Ca^{2+} release into the cytosol (Bers, 2002; Louch et al., 2010). Thus, an attractive hypothesis would be that preferential localization of NKAα2 and NCX in cardiac T-tubules could allow local Ca^{2+} modulation in specific subcellular domains involved in the excitation-contraction coupling. Similar to NCX (Frank et al., 1992; Despa et al., 2003; Sipido et al., 2013), NKAα2 is indeed relatively more abundant in the T-tubules, as suggested by immunofluorescence (Mohler et al., 2005; Silverman et al., 2005), super-resolution microscopy (Yuen et al., 2017), and NKA current measurements in de-tubulated cardiomyocytes (Berry et al., 2007; Despa and Bers, 2007; Swift et al., 2007) [although one early study did not find this pattern (McDonough et al., 1996)]. NKAα2 is also highly clustered in the T-tubules in skeletal muscles, where it constitutes the main NKA isoform (Radzyukevich et al., 2013; DiFranco et al., 2015).

However, NKAα1 is also present in the T-tubules in cardiomyocytes (Mohler et al., 2005). Despite NKAα2 being *relatively* abundant in the T-tubules (i.e. high T-tubule/surface sarcolemma ratio), the total amount of NKAα1 in the T-tubules is equal to or even higher compared to NKAα2 despite a low T-tubule/surface sarcolemma ratio for NKAα1 (Berry et al., 2007; Despa and Bers, 2007; Swift et al., 2007). For instance, Swift *et al.* found that NKAα2 comprises 10% of the total NKA activity in rat cardiomyocytes, and 50% of the total NKAα2 activity was of T-tubular origin, indicating that about 5% of the total NKA activity was due to NKAα2 pumps located in the T-tubules. In contrast, only 10% of the total NKAα1 was located the T-tubules (Swift et al., 2007), but these data nevertheless indicate that NKAα1 outnumbers NKAα2 in the t-tubules with a 2:1 ratio.

NKAα2 could be more closely associated with RyR at SR junctional sites than NKAα1. Data from astrocytes, neurons, and smooth muscles suggest that NKAα2 assembles with NCX in a microdomain linked to the ER/SR (Juhaszova and Blaustein, 1997; Lencesova et al., 2004; Song et al., 2006). However, a recent study using super-resolution microscopy failed to show a similar arrangement in rat cardiomyocytes, as NKAα1 and NKAα2 were equally distant from RyRs (Yuen et al., 2017). As this study analyzed NKA clusters within 0.2–1 μm from RyR, while the distance between L-type Ca^{2+} channels and RyR in the dyad is 10–20 nm, later studies with higher resolution might reveal different RyR proximity for NKAα2 versus NKAα1.

Macromolecular Complexes

Ankyrins are a family of anchoring proteins that couples membrane proteins to the membrane cytoskeleton, and both NKA and NCX co-assemble with Ankyrin B. Ankyrin B apparently does not structurally discriminate between NKAα1 and NKAα2, as Ankyrin B is found to interact and co-localize with both NKAα1 and NKAα2 in the T-tubules, in addition to NCX and InsP3 receptors in a shared macromolecular complex (Mohler et al., 2003; Mohler et al., 2005). Interestingly, the Ankyrin B macromolecular complex with NKA and NCX seems to have an extradyadic localization, as neither Ankyrin B, NKAα1, NKAα2, nor NCX co-localize with RyR or L-type Ca^{2+} channels in cardiomyocytes (Mohler et al., 2005). One possibility is that the NKA/NCX domains, rather than being directly involved in the excitation-contraction coupling, indirectly regulate dyadic Ca^{2+} by modulating transsarcolemmal Ca^{2+} fluxes at the dyadic border, but more studies are needed to investigate this hypothesis.

Local Na^+ Domains

Another possibility than differences in localization is that NKAα2 could, more tightly than NKAα1, regulate the local Na^+ pools sensed by NCX. Any effect on Ca^{2+} cycling would be mediated through Na^+, and differences in the ability to control local Na^+ pools in the vicinity of NCX could potentially have significant effects on Ca^{2+} cycling and cardiac contractility *independently* of the localization of the shared NKA/NCX-domain.

Several studies suggest that NKAα2 preferentially regulates NCX-sensed Na^+ and NCX activity. Yamamoto *et al.* first reported that local NCX-sensed (Na^+) was higher in heterozygous NKAα2$^{+/-}$ mice. Similarly, by using NKAα2 selective doses of oubain, Swift *et al.* later showed that NKAα2 regulated NCX-sensed (Na^+) and NCX activity (Swift et al., 2007; Swift et al., 2010). Other molecular studies suggest that both NKAα1 and NKAα2 co-immunoprecipitate with NCX in cardiomyocytes (Dostanic et al., 2004; Mohler et al., 2005), which apparently represents a discrepancy to the idea of NKAα2 as a preferential regulator of NCX activity. However, no quantitative measurements on the degree of co-localization of NKAα1 versus NKAα2 with NCX have been performed, and data from other cell types indicate that NKAα2 more than NKAα1 interacts with NCX (Golovina et al., 2003; Lencesova et al., 2004). In addition, it is possible that the microarchitecture or functional features of the shared NKA/NCX macromolecular complexes are different between NKAα1 and NKAα2 in a way that is not assessed with the interaction assays. In support of this concept, even though it has been shown that Ankyrin B co-immunoprecipitates with both NKAα1 and NKAα2, we observed that disruption of NKA from Ankyrin B only affected local Na^+ and NCX activity in the NKAα2 domains and not in the NKAα1 domains (Skogestad et al., 2019b).

Summary: Mechanisms for NKAα2 Mediated Regulation of Cardiac Contractility

In summary, there are several differences between NKAα1 and NKAα2 that could explain the observed role of NKAα2 as a regulator of cardiac contractility. NKAα2 is relatively abundant in the T-tubules of cardiomyocytes (Berry et al., 2007; Despa and Bers, 2007; Swift et al., 2007) and interacts with ER/SR junctions in other cell types (Juhaszova and Blaustein, 1997; Lencesova et al., 2004; Song et al., 2006), while it is questioned whether NKAα2 is more densely co-localized with the dyad in cardiomyocytes (Yuen et al., 2017). Regardless of localization, NKAα2 controls NCX-sensed Na^+ levels and subsequently NCX activity, excitation-contraction coupling, and contractility (Yamamoto et al., 2005; Swift et al., 2007). In addition, both the voltage-dependence and the extracellular [K^+] dependency are different between NKAα2 and NKAα1, possibly contributing to the ability of NKAα2 to regulate Ca^{2+} fluxes in cardiomyocytes.

Role of Subsarcolemmal Na^+ Gradients

Any effect of NKAα2 on intracellular [Ca^{2+}] and cardiac contractility must be mediated through the regulation of intracellular [Na^+], proposedly by altering local [Na^+] in specific domains. In other words, a given change in NKA activity leads to alterations in local [Na^+] sensed by NCX in the same compartment, with a more negligible (or no) effect on the [Na^+] in more distant compartments. A prerequisite for this hypothesis is the presence of intracellular Na^+ gradients between different compartments in cardiomyocytes.

The first reports of a subsarcolemmal space of Na^+, i.e., a distinct submembrane compartment where Na^+ is different from bulk cytosolic [Na^+], came from a landmark paper by Leblanc and Hume (Leblanc and Hume, 1990). They observed that Na^+ current activation was sufficient to induce Ca^{2+}-induced Ca^{2+} release (CICR) through activation of reverse NCX, a mechanism that localized elevations of [Na^+] in an undefined compartment coined “fuzzy space” (Lederer et al., 1990). Accumulation of Na^+ in submembrane compartments has also been observed in compartments not directly involved in CICR, e.g., around NKA (Su et al., 1998; Despa and Bers, 2003; Silverman, 2003; Despa et al., 2004; Swift et al., 2007; Despa et al., 2012), and the broader term “subsarcolemmal space” is frequently used to encompass a submembrane compartment with differential [Na^+] than the cytosol (Aronsen et al., 2013). We recently reported data that indicates that [Na^+] is different between the Na^+ channel compartments and the NKA compartments, arguing against a uniform distribution of Na^+ throughout the subsarcolemmal space. These data suggest rather that Na^+ is differentially regulated in distinct submembrane compartments (Skogestad et al., 2019a), i.e., "hotspots" and "coldspots" with higher or lower $[Na^+]$ than the cytosolic $[Na^+]$. In support of a shared NKA/NCX compartment, another study observed that the subsarcolemmal $[Na^+]$ is similar for NKA and NCX after manipulation of the Na^+ current (Su et al., 1998).

If such "hotspots" and "coldspots" exist, a fundamental question is how the proposed Na^+ gradients could be generated and maintained. Na^+ diffuses rapidly in the cytoplasm (Kushmerick and Podolsky, 1969), and similar diffusion kinetics in the subsarcolemmal space would lead to rapid dissipation of all Na^+ gradients. Calculations show that to maintain the accumulation of Na^+ in the subsarcolemmal space, the diffusion rates need to be 100-10,000 times slower than what is observed experimentally (Despa and Bers, 2003; Despa et al., 2004). It is possible that physical restrictions (e.g., membrane tortuosity, molecular and organelle crowding) and negative submembrane charges impede the free diffusion of ions.

A crucial aspect is the temporal duration of the proposed subsarcolemmal Na^+ gradients. Weber *et al.* observed that Na^+ current activation generates transient Na^+ accumulation near NCX early during the action potential. Due to the positive membrane potentials and the general Na^+ accumulation during the early phase of the action potential, NCX operates in reverse mode for a brief time before cytosolic Ca^{2+} levels increase. Local Na^+ accumulation due to opening of voltage-gated Na^+ channels could potentially contribute to CICR by increasing Ca^{2+} entry through NCX (Weber et al., 2003), but the very brief nature of these currents also questions their physiological relevance. Similarly, altered NKAα2 activity may create short-lived Na^+ gradients that exert short-lived effects on NCX activity.

Several studies, however, suggest that the Na^+ gradients are generated and maintained throughout several beats (Wendt-Gallitelli et al., 1993; Silverman, 2003). For example, we recently showed that several minutes of repetitive Na^+ current activation increased the $[Na^+]$ sensed by the NKA, whereas 10 s of repetitive Na^+ current activation had no effect on the $[Na^+]$ sensed by the NKA (Skogestad et al., 2019a), in line with previous findings (Silverman, 2003). Further, the subsarcolemmal Na^+ gradient dissipated very slowly (Skogestad et al., 2019a), suggesting that a Na^+ gradient between the subsarcolemmal space and bulk cytosol might be continuously present in the beating heart.

Collectively, these data suggest that NKAα2 can generate local Na^+ gradients that are further maintained by an unknown mechanism. We speculate that NKAα2 exerts short-term and long-term control of local $[Na^+]$ and, hence, NCX activity, allowing the functional NKAα2/NCX complex to regulate Ca^{2+} entry, with proposed effects on CICR, and Ca^{2+} extrusion. The underlying mechanisms are yet to be demonstrated, but we consider the undisputed role of NKAα2 in regulating cardiac NCX activity as a clear indication of Na^+ gradients in cardiomyocytes.

Role of NKAα2 in Cardiac Disease

Ca^{2+} plays an essential and complex role in the development of cardiac disease. Reduced cytosolic $[Ca^{2+}]$ could contribute to the contractile deficit in heart failure (Eisner, 2014), while overload of Ca^{2+} leads to activation of detrimental Ca^{2+}-dependent signaling pathways and promotes ventricular arrhythmias (Marks, 2003; Wehrens et al., 2005). As a regulator of intracellular $[Ca^{2+}]$, NKAα2 could play a role in the development of cardiac disease. Several studies have investigated the role of NKAα2 in cardiac hypertrophy and ventricular arrhythmias, and these results are briefly reviewed here.

Cardiac Hypertrophy

Compared to WT and NKAα1 overexpression, overexpression of NKAα2 attenuated cardiac hypertrophy 2, 10, and 16 weeks after pressure overload in mice (Correll et al., 2014). There were no differences in Ca^{2+}-dependent pro-hypertrophic mechanisms, such as NFAT and CaMKII, but the mice with NKAα2 overexpression had faster NCX-dependent Ca^{2+} extrusion. The authors concluded that the anti-hypertrophic effect of NKAα2 overexpression likely was due to lowering of $[Ca^{2+}]$ and $[Na^+]$ in strategic compartments (Correll et al., 2014). On the other hand, Rindler *et al* found that cardiac-specific NKAα2 inactivation delayed the onset of cardiac hypertrophy following pressure overload but that outcomes were similar to control animals at later stages (Rindler et al., 2013).

These contradictory findings can be reconciled by considering the following complicating factors: 1) Genetic models are impure systems because genetic modification of one protein leads to several secondary changes with unpredictable effects. Mice with overexpression of either NKAα2 or NKAα1 have reduced levels of the other isoforms, and direct functional interpretation is thus difficult. In addition, the expression of PLM and the Ser-63 and Ser-68 phosphorylation were reduced in the NKAα2 overexpression mice (Correll et al., 2014). 2) It is possible that endogenous glycosides at least partly mediate the effect of NKAα1 and NKAα2 on cardiac hypertrophy (Blaustein et al., 2016; Blaustein, 2017). Mice with ouabain-sensitive NKAα1 (SWAP mice) had increased cardiac hypertrophy following pressure overload, a response that was abolished following sequestration of endogenous cardiac glycosides (Wansapura et al., 2011). Predicting the hypertrophic effect of altering the NKAα isoforms is not straightforward when considering the different affinity of cardiac glycosides towards NKAα1 and NKAα2 and the altered expression of NKAα isoforms in the genetically modified mice [(Blaustein, 2017). 3] Overexpression and reduction of NKAα2 are expected to have opposite effects on intracellular $[Ca^{2+}]$, with different short- and long-term effects on cardiac contractility and hypertrophy. Although there were no baseline differences, the heterozygous NKAα2 mice showed increased contractility in the first weeks following pressure overload (Rindler et al., 2013). While increasing Ca^{2+}-dependent cardiac contractility could be temporarily beneficial, the consequences are potentially more dire over a longer time course (Lou et al., 2012). In contrast, the NKAα2 overexpression mice had lower Ca^{2+} transient amplitude and increased NCX-dependent Ca^{2+} extrusion compared to WT (Correll et al., 2014), which could exert beneficial effects by strategically lowering Ca^{2+} in specific domains involved in cardiac hypertrophy development.

Ventricular Arrhythmias

Reduced NKA activity increases intracellular [Na^+], reduces NCX-mediated Ca^{2+} extrusion, increases intracellular [Ca^{2+}], and increases the risk of triggered ventricular arrhythmias in hypokalemia (Eisner and Lederer, 1979; Aronsen et al., 2015; Pezhouman et al., 2015; Skogestad and Aronsen, 2018), digitalis toxicity (Gonano et al., 2011), and the Ankyrin B syndrome (Mohler et al., 2003; Mohler et al., 2005; Camors et al., 2012; Popescu et al., 2016). The increased intracellular [Ca^{2+}] following reduced NKA activity increases the frequency of arrhythmogenic Ca^{2+} waves (Camors et al., 2012; Aronsen et al., 2015) but also activates CaMKII (Gonano et al., 2011; Pezhouman et al., 2015; Popescu et al., 2016), which further promotes arrhythmias by activating Na^+ and Ca^{2+} currents (Hund and Mohler, 2015; Pezhouman et al., 2015). The specific role of NKAα2 in arrhythmias has been examined by two publications from our group. We found that hypokalemia increased Ca^{2+} transient amplitude and increased the frequency of Ca^{2+} waves, which was abolished following NKAα2 inhibition (Aronsen et al., 2015). We also studied the effect on intracellular [Ca^{2+}] and cellular arrhythmias following disruption of NKA from Ankyrin B, a proposed mechanism for ventricular arrhythmias in the Ankyrin B syndrome (Mohler et al., 2003; Mohler et al., 2004; Mohler et al., 2005). NKA/Ankyrin B disruption increased NCX-sensed Na^+, reduced Ca^{2+} extrusion through NCX, and increased the frequency of Ca^{2+} sparks and Ca^{2+} waves (Skogestad et al., 2019b), thus mimicking the phenotype from the Ankyrin $B^{+/-}$ mice (Camors et al., 2012), and all effects were mediated by NKAα2 (Skogestad et al., 2019b). These data collectively suggest that NKAα2 might be an upstream node for arrhythmias, where altered NKAα2 activity could influence intracellular [Ca^{2+}] and CaMKII activity downstream. Specific activation of NKAα2 might thus represent a future anti-arrhythmic target that warrants further investigation.

AUTHOR CONTRIBUTIONS

Both authors contributed to the writing of the manuscript.

ACKNOWLEDGMENTS

We are grateful to Carina Knudsen, Institute of Basic Medical Sciences, University of Oslo for the artwork included in this review.

REFERENCE

Acsai, K., Antoons, G., Livshitz, L., Rudy, Y., and Sipido, K. R. (2011). Microdomain [Ca(2)(+)] Near Ryanodine Receptors as Reported by L-type Ca(2)(+) and Na+/Ca(2)(+) Exchange Currents. *J. Physiol.* 589 (Pt 10), 2569–2583. doi:10.1113/jphysiol.2010.202663

Aronsen, J. M., Skogestad, J., Lewalle, A., Louch, W. E., Hougen, K., Stokke, M. K., et al. (2015). Hypokalaemia Induces Ca2+overload and Ca2+waves in Ventricular Myocytes by Reducing Na+,K+-ATPase α2activity. *J. Physiol.* 593 (6), 1509–1521. doi:10.1113/jphysiol.2014.279893

Aronsen, J. M., Swift, F., and Sejersted, O. M. (2013). Cardiac Sodium Transport and Excitation-Contraction Coupling. *J. Mol. Cell. Cardiol.* 61, 11–19. doi:10.1016/j.yjmcc.2013.06.003

Barcroft, L. C., Moseley, A. E., Lingrel, J. B., and Watson, A. J. (2004). Deletion of the Na/K-ATPase α1-subunit Gene (Atp1a1) Does Not Prevent Cavitation of the Preimplantation Mouse Embryo. *Mech. Dev.* 121 (5), 417–426. doi:10.1016/j.mod.2004.04.005

Baxter-Lowe, L. A., Guo, J. Z., Bergstrom, E. E., and Hokin, L. E. (1989). Molecular Cloning of the Na,K-ATPase α-subunit in Developing Brine Shrimp and Sequence Comparison with Higher Organisms. *FEBS Lett.* 257 (1), 181–187. doi:10.1016/0014-5793(89)81816-2

Berry, R., Despa, S., Fuller, W., Bers, D., and Shattock, M. (2007). Differential Distribution and Regulation of Mouse Cardiac Na+/K+-ATPase α1 and α2 Subunits in T-Tubule and Surface Sarcolemmal Membranes. *Cardiovasc. Res.* 73 (1), 92–100. doi:10.1016/j.cardiores.2006.11.006

Bers, D. M. (2008). Calcium Cycling and Signaling in Cardiac Myocytes. *Annu. Rev. Physiol.* 70, 23–49. doi:10.1146/annurev.physiol.70.113006.100455

Bers, D. M. (2002). Cardiac Excitation-Contraction Coupling. *Nature* 415 (6868), 198–205. doi:10.1038/415198a

Bers, D. M., and Despa, S. (2009). Na+transport in Cardiac Myocytes; Implications for Excitation-Contraction Coupling. *IUBMB Life* 61 (3), 215–221. doi:10.1002/iub.163

Bers, D. M. (2001). *Excitation-contraction Coupling and Cardiac Contractile Force. 2nd Ed. Developments in Cardiovascular Medicine*. Dordrecht ; Boston: Kluwer Academic Publishers. xxiv, 427.

Bibert, S., Roy, S., Schaer, D., Horisberger, J.-D., and Geering, K. (2008). Phosphorylation of Phospholemman (FXYD1) by Protein Kinases A and C Modulates Distinct Na,K-ATPase Isozymes. *J. Biol. Chem.* 283 (1), 476–486. doi:10.1074/jbc.m705830200

Blanco, G., and Mercer, R. W. (1998). Isozymes of the Na-K-ATPase: Heterogeneity in Structure, Diversity in Function. *Am. J. Physiology-Renal Physiology* 275 (5), F633–F650. doi:10.1152/ajprenal.1998.275.5.f633

Blaustein, M. P., Chen, L., Hamlyn, J. M., Leenen, F. H. H., Lingrel, J. B., Wier, W. G., et al. (2016). Pivotal Role of α2 Na+pumps and Their High Affinity Ouabain Binding Site in Cardiovascular Health and Disease. *J. Physiol.* 594 (21), 6079–6103. doi:10.1113/jp272419

Blaustein, M. P. (2017). How Does Pressure Overload Cause Cardiac Hypertrophy and Dysfunction? High-Ouabain Affinity Cardiac Na+ Pumps Are Crucial. *Am. J. Physiology-Heart Circulatory Physiology* 313 (5), H919–H930. doi:10.1152/ajpheart.00131.2017

Bossuyt, J., Ai, X., Moorman, J. R., Pogwizd, S. M., and Bers, D. M. (2005). Expression and Phosphorylation of the Na-Pump Regulatory Subunit Phospholemman in Heart Failure. *Circulation Res.* 97 (6), 558–565. doi:10.1161/01.res.0000181172.27931.c3

Bossuyt, J., Despa, S., Han, F., Hou, Z., Robia, S. L., Lingrel, J. B., et al. (2009). Isoform Specificity of the Na/K-ATPase Association and Regulation by Phospholemman. *J. Biol. Chem.* 284 (39), 26749–26757. doi:10.1074/jbc.m109.047357

Camors, E., Mohler, P. J., Bers, D. M., and Despa, S. (2012). Ankyrin-B Reduction Enhances Ca Spark-Mediated SR Ca Release Promoting Cardiac Myocyte Arrhythmic Activity. *J. Mol. Cell. Cardiol.* 52 (6), 1240–1248. doi:10.1016/j.yjmcc.2012.02.010

Correll, R. N., Eder, P., Burr, A. R., Despa, S., Davis, J., Bers, D. M., et al. (2014). Overexpression of the Na +/K + ATPase α2 but Not α1 Isoform Attenuates Pathological Cardiac Hypertrophy and Remodeling. *Circ. Res.* 114 (2), 249–256. doi:10.1161/circresaha.114.302293

Crambert, G., Füzesi, M., Garty, H., Karlish, S., and Geering, K. (2002). Phospholemman (FXYD1) Associates with Na,K-ATPase and Regulates its Transport Properties. *Proc. Natl. Acad. Sci. U.S.A.* 99 (17), 11476–11481. doi:10.1073/pnas.182267299

Despa, S., and Bers, D. M. (2007). Functional Analysis of Na+/K+-ATPase Isoform Distribution in Rat Ventricular Myocytes. *Am. J. Physiology-Cell Physiology* 293 (1), C321–C327. doi:10.1152/ajpcell.00597.2006

Despa, S., and Bers, D. M. (2003). Na/K Pump Current and [Na]i in Rabbit Ventricular Myocytes: Local [Na]i Depletion and Na Buffering. *Biophysical J.* 84 (6), 4157–4166. doi:10.1016/s0006-3495(03)75140-6

Despa, S., Bossuyt, J., Han, F., Ginsburg, K. S., Jia, L.-G., Kutchai, H., et al. (2005). Phospholemman-Phosphorylation Mediates the β-Adrenergic Effects on Na/K Pump Function in Cardiac Myocytes. *Circulation Res.* 97 (3), 252–259. doi:10.1161/01.res.0000176532.97731.e5

Despa, S., Brette, F., Orchard, C. H., and Bers, D. M. (2003). Na/Ca Exchange and Na/K-ATPase Function Are Equally Concentrated in Transverse Tubules of Rat Ventricular Myocytes. *Biophysical J.* 85 (5), 3388–3396. doi:10.1016/s0006-3495(03)74758-4

Despa, S., Kockskämper, J., Blatter, L. A., and Bers, D. M. (2004). Na/K Pump-Induced [Na]i Gradients in Rat Ventricular Myocytes Measured with Two-Photon Microscopy. *Biophysical J.* 87 (2), 1360–1368. doi:10.1529/biophysj.103.037895

Despa, S., Lingrel, J. B., and Bers, D. M. (2012). Na+/K+-ATPase 2-isoform Preferentially Modulates Ca2+ Transients and Sarcoplasmic Reticulum Ca2+ Release in Cardiac Myocytes. *Cardiovasc. Res.* 95 (4), 480–486. doi:10.1093/cvr/cvs213

Despa, S., Tucker, A. L., and Bers, D. M. (2008). Phospholemman-Mediated Activation of Na/K-ATPase Limits [Na] I and Inotropic State during β-Adrenergic Stimulation in Mouse Ventricular Myocytes. *Circulation* 117 (14), 1849–1855. doi:10.1161/circulationaha.107.754051

DiFranco, M., Hakimjavadi, H., Lingrel, J. B., and Heiny, J. A. (2015). Na,K-Na,K-ATPase α2 Activity in Mammalian Skeletal Muscle T-Tubules Is Acutely Stimulated by Extracellular K+. *J. Gen. Physiol.* 146 (4), 281–294. doi:10.1085/jgp.201511407

Dostanic, I., Lorenz, J. N., Schultz, J. E. J., Grupp, I. L., Neumann, J. C., Wani, M. A., et al. (2003). The α2 Isoform of Na,K-ATPase Mediates Ouabain-Induced Cardiac Inotropy in Mice. *J. Biol. Chem.* 278 (52), 53026–53034. doi:10.1074/jbc.m308547200

Dostanic, I., Paul, R. J., Lorenz, J. N., Theriault, S., Van Huysse, J. W., and Lingrel, J. B. (2005). The α2-isoform of Na-K-ATPase Mediates Ouabain-Induced Hypertension in Mice and Increased Vascular Contractility *In Vitro*. *Am. J. Physiology-Heart Circulatory Physiology* 288 (2), H477–H485. doi:10.1152/ajpheart.00083.2004

Dostanic, I., Schultz, J. E., Lorenz, J. N., and Lingrel, J. B. (2004). The α1 Isoform of Na,K-ATPase Regulates Cardiac Contractility and Functionally Interacts and Co-localizes with the Na/Ca Exchanger in Heart. *J. Biol. Chem.* 279 (52), 54053–54061. doi:10.1074/jbc.m410737200

Dostanic-Larson, I., Lorenz, J. N., Van Huysse, J. W., Neumann, J. C., Moseley, A. E., and Lingrel, J. B. (2006). Physiological Role of the α1- and α2-isoforms of the Na+-K+-ATPase and Biological Significance of Their Cardiac Glycoside Binding Site. *Am. J. Physiology-Regulatory, Integr. Comp. Physiology* 290 (3), R524–R528. doi:10.1152/ajpregu.00838.2005

Eisner, D. A., and Lederer, W. J. (1979). Inotropic and Arrhythmogenic Effects of Potassium-Depleted Solutions on Mammalian Cardiac Muscle. *J. Physiol.* 294, 255–277. doi:10.1113/jphysiol.1979.sp012929

Eisner, D. (2014). Calcium in the Heart: from Physiology to Disease. *Exp. Physiol.* 99 (10), 1273–1282. doi:10.1113/expphysiol.2013.077305

Feschenko, M. S., Donnet, C., Wetzel, R. K., Asinovski, N. K., Jones, L. R., and Sweadner, K. J. (2003). Phospholemman, a Single-Span Membrane Protein, Is an Accessory Protein of Na,K-ATPase in Cerebellum and Choroid Plexus. *J. Neurosci.* 23 (6), 2161–2169. doi:10.1523/jneurosci.23-06-02161.2003

Frank, J., Mottino, G., Reid, D., Molday, R., and Philipson, K. (1992). Distribution of the Na(+)-Ca2+ Exchange Protein in Mammalian Cardiac Myocytes: an Immunofluorescence and Immunocolloidal Gold-Labeling Study. *J. Cell Biol.* 117 (2), 337–345. doi:10.1083/jcb.117.2.337

Fuller, W., Howie, J., McLatchie, L. M., Weber, R. J., Hastie, C. J., Burness, K., et al. (2009). FXYD1 Phosphorylation *In Vitro* and in Adult Rat Cardiac Myocytes: Threonine 69 Is a Novel Substrate for Protein Kinase C. *Am. J. Physiology-Cell Physiology* 296 (6), C1346–C1355. doi:10.1152/ajpcell.00523.2008

Gao, J., Wymore, R., Wymore, R. T., Wang, Y., McKinnon, D., Dixon, J. E., et al. (1999). Isoform-specific Regulation of the Sodium Pump by Alpha- and Beta-Adrenergic Agonists in the guinea-pig Ventricle. *J. Physiol.* 516 (Pt 2) (Pt 2), 377–383. doi:10.1111/j.1469-7793.1999.0377v.x

Garcia, A., Liu, C. C., Cornelius, F., Clarke, R. J., and Rasmussen, H. H. (2016). Glutathionylation-Dependence of Na(+)-K(+)-Pump Currents Can Mimic Reduced Subsarcolemmal Na(+) Diffusion. *Biophys. J.* 110 (5), 1099–1109. doi:10.1016/j.bpj.2016.01.014

Golovina, V. A., Song, H., James, P. F., Lingrel, J. B., and Blaustein, M. P. (2003). Na+pump α2-subunit Expression Modulates Ca2+signaling. *Am. J. Physiology-Cell Physiology* 284 (2), C475–C486. doi:10.1152/ajpcell.00383.2002

Gonano, L. A., Sepúlveda, M., Rico, Y., Kaetzel, M., Valverde, C. A., Dedman, J., et al. (2011). Calcium-calmodulin Kinase II Mediates Digitalis-Induced Arrhythmias. *Circ. Arrhythm. Electrophysiol.* 4 (6), 947–957. doi:10.1161/CIRCEP.111.964908

Han, F., Bossuyt, J., Despa, S., Tucker, A. L., and Bers, D. M. (2006). Phospholemman Phosphorylation Mediates the Protein Kinase C-dependent Effects on Na +/K + Pump Function in Cardiac Myocytes. *Circulation Res.* 99 (12), 1376–1383. doi:10.1161/01.res.0000251667.73461.fb

Han, F., Bossuyt, J., Martin, J. L., Despa, S., and Bers, D. M. (2010). Role of Phospholemman Phosphorylation Sites in Mediating Kinase-dependent Regulation of the Na+-K+-ATPase. *Am. J. Physiology-Cell Physiology* 299 (6), C1363–C1369. doi:10.1152/ajpcell.00027.2010

Han, F., Tucker, A. L., Lingrel, J. B., Despa, S., and Bers, D. M. (2009). Extracellular Potassium Dependence of the Na+-K+-ATPase in Cardiac Myocytes: Isoform Specificity and Effect of Phospholemman. *Am. J. Physiology-Cell Physiology* 297 (3), C699–C705. doi:10.1152/ajpcell.00063.2009

Harada, K., Lin, H., Endo, Y., Fujishiro, N., Sakamoto, Y., and Inoue, M. (2006). Subunit Composition and Role of Na+,K+-ATPases in Ventricular Myocytes. *J. Physiol. Sci.* 56 (1), 113–121. doi:10.2170/physiolsci.rp001905

Hensley, C. B., Azuma, K. K., Tang, M. J., and McDonough, A. A. (1992). Thyroid Hormone Induction of Rat Myocardial Na(+)-K(+)-ATPase: Alpha 1-, Alpha 2-, and Beta 1-mRNA and -protein Levels at Steady State. *Am. J. Physiol.* 262 (2 Pt 1), C484–C492. doi:10.1152/ajpcell.1992.262.2.C484

Hund, T. J., and Mohler, P. J. (2015). Role of CaMKII in Cardiac Arrhythmias. *Trends Cardiovasc. Med.* 25 (5), 392–397. doi:10.1016/j.tcm.2014.12.001

Ishizuka, N., Fielding, A. J., and Berlin, J. R. (1996). Na Pump Current Can Be Separated into Ouabain-Sensitive and -insensitive Components in Single Rat Ventricular Myocytes. *Jjp* 46 (3), 215–223. doi:10.2170/jjphysiol.46.215

James, P. F., Grupp, I. L., Grupp, G., Woo, A. L., Askew, G. R., Croyle, M. L., et al. (1999). Identification of a Specific Role for the Na,K-ATPase α2 Isoform as a Regulator of Calcium in the Heart. *Mol. Cell* 3 (5), 555–563. doi:10.1016/s1097-2765(00)80349-4

Juhaszova, M., and Blaustein, M. P. (1997). Na + Pump Low and High Ouabain Affinity α Subunit Isoforms Are Differently Distributed in Cells. *Proc. Natl. Acad. Sci. U.S.A.* 94 (5), 1800–1805. doi:10.1073/pnas.94.5.1800

Kaplan, J. H. (2002). Biochemistry of Na,K-ATPase. *Annu. Rev. Biochem.* 71, 511–535. doi:10.1146/annurev.biochem.71.102201.141218

Katz, A., Lifshitz, Y., Bab-Dinitz, E., Kapri-Pardes, E., Goldshleger, R., Tal, D. M., et al. (2010). Selectivity of Digitalis Glycosides for Isoforms of Human Na,K-ATPase. *J. Biol. Chem.* 285 (25), 19582–19592. doi:10.1074/jbc.m110.119248

Khafaga, M., Bossuyt, J., Mamikonian, L., Li, J. C., Lee, L. L., Yarov-Yarovoy, V., et al. (2012). Na +/K + -ATPase E960 and Phospholemman F28 Are Critical for Their Functional Interaction. *Proc. Natl. Acad. Sci. U.S.A.* 109 (50), 20756–20761. doi:10.1073/pnas.1207866109

Kjeldsen, K. (2010). Hypokalemia and Sudden Cardiac Death. *Exp. Clin. Cardiol.* 15 (4), e96–9.

Kushmerick, M. J., and Podolsky, R. J. (1969). Ionic Mobility in Muscle Cells. *Science* 166 (3910), 1297–1298. doi:10.1126/science.166.3910.1297

Leblanc, N., and Hume, J. R. (1990). Sodium Current-Induced Release of Calcium from Cardiac Sarcoplasmic Reticulum. *Science* 248 (4953), 372–376. doi:10.1126/science.2158146

Lederer, W. J., Niggli, E., and Hadley, R. W. (1990). Sodium-calcium Exchange in Excitable Cells: Fuzzy Space. *Science* 248 (4953), 283. doi:10.1126/science.2326638

Lencesova, L., O'Neill, A., Resneck, W. G., Bloch, R. J., and Blaustein, M. P. (2004). Plasma Membrane-Cytoskeleton-Endoplasmic Reticulum Complexes in Neurons and Astrocytes. *J. Biol. Chem.* 279 (4), 2885–2893. doi:10.1074/jbc.m310365200

Liu, L., Wu, J., and Kennedy, D. J. (2016). Regulation of Cardiac Remodeling by Cardiac Na+/K+-ATPase Isoforms. *Front. Physiol.* 7, 382. doi:10.3389/fphys.2016.00382

Lou, Q., Janardhan, A., and Efimov, I. R. (2012). Remodeling of Calcium Handling in Human Heart Failure. *Adv. Exp. Med. Biol.* 740, 1145–1174. doi:10.1007/978-94-007-2888-2_52

Louch, W. E., Sejersted, O. M., and Swift, F. (2010). There Goes the Neighborhood: Pathological Alterations in T-Tubule Morphology and Consequences for Cardiomyocyte Ca2+ Handling. *J. Biomed. Biotechnol.* 2010, 503906. doi:10.1155/2010/503906

Lu, F.-M., and Hilgemann, D. W. (2017). Na/K Pump Inactivation, Subsarcolemmal Na Measurements, and Cytoplasmic Ion Turnover Kinetics Contradict Restricted Na Spaces in Murine Cardiac Myocytes. *J. Gen. Physiol.* 149 (7), 727–749. doi:10.1085/jgp.201711780

Marks, A. R. (2003). Calcium and the Heart: a Question of Life and Death. *J. Clin. Invest.* 111 (5), 597–600. doi:10.1172/jci18067

McDonough, A. A., Zhang, Y., Shin, V., and Frank, J. S. (1996). Subcellular Distribution of Sodium Pump Isoform Subunits in Mammalian Cardiac Myocytes. *Am. J. Physiol.* 270 (4 Pt 1), C1221–C1227. doi:10.1152/ajpcell.1996.270.4.C1221

McDonough, A. A., Geering, K., and Farley, R. A. (1990). The Sodium Pump Needs its β Subunit. *FASEB J.* 4 (6), 1598–1605. doi:10.1096/fasebj.4.6.2156741

Mohler, P. J., Davis, J. Q., and Bennett, V. (2005). Ankyrin-B Coordinates the Na/K ATPase, Na/Ca Exchanger, and InsP3 Receptor in a Cardiac T-Tubule/SR Microdomain. *PLoS Biol.* 3 (12), e423. doi:10.1371/journal.pbio.0030423

Mohler, P. J., Schott, J.-J., Gramolini, A. O., Dilly, K. W., Guatimosim, S., duBell, W. H., et al. (2003). Ankyrin-B Mutation Causes Type 4 Long-QT Cardiac Arrhythmia and Sudden Cardiac Death. *Nature* 421 (6923), 634–639. doi:10.1038/nature01335

Mohler, P. J., Splawski, I., Napolitano, C., Bottelli, G., Sharpe, L., Timothy, K., et al. (2004). A Cardiac Arrhythmia Syndrome Caused by Loss of Ankyrin-B Function. *Proc. Natl. Acad. Sci. U.S.A.* 101 (24), 9137–9142. doi:10.1073/pnas.0402546101

Moseley, A. E., Huddleson, J. P., Bohanan, C. S., James, P. F., Lorenz, J. N., Aronow, B. J., et al. (2005). Genetic Profiling Reveals Global Changes in Multiple Biological Pathways in the Hearts of Na, K-ATPase Alpha 1 Isoform Haploinsufficient Mice. *Cell Physiol. Biochem.* 15 (1-4), 145–158. doi:10.1159/000083647

Nakao, M., and Gadsby, D. C. (1989). [Na] and [K] Dependence of the Na/K Pump Current-Voltage Relationship in guinea Pig Ventricular Myocytes. *J. Gen. Physiol.* 94 (3), 539–565. doi:10.1085/jgp.94.3.539

O'Brien, W. J., Lingrel, J. B., and Wallick, E. T. (1994). Ouabain Binding Kinetics of the Rat Alpha Two and Alpha Three Isoforms of the Sodium-Potassium Adenosine Triphosphate. *Arch. Biochem. Biophys.* 310 (1), 32–39. doi:10.1006/abbi.1994.1136

Orlowski, J., and Lingrel, J. B. (1988). Tissue-specific and Developmental Regulation of Rat Na,K-ATPase Catalytic Alpha Isoform and Beta Subunit mRNAs. *J. Biol. Chem.* 263 (21), 10436–10442. doi:10.1016/s0021-9258(19)81535-1

Palmer, C. J., Scott, B. T., and Jones, L. R. (1991). Purification and Complete Sequence Determination of the Major Plasma Membrane Substrate for cAMP-dependent Protein Kinase and Protein Kinase C in Myocardium. *J. Biol. Chem.* 266 (17), 11126–11130. doi:10.1016/s0021-9258(18)99137-4

Periyasamy, S. M., Huang, W.-H., and Askari, A. (1983). Origins of the Different Sensitivities of Adenosinetriphosphatase Preparations to Ouabain. *Comp. Biochem. Physiology Part B Comp. Biochem.* 76 (3), 449–454. doi:10.1016/0305-0491(83)90274-2

Pezhouman, A., Singh, N., Song, Z., Nivala, M., Eskandari, A., Cao, H., et al. (2015). Molecular Basis of Hypokalemia-Induced Ventricular Fibrillation. *Circulation* 132 (16), 1528–1537. doi:10.1161/circulationaha.115.016217

Popescu, I., Galice, S., Mohler, P. J., and Despa, S. (2016). Elevated Local [Ca2+] and CaMKII Promote Spontaneous Ca2+release in Ankyrin-B-Deficient Hearts. *Cardiovasc Res.* 111 (3), 287–294. doi:10.1093/cvr/cvw093

Pressley, T. A. (1992). Phylogenetic Conservation of Isoform-specific Regions within Alpha-Subunit of Na(+)-K(+)-ATPase. *Am. J. Physiol.* 262 (3 Pt 1), C743–C751. doi:10.1152/ajpcell.1992.262.3.C743

Price, E. M., and Lingrel, J. B. (1988). Structure-function Relationships in the Sodium-Potassium ATPase .Alpha. Subunit: Site-Directed Mutagenesis of Glutamine-111 to Arginine and Asparagine-122 to Aspartic Acid Generates a Ouabain-Resistant Enzyme. *Biochemistry* 27 (22), 8400–8408. doi:10.1021/bi00422a016

Price, E. M., Rice, D. A., and Lingrel, J. B. (1990). Structure-function Studies of Na,K-ATPase. Site-Directed Mutagenesis of the Border Residues from the H1-H2 Extracellular Domain of the Alpha Subunit. *J. Biol. Chem.* 265 (12), 6638–6641. doi:10.1016/s0021-9258(19)39197-5

Radzyukevich, T. L., Neumann, J. C., Rindler, T. N., Oshiro, N., Goldhamer, D. J., Lingrel, J. B., et al. (2013). Tissue-specific Role of the Na,K-ATPase α2 Isozyme in Skeletal Muscle. *J. Biol. Chem.* 288 (2), 1226–1237. doi:10.1074/jbc.m112.424663

Rindler, T. N., Lasko, V. M., Nieman, M. L., Okada, M., Lorenz, J. N., and Lingrel, J. B. (2013). Knockout of the Na,K-ATPase α2-isoform in Cardiac Myocytes Delays Pressure Overload-Induced Cardiac Dysfunction. *Am. J. Physiology-Heart Circulatory Physiology* 304 (8), H1147–H1158. doi:10.1152/ajpheart.00594.2012

Silverman, B., Fuller, W., Eaton, P., Deng, J., Moorman, J., Cheung, J., et al. (2005). Serine 68 Phosphorylation of Phospholemman: Acute Isoform-specific Activation of Cardiac Na/K ATPase. *Cardiovasc. Res.* 65 (1), 93–103. doi:10.1016/j.cardiores.2004.09.005

Silverman, B. (2003). Is There a Transient Rise in Sub-sarcolemmal Na and Activation of Na/K Pump Current Following Activation of INa in Ventricular Myocardium? *Cardiovasc. Res.* 57 (4), 1025–1034. doi:10.1016/s0008-6363(02)00645-4

Sipido, K. R., Acsai, K., Antoons, G., Bito, V., and Macquaide, N. (2013). T-tubule Remodelling and Ryanodine Receptor Organization Modulate Sodium-Calcium Exchange. *Adv. Exp. Med. Biol.* 961, 375–383. doi:10.1007/978-1-4614-4756-6_32

Skogestad, J., and Aronsen, J. M. (2018). Hypokalemia-Induced Arrhythmias and Heart Failure: New Insights and Implications for Therapy. *Front. Physiol.* 9, 1500. doi:10.3389/fphys.2018.01500

Skogestad, J., Aronsen, J. M., Tovsrud, N., Wanichawan, P., Hougen, K., Stokke, M. K., et al. (2019). Coupling of the Na+/K+-ATPase to Ankyrin B Controls Na+/Ca2+ Exchanger Activity in Cardiomyocytes. *Cardiovasc Res.* 116 (1), 78–90. doi:10.1093/cvr/cvz087

Skogestad, J., Lines, G. T., Louch, W. E., Sejersted, O. M., Sjaastad, I., and Aronsen, J. M. (2019). Evidence for Heterogeneous Subsarcolemmal Na+ Levels in Rat Ventricular Myocytes. *Am. J. Physiology-Heart Circulatory Physiology* 316, H941–H957. doi:10.1152/ajpheart.00637.2018

Song, H., Lee, M. Y., Kinsey, S. P., Weber, D. J., and Blaustein, M. P. (2006). An N-Terminal Sequence Targets and Tethers Na+ Pump α2 Subunits to Specialized Plasma Membrane Microdomains. *J. Biol. Chem.* 281 (18), 12929–12940. doi:10.1074/jbc.m507450200

Song, J., Zhang, X.-Q., Ahlers, B. A., Carl, L. L., Wang, J., Rothblum, L. I., et al. (2005). Serine 68 of Phospholemman Is Critical in Modulation of Contractility, [Ca2+]itransients, and Na+/Ca2+exchange in Adult Rat Cardiac Myocytes. *Am. J. Physiology-Heart Circulatory Physiology* 288 (5), H2342–H2354. doi:10.1152/ajpheart.01133.2004

Stanley, C. M., Gagnon, D. G., Bernal, A., Meyer, D. J., Rosenthal, J. J., and Artigas, P. (2015). Importance of the Voltage Dependence of Cardiac Na/K ATPase Isozymes. *Biophysical J.* 109 (9), 1852–1862. doi:10.1016/j.bpj.2015.09.015

Su, Z., Zou, A., Nonaka, A., Zubair, I., Sanguinetti, M. C., and Barry, W. H. (1998). Influence of Prior Na+ Pump Activity on Pump and Na+/Ca2+ Exchange Currents in Mouse Ventricular Myocytes. *Am. J. Physiol.* 275 (5 Pt 2), H1808–H1817. doi:10.1152/ajpheart.1998.275.5.H1808

Sweadner, K. J., Herrera, V. L., Amato, S., Moellmann, A., Gibbons, D. K., and Repke, K. R. (1994). Immunologic Identification of Na+,K(+)-ATPase Isoforms in Myocardium. Isoform Change in Deoxycorticosterone Acetate-Salt Hypertension. *Circ. Res.* 74 (4), 669–678. doi:10.1161/01.res.74.4.669

Swift, F., Strømme, T. A., Amundsen, B., Sejersted, O. M., and Sjaastad, I. (2006). Slow Diffusion of K+ in the T Tubules of Rat Cardiomyocytes. *J. Appl. Physiology* 101 (4), 1170–1176. doi:10.1152/japplphysiol.00297.2006

Swift, F., Tovsrud, N., Enger, U., Sjaastad, I., and Sejersted, O. (2007). The Na+/K+-ATPase α2-isoform Regulates Cardiac Contractility in Rat Cardiomyocytes. *Cardiovasc. Res.* 75 (1), 109–117. doi:10.1016/j.cardiores.2007.03.017

Swift, F., Tovsrud, N., Sjaastad, I., Sejersted, O. M., Niggli, E., and Egger, M. (2010). Functional Coupling of α2-isoform Na+/K+-ATPase and Ca2+ Extrusion through the Na+/Ca2+-Exchanger in Cardiomyocytes. *Cell Calcium* 48 (1), 54–60. doi:10.1016/j.ceca.2010.06.006

Walaas, S. I., Czernik, A. J., Olstad, O. K., Sletten, K., and Walaas, O. (1994). Protein Kinase C and Cyclic AMP-dependent Protein Kinase Phosphorylate

Phospholemman, an Insulin and Adrenaline-Regulated Membrane Phosphoprotein, at Specific Sites in the Carboxy Terminal Domain. *Biochem. J.* 304 (Pt 2), 635–640. doi:10.1042/bj3040635

Wansapura, A. N., Lasko, V. M., Lingrel, J. B., and Lorenz, J. N. (2011). Mice Expressing Ouabain-Sensitive α1-Na,K-ATPase Have Increased Susceptibility to Pressure Overload-Induced Cardiac Hypertrophy. *Am. J. Physiology-Heart Circulatory Physiology* 300 (1), H347–H355. doi:10.1152/ajpheart.00625.2010

Weber, C. R., Ginsburg, K. S., and Bers, D. M. (2003). Cardiac Submembrane [Na+] Transients Sensed by Na+-Ca2+ Exchange Current. *Circ. Res.* 92 (9), 950–952. doi:10.1161/01.RES.0000071747.61468.7F

Wehrens, X. H. T., Lehnart, S. E., and Marks, A. R. (2005). Intracellular Calcium Release and Cardiac Disease. *Annu. Rev. Physiol.* 67, 69–98. doi:10.1146/annurev.physiol.67.040403.114521

Weiss, J. N., Qu, Z., and Shivkumar, K. (2017). Electrophysiology of Hypokalemia and Hyperkalemia. *Circ. Arrhythm. Electrophysiol.* 10 (3). doi:10.1161/CIRCEP.116.004667

Wendt-Gallitelli, M. F., Voigt, T., and Isenberg, G. (1993). Microheterogeneity of Subsarcolemmal Sodium Gradients. Electron Probe Microanalysis in guinea-pig Ventricular Myocytes. *J. Physiol.* 472, 33–44. doi:10.1113/jphysiol.1993.sp019934

Yamamoto, T., Su, Z., Moseley, A., Kadono, T., Zhang, J., Cougnon, M., et al. (2005). Relative Abundance of α2 Na Pump Isoform Influences Na-Ca Exchanger Currents and Ca Transients in Mouse Ventricular Myocytes. *J. Mol. Cell. Cardiol.* 39 (1), 113–120. doi:10.1016/j.yjmcc.2005.03.023

Yuen, G. K., Galice, S., and Bers, D. M. (2017). Subcellular Localization of Na/K-ATPase Isoforms in Ventricular Myocytes. *J. Mol. Cell. Cardiol.* 108, 158–169. doi:10.1016/j.yjmcc.2017.05.013

Zhang, J., Lee, M. Y., Cavalli, M., Chen, L., Berra-Romani, R., Balke, C. W., et al. (2005). Sodium Pump Alpha2 Subunits Control Myogenic Tone and Blood Pressure in Mice. *J. Physiol.* 569 (Pt 1), 243–256. doi:10.1113/jphysiol.2005.091801

Conflict of Interest: The authors declare that the research was conducted in the absence of any commercial or financial relationships that could be construed as a potential conflict of interest.

Frontiers in Physiology

Understanding how an organism's components work together to maintain a healthy state

The second most-cited physiology journal, promoting a multidisciplinary approach to the physiology of living systems - from the subcellular and molecular domains to the intact organism and its interaction with the environment.

Discover the latest Research Topics

See more →

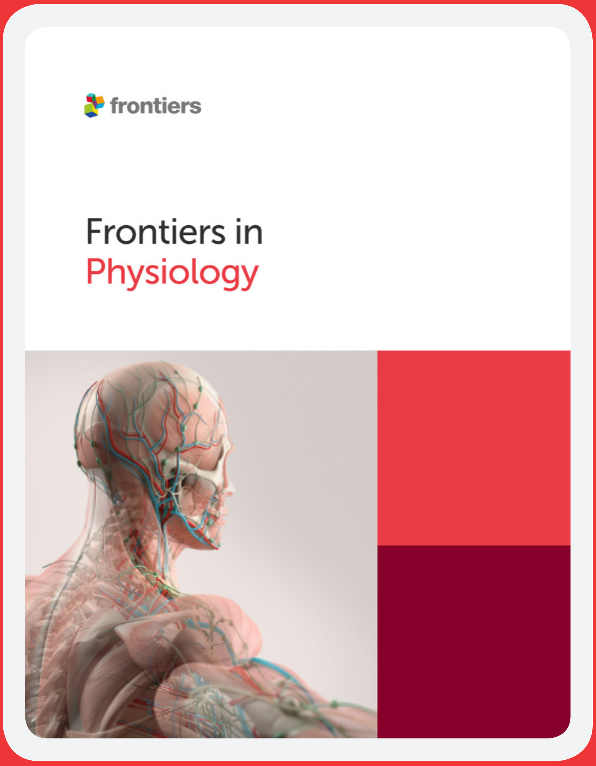
frontiers

Frontiers in
Physiology

Frontiers

Avenue du Tribunal-Fédéral 34
1005 Lausanne, Switzerland
frontiersin.org

Contact us

+41 (0)21 510 17 00
frontiersin.org/about/contact